SKYLAB

EREP
Investigations Summary

National Aeronautics
and Space Administration

Skylab EREP Investigations Summary

Skylab EREP Investigations Summary

Prepared by
NASA Lyndon B. Johnson Space Center

Many individuals of the scientific community and the NASA Lyndon B. Johnson Space Center (JSC) provided immeasurable assistance in preparation of this report, and their support is gratefully acknowledged. Special recognition is given to Willard J. Pierson, City University of New York, who served as senior editor, and to Victor L. Ettredge and Verl R. Wilmarth of JSC for their dedication and many contributions in completing this summary volume.

Foreword

ON FEBRUARY 8, 1974, the final Skylab mission ended with the splashdown of the Skylab 4 astronauts in the Pacific Ocean. The scientific and technological achievements from the Skylab manned space program are numerous and include new knowledge of solar phenomena, of man's capability for long-duration space flight, and of the Earth through the sophisticated sensors that comprise the Earth Resources Experiment Package (EREP).

The EREP acquired thousands of photographs and several miles of magnetic tape in which Earth surface features and phenomena of selected regions on five continents and two major oceans were recorded. Some data showed plumes of erupting volcanoes, circular patterns of a major hurricane, contrasting colors of ocean eddies and upwellings, and growth patterns of metropolitan complexes, whereas other data contained information on vegetation patterns, geological terrain, landforms, snowfields, and icefields. Investigators in the United States and 28 other countries have analyzed these data, and the results of their investigations are summarized in the discipline sections herein.

The success of EREP was due to the dedication and talents of many people in NASA, industry, and the scientific community. It remains, however, for the Earth scientists, design engineers, resource managers, and data analysts to capitalize on the EREP results to improve our future capability to monitor the Earth's dynamic systems from space and to effectively use and conserve our natural resources.

CHRISTOPHER C. KRAFT, JR.
Director, Lyndon B. Johnson Space Center

Page intentionally left blank

Preface

THE OVERALL PURPOSE OF THE Earth Resources Experiment Package (EREP) was to test the use of sensors that operated in the visible, infrared, and microwave portions of the electromagnetic spectrum to monitor and study Earth resources. During the three Skylab manned missions, the astronauts operated the EREP sensors according to instructions from the EREP planning team in the Mission Control Center at the NASA Lyndon B. Johnson Space Center. In this role, the crewmen were members of the scientific teams that performed Earth resources experiments. As a member of the Skylab 3 crew, I know that the part we played in the collection of these data for scientific study of the Earth was both fascinating and rewarding.

When the Earth is viewed from an altitude of 435 km (235 n. mi.), the multitude of features represented in many colors and tones are indicative of the complexity of processes and systems that are manifested on the Earth's surface. To understand these phenomena requires a synoptic view from space and sensors capable of obtaining high-resolution data in the appropriate parts of the electromagnetic spectrum. In reviewing the results of the EREP investigations summarized in this report, it is evident that major steps have been taken in developing a capability to conduct Earth science from space.

This document summarizes the analytical results of 139 investigators who used EREP data in their investigation of problems in the areas of agriculture, range, and forestry; land use and cartography; geology and hydrology; and oceans and atmosphere, and in their development of data analysis techniques. In future space exploration, the results of EREP will serve as a milestone for the development of an applications research technology for the study of Earth resources.

OWEN K. GARRIOTT
Science Pilot, Skylab 3

Page intentionally left blank

Contents

1

Introduction

REMOTE SENSING of the Earth from orbital altitudes was recognized in the mid-1960's as a potential technique for obtaining information important for the effective use and conservation of natural resources. These studies began when the Tiros satellites (1960) provided man's first synoptic view of the Earth's weather systems. The manned Gemini and Apollo Programs (1965-72) led to further consideration of space-age remote sensing for study of the Earth. The Earth Resources Technology Satellite, now designated Landsat, provided repetitive multispectral scanner data in the visible and infrared regions of the electromagnetic spectrum for large areas of the Earth. The Landsat series consisted of Landsat-1 launched in 1972 and Landsat-2 in 1975. Skylab, the largest manned space station ever placed in low Earth orbit, was launched in 1973 and carried into space the Earth Resources Experiment Package (EREP), which was designed to view the Earth with sensors that recorded data in the visible, infrared, and microwave spectral regions. Thus, EREP became another step in space exploration by testing the use of high-resolution camera systems with film return capability, narrow frequency bandwidth scanner systems in the visible through thermal-infrared spectral regions, and the initial use of active and passive microwave systems in Earth resource surveys. A significant feature of EREP was the use of man to operate the sensors in a laboratory fashion. Skylab objectives also included scientific observations of the Sun, the stars, and near-Earth space; materials research and manufacturing in a weightless environment; observation of living-organism functions in a near-zero-g environment; and development of techniques for long-duration manned-space-flight operations.

The Skylab spacecraft was launched eastwardly on a 50° azimuth from the NASA John F. Kennedy Space Center, Florida, on May 14, 1973, into a near-circular orbit at an altitude of 435 km above the Earth. It orbited the Earth every 93 minutes and repeated the groundtrack every 5 days. The launch azimuth inclined the orbital plane 50° with respect to the Equator and limited observations of the Earth to latitudes between 50° N and 50° S (fig. 1-1).

Skylab was occupied by three three-man crews during the period May 25, 1973, to February 8, 1974, for a total of 171 days in space (table 1-I). At the end of the Skylab 4 mission, the vehicle was deactivated and remains today in a near-circular orbit about the Earth.

The EREP was designed to explore the use of the widest possible portion of the electromagnetic spectrum for Earth resource investigations. It consisted of two photographic and four electronic sensor systems (table 1-II) that simultaneously permitted remote sensing of the Earth's surface in the visible, infrared, and microwave regions of the spectrum (fig. 1-2). The ground coverage for each sensor is shown in figure 1-3. The EREP sensor systems and their data products are described in appendix A.

The EREP Program began in December 1970 with the announcement by NASA that data collected by the EREP would be made available to qualified investigators for Earth resource investigations. From the response to this announcement, NASA selected 164 tasks to be performed by 148 Principal Investigators representing academic, governmental, and industrial firms in the United States and 19 other countries. (A list of the Principal Investigators is contained in appendix B.) These investigators analyzed EREP data and ap-
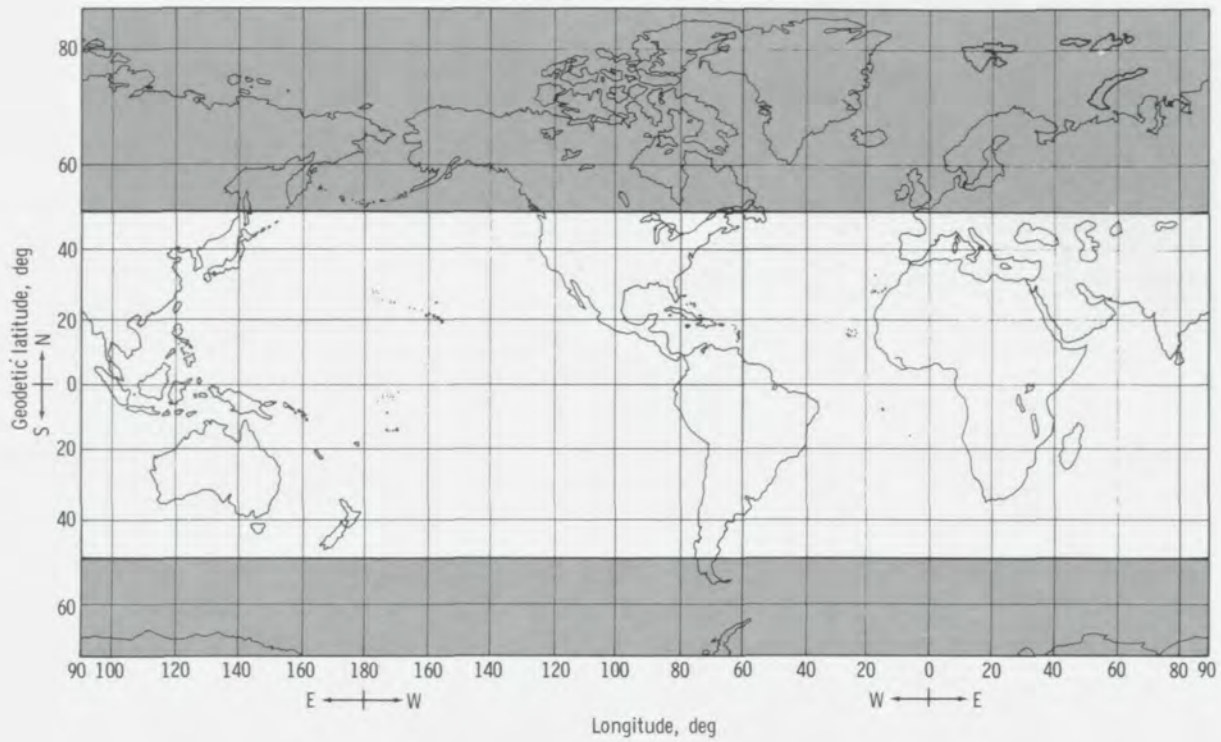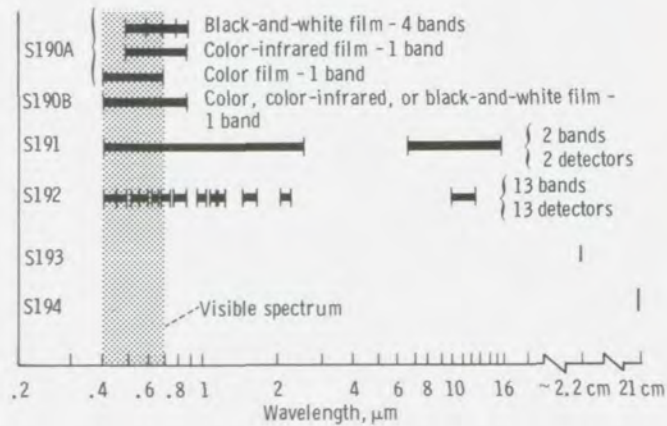
FIGURE 1-1.—Skylab ground coverage.

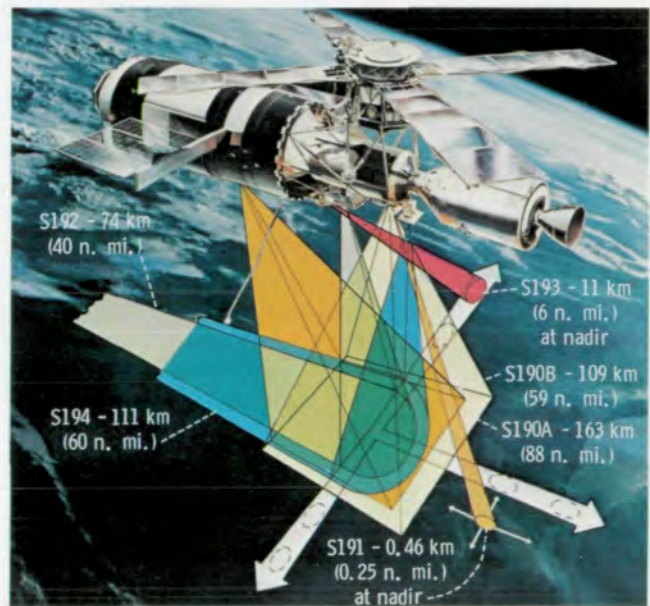FIGURE 1-2.—Wavelength sensitivity of Earth-viewing Skylab sensors.

FIGURE 1-3.—The ground area coverage provided by EREP sensors (S-73-005-S).

TABLE 1-I.— Skylab Mission Summary

Mission	Crewmembers	Launch date	Splashdown date	Duration, days
[a]Skylab 1	None	May 14, 1973	Not applicable (NA)	NA
Skylab 2	Charles Conrad, Jr., commander (CDR) Joseph P. Kerwin, science pilot (SPT) Paul J. Weitz, pilot (PLT)	May 25, 1973	June 22, 1973	28
Skylab 3	Alan L. Bean, CDR Owen K. Garriott, SPT Jack R. Lousma, PLT	July 28, 1973	Sept. 25, 1973	59
Skylab 4	Gerald P. Carr, CDR Edward G. Gibson, SPT William R. Pogue, PLT	Nov. 16, 1973	Feb. 8, 1974	84

[a]Launch of Skylab orbital workshop. The vehicle was operated unmanned between manned missions.

Integration of the data requirements for each investigative area resulted in a mission requirements document that was used by the EREP Team to plan, in the Mission Control Center at the NASA Lyndon B. Johnson Space Center (JSC), each EREP data pass on a daily basis during the three manned missions. Each EREP pass was planned within mission constraints to obtain the specific data needs of as many investigators as possible. Because most investigations required data obtained with minimum cloud cover, the Space Flight Meteorological Group of the National Weather Service at JSC was an essential part of the operation planning team. Before each EREP pass, a detailed time schedule for operation of each sensor was uplinked to the crew.

TABLE 1-II.— EREP Sensors

Sensor	Description	Wavelength range, μm	Frequency range, GHz
Multispectral Photographic Camera system (S190A)	Six 70-mm boresighted cameras; color, black-and-white, color-infrared, and black-and-white infrared films	0.4 to 0.9	—
Earth Terrain Camera (S190B)	Single 127-mm camera; color, black-and-white, and color-infrared films	0.4 to 0.88	—
Infrared Spectrometer (S191)[a]	Filter-wheel spectrometer; 1-sec scan rate; 16-mm camera that records Earth scenes; crew pointed	0.4 to 2.5; 6.6 to 16.0	—
Multispectral Scanner (S192)[a]	13-channel optical-mechanical scanner	0.4 to 2.35; 10.2 to 12.5	—
Microwave systems[a] K-band: Microwave Radiometer[b]/ Scatterometer[c] and Altimeter[c] (S193)	3-sensor facility; uses single 1.1-m, pointable, parabolic antenna	—	13.8 to 14.0
L-band: L-Band Radiometer[b] (S194)	Single sensor; fixed antenna	—	1.4 to 1.427

[a]Data recorded on magnetic tape.

[b]Passive sensors.

[c]Active sensors.

plied their results to nine major investigative areas that included agriculture, range, and forestry; geologic applications; continental water resources; oceanographic and atmospheric investigations; coastal zones, shoals, and bays; remote-sensing technique development; regional planning and development; and cartography. Within each of these areas, studies of specific features and phenomena were conducted using EREP, Landsat, aircraft, and ground measurement data.

Each investigation required specific EREP data, which were defined by the Principal Investigators and used to preplan the operation of the EREP during the mission. Depending on the scope of the investigations, the data requirements ranged from a series of photographs obtained by the S190A and S190B camera systems to computer-compatible tapes and color-composite images derived from the S192 multispectral scanner. The microwave sensors (S193 and S194) recorded data on magnetic tape for processing and analyzing with computers.

To conduct a conventional EREP pass, the crew oriented Skylab to point the EREP sensors normal (perpendicular) to the Earth's surface. In this position, the Z-axis of the spacecraft was alined with local vertical (Z-LV). With the exception of a few passes, all EREP data passes were accomplished in a Z-LV position.

During the 171 days of manned Skylab operation, 110 EREP passes were completed (table 1-III). These passes resulted in more than 35 000 frames of photography and 72 725 m (238 600 ft) of magnetic tape.

Skylab orbital groundtracks permitted the EREP sensors to view the United States; the continents of South America, Africa, and Australia; the southern part of Europe and Asia; and large areas of the Atlantic and Pacific Oceans (fig. 1-1). Each manned mission resulted in an abundance of Earth resource data, some of which is unique. Skylab missions were flown during the summer, fall, and winter months in the Northern Hemisphere, and some repetitive data were collected during each season for selected test sites. Mission constraints required that during the Skylab 2 mission, only descending (north to south) passes could be performed; during the Skylab 3 and 4 missions, both descending and ascending (south to north) passes were conducted. In general, the data collection period for each pass ranged from 15 to 25 minutes and covered a groundtrack distance of 6482 to 11 112 km (3500 to 6000 n. mi.).

During Skylab 2, EREP data were collected on descending groundtracks over the United States, the Gulf of Mexico, the Caribbean Sea, and northern regions of South America. About midway of this mission, an intense hurricane (Hurricane Ava), located approximately 1000 km (550 n. mi.) southwest of Acapulco, Mexico, was visible to the EREP sensors, and unique

TABLE 1-III.— EREP Data Summary

Mission	EREP passes	Photographs (frames)	Magnetic tape, m (ft)	
Skylab 2	13	5 275	13 716	(45 000)
Skylab 3	48	13 429	28 529	(93 600)
Skylab 4	49	17 000	30 480	(100 000)

photographs and microwave data were obtained concurrently with U.S. Air Force reconnaissance aircraft flights. The Skylab 3 crewmen returned large quantities of photographic and magnetic tape data obtained on ascending and descending groundtracks over the United States and 28 countries in Central and South America, Europe, western Africa, Asia, and Australia. Single data passes were accomplished over Japan and adjacent ocean, Israel, Ethiopia, Malaysia, Australia, and New Zealand. During the Skylab 3 mission, specific features sensed by the EREP included the active volcano Mount Etna, Sicily; the drought regions of Mali and adjacent countries; and tropical storm Christine in the Atlantic Ocean northeast of the coast of Venezuela.

Skylab 4 was flown during the winter months in the Northern Hemisphere; therefore, lighting conditions were not favorable for EREP data collection in December 1973. Nevertheless, the 84-day mission resulted in successful EREP passes over portions of the world generally covered during the Skylab 3 mission. In addition, some unique data collection passes were completed including predawn and near-local-noon sensing

of selected areas in California for testing the thermal-mapping capability of the S192, overflight of the largest extratropical cyclone in the North Atlantic in a decade, and a 360° S192 altimeter data pass that began at longitude 39° W and ended at longitude 61° W to measure the configuration of the Earth. Photographic data in both oblique (solar inertial) and Z-LV modes were obtained by the Skylab 3 and 4 crewmen over Paraguay to test the utility of space photography in topographic mapping of remote regions.

The vast quantity of EREP photographic, scanner, spectrometric, and microwave data returned from the 171 days of manned Skylab operations attest to the operational success of the sensor systems. To operate the sensor systems, the astronauts had to perform a series of tasks that included replacing film cassettes for the S190A and S190B cameras, manually pointing the telescope and operating the S191 spectrometer, and alining the S192 scanner detector system to optimize the signal received during data collection. Late in the Skylab 4 mission, the astronauts replaced the S192 channel 13 thermal detector with a more sensitive detector and thermal data were collected over sites in southern California. The complex S193 microwave system operated satisfactorily during the Skylab 2 mission; however, the scan motion compensator malfunctioned during the Skylab 3 mission. The Skylab 4 crew reestablished the antenna capability in the roll direction (normal to the groundtrack), but the pitch motion was not repaired. The loss of the S193 antenna came in the latter part of the Skylab 4 mission and resulted in degradation of the data. The S194 microwave radiometer operated without malfunctions for the three manned missions. In summary, EREP data collection provided, for each Principal Investigator (PI), a com-prehensive set of photographs and magnetic tapes containing data in the visible through microwave spectral regions over a wide variety of scenes, features, and phenomena of the Earth's surface.

Upon completion of each manned mission, the EREP data were returned for processing at JSC according to the requirements of individual investigators. The photographs were distributed soon after completion of each mission, but the complexity of the electronic data resulted in delays in the distribution of such data to the PI's. Information on geographic areas for which data were obtained by the EREP sensors is contained in the Skylab Earth Resources Data Catalog (ref. 1-1). The PI reports on analysis of the EREP data can be obtained from the National Space Science Data Center, NASA Goddard Space Flight Center, Greenbelt, Maryland 20771.

The purpose of this summary volume is to describe the significant accomplishments of the EREP data analysis program in the areas of agriculture, range, and forestry; geology and hydrology; oceans and atmosphere; land use and cartography; and data analysis techniques. The results presented in this report indicate the manner in which space remote sensing is applied in Earth resource surveys today, the needs of future space remote-sensing systems, and some potential applications of space data in conservation and utilization of natural resources.

REFERENCE

1-1. Skylab Earth Resources Data Catalog. NASA Rep. JSC 09016, U.S. Government Printing Office (stock no. 3300-00586) (Washington, D.C.), 1974.

Page intentionally left blank

2

Land Use and Cartography

ROGER M. HOFFER,[a][†] R. E. JOOSTEN,[b] R. G. DAVIS,[c]
AND F. R. BRUMBAUGH[c]

AN INCREASING POPULATION and a growing awareness of the finite nature of U.S. natural resources have created a demand for more effective land use planning and mapping programs. In the past decade, National, State, and local legislation has been enacted for better management of land and resources. Conflicts for alternate uses of the land are evident everywhere: urban expansion decreases land available for agriculture; increase in strip mining raises environmental concerns; forest timber production competes with recreational needs; and commercial developments can adversely affect residential communities. In examining these situations, effective land use planning requires accurate up-to-date information concerning the current use of the land and the potential capabilities of the land. Such information is often very difficult to obtain, particularly if large geographic regions are involved.

In discussing the application of the Earth Resources Experiment Package (EREP) data to land use and cartography, it is important to distinguish between these two discipline activities. The land use application includes natural resource inventories and planning relationships; the cartographic application is concerned with mapping activities. Therefore, this section has two major divisions, one devoted to land inventories, land use products, and related activities, and the other to the mapping potential of Skylab-acquired data.

---

[a]Purdue University.

[b]NASA Lyndon B. Johnson Space Center.

[c]Lockheed Electronics Company, Inc.

[†]Principal Investigator.

LAND USE

The term "land use" is normally considered to include both the type of land cover and the actual use of the land as opposed to the potential use of the land or land suitability. The actual use of the land can only be inferred from remotely sensed data collected at any altitude; direct interpretation is not possible.

Most of the investigators who analyzed the Skylab EREP data for land use determination adopted a hierarchical classification scheme based on that proposed in the U.S. Geological Survey (USGS) Circular 671 (ref. 2-1). This scheme defined two major levels of land use classification (table 2-I). Level I contains nine categories that are closely related to different Earth surface features (e.g., water, urban buildup, etc.) or vegetative cover types (e.g., tundra, rangeland, forest land, etc.). In Level II, these nine categories are further subdivided, but these categories generally do not indicate the specific use of the land (e.g., deciduous forest does not indicate whether the land is being used for timber production, for recreation, or for some other purpose). Such specificity is introduced at Level III (e.g., recreational facilities) and Level IV (e.g., golf courses). To fit the varied conditions and the specific requirements involved in different geographical locations, most of the investigators modified the USGS system to meet their own particular situations and needs. Many factors were considered by the investigators in their analysis and interpretation of the EREP data for land use purposes. These factors are grouped into three major categories: the characteristics of the test site, the types of data, and

the interpretative and analytic techniques used. Some of these factors are discussed in the following paragraphs.

The spectral contrast and geometry of surface features within a given scene are extremely significant to the overall interpretability of a particular scene. Hannah et al. (ref. 2-2) and Stoeckeler et al. (ref. 2-3) pointed out that roads contrasted with the surrounding green vegetation distinctly and could be easily defined on the Earth Terrain Camera (S190B) color photographs. Colwell et al. (ref. 2-4) found that, in one type of desert scene, tentative road locations that had been excavated by using a bulldozer had very high reflectance and, because of the lack of contrast of the roads in relation to the naturally occurring, highly reflective surrounding soils, were not easily detected. Thus, the ability to detect and identify roads or other features is often a function of the reflectance of the feature of interest in relation to the surrounding cover types. Spatial considerations also are important. Long linear features such as roads or powerline rights-of-way are more easily discerned than a small pinpoint feature such as an oil well, a small surface mine, or even a small water body. The contrast between the particular feature of interest and the surrounding cover types is of extreme importance in locating, identifying, and mapping such features.

Another site characteristic that must be considered involves temporal variation of data acquired in different seasons. For much of the United States, the Skylab 2 data were obtained during late spring, the Skylab 3 data during late summer and early fall, and the Skylab 4 data during winter. In many instances, the time of year at which the EREP data were collected became a critical factor in determining the effective use of such data. Two different investigations, Hoffer (ref. 2-5) and Poulton and Welch (ref. 2-6), found that the Skylab 2 data were less effective than the Skylab 3 photographic data for vegetative mapping because of the differences in the condition of the vegetation during the spring and the summer. Figure 2-1 illustrates, by color-infrared photographs, temporal variations in the San Juan Mountains, Colorado.

The level of detail in the mapping scheme to be used is a primary factor in land use classification. Many investigators found that the Level I land use categories could be mapped with a high degree of reliability. Some of the categories of Level II could be identified and mapped reasonably well; others could be mapped with

TABLE 2-I.—A Land Use Classification System for Use With Remote-Sensor Data

[From ref. 2-1]

| Level I		Level II	
Category	*Description*	*Category*	*Description*
1.0	Urban and built-up land	1.1	Residential
		1.2	Commercial and services
		1.3	Industrial
		1.4	Extractive
		1.5	Transportation, communications, and utilities
		1.6	Institutional
		1.7	Strip and clustered settlement
		1.8	Mixed
		1.9	Open and other
2.0	Agricultural land	2.1	Cropland and pasture
		2.2	Orchards, groves, bush fruits, vineyards, and horticultural areas
		2.3	Feeding operations
		2.4	Other
3.0	Rangeland	3.1	Grass
		3.2	Savannas (palmetto prairies)
		3.3	Chaparral
		3.4	Desert shrub
4.0	Forest land	4.1	Deciduous
		4.2	Evergreen (coniferous and other)
		4.3	Mixed
5.0	Water	5.1	Streams and waterways
		5.2	Lakes
		5.3	Reservoirs
		5.4	Bays and estuaries
		5.5	Other
6.0	Nonforested wetland	6.1	Vegetated
		6.2	Bare
7.0	Barren land	7.1	Salt flats
		7.2	Beaches
		7.3	Sand other than beaches
		7.4	Bare exposed rock
		7.5	Other
8.0	Tundra	8.1	Tundra
9.0	Permanent snow and icefields	9.1	Permanent snow and icefields
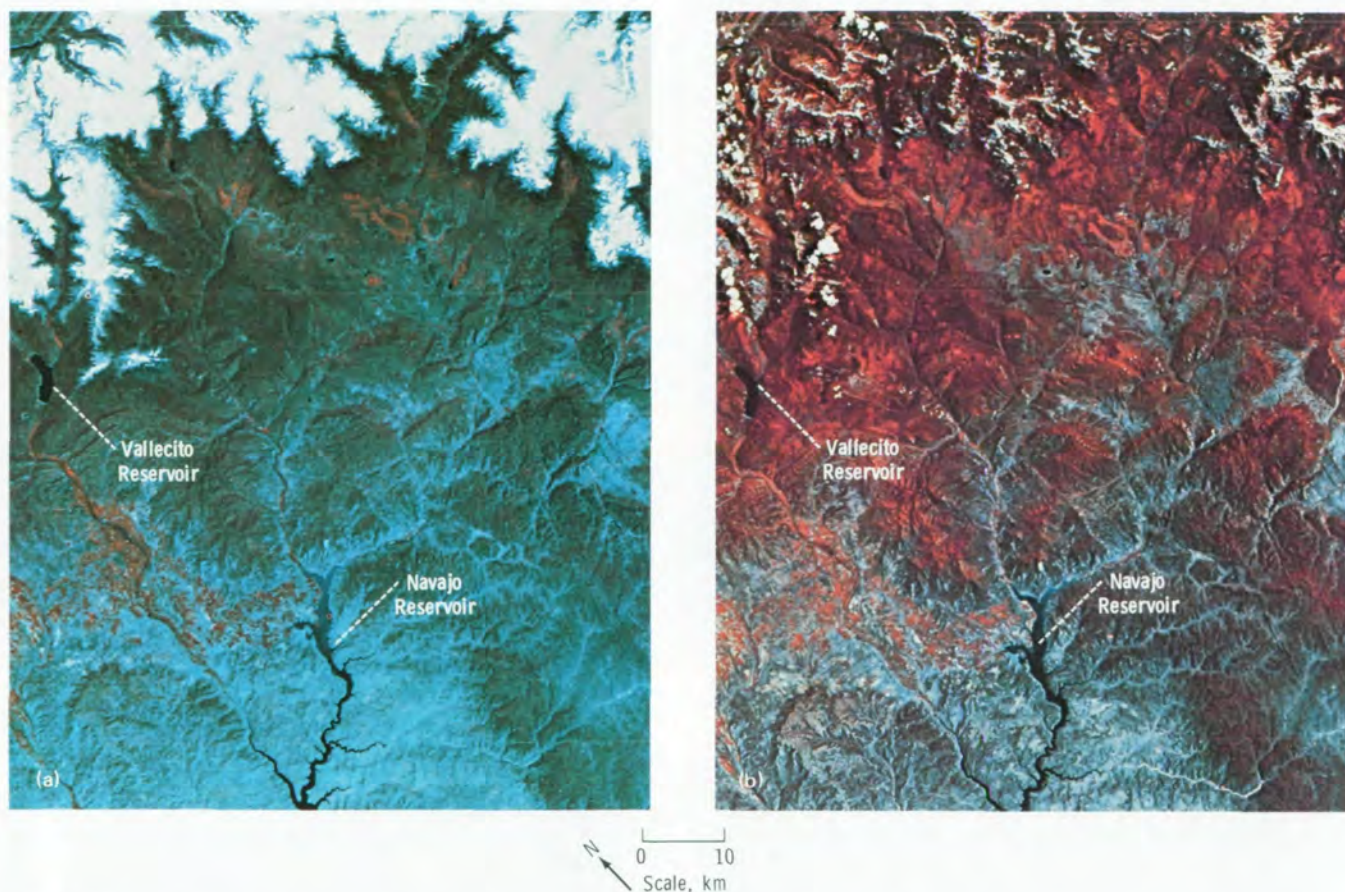
FIGURE 2-1.—S190A color-infrared photographs showing seasonal differences in vegetation for the San Juan Mountains of southwestern Colorado. This type of seasonal scene variation in vegetative condition was significant in data interpretation for many Skylab investigations. (a) Photograph taken in June 1973 (SL2-09-017). The area shown in blue tones indicates the general absence of green vegetation. (b) Photograph taken in August 1973 (SL3-21-331). The areas shown in several different red hues indicate healthy vegetation.

only moderate success. It was also found that different definitions influenced the apparent results. In a few cases, similar or even identical terminology was being used by different investigators to indicate different levels of difficulty in the mapping process.

The data used in land use mapping were of prime importance, in terms of both the analytic techniques used and the types of results that could be achieved. For land use mapping, the primary data were collected by the Multispectral Photographic System (S190A), the Earth Terrain Camera (S190B), and the Multispectral Scanner System (S192). The inherently better spatial resolution of the S190A and S190B photographs as compared to the S192 imagery permitted flexibility for the enlarge-

ment of the Skylab photographs. Despite the relatively small scales of the original photographs (approximately 1:2 900 000 for the S190A and 1:950 000 for the S190B), more usable scales were readily obtained by enlarging the original photographs by using photographic processes or viewing devices. It was demonstrated that enlarged scales ranging from 1:250 000 to 1:50 000 were feasible and practical for most applications. Fidelity of interpretative detail was excellent for this scale range. For the higher resolution films of the S190B camera, a scale of 1:50 000 is probably the largest for maximum usefulness; however, projections of S190B transparencies to scales of 1:24 000 and larger were used in detailed land use analysis.

General Land Use Results Obtained by Using S190/S192 Photographic Data

The types of EREP land use investigations ranged from academic research and theoretical examination of specific photographic products and analytic techniques to direct involvement with county planning agencies. The research-oriented investigators sought to determine why certain features on the Earth's surface appear as they do on certain types of film and how additional information can be derived through innovative interpretative methods. The direct-application investigations used the photographs to extract information that could be applied in the solution of specific problems.

In the evaluation of S190A and S190B film types for land use analysis, most investigators preferred the S190B color photographs because of the greater spatial resolution, but other investigators indicated the need for the better spectral discrimination provided by the color-infrared film for most land use categories (mainly cover-type features). For discrimination of urban categories, color film was most useful; but, for nonurban categories, the color-infrared data were better (fig. 2-2). These conclusions were substantiated by investigators who used the S190B color films as the prime data source and the S190A color-infrared data as complementary sources of information to improve the classification of natural features such as forest land, agricultural crops, rivers and lakes, and wetlands. Figures 2-3(a) and 2-3(b) illustrate how these two film types were used in land use planning and resource inventories.

Only one investigation (Hardy et al., ref. 2-7) involved the analysis of S190B black-and-white photographs for land use activities. Although this type of photograph contains the best spatial information, effective separation of Level II land units was impossible because of a lack of tonal characteristics.

The two black-and-white film types (panchromatic and infrared) used in the S190A camera system showed less information spectrally than either of the color-film types. The advantage of black-and-white multispectral coverage in the green, red, and infrared wavelengths is that different spectral responses of some land use categories can enhance feature identification from a comparative signature analysis. Additionally, each of the black-and-white bands can be combined with appropriate filters in the photoprocessing laboratory to produce a color-composite scene or can be enhanced by

a variety of other additive-color techniques. Spatially, the red wavelength of the two black-and-white panchromatic films was judged best, but it lacked the tonal qualities required to separate some land units for identification.

General land use mapping with use of S190 data.— Most land use investigators produced some type of land use map as a final product by using a variety of photographic data and extraction techniques. Figure 2-4, derived by photointerpretation of imagery and photographs, illustrates the level of land use information that can be obtained from different types of platforms and sensors. Cooper et al. (ref. 2-8) compiled these land use maps at a common scale of 1:63 360, using Landsat, Skylab S190A and S190B color-infrared, and RB-57/RC-8 aircraft imagery as the data sources. The interpretations were accomplished primarily from an analysis of transparencies that verified the discrimination between tonal characteristics and mapping units. In terms of hours, the compilation of these land use maps for the same area coverage required 1.5 hours for Landsat, 4 hours for S190A, 8 hours for S190B, and 10 hours for aircraft data. When these compilation times are extrapolated to full-frame interpretation for each different format size, it is evident that satellite platforms offer a distinct advantage over aircraft coverage. It must be emphasized that, although the time required to compile land use maps from Landsat and S190A photographs is considerably less, the quantity and quality of information for the S190B- and aircraft-data-derived land use maps are markedly superior (fig. 2-4). The S190B photographs, in particular, were found to be almost ideal for detailed as well as regional land use maps.

A broad assortment of land use products that vary in scale, type of data used, and extent of area involved is found in the reports of the individual investigators. One of these products is the detailed map of Alachua County in north-central Florida (Hannah et al., ref. 2-2), compiled from S190B color-infrared photographs at a scale of 1:40 000. This map was reviewed for completeness and accuracy by staff members of the North

FIGURE 2-2.—Comparison of S190B color and color-infrared film enlargements acquired over the Newburgh, New York, area. The higher spatial resolution of the color film (fig. 2-2(a)) is readily apparent. The color-infrared film (fig. 2-2(b)) is useful in discriminating vegetation (red) and bodies of water (black). (a) Color film (SL3-88-274). (b) Color-infrared film (SL3-87-300). ➝
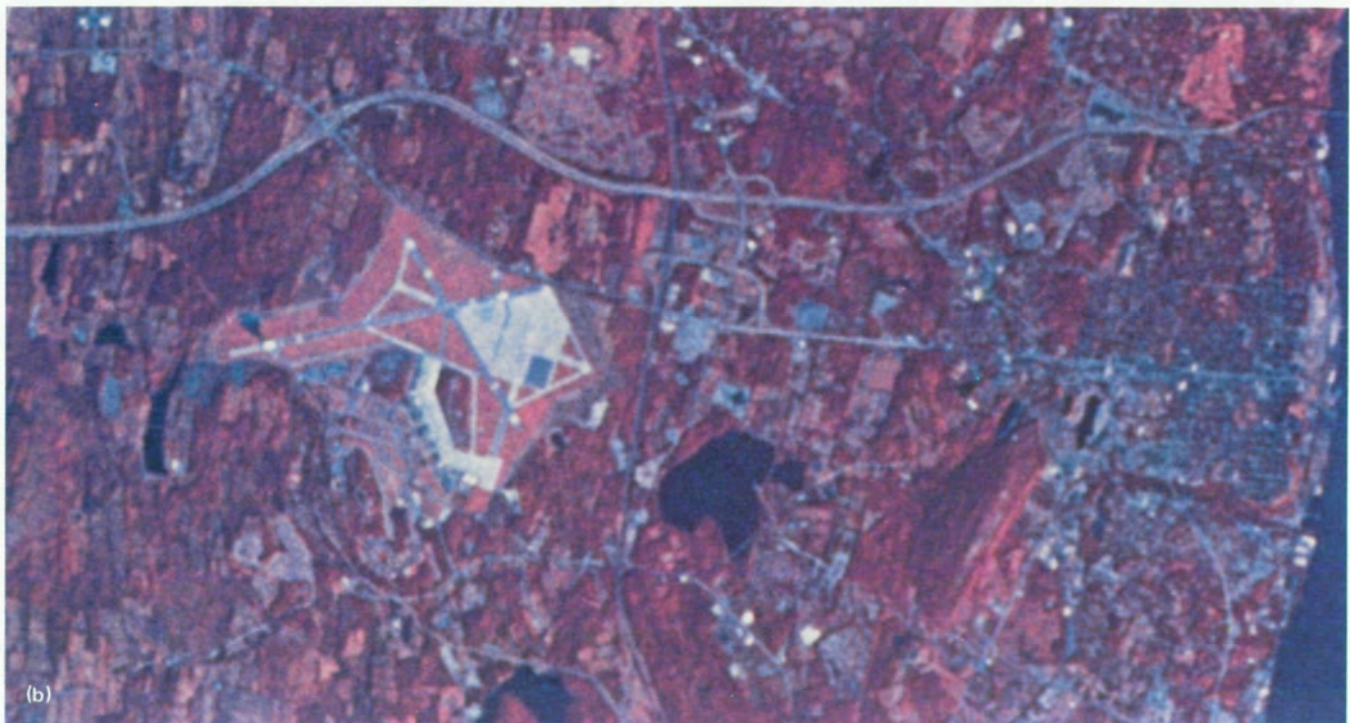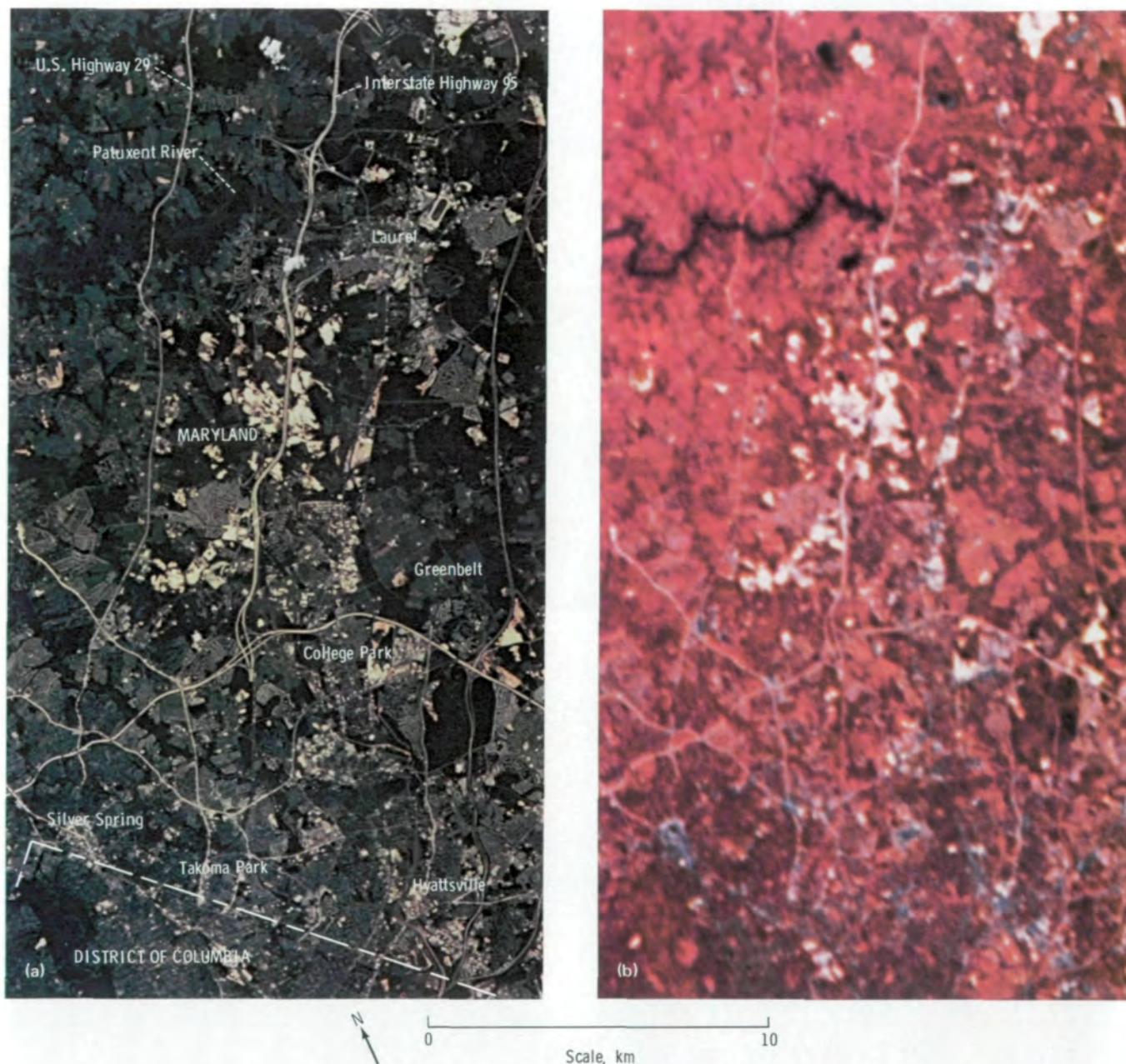
FIGURE 2-3.—A comparison of spatial and spectral characteristics of S190B color film and S190A color-infrared film. This scene, showing the rapidly developing urbanized corridor between Washington, D.C., and Baltimore, Maryland, is representative of the variation in spatial resolution and spectral sensitivities between Skylab photographic systems for enhancing particular land use features. For example, urban detail is visible on the S190B photograph (fig. 2-3(a)), whereas excellent enhancement of water features and improved discrimination within forested lands are provided by the S190A color-infrared photograph (fig. 2-3(b)). Photographs were taken in August 1973. (a) S190B color photograph (SL3-83-166). (b) S190A color-infrared photograph (SL3-15-172).

(a)

Merrimack River

Interstate Highway 95

Newburyport

Railroad

U.S. Highway 1

Salisbury

Salisbury Beach

Atlantic Ocean

Plum Island

N
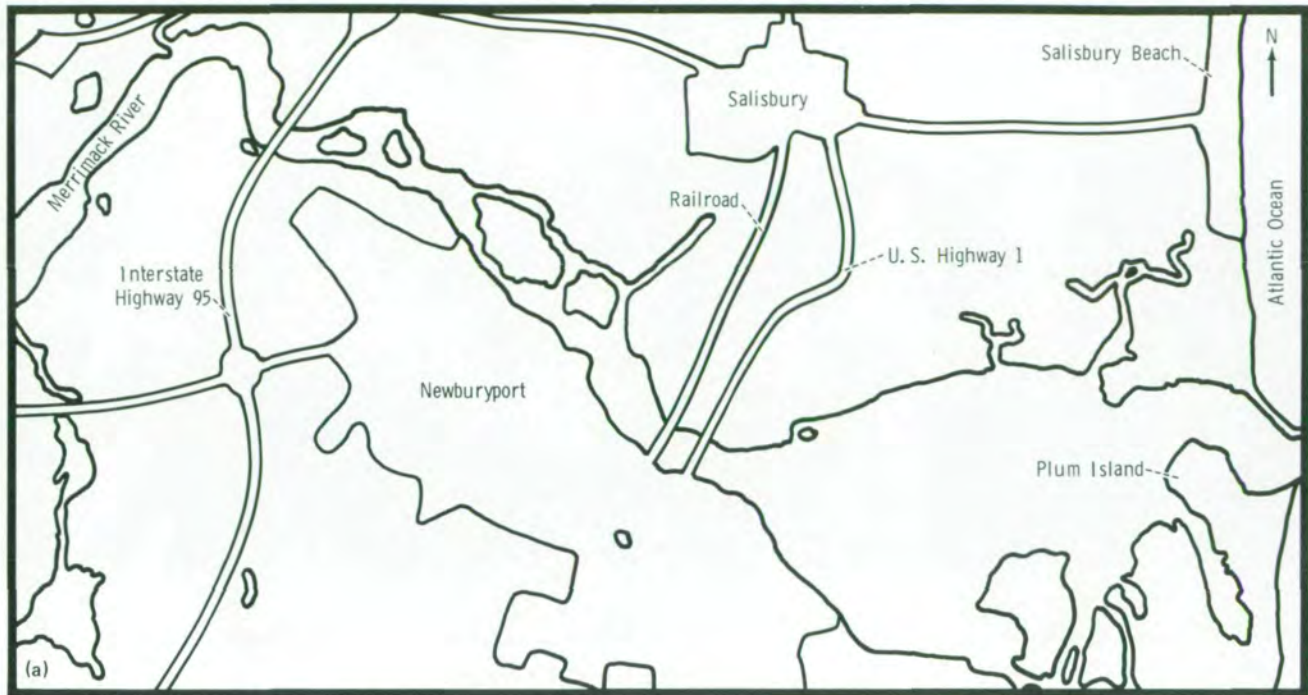
Explanation

| Color	Level I category	No.	Level II subcategory	Color	Level I category	No.	Level II subcategory
Red	Urban/built-up land	1	Residential, single family	Green	Forest land	3	Mixed
		2	Residential, multiple family	Blue	Water	1	Stream
		3	Commercial			2	Lake
		4	Industrial			3	Reservoir
		5	Extractive			4	Bay/estuary
		6	Mixed			5	Tidal channel
		7	Transportation, communi- cation, utilities			6	Ocean
		8	Institutional	Purple	Nonforested wetlands	1	Vegetated
		9	Open and other			10	Tidal marsh
Brown	Agricultural	1	Pasture	White	Barren land	1	Beach
		2	Row crop			3	Other
		3	Orchard				

0   1
Scale, km
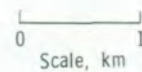
FIGURE 2-4.—A comparison of Landsat-, Skylab- (S190A and S190B), and aircraft-derived land use maps. This figure represents Level I and Level II categories mapped in the vicinity of Newburyport, Massachusetts. The land use maps illustrate the type of mappable units that can be derived from imagery obtained by using three different platforms and four different sensing systems. The land use classification system used was modified from reference 2-1. Specific colors represent Level I categories. Numbers represent subcategories, or Level II information, within the Level I categories. Hachuring is used in a few areas where positive identification could not be made for a single Level I category. The close correlation between specific-category patterns and areal extent on the Skylab S190B and aircraft maps should be noted. (a) Political map. (b) Landsat color-composite land use map. (c) Skylab S190A color-infrared land use map. (d) Skylab S190B color-infrared land use map. (e) Aircraft color-infrared land use map.
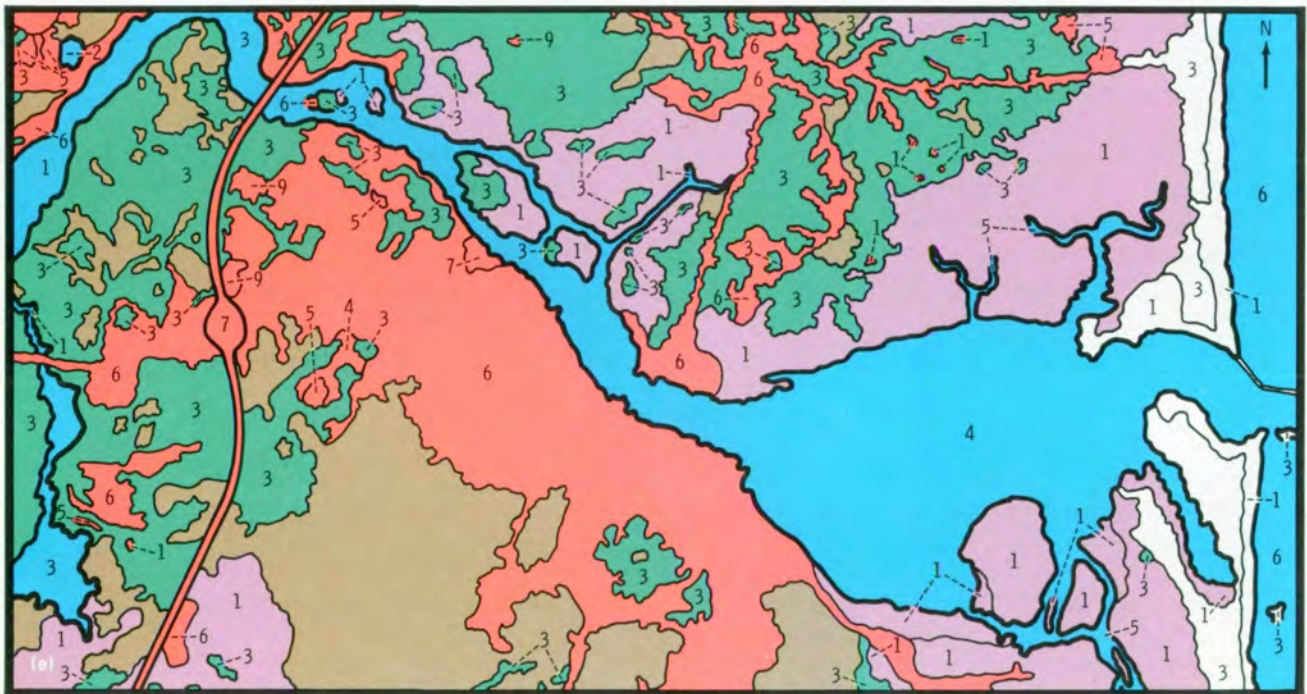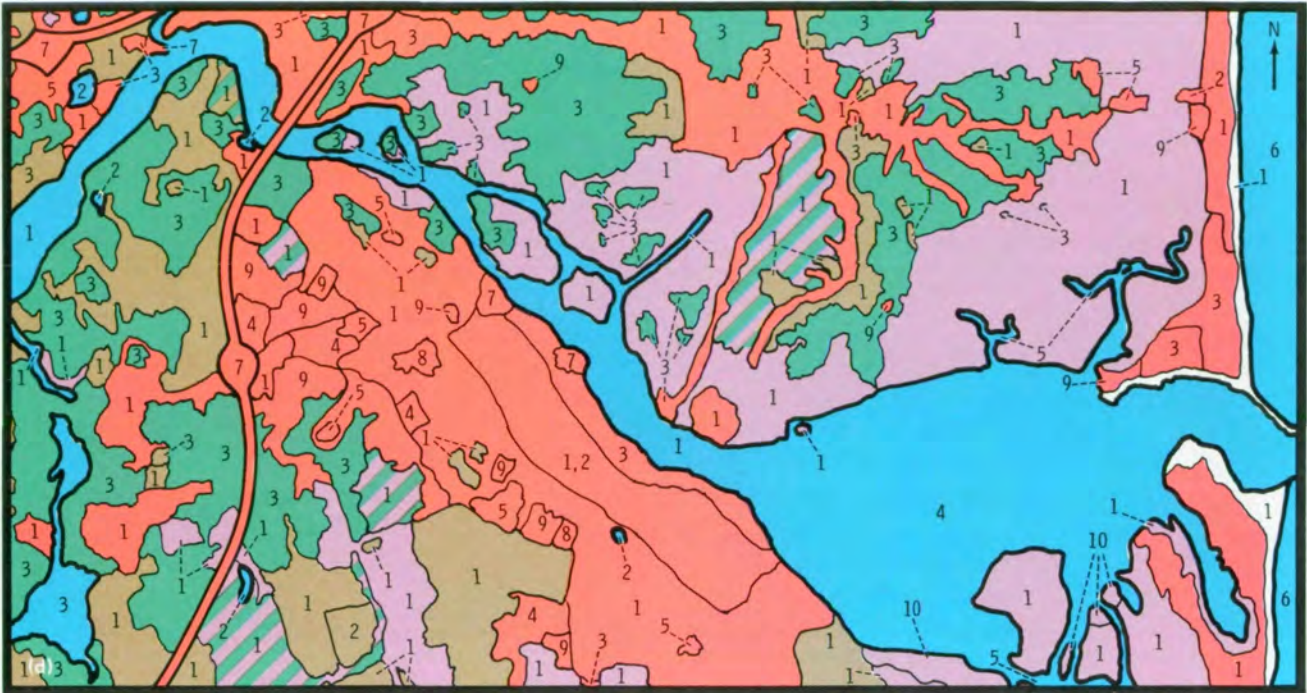
FIGURE 2-4.—Continued.

FIGURE 2-4.—Concluded.

Central Florida Regional Planning Council, who indicated that the mapping accuracy and the quality of detail were suitable for both regional and county planning endeavors. It was also compared with a recently released USGS land use map of the same area compiled from aircraft photographs, and only a few discrepancies were noted. Classification of the total county area varied by only 3 percent.

Coastal land use mapping from the S190B photographs was accomplished for Delaware and Maine. Klemas et al. (ref. 2-9), using S190B color photographs and a zoom transfer scope, compiled a map with a scale of 1:125 000 that delineated 10 land use and vegetation categories. Color-infrared S190A photographs of the Truk Watershed in Maine were used to provide additional definition of water boundaries and vegetative species.

Stoeckeler et al. (ref. 2-3) indicated that, in Maine, the S190B color-infrared data were valuable in delineating vegetation cover types and cultural features even though the only coverage available for evaluation was a snow scene (January 1974; fig. 18 from Woodman and Farrell's report in ref. 2-3). Logging roads that were approximately 6 m wide were identified. Several vegetation-cover-type maps were prepared from the S190A film types collected in September 1973. Vegetation types, especially forest stands, were best interpreted from color-infrared film, with black-and-white panchromatic film showing good delineations of most categories. The remaining film types contributed little additional information to this overall evaluation of general land use or vegetation-cover-type mapping.

Simonett (ref. 2-10) also cited several examples that indicated that good-quality land use maps could be derived from EREP data. One such example was the regional land use map (Level II) prepared at a scale of 1:126 720 from S190A (black-and-white and color-infrared) photographs for St. Marys County, Maryland. Interpreting the data, mapping the features, and preparing the final map of the 1088-km^2 area required 14 hours. By comparison, a similar map prepared from high-altitude-aircraft color-infrared data at the same scale required 32 hours for completion. Additional detailed information was derived from the analysis but

could not be adequately displayed on a map of this scale.

Hardy et al. (ref. 2-7) used a low-cost photographic enhancement process to convert black-and-white enlargements to color composites with use of the techniques discussed in section 6. Combinations of spectral bands, diazo hues, and exposures were selected to maximize the color contrast among the land use categories to be examined (figs. 2-5(a) and 2-5(b)). It should be noted that this process is used to achieve unique descriptions of classification units by means of color contrast; therefore, individual colors are not chosen to represent specific land uses. In a comparison of three test sites in New York, using the 1968 land use natural resource (LUNR) inventory as a data base, Hardy determined that more land use information was provided by the S190A enhanced color composites than by the individual S190A film types. In addition, the composites were nearly as effective as the individual S190B film types for classification. Accuracy ranges related to the USGS Level I and Level II categories for a scale of 1:62 500 are shown in table 2-II.

Table 2-III is representative of specific Level I and Level II accuracies achieved by comparing S190A color composites and S190B film types to the existing LUNR base. Accuracies were determined in terms of square hectometers, which were inventoried by using film from Skylab camera systems. Random ground checks of the LUNR data base, which was compiled in 1968

TABLE 2-II.—Accuracy Ranges for Level I and Level II Categories Calculated by Using Different Films and Techniques

[From ref. 2-7]

Film	Accuracy, percent	
	Level I	*Level II*
S190A enhanced color composites	88 to 93	71 to 78
S190B three film types	87 to 95	75 to 81
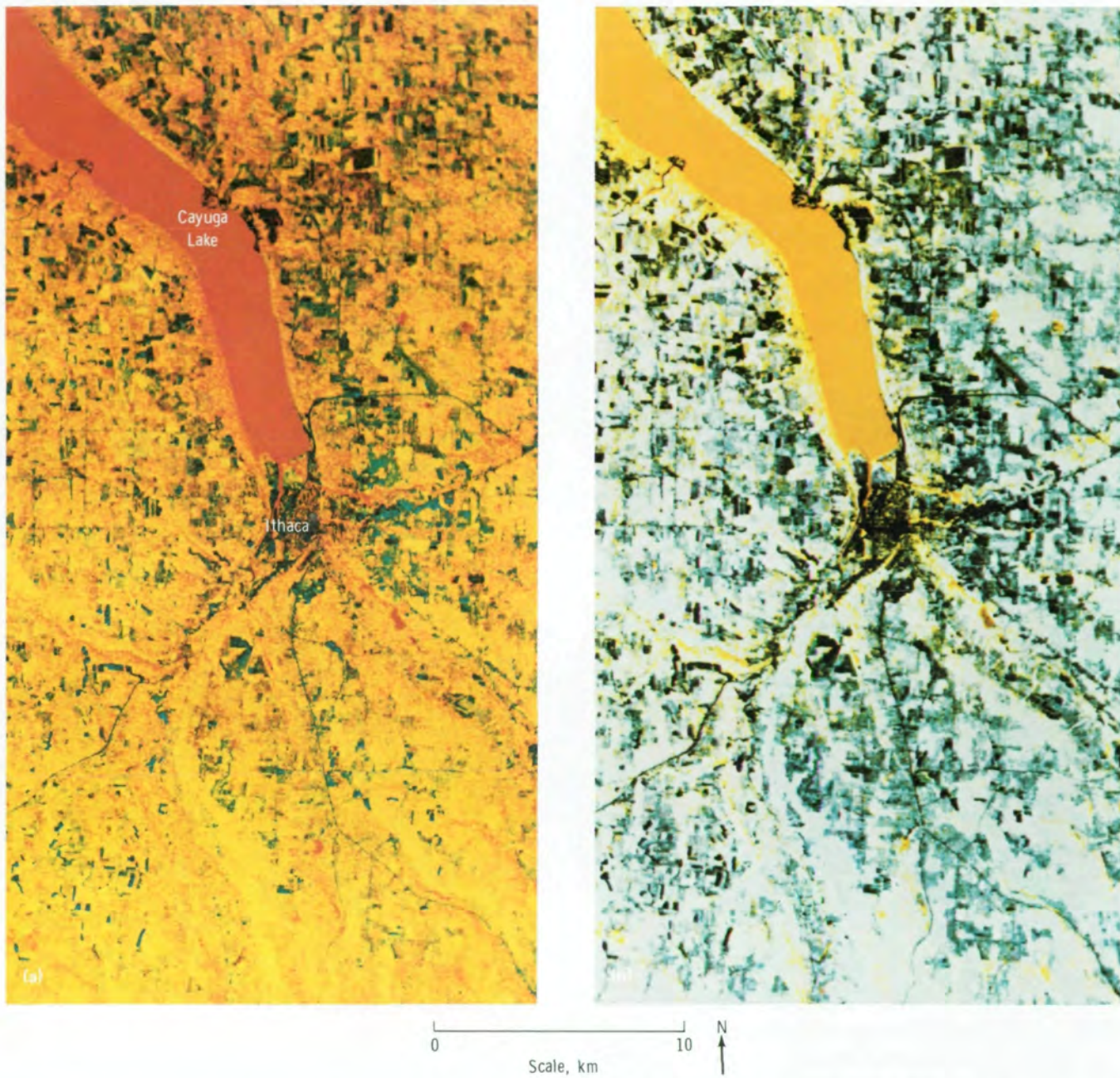
FIGURE 2-5.—S190A color composites of Tompkins County, New York, showing different color enhancements that assist in the interpretation of selected categories. These examples represent only two of several color composites that were generated for this test site. Lake Cayuga and the city of Ithaca are two prominent features in the scene. (Approximate scale, 1:250 000.) (a) S190A color composite designed to enhance natural features. (b) S190A color composite designed to enhance cultural features.

from 1:20 000-scale black-and-white aircraft photographs on overlays keyed to the 7.5' topographic map base, indicated an overall accuracy of 95 percent, based on the 1973 inventory for Tompkins and Suffolk Counties. However, for Orange County, the accuracy was 84 percent. If these adjusted figures were applied to the S190A data, table 2-III values would increase the Skylab inventory from 93 to 98 percent for Level I and from 78 to 83 percent for Level II, with comparable increases for the S190B data.

The numbers of classification units and the definitions used in the LUNR system are unrelated to the USGS classifications for Levels I and II. Several LUNR land use units had to be aggregated to provide the comparison presented in table 2-III. Difficulty was encountered in discriminating between light residential (Level III) and forested categories and between cropland and pasture. The reason for the difficulty was attributed, at least in part, to similar spectral responses for these categories. As previously mentioned, the season of data collection is significant in the inventory of natural resources. In this case, spring or late-fall coverage would have improved the overall classification results in the Level II categories. Hardy et al. (ref. 2-7) ranked the S190A and S190B sensors in terms of interpretation preferences as (1) S190B color, (2) S190A color composites, (3) S190B black and white for spatial patterns, and (4) S190B color infrared. The S190B black-and-white data had the best resolution properties, but tonal distinction for the various land use categories was often not sufficient to provide a high level of confidence for interpretability.

Agriculture, range, forest, and water-resource categories are discussed in detail in other sections of this report. To complete the representation of the major categories in land use, attention in the next part of this subsection is directed to the application of sample data to the urban category (with strip mining, wetlands, and other specific categories emphasized later).

Urban land use mapping with use of S190 data.—Primarily because of the high spatial resolution of the S190B system, almost all the investigators concerned with urban environment used this system for detection, identification, and mapping of urban categories. Table 2-IV shows a typical Level III classification unit within the "urban and built-up land" category. This table represents a compendium of the work of several investiga-

TABLE 2-III.—Comparison of Skylab S190A (Multispectral) and S190B (Color) Errors to 1968 LUNR Data for the Riverhead-Southampton, Suffolk County Test Area [a]

[Skylab scale: 1:62 500]

Category	1968 LUNR area, hm²	Error, hm²		Relative error	
		S190A	S190B	S190A	S190B
Level I					
1.0	9 239	−155	697	−0.02	0.08
2.0	12 818	2834	2369	.22	.18
4.0	17 737	3715	1527	.21	.09
5.0	18 575	55	−339	.00	−.02
6.0	1 142	−1054	−145	−.92	−.13
7.0	484	368	743	.76	1.54
Aggregate error				0.07	0.05
Level II					
1.1	5 065	−4693	−4285	−0.93	−0.85
1.2	261	7251	6123	27.78	23.46
1.4	381	−381	43	−1.00	.11
1.5	1 036	−348	−80	−.34	−.08
1.6	2 111	−1599	−859	−.76	−.41
1.7	384	−384	−344	−1.00	−.90
2.1	7 494	1626	2894	.22	.39
2.2	375	−367	−375	−.98	−1.00
2.4	4 949	−4093	−4888	−.83	−.99
4.2	16	−16	−16	−1.00	−1.00
4.3	17 721	3731	1543	.21	.09
5.1	111	−111	−87	−1.00	−.78
5.2	167	−147	93	−.88	.56
5.3	155	−155	−155	−1.00	−1.00
5.4	18 142	118	−190	.01	−.01
6.1	921	−837	−24	−.91	−.03
6.2	220	−216	−120	−.98	−.55
7.2	484	368	633	.76	1.31
7.4	0	0	80	0	∞
Aggregate error				0.22	0.19

[a] From reference 2-7.

TABLE 2-IV.—*Urban Features Discernible on Skylab S190B Photographs*

Level I	Level II	Level III	Qualitative evaluation of Level III categories
1.0 Urban and built-up land	1.1 Residential	1.1.1 Single-family household units	(a)
		1.1.2 Multiple-family household units	(b)
		1.1.3 Mobile home parks	(b)
		1.1.4 Transient lodging	(c)
	1.2 Commercial and services	1.2.1 Wholesale trade areas	(b)
		1.2.2 Retail trade areas	(b)
		1.2.3 Business, professional, and personnel services	(d)
		1.2.4 Cultural, entertainment, and recreational facilities	(b)
	1.3 Industrial	1.3.1 Major manufacturing plants	(b)
		1.3.2 Distribution centers	(c)
	1.4 Extractive	1.4.1 Stone quarries	(c)
		1.4.2 Sand and gravel pits	(c)
		1.4.3 Open-pit or strip mining	(a)
		1.4.4 Oil, gas, sulfur, salt, and other wells	(c)
	1.5 Transportation, communications, and utilities	1.5.1 Highways and related facilities	(a)
		1.5.2 Railroads and related facilities	(b)
		1.5.3 Airports and related facilities	(a)
		1.5.4 Marine craft facilities	(b)
		1.5.5 Telecommunications and related facilities	(c)
		1.5.6 Electric, gas, water, sewage disposal, solid waste, and related facilities	(c)
	1.6 Institutional	1.6.1 Educational facilities	(b)
		1.6.2 Medical and health facilities	(c)
		1.6.3 Religious facilities	(c)
		1.6.4 Military areas	(b)
	1.7 Strip and clustered settlement	(No further breakdown)	(b)
	1.8 Mixed	(No further breakdown)	(b)
	1.9 Open and other	1.9.1 Improved	(a)
		1.9.2 Unimproved	(b)

[a]Identification determined with ease.

[b]Identification possible often enough to make data useful without collateral data.

[c]Recognizable by geometry, texture, color, and/or alinement but not positively identifiable unless correlated with aircraft underflight or ground-truth data.

[d]Cannot be recognized.

tors and offers a qualitative evaluation of the S190B photographs as they relate to urban features. Figure 2-6 is an S190B color enlargement of Jackson, Mississippi, that is representative of the urban-type information present in such photographs. Photographs of this type can be enlarged to show the spatial relationships of individual features with the adjacent environments (1:125 000 scale) or can be effectively enlarged to common data-base scales (e.g., 1:50 000 or 1:24 000) by

photographic processes or viewing devices to enable more detailed urban analysis and general interpretation.

The type of urban land use interpretation accomplished by Alexander and Lins (ref. 2-11) for the Phoenix, Arizona, and New Haven, Connecticut, areas is shown in figures 2-7 and 2-8, respectively. A series of 20- by 20-km land use map sections was compiled by using 18- and 30-power microfiche viewers and transferring the land use polygon boundaries to scaled overlays

Explanation

1. Airport
2. Golf course
3. Shopping mall
4. Memorial Stadium

5. Medical center
6. Veterans Administration
   Hospital
7. Railroad yard

8. State fairgrounds
9. Central business district
10. Old residential areas
11. Cemetery

12. Park
13. Zoo
14. Park
15. Educational institution
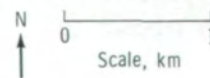
N

0   1
Scale, km

FIGURE 2-6.—A portion of an S190B color photograph (approximate scale, 1:50 000) showing the central city area of Jackson, Mississippi (SL4-92-295). Selected annotations show several Level III and Level IV land use categories. Transportation features and related components are visible but have not been annotated.

on which land parcels of 4 km² or larger were mapped. Their evaluation indicated that the S190B color photographs permitted the detection of higher levels of land use detail than any satellite imagery previously evaluated by using photointerpretative techniques. These areas are also part of the "Atlas of Urban and Regional Change" being produced in the USGS Geography Program.

The following paragraphs summarize the findings concerning the major Level II categories and several subcategories (Level III) for the Phoenix, Arizona, and New Haven, Connecticut, studies.

Residential: The residential land for both sites was identified on the S190B photographs and subdivided into single- and multiple-family categories. The individual signatures on the photographs differ somewhat between sites as a function of roof composition, quantity and type of vegetation, time of year, lot size, and block arrangement.

Commercial: Several types of commercial areas were identified. These types include central business districts, strip developments, and suburban shopping centers. Strip commercial developments extend along major transportation arteries and are usually no more than one block deep on either side of the road. Suburban shopping centers can be easily identified along major suburban highways by their large, brightly reflecting roofs and large, paved parking lots.

Industrial: Very large structures usually characterize the industrial category. Industrial activity commonly appears in groups or clusters as a mixture of crowded large buildings, fuel storage tanks, and numerous railroad sidings. These facilities resemble shopping centers except that many large buildings are present and parking areas are not oriented for convenient access to the buildings.

Transportation: The S190B photographs are valuable in delineating various types of transportation facilities. Major highways and interchanges are clearly visible and many lesser roads can be observed (although, in older residential areas, streets tend to be obscured by vegetation). Railroad yards, rights-of-way, and sidings have been identified. Airports with paved runways, aprons, and parking areas and with terminal buildings are readily evident. Many utility corridors (i.e., powerlines and pipelines) are visible, especially where they pass through forested land.

Institutions: Institutions appear in both scenes and consist primarily of educational facilities and large medical complexes. They appear as groups of long, connected buildings surrounded by extensive vegetated areas, parking lots, and—in some cases—athletic fields.

Open space: The open-space category includes improved open spaces such as golf courses, cemeteries, parks, and vacant lots. These land uses would be classified as Level IV in this classification matrix. The fairway patterns of golf courses are the easiest to identify within this category.

Industrial and commercial complexes: Although not a listed category under Level III, these "industrial parks" were identified on S190B photographs. They usually consist of a mixture of industrial and commercial land use, including light assembly, regional distribution facilities, and research and development sites. These "parks" exhibit none of the features associated with heavy industry, such as fuel tanks, railroad sidings, and piles of raw materials. They are usually located along, or at junctions of, major highways.

Additional, miscellaneous activities.—As part of the USGS Geography Program, Skylab S190B color photographs were compared to high-altitude-aircraft photographs collected in 1970 for selected urban scenes. The major objective of this study was to determine whether the S190B color photographs could be used effectively to determine the types of post-1970 land use changes that had occurred in the 3-year interval. This analysis was therefore one involving "change detection."

Several different urban scenes were studied to determine the level of detail that could be identified for very different environmental areas, extending from a desert setting to a forested setting. Only photointerpretation techniques were used to perform the analysis. A series of overlays containing different land use categories was prepared. When these overlays were superimposed on the 1970 aircraft-data-base land use maps, the areas of change were detected (fig. 2-9). The findings of this investigation were very positive. The resolution of the S190B photographs permitted detection of many Level III and some Level IV categories; it approached the quality of the high-altitude-aircraft color-infrared photographs, especially for the identification and mapping of urban changes. In figure 2-9, large parcels of agricultural land and rangeland that are undergoing changes were measured. From 1970 to 1973, many new
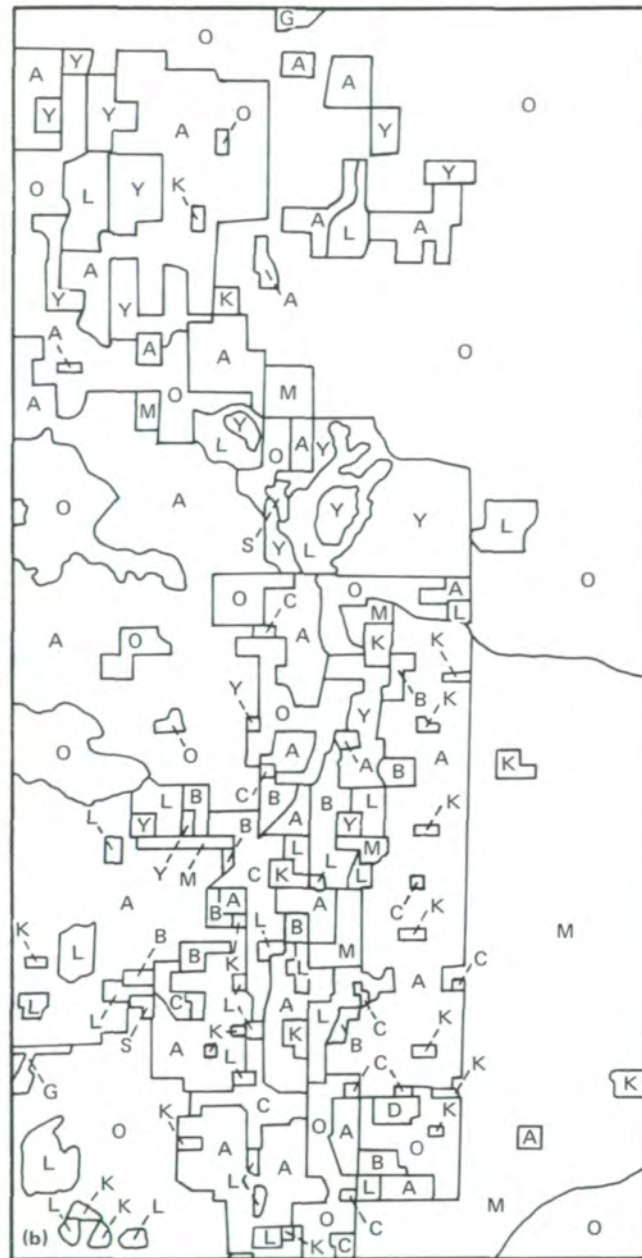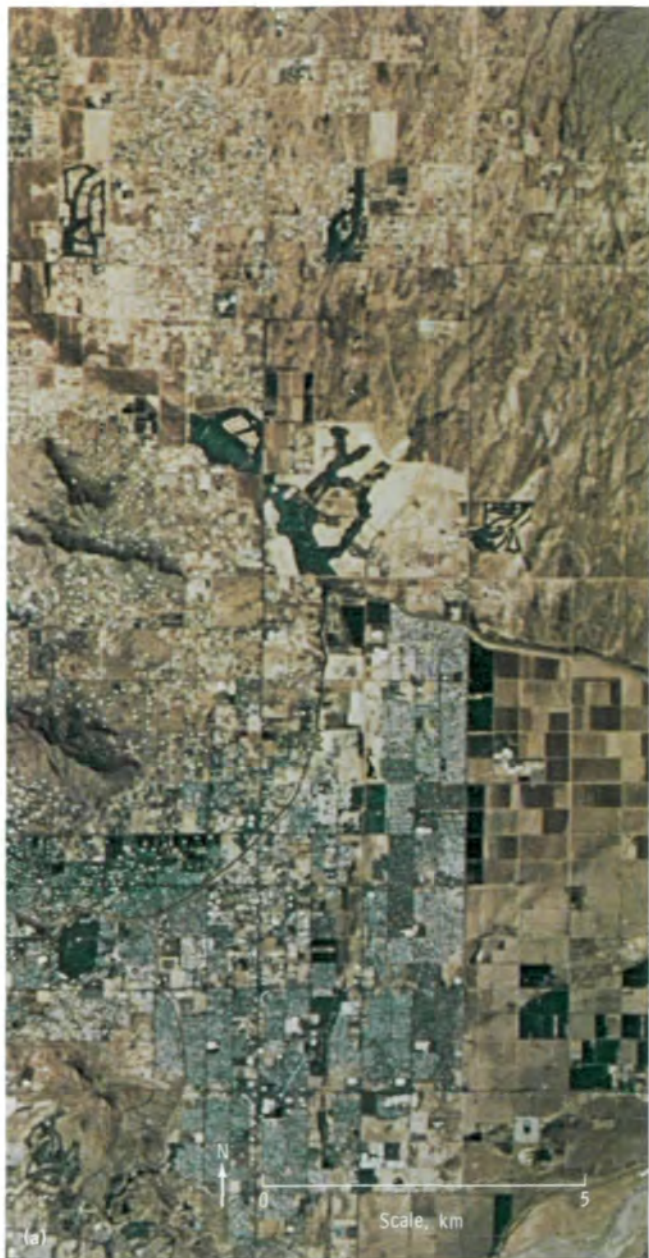
Explanation

A - 111, Single-family residential   G - 143, Airport facilities   N - 230, Confined feeding operations
B - 112, Multiple-family residential   K - 160, Institutions   O - 320, Shrub-brushland range
C - 120, Commercial and services   L - 170, Improved open space   S - 530, Reservoirs
D - 130, Industrial   M - 210, Cropland, pastures, and orchards   Y - 760, Transitional land
F - 142, Railroad facilities

FIGURE 2-7.—A portion of a land use map (fig. 2-7(b)) derived from an S190B color photograph (fig. 2-7(a)) for Phoenix, Arizona. This map is an example of a Level II and Level III land use map compiled at a scale of 1:100 000 for the Phoenix test site. The markedly different geographical settings (desert as opposed to vegetated landscapes) and the land use patterns should be noted and compared with figure 2-8. (a) S190B photograph (SL3-86-011). (b) Land use map.
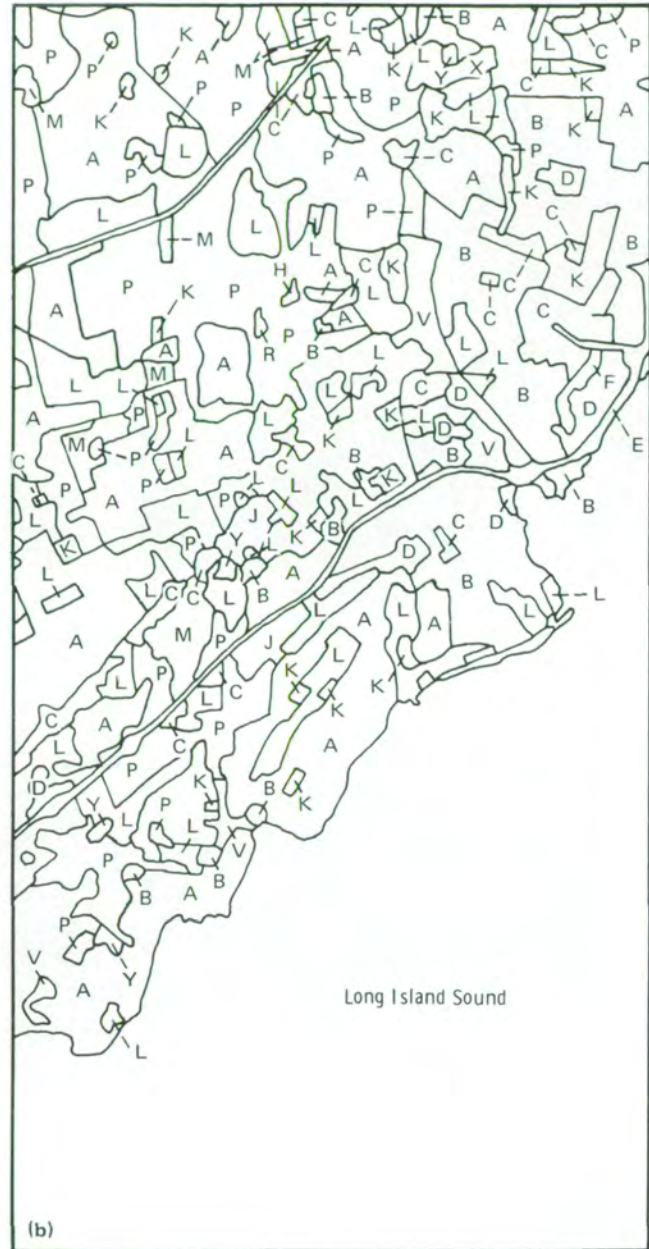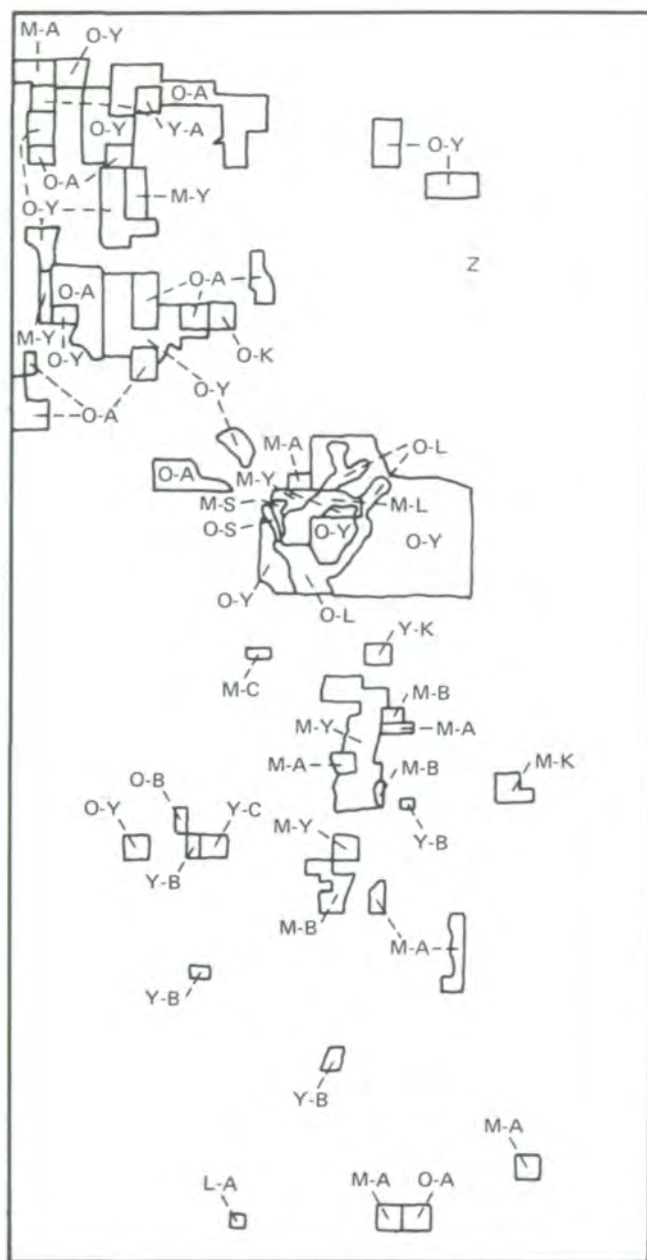
Explanation

A - 111, Single-family residential
B - 112, Multiple-family residential
C - 120, Commercial and services
D - 130, Industrial
E - 141, Highways
F - 142, Railroad facilities
G - 143, Airport facilities
H - 144, Utility rights-of-way

I - 145, Marine craft facilities
J - 150, Industrial and commercial complexes
K - 160, Institutions
L - 170, Improved open space
M - 210, Cropland, pastures, and orchards
P - 400, Forest land
Q - 510, Streams and canals
R - 520, Lakes

S - 530, Reservoirs
T - 540, Bays and estuaries
U - 610, Forested wetland
V - 620, Nonforested wetland
W - 720, Beaches and mudflats
X - 750, Strip mines, quarries, and gravel pits
Y - 760, Transitional land

FIGURE 2-8.—A portion of a land use map (fig. 2-8(b)) derived from an S190B color photograph (fig. 2-8(a)) for New Haven, Connecticut. This example of Level II and Level III land use categories represents the type of information that can be useful for regional planning and land use inventories. This map was compiled by using a 1:100 000-scale S190B photograph taken September 19, 1973. The overall scene contrast and land use patterns of this figure should be compared with those of figure 2-7. (a) S190B photograph (SL3-88-276). (b) Land use map.

LAND USE CHANGE -
First letter indicates 1970 land use interpretation;
second letter indicates 1970-73 change in land use.

A - 111, Single-family residential
B - 112, Multiple-family residential
C - 120, Commercial and services
K - 160, Institutions
L - 170, Improved open space
M - 210, Cropland, pastures, and orchards
O - 320, Shrub-brushland range
S - 530, Reservoirs
Y - 760, Transitional land
Z   No change in land use

N

0   5
Scale, km

FIGURE 2-9.—A portion of a Level II and Level III land use change map for the Phoenix test site. A dot planimeter was used for area measurement to permit calculation (in percent) of total amount of change in the test site for each category. (Fig. 2-7(a) contains a photographic display of this area.)

residential areas were developed and were mapped on the S190B photographs. Areas that showed evidence of some activity but that could not be accurately classified were placed into the transitional category (symbol Y in fig. 2-9). Mapping of nonurban land use categories, however, was more difficult with the use of S190B color photographs. For example, forests tended to be uniformly green on the natural-color film, and wooded residential areas were difficult to discriminate in some cases. Repetitive temporal coverage with use of a high-resolution color-infrared film in the S190B camera would improve the interpretability of these categories.

In a classification accuracy study, Alexander and Lins (ref. 2-11) used the S190B color-film data to produce a 1:24 000-scale land use map of Fairfax City, Virginia. This map product was evaluated against a similar map prepared from high-altitude-aircraft (U-2) color-infrared photography at the same scale and was field checked for accuracy. An accuracy of 83 percent was achieved with the EREP data for mapping Level III land units when compared to the aircraft data base. To quantify the results, Alexander used two methods to determine the accuracy of the resultant maps. First, a systematically alined sample (grid cells) of 69 sample points was examined; and second, the area measurements (square hectometers) of the land units were compiled for both the Skylab and the aircraft data maps. Of the 69 sample points, 57 were correctly classified. Of the units that were misclassified, nearly half the error was

attributable to the lack of spectral discrimination in the color film. Full foliage cover made detection of houses or other residential "keys" impossible. This difficulty is also true for high-altitude-aircraft data.

Another source of error was the difficulty of identifying and mapping the unimproved open-space category. These areas were confused with small plots of agricultural land. In a summary of the S190B data, Alexander and Lins (ref. 2-11) indicated an ability "to distinguish and map with considerable confidence such structural urban details as the location and extent of most single-family residential areas, even some residential structures themselves, commercial and industrial areas, even individual commercial and industrial structures, streets and roads of moderate size and considerable detail in the use patterns of surrounding nonurban land. If color infrared film of comparable spatial resolution to that of color film used in this evaluation had been available the investigators are confident that even greater detail and reliability of detection of the various land use categories would have been obtained. . . . The Skylab S-190B data here revealed a capability to distinguish Level III and in some cases, Level IV (trailer parks, tank farms, golf courses, drive-in theaters, cemeteries, etc.) in urban area land use analysis." Results of other investigators (Hannah et al., ref. 2-2; Simonett, ref. 2-10; and Baldridge et al., ref. 2-12) generally supported these findings.

When a suitable inventory data base (such as an aircraft mosaic) is available for an area, it is quick and easy to update that data base by using S190B-type photographs. Although the S190B color photographs provided the most meaningful source of information to update inventory bases in most land use inventories, the multispectral characteristics of the S190A also proved valuable. In several cases, the information provided by S190A film types was extremely beneficial to the analysis as a supplementary source for identification and delineation of specific nonurban categories. For example, in forested or generally vegetated scenes for which S190B color film was the primary source of detailed information, the S190A color-infrared film provided additional spectral information.

The pattern and extent of urban expansion into prime agricultural land were mapped for Columbus, Ohio, by Baldridge et al. (ref. 2-12), with the use of S190A photographs (fig. 2-10). With use of the map data, percentage figures were calculated to determine the rate of encroachment. This type of analysis, when coupled with long-range population density and pattern projections, can be meaningful to urban and regional planners and to decisionmakers; it can also be used as an input to test and update projection-type models.

In other urban-related activities, Welby and Lammi (ref. 2-13) used Skylab photographs for studying environmental issues involved with the expansion of the Raleigh-Durham, North Carolina, airport. Pressure to expand airport facilities (runway extensions, orientation of new runways, etc.) created problems concerning effective planning for this expansion with the least amount of adverse effect on the local area. Although the decisionmaking process for this type of problem is complicated and is influenced by social, political, and economic factors, Welby and Lammi concluded that Skylab photographs, even when used by a relatively inexperienced photointerpreter, are useful for this type of environmental analysis.

Another urban environmental problem in which Skylab photographs were used by Welby and Lammi involved a "greenspace" study. In urban planning, a greenspace (or greenbelt) is defined as an area of land covered with some form of vegetation. Planners are concerned with this type of area in terms of how to protect and manage it effectively and how to obtain additional areas when needed. The S190B color photographs, enlarged to a scale of approximately 1:62 500, provided the best source of, and format for, relevant information for greenspace analysis.

Welby and Lammi summarized their use of S190B color photographs with the following statements.

Land use, vegetative cover, and even the relative beauty and ugliness of the urban landscape can be seen or inferred from the photographs. The proximity and encroachment of commercial-industrial development into good quality residential areas, the tendency of many new residential developments to become open bulldozed biological deserts are examples of the environmental quality problems visible in Skylab Photography.

Another use of EREP data was explored by digitizing S190A and S190B photographs for generating land use classification maps. Hannah et al. (ref. 2-2) oriented their approach toward a direct application for urban planners, whereas Silva (ref. 2-14) directed his effort toward a quantitative, technical evaluation by comparing the digitized photographic results with Landsat and Skylab multispectral scanner results.
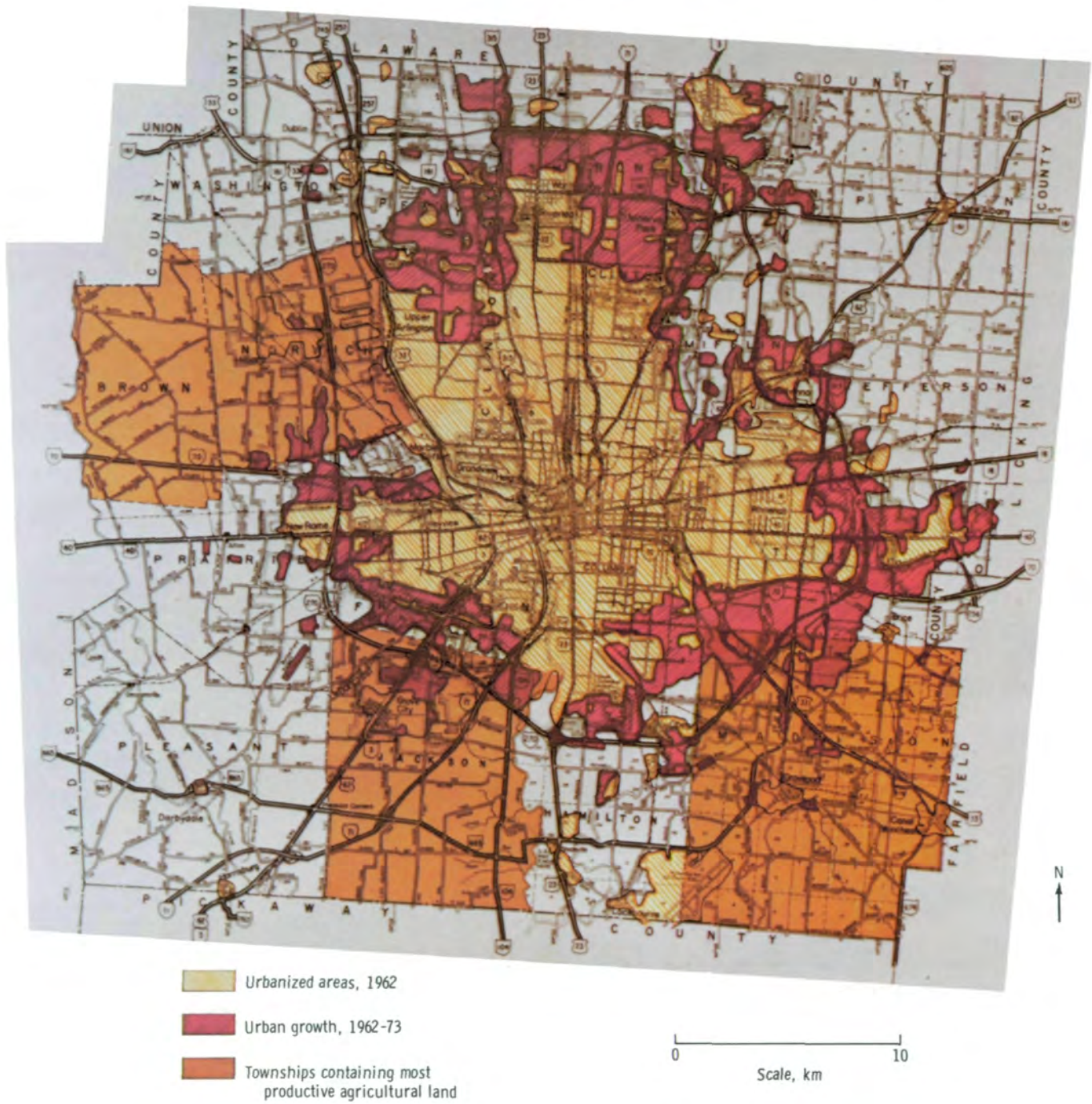
FIGURE 2-10.—Map of Franklin County, Ohio, showing urban encroachment on agricultural land in the Columbus, Ohio, area. This map graphically portrays the areal extent and pattern of urban encroachment into three predominantly agricultural townships surrounding Columbus. Conventional photographic techniques with the use of S190A photographs were used to plot the limit of the 1973 built-up area.

For the Gainesville, Florida, site, Hannah et al. generated a Level II classification map from three bands of digitized S190B color-infrared multiemulsion data. The result indicated that identification of various land classes on the basis of color tones can be accomplished more effectively by the human observer (photointerpretation); examples include identifying forest types and other vegetation types, such as waterhyacinths and marshlands, and relating land use units to their surroundings. By contrast, the maps produced with computer assistance reveal more details involving commercial-industrial classes because of the capability of machine processing to improve the degree of brightness of the spectral responses.

Silva digitized both S190A color-infrared (multiemulsion) and S190A multiband data, using the four-band black-and-white infrared films obtained over the Lake Monroe, Indiana, site. A classification perfor-

mance analysis based on training fields for nine land use classes was performed. Table 2-V shows the results compared to the Skylab S192 and Landsat multispectral scanner data for the same area. Although the performance levels were lower than those of the best four bands of the Skylab multispectral scanner (bands 3, 7, 8, and 11) and those of the Landsat multispectral scanner bands, the multiemulsion data were better than the digitized multiband black-and-white data.

Both investigators indicated that, although the achieved results were undramatic, digitized photography is a technique for which research and development should be continued for land use resource and inventory programs.

In the following subsections, land use results obtained by using S192 imagery and computer-aided analysis techniques are discussed.

TABLE 2-V.—*Classification Performance Results: Digitized S190A Photography Compared to Data From Two Multispectral Scanners for Selected Categories*

[Percent correct]

Category	Skylab S192		Landsat multispectral scanner	Skylab S190A	
	Bands 3, 7, 8, 11	Bands 3, 5, 6, 8		Color infrared	Four-band black and white
Residential	97	81	97	91	84
Commercial-industrial	73	33	61	76	46
Extractive	51	59	61	32	34
Soil	87	78	83	67	78
Grass	95	86	93	82	69
Sparse woods and deciduous forest	81	80	86	84	77
Coniferous forest	99	68	95	85	43
River	87	27	77	16	64
Lake	89	86	86	98	93
Class average[a]	84	66	82	70	65
Overall performance[b]	87	80	88	83	76

[a]Arithmetic mean of the performance results of the nine classes.

[b]Total number of points classified correctly divided by total number of points in test areas, times 100.

General land use mapping with use of S192 data.— Several investigators (Hannah et al., ref. 2-2; Hoffer, ref. 2-5; Klemas et al., ref. 2-9; Simonett, ref. 2-10; Silva, ref. 2-14; Gilmer and Work, ref. 2-15; Higer et al., ref. 2-16; Polcyn et al., ref. 2-17; and Sattinger et al., ref. 2-18) used computer-aided analysis techniques for the study of Skylab S192 data obtained over many test sites to map a variety of different types of land cover. The results, in general, indicated a considerable potential for mapping various land cover types through use of these techniques, even though the procedures used to train the computer, the classification algorithms, and the methods used in evaluating the results varied considerably. Some of the investigators conducted detailed analyses to determine the wavelength bands that were most valuable for mapping different cover types. These results show the value of the spectral range of the S192 system. Because some studies also involved analysis of Landsat-1 data obtained over the same test site as the EREP data, valuable comparisons of results obtained by using two very different satellite multispectral scanner systems were possible.

Most of the investigators used the USGS Circular 671 (ref. 2-1) system of land use classes in their analyses but modified it to meet their own particular requirements. In many studies, both Level I and Level II degrees of detail were mapped; and in some investigations, more detailed classifications were achieved for selected cover types. For the Level I cover types, the classification accuracies ranged from approximately 72 to 91 percent. For the Level II degree of detail, the results were more varied, with overall classification accuracies ranging from 43 to 89 percent. The exact reasons for these variations in results cannot be specifically determined. It is difficult to isolate the reasons for the variations because the different investigations involved diverse test sites that included a wide variation of cover types. Distinct differences in the analysis and evaluation techniques also must be considered.

The following paragraphs provide some insight into the similarities and differences among the many investigations by summarizing key aspects of the various studies. Only those investigations involving land use and land cover mapping by computer-aided analysis techniques are included here. Unless otherwise noted, each of these studies involved S192 data that had been digitally filtered and line-straightened at the NASA Lyndon B. Johnson Space Center data-processing facility.

A study by Simonett (ref. 2-10) involved the analysis of S192 data over a predominantly urbanized test site in the Washington-Baltimore region. The data were obtained on August 10, 1973, and all 13 wavelength bands were available for analysis. Extensive fieldwork provided the information for identifying many areas that could be located in the S192 imagery. A clustering technique was used to help define spectrally homogeneous training and test areas. The classification was performed by using a maximum-likelihood algorithm similar to that used by several other investigators (Polcyn, Silva, Hoffer, and Sattinger; refs. 2-17, 2-14, 2-5, and 2-18, respectively). A major difference in Simonett's approach was that a two-stage classification sequence involving different combinations of wavelength bands was used. This approach differed from that used by the other investigators because they generally defined a single optimal set of wavelength bands for classifying the data at the Level II degree of detail. The results of this Level II classification were then grouped into broader categories to display and tabulate Level I results.

Simonett defined five major Level I classes in the Washington-Baltimore test site: urban, agricultural, forest, water, and wetlands. The results were quantitatively evaluated by using a series of test areas that included approximately 13 600 picture elements (pixels), of which more than half (7000) were in the urban category. Simonett reported a 72-percent classification accuracy for the Level I classification of the test areas. This result compared with 73 percent for the training data sets and indicates that a fairly good statistical sample existed for both the training data sets and the test areas. Results obtained by using a combination of the training and test pixels (approximately half of each) are shown in table 2-VI. The Level II classification results yielded a classification accuracy of approximately 43 percent. Significant misclassification occurred at the Level II degree of detail in the agriculture and forest cover types, although other investigators reported reasonably good classification performances in similar categories of cover type. In some study sites, the number of training and test areas was insufficient to truly represent the various categories involved at this level of detail. As a result of this relatively poor classification performance at the Level II degree of detail, Simonett concluded that, in this particular study, only the Level I classification results would be of potential value for land use planning agencies. This general land use in-

vestigation also included a detailed evaluation of spectral bands for land use studies. The results of similar evaluations are discussed in the subsection entitled "Urban land use mapping with use of S192 thermal-infrared data." Simonett's conclusions, together with those of other investigators, are discussed in the subsection entitled "Wavelength band evaluation."

The Brevard County Planning Department in Florida conducted a land use investigation that included computer-aided analysis of the S192 data (ref. 2-2). A supervised approach was used to develop the training statistics for the analysis; and, as in other investigations, a maximum-likelihood-ratio algorithm was used for the classification. To obtain output products for land use planners, the generalized boundaries of computer-generated land use classes were manually delineated. The investigators indicated that acceptable results were obtained and that multispectral scanner mapping was a useful tool. In general, the computer classification maps tended to have more precise quantitatively defined land use patterns, whereas results from photointerpretation tended to generalize some of the patterns. This difference resulted in an overestimation of forest areas on the photointerpreted results as compared to the computer-derived results.

In a study by Polcyn et al. (ref. 2-17), the S192 data were used to classify an area in southern Ontario, Canada, largely covered by vegetation. The cover types involved in the classification included marsh, coni-fer/hardwood, hardwood/orchard, undifferentiated vegetation (including brush, idle, etc.), suburban, bare soil/quarry, herbaceous vegetation, and water. Only four wavelength bands of the S192 data from the Skylab 2 mission (0.56 to 0.61, 0.62 to 0.67, 0.78 to 0.88, and 10.2 to 12.5 μm) were available for analysis. The training statistics were obtained by applying two successive clustering-step analyses. The classification was based on a maximum-likelihood algorithm, as incorporated into the software system. Because of the difficulty in developing an adequate set of test areas for evaluating the classification results, Polcyn developed a different approach for quantifying the results. This approach involved defining the "probability of correct classification" for the eight categories mapped, based on a statistical analysis of the training data. The results indicated that all categories except two had probabilities of correct classification above 90 percent. (Undifferentiated vegetation and suburban categories had probabilities of correct classification of approximately 78 percent.) The training statistics that were used as a basis for these quantitative evaluation figures represented the best classification statistics. Polcyn also noted that the analysis indicated a likely misclassification of the suburban category as either "brush" or "bare soil"; this conclusion is not surprising because a suburban area is often composed of a mixture of cover types that would include these spectral classes.

TABLE 2-VI.—*Skylab Classification Results for the Heavily Urbanized Baltimore-Washington Area*

[From ref. 2-10]

Ground-truth category	No. of pixels	Skylab classification results, percent					Percent classified correctly
		1000: Urban	2000: Agricultural	4000: Forest	5000: Water	6000: Wetlands	
1000: Urban	12 993	71.3	19.3	7.4	0.5	1.5	71.3
2000: Agricultural	7 451	17.3	69.4	11.3	.1	1.9	69.4
4000: Forest	1 713	4.0	5.1	84.1	1.1	5.7	84.1
5000: Water	1 549	1.0	.3	.3	96.3	2.1	96.3
6000: Wetlands	928	4.4	9.3	33.6	6.6	46.1	46.1
Total	24 634	—	—	—	—	—	[a]72.2

[a]Percentage reflects correct classification of 17 796 pixels.

Silva (ref. 2-14), using unfiltered S192 data obtained on June 10, 1973, over the Lake Monroe area in south-central Indiana, conducted a land use study that identified residential, commercial-industrial, extractive, soil, grass, deciduous forest, coniferous forest, river, and lake. (Note that, in some instances, the investigators were working with land cover characteristics rather than land uses, such as "soil," which would actually be in the agricultural cropland land use category.) A combination of supervised and clustering analysis techniques was used to develop the statistics for classification. A divergence processor was used to define the best combination of 4 of the 12 wavelength bands available for use. This process indicated that bands 3, 7, 8, and 11 represented the best combination. It appeared that these wavelength bands also generally had the best data quality among those available. Therefore, there was some concern as to whether those bands were being selected for their spectral characteristics or for their data quality or for a combination of both. The classification was conducted by using a maximum-likelihood ratio based on the multivariant Gaussian distribution as incorporated into the software. An overall classification accuracy of 87 percent was obtained, based on tabulation of the results in the test areas. In this particular set of results, the test areas selected did not represent a statistically defined array of test areas, and Silva (ref. 2-14) stated that these performance figures might have been somewhat biased in an upward direction. It is important to note that this result is based on a Level II degree of detail; therefore, it does indicate a potentially significant improvement over the classification accuracy reported by some of the other investigators for this level of detail. A map display of these classification results is shown in figure 2-11.

Additional analyses of the S192 data over south-central Indiana were performed by Silva, using a statistically defined set of test areas. Many classifications of the test areas were conducted; different numbers and combinations of wavelength bands were used, for both the interim unfiltered and digitally filtered data sets. The best classification results were obtained with six wavelength bands (2, 3, 7, 9, 10, and 11) of the

filtered data set and the weighted a priori probabilities (as opposed to equal a priori probabilities). For the six-wavelength-band combination, the overall classification performance accuracy was 92 percent for Level I and 90 percent for Level II. For the best four wavelength bands (3, 7, 8, and 11), the Level I accuracy was essentially as good, 91 percent, and the Level II accuracy was 89 percent. Table 2-VII shows the results of the classifications for both Level I and Level II land use classes, based on the test-site data.

A study by Sattinger et al. (ref. 2-18) involved processing of the S192 data for application to recreational land analysis. The test site was of primary value for

TABLE 2-VII.—Level I and Level II Land Use Classification Results for an Area in Central Indiana

[From ref. 2-14]

Land use category	Percent of test-area pixels classified correctly			
	Optimum six bands [a]		Optimum four bands [b]	
	Level I	Level II	Level I	Level II
Urban	77.2		78.5	
Residential		80.2		79.1
Commercial-industrial		71.9		75.0
Extractive		50.0		65.4
Agriculture	88.7		88.9	
Soil		93.5		95.3
Grass		86.0		86.2
Forest	93.7		92.7	
Deciduous		92.2		90.4
Coniferous		56.4		59.0
Water	98.1		96.1	
River		89.2		73.0
Lake		98.9		98.5
Overall	91.6	89.7	91.1	88.8

[a] Bands 2, 3, 7, 9, 10, and 11.
[b] Bands 3, 7, 8, and 11.
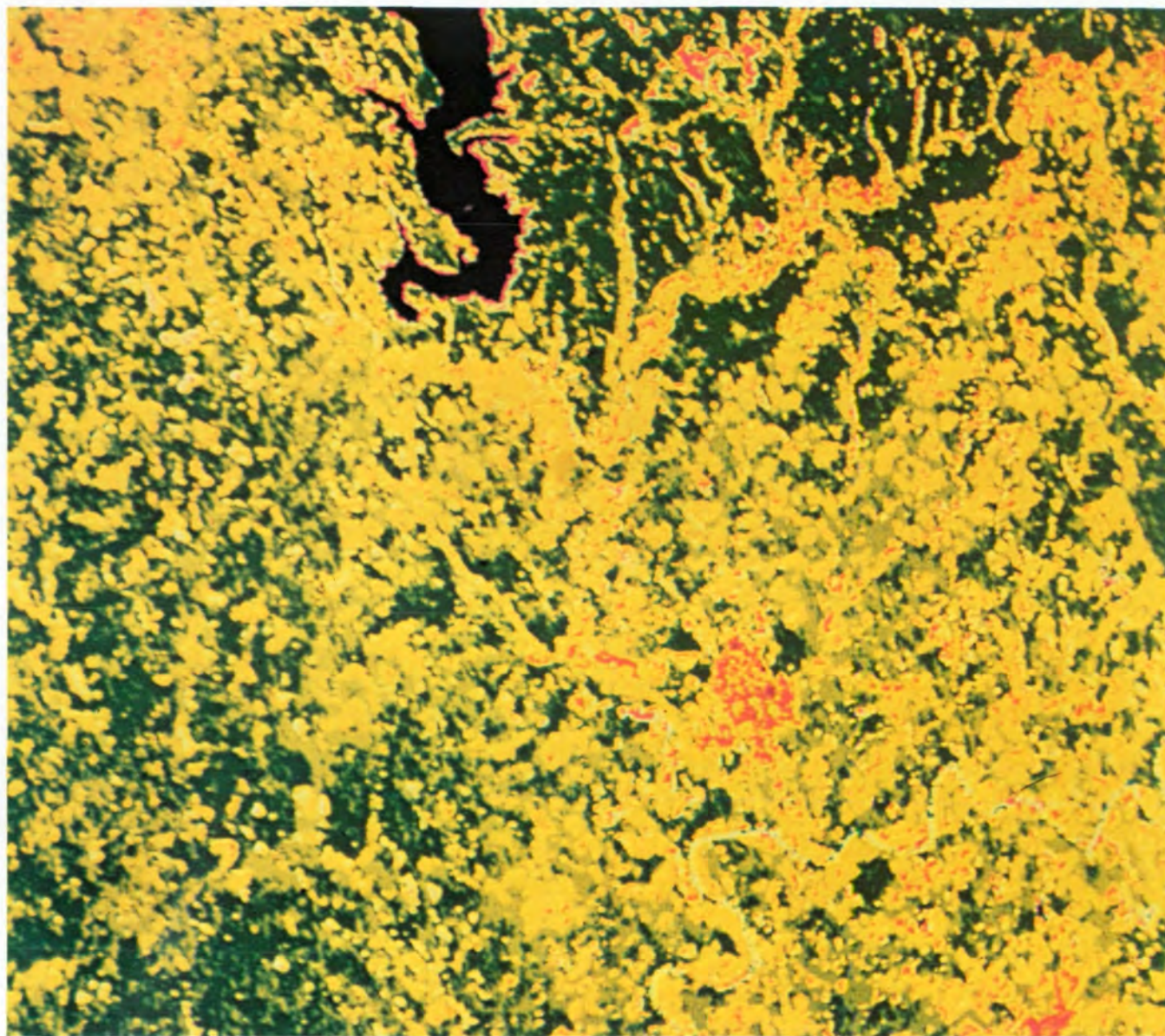
Explanation

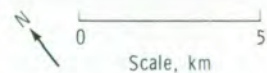|					
Red	Residential	Yellow	Bare soil	Pink	Coniferous forest
Dark gray	Commercial-industrial	Light green	Grass	Light blue	River
Cream	Extractive	Dark green	Deciduous forest	Dark blue	Lake

Scale, km 0 — 5

FIGURE 2-11.—Color-coded classification using S192 multispectral scanner data for an area south of Bloomington, Indiana. Monroe Lake is at the top. Nine land use classes are represented. Bands 3, 7, 8, and 11 were used for this classification. (Scale of original, 1:240 000.)

wildlife habitat and involved a relatively small (5300 hm²), mostly forested State game area in central Michigan. A maximum-likelihood algorithm was used for the classification. A total of 35 spectral training classes was initially defined; these classes were then combined to form 10 major informational categories. Six wavelength bands were used for the classification, based on a computer evaluation of the optimum combination for this particular analysis. The wavelength bands used, in order of preference, were 0.78 to 0.88, 1.55 to 1.75, 0.98 to 1.08, 0.68 to 0.76, 0.52 to 0.56, and 0.62 to 0.67 μm. The classified data were quantitatively evaluated by a summarization of the area of the various cover types over three 2.6-km² sections of land, and by a detailed quantitative comparison of the classified data with the Michigan Department of Natural Resources cover-type maps. These evaluations indicated that the 10 informational classes had been mapped with only a 54-percent classification performance. Consolidation of the 10 classes into 5 more generalized categories resulted in an accuracy of 72 percent. This low level of accuracy is attributed to the complexity of the test site, as indicated by the measure of many small stands, a condition that resulted in many "edge" pixels, or pixels containing more than a single cover type. Such factors are important to consider in classification. Sattinger (ref. 2-18) stated that S192 data can be used for regional surveys of existing or potential recreational sites, for delineation of open-space areas, and for preliminary site evaluation of geographically extensive sites.

The Green Swamp in central Florida was investigated by Higer et al. (ref. 2-16); S192 data were used to prepare maps showing environmental categories. The Green Swamp is not a continuous expanse of swamp, but a composite of many swamps with interspersed low ridges, hills, and flatlands. The water, land, and vegetation in the area are undergoing rapid changes caused by logging; reforestation; alteration of natural drainage by channelization and ponding; and burning and clearing for such purposes as sod farming, citrus farming, pasture improvement, and urban and industrial development. Improper planning and construction of new industrial and residential areas could clearly have a disastrous effect on such an environmentally sensitive area. For this reason, current cover-type maps are urgently needed for use in environmental appraisals to develop a rational basis for further planning and con-

trolled development. Higer's study was directed at evaluating the usefulness of Skylab S192 data for timely interpretation, assessment, and mapping of environmental categories. These categories included wetlands, water, cypress, pine, pasture, and uplands. A computer-aided analysis technique, incorporating supervised classification, was used. After classification, a qualitative evaluation of the results was conducted that involved comparison of the classification maps and aerial photographs of the study area. These comparisons indicated that the categorized S192 data were "found to be truly representative land-water cover conditions in the Green Swamp area." These results are discussed further in the subsection entitled "Comparison of Skylab S192 and Landsat multispectral scanner analyses."

Klemas et al. (ref. 2-9) used the S192 data and a computer interactive system to perform a land use classification of part of the Delaware Bay area. The system allowed a maximum of only four wavelength bands and eight spectral classes to be used in a single classification. Bands 4, 6, and 8 were selected because they roughly correspond to three of the Landsat bands; band 11 was included because other investigators have suggested that the use of wavelengths further into the reflective infrared could increase land use classification accuracies. The eight classes identified were water, sand and bare sandy soil, saltmarsh cordgrass, forest land, built-up land, plowed fields, cropland (planted fields), and a class composed of cattails and giant reedgrass. The classification results were displayed one class at a time and evaluated qualitatively. The investigator showed that classification accuracies ranged from 100 percent for water to 44 percent for the built-up-land category. In the latter group, most of the errors in classification were due to confusion with the agricultural category. However, photointerpretation of EREP S190A/S190B data indicated an accuracy for built-up areas of 81 percent. Klemas indicated that the results represented "a conservative indication of S192 capabilities because of the somewhat unsophisticated classification algorithm used and the limited number of categories and band combinations available."

Most of the investigations that included computer-aided analysis of S192 data were involved with test areas having little topographic relief. In contrast, a study by Hoffer (ref. 2-5) involved a 77 354-hm² test site in the San Juan Mountains of southwestern Colorado—an

area of rugged topographic relief and complex patterns of cover types. This study site was in a particularly important region from the standpoint of many conflicting demands for use of the land; e.g., timber production, wildlife habitat, grazing, recreation, and mineral production. Increasing public pressure for summer- and permanent-home developments is causing much concern on the part of the U.S. Forest Service, the National Park Service, the Bureau of Reclamation, and other agencies responsible for management of these lands. As a result of this pressure, personnel from these agencies indicated considerable interest in obtaining reasonably accurate and up-to-date cover-type maps that could be used for inventory purposes and for monitoring environmental alterations.

Computer classification of the S192 data involved several different analysis sequences. First, a detailed study of the data quality indicated considerable variation among the 13 wavelength bands, from both a qualitative and a quantitative standpoint. A newly developed "modified clustering" technique (discussed in sec. 6) was used to obtain training statistics. A divergence algorithm was used to determine the optimum combination of wavelength bands for various numbers of bands, and the best four bands were identified as 0.46 to 0.51, 0.78 to 0.88, 1.09 to 1.19, and 1.55 to 1.75 μm. The data were classified by using a maximum-likelihood algorithm. The cover types involved in this phase of the analysis were coniferous forest, deciduous forest, grassland, exposed rock and soil, water, and snow. Figure 2-12(a) illustrates the computer classification map of major land use classes for a sample portion of the entire test area as compared to a cover-type map (fig. 2-12(b)) developed by manual interpretation of the aerial photographs that were obtained in support of this Skylab mission. The figure shows that these two maps qualitatively compare quite well.

To obtain a quantitative evaluation of this classification of land use cover types, a test area consisting of a statistically defined grid of four by four resolution elements was used. A summary of classification performance for each land use class is shown in table 2-VIII. In this case, the overall classification accuracy was 85 percent. If the coniferous forest and the deciduous forest were combined, the overall accuracy for forest cover would be 98 percent. Several other investigators also indicated that forest cover, as a major cover type,

could be accurately mapped. The grassland category was the most difficult to classify; i.e., a considerable amount of grassland was misclassified as deciduous forest. Hoffer believed that this misclassification occurred primarily because foliation of much of the deciduous forest cover was not complete at the time of the Skylab 2 overpass (June 5, 1973). Therefore, the training field statistics for grassland tended to overlap those of deciduous forest. The cover-type category of "exposed rock and soil" is not included in table 2-VIII because none of the statistical-grid test areas fell on a sufficiently large area (approximately 8 hm² minimum size) of exposed rock or soil.

Evaluation of the computer-developed classification maps indicated that the classification was reasonably accurate, and an estimate of the areal extent of each cover type was then tabulated (table 2-IX). This tabulation required 45 seconds of computer time to complete the entire 77 354-hm² area.

Areal estimates of the major cover types obtained by photointerpretation were compared, on a quadrangle-by-quadrangle basis, to the areal summary based on computer-aided analysis of EREP data. This comparison resulted in a correlation coefficient of 0.929. Hoffer (ref. 2-5) stated that this correlation was particularly significant because it indicated (together with similar results obtained from Landsat-1) that reliable areal estimates can be obtained by using computer-aided analysis of satellite data, even for areas of rugged mountainous terrain. It was also noted that, for areal estimates obtained from computer classifications, commission and omission classification errors tended to balance, particularly as the geographic areas involved became larger. A similar comment concerning such areal estimates was made by Sattinger et al. (ref. 2-18).

Urban land use mapping with use of S192 thermal-infrared data.—Although relatively few detailed urban-mapping studies with S192 data were undertaken, several investigators concentrated their efforts on the value of the thermal-infrared band because it provided a type of data that could not be obtained with the higher resolution EREP photographic systems.

The thermal-infrared band and a density-slicing technique were used by Hannah et al. (ref. 2-2) to map Orlando, Florida. The resultant thermal map indicated that the thermal radiance is highest for commercial-industrial regions, next highest for "modern" residential
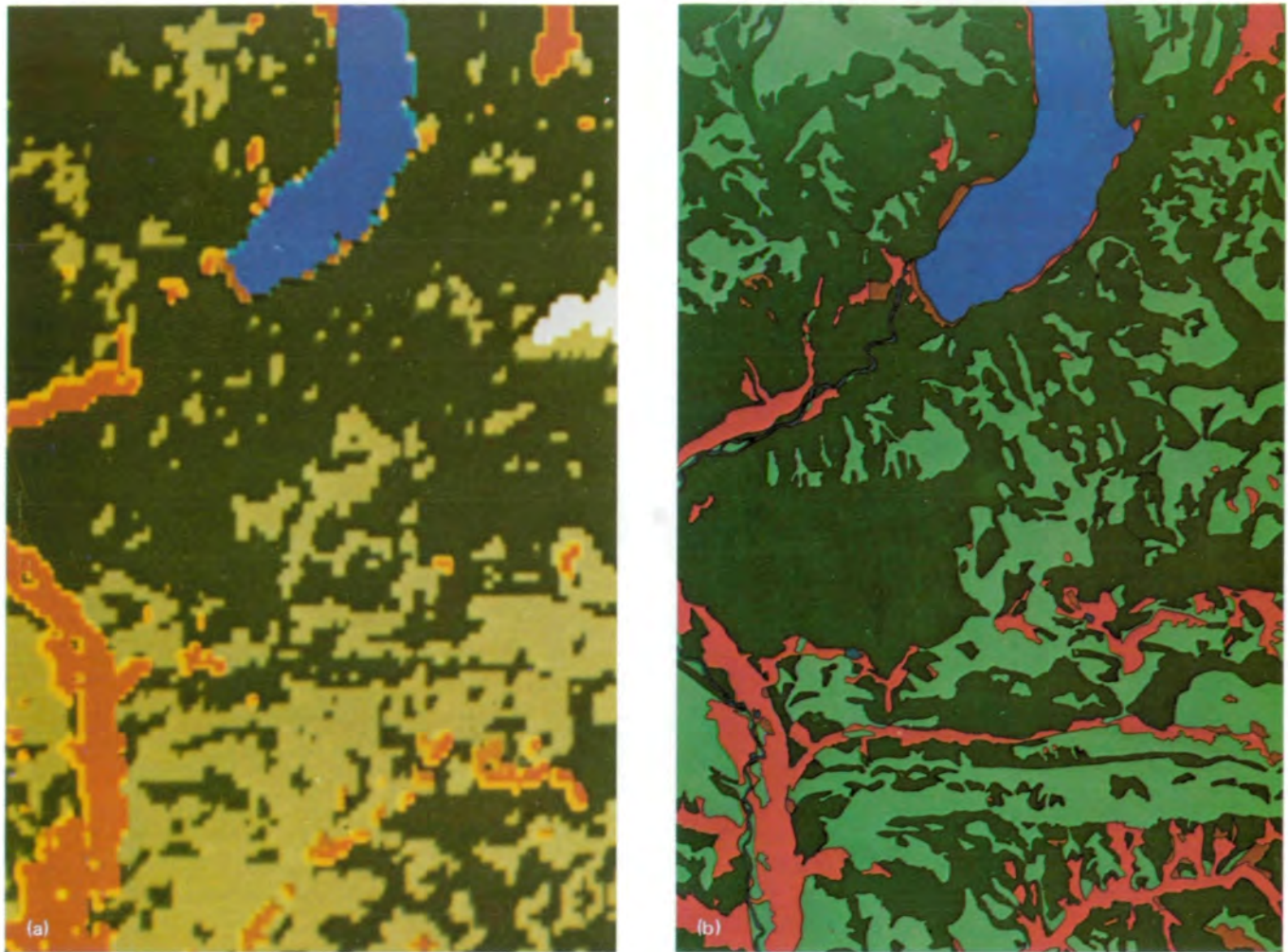
Explanation

White	Snow	Red	Grassland	N
Blue	Water	Brown	Exposed rock and soil	0 5
Dark green	Coniferous forest	Yellow	Mixed	Scale, km
Light green	Deciduous forest			

FIGURE 2-12.—Comparison between major cover types obtained by computer classification of S192 data (fig. 2-12(a)) and those obtained by manual interpretation of aerial photographs (fig. 2-12(b)) of the Vallecito Reservoir study area in southwestern Colorado. The reservoir is at the top. (a) Computer classification. (b) Manual interpretation.

areas having relatively few trees, and less for more wooded residential areas. The commercial-industrial sectors were identified and enhanced by computer-aided analysis of the thermal-infrared data. In this geographical area, even the "modern" residential and wooded residential areas were distinctly defined by this density-slicing technique. Hannah concluded that this type of "a thermal radiance map might be used to

classify sectors according to their environmental impacts (relative to amounts of trees and other vegetation and concrete) and certainly can be utilized by planners as a graphic indication of the value of landscaping."

Alexander and Lins (ref. 2-11) studied the Skylab S192 thermal-infrared data as a source of information on urban climates and surface energy balance in urbanized areas. In their experiment, a combination of

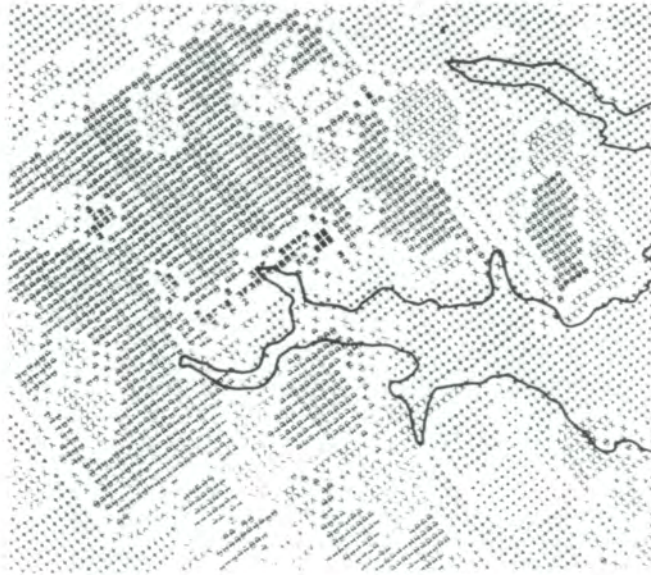| Cover-type category	No. of samples	No. of test-area samples classified as —						Percent classified correctly
		Water	Snow	Grassland	Deciduous forest	Coniferous forest	Rock/soil	
Water	96	91	0	0	0	5	0	94.8
Snow	112	0	112	0	0	0	0	100.0
Grassland	128	0	0	67	28	33	0	52.3
Deciduous forest	368	0	0	0	227	132	9	61.7
Coniferous forest	1696	0	2	1	132	1542	19	90.9
Totals	2400	91	114	68	387	1712	28	ᵇ85

ᵃBands 2, 7, 9, and 11 (optimum four).

ᵇOverall performance (2039/2400) = 85.0 percent.

modeling and observational techniques was used to assess the application of remote sensors to improve understanding of the relationships between surface properties and the mesoclimates of urbanized regions. Because drastic changes in land use, such as land clearing and urbanization, often have a significant climatic impact on urbanized areas, this study was undertaken to derive information useful for land use planners who are required to consider energy use and climatological effects of proposed changes in their planning jurisdictions.
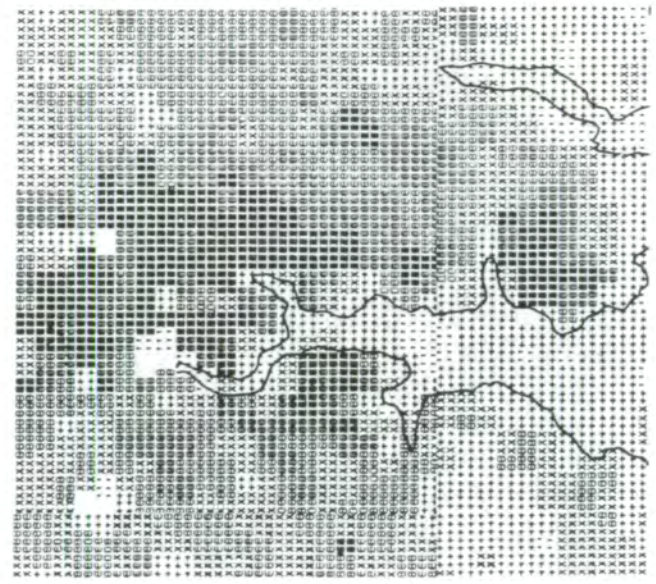
TABLE 2-IX.—Areal Estimates for Major Cover Types in the Colorado Granite Peaks Test Site Based on Computer Classifications of Skylab S192 Data

Cover-type category	No. of scanner resolution elements	Area, hm²
Water	2 064	959
Snow	16 852	7 828
Grassland	3 397	1 578
Coniferous forest	109 975	51 086
Deciduous forest	31 370	14 572
Exposed rock and soil	2 865	1 331
Totals	166 523	77 354

The climate of an urbanized region has been described simplistically as a group of heat islands set in a matrix of cooler, nonurban areas. The study of such heat islands clearly involves more than the analysis of the surface thermal state. The overall reflectance of an area will control the amount of energy being absorbed by the surface and thus affect the net radiation, which is the balance between energy absorbed and energy emitted. If one is limited to the use of ground-based data collection techniques, effective and accurate net radiation measurements over different locations and conditions are extremely difficult to obtain. The S192 scanner system, however, provided an effective method for obtaining a broad variety of data on cover types and conditions. The 10.2- to 12.5-μm band was calibrated by using a variety of reference data to correct for atmospheric effects. Alexander and Lins (ref. 2-11) then generated a map that showed the distribution of surface-radiation temperatures in the Baltimore, Maryland, area for the August 5, 1973, Skylab overpass (fig. 2-13(b)). The corresponding portion of an S190B photograph (fig. 2-13(a)) is shown for comparison. The radiation-temperature map shows the value of the synoptic view obtained from spacecraft altitudes for this type of study. The hypothesized urban heat islands are easily identified on the map, and the relative coolness of nonurban land is effectively documented. Thermal patterns and absolute values of radiation levels were obtained, documented, and later used to test the simulated model of

Absolute value range applying to each level
(maximum included in highest level only)

Minimum surface radiation temperature, K (°C)

| 293.15 | 295.98 | 298.82 | 301.65 | 304.48 | 307.32 |
| (20.00) | (22.83) | (25.67) | (28.50) | (31.33) | (34.17) |

Maximum surface radiation temperature, K (°C)

| 295.98 | 298.82 | 301.65 | 304.48 | 307.32 | 310.15 |
| (22.83) | (25.67) | (28.50) | (31.33) | (34.17) | (37.00) |

| Level | 1 | 2 | 3 | 4 | 5 | 6 |

(c)

Surface radiation
temperature, K (°C)

| | 298 | 301 | 304 | 307 | 310 | 313 |
| | (25) | (28) | (31) | (34) | (37) | (40) |

No. of cells

| 377 | 1237 | 4121 | 2748 | 1277 | 372 | 168 |

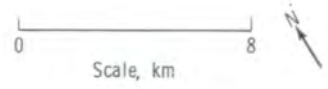| Level | 1 | 2 | 3 | 4 | 5 | 6 |

(b)

FIGURE 2-13.—An S190B photograph and computer-generated temperature maps of the Baltimore, Maryland, area. Chesapeake Bay protrudes from the right. The white patches in the photograph are clouds. (Original scale, 1:250 000.) (a) Small portion of an S190B photograph taken August 5, 1973, showing the surface features (SL3-83-166). (b) Computer-generated thermal-infrared surface-radiation-temperature map obtained from S192 data band 13. (c) Computer-generated, simulated surface-radiation-temperature map.

0 ——————— 8
Scale, km

the area (fig. 2-13(c)). These results indicate the value of such thermal-infrared data for observing the actual temperature characteristics of an urban area, despite the fact that the quality of these particular thermal-infrared data was less than optimal for the thermal-mapping purposes. Alexander and Lins (ref. 2-11) also noted that the conical scan pattern of the S192 scanner system was very desirable for this type of work because it enables maintenance of an optimal path of constant length for the scanner data.

A simulation experiment using the thermal-map information was conducted on the basis of the concept that each land use type has a particular mix of surface cover and building configuration associated with it. Therefore, if a land use map with an appropriate classification scheme is available, it should be possible to use the distribution of significant surface-cover characteristics in modeling the energy balance and distribution. The surface characteristics used by Alexander and Lins (ref. 2-11) as input for the energy balance model studies were (1) the building configuration, which provides information related to the surface roughness and solar radiation calculations; (2) the surface "wet fraction"; (3) the substrate thermal diffusivity and conductivity; (4) the surface albedo; and (5) the surface emissivity. The values of these factors for each different land use category were calculated and used as input to the model on the basis of the land use map of the test area.

A comparison of the S192-derived and the simulated surface-temperature maps (figs. 2-13(b) and 2-13(c), respectively) shows that the general heat distribution within the city of Baltimore is similar to that of outlying residential and commercial areas. Although both maps show the same generalized patterns of temperature distribution, differences are apparent in the shape of individual features. The map obtained from the S192 data has much more complex and intricate patterns than those on the simulated map. Also, the simulated map temperatures are as much as 6 to 8 K lower than the temperatures on the S192 map for the area in the center of the city heat island. Alexander and Lins stated that there is a considerable potential for further improvements in simulation-map studies through the use of such thermal-infrared scanner data. The results also indicated that the input from the land use map used for the simulation model did not have sufficient detail concerning phenomena that affect surface temperature.

The land use classes mapped in the simulation study tend to generalize many features such as houses, streets, lawns, forests, and fields.

Although the results of the S192 data analysis showed a potential urban application of a simulated surface-radiation-temperature map, the investigation indicated a need for further definition of those phenomena that affect surface temperature. In essence, the land use categories mapped may not represent the distribution of the features that actually affect the surface-temperature regime or the surface-energy-exchange phenomenon with sufficient realism. Consequently, the investigators recommend further work to refine and develop a more detailed classification for land cover that can be effectively used for climatological purposes.

An integral part of the land use investigation by Silva (ref. 2-14) over an area in northeastern Indiana was the analysis of S192 data obtained on January 25, 1974, for the city of Fort Wayne, Indiana. The land use classes involved were residential, commercial-industrial, hard surfaces (parking lots and runways), grass-covered areas (pastures, winter wheat, and golf courses), bare land, forest/snow, water, and snow. The analysis procedures Silva used were basically the same as those discussed in the preceding subsection. The classification performance of the scanner resolution elements, or pixels, used to train the computer is shown in table 2-X. The optimum combination consists of four wavelength bands—one band in the visible wavelength region (band 4, 0.56 to 0.61 μm), one in the near infrared (band 8, 0.98 to 1.08 μm), one in the middle infrared (band 11, 1.55 to 1.75 μm), and one in the thermal infrared (band 13, 10.2 to 12.5 μm). This combination resulted in an overall training-pixel classification performance of 90 percent. When the thermal-infrared band was excluded, the accuracy of the same training pixels decreased to 80 percent. When the middle-infrared band was excluded, a visible band (the only one available in this data set), two near-infrared bands, and the thermal-infrared band were selected for use; and the resultant classification performance was 79 percent. This comparison indicates the value of both the thermal-infrared and the middle-infrared wavelength bands in this land use classification sequence. One of the most significant results is seen in the extremely poor classification performance (even for the training data) of the residential and commercial-industrial land use classes when the thermal-infrared wavelength band is

TABLE 2-X.—Training-Pixel Classification Performance

Land use category	No. of training pixels	Percent classified correctly		
		Optimum four bands overall (4, 8, 11, 13)	Optimum four bands exclusive of thermal infrared (4, 7, 8, 11)	Optimum four bands exclusive of middle infrared (4, 8, 9, 13)
Residential	175	92	65	82
Commercial-industrial	61	95	18	90
Hard surface	52	73	71	52
Grass	141	90	89	81
Bare land	459	95	93	89
Forest/snow	81	79	86	54
Water	152	80	77	58
Snow	25	96	92	92
Overall performance	[a]1146	90	80	79

[a]Total number of training pixels.

not used. These two urban classes alone would account for most of the decrease in overall performance from 90 to 80 percent.

The importance of the thermal-infrared wavelength band in discriminating the urban land use classes from the other cover types is shown in figure 2-14. In these wintertime S192 data, the commercial and industrial classes and, to a somewhat lesser extent, the residential class have equivalent black-body temperatures significantly higher than those of the other land use classes. The effect of these parameters on determining area percentage of land use classes with S192 bands is shown in table 2-XI. Comparing the area estimates of the various land use classes obtained by the computer classification over the entire test site to the area estimates developed by conventional methods used by county and city planning agencies offers a procedure to establish the quality of the results. Such a method was pursued in this study and was found to be especially useful for showing the value of the thermal-infrared band in this analysis involving an urban area. Comparison of the computer-derived areal estimates with those provided by the county and city agencies for the five major categories in the data shows that the estimates obtained by using the thermal-infrared data for band 13 approximate the estimates provided by the city and the county. The differences in the urban class can be explained, for the most part, by the differences in the cover types that were included in the urban area. For example, cover
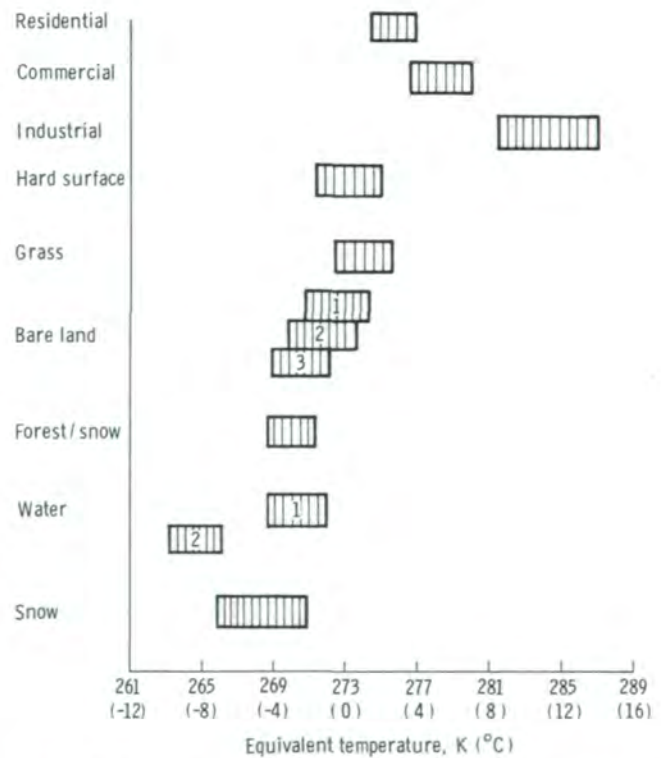

FIGURE 2-14.—Equivalent black-body temperatures computed from the S192 thermal-infrared band for training classes. Values include the mean plus or minus one standard deviation. Multiple classes are shown for bare land and water.

types such as golf courses and parks were classified, according to the data provided by the county and city agencies, as urban area; but these cover types were classified as grassland in the computer classification and therefore grouped with the winter wheat as agricultural land. The area classified as snow was largely agricultural land. The underestimate of commercial and industrial area was largely due to classification errors such as the railroad right-of-way through Fort Wayne; the right-of-way was considered as commercial in the estimates provided by the city but was classified by the computer as bare soil. Also, the Allen County Planning Commission estimates for the industrial and commercial category included the areas owned by businesses or industries (i.e., buildings, parking lots, and landscaped property). In the computer classification, the buildings themselves were largely delineated as commercial or industrial and the crushed stone lots as hard surface, or the asphalt parking lots were often identified as being residential. These results provide some insight into the comments by several of the investigators that the land use classes designated by user groups or USGS Circular 671 (ref. 2-1) often may not coincide with the cover types that can be spectrally discriminated by using remotely sensed data.

As in table 2-X, the value of the thermal- and middle-infrared wavelengths for accurate identification of land use classes, particularly the urban classes, is shown in table 2-XI. Absence of the thermal-infrared band causes a very significant overestimation of the area in the urban category. With the thermal- and middle-infrared bands present, the areal estimates obtained by computer classification compare favorably with those obtained by conventional techniques.

Comparison of Skylab S192 and Landsat multispectral scanner analyses.—Several investigators compared classification results obtained by using Skylab S192 and Landsat data. In essentially every case, both Level I and Level II land use cover types could be mapped with approximately the same overall degree of accuracy by using either the Skylab or the Landsat data. In general, the investigators found that the wavelength bands above 1.1 μm, which were available on the Skylab data but not on the Landsat data, were frequently selected by the various computer analysis routines as being very important and valuable bands to use in the classification. The data quality generally was much better for the Landsat data being used than for the Skylab data. The results did indicate that the improved spectral resolution available with the Skylab S192 data enabled improvement in classification accuracy.

One of the more precise comparisons between classification results obtained by using the Skylab S192 data and the Landsat data was accomplished by Hoffer

TABLE 2-XI.—Land Use Area Percentage Estimates for Major Portion of Allen County, Indiana

Land use category	Area estimate, percent (b)			
	Local Allen County reference data [a]	Skylab 4 S192 data		
		Optimum four bands overall (4, 8, 11, 13)	Optimum four bands exclusive of thermal infrared (4, 7, 8, 11)	Optimum four bands exclusive of middle infrared (4, 8, 9, 13)
Urban	12.6	9.9	27.7	7.3
Residential	(10.1)	(9.1)	(26.7)	(6.8)
Commercial-industrial-hard surface	(2.5)	(.8)	(1.0)	(.5)
Agricultural/forest	85.6	85.6	68.1	87.3
Water	—	1.4	1.4	1.6
Other land	1.8	—	—	—
Snow	—	3.1	2.8	3.8

[a] Data from the Allen County Planning Commission and the Fort Wayne Department of Community Development and Planning.

[b] Values in parentheses are subtotals.

(ref. 2-5). For this effort, a frame of Landsat data was used that had been digitally registered to both the S192 data and to a USGS 7.5′ quadrangle map base with a reasonably high degree of precision (±1 pixel). The Skylab S192 and Landsat data were obtained on the same day (within 2.5 hours) and under completely cloud-free conditions. Statistically defined grids of the test area (each, four by four pixels in size) were used to evaluate the classification results so that they could be quantitatively compared for exactly the same resolution elements on the ground with use of the different data sets.

Three classifications were conducted. First, the major cover types present in the area were classified by using the four optimum wavelength bands of Skylab S192 data (bands 2, 7, 9, and 11, as determined by the divergence algorithm). Second, the four S192 wavelength bands that most closely corresponded to the four Landsat bands (bands 3, 5, 6, and 8) were used to classify the data. Third, the Landsat data were classified.

Silva (ref. 2-14) followed a very similar procedure for comparing Skylab S192 and Landsat data obtained over a test site in central Indiana. In his study, the Landsat data were obtained a day before the Skylab data were obtained, and the two data sets were not digitally registered. The test blocks for Silva's study involved hand-selected test areas rather than a statistically defined grid. The basic approach was the same, although the optimum four Skylab bands used by the authors were different.

The overall results of these two land use studies are shown in table 2-XII. The four optimum combinations of wavelength bands from Skylab data produced classification results that were almost identical in both investigations. In both studies, the four wavelength bands of Skylab data that most closely corresponded to the Landsat bands produced less accurate results than those obtained using the actual Landsat data. Considering that the cover types were rather different in the two test locations, it is significant that the results of both comparisons are approximately the same. The Colorado

TABLE 2-XII.—*Comparison of Classification Performances Using Skylab and Landsat Multispectral Scanner Data*

Data	Wavelength bands used	Overall classification performance, percent	
		Hoffer's results [a] (ref. 2-5)	Silva's results [b] (ref. 2-14)
Optimum four wavelength bands of Skylab data	0.46 to 0.51, 0.78 to 0.88, 1.09 to 1.19, and 1.55 to 1.75 μm[c] (bands 2, 7, 9, and 11)	85.0	87
Skylab data using wavelength bands that correspond to Landsat	0.52 to 0.56, 0.62 to 0.67, 0.68 to 0.76, and 0.98 to 1.08 μm (bands 3, 5, 6, and 8)	82.5	80
Landsat data	0.5 to 0.6, 0.6 to 0.7, 0.7 to 0.8, and 0.8 to 1.1 μm (bands 4, 5, 6, and 7)	85.7	88

[a]Cover types were coniferous forest, deciduous forest, grassland, water, and snow.

[b]Cover types were residential, commercial-industrial, extractive, soil, grass, deciduous forest, coniferous forest, river, and lake.

[c]For Silva's data, the optimum combination of four wavelength bands included the 0.52- to 0.56-μm band (3) rather than the 0.46- to 0.51-μm band (2), and the 0.98- to 1.08-μm band (8) rather than the 1.09- to 1.19-μm band (9). In both cases, these bands are adjacent to those used by Hoffer. The other two bands were identical in both studies.

site (Hoffer, ref. 2-5) involved complex mountainous terrain consisting primarily of forest and rangeland cover types, whereas the Indiana test site (Silva, ref. 2-14) involved urban and agricultural cover types.

Both investigators concluded that the better spectral resolution and the extended spectral range of the Skylab S192 scanner contributed to an improvement in classification performance. This improvement was indicated by the difference in the classification results obtained by using the best four wavelengths that corresponded to the Landsat scanner systems. The fact that the Skylab data did not yield better classification results than the Landsat data was attributed to the noisy characteristics of the Skylab data. The investigators believed that the results obtained indicated the importance of good-quality data, the value of using the optimum combination of fairly narrow, properly located spectral bands for cover-type mapping, and the value of using computer-aided analysis techniques.

Polcyn et al. (ref. 2-17) also conducted a comparison of Skylab and Landsat classification results, for a test site in Ontario, Canada. The percentage of the total area classified into the various cover types by using four S192 bands (bands 4, 5, 7, and 13; 0.56 to 0.61, 0.62 to 0.67, 0.78 to 0.88, and 10.2 to 12.5 μm, respectively) was compared with the Landsat data classification. The results indicated that a reasonably similar classification was obtained with both data sets. A detailed comparison with aerial photographs indicated that both Skylab and Landsat data had enabled achievement of a reasonable classification, with some variation among categories within both data sets. The most severe misclassification occurred with the Landsat data in the manmade category of cover types. Overrecognition occurred, and, in general, the bare soil category caused the most confusion. It was concluded that the Skylab S192 and Landsat data appeared to be reasonably equivalent in terms of information content and distinction of the various cover types in the area involved. Most of the difference in the percentage of the area recognized as particular classes can be accounted for by differences in the training-set signatures used rather than by any fundamental difference in the information content in the spectral data from the scanner system.

Cover-type maps of the Green Swamp area in Florida were generated with the use of both Landsat and Skylab S192 data (Higer et al., ref. 2-16). The resulting classifications were representative of the cover types present, and the vegetation maps produced from S192 and Landsat categorized data were in accord with county land use maps by 82.8 and 87.2 percent, respectively. Hannah et al. (ref. 2-2) stated that computer classification of S192 data over an urban area (Orlando, Florida) resulted in cover-type maps that were of generally comparable quality to those previously obtained from Landsat.

To summarize, the comparison of Skylab and Landsat classification results showed that the increased number of spectral bands of the Skylab scanner system enabled definition of a better combination of four wavelength bands for computer analysis.

Wavelength band evaluation.—Detailed investigations were conducted to determine the combinations of wavelength bands that are optimum for land use mapping. This subsection is a brief summary of some of these results. The reports by Hoffer, Silva, and Simonett (refs. 2-5, 2-14, and 2-10, respectively) are particularly detailed on this subject.

In the initial phases of Hoffer's investigation of the use of S192 data in mountainous terrain, different approaches and techniques were applied to define the data quality of the different bands. These analyses resulted in a numerical data-quality index for each wavelength band (table 2-XIII). To interpret the numerical values, a quantitative evaluation designation was also defined. Comparison of the data-quality indexes with the imagery of the individual wavelength bands showed that, in several cases, the visual appearance of the imagery or the qualitative evaluation (table 2-XIII) was not a reliable indication of the spectral information content of the data. The investigators stated that the quality of multispectral scanner data can be effectively evaluated only by quantitative evaluation techniques (rather than qualitative techniques) if the data are to be analyzed by computer.

Another phase of Hoffer's investigation (ref. 2-5) was directed to determining the number of wavelength bands required for effective classification with use of the S192 data. Previous work has indicated that, as the number of wavelength bands increases, the classification performance initially increases rapidly when four to six wavelength bands are used but increases at a slower rate above this number. The amount of computer time required to classify the data increases significantly for more than four to six bands, as shown in figure 2-15. The effect of increasing the number of

TABLE 2-XIII.—*Data-Quality Evaluation Results*

[From ref. 2-5]

Spectral region	Band no.	Wavelength band, μm	Qualitative evaluation designation	Quantitative data-quality index	Quantitative evaluation designation
Visible	1	0.41 to 0.46	Very poor	7.1	Fair
	2	0.46 to 0.51	Poor	2.0	Good
	3	0.52 to 0.56	Very good	1.8	Very good
	4	0.56 to 0.61	Poor	14.8	Poor
	5	0.62 to 0.67	Fair	12.1	Poor
Near infrared	6	0.68 to 0.76	Fair	4.1	Fair
	7	0.78 to 0.88	Very good	2.2	Good
	8	0.98 to 1.08	Very good	5.6	Fair
	9	1.09 to 1.19	Very good	1.8	Very good
	10	1.20 to 1.30	Good	6.2	Fair
Middle infrared	11	1.55 to 1.75	Very good	1.6	Very good
	12	2.10 to 2.35	Good	2.9	Good
Thermal infrared	13	10.2 to 12.5	Poor	11.8	Poor

wavelength bands on performance results was tested on the S192 data. The divergence algorithm was used to determine the optimum combination of 1 to 13 wavelength bands. The data were then classified by using the maximum-likelihood algorithm. The results of this analysis indicated that classification performance was not significantly improved when more than four wavelength bands were used (fig. 2-16). These results were based on test-area classification performance for both major and forest cover types. The overall classification accuracy for the major cover types as a function of the number of wavelength bands is shown in table 2-XIV. For this data set, the 1.09- to 1.19-μm wavelength band in the near infrared was the single most valuable wavelength band. The best combination of four wavelength bands consists of one in the visible region (the 0.46- to 0.51-μm band, which, in table 2-XIII, was indicated to be visually of qualitatively poor data quality), two in the near-infrared region (the 0.78- to 0.88-μm and 1.09- to 1.19-μm bands), and one in the middle-infrared region (1.55 to 1.75 μm). The best

combination of six wavelength bands consists of two in the visible, two in the near infrared, one in the middle infrared, and one in the thermal infrared. Furthermore, detailed studies indicated that various combinations of four wavelength bands were required to achieve optimal classification performance for different individual cover types. The near-infrared portion of the spectrum (especially the 1.09- to 1.19-μm wavelength band) was shown to be of particular value for effective vegetation mapping. The relative importance of the different spectral regions and the individual wavelength bands varied significantly as a function of the cover types to be mapped.

Simonett (ref. 2-10), using a series of statistical procedures, also found that the 1.09- to 1.19-μm wavelength band was the most valuable single band for discriminating among land use categories. For overall land use mapping, in order of ranking, the most useful six spectral bands were band 9 (1.09 to 1.19 μm), band 3 (0.52 to 0.56 μm), band 6 (0.68 to 0.76 μm), band 1 (0.41 to 0.46 μm), band 11 (1.55 to 1.75 μm), and band
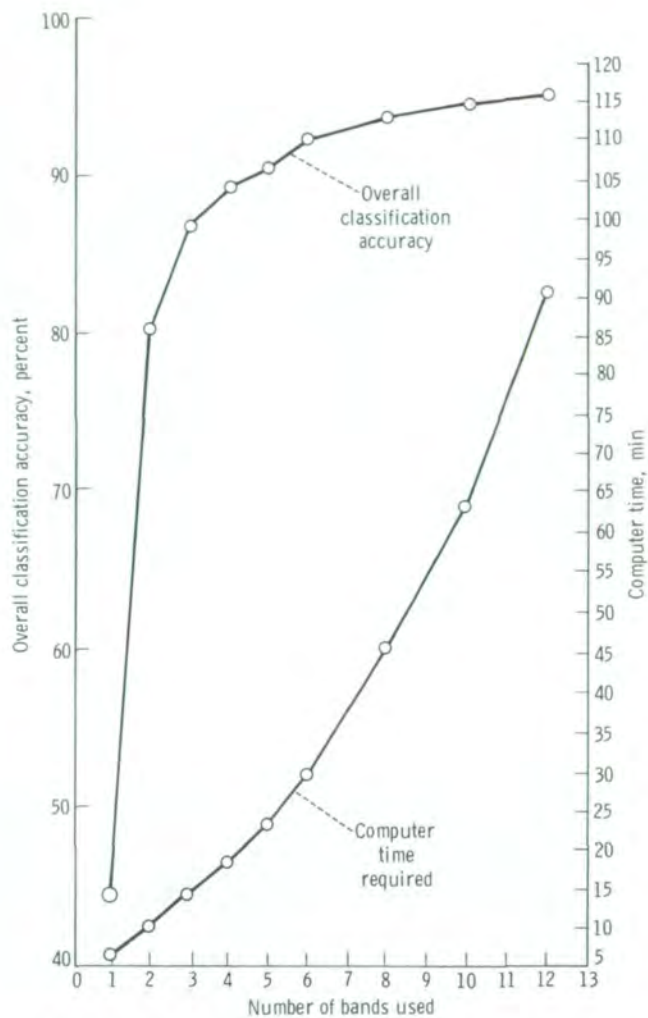
FIGURE 2-15.—Overall cover-type-classification accuracy and computer-processing time required compared to number of S192 bands used.
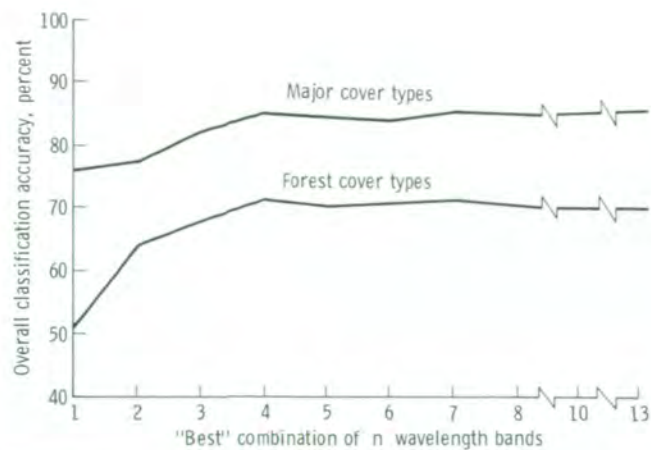

FIGURE 2-16.—Overall classification accuracy as a function of the number of S192 wavelength bands used for classifying two levels of detail of land use information.

13 (10.2 to 12.5 μm). The results indicated that the optimal spectral bands identified for discriminating among general land use categories were significantly different from the spectral bands identified for discriminating within specific land use categories.

Different sets of spectral bands were selected when analyzing different groups of Level II land use categories (all belonging to the same Level I land use catego-

ry). The following sets of spectral bands were selected as providing the best discrimination.

Category	Bands
Urban	9,3,11,6,13
Agricultural	9,7,1,11,6
Forest	9,3,5,4,11
Water	6,1,3,8,9
Wetlands	10,3,1,8,6

Silva's wavelength-band study (ref. 2-14) also included an evaluation of the various combinations of wavelength bands and a comparison of interim and filtered S192 data sets. These results are summarized in table 2-XV. Silva's results emphasize the value of the middle-infrared wavelength band (1.55 to 1.75 μm), the near-infrared bands (0.78 to 0.88 μm and 0.98 to 1.08 μm), and the visible band (0.46 to 0.51 μm) for identifying land use classes on the Skylab 2 data obtained on June 10, 1973. The combination of the thermal-infrared band (10.2 to 12.5 μm), the middle-infrared band (1.55 to 1.75 μm), and the visible band (0.56 to 0.61 μm) was particularly useful in analysis of the Skylab 4 data obtained on January 25, 1974. As these results indicate, there is no single set of bands that is best under all circumstances.

TABLE 2-XIV.—Optimal Wavelength Bands for Major-Cover-Type Classification Using Skylab S192 Data Obtained on June 5, 1973

Spectral region	Band no.	Wavelength band, μm	Data-quality index	Optimum wavelength-band combinations [a]									
				1	2	3	4	5	6	7	8	10	13
Visible	1	0.41 to 0.46	7.1								X	X	X
	2	0.46 to 0.51	2.0		X	X	X	X	X	X	X	X	X
	3	0.52 to 0.56	1.8									X	X
	4	0.56 to 0.61	14.8					X	X	X	X	X	X
	5	0.62 to 0.67	12.1										X
Near infrared	6	0.68 to 0.76	4.1										X
	7	0.78 to 0.88	2.2			X	X	X	X	X	X	X	X
	8	0.98 to 1.08	5.6										X
	9	1.09 to 1.19	1.8	X	X	X	X	X	X	X	X	X	X
	10	1.20 to 1.30	6.2									X	X
Middle infrared	11	1.55 to 1.75	1.6					X	X	X	X	X	X
	12	2.10 to 2.35	2.9							X	X	X	X
Thermal infrared	13	10.20 to 12.50	11.8						X	X	X	X	X
Overall classification performance, percent				75.7	76.8	81.9	85.0	84.1	83.7	85.3	84.1	85.2	86.0

[a]Band 9 was selected as the single best wavelength band, bands 9 and 2 were selected as the two best wavelength bands, etc.

TABLE 2-XV.—Optimum Combinations of Wavelength Bands for Mapping Land Use in Indiana

[Skylab 2 data]

No. of bands	Bands of optimum value [a]	
	Interim data set	Filtered data set
1	11	11
3	1, 2, 11	1, 2, 11
4	3, 7, 9, 11	2, 7, 8, 11
5	2, 3, 7, 9, 11	2, 7, 8, 9, 11
6	2, 3, 7, 9, 10, 11	2, 7, 8, 9, 10, 11

[a]Band 13 was not available in the interim data set, and bands 4, 5, 6, and 12 were not available in the filtered data set.

The results reported by Silva (ref. 2-14) (and partly summarized in table 2-XI) demonstrate the value of the thermal- and middle-infrared wavelengths for obtaining accurate areal estimates of the urban land use class (particularly the residential). The S192 data had been obtained during the winter when some snow was on the ground. In this area, the optimum combination of four wavelength bands (4, 8, 11, and 13) resulted in an areal estimate for the urban residential area of 15 000 hm^2, compared to 16 900 hm^2 estimated by the Fort Wayne Department of Development and Planning. When the thermal-infrared wavelength band was not used, the classification resulted in a residential areal estimate of 43 850 hm^2. Without the middle-infrared data (when using one visible, two middle-infrared, and the thermal-infrared bands), the areal estimate based on the computer classification was 11 200 hm^2, compared to 15 000 hm^2 when all four major spectral regions were represented.

In the Higer et al. study (ref. 2-16) of the Green Swamp (which involved mostly vegetation, wetlands, and water categories), the five wavelength bands that provided the largest contribution to the categorization of the cover types present were, in order of preference, bands 11, 8, 2, 10, and 6. Band 11 was particularly important for identifying vegetation; specifically, Higer indicated that the thermal-infrared band would also be very useful but that, in this case, it was excessively noisy. This investigator noted that bands 8, 9, 10, and 11, which, except band 8, are beyond the range of the Landsat scanner system, were "useful in detection and categorization of cover types in the Green Swamp."

Individual wavelength bands of S192 imagery obtained over several test sites in North Carolina were examined by Welby and Lammi (ref. 2-13), using a density-slicing technique. Their results showed that various vegetative cover types could be separated best by using the near-infrared wavelength bands, which were also fairly effective for separating the cropland areas from forest cover and in defining the boundaries between vegetation and water features.

A color-additive viewer was used by Welby and Lammi to combine selected wavelength bands of the S192 imagery. Their work showed that different combinations of wavelength bands produced variable results in terms of spectral discrimination of cover types or land use categories. They concluded that working with combinations of wavelength bands through use of the color-additive viewer was more effective than analysis of individual wavelength bands and that many of the cover types present could be effectively separated by using this technique. A particularly important conclusion was that "the breaking of the near-infrared portion of the spectrum into a series of relatively narrow bands appears to be a very useful approach to acquisition of earth resource information."

Welby and Lammi identified some of the complexities encountered in attempting to manually interpret and analyze many individual wavelength bands of multispectral scanner imagery. There are many wavelength bands to be considered, and distinct differences in reflectance levels are often found in different wavelength bands in the same spectral region (near infrared, in this case) for the various cover types of interest. These results also tended to emphasize the value of several discrete wavelength bands in the near-infrared portion of the spectrum. If differences in infrared reflectance among the cover types of interest were not present in one wavelength band, another band would enable effective discrimination.

To summarize, the wavelength-band evaluations showed that the optimum wavelength bands for effective classification of various land use cover types are the 1.09- to 1.19-μm band in the near-infrared region, the 1.55- to 1.75-μm band in the middle-infrared region, and the 10.2- to 12.5-μm thermal-infrared wavelength band. Also, each of the four major spectral regions (visible, near infrared, middle infrared, and thermal infrared) is significant with respect to accurate classification, and the importance of each region varies as a function of the cover type and scene characteristics.

Environmental Studies

The discussion on selected environmental studies includes strip mining, wetland mapping and ecology, and migratory waterfowl habitat evaluation.

Strip mining.—Increased energy demands have resulted in accelerated strip-mining activities, the environmental effects of which are of increasing concern. Estimates in 1970 of accumulated coal production (3992 Tg) from strip mining were slightly more than 3 percent of the total estimate of strippable coal reserves (116 119 Tg) in the United States. The potentially disturbed land areas (those to be strip mined) are estimated to exceed an area larger than the combined size of Pennsylvania and West Virginia. The photograph in figure 2-17 is an example of strip-mining endeavors covering an extensive area in Alabama. On the basis of the growing pressure to increase coal production, it is apparent that a more effective and efficient methodology will be required to map disturbed mining areas and to monitor mining and reclamation activities.

Skylab EREP investigations have provided substantial and positive evidence that remote-sensing data, specifically spacecraft-acquired photographs, can be of value in the overall planning, detection, and monitoring of surface mining activities. The Skylab strip-mining studies are of two major types: (1) the detection and mapping of disturbed areas and (2) the identification
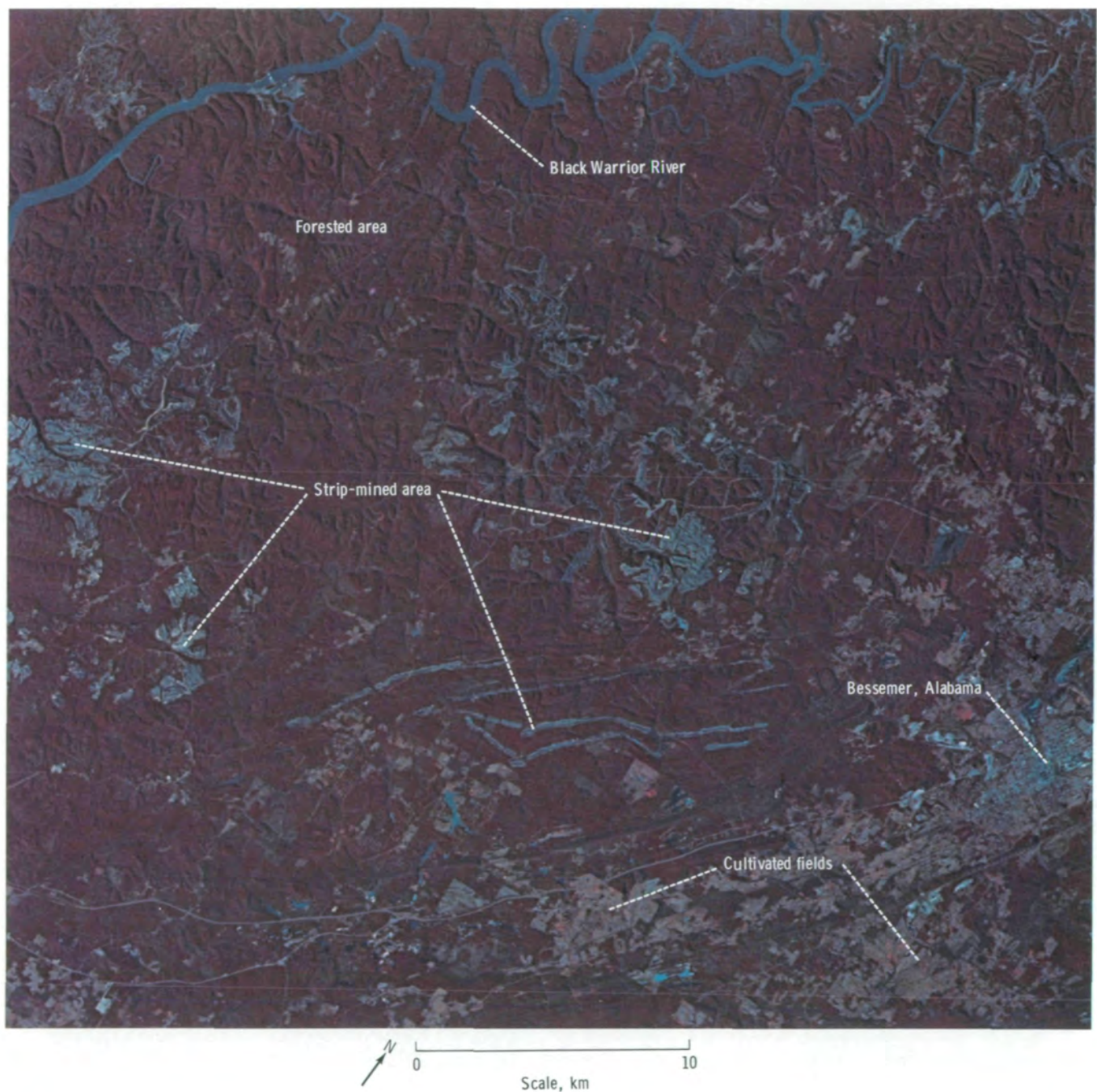
FIGURE 2-17.—A portion of an S190B color-infrared photograph illustrating the extent of strip-mining activities in an area west of Birmingham, Alabama. The well-defined boundaries formed by the strip-mining operations and the natural vegetation should be noted. Two distinctly different stripping patterns are easily discerned (SL4-93-152).

and interpretation of key physical features that are necessary to monitor the components of ongoing strip-mining operations and reclamation activities.

The simplified photointerpretation technique used by Brooks and Parra (ref. 2-19) requires the use of S190B 2× color positive transparencies, an overhead projector, and a white poster board as the projection screen. It enables mining officials who do not have extensive photointerpretation backgrounds or expensive scanning equipment to outline, on the basis of color tones and density patterns, salient strip-mining features (fig. 2-18).

Weir et al. (ref. 2-20) have shown that a 1:100 000-scale black-and-white S190B enlargement (made from color film) is satisfactory for accurately mapping past and current surface mines and for detecting several classes of reclamation assessment. Cultural details at this scale were adequate for preparation of new base maps or updating existing topographic maps that were enlarged from a 1:24 000 scale.

Disturbed strip-mining areas could be detected and discriminated on both S190A and S190B infrared photographs. For monitoring surface mining activities, S190B photographs, having high spatial resolution and spectral discrimination, provided the more detailed interpretation results for useful monitoring practices.

The Coshocton County, Ohio, S190B color-infrared photographs were used by Baldridge et al. (ref. 2-12) to define four major strip-mining-land categories: (1) active areas, (2) orphaned or abandoned land, (3) areas undergoing reclamation or restoration, and (4) natural or planned reclaimed lands. The regrading of stripping operations was the most apparent feature observed on the color-infrared images. Areas covered by varying degrees of vegetation, high walls, and water impoundments were also identified. Baldridge et al. stated that land that had been thickly revegetated had the appearance of being completely reclaimed and was difficult to identify as having been stripped. In some areas, high walls and pond water remained to indicate past stripping operations.
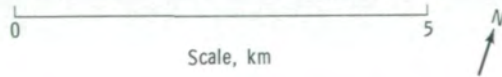
Table 2-XVI is a summary of key features identified by Baldridge, Brooks, and Weir (refs. 2-12, 2-19, and 2-20, respectively). Their results illustrate the positive attributes of using S190B-type photographs. The three

investigators used S190B enlargements to discriminate various categories of mining activity and reclamation (vegetation stages, refuse areas and slurry ponds, water bodies, high walls, haulage roads, unmined areas, orphaned areas, and possible acid drainage effects).

The most effective imagery scales for strip-mining and reclamation activities would encompass three ranges. The first range, 1:125 000 to 1:250 000, provides a synoptic overview of the general terrain and topography being mined. Over a period of time, this range would present a vivid pictorial history of extensive and evolving patterns. The second range extends from 1:62 500 to 1:100 000. Two of the Skylab experimenters did most of their investigative work within this range; specifically, at the 1:80 000 scale. For more subtle details, scales ranging from 1:24 000 to 1:50 000 are required. The S190B 2× positive transparencies were optically enlarged to achieve a usable 1:24 000-scale image.

Skylab photographs were also used by Baldridge et al. (ref. 2-12) in conjunction with frames of high-altitude-aircraft photographs to identify topographic features that are not measurable in the Skylab photographs alone because of inadequate stereographic parallax. This procedure involved simultaneous viewing of the aircraft photographs (acquired at an earlier date) and Skylab photographs of the same area and at the same scale. The resultant stereoscopic effect provided the investigator with a means to define the slope of land features and to evaluate the temporal impact on the landscape.

The potential of using S190B photographs for the detection of nonfuel surface mining (e.g., clay, sand, gravel, and phosphate mining) was also assessed by Hannah, Welby, and Weir (refs. 2-2, 2-13, and 2-20, respectively). Because clay mines range in surface area from 0.4 to 2 hm^2, they are difficult to detect in space-acquired imagery. However, the larger sand and gravel mines, with their lobate geometry and associated water bodies, provided a distinctive pattern and were easily detected and identified. The very distinct signature created by phosphate mining in central Florida (highly reflective surface produced by bare sandpiles) indicates that this type of excavating and associated reclamation activities can easily be identified and mapped by using space photographs (ref. 2-2).

Farms

Cultivated fields

U. S. Highway 41

Lake Peewee

Colonial Mine

Red Lake

Madisonville, Kentucky

Illinois Central Railroad

Orphans (unreclaimed)

Golf course

0   5
                  Scale, km

N

(a)

FIGURE 2-18.—An S190B photograph showing strip mines in the Madisonville, Kentucky, area (SL4-90-032). (a) This synoptic view allows identification of surface coal strip-mining operations in an agricultural region. (b) An enlargement of a small segment of figure 2-18(a). The features associated with an active strip-mining operation are identified. This scene shows the amount of detail that can be seen in an enlarged portion of an S190B photograph.

Explanation

1. Ramp roads
2. Active pit and minor roads
3. Graded
4. Planted
5. Reclaimed
6. Shadows from spoil hills

Scale, km

(b)
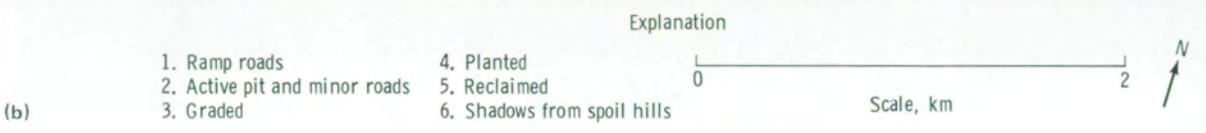
FIGURE 2-18.—Concluded.

*TABLE 2-XVI.—Summary of Qualitative Feasibility of Using Skylab S190B Data
to Identify Surface Coal-Mining/Reclamation Features*

Feature	Skylab Principal Investigator			
	Baldridge (ref. 2-12)		Brooks (ref. 2-19) results	Weir (ref. 2-20) results
	Results	Minimum area discernible using color-infrared film, hm²		
Active strip mine land				
Lack of vegetation	(a)	0.5	(a)	(a)
High walls	(b)	(c)	(a)	(a)
Slope (recognized but not measurable)	(b)	(d)	(e)	(e)
Coal seam	(b)	(c)	(f)	(e)
Spoil banks	(b)	(c)	(b)	(b)
Access roads	(a)	(c)	(a)	(a)
Equipment	(e)	(d)	(g)	(g)
Orphaned strip mine land				
No vegetation or sparse vegetation	(a)	0.5 to 1	(a)	(b)
High walls	(b)	(c)	(b)	(b)
Spoil banks	(b)	(c)	(b)	(b)
Impoundments	(a)	0.5 to 1	(a)	(a)
Impoundment quality	(e)	(d)	(b)	(g)
Access roads	(b)	(c)	(b)	(b)
Ongoing reclamation and reclaimed strip mine areas				
Equipment	(e)	(d)	(g)	(g)
Smooth slopes	(b)	(d)	(f)	(f)
Vegetation: 0- to 40-percent cover	(b)	1 to 5	(b)	(b)
Vegetation: 40- to 80-percent cover	(b)	1 to 5	(b)	(b)
Vegetation: 80- to 100-percent cover	(b)	1 to 5	(b)	(b)
Impoundments	(a)	0.5 to 1	(a)	(a)
Impoundment quality	(e)	(d)	(b)	(g)
Access roads	(b)	(c)	(b)	(b)

[a]Usually determined with ease from S190B.

[b]Determined often enough to make data useful.

[c]No information presented.

[d]Not applicable.

[e]Information desired but unobtainable from S190B.

[f]Rarely obtained from S190B.

[g]Information desired but not subjected to investigation with S190B.

The overall conclusion is that S190B-type photographs can be used for detection and mapping of the small surface mines and that this knowledge can be used by Federal and State agencies and local groups that are concerned with resources, reclamation, and land use management. Although none of the Skylab investigators specifically evaluated the S190B photographs for other types of surface mining activities (copper, uranium, and limestone), it is obvious that Skylab-type photographs could be useful for mapping and monitoring disturbed areas associated with such mining operations (fig. 2-19).

Welby and Lammi (ref. 2-13) indicated that S190A color-infrared film can be used effectively as an aid in detecting sediment discharge from active or abandoned quarry operations, providing the receiving-stream waters are approximately 60 m wide. Normally, water with high sediment content will have a more highly reflective surface than will other stream water.

Wetland mapping and ecology.—The fragile ecological zone that forms the boundary between land and water mass, termed the "coastal wetlands," has become an increasingly critical area requiring the establishment of effective management practices. Laws regulating the types of activity in wetlands have been enacted by most of the affected States. Anderson et al. and Klemas et al. (refs. 2-21 and 2-9, respectively) examined the potential of using spacecraft-acquired data to monitor and map these areas in a practical and inexpensive manner.

Anderson's findings (ref. 2-21), in particular, indicate that orbital photographs (primarily the S190A color-infrared and S190B color films) are the best data base being used for rapid, relatively low cost wetland mapping and monitoring on a regional basis. Figures 2-20(a) and 2-20(b) are two S190A color-infrared prints acquired over Anderson's test site at the mouth of the Nanticoke River in Dorchester County, Maryland; figure 2-20(c) is the compiled wetlands map. In mapping the marsh categories, the tonal contrast of the color-infrared film and the texture patterns were found to be the most important recognition elements in the photointerpretation analysis. Attempts with the use of
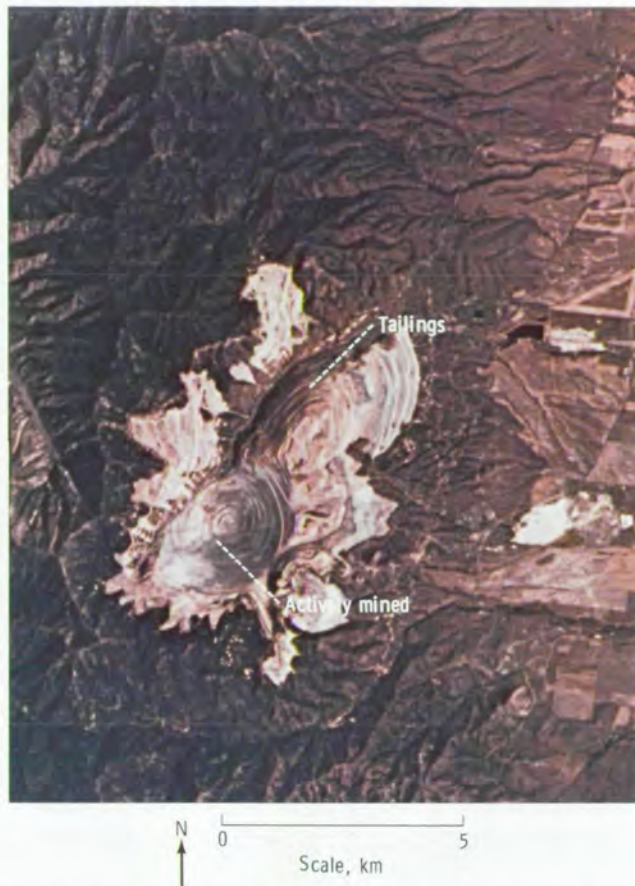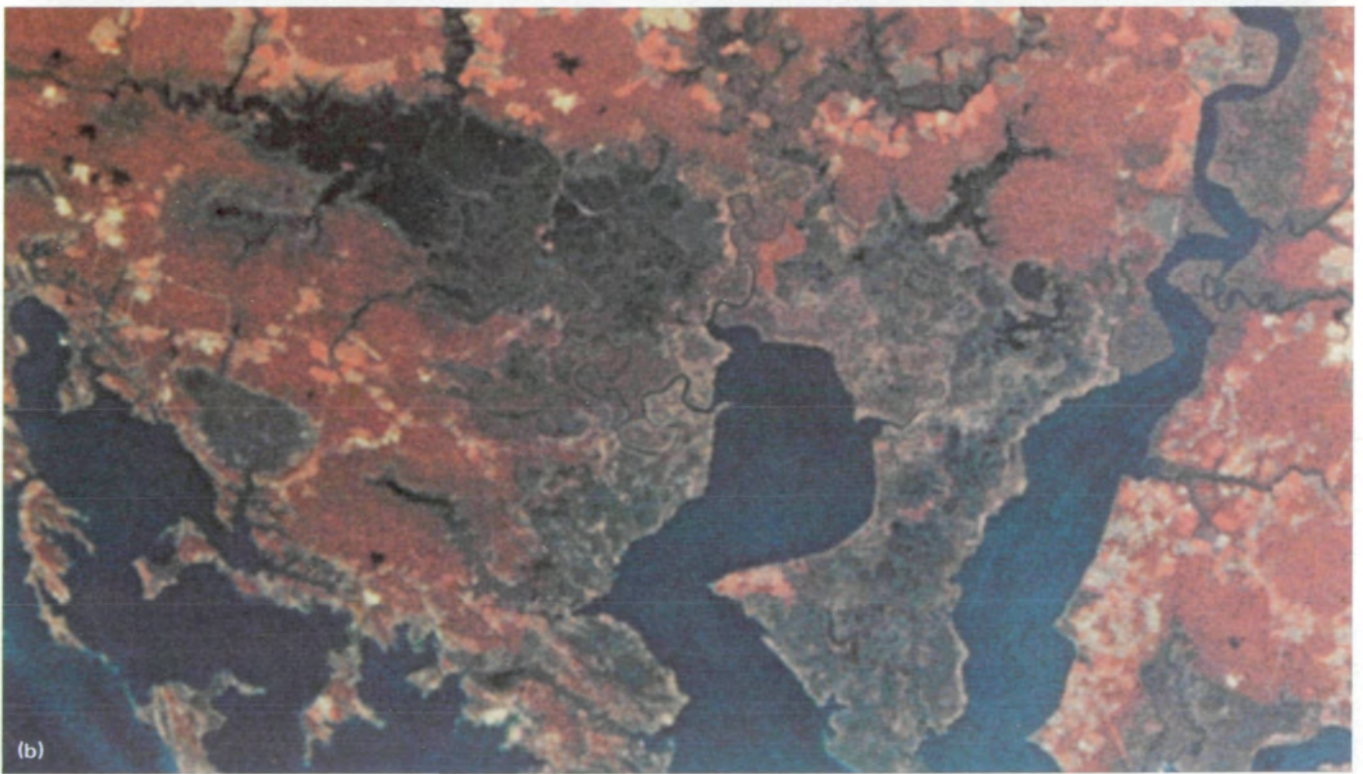

FIGURE 2-19.—An S190B color photograph showing the large open-pit copper mine in Bingham Canyon, Utah. The actively mined area and the mine tailings should be noted (SL3-83-300).

other enhancement techniques (color-additive viewing and density slicing) were unsuccessful in producing distinctive signatures in the areas of interest and effectively separating the various categories and individual species. The S190A color film provided slightly better resolution, but tonal contrast (greens and browns) was not as distinguishable as the shades of red and blue in the color-infrared film. The S190A black-and-white infrared film also provided some information in the

(a)

(b)

Upland
Water
Near saline
Type I, fresh estuarine river
Type III, fresh estuarine bay
Type II, brackish estuarine river
Type IV, brackish estuarine bay
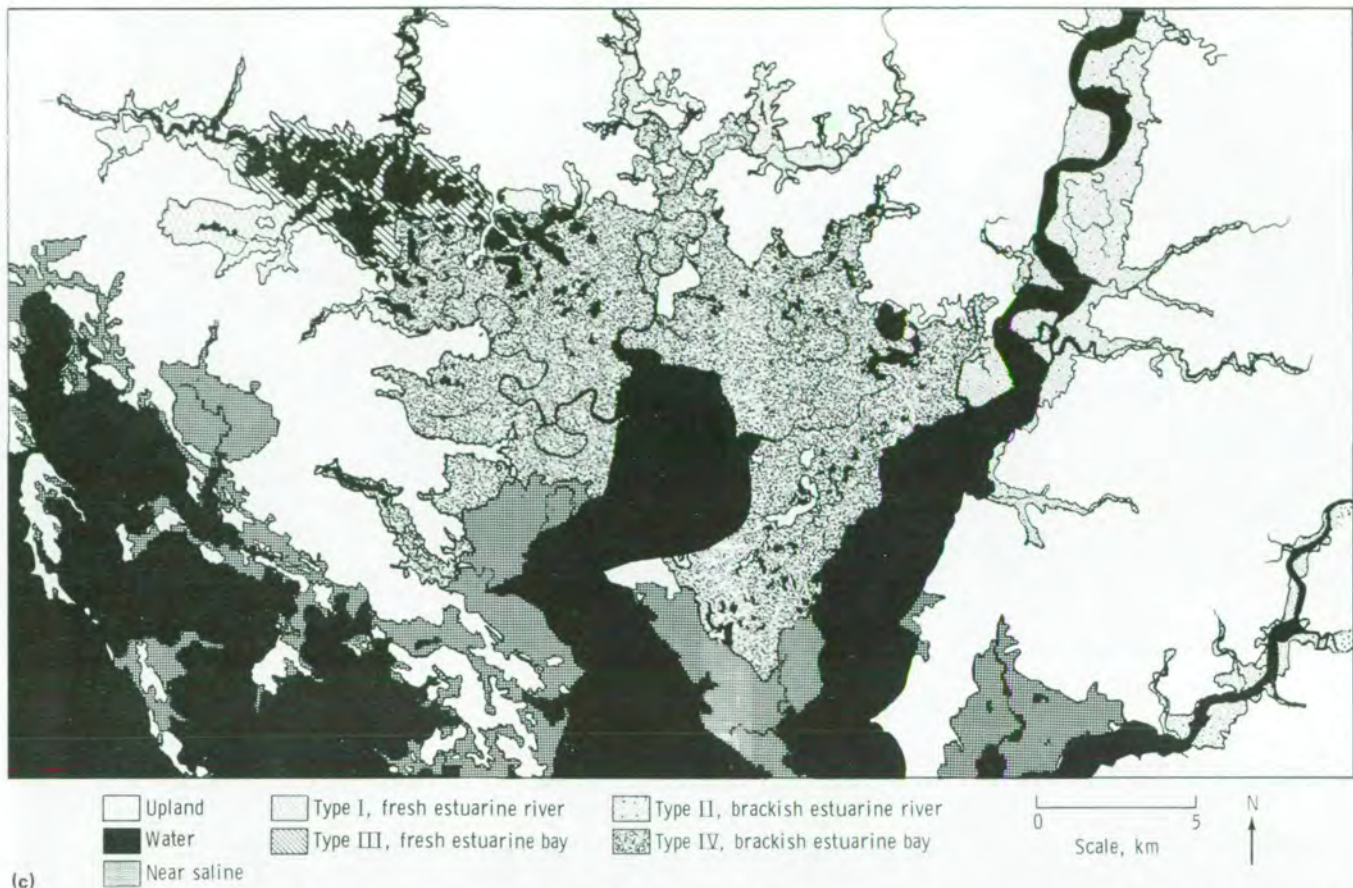
Scale, km
0   5
N

(c)

FIGURE 2-20.—S190A color-infrared photographs and a compiled wetlands map for the marshes of Dorchester County, Maryland. This type of temporal photographic coverage was useful for the delineation of wetland boundaries. (a) S190A color-infrared photograph obtained in June 1973 (SL2-15-174). (b) S190A color-infrared photograph obtained in September 1973 (SL3-39-123). (c) Compiled wetlands map.

marsh areas. The final product prepared from both scenes (June and September) indicated the value of temporal data in accurately determining boundary placement during the mapping of marsh categories and in identifying individual species. The June data were used to distinguish the marsh areas from the uplands and the brackish river marsh from the fresher water; they also enabled the delineation of certain individual species by their characteristic color. The September photographs were superior for delineating the upper marsh boundary (i.e., wooded swamps are drier in the fall and provide better contrast) and marsh/water interfaces because of reduced vegetation cover.

Anderson points out that, from analysis of the S190A data, it was possible to develop a wetland classification system that included freshwater tidal wet-

lands and also to detect individual species when they occurred in relatively large stands. Several different species (not shown in fig. 2-20) were identified and mapped, and several subcategories of marshes were also identified.

The S190B color photographs of Great Egg Harbor, New Jersey, were examined by Anderson, who indicated that these photographs were similar to high-altitude aerial data with respect to the amount and sharpness of detail. Within this area, the upper marsh boundary, the marsh/water interface, and the perimeters of marsh areas were easy to delineate with the S190B photographs, and less subjective judgment was involved than with the S190A photographs. Figure 2-21(b) is a map of the same area compiled from analysis of figure 2-21(a), an S190B photograph of the

FIGURE 2-21.—S190B color photograph (fig. 2-21(a)) of Great Egg Harbor, New Jersey, and a coastal wetland map (fig. 2-21(b)) compiled from an analysis of the Skylab photograph. The increased spatial resolution of the S190B color film enhanced boundary delineation and placement and also enabled identification of more botanical categories than was possible with the S190A photograph. (a) S190B color photograph (SL3-86-303). (b) Coastal wetland map.

New Jersey site with an approximate scale of 1:110 000. The land/water interface, drainage patterns, ditching activity, and vegetational distribution are well displayed on the photograph. As a result of the excellent tonal contrast on the S190B color photographs, it was possible to distinguish the boundary between saline and brackish wetland and to delineate the transition zone (between wetland and upland) with the brackish wetland. The transition zone was easier to delineate on the Skylab photograph than on low-altitude-aircraft photo-graphs. As a result of these studies, Anderson (ref. 2-21) modified the classification system to separate saline wetlands that have been affected by human activity from unaffected saline wetlands (a naturally occurring state).

Migratory waterfowl habitat evaluation.—The major objective of the migratory waterfowl habitat investigation (conducted in eastern North Dakota) was to monitor changes in the breeding habitat of migratory waterfowl between May (the peak nesting season for several

Brackish wetland

Upland

Transition zone

S Spoil

+ + +
+ + + Saline wetland,
+ + + not ditched

(b)

:::: Saline wetland, ditched

Water

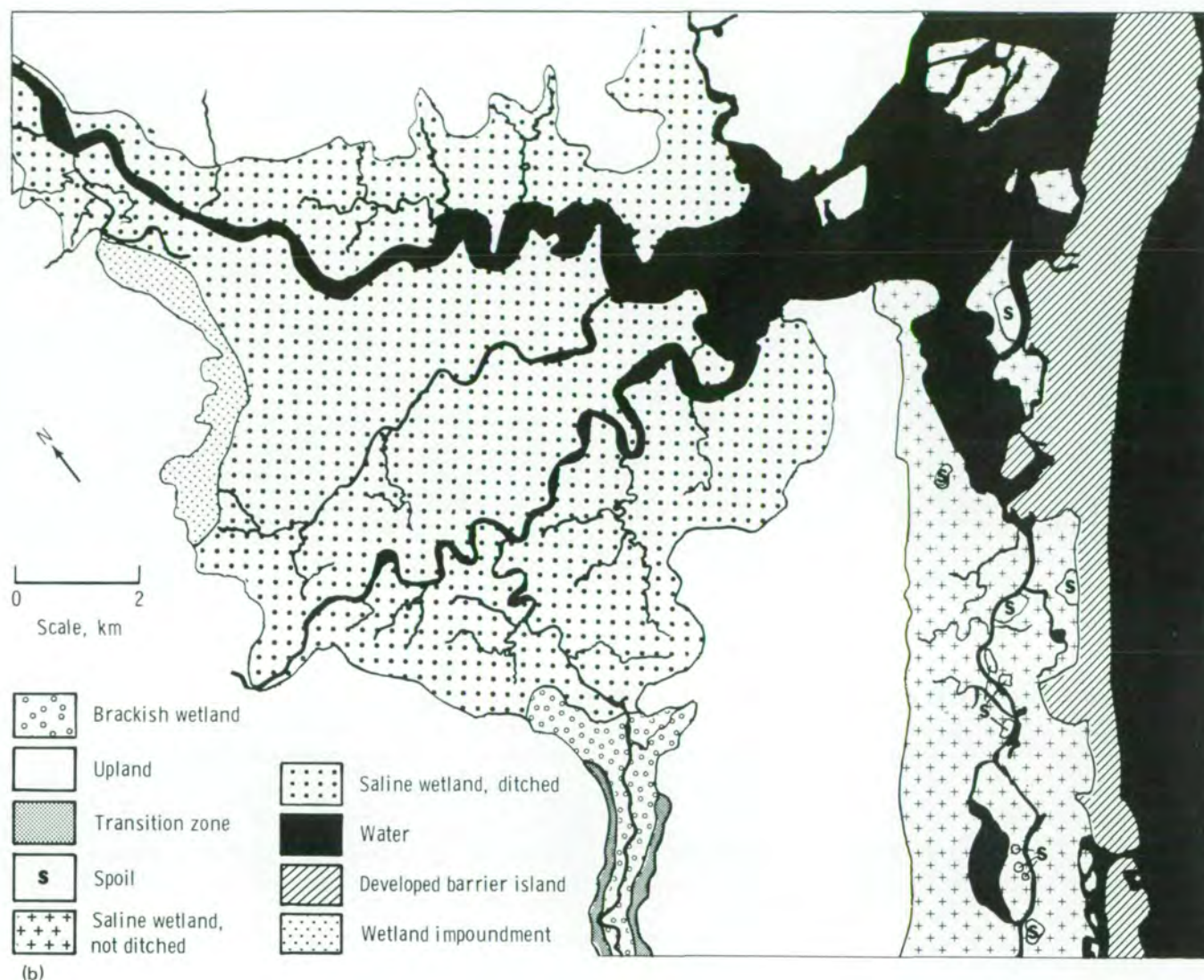Developed barrier island

Wetland impoundment

FIGURE 2-21.—Concluded.

species of ducks) and July or early August (when most duck broods have hatched). Proposed indicators of habitat quality were surface water, general degree of terrain wetness, plant phenology, and land use patterns. Primary emphasis was placed on the observation of surface-water features (ponds and lakes) to obtain statistical data on the number of surface-water features and their areal extent, distribution, and frequency. Such information is used in models for predicting annual waterfowl production. The EREP data were not obtained over the test site during the May 1973 breeding period but were obtained on June 12, 1973, between the May and July dates desired. Results of the analysis of the EREP data were therefore compared to those obtained by Landsat on May 14 and July 7, 1973.

In this Skylab study, the S192 scanner system data were analyzed by digital computer analysis techniques. The use of computer data-processing techniques is particularly well suited to this type of analysis because of the wide expanse of prime waterfowl-breeding area involved and because of the need to quickly assimilate and collate information on habitat conditions.
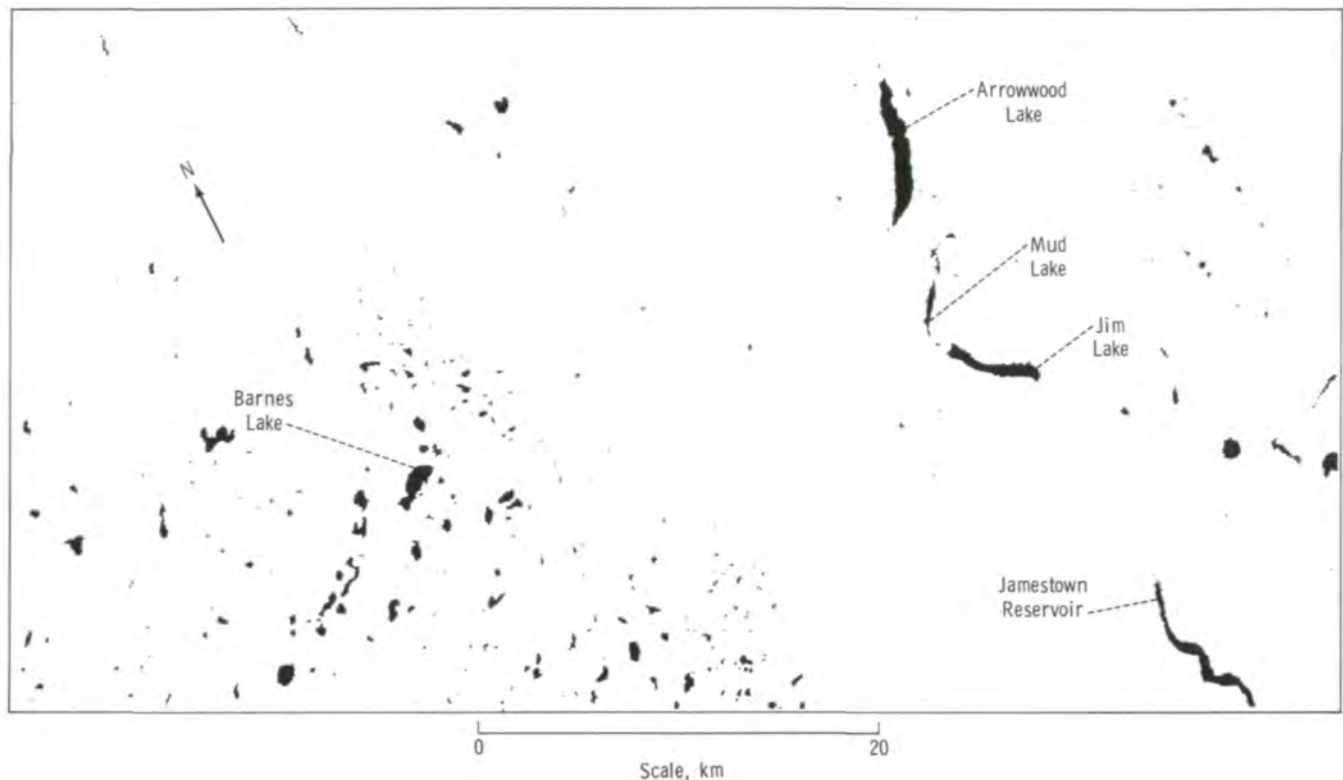
FIGURE 2-22.—A segment of a computer-generated surface-water map produced by processing band 11 (1.55 to 1.75 μm) data from the Skylab S192 multispectral scanner observation of an area north of Jamestown, North Dakota. The open surface water is shown in black.

To delineate surface-water boundaries, a level-slicing technique was used to analyze the data from a single near-infrared band. This reasonably reliable and fairly simple method was effective because of the very high absorption and therefore low reflectance of water in these near-infrared wavelengths. Preliminary study of the data indicated that any one of the five wavelength bands from 0.78 to 1.75 μm would be potentially useful for discriminating open surface water by using such a thresholding technique. Thus, the EREP data offered an opportunity to appraise the relative usefulness and reliability of several different near-infrared wavelength bands. The results of this evaluation indicated that bare soil was the terrain feature most likely to be mistaken for open surface water. Although the problem was not severe, there did seem to be a tendency for water and bare soil to have some overlap in level of spectral response. The preliminary work with the S192 data indicated that this overlap decreased with increasing wavelengths. Thus, the 1.55- to 1.75-μm wavelength

band was the most useful single band for effective water discrimination. Using the thresholding technique and the 1.55- to 1.75-μm wavelength band, a computer-generated thematic map identifying open surface water was obtained for a 3618-km^2 area (fig. 2-22).

In a comparison of the Skylab results with those from analysis of Landsat data collected in May and July 1973, Gilmer and Work (ref. 2-15) found that, on a synoptic basis, the two sensor systems appeared to provide consistent answers in that both data sets indicated a decline in area and number of surface-water features. A more detailed comparison of the size of 21 individual lakes that appeared on all data sets indicated that the Skylab multispectral scanner was not capable of achieving as consistent a measure of area as the Landsat scanner. The investigators attributed this result to the conical scan configuration used by the Skylab S192 scanner. Gilmer and Work believed that both the scanning format and the associated techniques for data processing appeared to have the net effect of slightly but

systematically altering the measurements and the geometric fidelity of small ponds.

Another phase of this study involved a more limited testing of a different technique for improving the apparent spatial resolution of the Skylab S192 data. This technique was described as a proportion estimation technique and involved the use of a computational algorithm for estimating the fractions of pure materials present within the resolution cell of a multispectral scanner. The details of this technique are described in section 6. Results of this analysis indicated that the minimum discernible size of a water body was four-tenths of the minimum size that could be detected by using the single-band thresholding algorithm. Therefore, this technique seemed to offer considerable promise for mapping and tabulating much smaller water bodies than could be achieved by using the thresholding technique. Gilmer and Work also found that, by using the proportion estimation technique, some lakes that had been only partly defined with Landsat data could be fully defined with the S192 data. Such lakes were shallow and alkaline, with a high level of suspended solids and/or precipitated alkali sediment. The improved capability for delineating such lakes was attributed to the middle-infrared spectral bands associated with the S192 data that extended to 2.35 μm, whereas the Landsat scanner system had only two near-infrared wavelength bands with a maximum wavelength of 1.1 μm. The 1.55- to 1.75-μm wavelength band is particularly effective in the delineation of water and hygric-scene features in general.

User Evaluations

In addition to yielding the specific benefits derived by the individual investigations, the Skylab Program promoted a much broader concept of technology transfer to a diverse user audience. Through the efforts of the Principal Investigators and their direct contact with different user-agency groups, including local, county, regional, State, and Federal user communities, the use and evaluation of the Skylab EREP data have received a significant amount of exposure.

From the initial selection of the Skylab Principal Investigators and extending through the data analysis period, considerable emphasis was directed toward actual or potential user involvement with the data products generated from this unique remote-sensing system.

TABLE 2-XVII.—
Non-Principal-Investigator User Agencies

Skylab Principal Investigator	*Geographic area*	*User agencies*
P. E. Baldridge	Ohio	Department of Economics (community development), Department of Natural Resources (city, county, and regional agencies)
R. L. Brooks	Kentucky	State coal strip mine inspectors, other State officials
J. W. Hannah	Florida	City, county (regional planning)
E. E. Hardy	New York	City, county, regional (State planning and environmental research)
R. M. Hoffer	Colorado	U.S. Forest Service, National Park Service
I. J. Sattinger	Michigan	Bureau of Outdoor Recreation, Oakland County Planning Commission, Michigan Department of Natural Resources
C. W. Welby	North Carolina	Department of Natural Resources (economic resource planning, evaluation)

In some cases, the Principal Investigators themselves were representing various user agencies. In many other instances, the Principal Investigators contacted various agencies having responsibility within their test-site area and worked with the personnel of those agencies to produce specific Skylab products for use and evaluation by those agencies. Table 2-XVII is indicative of the number and variety of non-Principal-Investigator user agencies that were involved indirectly in Skylab land use investigations. The following paragraphs cite some examples of the specific types of activities that were involved.

The major user of remote-sensing data for surface mining applications in Ohio (the Ohio Department of Natural Resources) indicated that the potential usefulness of EREP-type data for current mining and

reclamation activities has been satisfactorily demonstrated and that both satellite and aircraft data are now being used in State of Ohio mining and reclamation programs. Another Skylab investigator worked directly with State of Kentucky coal-mining officials who indicated that if Skylab quality imagery were available on a regularly recurring basis, the overall strip-mining program could be upgraded through its use.

The usefulness of space photographs was cited by the members of the Ohio Department of Economic and Community Development in their study on urban growth encroachment on agricultural land. Participating regional planners concluded that the capability to measure urban growth and its impact on the region could be of immediate use to planners in evaluating the effectiveness of both regional and local policies.

The S192 digital data and S190 imagery were used to derive computer-generated classification maps and photointerpreted land use maps, respectively, for different levels of planning agencies in Florida. A majority of the user group surveyed expressed a strong preference for the largest scale map possible, regardless of the data source used.

In surveying the user evaluation of EREP data, a two-phase approach was initiated—an introductory phase during which the potential user was familiarized with the concept of multispectral analysis and with the use of EREP data products to delineate certain land uses and natural characteristics and an in-depth followup interview structured around a detailed questionnaire. These surveys showed distinct differences in response between different categories of users. The regional planners were more interested in long-term interrelationships and were enthusiastic about the EREP data because the synoptic view obtainable from space offers an unparalleled method for accurately showing various land use patterns on a regional scale. Local agencies, involved in day-to-day decisions, generally indicated a requirement for more detailed information than could be obtained from the EREP products. In most instances, their needs could best be met by using data collected from aircraft. The important point to be made is that certain user groups do have a need for such synoptic data, whereas other user groups require more detailed data over smaller areas.

Summary

A significant number of Skylab investigators developed and demonstrated the usefulness of the photographic sensor systems and their application to resource inventories and analysis for large geographical areas, as well as to regional and local uses. Both conventional photointerpretation and computer-assisted procedures were effective in the analysis of EREP data. Many special applications (including surface mining operations, wetland area mapping, change detection of urban patterns, and general land use mapping) involving the use of multiband and color-infrared photographs were successfully demonstrated. With few exceptions, repetitive data of the type obtained by Skylab (primarily with the S190B) can meet most inventorying and mapping requirements. Participating planners concluded that the capability to monitor urban growth and its impact on the region has immediate value to land use planners in evaluating the effectiveness of both regional and local policies related to growth.

The Skylab S190B photographs enlarged to scales of 1:63 360 and 1:24 000 provided significant detail for easy and efficient mapping. The S190B photographs were cited by most investigators as being superior to the S190A photographs because of the greater amount of detailed information that could be derived from these photographs. Studies involving urban areas were particularly amenable to the use of the S190B color film because this film provided adequate spatial resolution and therefore the most detailed information. Also, many investigators stated that the color-infrared photographs were invaluable for many applications requiring identification of vegetative cover. Therefore, an optimum system for many investigations would have combined the high-resolution color film and the high-resolution color-infrared film (SO-131) into a dual S190B camera system. A specific recommendation was that future orbiting space stations include a multispectral camera array composed of four S190B-type cameras. This design would incorporate the added flexibility that is essential to expand and enhance the type and quality of information for general land use programs.

A group of Skylab investigators provided much in-

sight into the use of computer-processing techniques for analyzing S192 multispectral scanner data for land use applications. Overall accuracies of 75 to 90 percent for classification of Level II land use maps were achieved by using such analysis techniques. Areal estimates based on computer-aided analysis were highly correlated with those obtained through standard photointerpretation techniques applied to aircraft photographs.

The increased spectral range, from the visible through the thermal-infrared wavelength, offered by the S192 scanner system provided investigators with the first opportunity to analyze this wide spectrum of data from satellite altitudes. The consensus of the investigators was that at least one wavelength band from each of the four major portions of the electromagnetic spectrum (visible, near infrared, middle infrared, and thermal infrared) was necessary to achieve optimal computer classification of land use categories. The near-infrared portion of the spectrum was found to be particularly important for accurate discrimination among various vegetative cover types. In other studies, a combination of six wavelength bands was cited as being optimal for land use mapping with the use of computer-aided analysis techniques.

In general, the Skylab S192 land use investigators concluded that the improved spectral resolution and the increased spectral range available in the S192 scanner systems (as compared to the Landsat-1 system) enabled significant improvement in classification performance for land use mapping. A few investigators indicated that the improved spectral resolution obtained in the Skylab scanner data was more important for mapping many cover-type features than was the spatial resolution obtained through use of the S190 photographic sensor systems.

In one investigation, camera data from Skylab and Landsat were geometrically corrected to a topographic map (scale, 1:24 000) of the Durango, Colorado, area for the purpose of quantitative and qualitative comparisons and analyses. The use of various analysis techniques with this data set provided some insight into the value of working with topographic data in conjunction with multispectral scanner data for land use and major-cover-type mapping in a topographically and vegetationally complex mountainous region.

In nearly every study in which S192 data were used in conjunction with computer-aided analysis techniques, the investigators concluded that traditional definitions of land use categories often will not produce spectrally separable informational classes of data output. To obtain maximum benefit from multispectral scanner data, it will be necessary, in many cases, to establish land use category definitions that are based on spectrally discriminable classes of cover type.

The Skylab EREP experiment demonstrated the value of photographic and multispectral scanner data obtained from satellite altitudes for many land use mapping activities.

CARTOGRAPHY

The process of producing and maintaining quality maps and other precision cartographic products is complex, time consuming, and costly. Despite the obvious need for more and better maps and the use of highly sophisticated equipment and techniques in their production, it is estimated that only about 30 percent of the Earth's landmass is now adequately mapped. Furthermore, in rapidly developing locales, maps are often obsolete by the time they are constructed and published.

Before the advent of practical aerial photography, maps were made in the field by teams of cartographers who painstakingly measured their way over the landscape. During the 1920's and 1930's, significant advances were made in the development of aircraft, photography, and optics. These advances made photogrammetry—the art and science of deriving reliable measurements from photographs—increasingly important in the production of maps. Through the use of specialized cameras, customized photographic flight equipment, and complex monoscopic and stereoscopic plotting equipment, a major portion of the mapmaking process was shifted from the field to the office. This use of aerial photographs made it possible to accelerate map production and to produce maps having increased geometric accuracy and detail. In recent years, cartographers have turned to large-scale, high-speed electronic computers and improved mathematical techniques to increase the speed and accuracy of map pro-

duction. Today, photogrammetrists and cartographers consider photographs and digital imagery from orbiting spacecraft as the next major step in the preparation and revision of many types of maps.

The Skylab S190A and S190B camera systems produced satellite photographs of relatively high metric and resolution qualities and provided cartographers with a viable means of testing and evaluating the cartographic potential of space photographs. In the United States, the primary problem in mapping is the revision and updating of existing maps. In many other regions of the world, particularly in developing countries and/or remote areas, the production of new maps is of paramount concern. Most of the investigations using Skylab S190A and S190B photographs for original mapping were conducted by agencies or organizations outside the United States. The purpose of this subsection is to summarize the results of the Skylab EREP cartographic investigations and to indicate possible improvements in cartographic instrumentation and techniques for future space missions.

Sensor Technology

In considering the results of experiments performed by the cartographic investigators, it is important to note that neither the S190B terrain camera nor the cameras comprising the S190A multispectral array were designed for cartographic applications. However, the S190A and the S190B did represent significant metric and resolution advances in camera systems for Earth photographic observations from space, and several cartographers attempted to exploit fully some of the photographs.

Applications

Aside from charts, which are special-purpose maps used for air or water navigation, the most widely used cartographic products are planimetric and topographic maps and controlled photomosaics. Planimetric maps reveal only the horizontal locations of surface features, whereas topographic maps show additionally the vertical positions of features by displaying relief in some measurable form. On maps, relief is depicted by a contour line, which is an imaginary line on the ground that connects all points that are at the same elevation above

a specific datum surface (usually mean sea level). A photomosaic is a continuous photographic representation of a portion of the Earth's surface, prepared by assembling individual photographs that have been rendered "tilt free" by a process termed rectification.

Planimetric and topographic maps and photomosaics are produced in a wide range of scales; however, most of these items range from 1:24 000 (1 cm equals 0.24 km) to 1:500 000 (1 cm equals 5 km). In the United States, scales of the standard national cartographic products are 1:24 000, 1:62 500, and 1:250 000. In metric-system-oriented parts of the world, the more commonly used scales are 1:25 000, 1:50 000, 1:100 000, 1:250 000, and 1:500 000. Maps having scales between 1:75 000 and 1:600 000 are generally classed as medium-scale maps, whereas maps having scales greater than 1:75 000 are considered large-scale maps. In most usages or applications, one generally seeks the smallest scale map capable of depicting the degree of detail required to support the particular application.

Photogrammetric mapping requires that the position and the orientation of the camera taking the photograph be determined at the instant of exposure. This information is generally obtained by means of a network of photoidentifiable "control points," for which the horizontal and/or vertical locations have been established by ground survey. After a basic network of ground control has been established, photogrammetric triangulation methods are usually used to extend the basic control network. For each photograph being used in photogrammetric mapping or in the preparation of controlled photomosaics, six to nine control points, well distributed over the format, are required. The establishment of basic ground control and densification of the control network are usually the most costly and time-consuming portion of the overall photogrammetric mapping process, especially in remote regions.

If camera parameters such as lens focal length and film format remain constant, the higher the altitude from which a photograph is taken, the greater the ground area that appears on the photograph. An increase in altitude reduces the number of photographs required to cover a given area and, most importantly, increases the distance between the required surveyed ground control points and thus reduces the overall number of mandatory control points. The formats of the S190A and S190B are significantly smaller than conventional mapping cameras (5.7 cm and 11.4 cm,

respectively, compared to 22.8 cm), and the 45.72-cm focal length of the S190B is three times longer than the lens used in many conventional mapping cameras. Nevertheless, as shown in figure 2-23, the increase in area of ground coverage by the S190A and S190B systems is striking by comparison to conventional aircraft photographs.

Most of the Skylab EREP investigative efforts in cartography were directed toward (1) the revision and updating of existing maps, (2) the establishment of photogrammetric ground control, and (3) the construction of new planimetric and topographic maps and photomosaics. In almost all investigations, the emphasis was directed toward determining the largest scale mapping task or product that the S190A and S190B Skylab photographs were capable of supporting.

Map Revision and Updating

Many innovations of procedures and techniques have been developed over the past few years to improve the technology of revising and updating maps. The use of remote-sensing data from space platforms for this purpose is not new; limited experimental revision products have been published, based on Gemini, Apollo, and Landsat data. Because Skylab photographs have improved spatial and spectral resolutions, several map revision projects have been accomplished with the use of Skylab data.

The most extensive cartographic investigation was conducted by 17 Latin American cartographic agencies through the Inter-American Geodetic Survey at Fort Clayton in the Panama Canal Zone (Staples et al., ref. 2-22). A few representative examples are cited in the following paragraphs to provide some insight into the usefulness of and the economic benefits derived from Skylab-quality photographs.

A map revision project performed by Fernandez (ref. 2-22) for a 1:50 000-scale map of Santa Cruz, Bolivia, reveals the economy of such revision procedures. Stereopairs of black-and-white S190A (0.6 to 0.7 μm) photographs at a 1:1 500 000 scale (enlarged 2× from the original scale) were used in a stereoplotter to compile planimetric features. In this study, the image quality of the S190A photographs limited the detection of changes to linear cultural features (roads) and the extent of new major urban growth patterns. Major changes to the river channels were also compiled. Sig-

nificantly, the map revision was accomplished within a 24-hour period, with the use of existing photogrammetric equipment.
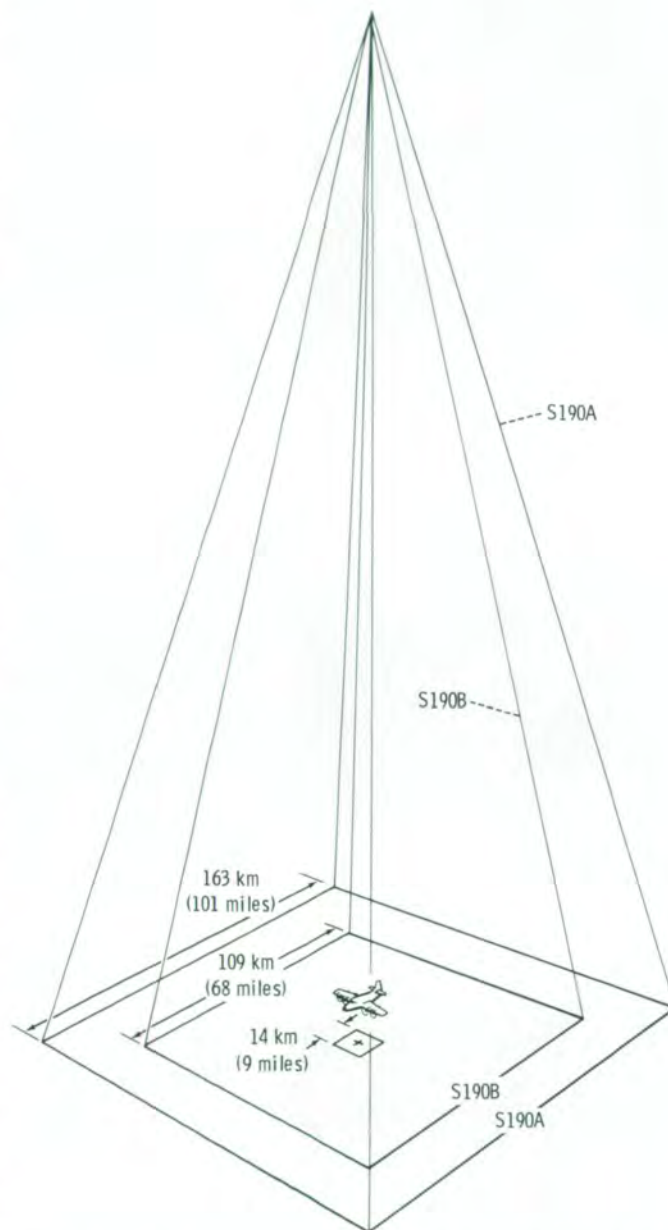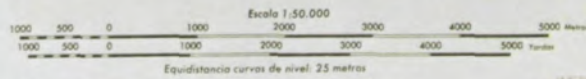

FIGURE 2-23.—Relative areal coverage of the S190A, S190B, and conventional aircraft camera systems. The coverage is roughly square; therefore, the side dimensions given in kilometers and statute miles are typical.

EXPERIMENTO DE ACTUALIZACIÓN
SOBREIMPRESA

CHILE 1:50.000   CONCEPCIÓN   SKYLAB—EXPERIMENTO

CONCEPCIÓN, CHILE

Investigators in several other Latin American countries updated existing maps with S190A photographs. In Chile, Puccio (ref. 2-22) also used S190A (0.6 to 0.7 μm) film to revise a 1:50 000-scale map (fig. 2-24). The black-and-white negatives were photographically enlarged and rectified, then registered to the topographic map. Puccio indicated that the technique was inexpensive and that significant planimetric features such as urban density patterns and major new roads were extracted easily.

Although the S190A photographs were used in some map revision activities, most investigators preferred the S190B photographs because of the spatial resolution of as much as 15 m. The type of scene contrast and image quality determines the extent to which S190B photographs will enable identification of individual features that can be compiled onto 1:50 000-scale maps. With optical enlarging viewers and/or stereoplotters, many small nonlinear surface features are discernible and can be plotted. However, the capability to define some required features depends on the availability of ground-truth data. The S190B data are mainly color photographs, but selected data passes were also taken with black-and-white and color-infrared film. The S190B field of view of 11 881 km² provides coverage of most major metropolitan areas with excellent image quality for map scales of 1:250 000 and larger. A 9.5× enlargement will provide a scale of approximately 1:100 000, and enlargements of twice this scale to a 1:50 000 scale still provide sufficient image quality to enable extraction of map data directly from the photographic print or from optical enlargers and/or stereographic plotters.

In Argentina, Micro (ref. 2-22) prepared a partial revision of the Chascomús 1:250 000-scale planimetric map, using a black-and-white print from the S190B color film. He indicated that the data enabled the mapping of new roads, rivers, lakes, small urban areas, and shorelines in this topographically subdued region along the Atlantic coastline of eastern Argentina. Railroads could be detected when they were parallel to roads, and farm buildings were visible when grouped. Other investigators (Romero, Venezuela (ref. 2-22); Morrell, Dominican Republic (ref. 2-22); Stewart, Canada (ref. 2-23); and Mott et al., England (ref. 2-24)) indicated that the S190B color film provided better interpretative details for updating 1:100 000- and 1:50 000-scale products. This detail is primarily due to the scene contrasts in the particular frames used rather than the resolution characteristics of the color film.

Excellent examples of large-scale planimetric map revision are two 1:24 000-scale maps of Lubbock, Texas, prepared by the Defense Mapping Agency Aerospace Center in St. Louis, Missouri. The S190B color film for this task was used in January 1974 when the vegetation was dormant, and this condition afforded excellent scene contrast. The revision mapping was accomplished at the original 1:24 000 scale, and polyester matte positives of two topographic map sheets were used for the compilation base. A color photographic print (1:48 000 scale) and a color transparency (1:200 000 scale) were enlarged from second-generation materials. The area of interest on this Skylab frame covered approximately 3 percent of the total photographic area. Planimetric features were transferred to the map base compiled by use of a zoom transfer scope. This instrument provides a capability for viewing the photographic image and the map base simultaneously and thus enables the operator to revise or add detail in relationship to existing map features. A portion of an enlarged S190B photograph used for this revision is shown in figure 2-25(a). Figures 2-25(b) and 2-25(c), respectively, depict only a small part of a 1:62 500-scale map produced in 1957 and the changes and revisions derived from the Skylab imagery. The photointerpretation and compilation for this map revision effort of the two 1:24 000-scale Lubbock topographic sheets required 72 man-hours. In this case, reliable interpretation of ground features was accomplished on 40× enlargements (from the original scale).

In other examples, both Stewart (ref. 2-23) and Colvocoresses (ref. 2-25) indicated that, because of errors in photointerpretation, revisions to 1:50 000-scale maps with the use of S190B data were not completely reliable. They do, however, indicate that the S190B data can be used for partial map revision activities if the quality of the original film data is maintained.

FIGURE 2-24.—Example of map revision using Skylab S190A station 5 photographs. Original map scale is 1:50 000. Changes to original map are overprinted in pink.
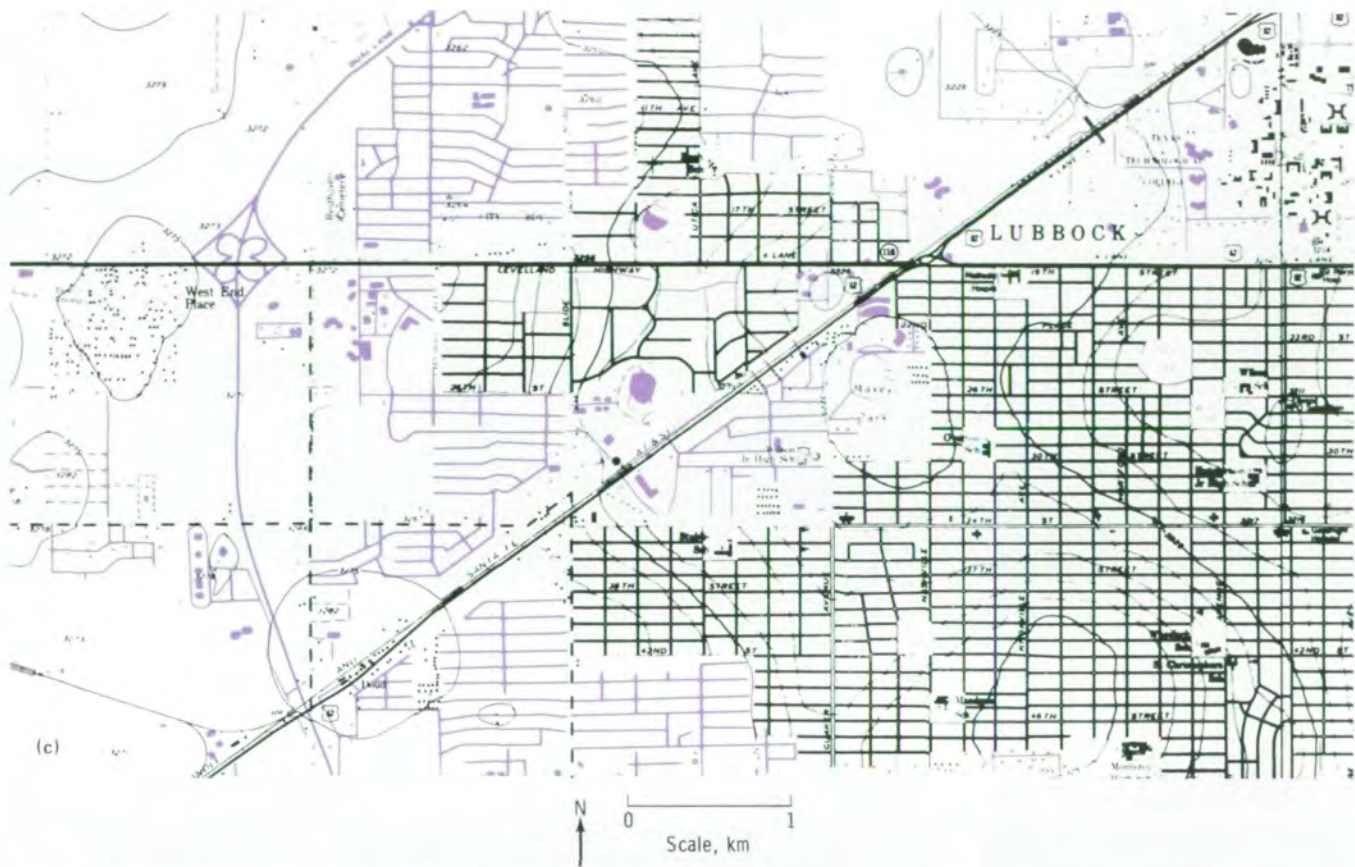
(a)

(b)
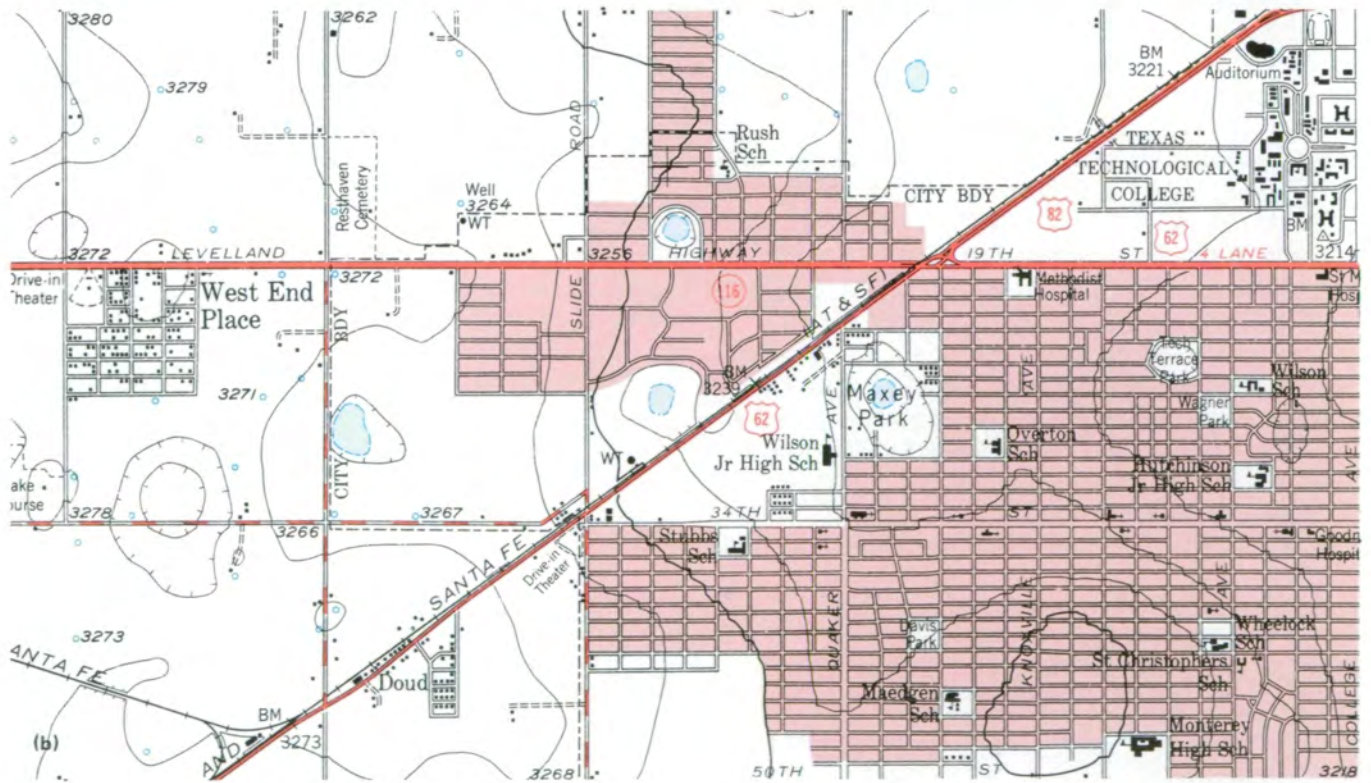
FIGURE 2-25.—Planimetric map revision of Lubbock, Texas, and vicinity. (a) Enlargement of a portion of an S190B color photograph (SL4-94-111). (b) Planimetric map produced in 1957 by using conventional photogrammetric methods. Scale of original map is 1:62 500. (c) Revision to planimetric map shown in figure 2-25(b) as derived from S190B photograph. Changes are shown in color.

Photogrammetric Establishment Of Ground Control

The establishment of ground control is one of the most expensive and time-consuming tasks in cartography. Three quantitative investigations by three separate agencies in Canada, each using different techniques of aerial triangulation adjustment (Stewart, ref. 2-23), and an investigation in England (Mott et al., ref. 2-24) demonstrated that horizontal photogrammetric control capable of supporting planimetric mapping at scales of 1:250 000 and smaller can be derived from Skylab S190A photographs. These same investigators, and Keller (ref. 2-26) of the National Oceanic and Atmospheric Administration, found that photographs from the S190B camera system, with its longer focal length and higher resolution, were capable of providing

horizontal control sufficient to sustain the compilation of planimetric maps at scales of 1:50 000 and smaller.

In his triangulation investigation, Keller used a strip of 12 S190B photographs that covered a 648-km-long swath from Charlotte, North Carolina, to the Rappahannock River in Virginia. Within this area were 29 highly identifiable ground control points (road intersections, aeronautical aids, and airport runway ends) for which position could be determined from standard 1:24 000-scale USGS quadrangle maps and National Ocean Survey (NOS) airport surveys. A standard NOS computational program to perform numerous simultaneous adjustments of the 12-photograph strip was used in the analysis. In these adjustments, different subset combinations of the ground control and different empirical weightings of the ground control and photographic measurements were tried. The best results were

obtained using a 14-point network of ground control. The remaining 15 points of known location were used for accuracy evaluation. This "best" solution yielded a root-mean-square (rms) horizontal position error of 15 m, with 25 m being the maximum error observed.

The ability to derive vertical control or contour information from aerial or orbital photographs is largely a function of a characteristic of overlapping stereoscopic pairs of photographs, termed base/height (B/H) ratio. The B/H ratio of such a pair of photographs is the ratio of the distance between the camera exposure stations to the distance, or altitude, of the cameras above the ground. In conventional aerial photography (15.25-cm focal length, 23- by 23-cm format) with 60-percent forward overlap, this ratio is approximately 0.6. Because of the higher altitude of the EREP and smaller film format (and longer focal length for the S190B), with 60-percent forward overlap, the B/H ratio is 0.15 for the S190A and 0.10 for the S190B. Despite the small B/H ratio, Mott et al. (ref. 2-24) performed a vertical adjustment of a strip of seven S190B photographs taken over the rugged terrain of Nepal and achieved an rms height error of 117 m.

In an effort to overcome the small B/H ratio of vertical EREP photographs, triangulation was performed on a two-strip block of obliquely convergent photographs taken over Paraguay (ref. 2-22). Horizontal accuracies of approximately 15 m and vertical accuracies of approximately 25 m were achieved with an rms error for photographic image measurements of 8 μm. Only 10 original ground control points were minimally required to accomplish triangulation over a 50 000-km^2 area; however, because of availability, 40 ground control points were used. This block had a B/H ratio of approximately 0.9 and consisted of a vertical strip of S190A photographs from one EREP orbital pass and a strip of S190B photographs from a solar inertial pass from an adjacent orbit. During the S190B pass, the spacecraft
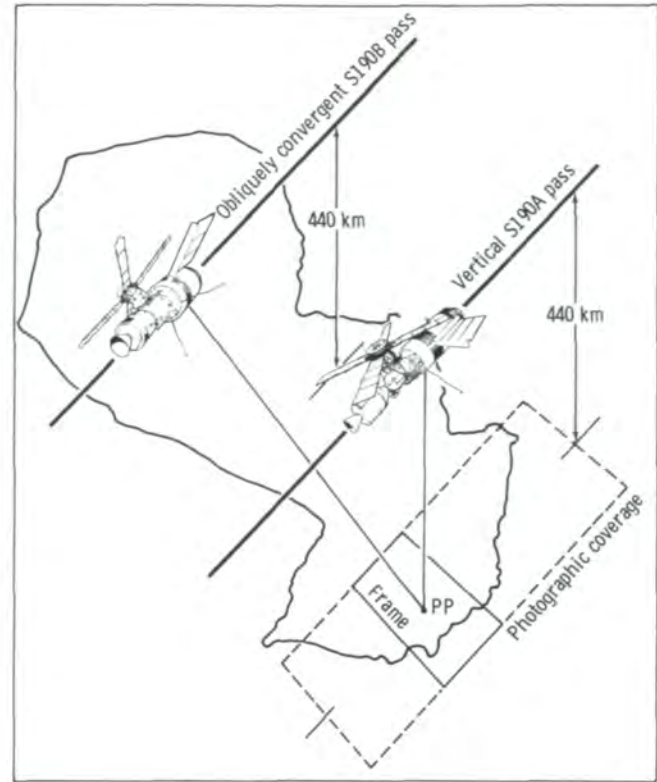

FIGURE 2-26.—Conceptual geometry of vertical S190A and obliquely convergent S190B coverage over Paraguay with a 0.9 base/height ratio. The designator "PP" represents the principal point.

was oriented (pitched and rolled) such that the S190B camera photographed almost the identical ground area photographed during the S190A pass, as conceptually demonstrated in figure 2-26. This triangulation is capable of supporting planimetric mapping at scales of 1:50 000 and smaller and topographic mapping at scales of 1:100 000 and smaller.

Original Mapping Activities

The use of Skylab photography to revise reconnaissance maps of regions in Central America and South America was reported by Staples et al. (ref. 2-22). In Guatemala, a 1:50 000-scale planimetric map (shown in reduced form in fig. 2-27(b)) was produced from a pair of S190B black-and-white photographs enlarged to 23 by 23 cm (9 by 9 in.), by using a stereoplotter. Outlines of urban areas, highways, railroads, and natural features were mapped. A 2486-km^2 region in and around Concepción, Paraguay, was planimetrically mapped at a scale of 1:100 000 by using approximately 25 percent of the stereomodel of two S190B 2× enlargements. A total of 36 man-hours was expended on compiling this map. If aircraft photographs had been used, 50 stereomodels and approximately 250 man-hours would have been required to accomplish the same task.

A planimetric map (scale, 1:100 000) of Fundación, Colombia, was prepared from 29.2- by 29.2-cm S190B color diapositives and a universal stereoplotter (Fletcher, ref. 2-22). A portion of this map (fig. 2-28(b)) shows the location of the transportation networks, other cultural features, hydrographic features, and forests, as compared to a similar map of this area published in 1954 (fig. 2-28(a)). Topography on the Skylab map was transferred from the 1954 map sheet. A similar map (not shown) was constructed from 1:50 000-scale aircraft photographs to serve as a basis of comparison; the precision of the map prepared from Skylab photographs was found to be within acceptable limits for the 1:100 000 scale. With use of the Skylab photographs, the mapping of the 2400-km^2 area was accomplished in 72 man-hours, a time element approximately 8 times less than that required for mapping with use of the 1:50 000-scale aircraft photographs.

Despite the poor B/H ratios, vertical Skylab imagery and the previously mentioned obliquely convergent photographs were used to produce topographic maps of portions of the Himalaya Mountains, Arizona, and Paraguay.

Mott et al. (ref. 2-24), using 2.5× glass diapositives of vertical S190A photographs and a first-order photogrammetric stereoplotter, produced 1:500 000- and 1:62 500-scale maps, both with 250-m contour intervals, of portions of the rugged Himalaya Mountains. In this analysis, only techniques and instrumentation commonly used in commercial mapping companies were used. Topographic mapping was performed by Goetz et al. (ref. 2-27) with the use of partial frames of S190B color photographs of central Arizona (fig. 2-29). An analytical plotter, contact diapositives, and ground control from 1:24 000- and 1:62 500-scale USGS topographic maps were used to produce a 1:100 000-scale topographic map with 150-m contours covering a 57- by 66-km area of the Verde Valley. A portion of this map, at one-half scale, is shown in figure 2-29(b). The highly convergent configuration created by a vertical strip of S190A photographs coupled with an oblique-looking strip of S190B photographs was used to map portions of Paraguay for which reconnaissance maps were available. An analytical plotter was used to produce 16 full and 13 partial topographic map sheets at a scale of 1:100 000 with 200-m contour intervals. An example of one of these map sheets, reduced to page size, is shown in figure 2-30 and illustrates the value for this type of mapping activity.

An experimental 1:250 000-scale photomap covering the same area as the standard 1° by 2° topographic sheet of Hartford, Connecticut, was produced by the USGS. The mosaic (fig. 2-31) was assembled from portions of four S190A black-and-white (0.6 to 0.7 μm) frames by using a photomechanical film mosaic process. Another photomap of the Hartford area was prepared at a 1:100 000 scale with use of the S190B color-infrared (0.5 to 0.88 μm) film. Both products meet national map accuracy standards for positional accuracy.
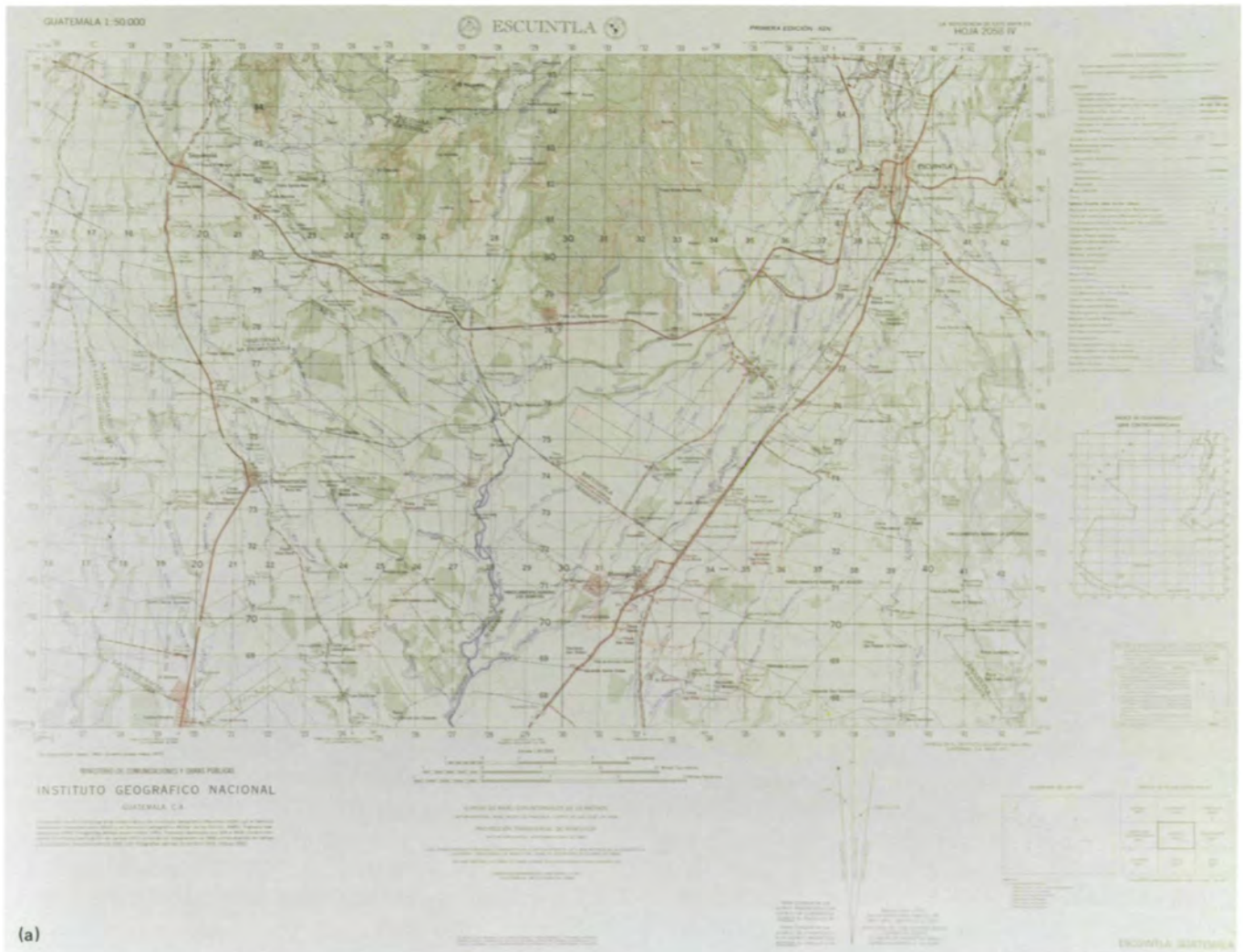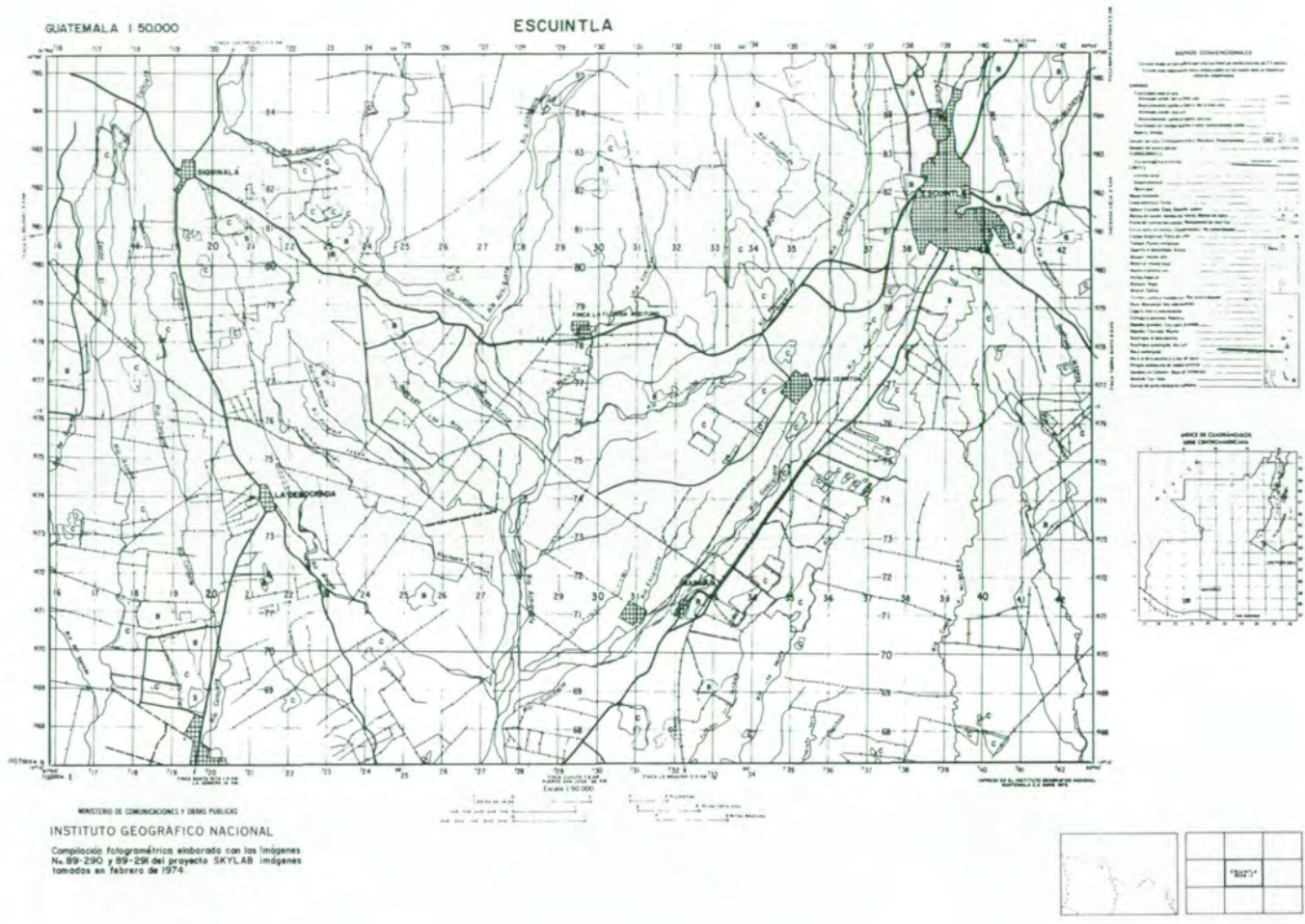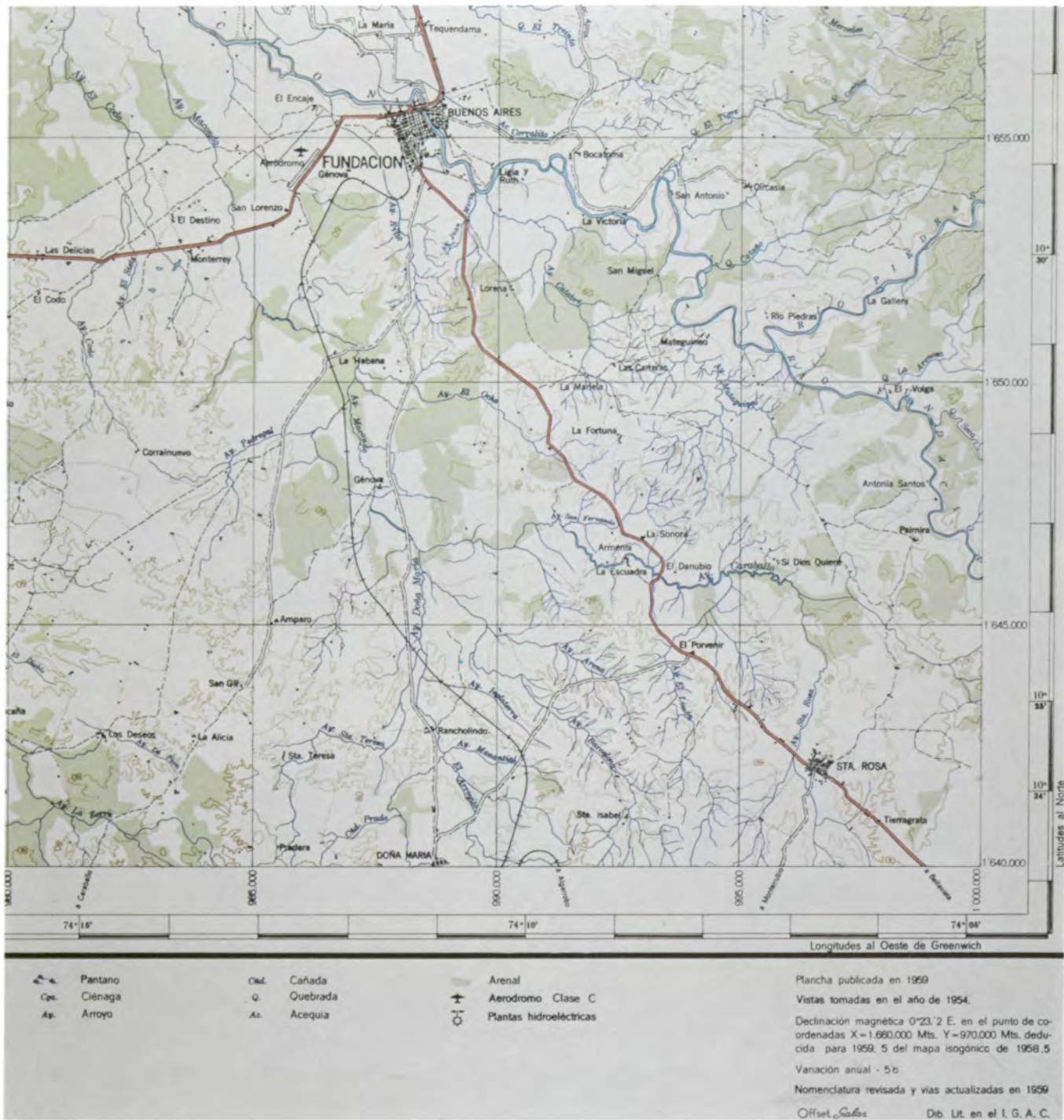
FIGURE 2-27.—Maps of Escuintla, Guatemala, and vicinity. (a) Conventional topographic map published in 1973 at a scale of 1:50 000. (b) Planimetric map compiled from S190B frames SL4-89-290 and SL4-89-291 obtained in February 1974.

(b)

FIGURE 2-27.—Concluded.

Map legend:

Pantano		Cñd.	Cañada		Arenal	
Cga.	Ciénaga	Q.	Quebrada		Aerodromo Clase C	
Ay.	Arroyo	Ac.	Acequia		Plantas hidroeléctricas	

Plancha publicada en 1959

Vistas tomadas en el año de 1954.

Declinación magnética 0°23.'2 E. en el punto de co-ordenadas X = 1.660.000 Mts. Y = 970.000 Mts. dedu-cida para 1959. 5 del mapa isogónico de 1958.5

Variación anual - 5'6

Nomenclatura revisada y vias actualizadas en 1959

Offset Salas   Dib Lit. en el I. G. A. C.

0   Scale, km   10

(a)

FIGURE 2-28.—Maps of Fundación, Colombia, area. (a) Conventional topographic map published in 1954 at a scale of 1:100 000. (b) Planimetric map prepared in 1975 from S190B color photograph. Topographic details were transferred from the map shown in figure 2-28(a).

(b)

FIGURE 2-28.—Concluded.

FIGURE 2-29.—Verde Valley, central Arizona. The broad, flat valley dominates the right half of the area shown. (a) S190B photograph (SL4-90-305). (b) Topographic map prepared using photograph shown in figure 2-29(a). (Original scale, 1:100 000.)
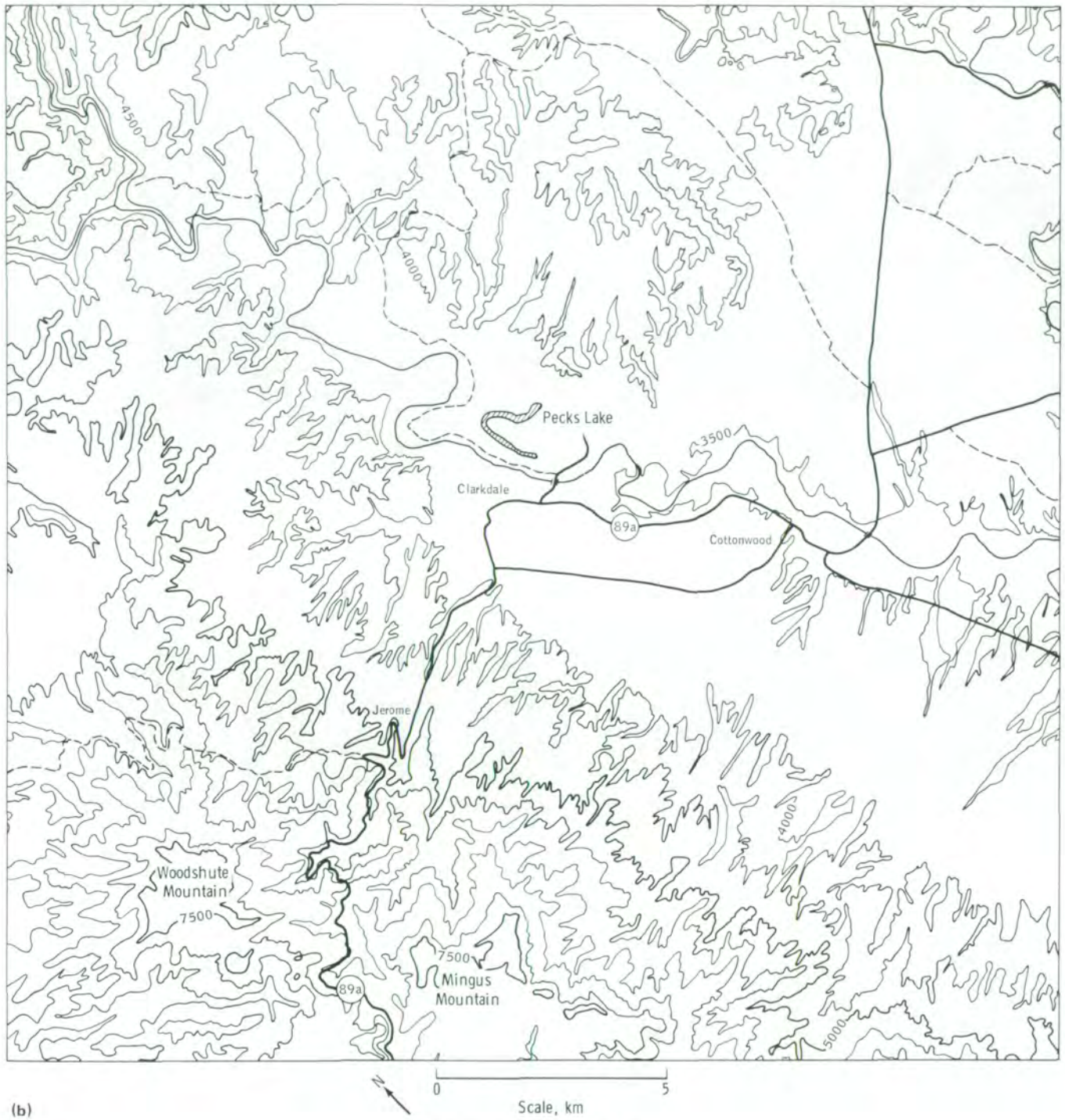
(b)

FIGURE 2-29.—Concluded.

FIGURE 2-30.—A topographic map of a portion of Paraguay produced from a vertical S190A frame coupled with an obliquely convergent S190B frame. The map is a reduction of the 1:100 000-scale compilation.

FIGURE 2-31.—A photomap of Hartford, Connecticut, and vicinity, produced from portions of four S190A black-and-white photographs. The format of the photomap corresponds to the existing USGS 1° by 2° series map sheet. The map is a reduction of the 1:250 000-scale compilation.

In Canada, Stewart (ref. 2-23) prepared a sample photomap that covered approximately one-third of a standard 1:250 000-scale map sheet. The S190B black-and-white data were rectified directly, in one stage, and provided an excellent image (3.8× enlargement) base and planimetric accuracy. Photomapping the same area from standard aerial photographs (1:36 000 scale) required 240 prints. With an increase in the number of photographic prints required to cover an area, density- and contrast-matching problems, as well as defects due to banding and tone control, occur. Space photographs such as those obtained from the S190B system eliminate the majority of these defects, and large areas can be mapped by using relatively few space photographs.

A very practical feature of vertical S190A- and S190B-type data is the capability for use as uncontrolled photomaps. Individual frames can be directly enlarged to the specific scale and format that permits direct comparison between the enlarged photograph frame and existing line maps. The enlarged frame is relatively free of distortions, and positioning to map control is more than adequate for visual comparisons of changes in map detail. Photographs from the S190B system have been enlarged to the 1:24 000 scale of standard topographic maps (approximately 40× enlargement) to permit visual comparisons of the cultural changes that have occurred since the map was published.

Summary

The accomplishments and results of the various Skylab EREP cartographic experiments have demonstrated the potential and the practicality of using quality photographs from orbiting spacecraft as a means of preparing and updating certain types of maps and other cartographic products. It was clearly shown that, with suitable spectral resolution and geometric fidelity, photographs from space can serve as an adequate source for a variety of cartographic products at scales of 1:100 000 and smaller. With improved resolution, this scale limit might be improved to 1:50 000 or even 1:24 000. It was concluded that Skylab EREP space

photographs cannot completely supplant aircraft photographs and ground-truth information for cartographic applications at scales of 1:100 000 and larger. The need for convergent photographs to enable detailed topographic mapping from space images was demonstrated.

Little effort was expended on investigating the spectral aspects of the Skylab imagery in cartographic applications. This area should be specifically marked for future study.

To accomplish most cartographic objectives, cloud-free photographic coverage at repeated intervals is required over most regions. Because of problems created by weather, a satellite totally dedicated to cartography seems to offer the highest potential for satisfying this need. Such a satellite, with one or more high-resolution, large-format, long-focal-length cameras designed to photogrammetric standards, would provide a practicable means of solving many terrestrial mapping problems. Such a system would prove especially valuable for the establishment and densification of ground control, the construction of new maps and photomosaics in the more remote regions of the Earth, and the revision and updating of existing cartographic products.

REFERENCES

2-1. Anderson, J. R.; Hardy, E. E.; and Roach, J. T.: A Land-Use Classification System for Use With Remote Sensor Data. U.S. Geol. Survey Circ. 671, 1972.

2-2. Hannah, John W.; Thomas, Garland L.; and Esparza, Fernando: Planning Applications in East Central Florida. NASA CR-145415, 1975.

2-3. Stoeckeler, E. G.; Woodman, Raymond G.; and Farrell, Robert S.: Multidisciplinary Analysis of Skylab Photography for Highway Engineering Purposes. NASA CR-141942, 1975.

2-4. Colwell, Robert N.; Bowden, Leonard W.; et al.: Use of Skylab Imagery to Assess and Monitor Changes in the Southern California Environment. NASA CR-147561, 1974.

2-5. Hoffer, Roger M.: Computer-Aided Analysis of Skylab Multispectral Scanner Data in Mountainous Terrain for Land Use, Forestry, Water Resource, and Geologic Applications. NASA CR-147473, 1975.

2-6. Poulton, Charles E.; and Welch, Robin I.: Plan for the Uniform Mapping of Earth Resources and Environmental Complexes From Skylab Imagery. NASA CR-144484, 1975.

2-7. Hardy, E. E.; Skaley, J. E.; et al.: Enhancement and Evaluation of Skylab Photography for Potential Land Use Inventories. NASA CR-144473, 1975.

2-8. Cooper, Saul; Anderson, Duwayne; et al.: Skylab Imagery: Application to Reservoir Management in New England. NASA CR-144514, 1975.

2-9. Klemas, Vytautas; Bartlett, David S.; et al.: Skylab/EREP Application to Ecological, Geological, and Oceanographic Investigations of Delaware Bay. NASA CR-144910, 1976.

2-10. Simonett, David S.: Application of Skylab EREP Data for Land Use Management. NASA CR-147457, 1976.

2-11. Alexander, Robert H.; and Lins, H. F., Jr.: Selected Applications of Skylab High-Resolution Photography to Urban Area Land Use Analysis. NASA CR-139997, 1974.

2-12. Baldridge, Paul E.; Goesling, P. H.; et al.: Utilizing Skylab Data in On-Going Resources Management Programs in the State of Ohio. NASA CR-134938, 1975.

2-13. Welby, Charles W.; and Lammi, J. O.: Utilization of EREP Data in Geological Evaluation, Regional Planning, Forest Management, and Water Management in North Carolina. NASA CR-144104, 1975.

2-14. Silva, Leroy F.: A Study of the Utilization of EREP Data From the Wabash River Basin. NASA CR-147412, 1976.

2-15. Gilmer, Davis S.; and Work, Edgar A., Jr.: Utilization of Skylab (EREP) System for Appraising Changes in Continental Migratory Bird Habitat. NASA CR-147542, 1975.

2-16. Higer, A. L.; Coker, A. E.; Schmidt, N. F.; and Reed, L. E.: An Analysis and Comparison of Landsat-1, Skylab (S-192), and Aircraft Data for Delineation of Land-Water Cover Types of the Green Swamp, Florida. NASA CR-144855, 1976.

2-17. Polcyn, Fabian C.; Rebel, Diana L.; and Colwell, John E.: Analysis of Hydrological Features of Portions of the Lake Ontario Basin Using Skylab and Aircraft Data. NASA CR-147456, 1976.

2-18. Sattinger, I. J.; Sadowski, F. G.; and Roller, N. E. G.: Analysis of Recreational Land Using Skylab Data. NASA CR-144471, 1976.

2-19. Brooks, Ronald L.; and Parra, Carlos G.: Applicability of Satellite Remote Sensing for Detection and Monitoring of Coal Strip Mining Activities. NASA CR-144474, 1975.

2-20. Weir, Charles E.; Powell, Richard L.; et al.: Application of EREP Imagery to Fracture-Related Mine Safety Hazards in Coal Mining and Mining-Environmental Problems in Indiana. NASA CR-144495, 1975.

2-21. Anderson, R. R.; Carter, V. P.; and Alsid, L. J.: Skylab-EREP Investigations of Wetlands Ecology. NASA CR-139224, 1974.

2-22. Staples, Jack E.; Eoldan, J. J. M.; et al.: Overall Evaluation of Skylab Imagery for Mapping of Latin America. NASA CR-144476, 1975.

2-23. Stewart, R. A.: Investigation of Selected Imagery From Skylab/EREP S190 System for Medium and Small Scale Mapping. NASA CR-144542, 1975.

2-24. Mott, P. G.; Fullard, H.; et al.: Cartographic Research in EREP Program for Small Scale Mapping. NASA CR-144478, 1975.

2-25. Colvocoresses, Alden P.: Overall Evaluation of Skylab (EREP) Images for Cartographic Application. NASA CR-147423, 1975.

2-26. Keller, Morton: Analytic Aerotriangulation Utilizing Skylab Earth Terrain Camera (S-190B) Photography. NASA CR-144387, 1975.

2-27. Goetz, A. F. H.; Abrams, M. J.; et al.: Comparison of Skylab and Landsat Images for Geologic Mapping in Northern Arizona. NASA CR-147503, 1976.

Page Intentionally Left Blank

3

Agriculture, Range, and Forestry

ROBERT N. COLWELL,[a†] *F. PHILIP WEBER,*[b]
AND RYBORN R. KIRBY[c]

AGRICULTURISTS, RANGE MANAGERS, and foresters are primarily concerned with the management of resources such as crops, forage, livestock, timber, soil, and water. If wisely managed, these resources will continue to provide mankind with food, fiber, and shelter; if they are not wisely managed, man's survival will become threatened. During the past 100 years, the extent of resource management and production has accelerated rapidly. Resource managers have identified the need for timely and accurate information on what is being produced; where it is being produced; the general state of health, or condition, of the resource; and the amounts expected to be produced.

In the past decade, the data acquired by spacecraft have provided a new tool to assist in the decisionmaking processes of the resource managers. The purpose of this section is to show, with specific examples, how the data acquired by the Earth Resources Experiment Package (EREP) can be used to satisfy some of the information needs of resource managers. Numerous investigators addressing different information requirements submitted findings, and the most pertinent examples are cited in this report. The EREP investigators have demonstrated the capability to inventory many different types of agricultural, range, and forestry resources. The results show that the findings obtained at their test sites are applicable to analogous areas throughout the world.

The wise management of Earth resources requires implementing a three-step process: inventory, analysis, and operations. In the inventory step, an area-by-area determination is made of the amount and quality of the existing resources. In the analysis step, management decisions are made with respect to the ultimate use of the resources after consideration of the type and condition of the resources and the cost benefits. In the operations step, the resource manager implements each decision made in the analysis phase; e.g., the decision to apply the appropriate fertilizer in certain mineral-deficient parts of an agricultural area; the decision to practice deferred, rotational grazing in certain parts of a rangeland area; or the decision to cut only the overmature trees in a certain part of the forest area. The resources are highly dynamic rather than static; to effectively manage them, a new inventory must be obtained periodically (a process known as monitoring).

DATA REQUIREMENTS AND APPLICATIONS

The types of information necessary for monitoring vegetation resources are provided in table 3-I. Federal, State, and county agencies, as well as industrial firms (identified in table 3-II), use this information, which currently is largely obtained by means of ground surveys. Although relatively small amounts of the resource data are obtained by remote-sensing techniques, the use of such remotely sensed data has greatly increased during the last decade. Satisfying the requirements for all these users is complicated because the users want different information about vegetation groupings in

---

[a]University of California at Berkeley.

[b]U.S. Department of Agriculture Forest Service.

[c]NASA Lyndon B. Johnson Space Center.

[†]Principal Investigator.

TABLE 3-I.—Types of Resource Information Desired

Agricultural crops	Timber stands	Rangeland forage	Brushland vegetation
Present crop vigor and stage of maturity	Present tree and stand vigor by species and size class	Present "range readiness" (for grazing by domestic or wild animals)	Vegetation density
Prevalence of crop-damaging agents by type	Prevalence of tree-damaging agents by type	Prevalence of forage-damaging agents (weeds, rodents, diseases, etc.) by type	Information desired as a function of vegetation (i.e., for watershed protection, game habitat, esthetics, etc.)
Prediction of time of maturity and eventual crop yield per square hectometer by crop type and vigor class	Present volume and prediction of probable future volume per square hectometer by species and size class in each stand	Present animal-carrying capacity and probable future capacity per square hectometer by species and range condition class in each forage type	Information desired as a function of vegetation (i.e., for watershed protection, game habitat, esthetics, etc.)
Total area in each crop type and vigor class	Total area in each stand type and vigor class	Total area in each forage type and condition class	Information desired as a function of vegetation (i.e., for watershed protection, game habitat, esthetics, etc.)
Total present yield by crop type	Total present and probable future yield by species and size class	Total present and probable future animal capacity	Information desired as a function of vegetation (i.e., for watershed protection, game habitat, esthetics, etc.)

TABLE 3-II.—Users Desiring Resource Information

Level	Agricultural crops	Timber stands	Rangeland forage	Brushland vegetation
Federal	Agricultural Stabilization and Conservation Service, Agricultural Conservation Program, Commodity Credit Corp., Agricultural Marketing Service, Statistical Reporting Service, Economic Research Service, Soil Conservation Service, Federal Crop Insurance Corp., Farmers Home Administration, Rural Community Development Service, Foreign Agricultural Service, Famine Relief Program, Foreign Economic Assistance Program, Department of Commerce Agricultural Census Program	U.S. Forest Service, Bureau of Land Management, and many Federal agencies listed previously	U.S. Forest Service, Bureau of Land Management, and many Federal agencies listed previously	Primarily U.S. Forest Service and Bureau of Land Management
State and county	Agricultural Extension Service, State tax authority	Division of Forestry, Forest Extension Service, State tax authority	Livestock Reporting Service, Range Extension Service, State tax authority	Division of Forestry, Division of Beaches and Parks, Water Resource Agency, State tax authority
Private	Fertilizer and pesticide producers, crop-harvesting industry, food-processing and packing industry, transportation industry, food and fiber advertising and marketing industry	Fertilizer and pesticide producers, logging industry, wood-processing industry, transportation industry, wood and wood products advertising and marketing industry	Fertilizer and pesticide producers, meatpacking industry, tanning industry, transportation industry	Hunting and fishing commissions, public utilities commissions, local irrigation districts

different places, at different times, and with different levels of accuracy. In addition, they have different requirements as to the speed with which vegetation information must be processed after the raw data have been collected, and the frequency with which the information must be updated (table 3-III).

The EREP investigators considered the remote-sensing capabilities that would be necessary to satisfy some of the resource information requirements in table 3-I, and, in this context, they analyzed the EREP data to determine the potential for providing needed information. Although the primary emphasis was given to vegetation resources, it was recognized that agriculturists, range managers, and foresters are also interested in animal resources such as livestock and wildlife. Moreover, they are interested in the entire complex of Earth resources (including soils, water, minerals, and atmosphere) in the areas for which they have management responsibilities. In the following subsections, the results of the EREP investigations are presented for most types of data required to monitor vegetation resources.

Agriculture

Recently, agriculturists were asked to list the specific applications of remote sensing that might prove profitable in terms of cost/benefit ratios and the total savings that might be achieved for each crop. In addition to the types of data shown in table 3-I, they selected the most important candidate problem in U.S. agriculture—the extent of damage done each year to specific crops by specific insects or pathogens.

Range

Range managers are concerned with land management and with animal management on lands that produce mature forage for animal (wild or domestic) consumption. One of the major objectives of a range manager is maximization of the production forage concurrent with conservation of the land resources. In the United States, there are two basic types of range areas, for which the same resource information is required.

TABLE 3-III.—Frequency With Which Resource Information Is Desired

Time interval	Agricultural crops	Timber stands	Rangeland forage	Other vegetation (mainly shrubs)
10 to 20 minutes	Observe advancing waterline in croplands during disastrous floods; observe the start of locust flights in agricultural areas	Detect the start of forest fires during periods when there is a high "fire-danger rating"	Detect the start of rangeland fires during periods when there is a high fire-danger rating	Detect the start of brushfield fires during periods when there is a high fire-danger rating
10 to 20 hours	Map perimeter of ongoing floods and locust flights; monitor the wheat belt for outbreaks of black-stem rust caused by spore showers	Map perimeter of ongoing forest fires	Map perimeter of ongoing rangeland fires	Map perimeter of ongoing brushfield fires
10 to 20 days	Map progress of crops as an aid to crop identification (using "crop calendars") and estimate date to begin harvesting operations	Detect start of insect outbreaks in timber stands	Update information on range readiness for grazing	Update information on times of flowering and pollen production in relation to the bee industry and to hay fever problems
10 to 20 months	Facilitate annual inspection of crop rotation and compliance with Federal requirements for benefit payments	Facilitate annual inspection of firebreaks	Facilitate annual inspection of firebreaks	Facilitate inspection of firebreaks
10 to 20 years	Observe growth and mortality rates in orchards	Observe growth and mortality rates in timber stands	Observe signs of range deterioration and study the spread of noxious weeds	Observe changes in "edge effect" of brushfields that affect suitability as a wildlife habitat
20 to 100 years	Observe shifting cultivation patterns	Observe plant succession trends in timber stands	Observe plant succession trends on rangelands	Observe plant succession trends in brushfields

These areas are (1) Federal and publicly owned lands and (2) State and privately owned grasslands. The Federal and publicly owned lands are located primarily in the 17 Western States and are managed by the U.S. Government. The State and privately owned lands are generally east of the Rocky Mountains and are managed by State governments and/or private owners. The managers for both types of areas have the same objectives, and their management efforts are governed by the information requirements given in table 3-I. Satisfying these objectives requires continual monitoring of all vegetation to avoid forage waste, overgrazing, and damage to the range resources. The private owner acquires this information by frequent in situ observations, but managers of the larger, publicly owned lands can only inspect representative portions and extrapolate the information obtained from sample areas to other nearby regions. This extrapolation is difficult and unreliable because of the many unknown factors, including rainfall patterns, vegetation differences, and habitats of livestock and wildlife.

Forestry

Foresters need essentially the same information (table 3-I) as that required by agriculturists and range managers. Using a somewhat different approach, foresters indicated that remote sensing can be especially helpful by providing information on which to base multiple-use decisions relative to each part of the forest. The multiple-use concept is complex and more applicable to forestry than to agriculture. Some foresters prefer to have all parts of an area managed with respect to maximization of timber production; others want to preserve the forests as primeval museums to be enjoyed in perpetuity. Between these two extremes are those who condone each of these uses for specific parts of a forest if such use does not interfere with the use of the forest primarily as a source of water for domestic use and minerals for industrial use and the preservation of esthetic qualities for recreational use. To support intelligent decisionmaking processes regarding the best use of each part of the forest, two major types of information are needed: (1) a resource map that accurately delineates the forest vegetation and all associated resources (soils, water, minerals, etc.) and (2) adequate sociological, economic, and technological data to ensure that the forests can produce "the greatest good for the

greatest number." Forestry applications addressed only the first of these two complex and interrelated requirements, a resource map of forested areas. The authors of this section believe that management techniques can be enhanced by the use of space-acquired information, which will assist the large-area manager in decisionmaking processes.

INVENTORY BY PHOTOINTERPRETATION

A primary objective of this section is to discuss the extent to which EREP data will satisfy the informational needs of various users in the fields of agriculture, range management, and forestry. The EREP investigators identified the type of data and analysis techniques that would provide the required information for resource management. The usefulness of the information was evaluated in terms of type of data, frequency of observations, need for ancillary data, and method of using the data for resource management decisions. The EREP investigators, both domestic and foreign, have demonstrated the capability to inventory many different resources within the disciplines of agriculture, range management, and forestry.

Crop and Acreage Inventory

Agricultural land use and crop-producing areas are discernible in photographs taken with the Multispectral Photographic Camera (S190A) and the Earth Terrain Camera (S190B) when the photographs are analyzed by standard photointerpretative techniques. The crops identified were citrus, coffee, sugarcane, and wheat.

The S190B color and color-infrared photographs of the Rio Grande Valley, enlarged to a scale of 1:63 000, were projected onto a standard viewing screen, resulting in a scale of 1:10 000 (Hart et al., ref. 3-1), and interpreted by an agricultural analyst to identify vegetative patterns and to discriminate citrus, sugarcane, and crops grown in larger fields. This data format (figs. 3-1(a) and 3-1(b)), when supported by transect low-altitude-aircraft data (fig. 3-1(c)) and ground truth (fig. 3-1(d)), provided the information required for a field-by-field interpretation. When color-infrared photographs were analyzed, only annual crops and fallow land were identified with 100 percent accuracy. Citrus
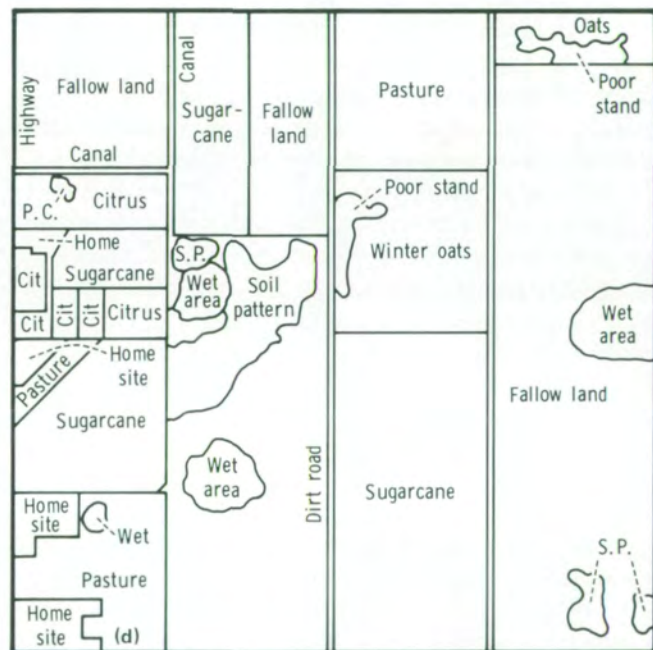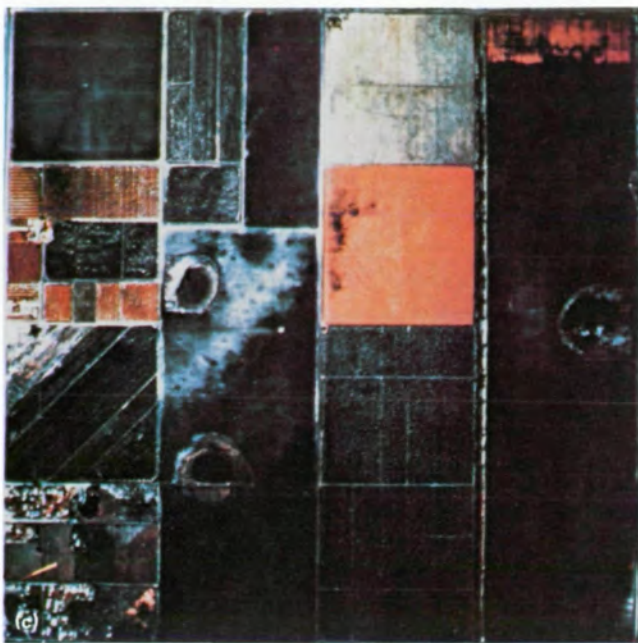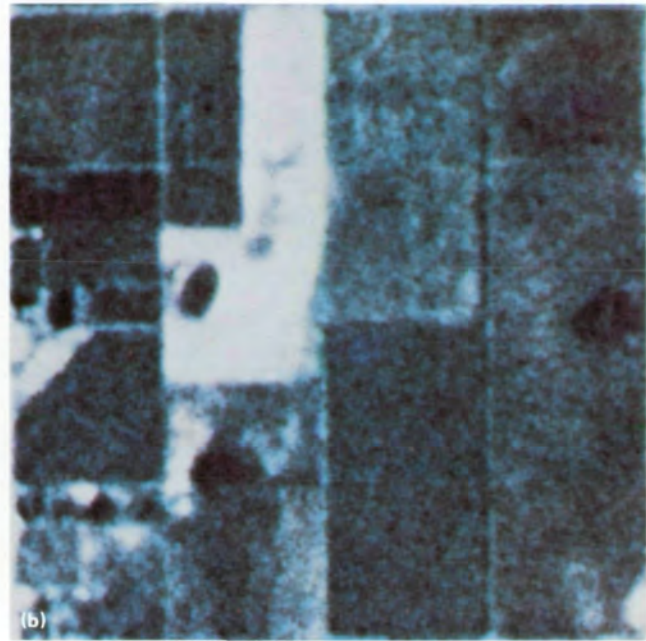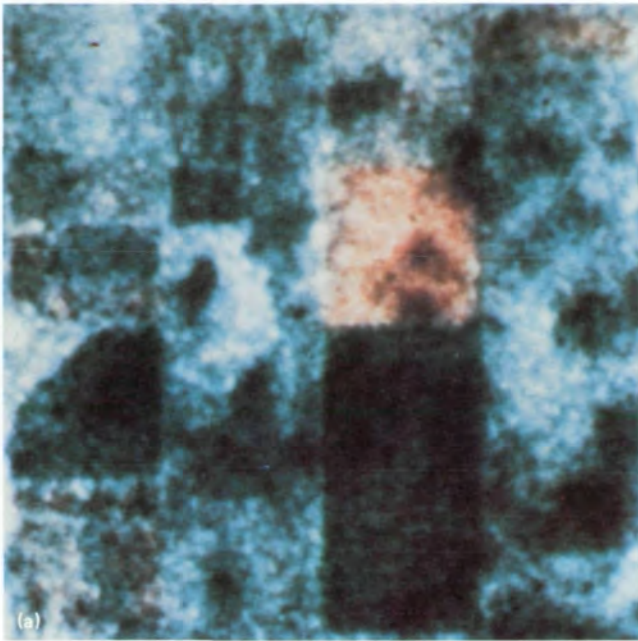
FIGURE 3-1.—An intensive agricultural area near Weslaco, Texas, with major crops of sugarcane, citrus, and vegetables. (a) S190B color-infrared photograph taken January 28, 1974 (SL4-93-326). (b) S190B color photograph taken December 5, 1973 (SL4-91-005). (c) Aircraft color-infrared photograph. (d) Ground-truth map. The abbreviation P.C. indicates poor cover; S.P., soil pattern.

was identified with an accuracy of 93 percent when color-infrared film was used and with an accuracy of 80 percent when conventional color film was used. However, when both film types were analyzed concurrently, citrus was identified with 100 percent accuracy. This analysis identified the areal extent of frost damage to sugarcane growing in the test area.

The areal extent of frost damage in July 1973 (de Mendonca et al., ref. 3-2) to the coffee of Maringá, Paraná, Brazil, was assessed using a multilevel surveying system in which Landsat, Skylab, low-altitude aircraft, and field visits were the information sources. An S190B high-resolution color photograph (fig. 3-2(a)) acquired on August 8, 1973, was used to delineate the coffee- and wheat-growing areas (fig. 3-2(b)) and to serve as a training area for analysis of Landsat computer-compatible tapes using an interactive multispectral image analysis system. The descriptor, which enabled identification of the two crops, was the cultural pattern shown in figure 3-2(a). The analysis, in which classification results based on multistage sampling were used, indicated that 852 884 hm² (2 107 522 acres) of frost-affected coffee, 33 864 hm² (83 680 acres) of normal coffee, and 302 342 hm² (747 103 acres) of wheat were present in the study area. This multilevel survey of a major agricultural commodity provided a rapid assessment of the economic losses sustained from an act of nature.

When a statistical approach was used to inventory an agricultural area for crop types and acreage, color and color-infrared photographs in a 23.0- by 23.0-cm format were used to identify the differing cultural patterns or strata and were outlined directly on the working data. The photographic texture, tone, color, pattern, size, shape, shadow, location, and associated features were used to identify a stratum (a large homogeneous area) (Colwell et al., ref. 3-3). The textures (coarse, medium, and fine) (fig. 3-3) were indicative of the field sizes in the areas of interest. From experience, the analyst knows that a coarse texture (65- to 32-hm² (160 to 80 acre) field size) indicates a predominance of field crops, a medium texture (12- to 32-hm² (30 to 80 acre) field size) indicates a mixture of field and vegetable crops, and a fine texture (4- to 12-hm² (10 to 30 acre) field size) indicates vineyards and pastures. Color and color-infrared photographs from the S190A system, enlarged to a scale of 1:805 000 (20.3 by 20.3 cm), provided a scale that was considered optimum for this task.

Color within each stratum indicated the crop type and degree of maturity. Based on photographic texture and color, areas were identified in which to obtain ground-based transects for the development of agricultural statistics (acreage, crop type, crop maturity, irrigated fields, etc.). The image analyst used these statistics to perform stratum-by-stratum inventories for crop acreage and crop class. (Classes were mature or immature for wheat, barley, and safflower.) When this procedure was used, sampling efficiency was increased, classification errors were reduced, and an agricultural stratum inventory was achieved with an accuracy of 10 to 20 percent at the 95-percent-confidence level, with a cost reduction of 15 to 1 (ref. 3-3).

Acreage measurements of three land use categories were made by using stereoscopic study and image magnification of the S190A and S190B photographs. When the S190A photographs were enlarged (20×), forest, bare soil, and wetlands were readily identified.[1] Generally, the S190A photographs were satisfactory for interpreting gross characteristics only at the regional level. Major boundaries, such as roads and section lines, could not be identified. When forests and generalized crop categories were delineated by using late-summer photographs or the most cloud-free photographs, accuracies of 93 and 94 percent, respectively, were achieved. The quality of the S190A photographs acquired over a Michigan test site was highly variable between passes and film/filter combinations and between duplicates of the filmstrips. The resolution was marginal for purposes of crop acreage estimation. Analysis of S190B black-and-white photographs acquired from this same Michigan test site in late summer indicated that section lines, roads, and field boundaries were readily visible because of the improved resolution of the sensing system. The acreage measurements were performed on magnifications of 15×, with an ocular grid having a 0.25-mm line spacing.

When stereoscopic and image magnification procedures were used to estimate the acreage of 170 fields, there was a tendency to underestimate the acreage of fields larger than 4 hm² (10 acres) and a tendency to overestimate on fields smaller than 4 hm² (10 acres).

---

[1] Lester V. Manderschied, "Economic Evaluation of Crop Acreage Estimation by Multispectral Remote Sensing," EPN 472-II, Mich. State Univ., Dept. of Agriculture Economics, East Lansing, Mich., 1975.
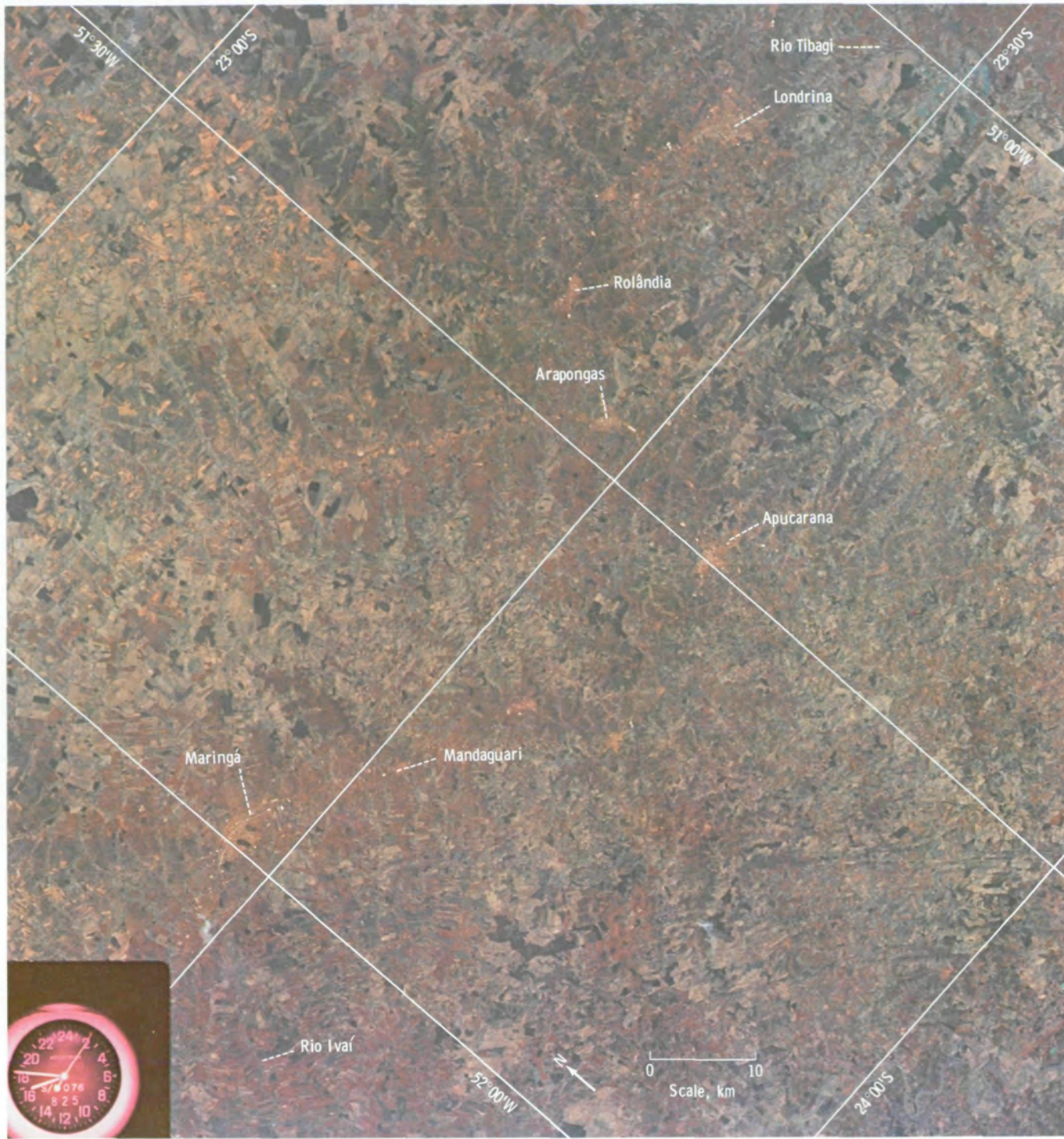
FIGURE 3-2.—Maringá, Paraná, Brazil. (a) S190B high-resolution color photograph of the coffee-growing area near Maringá, Paraná, Brazil, taken August 8, 1973 (SL3-83-361). (b) Coffee plantations delineated using the cultural pattern shown in figure 3-2(a).
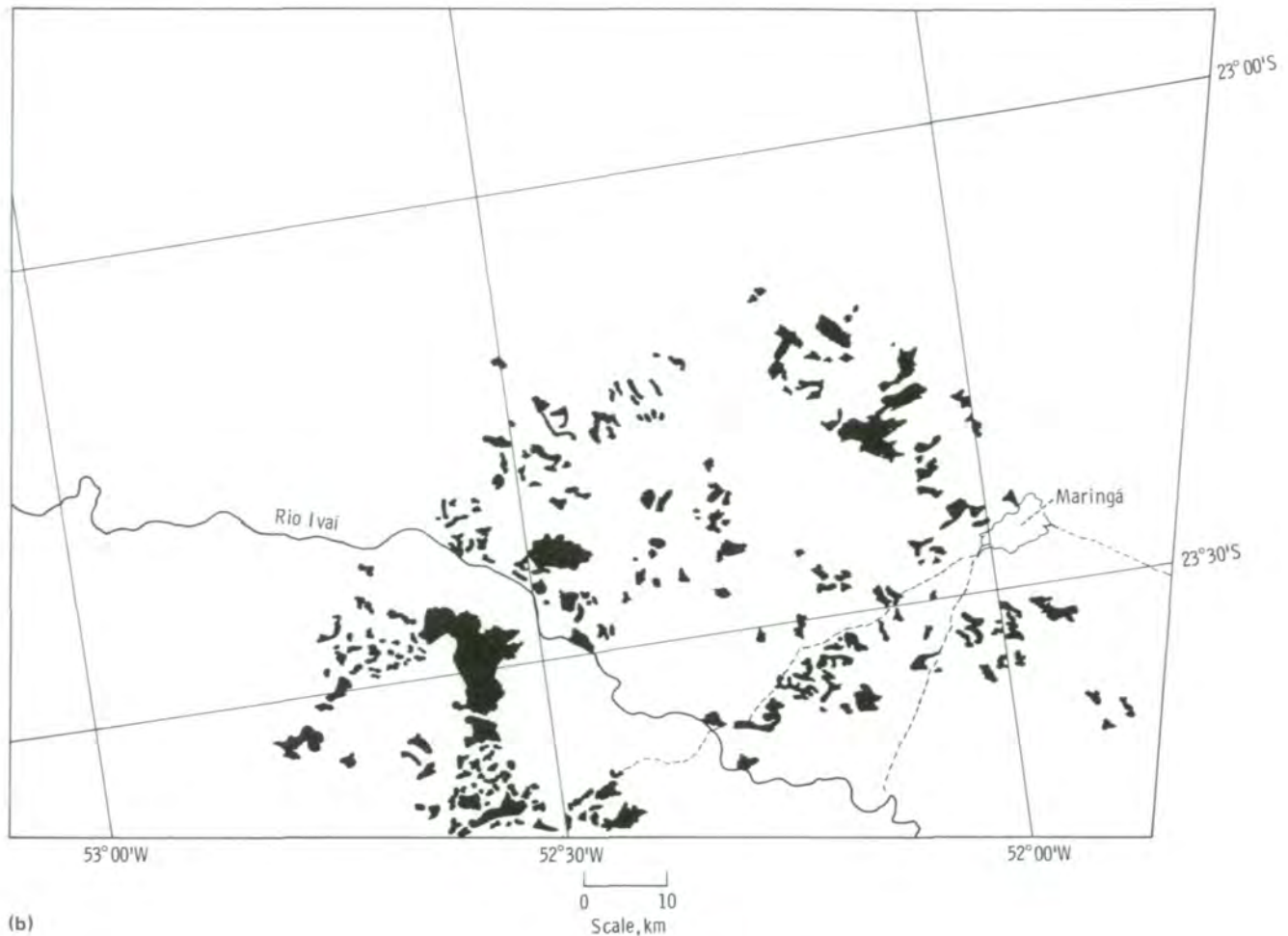
(b)

FIGURE 3-2.—Concluded.

Even with these biases, an aggregated percentage error of 6 percent below the actual acreage in the test site was achieved. The resolution obtained by the S190B system was judged to be adequate for crop acreage assessment for major field crops, but further improvement in resolution will be useful for crops, such as vegetables, that are often grown on small plots.

Analysis of Digitized Photographs

Automatic data-processing techniques were used in the analysis of EREP photographs converted to a digital format to determine the extent to which agricultural information could be extracted (Colwell et al., ref. 3-3). The four bands of S190A black-and-white photographs

acquired over the Salinas Valley of California during the Skylab 2 and 3 missions were digitized with a microdensitometer and stored on magnetic tape. The scale of the photographs was approximately 1:2 850 000, and the scan interval along the X- and Y-axes was 0.0254 cm with an aperture setting of 0.00254 cm. The resulting resolution cell represented a 0.45-hm^2 (1.12 acre) area on the ground. Actual scanning time was 0.5 hr/band, with 0.5 hour for setup, for a total time of 2.5 hours to digitize four bands of data.

The magnetic tapes were reformatted to be compatible with a computer program that used a five-step procedure to identify the predominant crops present in the valley (i.e., tomatoes, carrots, lettuce, asparagus, and cauliflower). Because tomatoes and lettuce were in distinct stages of development during the September

FIGURE 3-3.—Southwestern San Joaquin Valley, California, June 3, 1973. Land use strata (fig. 3-3(b)) are correlated fairly well with the boundaries between the valley basin and valley basin rim soils and with the boundaries between the alluvial and bedrock soils (fig. 3-3(a)). However, the boundary between the valley basin rim soils and the alluvial fan soils does not correlate with any of the agricultural land use strata boundaries. (a) Natural color S190A photograph (SL2-04-121). Boundaries between major soil types have been transferred from a soil map. Red crosshatched areas represent the valley basin soils, blue hatching shows the valley basin rim soils, and yellow hatching correlates with the alluvial fan soils. Unhatched areas represent soils that developed on bedrock material. (b) False-color-infrared S190A photograph showing land use strata (SL2-03-121).

Skylab 3 overpass, they were further divided into two subclasses: immature and mature.

The initial analysis program stratified the test area and produced gray-scale maps of discrete features to assist in the selection of training areas for the computer. With use of the training area, statistics for classifying each stratum were derived, identifying the mean density, the standard deviation, the spectrograms, and the histograms for each field and class of each band; correlation and covariance matrices were developed for each field and class for all bands. An optimization of the combination of data bands was performed to give

the interclass divergences of each combination of crops for each combination of bands. When each stratum was inventoried, the statistics that had been developed and the optimum bands for classification were used to address each data point (0.45 hm^2 (1.12 acres)) of the test area, assigning a character to each point that corresponded to one of the training classes. For validation, the stratum was reclassified by using a nearest neighbor algorithm, which also produced an accuracy statement.

When the six bands of the S190A photography were analyzed for crop discrimination, the four bands (i.e., an optimum number of bands for classification is four or less bands of data) that consistently provided the highest accuracies for both the June 2, 1973, and September 13, 1973, Skylab data takes were (1) green (0.5 to 0.6 μm), (2) red (0.6 to 0.7 μm), (3) infrared 1 (0.7 to 0.8 μm), and (4) infrared 2 (0.8 to 0.9 μm). Of all the combinations, the green band contributed more information, particularly when used in conjunction with the other bands, because the vegetative cover of the fields was particularly dense and, as a consequence, the reflectance in the green band was high.

When this analysis procedure was applied to the digitized June 2, 1973, S190A photographs, the classification accuracy was low, with an overall 49.5 percent correct and an average of 58.3 percent correct by crop class. However, the training classes of two vegetables (carrots and asparagus) that were in an advanced state of maturity were classified with a high degree of accuracy (89.2 and 98.1 percent, respectively).

When the digitized September 13, 1973, S190A photography was classified, an overall accuracy of 85.1 percent was achieved. Most of these crops were in an advanced state of maturity. For all crops except beans, the correct classifications exceeded 80 percent. The low performance (60.3 percent correct) for beans was attributable to the harvesting of beans throughout the area. These results indicate that when vegetable crops are inventoried by means of remotely sensed data, the proper timing of data collection is more critical than it would be for field crops. Frequently, in a given area, individual vegetable crops will be in different stages of development, whereas individual field crops will be in a common stage of maturity. Therefore, if single-date data are not acquired at precisely the correct time, multidate data will be required for vegetable crop inventories.

Analysis of Multispectral Scanner Data

The Multispectral Scanner (S192) provided vast quantities of narrow-band spectral data that were used for developing techniques to perform automatic classification of agricultural crops and to assist in large-area crop inventories. However, even with the use of a computer, the large volume of data presented a major analysis problem.

Based on knowledge derived from analysis of aircraft scanner and multidate Landsat data, the consensus is that when no more than six or eight bands of data are available for analysis, classification accuracies increase as the number of bands of analyzed data increases. The cost of analysis, in both time and money, also increases with an increase in the number of bands of analyzed data. Therefore, the prime task is to select the optimum bands for future classification and to minimize the number of bands required to achieve a specified level of accuracy.

Crop class and subclass signatures were developed from S192 data[1] by using 12 bands. Because of large anomalies in the data, band 2 was deleted. Supervised field clustering using center picture elements (pixels) produced distinct signatures of each class that were not contaminated by border-area pixels. To reduce the cost of classification, the number of signatures was reduced by a band-ranking criterion, which used an average pairwise probability of misclassification based on this selection, and the combination of bands most probable for identification was chosen. This process indicated that bands 5, 8, and 9 provided little aid for discrimination between major ground-cover types. Recognition signatures on three different training sets were identified, and the selected bands are shown in table 3-IV. A test site, approximately 233 km^2 (90 sections), in eastern Ingham County, Michigan, was chosen for reclassification. The signatures developed from the training sets in the northern half of the test site were used to reclassify 104 km^2 (40 sections) in the northern half of the county and then to classify 124 km^2 (48 sections) in the southern half of the test site. The accuracies for

[1]Lester V. Manderschied, "Economic Evaluation of Crop Acreage Estimation by Multispectral Remote Sensing," EPN 472-II, Mich. State Univ., Dept. of Agriculture Economics, East Lansing, Mich., 1975.

TABLE 3-IV.—Recognition Signature Bands

Training set, no. of sections (a)	Band (b)
40	3
	6
	7
	11
	10
	8
	9
20	3
	6
	7
	11
	12
	10
	8
	9
10	3
	7
	11
	12
	10
	8

aEach section within a training set represents 2.6 km² (1 s. mi²).

bSee table 3-VI for band wavelengths.

reclassification and signature extension for the different signatures are listed in table 3-V. Initial observations indicate an exception to the rule that the more training sets used for signature development, the higher the accuracy of classification. As given in table 3-V, signatures developed from the 20-section training set achieved a better performance accuracy. This accuracy is a result of the procedures followed when developing the signatures from the 40-section training set, in which more signatures were combined or dropped in the initial signature-analysis procedures.

Man/machine interactive analysis of the S192 data was performed by Colwell et al. (ref. 3-3), by using all the 22 data outputs from the 13 channels. The analysis processes were the same as those described in the discussion of the analysis of digitized photographs, except that there was a larger array of data channels (table 3-VI). An optimization program identified the bands of data most appropriate for classifications of the scene.

The selection process was one of either selecting different bands or discriminating between two data outputs within a discrete data band. The process was one of data source selection in which the 22 data outputs (table 3-VI) were displayed on a television monitor to screen out data outputs that were unusable because of saturation or high systematic noise. Three data outputs from the remaining data of each area of interest were displayed on a color monitor, and the training area within each stratum of interest was identified. A grid coordinate that was displayed simultaneously on the monitor assisted in locating the training sets.

When a complex agricultural scene west of Fresno, California (fig. 3-4), was analyzed, an overall classification accuracy of 81.8 percent and an average performance, by class, of 78.9 percent were achieved. During the analysis of a less complex agricultural stratum (i.e., wheat, barley, and safflower in an annual grass region of the Pacific coast range), a significant increase in accuracies was achieved. For an area in the western San Joaquin Valley, classification accuracies of 100, 100, and 98.6 percent were achieved for wheat, barley, and safflower, respectively; and class designations in each crop type were identified.

When analysis for the selection of the optimum bands for crop classification was performed on the 22

TABLE 3-V.—Accuracies Achieved for Crop Classification

Training set, no. of sections	Classification accuracy, percent
Reclassificationa	
40	70.0
20	75.1
10	67.0
Signature extensionb	
40	63.0

aOnly reclassification of the 40-section training set area was performed using the signatures developed from each of the respective training sets.

bFor signature extension, 48 sections in the southern portion of the test area were evaluated using signatures developed from the 40-section training set in the northern portion of the test area.

Scale, km
0 — 1
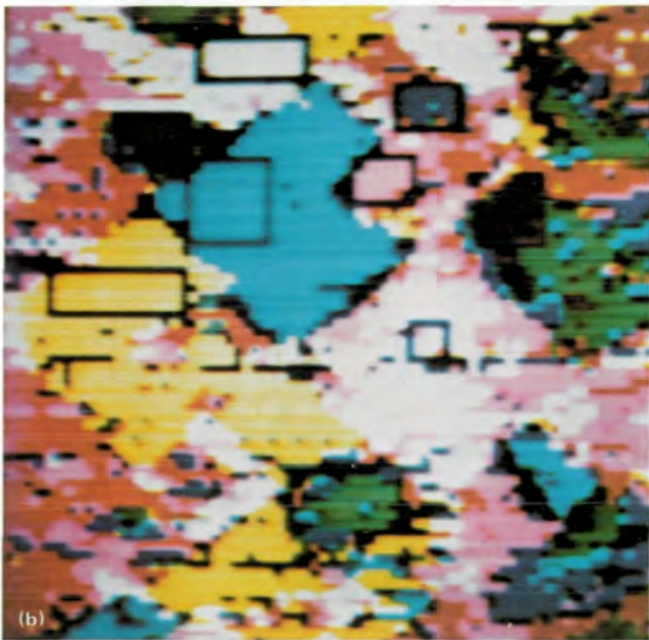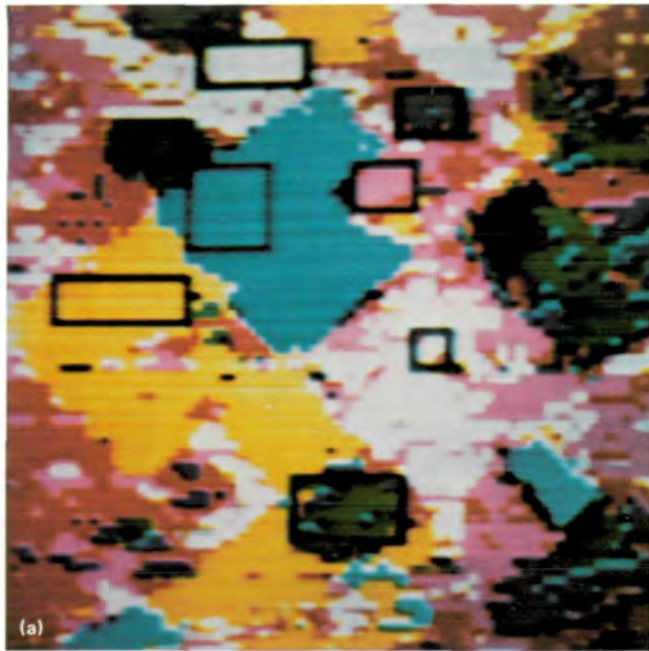
Yellow - Mature barley
Red - Tomatoes
White - Cotton
Orange - Fallow
Pink - Potatoes

Purple - Cucumbers
Aqua - Barley stubble
Blue - Safflower
Green - Alfalfa
Black - Other

TABLE 3-VI.—S192 Spectral Bands Used in the 22-Feature Format

Band	Spectral feature (a)	Wavelength, μm		Description	Sampling scheme (b)
1	1	0.41 to	0.46	Violet	Low
2	2	0.46 to	0.51	Violet-blue	Low
3	3	0.52 to	0.56	Blue-green	High odd
4	4	0.56 to	0.61	Green-yellow	High odd
5	5	0.62 to	0.67	Orange-red	High odd
6	6	0.68 to	0.76	Red	High odd
7	7	0.78 to	0.88	Reflectance infrared	High odd
8	8	0.98 to	1.08	Reflectance infrared	Low
9	9	1.09 to	1.19	Reflectance infrared	Low
10	10	1.20 to	1.30	Reflectance infrared	Low
11	11	1.55 to	1.75	Reflectance infrared	High odd
12	12	2.10 to	2.35	Reflectance infrared	High odd
13	13	10.20 to 12.50		Thermal infrared	Low
13	14	10.20 to 12.50		Thermal infrared	High odd
3	15	0.52 to	0.56	Blue-green	High even
4	16	0.56 to	0.61	Green-yellow	High even
5	17	0.62 to	0.67	Orange-red	High even
6	18	0.68 to	0.76	Red	High even
7	19	0.78 to	0.88	Reflectance infrared	High even
11	20	1.55 to	1.75	Reflectance infrared	High even
12	21	2.10 to	2.35	Reflectance infrared	High even
13	22	10.20 to 12.50		Thermal infrared	High even

[a]In the context of the discriminant analysis of remote-sensing data, a feature is any continuous function over a specified range that describes a particular point or area on the ground. In part, this function may consist of spectral data (e.g., multispectral data or digitized multiband photographs), textural data generated from the spectral data, or nonspectral data (e.g., topography, rainfall, or soil type).

[b]The 13 S192 bands were sampled at 2 rates: low (72.6 m) center-to-center spacing and high (36.3 m) center-to-center spacing. On the digital tapes, the high sampled bands were handled as either an odd or an even low-rate band.

FIGURE 3-4.—Computer classification of a complex agricultural area west of Fresno, California, by analysis of S192 data. The data within the black rectangular boxes were used to train the automatic classifier. (a) Classified using a medium threshold for analysis. (b) Classified using a fine threshold for analysis.

features of the S192 data, 4 spectral features were selected. They were (1) the high-density yellow data output, (2) one of the high-density reflectance-infrared data outputs (7 or 19), (3) one of the three low-density reflectance-infrared data outputs (8, 9, or 10), and (4) one of the high-density reflectance-infrared data outputs (11 or 20). Studies indicate that when discriminant analysis techniques are applied to more than four bands of data, the cost becomes prohibitive (i.e., the cost of analysis increases approximately by the square of the number of bands used) without significantly improving the classification accuracy. The S192 narrow spectral bands appear to provide more useful information for discriminating among crop types but require precise timing for highly dynamic crop types such as vegetables.

SOILS

Soil is the basic medium for sustaining the plant, animal, insect, mineral, and hydrological ecosystem on which man depends for his existence. The basic soil units were mapped by using the standard EREP photographic products, and the soil salinity characteristics were discriminated by analysis of the spectral data recorded by the S192 instrument. The quantity of free water in the soil and of crystalline moisture in snow was measured by the use of microwave data.

Mapping by Photointerpretation

The S190A and S190B color and color-infrared photographs were analyzed visually to delineate regional vegetative patterns indicative of the agriculture, the hydrology, the soil resources, and the insect habitats of a citrus-producing area. When the S190B photographs were enlarged to a 1:63 000 scale and projected for a subsequent enlargement to 1:10 000, agriculture analysts (Hart et al., ref. 3-1) identified host plants and plant distributions, which are the avenues of citrus-insect migration between Mexico and the Texas citrus belt. Supportive information identifying physical features of the area such as drainage patterns, watercourses, and some soil characteristics was derived from the S190A photographs.

Soil units and drainage patterns were mapped by de Mendonca et al. (ref. 3-2) on Skylab photographic data

of Campo Grande, Mato Grosso, Brazil. The S190A color-infrared film (fig. 3-5(a)) was used to separate and map eight types of soil (fig. 3-5(b)). This map derived from the S190A data coincided with the current soil map of the area (fig. 3-5(c)), which was prepared by the use of ground transects. The map derived from the S190A photograph identified the vegetative patterns, the extent of good-quality soil, and the extent of human exploitation of the region. Using the same type of data (fig. 3-6(a)), Bannert (ref. 3-4) mapped pedological units in the Province of Corrientes, Argentina (fig. 3-6(b)), that compared favorably with soil delineations on the soil map of the world (1:5 000 000 scale).

Salinity Discrimination by Analysis of S192 Data

Vegetated areas that exhibited differences in quantity and quality of reflectance as compared with the reflectance from bare soil were analyzed through digital processing (Wiegand, ref. 3-5), and the results were correlated with field measurement of the electrical conductivity of soils of varying salinity. Data were acquired by the 13-band S192 scanner, and analysis was made by linear correlation in each discrete band. As the reflectance ratio between vegetated areas and bare soil increased (i.e., as more reflectance was received from the vegetation), the salinity level of the study area was observed to be lower. The correlations for the six continuous bands (6 to 11) in the wavelength region of 0.68 to 1.75 μm were -0.739, -0.946, -0.862, -0.876, -0.963, and -0.722, respectively.

Vegetative patterns, as extracted from the S190B color and color-infrared photographs, were used to identify subterranean freshwater levels in the pampa region of Argentina (Bannert, ref. 3-4). In the area of investigation, ground water occurs at the surface and to a depth of 20 m. On the ground, surveys revealed relationships among the morphology, the depth, and the salinity of ground water. These features on the Earth's surface can be observed in EREP color-infrared photographs (fig. 4-26(a) in sec. 4). These areas are delineated on a ground-water-depth map (fig. 4-26(b) in sec. 4); the regions with a ground water table at a depth of less than approximately 5 to 7 m appear light blue and are characterized by high evaporation and increased soil and ground water salinity, which lead to unfavorable conditions for certain plant species and to sparse vegetative cover. These regions are favored predominantly by halophytes.
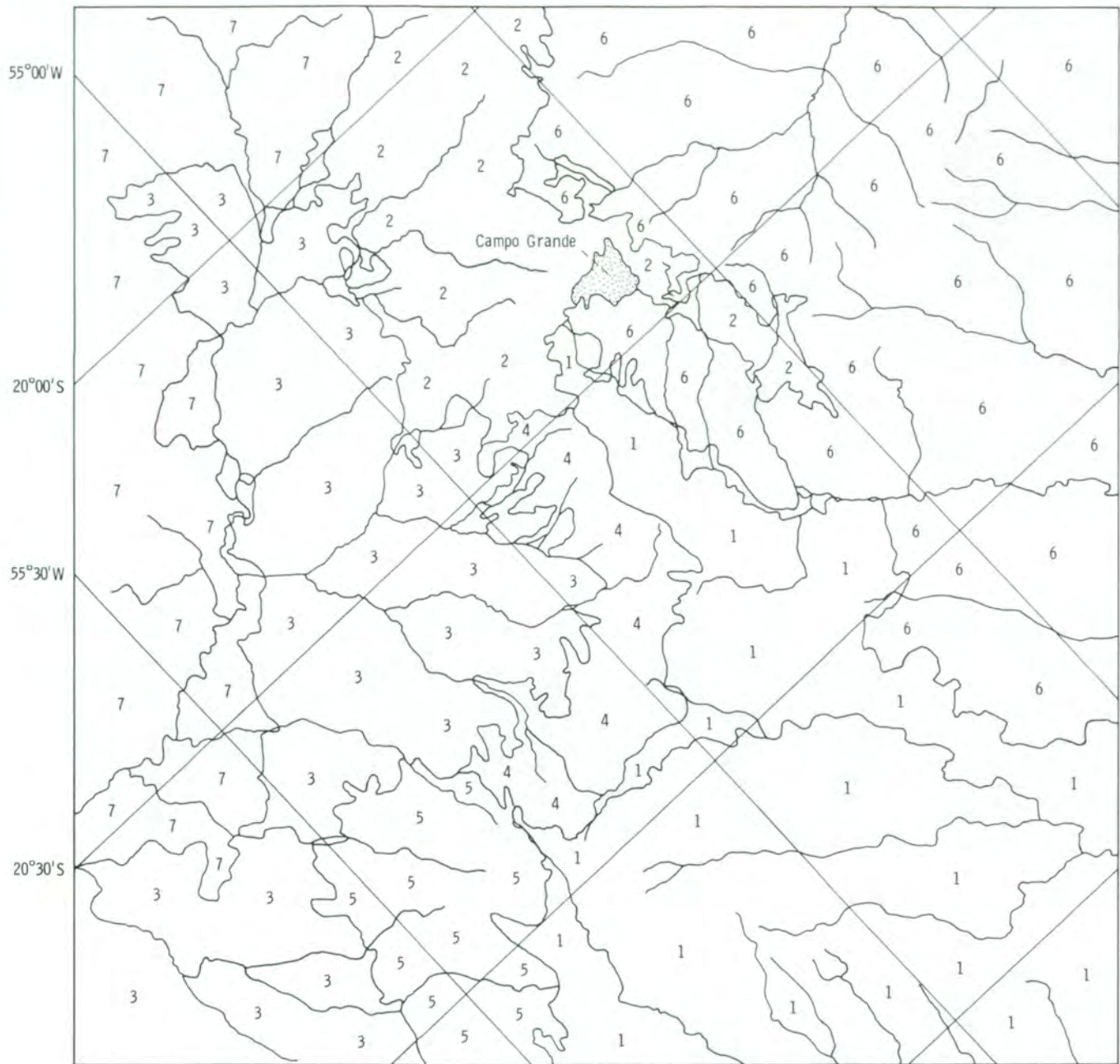
(a)

0 10
Scale, km

N
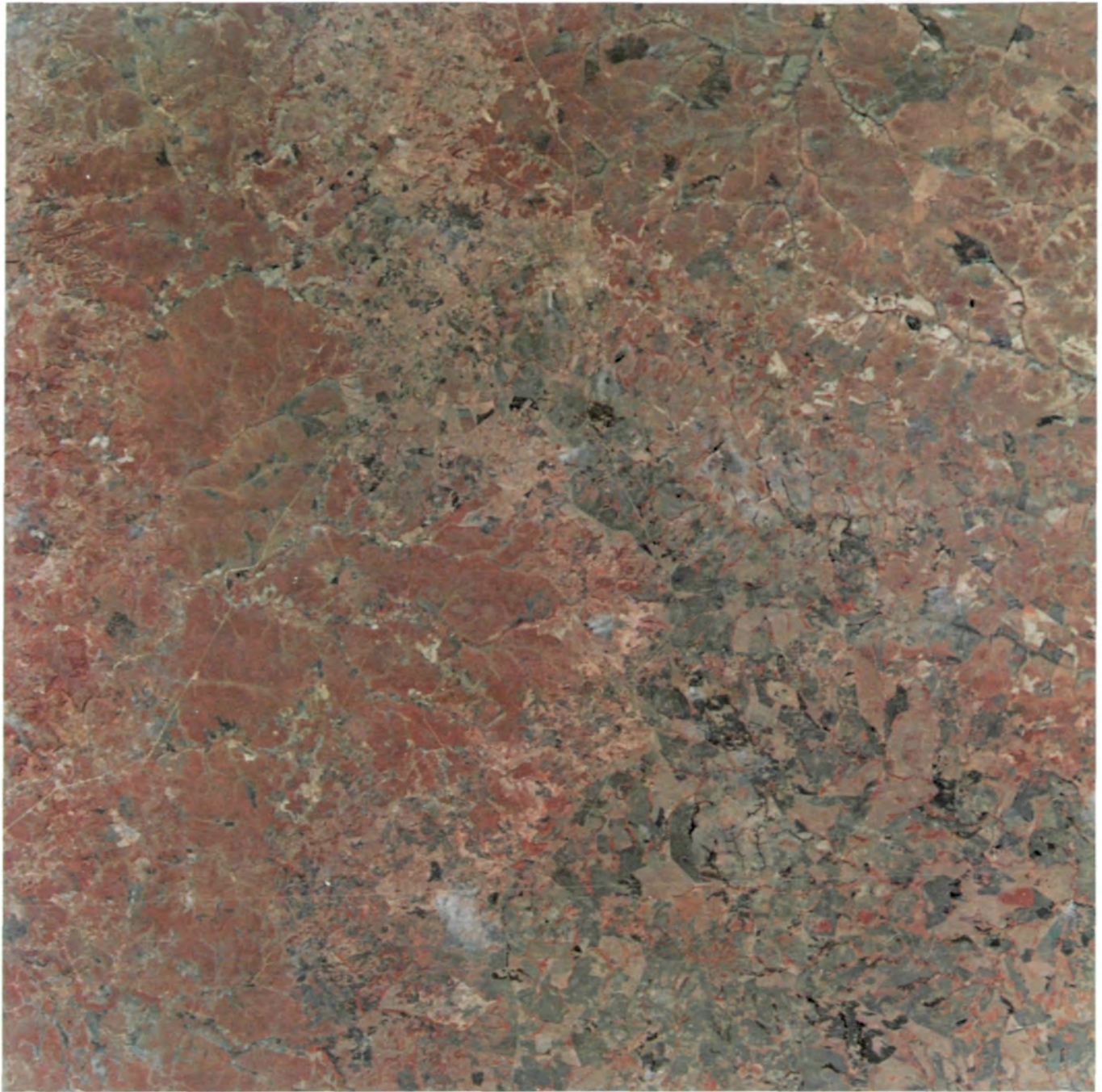
FIGURE 3-5.—Campo Grande, Mato Grosso, Brazil. (a) Skylab 3 S190A color-infrared photograph taken in September 1973 used as base data for soil suitability mapping (SL3-33-093). (b) Soil suitability map derived from imagery of figure 3-5(a). (c) Current soil suitability map derived by conventional means.

55°00'W

20°00'S

55°30'W

20°30'S

Campo Grande

N

0   10
Scale, km

(b)

Explanation

1 Areas of intensive agricultural activity
   with large-scale plantations predominant
2 Areas of intensive agricultural activity
   with small-scale plantations predominant
3 Relatively unexplored forest areas

4 Intensively explored cleared pastureland
5 Relatively unexplored areas of cerradão vegetation
6 Relatively unexplored areas of cerrado vegetation
7 Relatively unexplored areas of varying topography
   with cerradão vegetation predominant

FIGURE 3-5.—Continued.
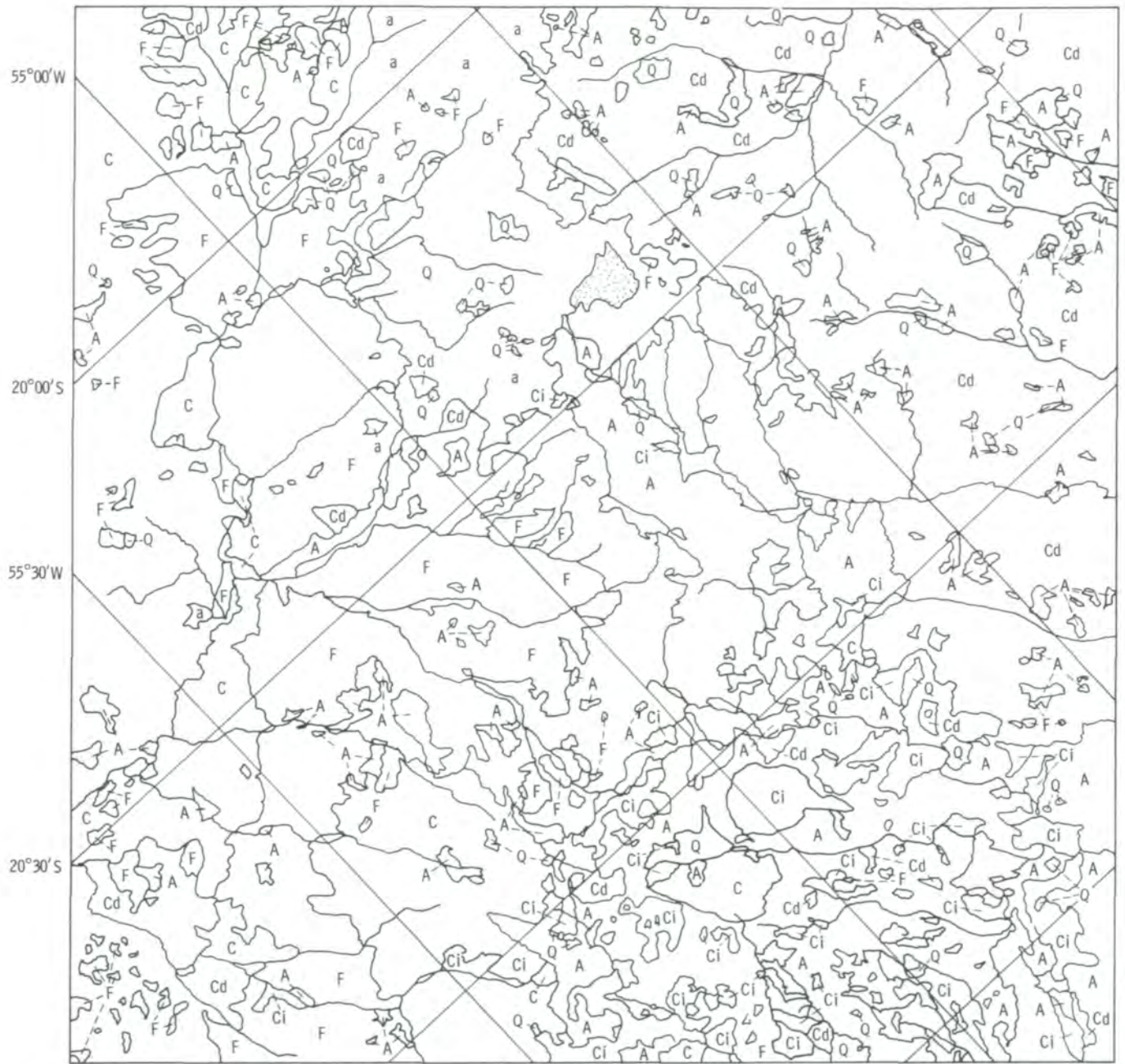
Explanation

a Small-scale agricultural area   C Cerradão vegetation
A Large-scale agricultural area   F Forest vegetation
P Cleared pastureland   Ci Native rangeland
Cd Cerrado vegetation   Q Burned areas

(c)

FIGURE 3-5.—Concluded.

Moisture

Area and regional managers responsible for the allocation and control of surface water have attempted to forecast the available moisture either in the soil or as free crystalline water in the snowpacks, using the aridity and antecedent precipitation index models. The implications are great in terms of use for agricultural endeavors that depend on soil/water resources and flood forecasting for large watersheds. The quantity of runoff produced by a storm depends on the moisture deficiency of the basin at the onset of rain and on characteristics such as rainfall amount, intensity, and duration. The characteristics of moisture-delivering phenomena can be determined from an adequate network of meteorological gages; but the direct determination of moisture conditions throughout a storm is not feasible, and the antecedent precipitation index models can only be used to estimate relative values for soil moisture conditions.

Microwave instruments of the type onboard Skylab are potentially useful for determining moisture conditions of an area. Those on Skylab operated in active and passive modes and responded to an average value of surface or near-surface moisture content. Those instruments were not dependent on visible reflectance. Microwave backscatter (active) and emission (passive) are strongly dependent on the dielectric constant and the moisture content of soil, vegetation, and snow being sensed. The dielectric constant is a measure of the electric charge on a surface within an electric field. For water, at microwave frequencies, the dielectric constant is quite large (as much as 80), whereas that of dry soil is typically less than 5 and that of snow is less than 2. Therefore, the water content of soil or snow can greatly affect the dielectric constant.

Analysis of the response of the microwave instruments (Eagleman et al., ref. 3-6) indicates that passive radiometers, particularly the L-Band Radiometer (S194), were most sensitive to the percentage of moisture in either the surface layers of the soil or snow cover. The first step of the analysis consisted of obtaining, by direct measurement, detailed ground soil moisture information at the time the EREP instruments were collecting data. The resulting soil moisture maps showed the percentage of moisture available in each 2.5-cm increment to a total depth of 15 cm. The correlations of the radiation received by the radiometer with the moisture content of the various layers beneath the surface were computed for each of the 2.5-cm layers to evaluate the effective depth from which the L-band signal originated. In one case, the antenna temperatures correlated with the moisture content in the top 5 cm; but for the four other cases, the moisture within the top 2.5 cm provided the best correlation. This result agrees with the theoretical calculations. When data for the five different passes were combined, the correlation between the S194 radiometric temperature and the soil moisture content remained high, with a value of −0.96.

The results of the radiometer component of the Microwave Radiometer/Scatterometer and Altimeter (S193) were less definitive than for the S194 instrument. For the same test site and for the same area, when several of the S193 footprints were averaged to obtain the same area covered by the S194, the correlation of antenna temperatures with moisture content was −0.988 for the S193 as compared with −0.996 for the S194. The particular pass was across Texas on June 5, 1973. When the S193 was used as a scatterometer, the response to soil moisture, which is not as good as that for the radiometers, resulted in a correlation of 0.75.

The analysis of S190A photographs and of imagery generated from the S192 has shown that, for some areas, the infrared bands of these sensors can be used to identify significant differences in soil moisture. However, direct measurements of subsurface soil moisture content by optical and multispectral scanner data are difficult because the presence of a vegetative cover tends to shield soil moisture from detection by these methods. (See methodology by J. Colwell, sec. 6.) Although optical or multispectral scanners cannot gather quantitative soil moisture information on a practical basis, they can be used very effectively with microwave data to increase the accuracy of soil moisture measurements by providing information about vegetation type and density. Analysis of multispectral scanner thermal-band data can aid in collecting and assembling surface-temperature information.

When the microwave antenna temperatures were analyzed for surface emission, which is a function of the percent of soil moisture by weight, it was concluded (Eagleman et al., ref. 3-6) that there is a very high correlation between antenna temperature and soil moisture

FIGURE 3-6.—Corrientes Province of Argentina. (a) S190A color-infrared photograph (SL3-34-165). (b) Soil units as outlined on figure 3-6(a).

Wes - Eutric planosols, sandy
Wec - Eutric planosols, clayey
Wms - Mollic planosols, sandy
Wmc - Mollic planosols, clayey
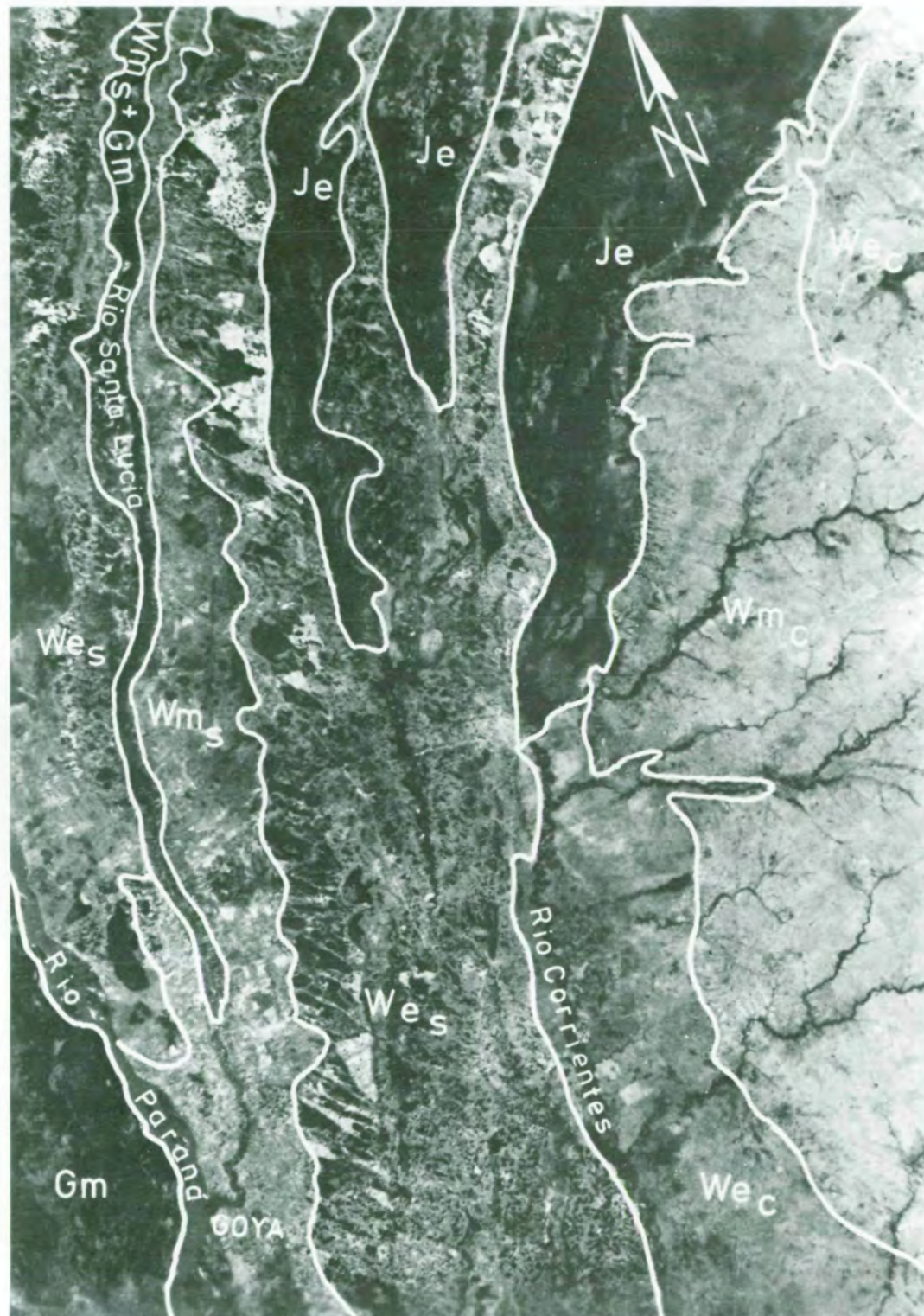Je - Eutric fluvisols
Gm - Gleysols

N

0 — Scale, km — 25

(b)

FIGURE 3-6.—Concluded.

for values of 0 to 35 percent. As the moisture content of the soil increased above approximately 35 percent, larger dispersions in the data occurred. It should be noted that this correlation is inverse (i.e., the microwave temperature increases as the soil moisture percentage decreases). Analysis of the microwave temperatures from S193 and S194 instruments recorded over snow-covered terrain in the Great Plains has shown that the relationship between brightness temperatures and the water content of the surface of the snow did not resemble that observed in soils. Over the snow-covered terrain, the temperatures were proportional to the water content of the surface of the snow, and there was a high degree of correlation only when the free-water content was between 0 and 2.5 percent. The results of this study, based on limited microwave data, indicate that it is possible to measure moisture content with a high degree of precision over relatively large areas having low quantities of moisture. Better correlations were obtained with the S194 instrument than with the S193.

RANGE

In most of the nonagricultural test sites that were studied by EREP investigators, rangelands were intermixed with forest lands. In fact, this same intermixing occurs quite commonly throughout the wild-land areas of the world. For this reason, timber resources are referred to in this subsection and, conversely, range resources are referred to in the subsection on timber resources.

Range and Wild-Land Classification Systems

A significant contribution of the rangeland investigations to the EREP program was the adaptation of existing vegetation classification systems for use with Skylab data. Classification systems are probably the most important components in the transfer of remote-sensing information, such as that provided by Skylab, to resource managers, planners, and government agencies. Among the various hierarchical classification systems,

ECOCLASS[2] is frequently used for ecosystem classification and for improved multiple-use planning and management of forest and range resources. The ECOCLASS system links vegetation, land, and aquatic systems with the description and classification of relatively permanent ecosystems. The system defines five categories, proceeding from the most general to the most specific, as follows.

V. Formation—The most general class of vegetation, characterized by general appearance: grassland, coniferous forest, deciduous forest, etc. The basis for this category is continental in scope (i.e., all the United States) and is controlled by continental climatic differences.

IV. Region—Subdivisions of the formation, associated regionally and therefore determined by subclimates within continental climates: montane grassland, temperate mesophytic coniferous forest, alpine grassland, etc.

III. Series—A group of vegetation systems in the region category, with a common dominant climax species: ponderosa pine forest, fescue grassland, herbaceous meadow, etc.

II. Habitat type—Units in a series, each with relatively pure internal biotic and abiotic structure: ponderosa pine/Arizona fescue habitat type, Arizona fescue/mountain muhly habitat type, etc. These are the elemental units of the classification scheme on which primary management is based. These units are frequently related to climax vegetation or to vegetation held in a relatively stable state of high succession by proper management.

I. Community type—A system that appears relatively stable under management and may be equivalent to the habitat type. The biotic components usually are dissimilar, but abiotic components are analogous to habitat type.

Of the five ecological levels of classification most useful for evaluating remote-sensing data, habitat type represents the level of information required by vegetation and land managers for making resource management decisions.

Several Skylab investigators evaluated EREP data for range resources inventory and analysis applications (Poulton and Welch, ref. 3-7; Hoffer, ref. 3-8; and Aldrich et al., ref. 3-9). They found that S190A color-infrared photographs were consistently most useful for interpreting a wide range of natural vegetation types in Nevada and Colorado/New Mexico test sites. The

S190A color-infrared film was significantly better for identifying vegetation complexes than any other film tested, although S190B color film was nearly as good for other aspects.

A rigorous classification of range plant communities performed by the U.S. Forest Service range scientists was based on the ECOCLASS system. Identification at two levels, three regional and eight series, was attempted (Aldrich et al., ref. 3-9). Photographs from the S190A multiband camera and the S190B terrain mapping camera (June and August 1973), photographs from high-altitude aircraft (June and August 1973), and large-scale photographs from aircraft were used in the tests. Both visual and microdensitometer techniques were tested.

Training and test sample cells were selected for interpretation on a restricted random basis. To be selected, a specific plant community had to occupy an area at least 500 m square. A 10-percent sample was selected at random from each plant community class for field validation. Overlays of sample cell locations and plant community keys were used to aid interpretation. Procedures were also developed to map cultural features from the EREP photographs.

Range ecologists, interpreting S190A and S190B photographs, classified grassland and conifer region classes with a mean accuracy of 98 percent or greater on both Skylab and support-aircraft photographs, regardless of date or film type. However, tree series classification was inconsistent. Aspen was classified with 80 percent accuracy on August color-infrared 1:10 000-scale aircraft photographs, but this accuracy was not obtained on EREP photographs. Accuracies for coniferous classification at the series level were dependent on date, film type, and scale. For instance, the Douglas fir class was accurately classified on June color-infrared EREP photographs but not on aircraft photographs. Lodgepole pine and ponderosa pine classes were interpreted accurately on EREP color photographs for June but not on aircraft photographs. Aircraft color and color-infrared medium-scale photographs made in June were best for interpreting the spruce/fir class. The greater accuracies at smaller scales were probably due to the mixing of tree species into homogeneous units with a dominant species signature and a lower resolution.

In the grassland series, shortgrass was classified with 95 percent or greater accuracy on both Skylab and aircraft photographs, regardless of date or film type. Wet meadows were classified with greater than 90 per-

cent accuracy on both June and August aircraft photographs, regardless of film type or scale. The classification of wet meadows was also acceptable on both color and color-infrared EREP photographs taken in August. Mountain bunchgrass was not accurately classified on S190A and S190B photographs; but on the August aircraft photographs, the classification was acceptable, regardless of film type or scale. Topographic slope and aspect, mountain shadows, ecotones (interfaces between two ecosystems), season, and class mixing affected the classification of plant communities.

Experimental results in the EREP rangeland studies (Aldrich et al., ref. 3-9) were much affected by seasonal timing of S190A and S190B photograph acquisition. Although quantitative results were data dependent, it was emphatically stated that the best time for imaging natural vegetation with color-infrared film is when the vegetation types are approaching the mature growth period. The EREP investigations indicate that the peak growing season (high phenological activity) is the poorest time of year for photographing natural vegetation from space. Multidate photographs, therefore, provided the only means for consistent identification of some vegetation complexes.

Microdensitometric point sampling of region-level conifer, deciduous (aspen), and grassland classes showed significant differences in mean optical densities at the 95-percent-probability level. However, the deciduous class could be separated from the other classes with significant differences only on color film. Ponderosa pine was the only series-level conifer that showed a significant difference in mean optical density from the other three conifers, regardless of date or film type. Spruce/fir and lodgepole pine were not separable at any date or on any scale or film type. The mean optical density for aspen was significantly different from that for the conifer classes, but the differences were dependent on date, scale, and film type. Douglas fir was separable from the other three conifers on both the June color-infrared and the August color S190A EREP photographs. Grassland classifications at the series level varied in acceptability. However, shortgrass, mountain bunchgrass, and wet meadows did have mean optical density differences that were significant on August S190A color photographs. The optical density was more dependent on community mixing than on the growth stage of the plants at the time (season).

Both EREP and aircraft photographs were useful for mapping the areal extent of conifer and grassland.

These two classes were usually mapped with greater than 90 percent accuracy. The deciduous class could not be mapped with acceptable accuracy at either the region or the series level. Series-level conifer and grassland could be mapped with acceptable accuracy only if class complexes were formed. Class complexes were ponderosa pine and Douglas fir, lodgepole pine and spruce fir, shortgrass and mountain bunchgrass, and wet meadow.

Many disturbances to natural rangeland vegetation communities were recorded. For example, paved and gravel roads, utility corridors constructed within the last 10 years, larger mining excavations, and clusters of buildings could be mapped on S190A and S190B photographic enlargements. However, 1:100 000-scale aircraft photographs were needed to map dirt roads, minor soil excavations, utility corridors more than 10 years old, and individual buildings. Foliar cover and plant litter measured on large-scale color-infrared photographs of nondiverse grasslands were related to ground measurements with a correlation coefficient of 0.75. This coefficient is considered acceptable for range surveys. The relationship for foliar cover of shrubs was acceptable only on diverse grasslands.

The use of EREP photographs for vegetation delineation was illustrated by a legend system (Poulton and Welch, ref. 3-7) in which a multidigital fraction was used to depict the vegetative associations (numerator) and landforms (denominator). This system is especially suited to multistage remote-sensing applications and is in decimal form for computer compatibility. The numerator is a three-digit number with decimal components identifying the vegetation analog or land use conditions. The denominator uses a three-component decimal system for landscape characterization. The components are macrorelief, landform, and microrelief. Macrorelief refers to the largest category of classification of major relief change within the landscape system being studied, with the landform feature addressing the geomorphological categories as fluvials or deserts and the microrelief characters defining the local contours.

An arid region of the Southwestern United States (fig. 3-7(a)) was classified, and a photograph was annotated (fig. 3-7(b)) using this hierarchical classification system. The numerical classifiers used for this illustration are listed in appendix A of reference 3-7.

Evaluation of Film for Classification

Although the legend system is difficult for resource managers to use, it can be applied to landscape boundary determination on a Skylab-quality satellite photograph, as shown in figure 3-8(a) (an S190A color photograph) and in figure 3-8(b) (an S190A color-infrared image of the Uncompahgre area). The photographs in figure 3-9 show separation between landscape types as viewed from low-altitude aircraft. High-definition S190B color film was preferred for mapping vegetation boundaries because it has better spatial resolution (fig. 3-8(c)). Ranking beneath S190B color for vegetation boundary delineation were, in descending order, S190A color (fig. 3-8(a)), S190A color-infrared (fig. 3-8(b)), and S192 (fig. 3-8(d)) imagery. When cost was considered, high-definition S190B color film (fig. 3-8(c)) was considered best for delineating vegetation boundaries. In most cases, Skylab stereoscopic data provided the best identification of vegetation complexes and delineation of vegetation boundaries, particularly in areas where changes in relief were related to changes in vegetation types (a common occurrence in wild-land vegetation communities).

FORESTS

Skylab provided the first opportunity for foresters to test the concept of a manned space laboratory for resource surveys. Thus, remote-sensing investigations in which widely separated forest and wild-land sites were studied were conducted to investigate the applicability of EREP data to forest resources inventory and analysis problems.

Interpretation techniques and instruments used by the investigation teams to analyze EREP data varied from one application to another. When the EREP photographic products were studied, a zoom transfer scope was used for mapping and dual-image correlations. In forest-stress impact analysis, a stereomicroscope was used to test, monocularly and stereoscopically, a wide range of image magnifications. Other forms of manual photointerpretation included the use of rear projection viewers that provided image magnifications as large as 29.5×. On one forest inventory

task, a scanning stereoscope and a lamp magnifier were used for conventional photointerpretation.

Two types of digital methods were used to analyze EREP photoproducts. Microdensitometers were used to scan and digitize S190A and S190B photographs, and television scanning systems were used to analyze digitized photographs that were displayed at different gray-scale levels. With digital tapes from the S192 Multispectral Scanner, investigators used several types of computer hardware systems and analysis algorithms.

Various forest resource applications problems were addressed with the aid of EREP products. Forest classification, a specialized area of land use classification and a function of forest inventory, was the cornerstone activity of all forestry investigations. The specific tasks related to the data needs of forest resource managers involved determining forest timber volume, stand vigor (stress), and ownership boundaries.

Classification

The EREP investigators indicated that, with S190B color photographs, Level I forest and nonforest land areas can be classified with 90 to 95 percent accuracy. (See table 2-I for Level I and Level II classification definitions.) The accuracy of classifying Level II forest and nonforest classes varied from fair to poor. Hardwood and pine (fig. 3-10) could be separated with a confidence level of 95 percent and an accuracy of 90 and 70 percent, respectively (ref. 3-9).

The computer map shown in figure 3-11(a) provides a visual comparison with the S190B photograph (fig. 3-11(b)). A point-by-point comparison was made between points located on a ground-truth map and the same points on the computer map. Investigators found that 93 percent of the forest points were correctly classified as printed on the computer map. The pine points were classified with an accuracy of 83 percent. Points falling in hardwood were classified with 74 percent accuracy, and nonforest points were classified with 85 percent accuracy. The results of the Aldrich et al. research (ref. 3-9) revealed that forest area could be classified and, therefore, stratified on high-resolution S190B photographs with an accuracy of approximately 96 percent. Thus, with S190B photographs, forest area

can be mapped and an estimate of the land use areas can be made within limits that can be accomplished using aerial photographs.

The results of plant community classification tests indicate that both visual and microdensitometric techniques can be used to separate deciduous, coniferous, and grassland classes to the region level in the ECOCLASS hierarchical classification system. By visual analysis techniques, the classification accuracy was more than 90 percent on S190B photographs. However, the classification of deciduous forest was dependent on the date, the film type, and the scale of the photographs. By means of microdensitometry analysis of S190A photographs, an average accuracy of more than 80 percent was achieved, although this accuracy is subject to change depending on the film type and the season of data acquisition. There was no consistency in classifying tree categories at the series level by visual photointerpretation. Conifers were classified most accurately (80 percent) on S190A photographs, whereas, under certain conditions, grassland plant communities were classified at accuracies greater than 80 percent. The results of microdensitometric techniques were variable and highly dependent on the photograph date, film type, and scale.

The analysis of S192 data (fig. 3-12) involved classification of major cover types (corresponding to the Level II land use classes in table 2-I) and forest cover types. The results (Hoffer, ref. 3-8) indicated that the major cover types could be mapped with approximately 85 percent accuracy and that the forest cover types could be mapped with approximately 71 percent accuracy. When areas of major cover types obtained from photointerpretation of S190A or S190B imagery were compared to the area summary based on two computer-aided analysis techniques, ECHO and per-point classification, using S192 data, a correlation coefficient of 0.929 resulted.

Comparison of the results obtained with S192 data and Landsat multispectral scanner data indicated that the improved spectral resolution of the S192 narrow-band data enabled a higher classification accuracy for forest cover types, although the classification performance for major cover types was not significantly different. The investigators believe that, had the S192 performance been optimal throughout the mission,

FIGURE 3-7.—Uncompahgre Plateau area of Colorado. (a) S190A high-resolution color-infrared photograph (SL3-21-004). (b) Land use classification using the hierarchical numbering system to depict landforms and vegetative patterns.

FIGURE 3-7.—Concluded.

FIGURE 3-8.—Uncompahgre Plateau area in Colorado. (a) S190A color photograph taken June 1973 (SL2-15-010). (b) S190A color-infrared photograph taken June 1973 (SL2-15-009). (c) S190B high-definition color photograph taken June 1973 (SL2-81-020). (d) S192 electronically acquired image obtained September 1973.

FIGURE 3-8.—Continued.

FIGURE 3-8.—Continued.

N

0   10
Scale, km

(d)
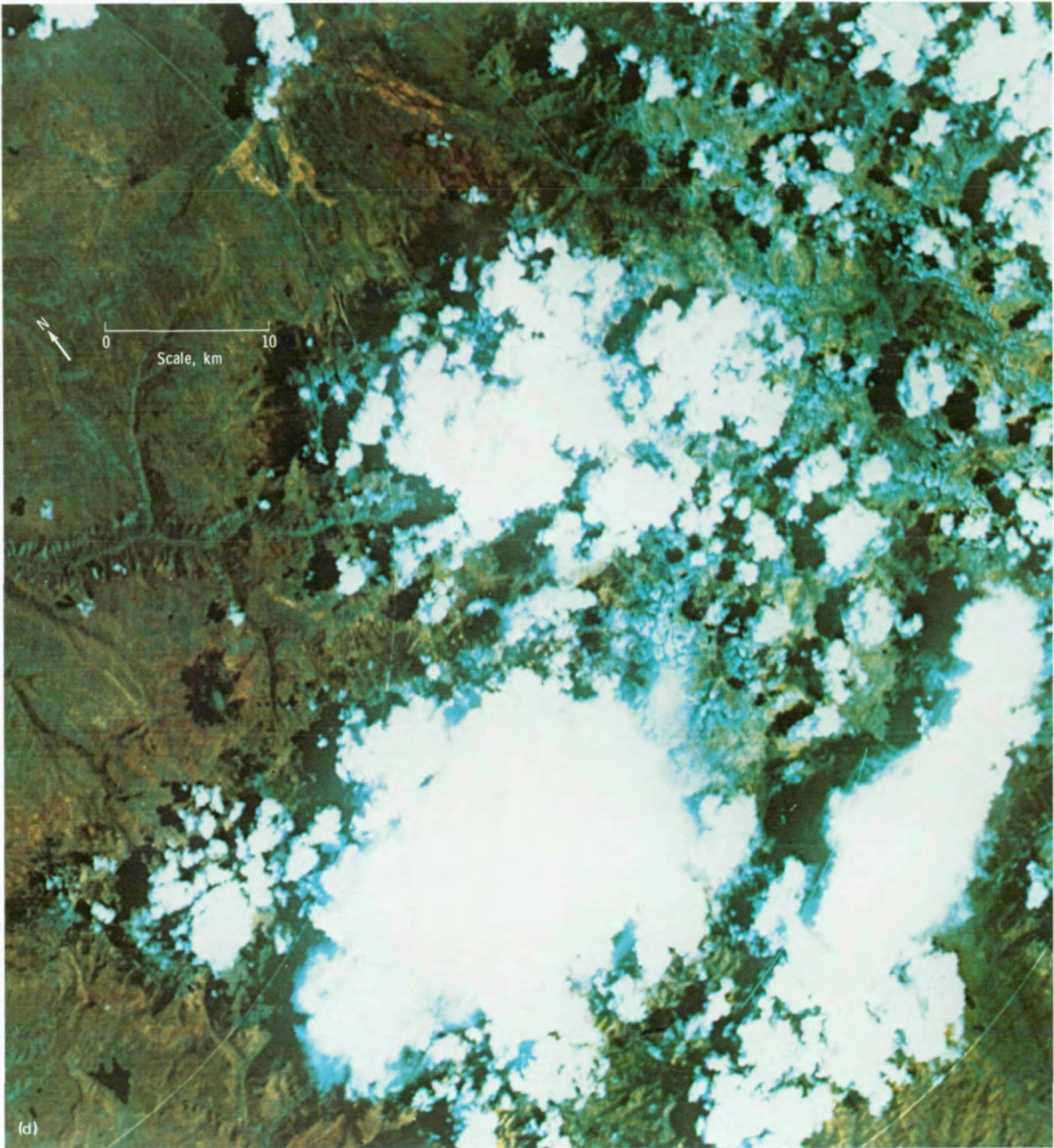
FIGURE 3-8.—Concluded.

FIGURE 3-9.—Low-altitude-aircraft photographs of the Uncompahgre Plateau area in Colorado used for vegetative mapping. (a) Spruce, fir, and grassy parks atop the Uncompahgre Plateau, with some aspen patches intermixed. (b) Formation between mountain meadows, aspen, spruce, fir, and the timberline. (c) Color-infrared aerial oblique photograph showing spruce/fir timberline. (d) Color-infrared aerial photograph showing the boundary between aspen and spruce/fir.

(a)

N

(b)

Pine   Hardwood   Nonforest   Water
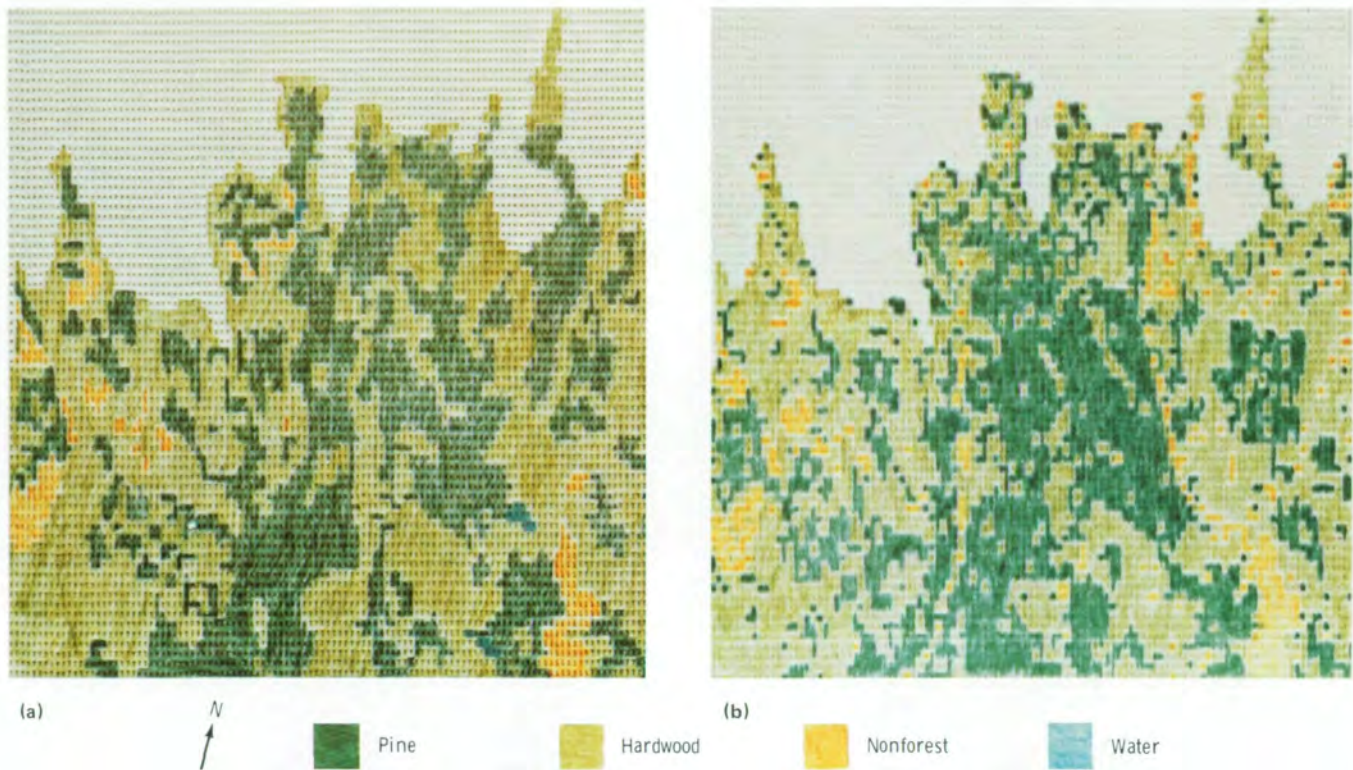
FIGURE 3-10.—Pine and hardwood separation maps of portions of McDuffie County, Georgia. Many nonforest areas, mostly roads or road segments that are below the minimum mapping size to separate on the land use ground-truth map (fig. 3-10(a)), are shown on the map in figure 3-10(b). (a) Map produced from data digitized from a land use map. (b) Map produced from classification of microdensitometer scans on an S190B color transparency.

the classification results would have improved significantly. Also, the results indicated that the increased spectral range of the S192 system enables selection of a better combination of four wavelength bands for computer analysis than is present in the Landsat data. Specific results of the wavelength band evaluation study indicated that classification performance was not significantly improved when more than four wavelength bands were used in the computer analysis. Analysis of S192 data indicated that the near-infrared part of the spectrum, especially the 1.09- to 1.19-μm wavelength band, was of particular value for vegetation mapping

(Hoffer, ref. 3-8), with additional wavelength bands in the visible (0.52 to 0.56 μm), near infrared (0.78 to 0.88 μm), and middle infrared (1.55 to 1.75 μm) also shown to be of significant importance. However, the combination of four wavelength bands that were of most value for classifying various cover types varied considerably.

The S192 data collected on August 5, 1973, were processed to produce a classification map of part of the Gratiot-Saginaw State game area in south-central Michigan (fig. 3-13). A preliminary 10-category classification map was prepared for an area consisting of diverse vegetation cover types, including hardwood
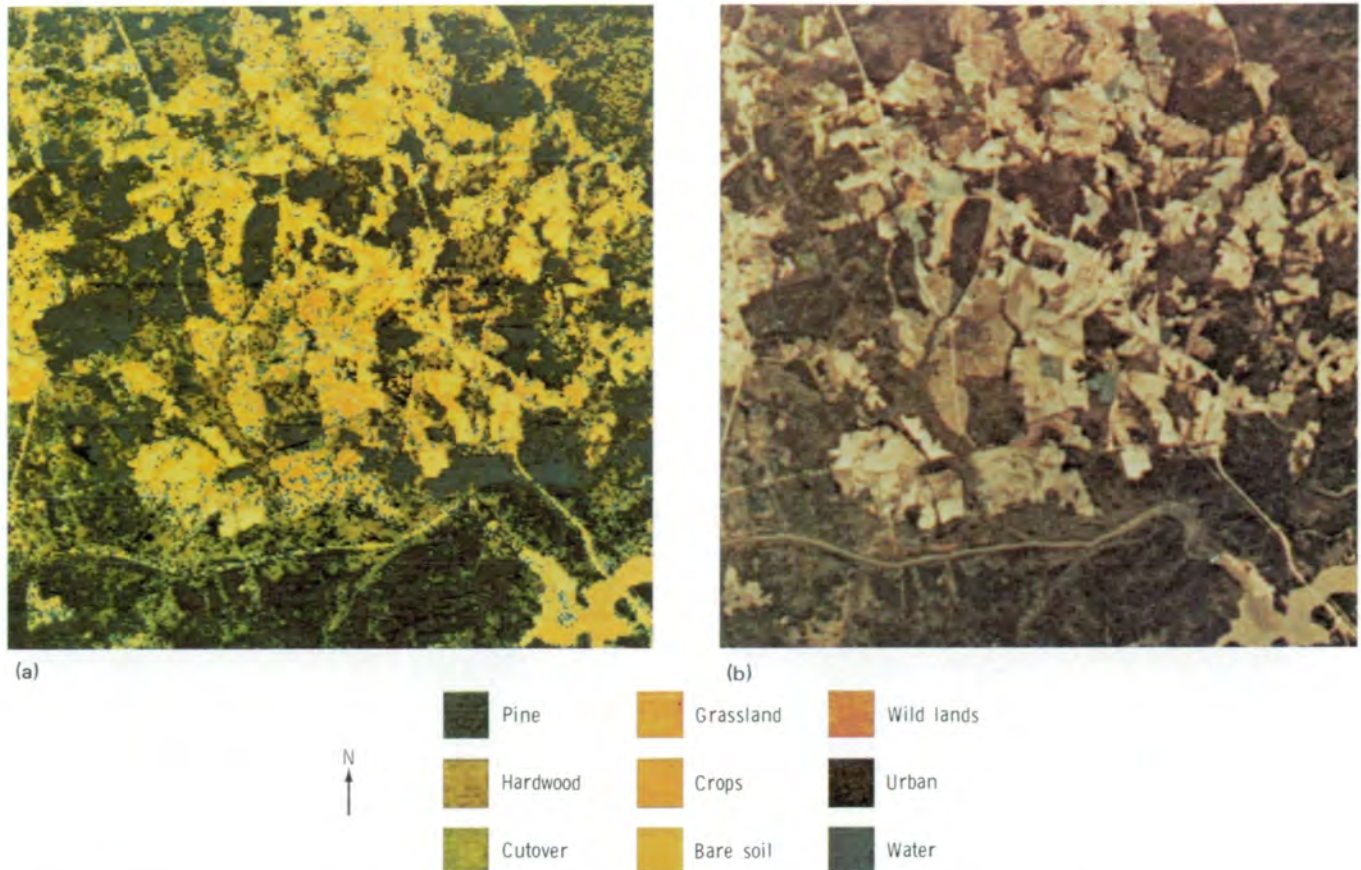
FIGURE 3-11.—Level II classification of forest types by computer analysis. (a) Computer map made using diffuse densities converted from optical densities measured on figure 3-11(b). (b) S190B photograph taken November 30, 1973 (SL4-90-046).

and conifer forests, wetlands, brushland, and herbaceous vegetation. Field checks indicated an overall pixel recognition accuracy of 54 percent, although accuracy of the more poorly classified categories ranged from 25 to 52 percent. After the categories were limited to five, the overall classification accuracy increased from 54 to 72 percent. When the output statistics were reduced for a square-mile grid, the accuracy increased to 82 percent, as the result of compensating for errors of omission and commission (Sattinger et al., ref. 3-10). The signal-to-noise ratio of each S192 band presented many problems. Sattinger et al. (ref. 3-10) identified the remaining usable bands in order of preference for scene classification: (1) 0.78 to 0.88 μm, (2) 1.55 to 1.75 μm, (3) 0.98 to 1.08 μm, (4) 0.68 to 0.76 μm, (5) 0.52 to 0.56 μm, and (6) 0.62 to 0.67 μm.

Type Determination

Density-slicing analyses of S190A and S190B color and color-infrared photographs, converted to gray-scale levels, have demonstrated the feasibility of using such data for differentiating major timber classes (including pines, hardwoods, mixed, cut, and brushland), provided such analyses were made at scales of 1:24 000 or larger (Baldridge et al., ref. 3-11). Detailed machine analyses, reinforced with data from knowledgeable field personnel, indicate that sufficient spectral differences exist to make automatic (computerized) machine separation of pine and hardwood stands possible. Further differentiation of mixed hardwood and softwood types in western Ohio study sites, which have small, extensively mixed forest stands, was not possible with the use of EREP
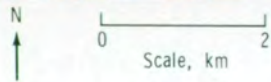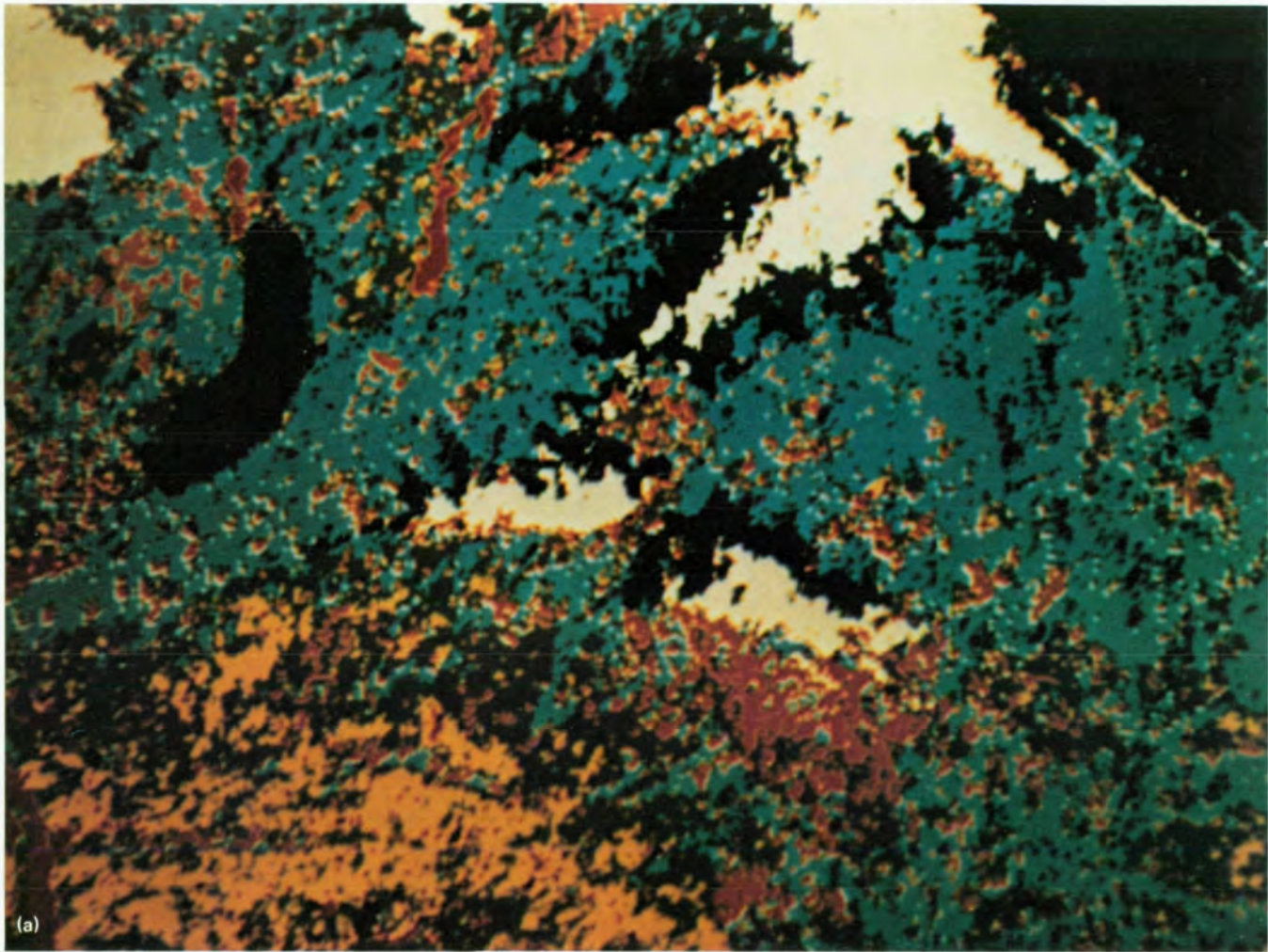
N
↑

0 ——————————— 2
Scale, km

FIGURE 3-12.—A comparison of two classification systems, "ECHO" and "per-point," using forested terrain as a test site. The per-point classification gives a salt-and-pepper effect, whereas the ECHO gives a classification similar to that achieved by standard photointerpretative techniques. The various cover types are designated by the following color codes: white, snow; light red, deciduous forest; dark red, grasslands; black, water and cloud shadows; and blue, coniferous forest. (a) Per-point classification. (b) ECHO classification.

photographs. Sample results indicate that density slicing of EREP color and color-infrared film may be used to classify forest-stand maturity in Ohio into the following categories of commercial interest: mature timber, intermediate and pole timber, seedling/sapling stands, brushland, and clear cut areas.

Forest investigators in Australia were able to correlate the occurrence of different forest types with variations in color on the S190A color-infrared photographs

(Lambert et al., ref. 3-12). They also separated native forest areas into tree/crown density (crown closure) classes and delineated the major forest species, even though the vegetation boundaries were less sharp than on midsummer Landsat-1 imagery. The black-and-white photographs were of little value for vegetation classification of forest lands. The investigators recommend the use of midsummer S190B color-infrared photographs for forest mapping.
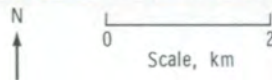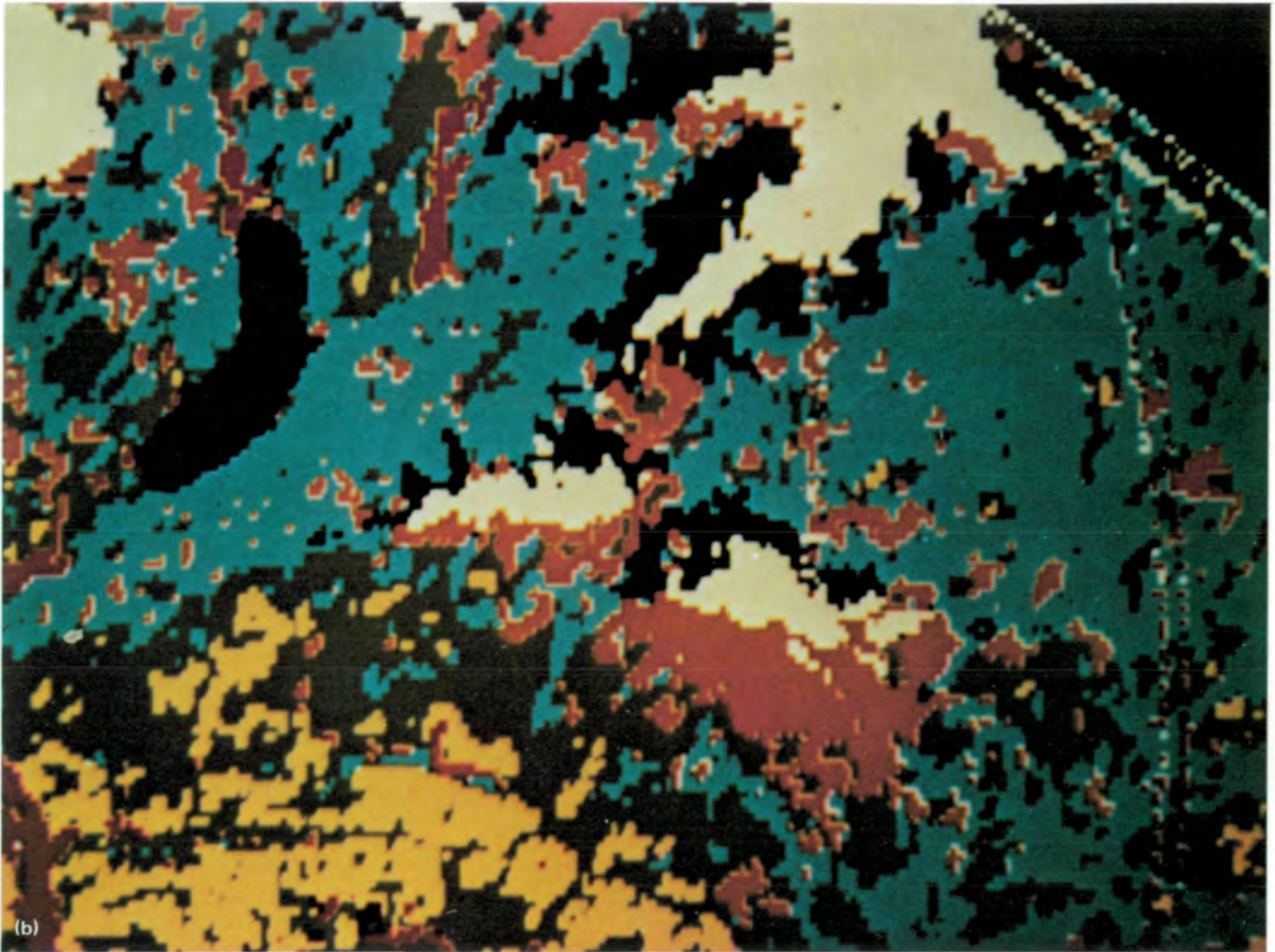
N ↑

0 ─────── 2
Scale, km

FIGURE 3-12.—Concluded.

Inventory

The EREP S190A and S190B photographs were successfully used to inventory and map a large woodland area in Ohio, an accomplishment demonstrating the minimal requirement for supportive ground and aircraft data (ref. 3-11). Both conventional photointerpretation and machine-assisted procedures were used effectively. It was learned that, for the determination of forest cover by counties, Skylab photographs were more accurate and economical than conventional surveys involving the use of aerial photoplot techniques.

However, this assessment is not meant to imply that cost effectiveness was maintained in providing all the inventory and mapping information generally required for forest surveys.

Volume Determination

Scientists at the University of California at Berkeley (Colwell and Benson, ref. 3-13) used S190A photographs as the first stage in a multistage sampling design to determine the abilities of human photointerpreters to

N

0 ⊢———————————⊣ 5
Scale, km

White - Snow
Blue - Water
Dark green - Coniferous forest
Light green - Deciduous forest
Red - Grassland
Brown - Exposed rock and soil
Yellow - Boundary areas

FIGURE 3-13.—Map of major cover types obtained by computer classification of S192 data. The two vertical lines of yellow dots represent "bad data."

distinguish timber-volume classes. Gross timber volume was the variable estimated in the sampling design, based on random sampling at each of three stages. Sampling units were randomly selected at each stage because it was not known how well human interpreters could differentiate between timber and non-timber classes on S190A photographs in the first stage; therefore, the classes could be established quantitatively, as desired. After all combinations of sampling procedures had been tested, it was concluded that S190A color-infrared photographs did not have sufficient resolution to provide timber-volume information for inventory purposes. When the same analysis procedures were applied to high-flight-aircraft data, the investigator was able to estimate timber volume in the test area.

Stress Detection

A comprehensive evaluation of EREP data showed that mountain pine beetle infestations in the Black Hills National Forest of western South Dakota could not be detected on color-combined multiband, black-and-white, normal color, or color-infrared photographs from the S190A multiband camera system (Aldrich et al., ref. 3-9). All positive identifications were made using S190B color photographs. The infestations detected were always more than 26 m in the longest dimension. On one site, only infestations of more than 50 m could be detected. It was concluded that poor detection was due to timing of the imagery (June) and low Sun angle. Optimum viewing was achieved with a microscopic viewer on a good-quality light table at a 1:75 000 scale. Stereoscopic viewing resulted in fewer errors of commission. Because of poor quality and misregistration between bands, infestations could not be detected by computer processing of the S192 data. Foresters in Ohio reported that S190A photographs, regardless of film emulsion, were inadequate to detect tree stress and damage conditions in northeastern Ohio (Baldridge et al., ref. 3-11).

Image Annotation and Overlays

A precision image annotation system was developed as a critical part of a forest investigation in northern California (Langley and Van Roessel, ref. 3-14). The technique extended the existing capability of annotating the corners of primary sample units on aerial photographs, Landsat imagery, and the Landsat multispectral scanner data to S190A and S190B photographs and to gray-scale maps made from S192 data. Image overlays were produced by computer methods to provide visual identification of the sample-unit corners on each of the image types. Concurrently, the coordinates of the points in the computer tape system were determined. Hence, specific sample units were addressable over spectral bands and time for interpretation purposes. The annotation system developed is capable of correcting for image distortions caused by Earth curvature, terrain relief, and distortions inherent in the imaging system.

One of the significant results achieved with the annotation system was the determination that the root-mean-square error of point location of S190A imagery was 100 m and 90 m in the X and Y directions, respectively. It was also learned that the potential gains in sampling precision attributable to space-derived imagery ranged from 4.9 to 43.3 percent depending on the image type, interpretation method, time of year, and sampling method applied. These results can be compared with the 55.1-percent gain achieved by human interpretation methods applied to high-altitude-aircraft photographs.

A significant "first" by Hoffer (ref. 3-8) was to analyze Skylab, Landsat, and topographic data all in a common format. The Skylab data were corrected geometrically, and the Landsat data were corrected to a corresponding scale for analysis. Topographic map data, which included aspect, slope, and elevations, were digitized and corrected to the appropriate scale for analysis with the Skylab and Landsat data. This process required the development of new techniques, including the production of a digital data tape containing 13 S192 wavelength bands, 4 Landsat bands, and 3 bands containing topographic data. These different data sets were all geometrically corrected and registered to a 1:24 000-scale data base. Digital display images in either a gray tone or color format and line-printer outputs were generated from topographic data; by this means, elevation, slope, or aspect could be indicated with different gray tones or colors on the digital display imagery or with different symbols on the line-printer output.

Area Determination

Random and systematic sampling designs were tested for measuring forest area proportions by using a digitized ground-truth map for one county (Aldrich et al., ref. 3-9). The variance in forest area proportions was always less with the use of systematic sampling, which stratified the area into forest and nonforest and sampled the forested area before analysis. Systematic sampling, with the use of digitized S190B optical densities and linear discriminant functions for postsampling stratification, reduced variance in forest area proportions at the lower sampling rates. (At sampling fractions of more than 0.0004, the advantage decreased rapidly. This sampling fraction represents the percentage of the stratified forest that was sampled on a grid coordinate basis.) In addition, Hoffer (ref. 3-8) substantiated that reliable areal estimates can be obtained using computer-aided analyses of satellite data even in areas of rugged, mountainous terrain.

Recreational Potential

Sattinger et al. (ref. 3-10) provided a qualitative evaluation of both S190A and S190B photographs and concluded that S190A has limited application for recreational land use analysis, but that S190B, with a resolution approaching that obtainable from high-altitude aircraft, is useful for many land analysis applications. The investigators have stated that S190B photographs contain sufficient detail to map Level I and Level II categories of land use and land cover. Applications included mapping existing recreational facilities, identifying open spaces that might be suitable as recreational land, and site planning of geographically extensive areas, such as river basins.

Temporal Variations

The evaluation of temporal S190A and S190B photographs showed the importance of season in relation to the analysis of multispectral scanner data (Hoffer, ref. 3-8). The photointerpretation results indicated that,

because of differences in vegetative condition, the Skylab 2 data obtained in June over Colorado were better for vegetation mapping than those obtained in August.

Langley and Van Roessel's results (ref. 3-14) confirmed that seasonal variations, as recorded on film, were significant for forest interpretations. In their study conducted in California, the S190A photographs obtained during Skylab 3 (September) yielded higher interpretation accuracy than those obtained in June; however, S190A color-infrared composites from both time periods yielded the highest results of all S190A products analyzed. No S190B photographs were available for this study; therefore, no S190B temporal combinations were possible.

Although mapping of all the forest and rangeland (6070×10^9 m² (1.5×10^9 acres)) in the United States at frequent intervals is desirable, limitations in computers and computer storage make detailed and repeated inventories unfeasible at the present time. Instead, it is much more reasonable to think of sampling applications. For example, it was demonstrated (Aldrich et al., ref. 3-9) that a systematic sample grid can be overlaid on digitized land use map data by computer to estimate forest and nonforest land in an entire county. (The variance was always lower than that resulting from simple random sampling.) Using Skylab color film to classify forest and nonforest land in an entire county resulted in an accuracy of 80 percent for forest land, with a 30-percent commission error. Types of forest and other land covers may be estimated by sampling digitized data from future satellite coverage if color-infrared film is made available and if a classification system based on the existing land cover rather than on intended use is designed.

The primary advantage of Skylab S190A and S190B photographs in forest resource surveys is the broad area coverage within a single frame. In the 4-county experiment, 183 aerial photographs (1:20 000) were required to cover an estimated 80 percent of the total area. This was single photographic coverage without the advantage of stereoscopic overlap. A single S190B photograph, however, will cover these four counties and from two to four additional counties as well. Complete county coverage offers better distribution of photograph samples and reduces data handling and photoacquisition costs, on the assumption that only printing and processing costs are involved.

If all other survey costs are considered equal, the costs of Level I and Level II land use and forest stratification would be 49 percent lower using S190B photographs than on conventional 1:20 000-scale aerial black-and-white photographs. The major difference between the two methods is the cost of the photographs. Because of the small scale and the use of normal color film, more time was required to make interpretative decisions on S190B photographs. However, if high-resolution color-infrared photographs were available on a regular, recurring basis, the advantages of current information would far outweigh the disadvantage of any additional interpretation time.

SUMMARY

Several scientific investigations in the disciplines of agriculture, range management, and forestry analyzed the EREP data to contrive techniques and procedures for extracting the required resource information. The imagery was acquired in a multispectral format, analyzed by visual interpretation, and digitized for computer analysis. The narrow-band spectral data as acquired by the S192 instrument were analyzed by computer processing to identify the optimum spectral bands and combinations of these bands that would provide maximum amounts of resource information at a minimum cost. Microwave data recorded in an electronic format provided an insight into the mapping and monitoring of available moisture for natural resource consumption. Evaluations of the utility and recommendation of data formats and required observation frequency for discrete resource monitoring or measurements using EREP-quality data were also made.

For identifying and measuring field crops (i.e., crops grown in larger tracts (32 to 65 hm² (80 to 160 acres)) and in the categories of cereal or large-area crops, as differentiated from vegetables), it was found that the multispectral photographs were appropriate for inventorying within an accuracy range of 82 to 98 percent. To identify large-area crops using single-date data, it was determined that the data would have to be acquired precisely when the crops were maturing; but when temporal or multidate data were used, the acquisition time was not as critical and data could be acquired throughout the development phase and before maturity. When data acquired from these same types of

crops were analyzed, the results were equally as good with either digitized photographs or electronically recorded S192 data. Large-area crops generally follow a uniform planting and harvesting calendar for a given geographical region and meteorological environment and are compatible with the identifiable types of required data and the appropriate times for acquisition of the data.

When intensively cultivated crops (vegetables) were studied, it was concluded that the timing of data acquisition was extremely critical and that data should be acquired at discrete stages of maturity. Acquisition of these temporal data constituted an additional problem because vegetable production areas frequently have one type of crop in two adjacent fields at different stages of maturity and thus require more frequent observation intervals.

Generally, field sizes smaller than 2 hm² (5 acres) were difficult to discriminate with the resolution of the EREP sensors. As the field sizes increased, the identification and areal measurement accuracies also increased.

With use of the full range of the multispectral photographic system, four bands (green, red, and two infrared) were the most useful for inventorying and monitoring vegetative resources, although only two bands were analyzed for vegetative resources. The natural color and color-infrared bands were the most frequently used. Analysis of the narrow 13-band electronic data indicated that a yellow band and 3 infrared bands provided the greatest amount of information.

The photographic system, the 13-band S192, and the microwave systems were used to map various soil parameters. The areal extent of soil units was mapped using the color and color-infrared photographs. When the soil was visible, color was the indicator of soil units; and when the soil supported vegetation, the vegetation boundaries were considered synonymous with soil units and used for mapping.

Soil salinity was mapped over a limited test site by analyzing S192 data. The indicator was the quality of vegetation as correlated with the electrical conductivity of the soil. This technique is promising for saline soil mapping but will require additional study for refinement.

The available soil moisture in the top 15 cm for plant consumption was mapped from S193 and S194 microwave data. Correlations of soil moisture between 0 and 35 percent by weight were very good; but for larger percentages of moisture, the instrument responses were saturated. Similar results were obtained when the water equivalent of snow covering the Great Plains area was mapped.

When mapping wild-land resources, which include rangeland and forest environments, accuracies for Level I and Level II were 90 to 95 percent and 70 to 90 percent, respectively. Conventional photointerpretation techniques were used, with the preference of film types being high-definition color from the S190B because of its better spatial resolution, followed by S190A color and S190A color infrared, respectively. Level II land use classes, as identified in table 2-I, were identified by analysis of S192 data at an accuracy of 85 percent.

Investigators achieved limited success in detecting insect damage by analysis of EREP data. They indicated that the residual effect, or change in vegetative state, was sufficiently limited to prevent detection with the resolution-cell capability of the sensors and that the data were not acquired at the optimum biological periods of insect activities. In the case of the pine bark beetle damage to conifer forests and mealybug infestation on citrus, the period of maximum biological activity produces the maximum visual change in the character of the vegetation. The general conclusion of most of the investigators was that the EREP-quality data are acceptable for Level I and II monitoring but require acquisition at optimum times within the developmental stages of the vegetation and should be analyzed by personnel thoroughly familiar with the resource in question.

REFERENCES

3-1.   Hart, W. G.; Ingle, S. J.; and Davis, M. R.: A Study of the Early Detection of Insect Infestations and Density Distribution of Host Plants. NASA CR-144483, 1975.

3-2.   De Mendonca, F.; Machado, J. B.; et al.: Collection of Relevant Results Obtained With the Skylab Images. NASA CR-147502, 1975.

3-3.   Colwell, Robert N.; Benson, Andrew S.; et al.: Agriculture Interpretation Technique Development. NASA CR-144486, 1975.

3-4.   Bannert, D.: Hydrological Investigations in the Pampa of Argentina. NASA CR-144488, 1975.

3-5.   Wiegand, Craig L.: Soil Salinity Detection. NASA CR-144403, 1975.

3-6.   Eagleman, J. R.; Lin, W.; et al.: Detection of Soil Moisture and Snow Characteristics From Skylab. NASA CR-144485, 1975.

3-7.   Poulton, C. E.; and Welch, R. I.: Plan for the Uniform Mapping of Earth Resources and Environmental Complexes From Skylab Imagery. NASA CR-144484, 1975.

3-8.   Hoffer, Roger M.: Computer-Aided Analysis of Skylab Multispectral Scanner Data in Mountainous Terrain for Land Use, Forestry, Water Resource, and Geologic Applications. NASA CR-147473, 1975.

3-9.   Aldrich, Robert C.; Dana, Robert W.; et al.: Evaluation of Skylab (EREP) Data for Forest and Rangeland Surveys. NASA CR-147440, 1975.

3-10.   Sattinger, I. J.; Sadowski, F. G.; and Roller, N. E. G.: Analysis of Recreational Land Using Skylab Data. NASA CR-144471, 1973.

3-11.   Baldridge, Paul E.; Goesling, P. H.; et al.: Utilizing Skylab Data in On-Going Resources Management Programs in the State of Ohio. NASA CR-134938, 1975.

3-12.   Lambert, B. P.; Benson, C. J.; et al.: A Study of the Usefulness of Skylab EREP Data for Earth Resources Studies in Australia. NASA CR-144493, 1975.

3-13.   Colwell, Robert N.; and Benson, Andrew S.: Skylab Data as an Aid to Resource Management in Northern California. NASA CR-144487, 1975.

3-14.   Langley, Philip G.; and Van Roessel, Jan: The Usefulness of Skylab/EREP S190 and S192 Imagery in Multistage Forest Surveys. NASA CR-147439, 1976.

Page Intentionally Left Blank

4

Geology and Hydrology

RICHARD A. HOPPIN,[a†] DUWAYNE M. ANDERSON,[b†]
ROBERT K. STEWART,[c] DAVID L. AMSBURY,[c]
VON R. FRIERSON,[d] A. VICTOR MAZADE,[d]
AND MARTIN L. MILLER[c]

THE APPLICATION OF REMOTE SENSING to geological studies began in the early 1920's through the use of visual analysis of aerial photographs, and their use advanced rapidly after World War II for regional geological mapping and for petroleum and mineral exploration. The use of photogeology reached its peak in the United States by the middle 1950's. The distribution of handheld-camera photographs taken during the Gemini Program in the mid-1960's and of data from the Apollo, Landsat, and Skylab Programs in late 1960 and the early 1970's increased the interest in the use of space remote-sensing surveys for geological and hydrological studies.

Several types of geological and hydrological studies were conducted by approximately one-third of the Skylab investigators. Geologic studies included regional mapping of structure and lithology; mineral, petroleum, and geothermal exploration; mapping of volcanic phenomena; mapping of fault systems for location of active earthquake zones; and mapping of fracture zones in a coal mining area for mine safety purposes. Water resource studies included analysis of such features as streamflow, effluent discharge, river stage, flooding, snow accumulation and ablation, estuarine circulation, sedimentation, stream erosion, and shoreline retreat.

Hydrological studies were directed to generation of models of ground water movement, detection of trapped ground water along faults, and studies of the relationship of ground water to photolinears. Although the Earth Resources Experiment Package (EREP) investigators studied a wide variety of terrain and geographic areas, domestic investigations were concentrated in the Great Plains area and the Central and Western United States. Three investigators analyzed data of the Appalachian Mountains of the Eastern United States. Investigations were also conducted in Central and South America, Europe, Africa, and Australia.

Results of the Skylab EREP studies show that the most practical and useful space sensor for geological studies is a high-resolution camera. The photographs from the Earth Terrain Camera (S190B) will probably continue to be the data most in demand by geologists. The main advantages of the EREP camera systems are synoptic view, stereoscopy, and resolution. For field geologists, the synoptic view is a particularly important aid in understanding and interpreting the regional geology of an area because it provides an expanded opportunity to look at the total area of interest. Space data in the format of color or color-infrared photographs enable the geologist to map and extend trends for great distances and to perceive anomalous areas that may be indicators of subsurface structures capable of trapping oil or gas or of containing prospective mineral deposits. Fracture systems and rock alteration zones are probably the two most useful indicators of mineralization. These

---
[a]University of Iowa.

[b]U.S. Army Corps of Engineers.

[c]NASA Lyndon B. Johnson Space Center.

[d]Lockheed Electronics Company, Inc.

[†]Principal Investigator.

119

often appear as tonal lineaments and color anomalies on the photographs. Space photographs and images do not provide direct evidence of oil, gas, or mineral deposits; but they can often provide geological clues on where to conduct further exploratory surveys, such as aerial photography, surface mapping, geophysical surveys, and exploratory drilling. They can be useful also in geothermal exploration for mapping major fault trends that may be conduits for magma and hot water moving upward near the surface, where the heat can be tapped economically. In addition, the view from space may serve as a stimulus for new concepts concerning the fundamental geological structure of the Earth and lead to the formulation of new hypotheses to be tested.

Geologists and hydrologists tend to use initially simple, economical methods of analysis. The basic technique consists of photointerpretation of transparencies using a stereoscope or zoom transfer scope. In most areas, only the morphology is directly observable by photointerpretation; and the geology is inferred. For example, sinkholes, sand dunes, alluvial fans, flood plains, glacial features, and volcanic cones were identified on the basis of shape and color. Drainage patterns can aid in the recognition of folds, faults, and areas of bedrock. Drainage anomalies can be seen on many images and photographs and marked for ground checking. Many investigators enhanced the EREP photographs by selective color-additive techniques. However, for most investigations, these techniques did not provide much additional information. The digital Multispectral Scanner (S192) data were converted to images and studied in a similar manner. The results of these analyses indicate that S192 bands 8 (0.98 to 1.08 μm), 10 (1.20 to 1.30 μm), 11 (1.55 to 1.75 μm), and 12 (2.10 to 2.35 μm) provide the best contrast for mapping rocks. This finding may prove to be very important for geological mapping because these infrared bands are not available on film from camera systems.

Studies of the spectral reflectance and radiance of rocks using computer-processed S192 digital tapes were supplemented by spectroradiometric measurements made on the ground during the Skylab overflights. Other investigations included comparisons of the film products of the Multispectral Photographic Camera (S190A) and the S190B camera as well as comparisons of the different bands of the S192 scenes.

Verification of observations and interpretations was a necessary part of each investigation. Field checking and correlation with published geological, gravity, and magnetic or earthquake-epicenter maps were conducted by most investigators. To aid in determining the usefulness of EREP data for Earth resources studies, EREP investigators compared photographs from Skylab, U-2 and RB-57 aircraft, and Landsat-1.

The summary results presented in the following subsections represent only a small percentage of the total geologic, hydrologic, and engineering information that will ultimately be derived from the analysis of the data collected during the EREP program. These results, however, are indicative of the wide variety of the use to which such data can be applied for study of the Earth's features and phenomena.

MAPPING AND ANALYSIS

Geological Mapping

Maps are the fundamental data base of geology; they are used for various applications such as exploration for mineral and water resources, determination of land use, investigation of the environment and potential hazards, and resolution of engineering problems. Maps prepared from EREP data analysis were of two types: (1) general geological maps showing patterns of rock-unit outcrops, faults, and folds; and (2) linear-lineament maps showing the location and orientation of continuous or en echelon linear features.

Geologic maps prepared by EREP investigators were less detailed than the published maps derived from aerial photographs and field investigations because of the lower resolution of the EREP photographs. In addition, the photographic units derived from the EREP data may not correspond to field geologists' stratigraphic units, which are based on fossil content or rock type. Nevertheless, regional structures were defined and several previously unmapped structures were recognized. Quade et al. (ref. 4-1) identified a 19-km-long anticline in Gabbs Valley, Nevada, that is not shown on the State geological map. In several investigators' areas, many more faults were interpreted from photographs than appear on published maps; field checking validated some of these faults but eliminated others. In semiarid regions such as the Southwestern United States, geologists found that the large structures and distinctive rock units or contacts could be mapped with EREP photographs, and the following examples illustrate their use in photogeologic analysis of areas that differ in terrain features.
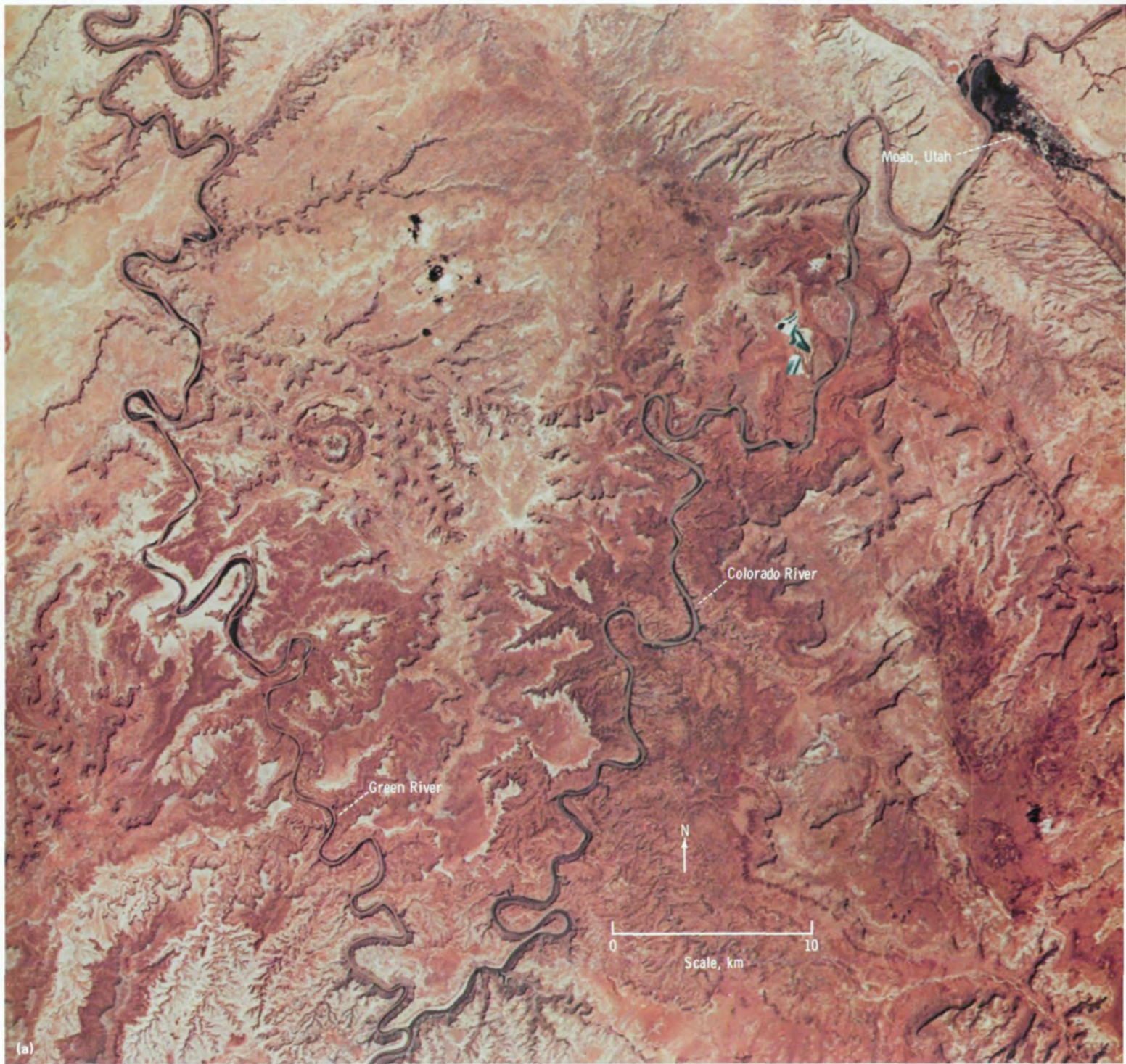
FIGURE 4-1.—Area southwest of Moab, Utah, showing the junction of the Colorado and Green Rivers. (a) S190B photograph (SL2-81-016). (b) U.S. Geological Survey map (1:250 000 scale) based on aerial photographs and fieldwork (ref. 4-3). (c) Detailed geological map (1:62 500 scale) prepared from S190B photographs by Lee (ref. 4-2).
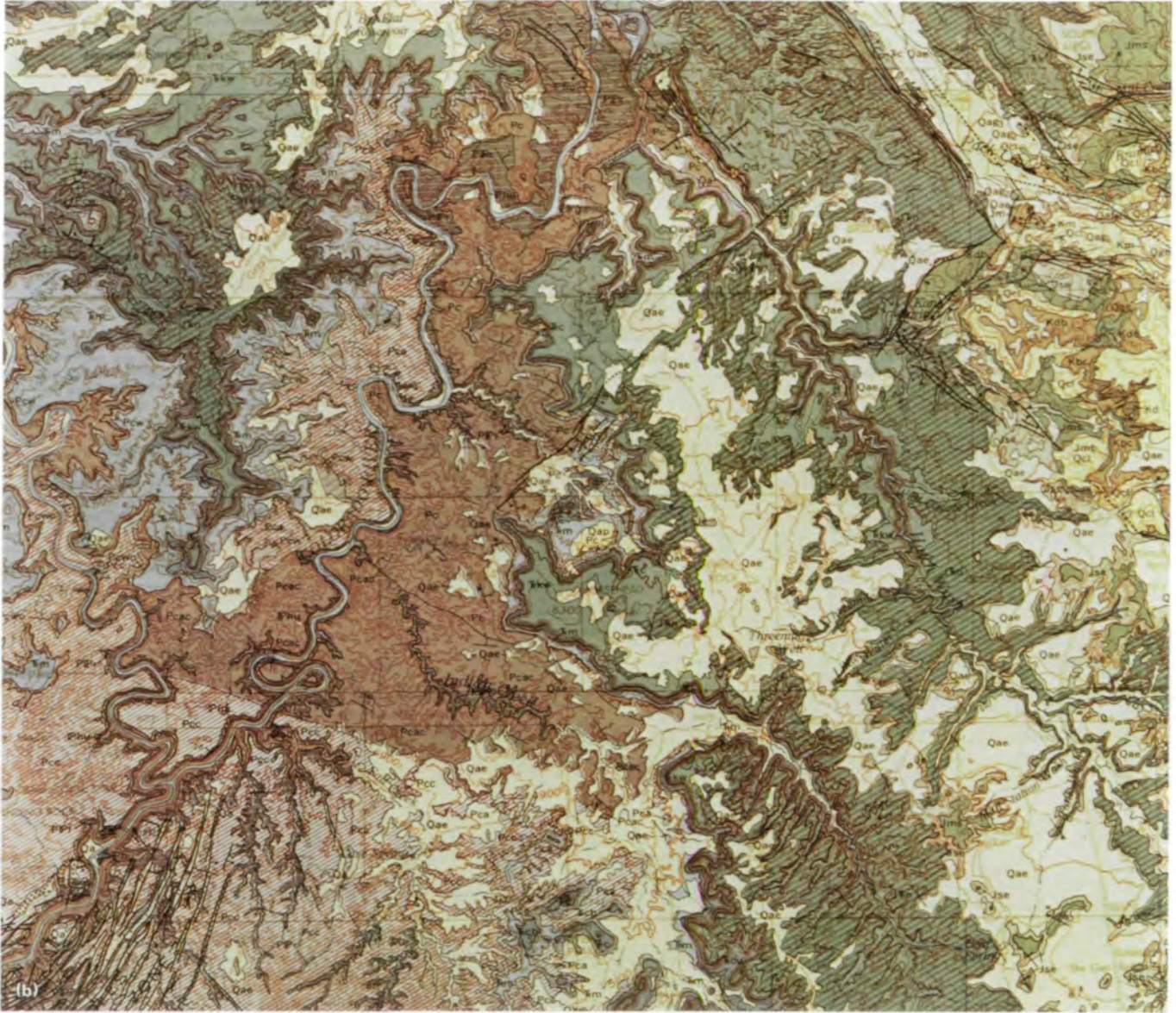
FIGURE 4-1.—Continued.

In the Canyonlands National Park in Utah, Lee et al. (ref. 4-2) used an EREP photograph (fig. 4-1(a)) to map all the sedimentary rock formations ranging in age from Pennsylvanian to Quaternary that appear on the published U.S. Geological Survey 1:250 000-scale map of this region (fig. 4-1(b)). At this scale, EREP photographs made possible some subdivision of formations into members as well as the mapping of stratigraphic pinchouts, intertonguing sedimentary rocks, and lateral facies changes. The photographs and the topographic maps were used to estimate the thickness of major stratigraphic units. Most major geological structures were recognized, and the dip of beds was estimated within 2° of field measurements. During this investiga-

FIGURE 4-1.—Concluded.

tion, mapping was accomplished at scales of 1:250 000 to 1:62 500. At this latter scale, a geologic map of a portion of the area was prepared that demonstrates the use of space data for detailed photogeologic analysis (fig. 4-1(c)).
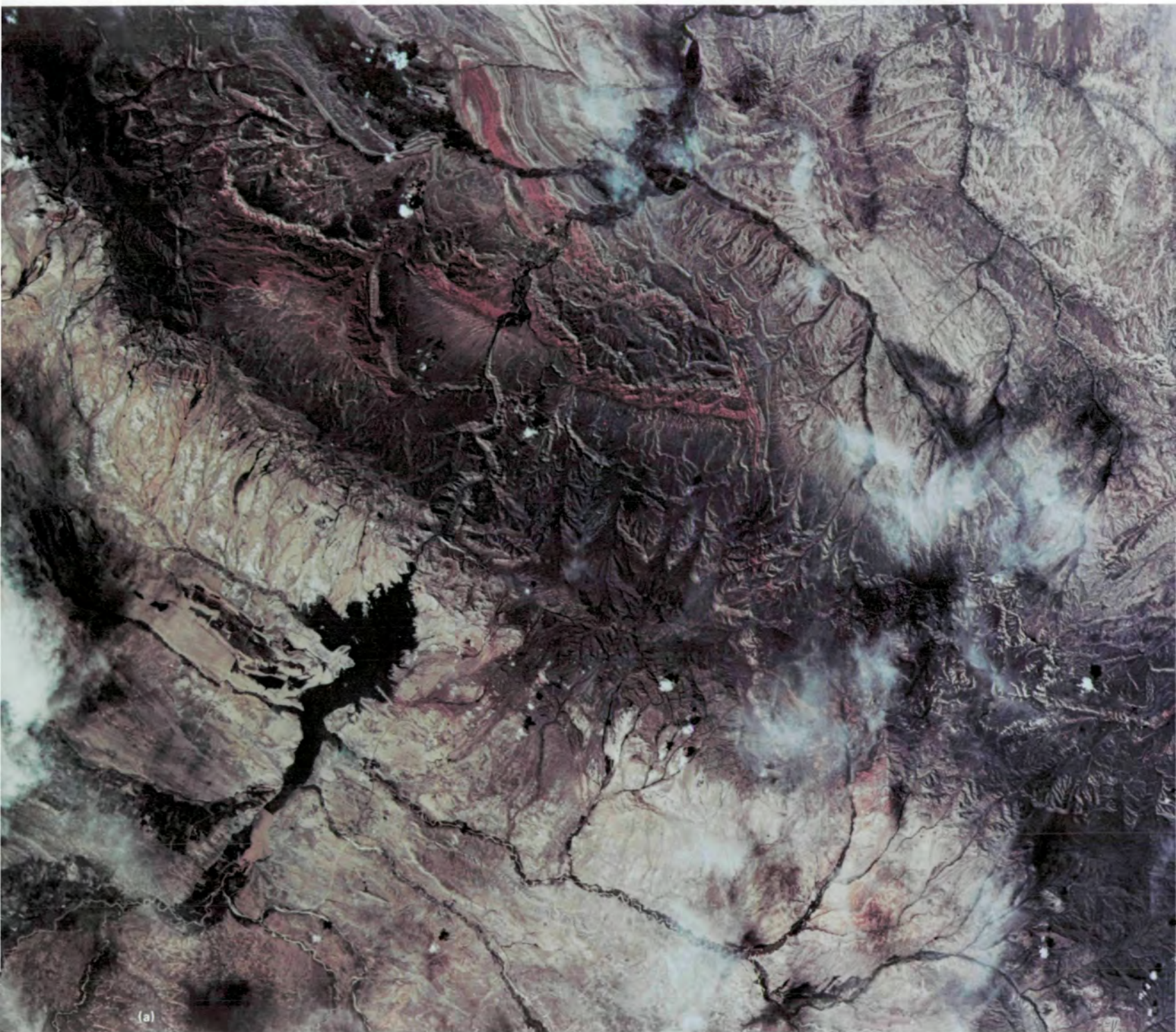
Skylab color photographs of the San Rafael Swell, a well-exposed, 116-km-long anticline in Utah, were used to map rock types and structural and linear features (fig. 4-2(a)). The results of this photogeologic mapping are shown in figure 4-2(b). Other regions photogeologically mapped from EREP photographs include Owl Creek Mountains and Bighorn Mountains, Wyoming (figs. 4-3 and 4-4). In the Owl Creek area (ref. 4-4), the Triassic red beds are vividly portrayed and were used as a

FIGURE 4-2.—San Rafael Swell area, Utah. (a) S190A color photograph (SL2-10-010). (b) Photogeological map derived from stereoscopic examination of Skylab S190A and S190B photographs.

(b)

Legend:

Tertiary Quaternary
- QAL. — Alluvium deposits

Tertiary
- TPC — Paleocene continental deposits

Cretaceous
- KMUG — Mesa Verde Group
- KM — KMFE-Ferron member Mancos Shale

Jurassic — San Rafael Group
- KJSR — Morrison Formation, Summerville Formation, Entrada Sandstone

Triassic — Glen Canyon Group
- JᴿRG — Navajo Sandstone, Kayenta Formation, Wingate Sandstone
- ᴿRC — Chinle Formation unconformity
- ᴿRM — Moenkopi Formation

Permian
- PKC — Kaibab Limestone and Coconino Sandstone of Utah

Symbols:
- ⊕ Horizontal bedding
- ⊥ Dip 0° to 5°
- ⊥ Dip 6° to 45°
- △ Dip 45° to vertical
- ᴅ⊢f Fault
- --f Fault, inferred
- — Lineament
- +▸ Anticline
- + Syncline
- — Geological contact, dashed where indefinite

Scale, km 0 — 20

N

FIGURE 4-3.—Owl Creek Mountain area in western Wyoming. (a) S190B photograph (SL3-88-018). (b) Geological interpretation showing the major structural and stratigraphic units mapped from Skylab photography.

Tu   - Tertiary, undifferentiated
Tf   - Fort Union (Paleocene)
Ju-Ku - Jurassic-Cretaceous, undifferentiated
Ŕc   - Triassic, Chugwater Formation
Pp   - Permian, Phosphoria Formation
Є-Pp   - Cambrian to Permian units
PЄ   - Precambrian

High-angle faults
Linears
Anticline
Syncline
Monocline
Dip direction

0   Scale, km   10   N
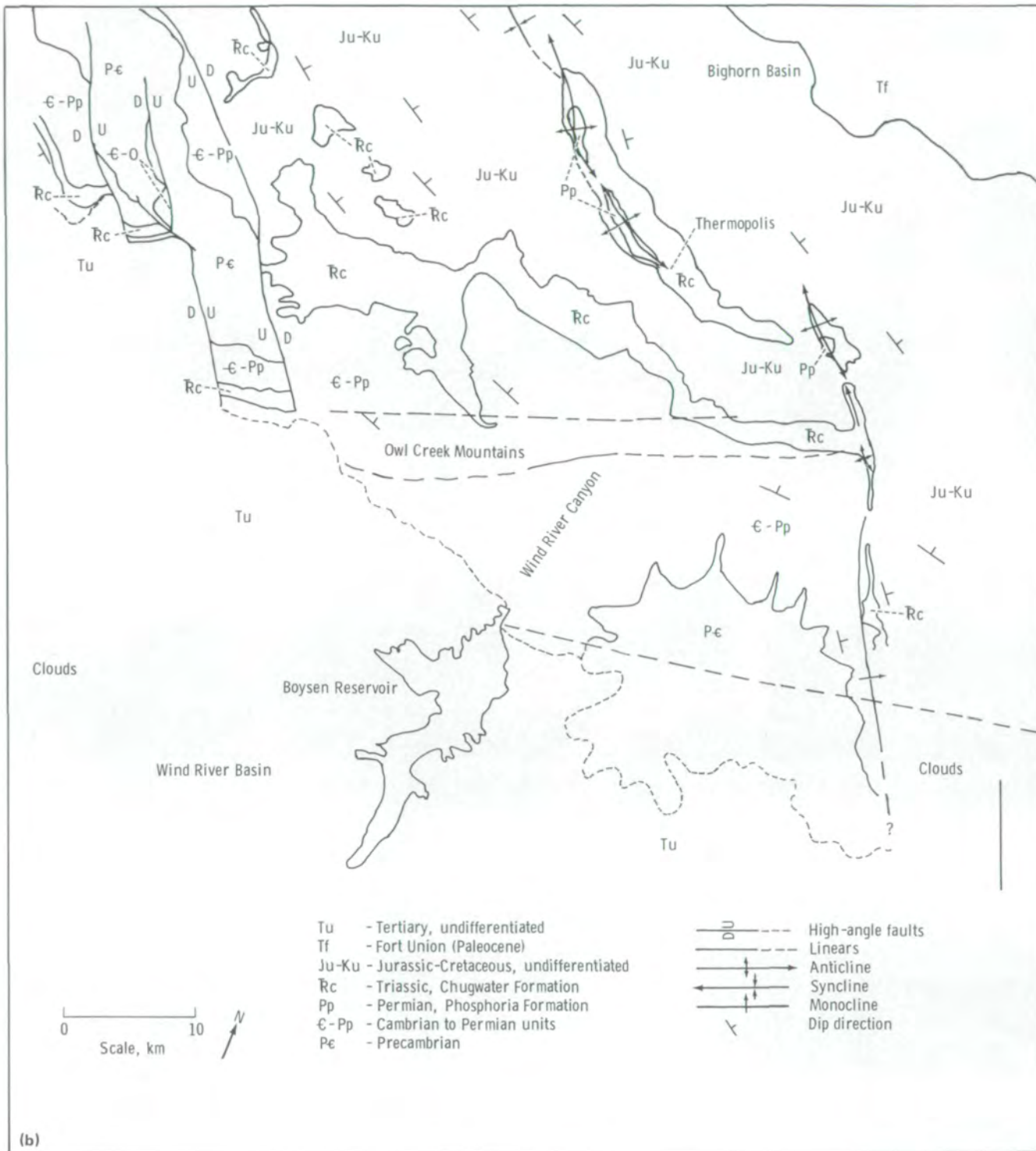
FIGURE 4-3.—Concluded.
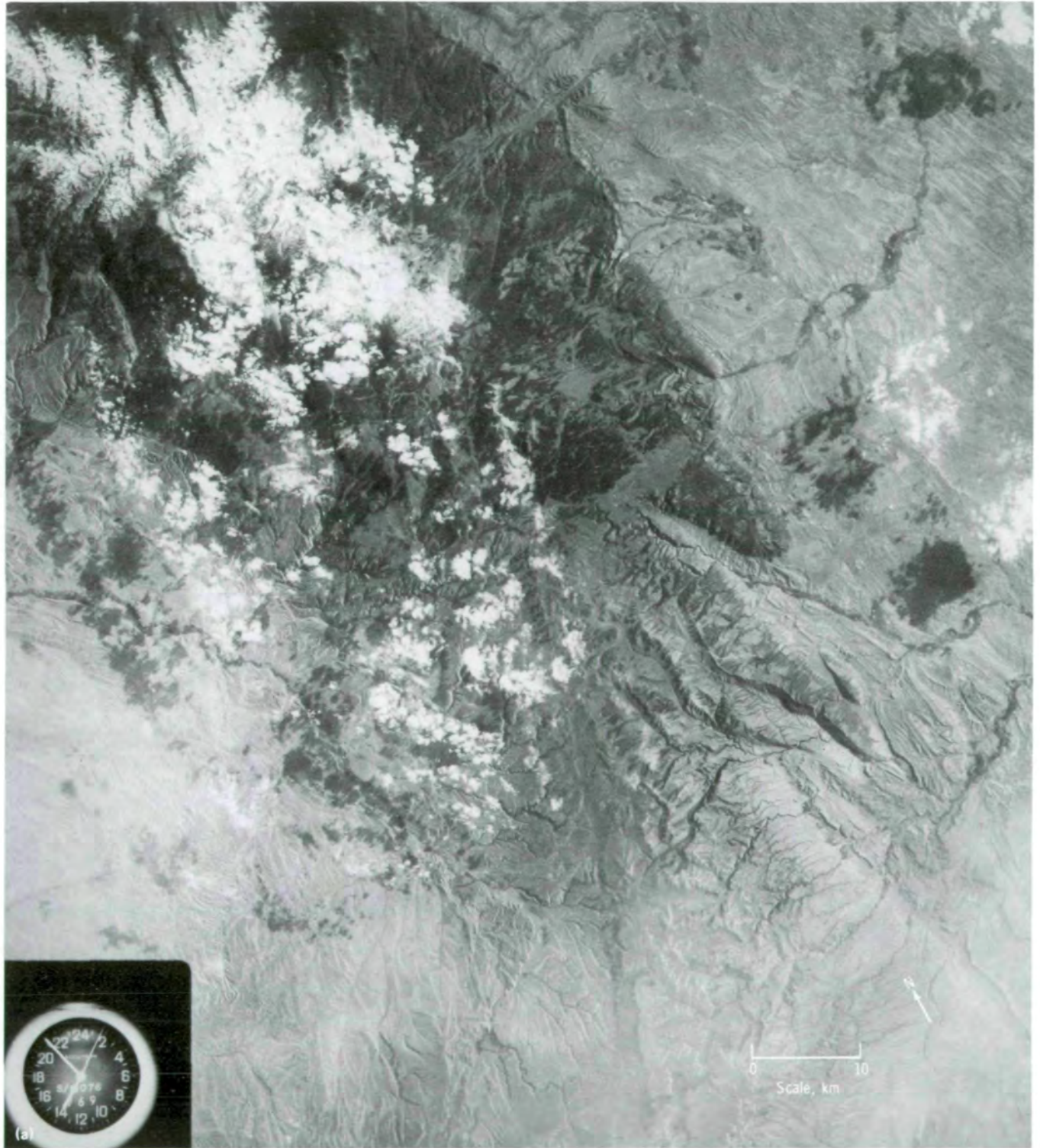
FIGURE 4-4.—Horn area of Bighorn Mountains in north-central Wyoming. (a) S190B photograph (SL2-82-146). (b) Reconnaissance geological map made by stereoscopic interpretation of Skylab S190A and S190B color, color-infrared, and black-and-white photography.

FIGURE 4-4.—Continued. (Symbols are explained on the following page.)

Photogeologic Map Units and
Approximate Geologic Map Unit Equivalents

Quaternary

Qal
Alluvium

Qpg
Pediment gravels

Tertiary

Tu
Undivided

Cretaceous

Kmv
Mesa Verde Formation at base; Lance Formation at top

Ksh
Basal contact of Shannon Sandstone; member of Cody Shale

Kc
Mostly Cody Shale

Kf
Mostly Frontier Formation

Kmr
Siliceous shales of the Mowry Formation

Kt
Black shales of the Thermopolis and Mowry Formations

Kcv
Cloverly Formation

Permotriassic

PRrb
Includes Permian Goose Egg Formation, and Triassic Chugwater Formation mostly

Pennsylvanian

Pt
Mostly Tensleep Sandstone

Mississippian

Mm
Mostly Mississippian Madison Limestone; includes some Bighorn Dolomite of Ordovician age

Cambrian

€u
Undivided

Precambrian

P€u
Undivided

FIGURE 4-4.—Concluded.

marker bed for interpreting the structural features. High-resolution black-and-white photographs of the "Horn" area (ref. 4-5) in the Bighorn Mountains portray the structural setting of the region, which aids in planning detailed geologic analysis.

The Alice Springs area in the arid central part of Australia was mapped by Lambert et al. (ref. 4-6) from EREP photographs, and the results were verified by field studies. These analyses showed that the strike of outcropping units was mapped accurately, that known folds were identified, and that areas of metamorphic and younger sedimentary rocks and Tertiary surficial deposits were delineated. Circular features detected on the photographs were found by field studies to be a ring dike, a granite intrusive, and a landslide.

In contrast to the application of color photographs in photogeologic analysis of semiarid regions, color-infrared and black-and-white infrared photographs are most useful in heavily vegetated regions. Structure can be revealed by landforms as in the Appalachian Mountains, where long, vegetated ridges are caused by resistant sandstones that resulted from the folding that occurred in this region. In the Black Hills of South Dakota, the Precambrian metamorphic and granitic rocks and the Paleozoic sedimentary sequences are tree covered and appear dark in the infrared photographs (figs. 4-5(a) and 4-5(b)). The color-infrared photograph (fig. 4-5(b)) shows the distribution of the Triassic red bed that outlines the regional extent of the Black Hills uplift. The lineament map (fig. 4-5(c)) derived from the photographs suggests a variation in pattern in the Paleozoic and Precambrian rocks that is an aid in delineating the contact.

In the areas of limited geological information, such as Central America, Skylab photographs have aided in the compilation of new information that can form the basis for further specialized mapping. Good examples are in Central America (ref. 4-7) and northeastern Spain (ref. 4-8). The usefulness of the photographs from spacecraft sensors varies with regional setting and environmental conditions at the site; table 4-I provides a comparison of the information content of the data acquired over the Great Plains area, which has subdued topography, heavy soil and vegetation cover, and a large amount of manmade disturbance (ref. 4-9).

Linear and lineament maps are common products of photographic analysis. A lineament is defined as any unidimensional straight or continuously curved combination of picture elements that appears on photographs or images and that is thought to have geologic significance (ref. 4-2). Straight or linear features on photographs have many possible causes. They may appear as alined sags and depressions, ridge gaps, tonal differences, alined springs, vegetational trends and types, straight drainage segments, ridges, textural differences, and cultural features. Many linears are faults or fracture traces, but unequivocal identification of all linears cannot be made from photographs; sometimes, identification cannot even be made after field checking.

Olson (ref. 4-10) found many topographic linears in South Carolina and northern Georgia to be parallel to
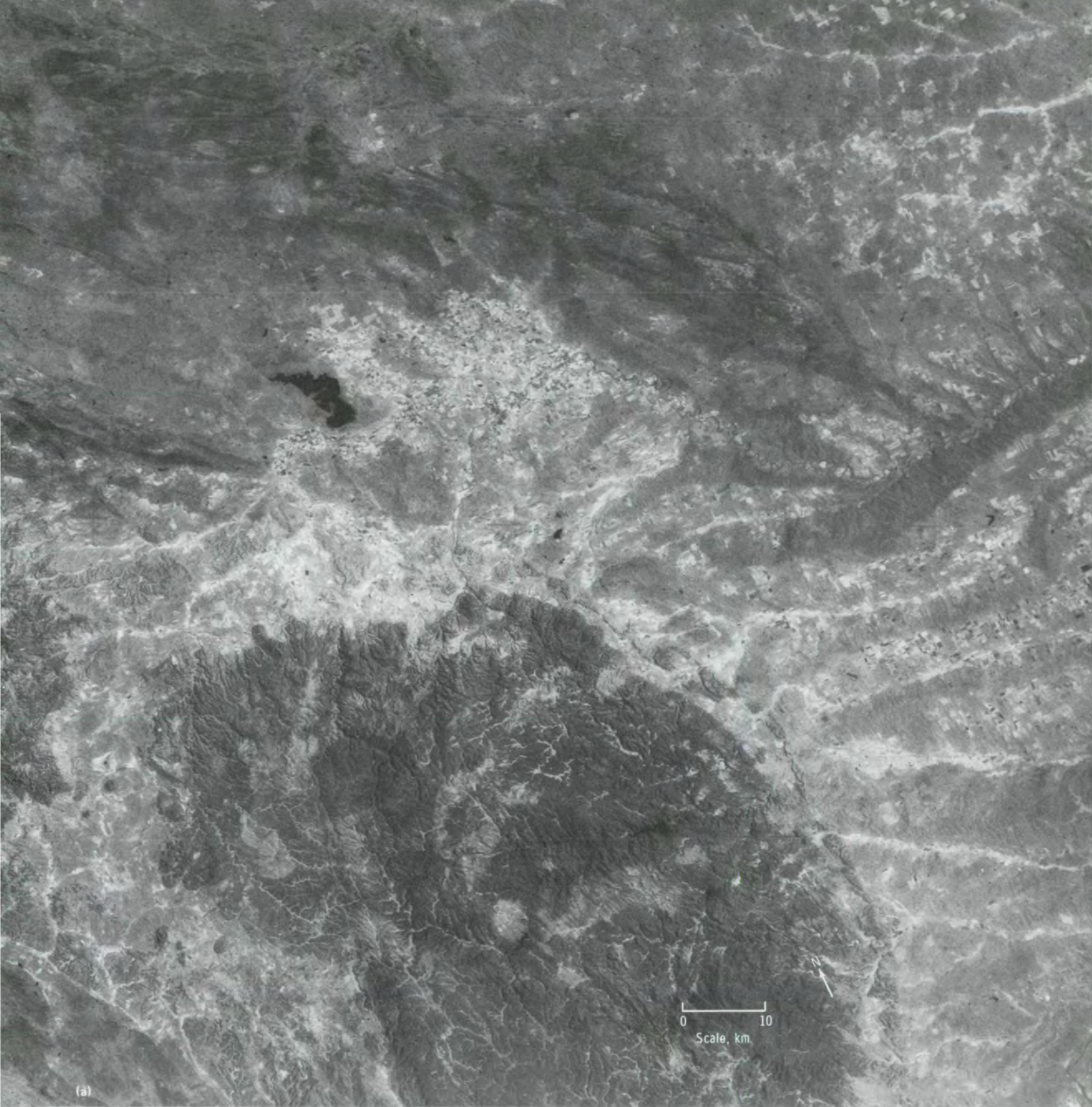
FIGURE 4-5.—Black Hills, South Dakota. (a) Black-and-white infrared photograph (SL2-08-113). (b) Color-infrared photograph with Paleozoic rock outlined (SL2-09-121). (c) Lineament map of lower portion of photographs.

Cretaceous

Cretaceous

Triassic
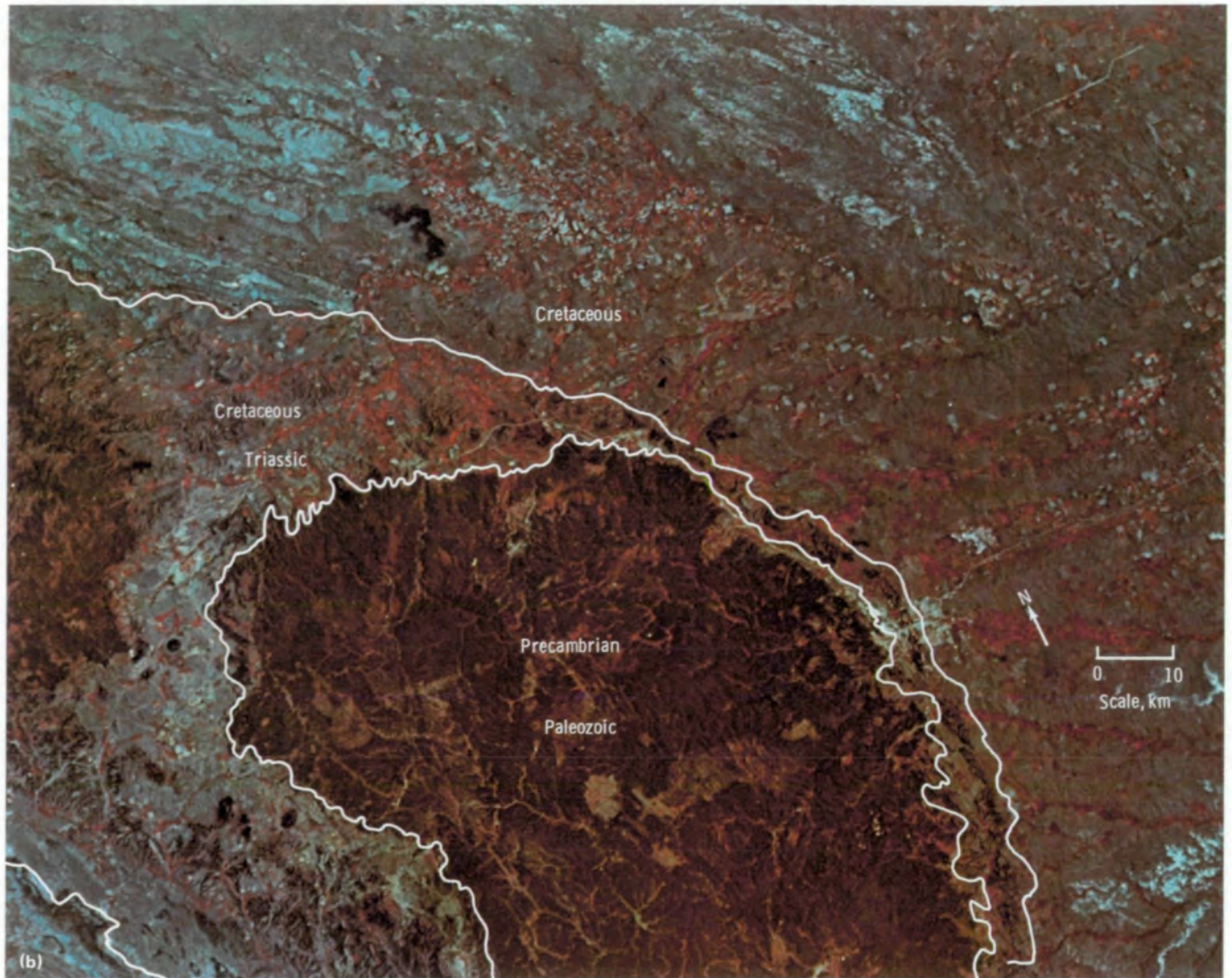
Precambrian

Paleozoic

N

0   10
Scale, km

(b)

FIGURE 4-5.—Continued.

zones of crushed rocks or to coincide with previously mapped regional fracture trends. Because linear patterns are often parallel to fracture and/or fault patterns as determined on the ground, linear diagrams are commonly considered to be reasonable approximations of fracture trends. In the Black Hills of South Dakota, Hoppin et al. (ref. 4-4) noted a strong north-northwest linear trend in the Precambrian core that parallels a widespread, closely spaced fracture system common throughout the region.

A major goal of the geology studies was to determine the scale, the resolution, and the spectral bands best suited for interpretation. Many investigators compared the number and length of linears observed on Landsat

FIGURE 4-5.—Concluded.

imagery, Skylab S190A and S190B photographs, and aircraft photographs. In general, more linears were found on Skylab photographs than on Landsat images. Longer linears were noted on Landsat images and shorter ones on aircraft photographs. The actual number observed can be a function of the season of the year in which the imagery is obtained. Cassinis et al. (ref.

4-11) noted that linear detection on the Skylab photographs acquired over Italy in September 1973 was not as good as on the Landsat imagery, because of the low contrast caused by uniform reflectance from vegetation. From geologic study of western Colorado, Lee et al. (ref. 4-2) showed that linears are selectively enhanced as a function of Sun elevation, Sun azimuth, and linear

TABLE 4-I.—*Comparison of the Content of Environmental Data Acquired by Different Sensors Over the Great Plains Area of the United States*

Imaging system	Spectral band	Attribute[a]							
		Sharpness of definition (ground resolution)	Color quality (color and color-infrared photographs)	Gray-scale or color-scale discrimination	Signal-to-noise ratio (multispectral scanner images)	Haze penetration	Shadow rendition	Repetitive, multiseasonal coverage	Regional coverage (comprehensiveness without gaps)
Skylab S190A multispectral photographs[b]	Color (0.4 to 0.7 μm)	3 to 3.5	3 to 4	3 to 4	—	2	2 to 3	2	2.5
	Color infrared (0.5 to 0.88 μm)	2 to 3	3 to 4	2.5 to 3.5	—	3.5	2	2	2.5
	B&W[c] infrared (0.7 to 0.8 μm)	0.5 to 1.5	—	1 to 2	—	3	1	2	2.5
	B&W infrared (0.8 to 0.9 μm)	0.5 to 1.5	—	0.5 to 2	—	3.5	1	2	2.5
	B&W red (0.6 to 0.7 μm)	3 to 3.5	—	2.5 to 3.5	—	2	2.5 to 3.5	2	2.5
	B&W green (0.5 to 0.6 μm)	2.5 to 3	—	1 to 2.5	—	1	1	2	2.5
Skylab S190B Earth Terrain Camera[b]	Color (0.4 to 0.7 μm)	3.5 to 4	3.5 to 4	3.5 to 4	—	2	2 to 3	2	2
Skylab S192 Multispectral Scanner images[d]	2 (0.46 to 0.51 μm; blue green)	0 to 1	—	0.5 to 1.5	3	.5	0	.5	.5
	3 (0.52 to 0.56 μm; green)	1 to 1.5	—	1 to 2	3	1	0.5 to 1	.5	.5
	4 (0.56 to 0.61 μm; yellow green)	1 to 1.5	—	1 to 2	3	1.5	0.5	.5	.5
	5 (0.62 to 0.67 μm; yellow red)	1 to 1.5	—	0.5 to 2	3	2	0.5	.5	.5
	6 (0.68 to 0.76 μm; red)	0 to 1	—	0.5 to 1.5	3	2	0	.5	.5
	7 (0.78 to 0.88 μm; near infrared)	1 to 1.5	—	1 to 2	2.5	3	0.5 to 1	.5	.5
	8 (0.98 to 1.08 μm; near infrared)	1 to 1.5	—	1 to 2	2	3	0.5 to 1	.5	.5
	9 (1.09 to 1.19 μm; near infrared)	1 to 1.5	—	1 to 2	2	3	0.5	.5	.5
	10 (1.20 to 1.30 μm; near infrared)	1 to 1.5	—	0.5 to 2	1.5	3	0	.5	.5
	11 (1.55 to 1.75 μm; near infrared)	0.5	—	0 to 1	1	3	0	.5	.5
	12 (2.10 to 2.35 μm; near infrared)	0 to 0.5	—	0 to 0.5	0.5	3	0	.5	.5
	13 (10.20 to 12.50 μm; middle infrared)	0 to 0.5	—	0 to 0.5	0.5	3	0	.5	.5
Landsat-1 multispectral scanner images[e]	4 (0.5 to 0.6 μm; green)	0.5 to 2	—	0.5 to 2	2 to 3	1	1	4	4
	5 (0.6 to 0.7 μm; red)	2 to 2.5	—	2 to 3.5	3.5	2	3	4	4
	6 (0.7 to 0.8 μm; near infrared)	2	—	2 to 3	3.5	3	2.5	4	4
	7 (0.8 to 1.1 μm; near infrared)	2	—	2 to 3.5	3.5	3.5	2.5	4	4

[a]Numerical rating system: 0 = very poor, 1 = poor, 2 = fair, 3 = good, and 4 = excellent.

[b]Better quality unenlarged third-generation transparencies of the project region.

[c]Black and white.

[d]Based on three snow-covered scenes from the Skylab 4 mission, groundtracks 1 and 58.

[e]Better quality photographic images (70-mm and/or 1:1 000 000-scale formats) of the project region.

TABLE 4-I.—Concluded

			Attribute[a]						
Stereoscopic coverage; stereovision	Metric (planimetric) capability	Water-body discrimination/ detail	Cloud/snow discrimination	Water penetration	Vegetation discrimination	Agricultural and urban land use detail	Topographic (landform and stream pattern) detail	Geological linear detectability	Average value
0 to 2.5	3	1 to 2.5	2	0.5	2 to 3	3 to 3.5	3 to 3.5	2 to 3	2.6
0 to 2.5	3	2 to 3	1	0	3.5	2 to 3	2 to 3	2 to 3	2.4
0 to 2.5	2.5	1 to 3.5	1	0	0.5 to 2	1	0.5 to 1	0.5 to 1.5	1.5
0 to 2.5	2.5	1 to 3.5	1	0	0.5 to 2	0.5	0.5	0.5 to 1	1.3
0 to 2.5	3	1 to 3	1	0	2.5	3	3 to 3.5	2.5	2.3
0 to 2.5	3	1	.5	2	1	1.5 to 3	1 to 2.5	0.5 to 1	1.7
0 to 3	3.5	1 to 3	2	1	2 to 3	3.5 to 4	3.5 to 4	2.5 to 3.5	2.7
0	2	0 to 1	0	—	—	0.5	0 to 1	0.5	.7
0	2	0 to 1	.5	—	—	0.5	1 to 2	0.5 to 2	1.1
0	2	0 to 1	.5	—	—	0.5	1 to 2	0.5 to 2	1.1
0	2	0 to 1	.5	—	—	0.5	0.5 to 2	0.5 to 2	1.1
0	2	0 to 1	0	—	—	0 to 0.5	0 to 1	1	.8
0	2	0 to 1.5	2	—	—	0.5 to 1	1 to 2	2.5	1.4
0	2	0 to 1.5	2	—	—	0.5	1 to 2	1 to 2	1.3
0	2	0 to 1.5	2	—	—	0.5	1 to 2	1 to 2	1.2
0	2	0 to 1	2.5	—	—	0 to 0.5	1 to 2	1 to 2	1.2
0	2	1 to 2	3	—	—	0	0 to 1	0 to 0.5	.9
0	2	0 to 1	3	—	—	0	0 to 0.5	0	.8
0	2	1	0	—	—	0	0	0	.6
1.5	3.5	0.5	.5	2	0.5	0.5	0.5	0.5 to 1.5	1.6
1.5	3.5	1 to 2	1	0	2.5	1 to 3	1 to 2.5	2 to 3.5	2.3
1.5	3.5	2 to 3.5	1	0	2	1 to 2.5	1 to 2	1.5 to 3	2.4
1.5	3.5	2 to 3.5	1	0	2	1 to 3	1 to 2.5	1.5 to 3	2.4

[a]Numerical rating system: 0 = very poor, 1 = poor, 2 = fair, 3 = good, and 4 = excellent.

orientation. Fractures as short as 1 km can be recognized on S190B photographs and joint spacing less than 200 m can be resolved.

Lambert et al. (ref. 4-6) compared the number of faults shown on a 1:250 000-scale geological map and the number of faults detected by interpretation of satellite images for the Alice Springs, Australia, area. The results, shown in table 4-II, include the following observations.

1. Many more faults were interpreted from S190B photographs than from any other type of image.

2. When faults shorter than 10 km are excluded from computation, the number of faults interpreted

3. Approximately the same number of known faults was detected on S190A and S190B photographs. Many more new faults were interpreted on S190B than S190A photographs, probably because the high resolution of the S190B camera makes it easier to discriminate faults from other linear features. Approximately 50 percent of the faults detected on S190B photographs are shorter than 10 km.

4. Almost 70 percent of the faults detected by analysis of Landsat-1 imagery were also interpreted on S190B photographs. However, the total number of faults detected on S190B photographs is twice that detected on Landsat imagery.

Merifield and Lamar (ref. 4-12) conducted extensive field studies in an effort to determine the origin of the linears they mapped from Skylab photographs of southern California. Although unable to assign a cause to all linears, they did correlate many linears with faults, foliation, and closely spaced fracture sets. Faults were indicated by topographic scarps; offset drainage or ridges; linear valleys and mountain fronts; contrasting tone, color, and texture; and vegetational differences caused by ground water blockage.

TABLE 4-II.—Comparison of the Number of Faults Identified From Various Sources for the Area of Alice Springs, Australia

(a) All sources

Source	Number of faults identified		
	> 10 km	< 10 km	Total
Map	26	39	65
Landsat-1	48	26	74
S190A	48	4	52
S190B	72	71	143

(b) Comparison of S190A and S190B photographs

Source	Number of faults in area			New faults interpreted
	Previously known	Detected	Not detected	
S190A	65	22	43	30
S190B	65	29	36	114

(c) Comparison of Landsat-1 and S190B photographs

Faults from Landsat-1	Faults detected on S190B	Faults not detected on S190B	New faults interpreted on S190B
74	50	24	93

Structural and Tectonic Synthesis[1]

Results of photogeologic analysis have shown that Skylab photographs are valuable for preparation of regional structural maps. From such maps, geologists can select areas for detailed ground studies, leading to definition of targets for further exploration of potential mineral resources or suspected geological hazards.

New maps based on EREP data of areas that have been studied previously can lead to reinterpretations of the geology and new hypotheses of regional structure. During a structural analysis of the Anadarko Basin (Oklahoma-Texas), Collins et al. (ref. 4-13) found a substantial correspondence between lineaments interpreted from the photographs and faults indicated by seismic data. This correspondence suggests a greater

---

[1]Structure refers to individual features such as folds, faults, or joint swarms. Tectonics refers to the origin of large-scale structural patterns of subcontinental size—the arrangement of mountain belts, basins, and fault systems.

amount of normal faulting on the northern side of the basin than has been recognized. The lineaments and faults could have associated structural closures, which might contain hydrocarbon accumulations. Further exploration to test the hypothesis appears to be warranted.

Whether or not a particular fracture originated by tension or by shear is much debated. Determining which model is applicable to the rocks in an area is an important step toward determining the orientation of the stresses that were responsible for the deformation of the rocks. McMurtry and Petersen (ref. 4-14) stated that lineaments, fracture traces, and joints mapped on Skylab photographs are coincident in direction in an area of the Allegheny Plateau. They postulate that the relationship is more consistent with a tensional than a shear model of origin.

The EREP photographs provided synoptic views of mapped lineaments (complex, long, rectilinear fracture zones). Geologists believe these structures are important to understanding the global tectonic systems, but their nature and origin are not yet well established. Lee et al. (ref. 4-2) noted that lineaments cut across young structural trends in the Colorado Front Range. The origins of these lineaments are not known, but they probably result from recurrent movement along old fracture systems.

In areas where linears and lineaments can be shown by field studies to be faults, the kind and amount of displacement along them may still be a matter of conjecture. When considering several tectonic hypotheses, it is necessary to determine not only the sense of displacement (horizontal or vertical movement) but also the length. Direct evidence of the sense of horizontal displacement along faults could seldom be obtained from Skylab photographs. In the Peninsular Ranges, southwestern California, Merifield and Lamar (ref. 4-12) used Skylab photographs and Landsat images to discover four faults in the basement rocks and to determine from fieldwork the direction of displacement (fig. 4-6). They noted a regional alinement of features possibly revealing unrecognized segments of the San Andreas Fault system southeast of the Salton Sea along which predominant right-horizontal slip is known to occur.

Abdel-Gawad and Tubbesing (ref. 4-15) analyzed Landsat imagery and Skylab photographs for a large area of the Southwestern United States and northwestern Mexico (fig. 4-7). Linears interpreted as faults were used to develop a tectonic model relating major fault zones to fragmentation and rotation of crustal blocks. The model supports the interpretation that the Texas shear zone is one of three elements in a broad zone of deformation 2000 km long and 250 km wide that trends northwest from the Gulf of Mexico to the Transverse Ranges in California. The zone is postulated to have a left-lateral offset of 500 km. The investigators suggest that the Mojave block and the Sierra block may have rotated 25° counterclockwise and the Colorado Plateau, 15° clockwise.

Lineaments have been extended speculatively by some authors for considerable distances beyond their known limits. Hoppin et al. (ref. 4-4) used EREP photographs to test some of these predictions. No evidence of an extension of the Nye-Bowler lineament east of its presently mapped limit in the Pryor Mountains could be found on an S190B color scene of the northern Bighorn Mountains in Wyoming. Other lineaments in this region also appear to be limited in length. Extending lineaments to great distances on the basis of analysis of space photographs may be unwarranted.

The nature of geologic structures is a key to understanding the location and types of past movements that are now inactive. There are, however, geologic structures actively forming that are evidence of crustal movement. (See the subsection on earthquake hazards.) Surface displacement not related to known faults can be inferred from the distribution and occurrence of youthful landforms. In Utah, Jensen and Laylander (ref. 4-16) noted that recent alluvial fans cover old Lake Bonneville terraces and are interpreted as indicative of recent regional uplift of the Wasatch Range. Such information may lead to a better understanding of Earth dynamics.

Photolinear maps of southwestern Guatemala and Chiapas document the structural complexity of the junction of the Cocos, Americas, and Caribbean plates and show the structural relationships to volcanic regions. Stoiber and Rose (ref. 4-7) found that the photolinear patterns within the Central American volcanic chain support their segmented model of the Benioff zone by showing a concentration of transverse, northeast-trending linears in the predicted locations.

Tectonic synthesis, one of the final goals of structural analysis, begins with mapping on the best Skylab photographs followed by field checking, detailed mapping of key areas, interpretation, and verification of hypotheses. The resulting regional geological maps are excellent for such a synthesis.
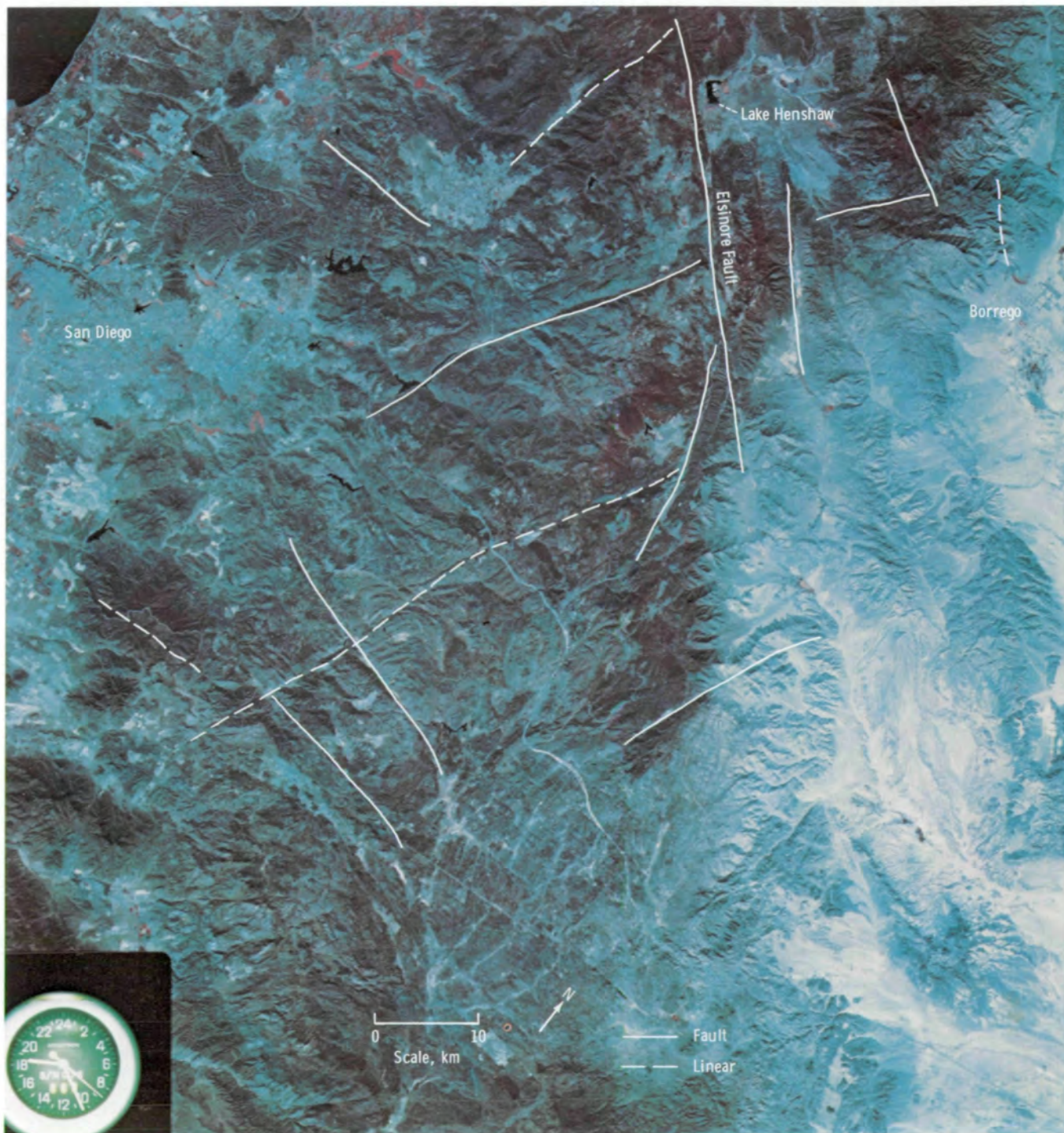
FIGURE 4-6.—S190B color-infrared photograph of the Peninsular Ranges in southwestern California, showing the major faults and linears (SL3-87-111).
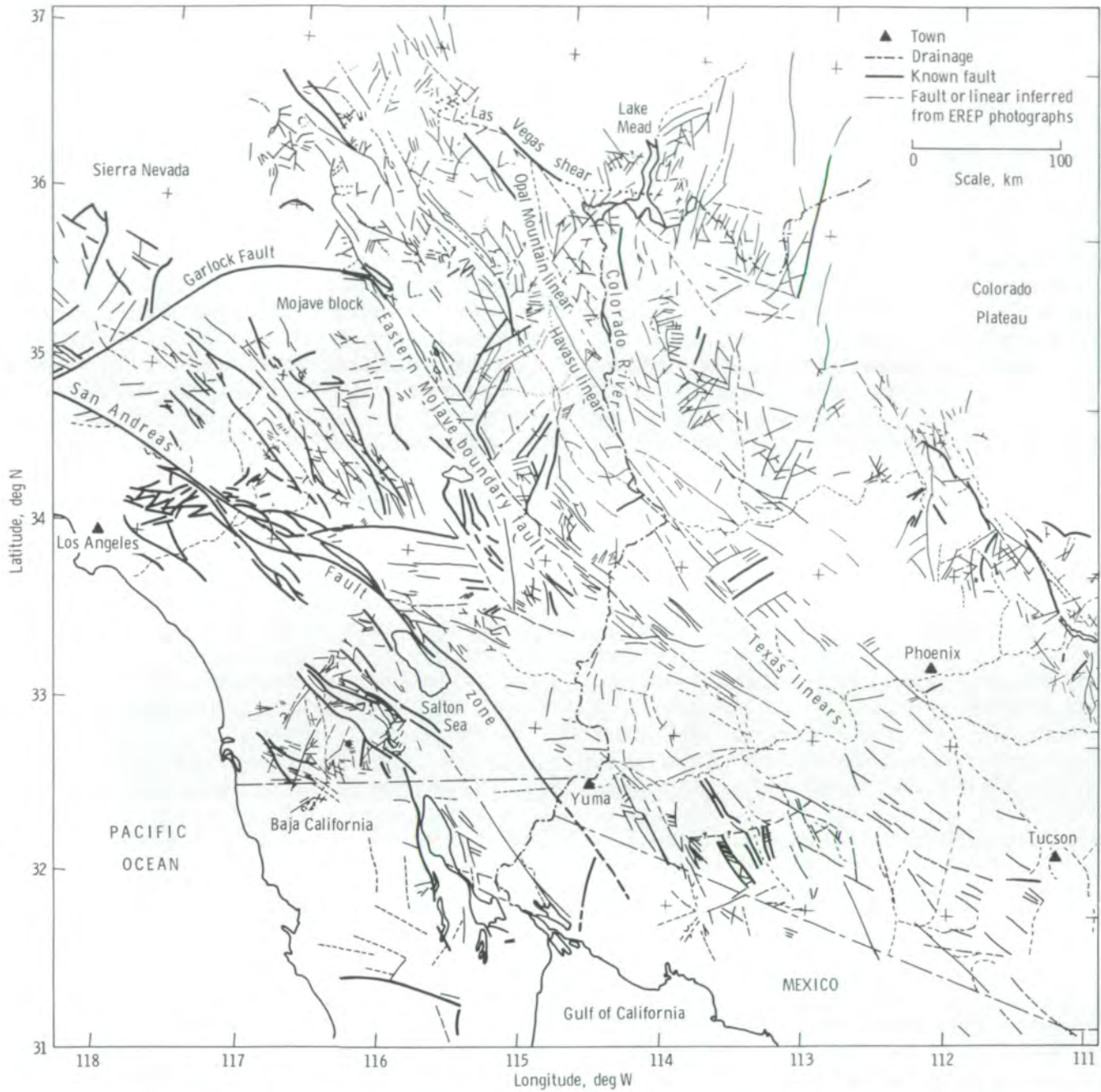
FIGURE 4-7.—Map of the Southwestern United States and northwestern Mexico showing known faults and lineaments. The lineaments were interpreted from Skylab photography and are possibly fault zones.

Rock Types

A major effort in remote sensing has been directed toward the identification and discrimination of rocks and minerals. Discrimination is the separation of one rock type from another; identification is the classification of a specific rock or mineral according to unique physical properties. The results of this effort show that detailed information is needed for the discrimination and identification of rock types. Most attempts at rock discrimination are made for regional mapping inventories, whereas most mineral identification is made for exploration for a single type of material.

As described by Morrison et al. (ref. 4-9) in the Great Plains States, by Morrison[2] in Arizona, and by Lee et al. (ref. 4-2) in Colorado, most regional mapping is conducted at the State government level or by private exploration companies. The distribution of all surface materials in the area is examined. Specialized rock-type or surface-type maps are prepared for specific purposes, such as selecting sites suitable for locating public utilities, providing construction materials, or routing new highways.

The work of Jensen and Laylander (ref. 4-16) and Bechtold et al. (ref. 4-17) illustrates the efforts of private interests in locating deposits of minerals that may have potential value. Using their approach, an investigator searches for areas where geological events altered the composition or structure of the rock in such a way that it serves as a host rock for the ore minerals or hydrocarbons. When an area of potential interest has been located, intensive geophysical and field surveys are initiated to provide more detailed information on which to base development plans.

Skylab investigators used the characteristics of sunlight reflected from surface materials as a means of identifying and mapping rock and mineral types. This process has been used for many years in field identification and aircraft reconnaissance to determine the color, brightness, texture, and geographical position of the material. A preliminary identification can be made from this information by an experienced geologist. However, many more field and laboratory tests are required to make a positive identification after an area of specific interest has been defined.

The discrimination factors examined by most Skylab investigators were those of visible color and brightness. Color and brightness of the remotely sensed surface were compared with the characteristics of a known standard. Identification was then made on the basis of the degree of similarity between the test material and the standard. The work of Lambert et al. (ref. 4-6) in Australia and the examination of Nevada surface materials by Quade et al. (ref. 4-1) exemplify this technique. Color photographs from the S190A and S190B camera systems were compared with aircraft color photographs and with field photographs and samples of materials. Although primary color comparisons were possible, atmospheric dispersion of light and laboratory processing of the photographs modified the Skylab photograph color, color balance, and brightness to such an extent that the photographs could not be used as accurate indicators of the sampled ground color. Laboratory modification of the Skylab photograph colors was made to match the colors visible in field examination. It was found that, when one specific sample area was color-corrected to match the ground sample, other sample areas might be degraded in color representation. High-quality photographic processing was considered to be essential to the interpretation. Quade et al. (ref. 4-1) stressed that differences in photograph colors enhance an interpreter's ability to separate one surface unit from another, even though the colors may not exactly match ground color (figs. 4-2 and 4-8).

To emphasize specific types of rocks and to enhance the contrast between different materials, a variety of color combinations and single-bandwidth spectral regions was used. Multiband photographs in the visible and near-infrared spectral regions were used in combination and separately by Lee et al. (ref. 4-2), Houston et al. (ref. 4-5), Bechtold et al. (ref. 4-17), Goetz et al. (ref. 4-18), Lee and Raines (ref. 4-19), and others to produce photographs that enhanced the differences between adjacent surfaces for visual interpretation. As an example, an improvement in discrimination of alluvium-covered and hydrothermally altered areas was evident in some false-color-composite photographs formed from the black-and-white S190A photographs. This technique enabled the interpreter to vary the emphasis within the four spectral regions to accentuate the desired color balance. Particular value was noted for the S190A photographs in the 0.6- to 0.7-μm bandwidth. Discrimination of red beds was improved using the infrared spectral regions because of the distinctive reflectance of these rocks.

---

[2]R. B. Morrison, "Application of Skylab EREP Photographs to Study of the Modern Episode of Accelerated Erosion in Southern Arizona," unpublished Final Report, NASA-USGS Agreement T-4113-B, 1975.
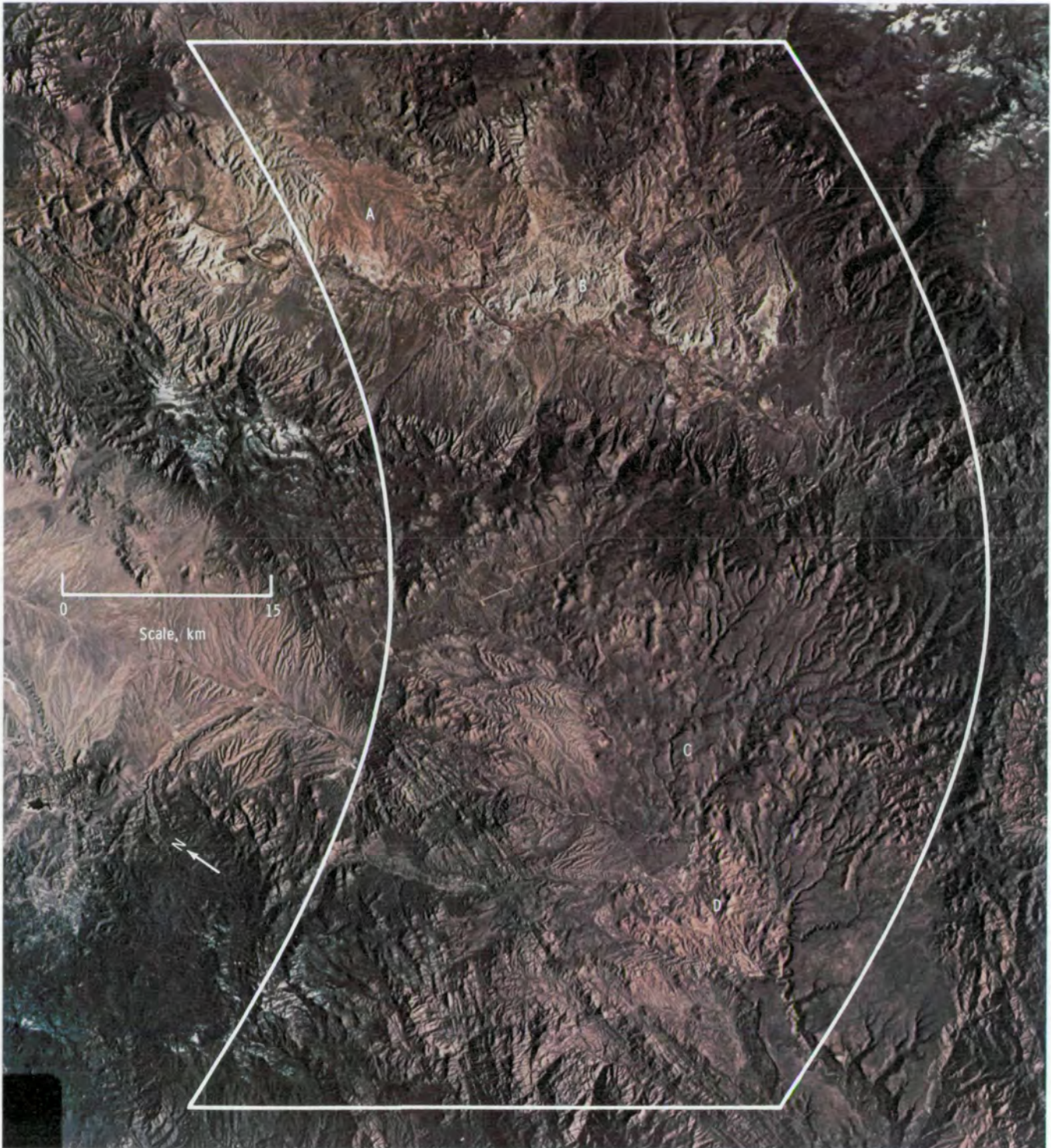
FIGURE 4-8.—S190B color photograph of the Prescott, Arizona, area, taken at 16:53 GMT on December 4, 1974 (SL4-90-306). Differences in tone and texture can be used to discriminate between surface materials. Sites A and B are sedimentary rocks, site C is mostly basalt, and site D is an area of granite. The approximate area shown in figure 4-10 is outlined.

Skylab experiments have demonstrated that it is possible, from orbital altitudes, to discriminate effectively among general types of surface materials on a regional scale. Experience using EREP data for identification of specific rock and mineral types indicates that only a few of the many component materials of rocks and minerals exhibit a distinctive reflectance-response pattern within the spectral regions sampled by EREP sensors. Two common rock components, water and carbonate materials, exhibit characteristic responses within the EREP infrared spectral regions at

1.4, 1.9, 2.2, and 2.35 μm. These materials are also present in many other forms on the Earth's surface as well as in the atmosphere. The result is that differences in reflected energy in these spectral regions are often greatly obscured by surface moisture, organic compounds in surface vegetation, and atmospheric effects.

Compounds of iron are found in many surface materials and exhibit characteristic reflectance features in the wavelength areas of 0.55, 0.75, 1.0, 1.6, and 2.0 μm. The response features are rather broad and occur at slightly higher or lower wavelengths in different
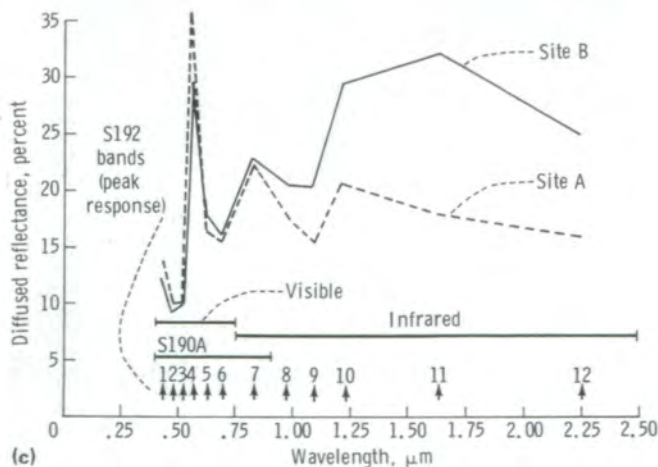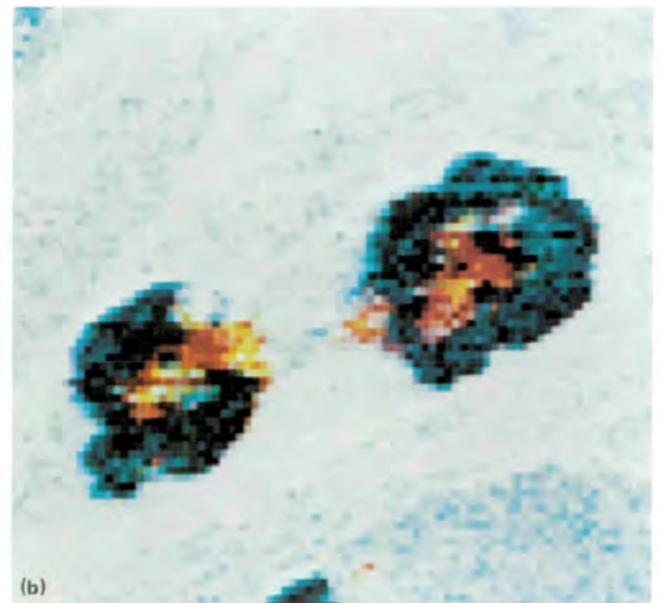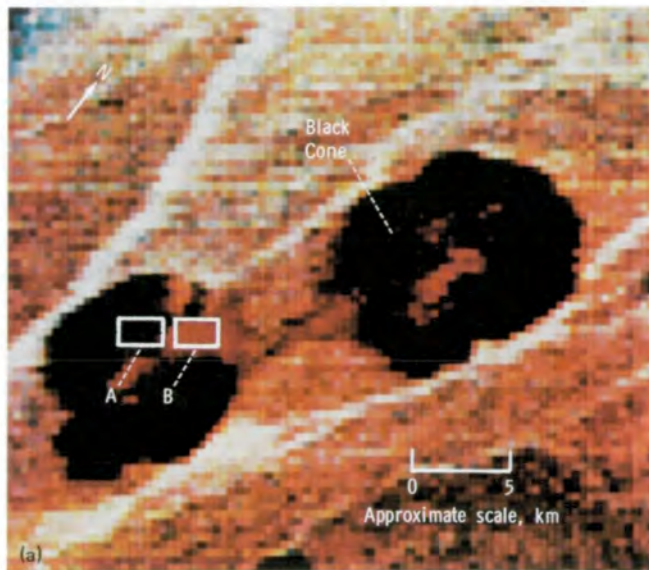
FIGURE 4-9.—Area of Black Cone, Nevada, on June 9, 1973. (a) Color composite of S192 data in which bands 12 (red), 7 (green), and 2 (blue) were used. The image contrast is typical of the normal scene reflectance. Site A is composed of materials inside the cone. Site B is adjacent materials demonstrating an anomalous reflectance possibly caused by a very fine coating of iron oxides deposited by posteruptive volcanic steaming. (b) Color composite of the same data, in which the image contrast was stretched to emphasize reflectance differences in the rocks near and inside the cones. (c) Spectral response curve showing the diffused reflectance signatures for sites A and B. These signatures demonstrate strong similarities in the visible range but significant differences in the infrared region.

minerals. A very small percentage of iron may dominate the reflectance response measured at the spacecraft, as exemplified by figure 4-9.

The EREP investigations of atmospheric effects by Thomson (ref. 4-20), Chang and Isaacs (ref. 4-21), and others illustrate the influence of atmospheric absorption and scattering on spectral reflectance data (fig. 4-10). Many major atmospheric effects coincide with the spectral bands required for accurate identification of rocks, which suggests that future progress in rock-type classification from orbital altitudes should be linked closely to atmospheric-correction models based on surface altitude and aerosol absorption.

EXPLORATION FOR MINERAL AND ENERGY RESOURCES

Exploration for economically useful mineral resources involves surveys or reconnaissance studies of large regions to locate the much smaller areas that may be worth the expense of detailed study. Geologists routinely use surface traverses, geophysical surveys, and interpretation of aerial photographs for reconnaissance. Photographs of the Earth obtained from spacecraft are useful because they can provide views of large areas under uniform lighting conditions with spatial resolution adequate for photointerpretation. The EREP investigators studied different types of data to determine the most useful spatial resolution, spectral resolution, scale, and format for resource exploration. Their results indicate that color or color-infrared, synoptic, stereoscopic photographs with approximately 10-m ground resolution are the best tools for photointerpretation. Positive transparencies are best for laboratory study, 23- by 23-cm positive paper prints are most useful for field checks, and larger paper prints are best for compiling information.

Mineral Exploration

Fracture systems (i.e., combinations of faults and joints) provide pathways for ore-bearing fluids and tend to localize deposition of ore minerals. Fractures may be expressed at the Earth's surface as straight valleys if the material along the fracture is crushed or altered, or as straight ridges if the fracture is filled with resistant vein deposits. Straight topographic features such as these are

visible on EREP photographs as linears that can be mapped, and their significance can be determined by field check. For example, Stoiber and Rose (ref. 4-7) found that trends of linear features mapped on S190A and S190B photographs agreed with previously mapped trends of lead-zinc, gold-silver-mercury-tin, and copper veins in Central America. Prost (in ref. 4-2) found a general correspondence between density of linears and location of mineral districts in Colorado. He and other investigators emphasize the necessity of careful field checking to eliminate linear features that do not represent the surface expression of geological fractures or rock-body contacts.

Bechtold et al. (ref. 4-17) studied S190A and S190B photographs and S192 imagery of California, Nevada, and Arizona to define combinations of linear and curvilinear features that might be correlated with mineral deposits. As an example, they described a nearly circular topographic feature near Hunter Mountain (fig. 4-11) in the Panamint Range, California. Similar circular features mark the location of bodies of intrusive igneous rocks in the Southwestern United States; many of these rock bodies are permeated with low-grade (0.5 to 3.0 percent) copper sulfide and/or molybdenum sulfide. The circular topographic features are caused by erosion of fractured rock. Some fractures are lined by soft, altered material; others are filled with resistance quartz. The net result is a dense network of short, straight, and curvilinear valleys and ridges that outline the potential ore body. The Hunter Mountain feature is not differentiated from other granitic bodies in the area (fig. 4-11(d)), although it is easily distinguished on the Skylab photographs. Field checks showed that copper and iron sulfides and their alteration products occur most of the way around the periphery of the circular body. Features such as these are targets for more detailed investigation because they may represent large, hidden ore bodies.

Another useful indication of possible large, low-grade ore deposits is an area of altered material at the surface (ref. 4-22). The alteration is caused by chemical solutions in heated water that spread from the source of mineralization into surrounding rocks. Surface indications of alteration zones range from brightly colored in shades of red and yellow due to oxidation of iron minerals, to white resulting from bleaching of the rocks and deposition of clay minerals. In reference 4-23, Levandowski and Borger report that computer-aided analysis of S192 data from the San Juan Mountains,
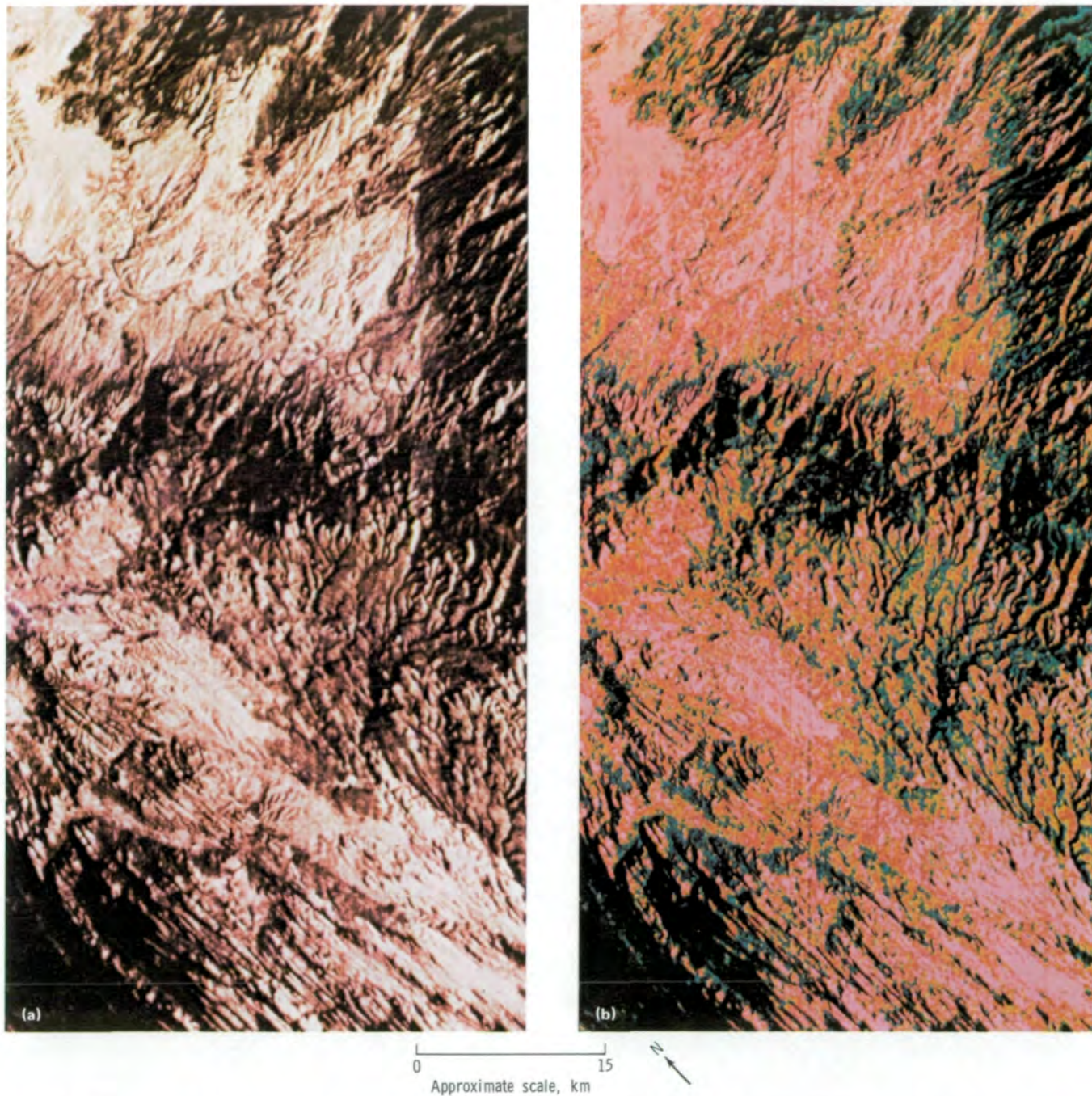
FIGURE 4-10.—Imagery of the Prescott, Arizona, area. (a) S192 image taken at the time of the photograph in figure 4-8 and presented in a conical format of band 11 (1.55 to 1.75 μm). This band has been suggested as having excellent potential for rock- and mineral-type discrimination. (b) False-color image of the data shown in figure 4-10(a). This type of enhancement can be used to improve the interpretability over an extensive scene. (c) Color composite of S192 data of the outlined area in figure 4-8, presented in a conical format of visible-wavelength band 6 (0.68 to 0.76 μm), band 3 (0.52 to 0.56 μm), and band 1 (0.41 to 0.46 μm). The subdued scene contrast, partially caused by the influence of atmospheric scattering, is noteworthy. (d) Color composite of the area shown in figure 4-10(c), using band 12 (2.10 to 2.35 μm) and band 8 (0.98 to 1.08 μm). The significant increase of contrast from figure 4-10(c) is evident.
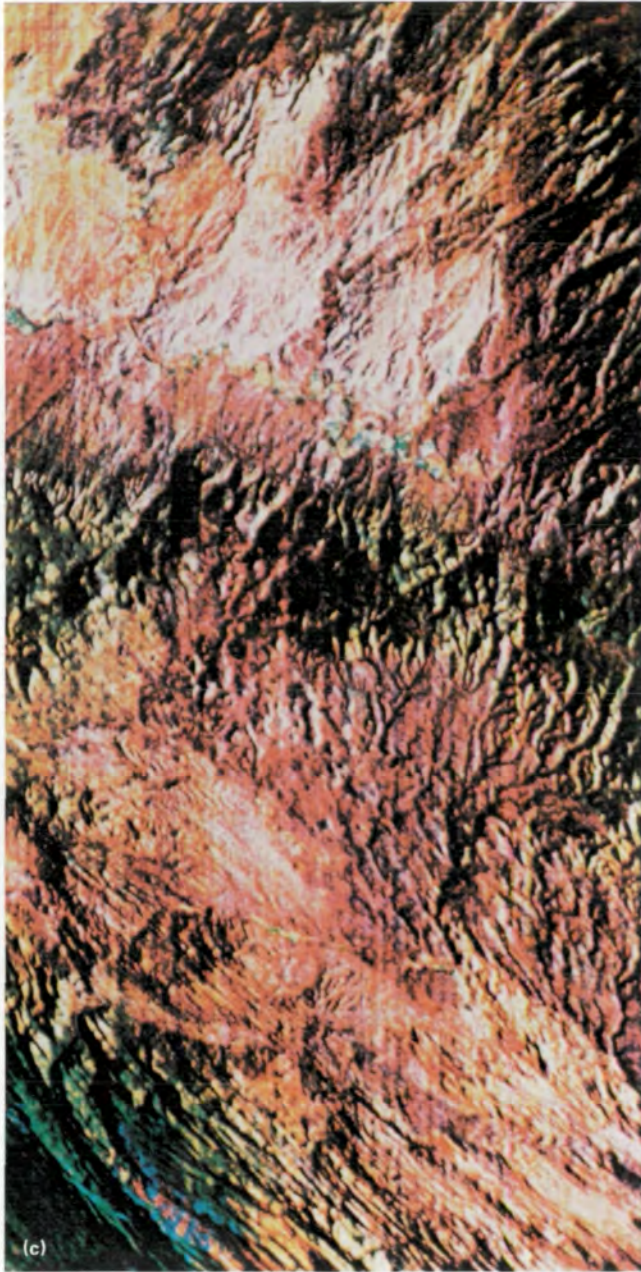
0 _____ 15
Approximate scale, km

N ↗

FIGURE 4-10.—Concluded.
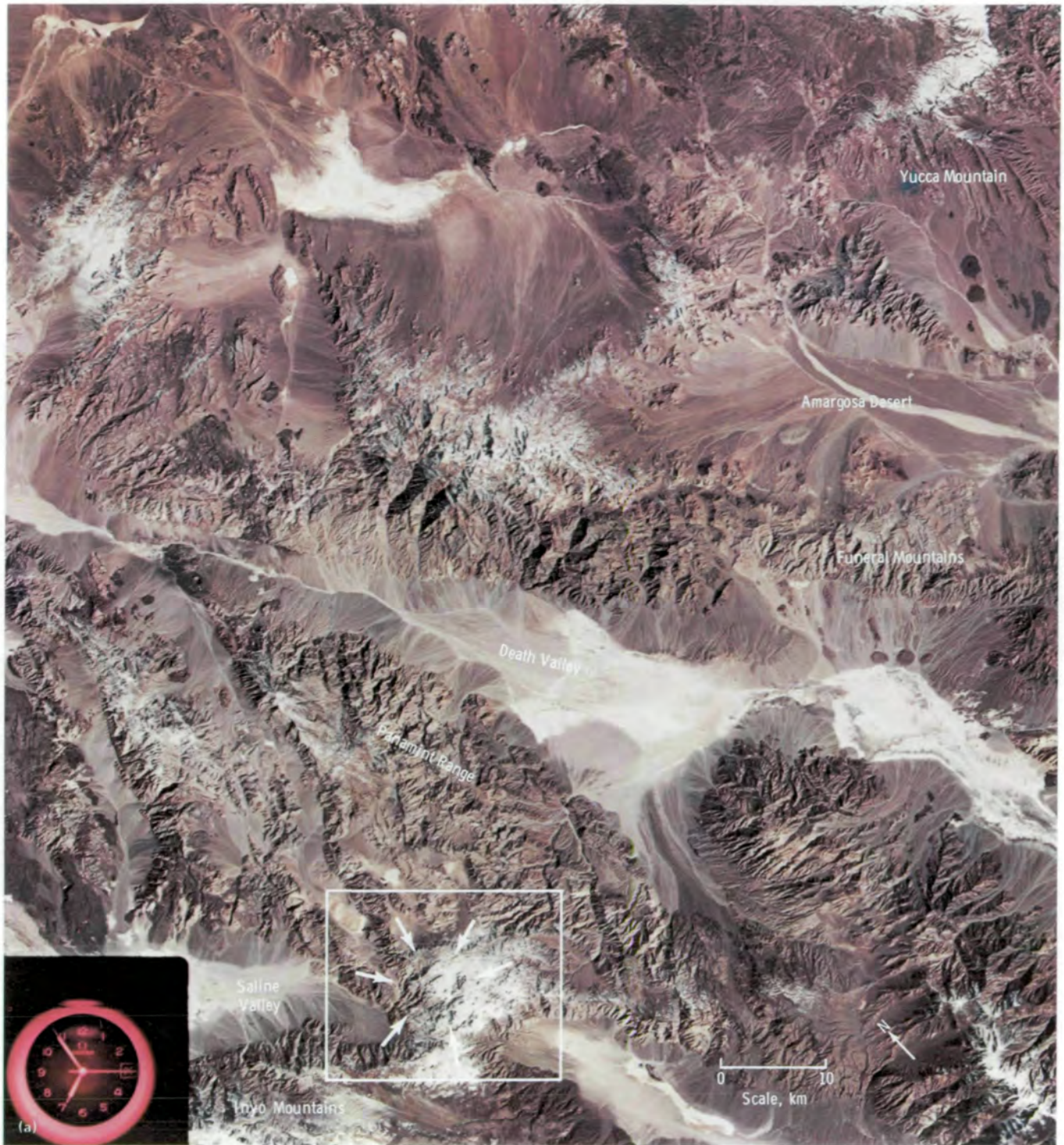
FIGURE 4-11.—Anomalous circular feature near Hunter Mountain in the Death Valley area of California. (a) S190B color photograph (SL4-94-013). The area shown in figure 4-11(b) is outlined. (b) Enlargement of circular feature. (c) View looking westward across the circular feature from a mineral prospecting pit on the rim of the feature (NASA S-75-31982). (d) Geological map of the area in which the circular feature is located, compiled from previously published sources (ref. 4-17).
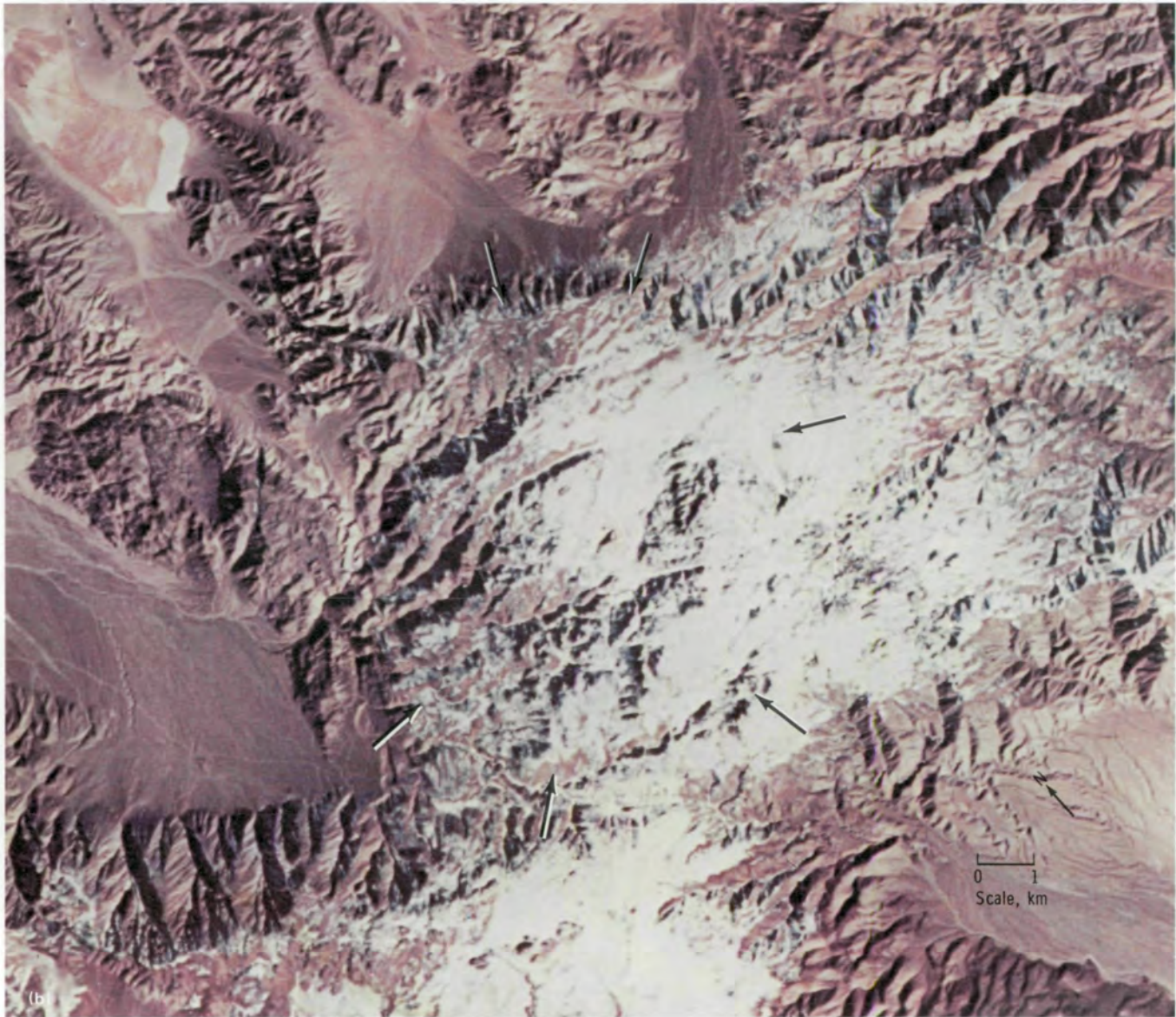
FIGURE 4-11.—Continued.

Colorado, allowed the delineation of alteration zones associated with vein mineralization, provided adequate field studies and ground-training samples were available. Investigators who studied Skylab imagery for color clues to possible mineral deposits include Quade et al. (Nevada; ref. 4-1), Lee et al. (Colorado; ref. 4-2), Houston et al. (Wyoming; ref. 4-5), Lambert et al. (Australia; ref. 4-6), Jensen and Laylander (Utah and Nevada; ref. 4-16), Bechtold et al. (Arizona, Nevada, and California; ref. 4-17), and Watson et al. (Nevada; ref. 4-24). Figure 4-12 illustrates the altered zone associated with the mineralized area in Goldfield, Nevada, in comparison with previous mapping. It should be emphasized that color, as do fracture patterns, forms only one piece of evidence in a long chain of logic that may lead to the discovery of mineral deposits.
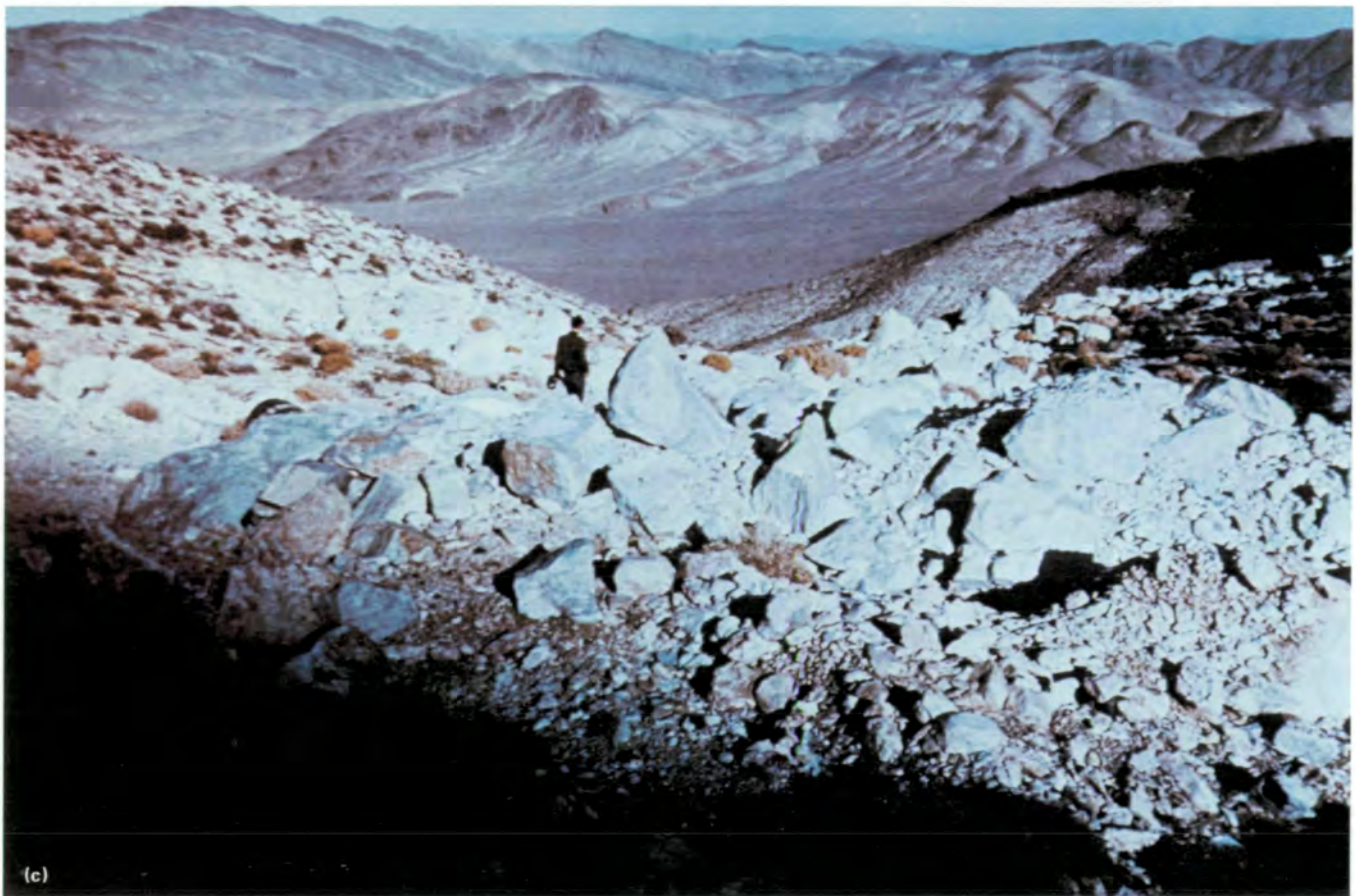
FIGURE 4-11.—Continued.

Jensen and Laylander (ref. 4-16) reported that study of S190A color photographs from the Skylab 2 mission suggested that portions of an area in the northern Egan Range in Nevada are underlain by light-colored carbonate rocks rather than by dark-colored volcanic rocks as previously mapped. This observation is significant because a large magnetic anomaly in the area coincides approximately with the extent of volcanic rocks (ref. 4-25). Jensen suggested that the magnetic anomaly might be caused, in part, by a body of igneous rock that intruded the carbonate rocks. If so, mineralization similar to that at Ely, Nevada (25 km to the south), might be present. Geologists from universities, industry, and governmental agencies promptly investigated the area. For example, Quade (ref. 4-1) enlarged the S190A photographs to the scale of published maps (ref. 4-26), compared them with aerial photographs, and per-

formed a field check. He decided that the geology had been mapped correctly by Carlson and Mabey (ref. 4-25), that the magnetic anomaly is coincident with outcrops of volcanic rocks, and that no mineralization could be found in the outcropping carbonate rocks. Explorative work is being continued in the area.

Prost (in ref. 4-2) investigated the hypothesis that anomalous reddish or pinkish areas that are caused by a concentration of iron oxide and that occur in regions marked by dense fracture networks might be indicators of potentially economical ore minerals in central Colorado. Anomalous reddish areas were observed on EREP color photographs of two test sites (Cripple Creek and Weston Pass). Field checks showed that one such area was caused by iron oxide derived from weathering of sulfide minerals, one by iron oxide and feldspar, and two by feldspar alone. Anomalous tannish

Qal   Alluvium
Ps   Plio-Pleistocene sediments
Pv   Plio-Pleistocene volcanics
gr   Mesozoic granitics
ℾP   Paleozoic rocks
— — —   Mapped faults
• • • •   Imagery anomaly
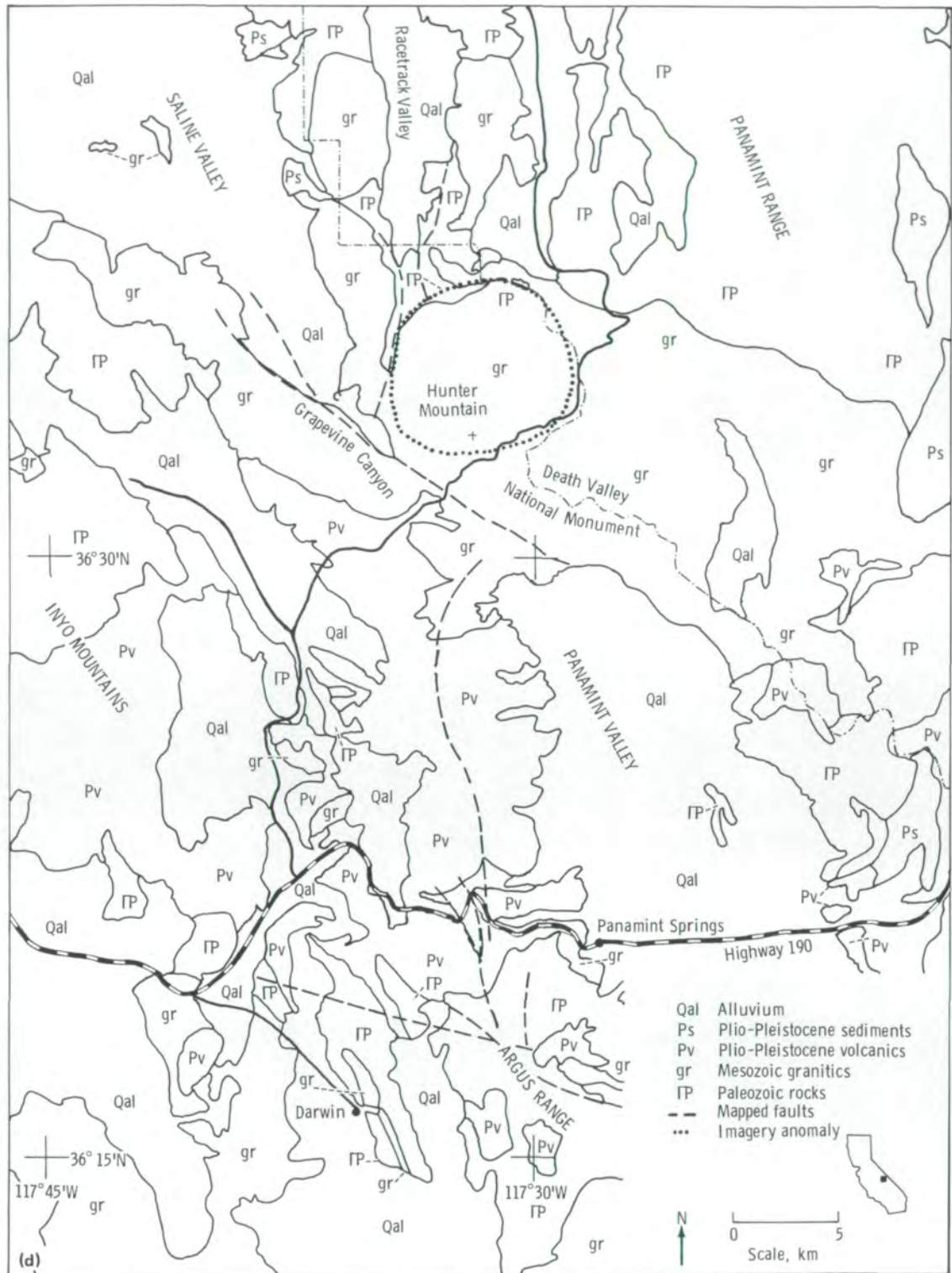
FIGURE 4-11.—Concluded.

FIGURE 4-12.—Goldfield, Nevada, area. (a) S190A color photograph (SL3-28-057). (b) Map showing areas of hydrothermal alteration and location of ore deposits.

117° 15' W   117° 10' W

Explanation

Argillized areas

Surface projections of ore-bearing areas

Kendall Mountain   McMahon Ridge   Black Butte

37° 45' N

Vindicator Mountain

Columbia Mountain   Banner Mountain

Goldfield

Preble Mountain

Blackcap Mountain

Myers Mountain

Esmeralda County   Nye County

0   Scale, km   3

(b)
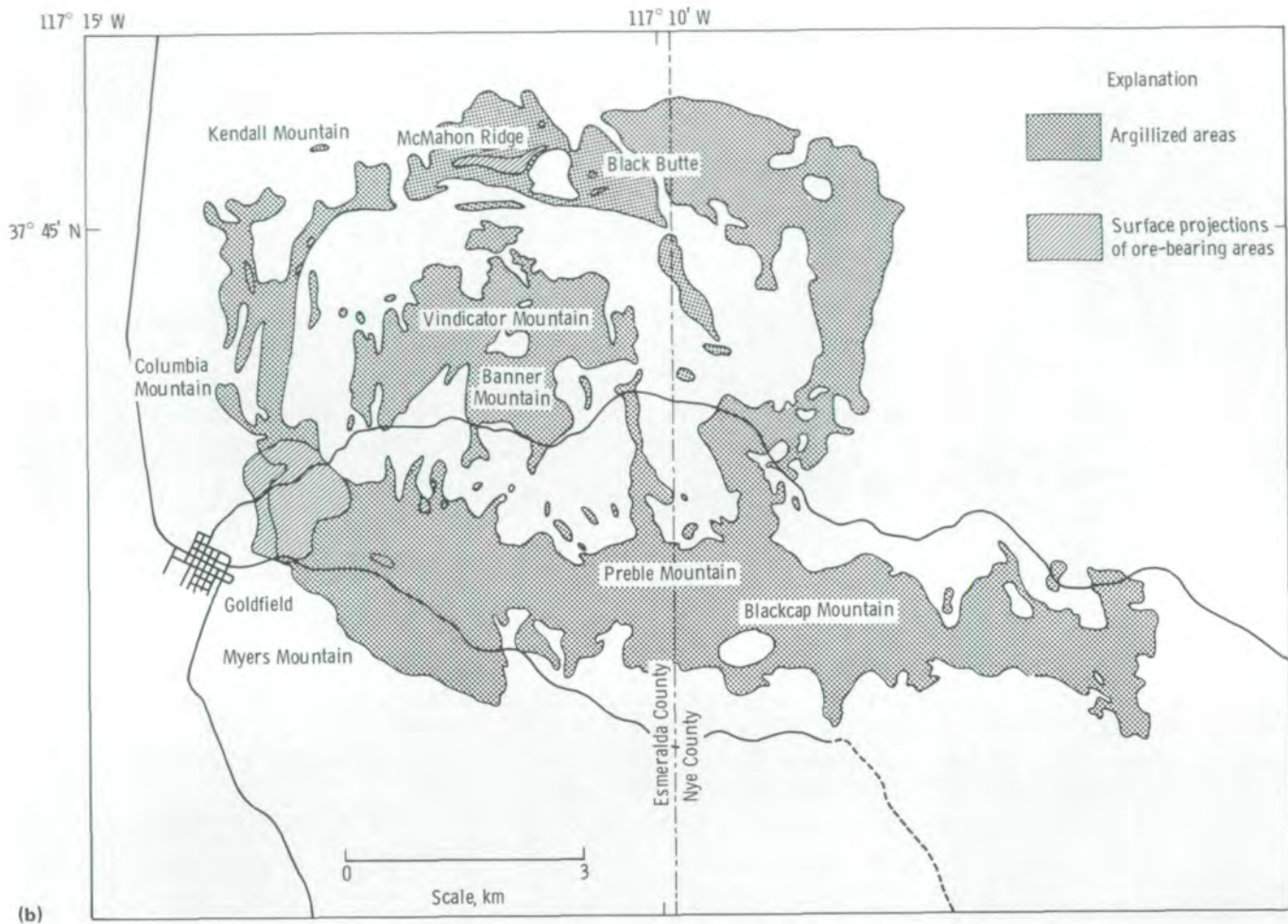
FIGURE 4-12.—Concluded.

areas in this region were attributed to quartz-rich pegmatites and light-colored sedimentary rocks and altered intrusives.

No mineral finds based on the study of EREP data have been reported. The three examples just described illustrate the use of space data in developing testable hypotheses of potential mineral occurrences. Exploration programs are usually of 5 to 10 years duration, and it is anticipated that use of the EREP data will lead to some significant discoveries over the next decade.

Petroleum Exploration

Although hydrocarbon accumulations cannot be directly detected, the interpretation of EREP data can provide information on regional lithologic and structural relationships and quickly draw attention to anomalous features and areas that are of the greatest interest in petroleum exploration. To be useful, EREP information must be integrated effectively with a wide variety of other types of data (geophysical, subsurface geology, and production history) and included within the structure of a rational exploration strategy. The advantages of Skylab data can be obtained with little additional cost to a conventional exploration program (ref. 4-13). Cost-saving benefits accrue from decreases in reconnaissance time, in seismic exploration, and in lease-acquisition expenses. The cost savings have been estimated to be as great as 40 percent in an exploration program (table 4-III).

FIGURE 4-13.—Anadarko Basin of western Oklahoma. (a) S190B color photograph (SL4-90-144). (b) Map showing linear features and circular anomalies interpreted from Skylab photography. The linear features may represent fault zones, and the circular anomalies are structures possibly containing oil or gas.
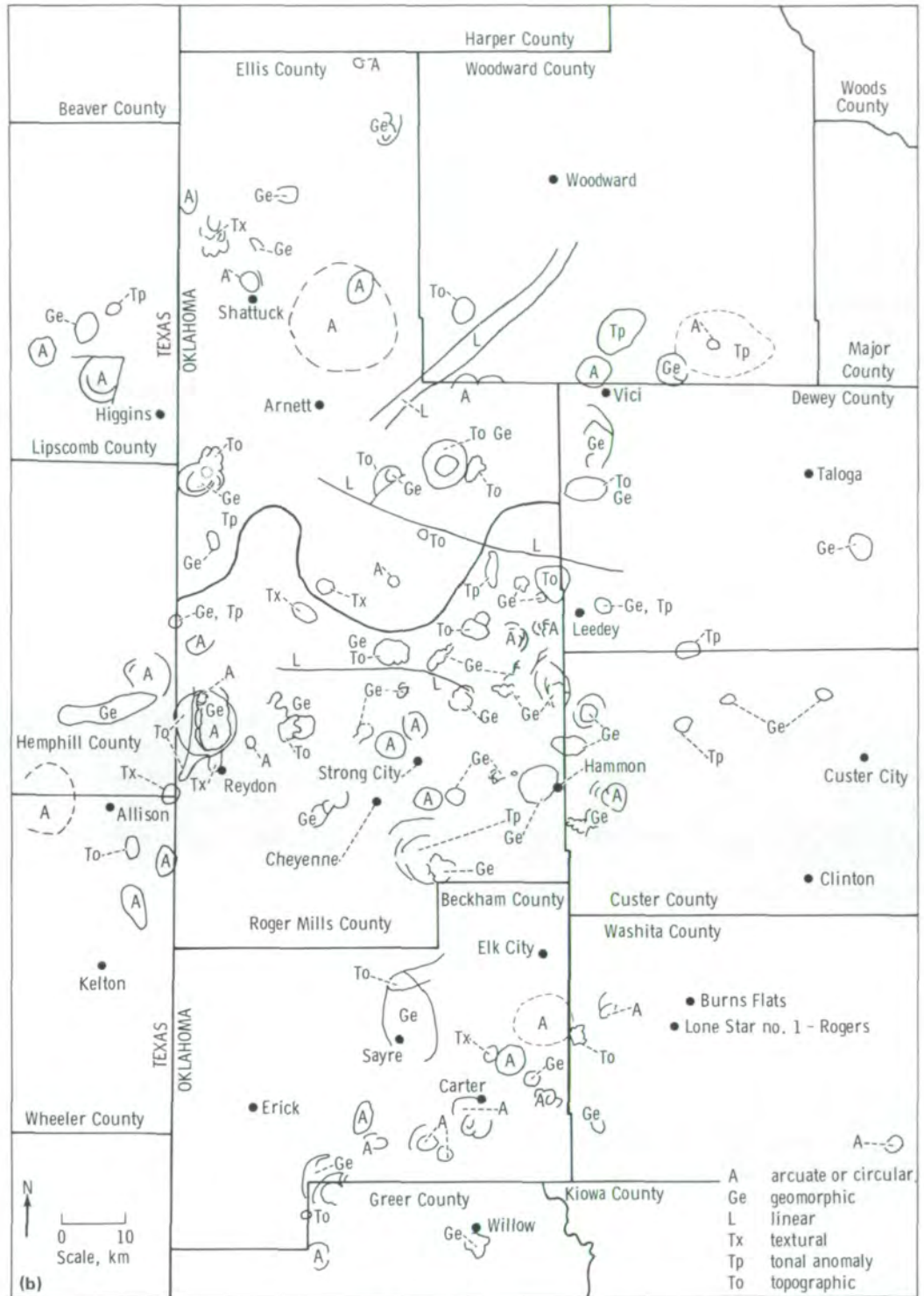
FIGURE 4-13.—Concluded.

TABLE 4-III.—Comparison of Estimated Costs of Petroleum Exploration Using Skylab and Conventional Exploration Techniques

Exploration method	Estimated cost
Conventional	
Aircraft photointerpretation of 80 000 km²	$ 64 000
Reconnaissance surface geology of 80 000 km²	200 000
Reconnaissance seismic survey of 4600 km² to locate anomalies	420 000
Detailed seismic survey of 600 km²	720 000
Total	$1 404 000
Skylab	
Interpretation of data including comparison with aircraft photographs	$ 24 000
Aircraft photointerpretation of 6000 km²	15 000
Reconnaissance surface geology of 6000 km²	21 000
Detailed seismic survey of 600 km²	720 000
Total	$780 000

In the study of the Anadarko Basin in Oklahoma, Collins et al. (ref. 4-13) found the S190A and S190B photographs to be exceedingly valuable for obtaining a rapid geological assessment of large areas and for conducting a relatively detailed study of specific areas of interest. Linears interpreted from Skylab data and Landsat imagery relate well to joints and subsurface faults. Some known surface faults were mapped and several unknown faults were inferred from Skylab data by Collins et al. (fig. 4-13). Field studies show that many long linears coincide with disturbed zones in surface rock exposures; these may represent major faults at depth. Tonal and drainage anomalies were detected in many photographs. Circular drainage patterns and tonal anomalies show the highest correlation with known hydrocarbon occurrences. Collins et al. (ref. 4-13) stated that lithologic interpretations from the EREP data are generally accurate but do not always match published interpretations. These interpretations indicate areas where remapping is desirable to verify new ideas derived from the reevaluation of supposedly well-known petroleum provinces (ref. 4-27).

Using S190A photographs, Rivereau, of the Institute Français du Petrole (in ref. 4-28), reinterpreted the geology of a Permian basin on the southwestern border of the French central massif. In the central southern part of the basin, a relatively thinly bedded unit (unit A, fig. 4-14) composed of fine sediments (siltstone and clayey sandstone) is surrounded by thickly bedded sandstone to the west and north (unit B) and conglomerates to the south (unit C). Unit A was considered by field geologists to represent lateral lithological changes with only the western boundary being structurally controlled by a northwest-trending fault (F1). A conventional photogeological map of the area showed that unit A was very homogeneous and that it was crossed by numerous faults having a northwest trend, thereby causing small displacements of bedding. However, because of the strike of bedding in units A and B and the same dislocation of bedding caused by the northwesterly trending faults, nothing else was suspected about the relationship between units A and B. The synoptic view of the Skylab photographs (and, to a lesser degree, of the Landsat imagery) showed the distinct regular pattern of unit A, which is bounded on all sides by straight lines. From these photographs, it was obvious to the investigator that the distribution of unit A is structurally controlled by faulting. It is currently believed that unit A occupies a collapsed part of the basin in which the top sediments of the trough have been preserved from erosion. Therefore, unit A should no longer be chronologically correlated with unit B; that is, unit A no longer appears as a local lithological variation of unit B. It is probable that unit A is younger than unit B and has been removed from the top of unit B in other parts of the area and only preserved in the collapsed area. Rivereau emphasized that, even though the

Fault and lineament
Limit of Triassic Formation
Limit of Permian trough visible on Skylab imagery
Area of unit A as discriminated from Skylab imagery

N 0 Scale, km 10

FIGURE 4-14.—Portion of the Aquitaine Basin in southern France with an interpretation of lithologic contacts and faults on an S190A photograph (SL3-34-321). Original scale, 1:320 000.

feature is visible on Landsat images, it is prominent in the Skylab photographs only because of the well-defined spectral contrast in S190A color film. The appearance of the feature was enhanced by making false-color composites using various combinations of the S190A black-and-white photographs. Drilling and geophysical surveys are now underway in the area, and confirmation or nonconfirmation of this hypothesis will be determined from the results.

Anticlinal folds often provide structural traps for hydrocarbons. Numerous examples of folds mapped on Skylab photographs can be found in EREP reports (e.g., refs. 4-4 and 4-5). Vargas (ref. 4-29) reports the detection of lineaments and drainage anomalies that may indicate subsurface faults and anticlines in north-central Bolivia, an area undergoing active exploration for oil and gas. These investigators believe that the EREP photographs will be of direct help in locating prospective structures.

Exploration for Geothermal Energy

The indirect methods used to search for minerals and petroleum are also used to search for geothermal energy. In addition, investigators are attempting to use the direct method of mapping hot ground using thermal scanners. An example of indirect methods is provided by Bechtold et al. (ref. 4-17) for the Coso Hot Springs area in California (fig. 4-15). This is a well-known thermal area that has been studied thoroughly (refs. 4-30 and 4-31). Evidence of recent volcanism in the area includes lava flows, vents, cones, hot springs, and areas of steaming ground. Fracturing of the rocks is intense, and patches of hydrothermally altered material occur. The Coso Hot Springs area is a potential source of geothermal power. Study of S190A and S190B photographs by Bechtold et al. indicated that, 70 km south of Coso Hot Springs, in the Lava Mountains, there is a similar (though smaller) area of repeated volcanism, intense fracturing, and hydrothermally altered material (fig. 4-15). A well drilled in the 1920's revealed hot rock and steam at 120 m (ref. 4-32), but the resource was never commercially developed. Study of Skylab photographs,

together with brief field checking, suggests that an area of approximately 15 km^2 may be potentially exploitable for geothermal power.

McMurtry and Petersen (ref. 4-14) analyzed S190A photographs of the Susquehanna River basin in Pennsylvania to determine the relationship of a warm spring, a large circular feature, and a major lineament; and to establish the regional geologic structure for use in detailed studies. Aerial thermal surveys and fieldwork are continuing to determine the size and significance of the thermal feature.

During the Skylab missions, particularly Skylab 4, some predawn thermal imagery was obtained (fig. 4-16) that demonstrates the sufficiency of the S192 spatial and thermal resolutions for discrimination of different types of material on the Earth's surface. Daytime thermal imagery was obtained over the Geysers geothermal power field in California. Analysis of this imagery by Siegal et al. (ref. 4-33) demonstrated that spots approximately 1 K warmer than the surrounding areas can be distinguished (fig. 4-17). Comparison with S190B photographs, aerial photographs, and previous field mapping showed that many of the warm spots coincide with sites of geothermal wells and steaming ground. However, these known warm sites also are bare of vegetation and, coincidentally, tend to occur on south-facing slopes where solar heating is at a maximum. Calculations indicate that solar heating can account for the effects recorded by the S192 scanner. The results are encouraging because they suggest that similar, perhaps more sensitive, predawn images might provide useful clues to sites for geothermal exploration. Such factors as slope direction (aspect), slope angle, previous weather (temperature history at the site, rainfall), and vegetation will have to be considered when using such thermal imagery.

ENVIRONMENTAL GEOLOGY

The use of EREP data to identify and study geological hazards and the testing of those data in engineering- and environmental-geology applications are described in this subsection. Geological hazards studied include
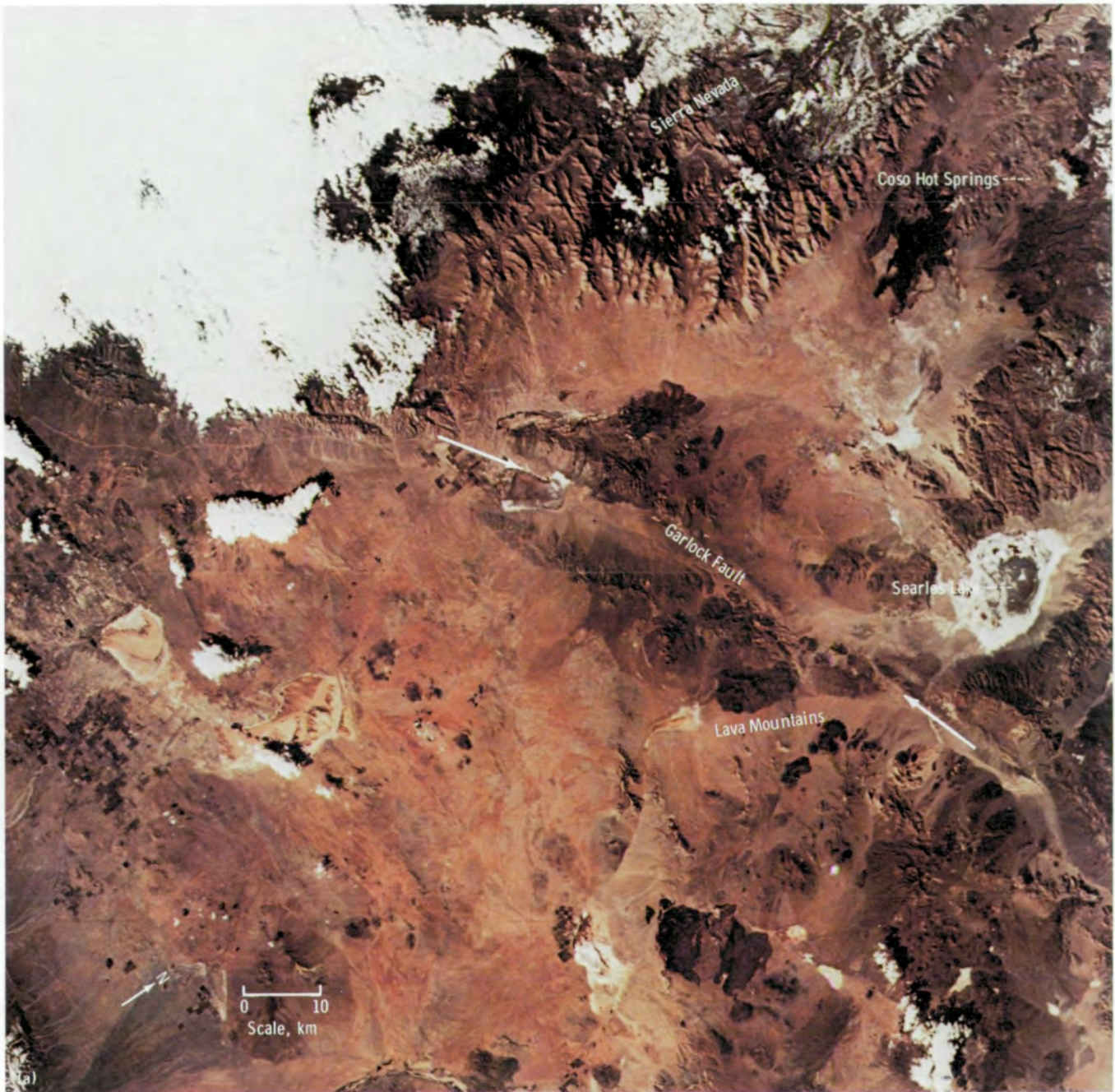
FIGURE 4-15.—Coso Hot Springs and the Lava Mountains, California. (a) S190A photograph (SL4-76-078). (b) Enlargement of the Coso Hot Springs area.
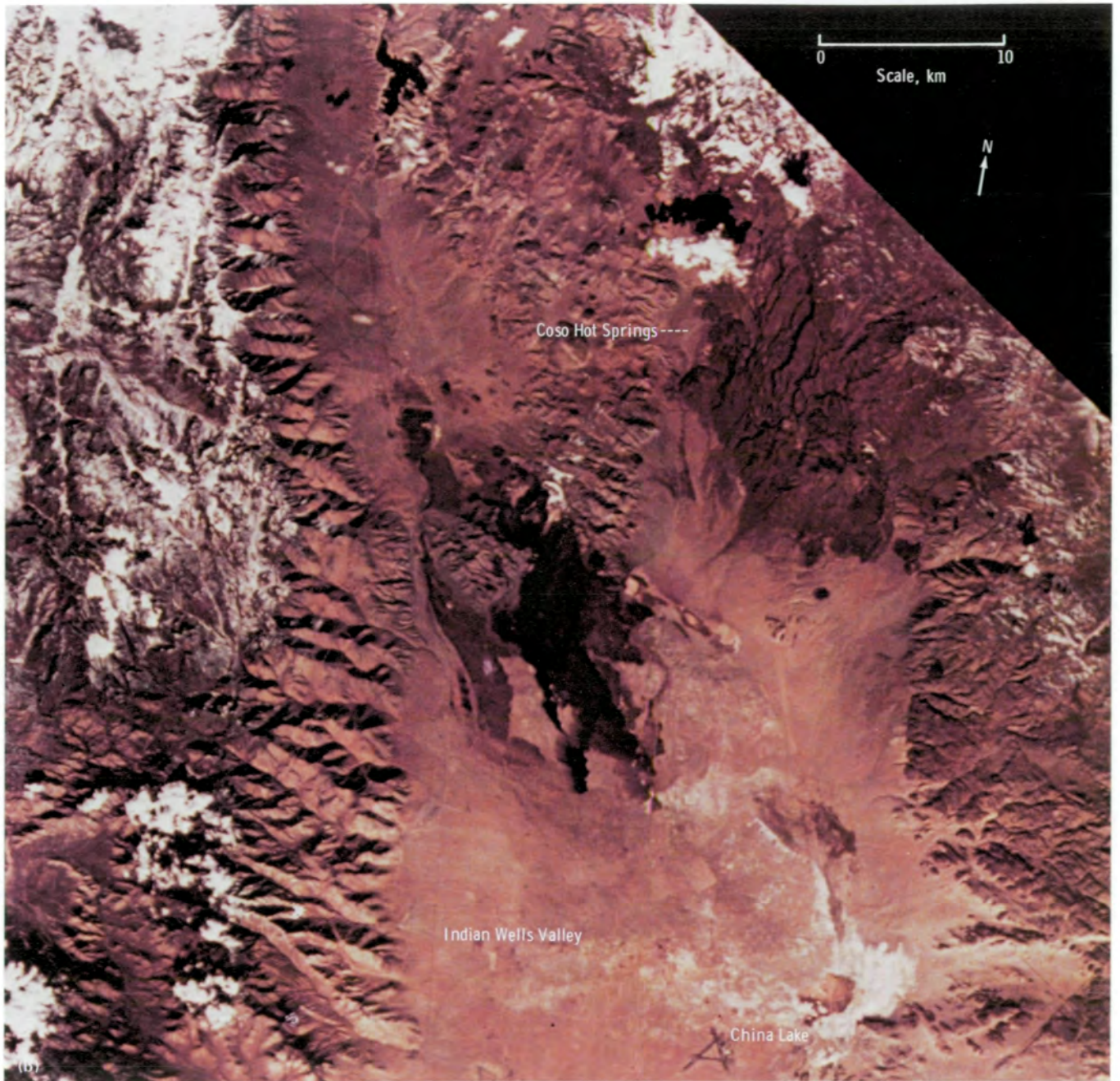
FIGURE 4-15.—Concluded.

FIGURE 4-16.—Color-coded density-sliced enhancement (band 13) of a predawn image of Hot Creek Valley, Nevada, acquired January 27, 1974.
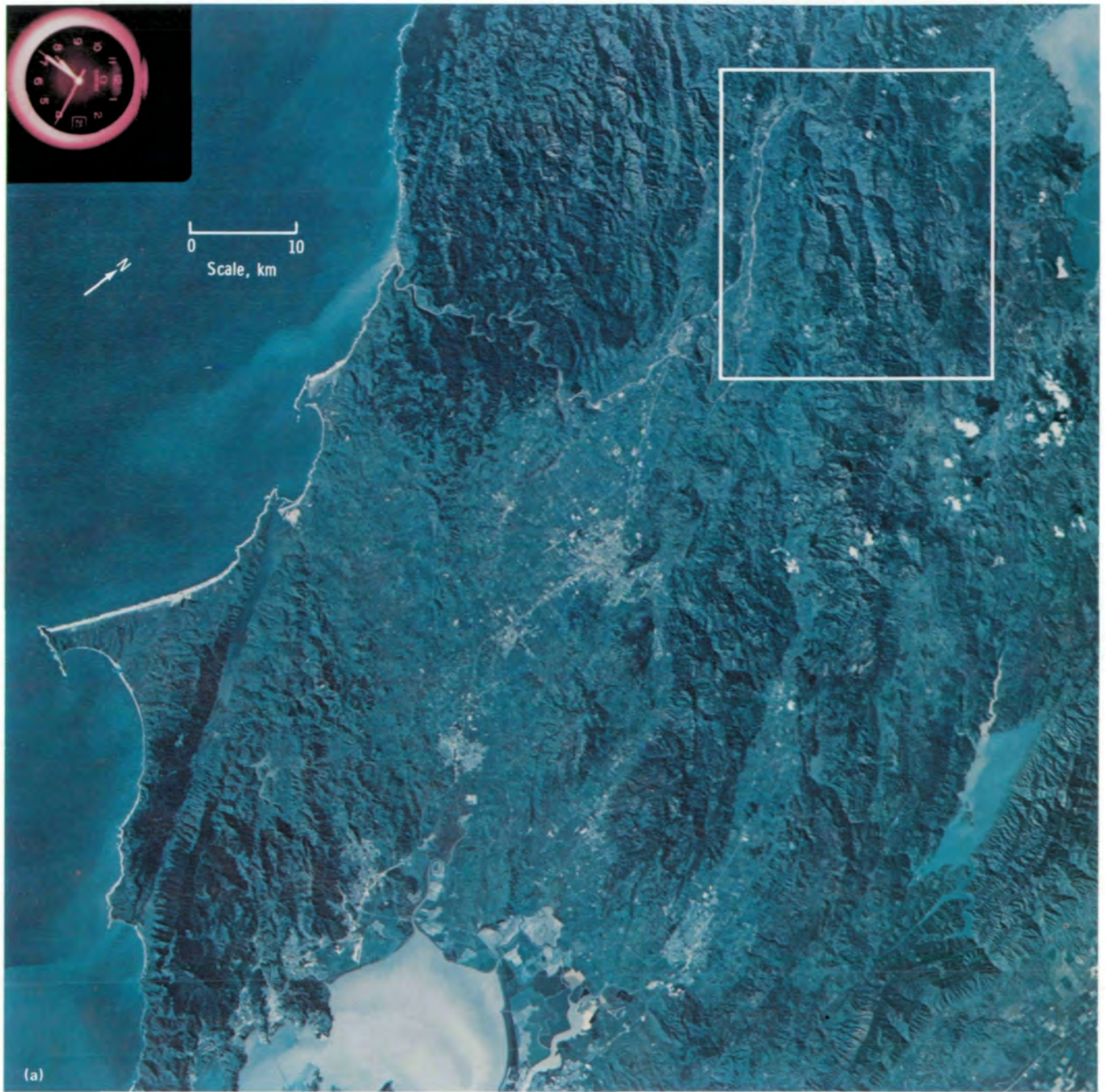
FIGURE 4-17.—Geysers area in California. (a) S190B color photograph (SL4-92-335). (b) Portion outlined in figure 4-17(a). (c) S192 image enhancement of the Geysers area (ref. 4-33) at approximately the same scale as figure 4-17(b).

FIGURE 4-17.—Continued. ⟶

Scale, km
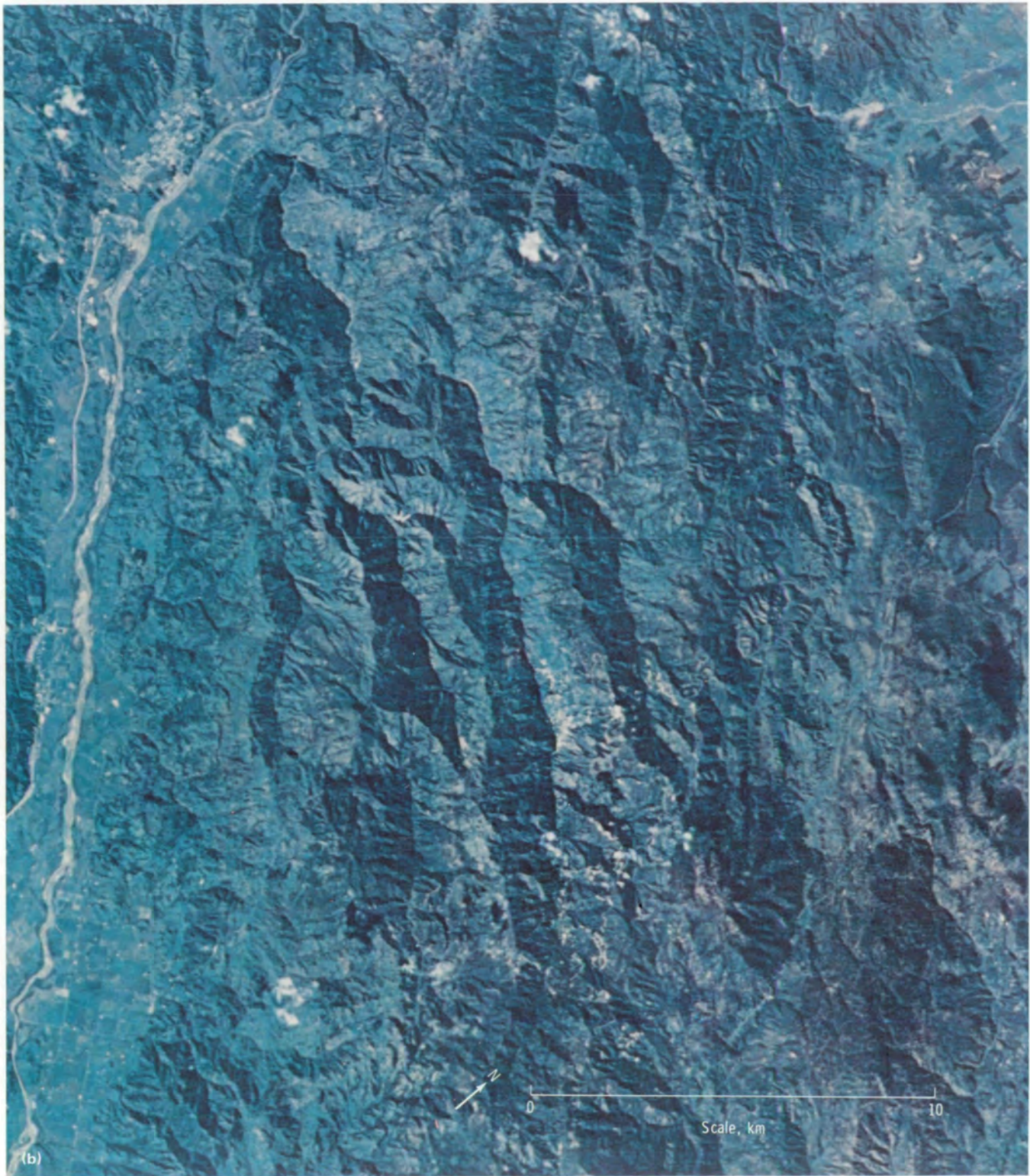
FIGURE 4-17.—Concluded.

earthquake zones, landslides, and volcanoes. Engineering-geology applications include, from a disciplinary standpoint, assessment of the previously mentioned hazards, studies of tunnel sites, and inventories of construction materials. Finally, environmental geology includes the preparation and assessment of "erosion susceptibility/ease of excavation" maps and "analytic landform" maps. These maps show surficial materials and conditions important in environmental, land use, and geological applications.

Geological Hazards

The geological hazards discussed are earthquakes, landslides, and volcanoes.

Earthquakes.—Several investigators used EREP photographs to map linear features and to investigate the relationship of these features to faults with historical earthquake activity. For example, Olson (ref. 4-10), using S190B transparencies, stated that the most significant finding of his investigation was the detection of

fracture traces and related lineaments crossing the Clark Hill Reservoir on the Savannah River, north of Augusta, Georgia. He noted that epicenters of some earthquakes (maximum magnitude of 4.5 on the Richter scale) that occurred in 1974 were plotted in the same area. The EREP data were being used to develop field evidence for assessing the causes of the earthquakes.

Abdel-Gawad and Tubbesing (ref. 4-15) identified segments of faults in the western Mojave Desert adjacent to the San Bernardino and San Gabriel Mountains and the San Andreas Fault zone. They produced maps delineating specific areas of seismic risks based on geomorphic evidence of recent faulting (visible breaks in the surficial alluvium and surface rocks, stream offsets, etc.). Merifield and Lamar (ref. 4-12) mapped faults in the Peninsular Ranges of southwestern California and conducted extensive field investigations to determine their potential for seismicity. Using Skylab photographs, they found two previously unmapped faults but determined, through field studies that revealed no signs of recent movement, that the faults posed little threat for generating earthquakes. Quade et al. (ref. 4-1) mapped lineaments in the Mina region of Nevada and then compared the map with a plot of earthquake epicenters for 1971-73. They found a correspondence between the epicenter locations and the east-northeast-trending faults west and southwest of Mina.

Landslides.—Although EREP photographs generally lack the necessary spatial resolution and vertical exaggeration (for stereoviewing) required to study small landslides, some positive results were reported. Large landslides were recognized and mapped by Quade et al. (ref. 4-1), Hoppin et al. (ref. 4-4), Houston et al. (ref. 4-5), Lambert et al. (ref. 4-6), and Lee and Raines (ref. 4-19). McMurtry and Petersen (ref. 4-14) noted a good correlation between lineaments observed on Skylab photographs and Landsat imagery and a zone of fractured material that was collecting and channeling ground water. This zone appeared to be the cause of landslides on slopes along a major highway in Pennsylvania. This example again demonstrates the usefulness of identifying linear features in relation to specific geological hazards.

Volcanoes.—Cassinis et al. (ref. 4-11) noted that an S190B color-infrared photograph (fig. 4-18) taken over Sicily showed an anomalously low infrared reflectance in an area of Mount Etna that later erupted. The investigators postulated that this type of anomaly might be caused by stressed vegetation resulting from small but continuous amounts of volcanic gases filtering through the soil. They analyzed 17 anomalies and found that most were caused by different vegetation assemblages rather than by stressed members of the same type. In an attempt to correlate lineations and eruptions, they mapped and analyzed lineations on the western flank of Mount Etna. It was found that (1) the maximum density occurred in the eruption zone, (2) the first effusive opening of the February 1974 eruption occurred at the intersection of four linears that were 0.5 to 2.5 km in length, and (3) the vegetative anomalies correlated well with the geometry of the lineations. From these results, the investigators concluded that their hypothesis, which suggested volcanic gases could stress vegetation and result in reflectance anomalies, might be valid, even though they were not able to verify it in this investigation of Mount Etna. They did determine that the relationship between lineations and eruption features was significant.

Stoiber and Rose (ref. 4-7), using EREP photographs of the Guatemalan highlands, mapped circular and arcuate features that correlated with distributions of early Quaternary and Tertiary volcanoes.

Engineering Geology

This discussion of engineering geology includes tunnel-site studies and construction materials inventory.

Tunnel-site studies.—Lambert et al. (ref. 4-6) used Skylab photographs of the Snowy Mountains area of Australia to prepare structural maps for comparison with detailed structural information obtained in the construction of long tunnels. The tunnels, built for irrigation and hydroelectric purposes, are an average of 247 m below the surface. The comparison enabled the investigators to determine directly the value of remote sensing in identifying fractures of concern in tunnel-site studies. They concluded that "The combination of three

factors: (1) means of measuring and achieving acceptable standards of data quality, (2) empirical evidence that approximately 50 percent of surface features will be detected underground, and (3) sufficient resolution to identify the location of these features indicates a potential operational role in 1:100 000 survey mapping and in engineering and mining investigations."

Construction materials inventory.—Several investigators used Skylab photographs to study and map surficial materials containing sand and gravel, but very few used the photographs specifically to locate new sources of these deposits. Three investigators who spent considerable time on this last objective reported worthwhile results. Woodman (ref. 4-34) used the photographs of Maine to map moraines and eskers, which are the State's major sources of sand and gravel for road construction. Cassinis et al. (ref. 4-11) used multispectral analysis of S190A photographs to identify and map the locations of ancient river channels in the Venetian Plain of Italy. As is the glacial material in Maine, these old riverbeds are sources of sand and gravel for construction and freshwater. Cassinis stated that he determined for the first time the regional extent of these resources. Furthermore, he estimated a cost saving of 90 percent in locating the buried channels with Skylab photographs as compared to locating them with electrical resistivity surveys. While working in Puerto Rico, Trumbull (ref. 4-35) was able to locate coral reefs, offshore sand and gravel deposits (potentially a valuable resource), and areas of coastal erosion, and to identify patterns of sediment transport.

Geoenvironmental Mapping

The EREP photographs were used with varying degrees of success in several geology studies in which surface geological features of environmental interest were examined. Among the most significant results are those reported by Morrison (ref. 4-9). He used EREP photographs in constructing erosion-susceptibility maps of areas of southeastern Arizona[2] and, in conjunction with associates from six Great Plains and Midwestern States, in preparing analytical-geomorphology maps of areas within the six States (ref. 4-9).

The maps of Arizona combine information on soil types, surficial deposits (including particle size and character of the deposits for several meters below the soil profile), and occurrences of exposed bedrock. The maps also provide background data on the susceptibility of various types of surface materials to erosion and, hence, on the potential magnitude of the modern accelerated-erosion problem in southeastern Arizona. Additionally, the maps indicate the ease of excavating near-surface materials for construction. The maps were prepared by direct photointerpretation of 1:250 000-scale Skylab photographs using a stereoplotter and without supplemental ground control. Published geologic reports and maps were then used for constructing detailed descriptions of the mapped units. These maps offer the land use planner or manager a low-cost tool because they can be prepared in a portion of the time required by standard field studies and map-preparation procedures. An example of one of these maps is shown in figure 4-19; the explanation of the map units is contained in table 4-IV.

The maps prepared for areas of the Great Plains and Midwestern States (e.g., fig. 4-20) show surficial features and contain rating systems (table 4-V) for each map unit in terms of limitations or advantages of topography, availability of shallow ground water, availability and quality of gravel and rock, slope stability, foundation conditions, ease of excavation, road construction, surface drainage, and soil (internal drainage, erodibility of soils, and sites for sanitary landfills, sewage lagoons, and septic tanks). The maps were prepared without field studies by using ancillary information such as topographic maps, geological and soil maps, reports, and high-altitude aerial photographs in conjunction with the EREP photographs. They contain information that should become increasingly useful as regions develop and detailed plans and environmental assessments are needed.

[2]R. B. Morrison, "Application of Skylab EREP Photographs to Study of the Modern Episode of Accelerated Erosion in Southern Arizona," unpublished Final Report, NASA-USGS Agreement T-4113-B, 1975.

FIGURE 4-18.—A portion of an S190B color-infrared photograph of the Mount Etna Volcano in Sicily (SL3-87-355). Shades of red indicate areas of vegetation; black areas show volcanic material from previous eruptions. ⟶

Eruption cloud

Clouds

Scale, km
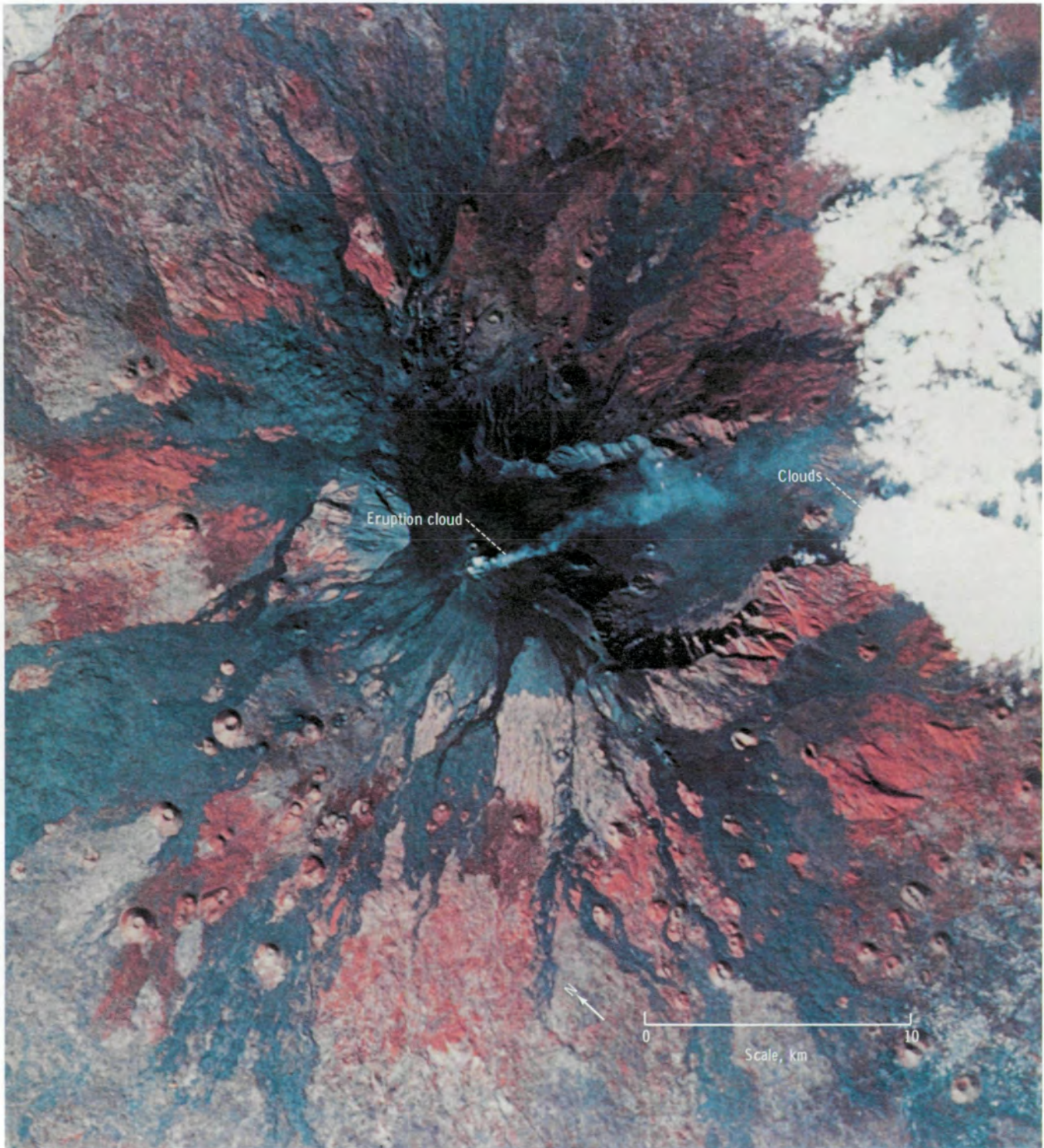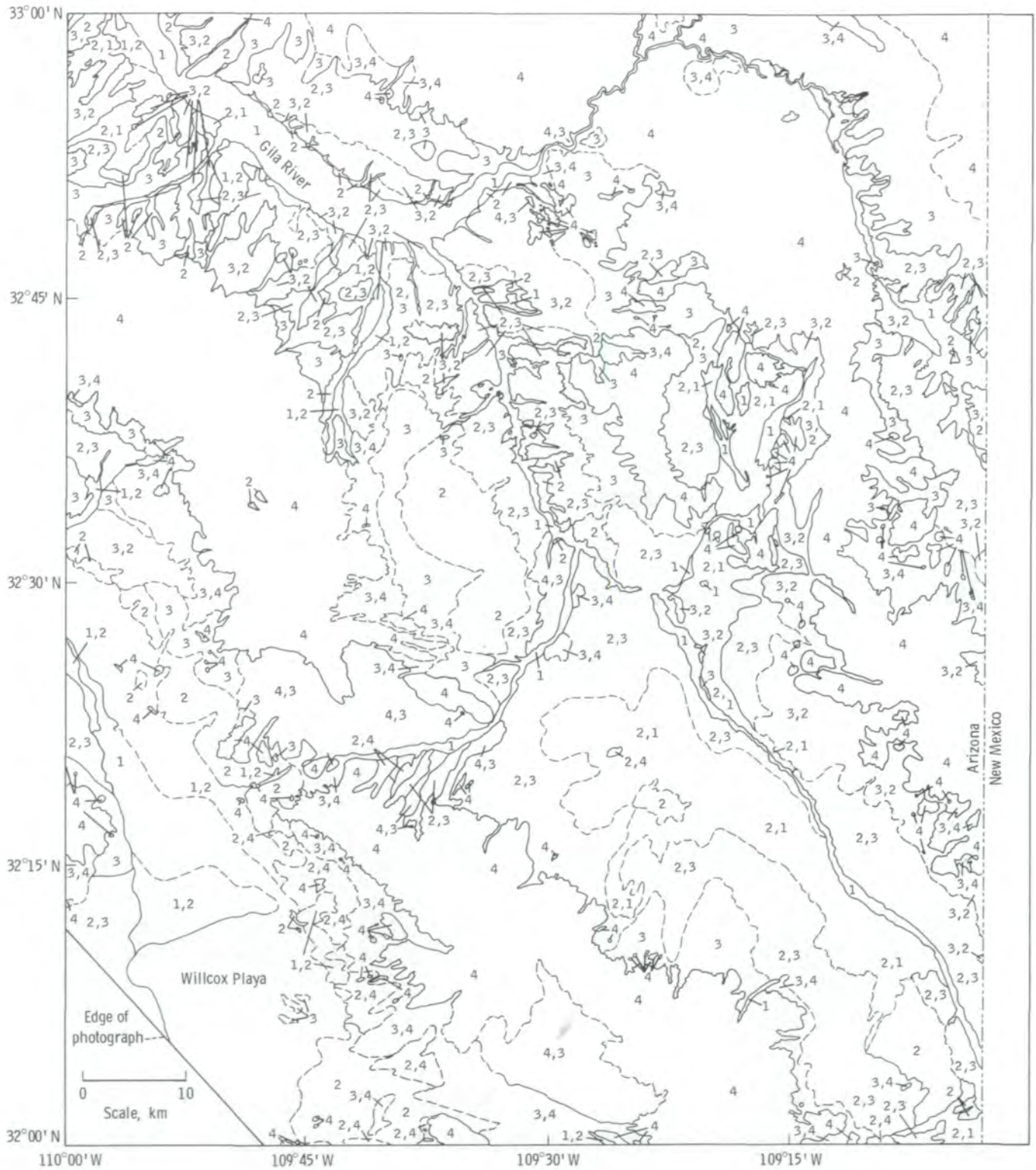
(a)
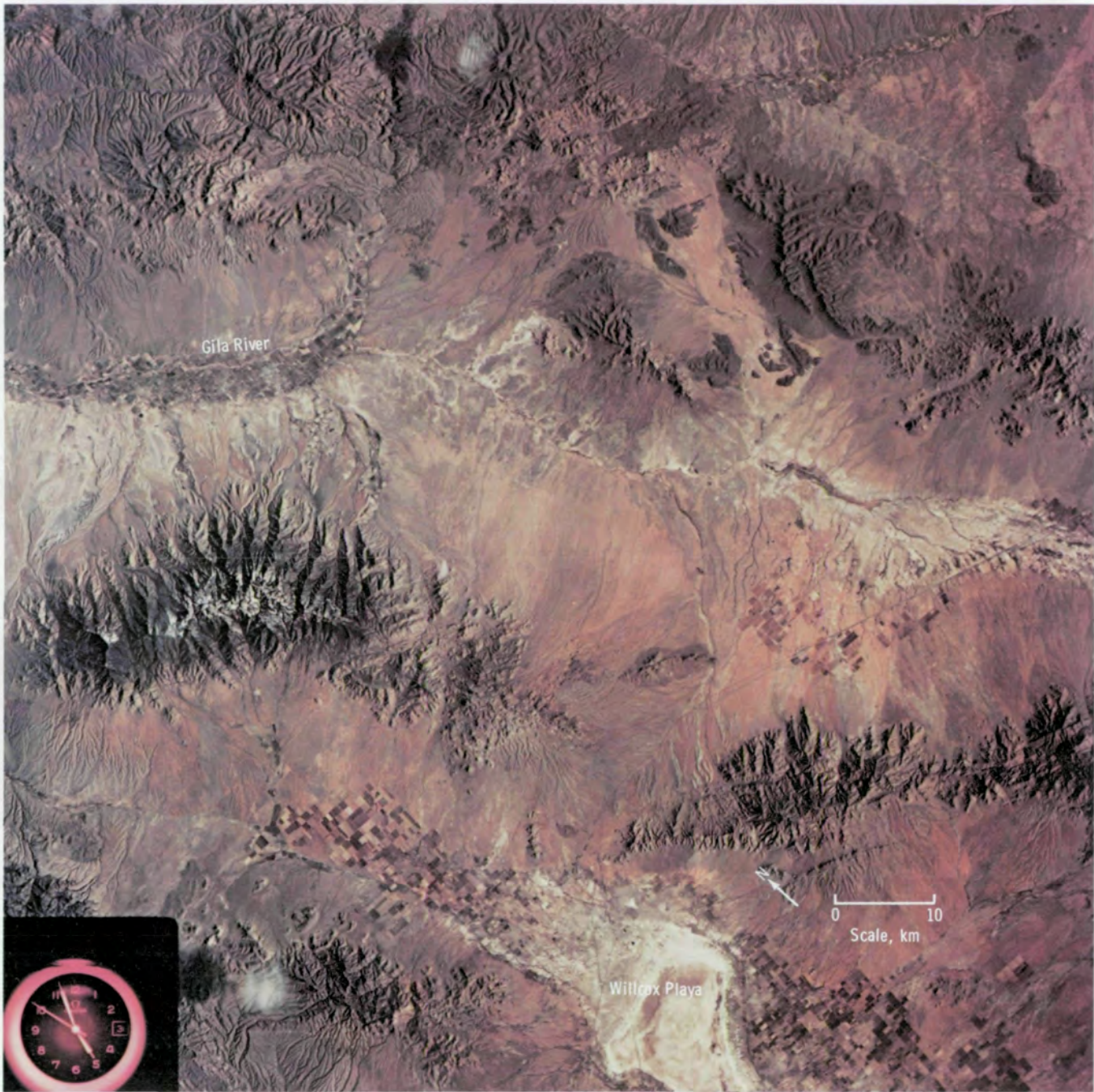
(b)

FIGURE 4-19.—Willcox Playa and Silver City, Arizona, area. (a) Erosion-susceptibility/ease-of-excavation map prepared from the interpretation of S190B photographs. Map units are defined in table 4-IV. (b) S190B color photograph of the Willcox Playa area (SL4-94-237).

TABLE 4-IV.—Explanation of Map Units

Map unit	Ease of excavation	Erosion susceptibility	Description
		Easily excavated and readily erodible materials	
1a	Excavation easy (light power equipment or handtools suitable for excavation)	Highly erodible	Unconsolidated fine-textured alluvium on flood plains and lowermost stream terraces; mainly silt, some sand, little or no gravel; very little or no soil development
1b	Excavation easy (light power equipment or handtools suitable for excavation)	Generally highly erodible	Unconsolidated sandy, silty to locally clayey, and somewhat gravelly alluvium of basin-interior lowlands and bajada toe slopes; soil development generally nil or weak, locally moderate
		Materials generally easily excavated (locally moderately difficult) and generally moderately erodible	
2	Excavation generally easy, locally moderately difficult	Erodibility moderately high to moderate	Mostly silty to pebbly sandy alluvium with moderate soil development (clay and/or carbonate accumulation); local pebble to cobble gravel with moderate to no soil development
		Materials generally moderately difficult to excavate and only slightly erodible	
3	Excavation moderately difficult (light or heavy power equipment necessary for excavation)	Erodibility mostly slight, locally moderate	Alluvium with very strong soil development including strong calcium carbonate (caliche) accumulation and/or moderate induration below the soil profile and/or coarse particle size (cobble and boulder gravel)
		Materials moderately difficult or difficult to excavate and generally least erodible	
4	Mostly rock excavation, moderately difficult to difficult (heavy power equipment needed for excavation; ripping may be necessary, and, in places, blasting)	Erodibility mostly negligible, locally slight to moderate	Consolidated bedrock is widely exposed; thin deposits of gravelly colluvium or alluvium occur locally, which are class 2 or 3 excavatability/ erodibility

WATER RESOURCES

Surface-Water Management

One of the most striking differentiations possible from multispectral aerial and EREP satellite imagery is the identification and delineation of surface-water bodies. Accurate delineation of regional drainage networks has been made possible by space photographs as demonstrated by Stoeckeler et al. (ref. 4-34), Colwell et al. (ref. 4-36), and Baker et al. (ref. 4-37). In instances in which overlap of the photographs enabled stereoscopic viewing, investigators were better able to detect and compare topographic relief. This capability enabled the accurate delineation of watershed boundaries by locating the ridge lines that circumscribe individual surface-water drainage systems. For this purpose, the S190B photographs were nearly equal to the best high-altitude-aircraft photographs available to the investigator (from an RC-10 camera at 18 300 m). This conclusion is important because frequent high- and low-altitude-aircraft coverage is expensive. The demonstration of the capability of the Skylab camera systems to provide accurate resolution of drainage basins and surface-water bodies offers the possibility of significant cost savings when applied on a nationwide or worldwide basis.

The Skylab multispectral photographic system provided coverage of the spectrum from the visible through the near-infrared. Piech et al. (ref. 4-38) used these photographs to assess the value of remote sensing from space for determining the eutrophication of lakes. Comparisons were made between conventional water-quality indices and relative values of reflectance in the blue and green portions of the visible spectrum at various locations in Lake Erie, Lake Ontario, and Conesus Lake, New York. Reflectances measured from the S190A color photographs were in excellent agreement with those determined from simultaneous aircraft flights. Changes in the balance acquired on organic-compound concentrations of the surface waters caused variations in the blue-to-green reflectance ratios. The ratio of blue-to-green reflectance in Lake Ontario is

shown in figure 4-21. Similar results were reported by Hannah et al. (ref. 4-39) using data acquired over lakes in Florida. Because the atmosphere can reduce the measured reflectance by as much as 60 percent, it was necessary to correct for this effect. Correction made by reference to reflectance standards was used by Piech et al. (ref. 4-38) in this successful application. It was predicted that an additional advance in resolution would permit use of the shadow-calibration procedure now used in the measurement of eutrophication indices by low-flying aircraft. The synoptic view provided by satellite imaging systems with repetitive coverage would enable the monitoring of natural and artificial lakes for the onset or amelioration of eutrophication. The resolution of the Skylab camera systems also greatly facilitated this application.

Yarger and McCauley (ref. 4-40) achieved good results by applying the band-ratioing technique to the problem of detecting the presence of suspended solids in reservoirs. They found that reflectance values in both S190A and S190B photographs correlated well with suspended (mostly inorganic) sediment. Band ratios of blue-green to red reflectances provided quantitative correlation at concentrations greater than 200 p/m in three small reservoirs in Kansas. Repetitive coverage provided by satellites could improve the regulation and management of lakes and reservoirs with respect to this water-quality parameter.

Snow Cover

An ever-increasing need in agricultural, industrial, and metropolitan areas for reliable sources of water makes efficient management of water resources a continuing concern. In many areas, winter storage of water in the form of mountain snow, together with its runoff regime, governs the availability of water during the periods of greatest need. Because of the general inaccessibility of high-mountain snowpacks and their relatively inhomogeneous distribution and irregular boundaries, estimation of total water content in them
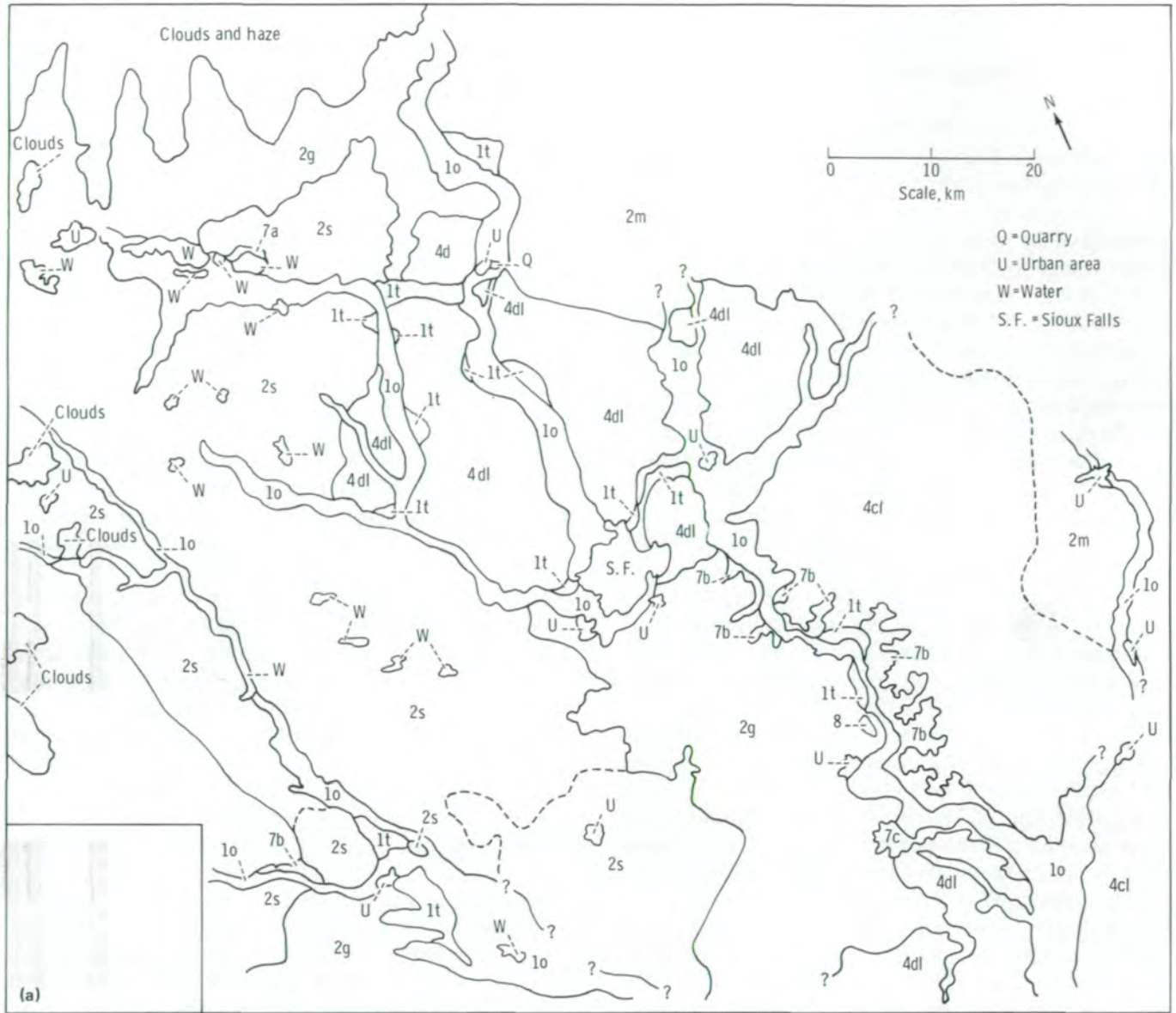
FIGURE 4-20.—Sioux Falls, South Dakota, area. (a) Analytic-geomorphology map prepared from following S190B color photograph. Symbols are defined in table 4-V. (b) S190B color photograph (SL2-81-316).
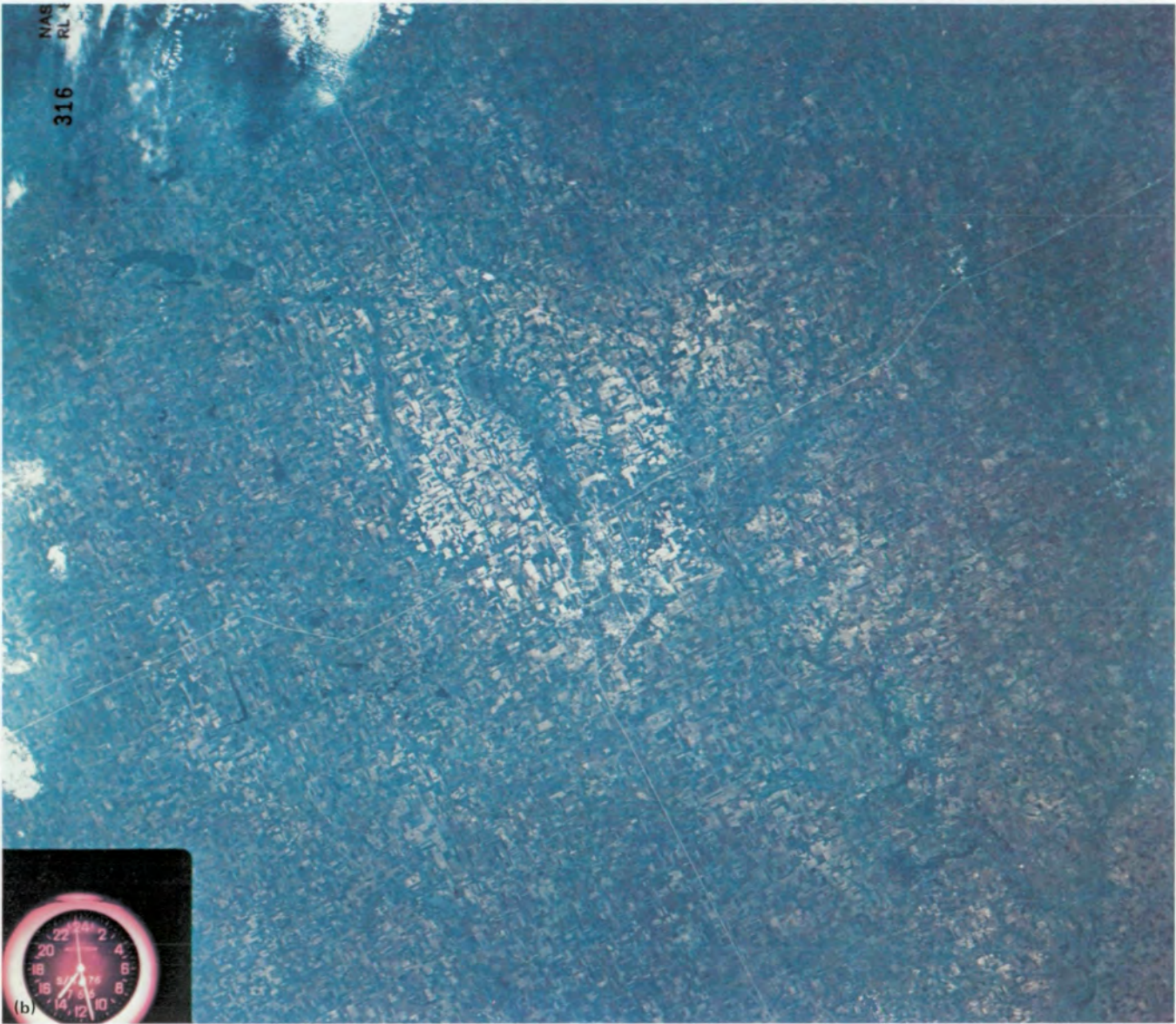
FIGURE 4-20.—Concluded.

(a) Attributes identifiable on Skylab photographs

Map units	Landform characteristics					Soil characteristics		Surficial-geologic deposits	Special problems or attributes
	Land-surface form symbol	Local relief, m	Stream dissection			Surface color	Soil drainage		
			Density	Pattern	Interfluves				
1	Ala, V, Vf	< 10	—	Not applicable	—	Dark	Poor to fair	Alluvial clay, silt, sand, and gravel	Commonly subject to flooding near streams; high water table in many places
lo	Ala, V, Vf	< 10	Low	Not applicable	—	Dark	Poor to fair	Alluvial sand and gravel, some silt	Commonly subject to flooding near streams; high water table in many places
lt	At, Ala, Alb	< 20	—	Not applicable	—	Medium	Fair to very good	Alluvial sand and gravel, some silt	None
2g	Ala, Alb, Bla, Blb	< 30	Low	Deranged	Wide, flat	Dark	Very poor to fair	Ground moraine; clayey till - unsorted clay, silt, sand, gravel, and boulders	Poorly drained depressions in places
2s	B2b, Clb, C2b	15 to 30	Low	Deranged	Very wide, irregular topography	Dark with light mottles	Very poor to very good	Stagnation moraine; clayey till - unsorted clay, silt, sand, gravel, and boulders	Poorly drained depressions in places
2e	Clc, C2c	15 to 30	Low	Deranged	Rounded	Medium with light mottles	Fair to very good	End moraine; unsorted clay, silt, sand, gravel, and boulders	None
2m	Ala	< 20	Medium	Dendritic	Flat	Dark	Fair to very good	Loess, commonly several meters thick, over somewhat-leached till like above	None
3c	Clc, C2c	< 30	Medium	Trellis	Rounded	Dark to medium	Poor to good	Unsorted clay, silt, gravel, and boulders	None
4ce	C3c, C3d, D2d, D3d	30 to 60	Medium	Trellis	Some rounded, some flat	Medium to light with light mottles	Fair to very good	Unsorted clay, silt, sand, gravel, and boulders	None
4cl	C2c	20 to 45	High	Pseudo-rectangular	Many flat-topped, rounded edges	Light	Fair to excellent	Loess, commonly several meters thick, over weathered and leached clayey till	None
4d	C2d	20 to 45	Medium	Deranged	Rounded	Medium	Fair to excellent	Loess, commonly several meters thick, over weathered and leached clayey till	None
4dl	C2d	20 to 45	High	Pseudo-rectangular	Some flat-topped ridges	Very light	Fair to excellent	Loess, commonly several meters thick, over weathered and leached clayey till	None

TABLE 4-V.— Continued

(a) Continued

Remarks

Young valley lowlands - flood plains and lower stream terraces of Holocene and in places of Wisconsinan age

Glacial outwash terraces, channels, and plains of late Wisconsinan age

Stream terraces, mainly of Wisconsinan age

Ground moraine of late Wisconsinan age; nearly level to gently rolling plains; some poorly drained depressions, marshes, ponds, and lakes

Stagnation moraines of late Wisconsinan age; gently rolling plains; many poorly drained depressions, marshes, ponds, and lakes

End moraines of late Wisconsinan age; low ridges, mostly gently sloping, in places discontinuous

Gently rolling drift plain of early Wisconsinan age covered with late Wisconsinan loess; drainage generally well integrated

Topographically similar to Illinoian drift plain (4cl) but much darker toned and slightly subdued relief

Highest end moraines of late Wisconsinan age (surrounding Turkey Ridge)

Illinoian drift plain; weathered clayey till mantled generally with several meters of late Wisconsinan loess; well-dissected upland plain

has been difficult. Hoffer (ref. 4-23) demonstrated that photographs from the S190A camera and imagery from the S192 scanner have potential use in delineating snow cover (fig. 4-22). A simple delineation of snow-covered areas usually is not possible because of obscuration by clouds, vegetation canopies, or shadows of clouds. However, digital processing of the S192 imagery data enabled recognition of five spectral classes of snow-covered areas (table 4-VI) according to differences in the proportion of the forest or vegetation canopy constituting each picture element (pixel) of the scanner data. Computer processing of the data permitted the digital overlay of 13 bands of EREP data, 4 bands of Landsat multispectral imagery, and topographic data (including elevation, slope, and aspect). The capability of comparing multiple data sets provides an effective means for rapidly generating accurate snow-cover maps using the repetitive coverage that will be provided by future satellites.

According to Barnes et al. (ref. 4-41), the differentiation of cloud cover from snow cover can be accomplished by selective use and analysis of S192 imagery data. Snow reflectance is high in the visible part of the electromagnetic spectrum but drops to comparatively low levels in the 1.55- to 1.75-μm and 2.10- to 2.35-μm bands. In the imagery covering this range (S192 bands 11 and 12), snow appears to be nearly black regardless of age and condition, but water and cloud-top reflectances are uniformly high throughout the range. Through computer processing of the data, a clear distinction can be made between cloud tops and snow cover. An area showing a high reflectance in the visible range but a low reflectance in the near-infrared range (S192 band 11 or 12) can be recognized as snow; an area showing high reflectance in both spectral regions can be recognized as water or clouds. Most snow-free areas exhibit relatively low reflectances in the visible range and medium reflectance in the near-infrared range (fig. 4-23). Exploitation of this technique for automatic snow-cover recognition and mapping was shown to be possible; when fully developed, it may aid in better management of large watersheds for flood protection and maximum water storage and utilization.

Hydrological Factors

The hydrological factors discussed are flood prediction, watershed management, and ancient water systems.

TABLE 4-V.— Continued

(a) Continued

Map units	Landform characteristics					Soil characteristics		Surficial-geologic deposits	Special problems or attributes
	Land-surface form symbol	Local relief, m	Stream dissection			Surface color	Soil drainage		
			Density	Pattern	Interfluves				
7a	Blc, Cld, Dlc, Dld, Dle	< 30	Very high (gullied)	Semi-par-allel	Few to no gently sloping interfluves	Dark	Excellent	Variable	None
7b	C2d, D2c, D2d, D2e	30 to 60	Very high (gullied)	Semi-par-allel	Few to no gently sloping interfluves	Medium	Excellent	Variable; commonly like 4cl; bedrock exposed locally	None
7c	D3c, D3d, D3e, D4e	>60	Very high (gullied)	Semi-par-allel	Few to no gently sloping interfluves	Medium	Excellent	Variable; commonly like 4cl; bedrock exposed locally	None
8	C2c, C2d	15 to 45	Low	Radial	—	Medium to light	Excellent	Kame - sand, gravel, boulders	Good source of sand and gravel

(b) Environmental-geomorphic /geological limitations[a]

Map units	Topographic limitations	Shallow ground water availability	Gravel availability/quality	Rock availability/quality	Construction			
					Slope stability	Foundations	Ease of excavation	Roads
1	3	3	2,3	1	1,2	1,2	3	3
lo	3	3	3	1	1,2	2,3	3	3
lt	3	3	3	1	1,2	2,3	3	3
2g	3	1,2,3	1,2	1	2	1,2,3	3	3
2s	2,3	1,2,3	1,2	1	2	1,2,3	3	3
2e	2,3	1,2,3	1,2	1	2	1,2,3	3	2,3
2m	3	1,2,3	1,2	1	2	2	3	3
3c	2	2	2	1	2	2,3	3	2
4ce	1	1,2	1,2	1	2	2,3	3	1
4cl	1,2	1,2	1	1	2	2,3	3	2,3
4d	1,2	1,2	1	1	2	2,3	3	2,3
4dl	1,2	1,2	1	1	2	2,3	3	2,3
7a	1	1	1	1	2,3	2,3		1
7b	1	1	1	3	2,3	2,3	1,2,3	1
7c	1	1	1	3	2,3	2,3	1,2,3	1
8	1	3	3	1	1,2	2,3	3	1

[a]1 is severe, 2 is moderate, and 3 is few.

TABLE 4-V.— Concluded

(a) Concluded

Remarks

Bluffs; units 7b and 7c generally have, at top, several meters of loess over weathered clayey till of Illinoian age over Sioux Quartzite (exposed locally)

Glacial kames (gravelly hills)

(b) Concluded[a]

Drainage		Erodibility	Waste disposal		
Surface	Soil (internal)		Sanitary landfills	Sewage lagoons	Septic tanks
1,2	1,2	1,2	1,2,3	1,2,3	1,2,3
3	3	2,3	1,2	1,2	3
3	3	2,3	1,2	1,2	3
1,2	1,2	2,3	2,3	2,3	1,2
1,2,3	1,2	2,3	2,3	2,3	1,2
3	1,2	1,2	2,3	2,3	1,2
2,3	1,2	2,3	2,3	2,3	1,2
3	1,2	2	2,3	2,3	1,2
3	1,2	1,2	2,3	2,3	1,2
3	1,2	1,2	2	2	2,3
3	1,2	1,2	2	2	2,3
3	1,2	1,2	2	2	2,3
3	2,3	1	2	2	2
3	2,3	1	2	2	2
3	2,3	1	2	2	2
3	3	2	1	1	3

[a]1 is severe, 2 is moderate, and 3 is few.

Flood prediction.—Flood-hazard indices are often used by insurance companies, banks, and others concerned with evaluating investment risk. Multispectral photographs are useful in defining relationships between the local geomorphology and land use within a given watershed. For example, in central Texas, where the orographic influence of the Balcones Escarpment tends to localize thunderstorms, it has been suggested by Baker et al. (ref. 4-37) that local geomorphology of the several drainage basins governs the conversion of storm precipitation to floods. A test of this idea and the beginning of the development of a quantitative hydrogeomorphic model to describe the floods are made possible by the availability of repetitive satellite imagery. A similar application was made by Colwell et al. (ref. 4-36) in defining patterns of runoff and alluviation in the San Bernardino Mountains. Geohydrological units within drainage basins were easily recognized and delineated by ridge lines, drainage divides, faults, and contact between different lithological units. A generalized model of ground water movement was constructed that includes a prediction of flood hazards in the south-central Mojave Desert. This model can be very useful in planning for the orderly growth and development of rapidly expanding communities in this region. The S190B photographs bridged the gap between high-altitude aerial photographs and relatively low-resolution multispectral imagery. Similar results were obtained at study sites in Illinois, Iowa, Kansas, Missouri, Nebraska, and South Dakota (ref. 4-9).

Watershed management.—A detailed comparison of Skylab S190A and S190B photographs and high-altitude-aircraft photographs of the New England area was made by Cooper et al. (ref. 4-42) to provide hydrological information needed for reservoir management. The relationship between the land use within a watershed and its hydrological characteristics is generally believed to be fundamental to an understanding of watershed functioning. The EREP S190B photographs made possible the identification and delineation of all 6 Level I classification units (ref. 4-43), 17 Level II units, and 1 Level III unit. (See table 2-I in sec. 2.) These results are almost as good as those obtained with the best high-altitude-aircraft photographs (6 Level I, 21 Level II, and 5 Level III units); at Level II, they are practically equal in utility. The S190B photographs meet the remote-sensing requirements for regional land use mapping and for evaluation of runoff potentials in situations requiring regional hydrological surveys for urban planning or
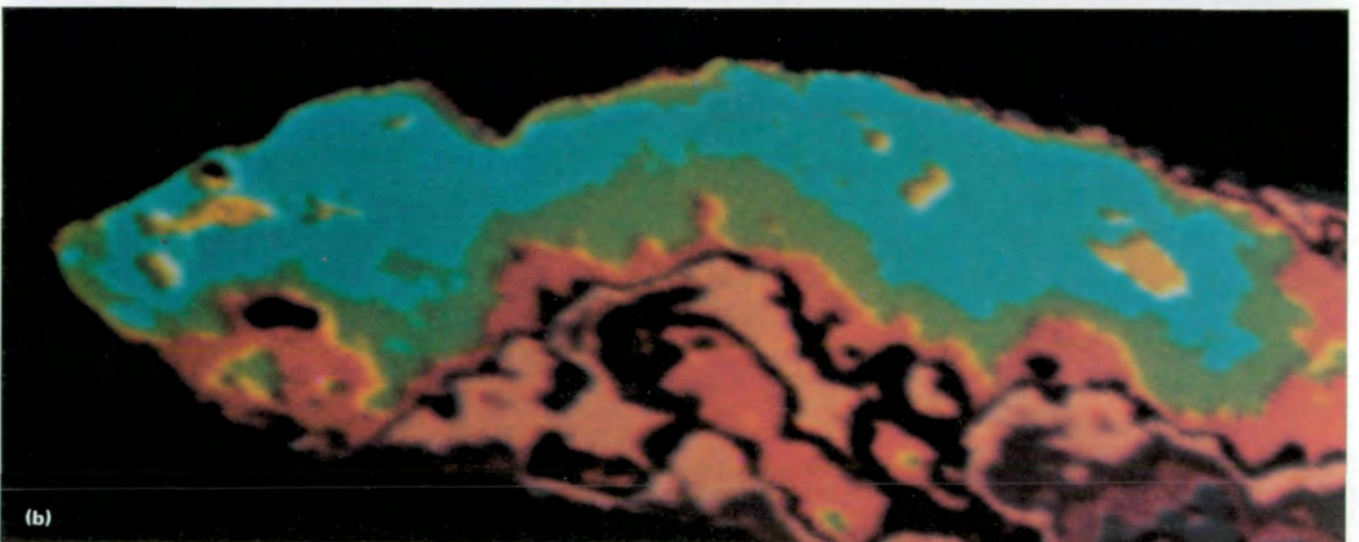
				Blue-to-green ratio			
Blue	Red	Violet	Pink	Orange	Green	Light blue	Yellow
1.2	1.4	1.5	1.8	2.0	2.4	3.1	4.2

FIGURE 4-21.—Western Lake Ontario. (a) S190A color photograph (SL3-40-016). (b) Color-coded ratio of the blue-to-green lake reflectance in figure 4-21(a). A low blue-to-green ratio indicates a high chlorophyll concentration.
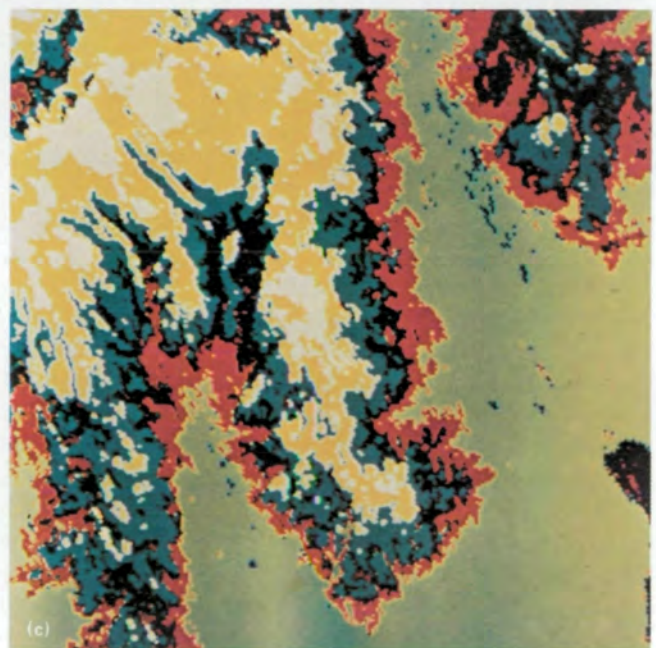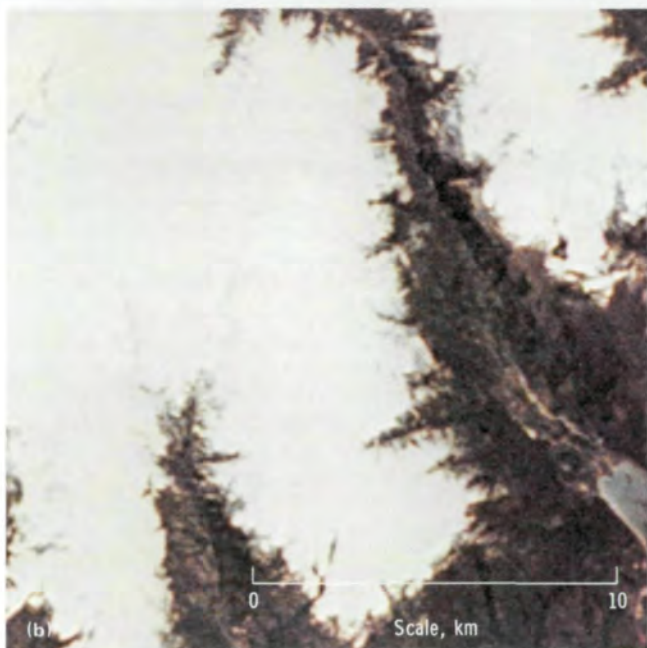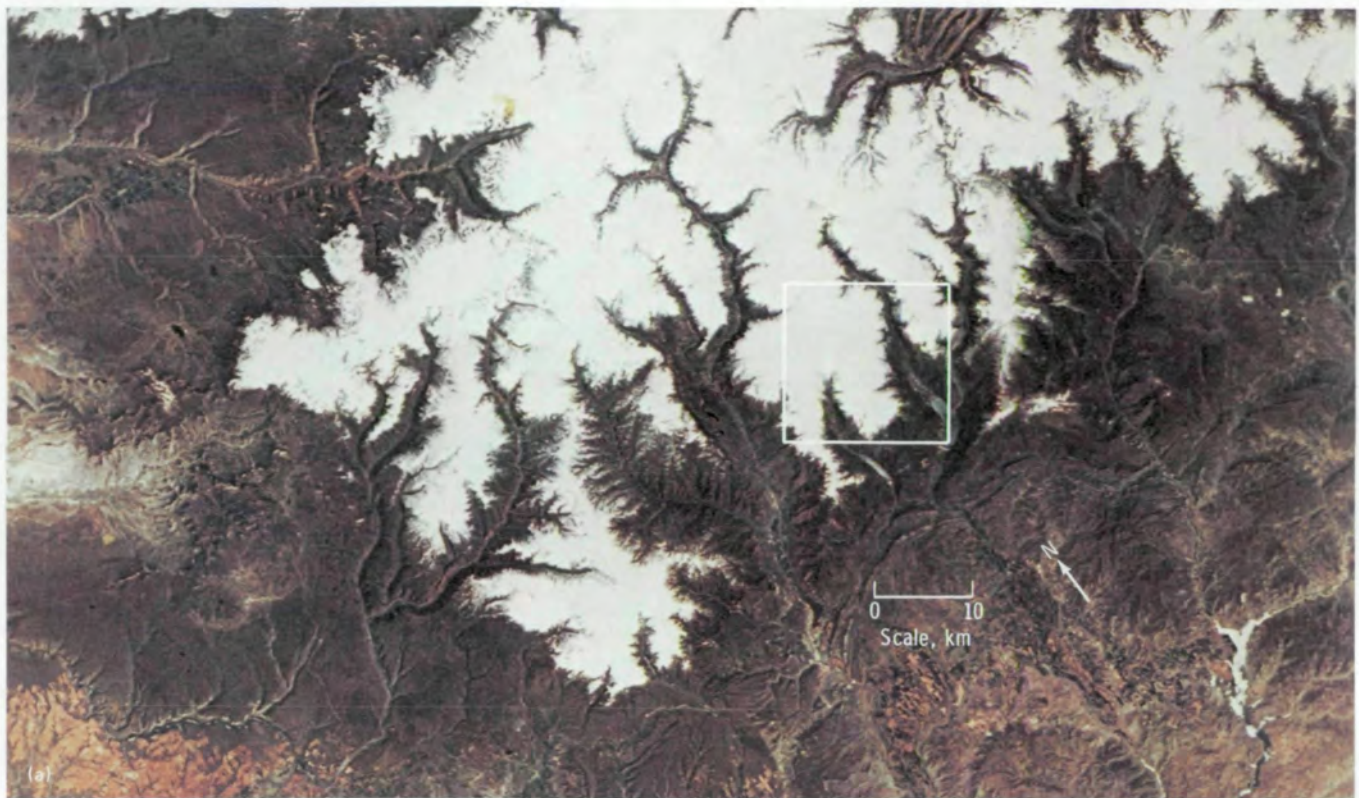
FIGURE 4-22.—San Juan Mountains in southwestern Colorado. (a) S190A color photograph, showing the extent of snow cover (SL2-10-016). Outlined area is shown in figure 4-22(b). (b) Area outlined in figure 4-22(a). (c) Color-coded snow classification map of S192 digital data in which five spectral classes of snow have been separated. The data can be used to determine the areal extent of the snowpack.
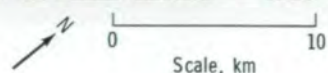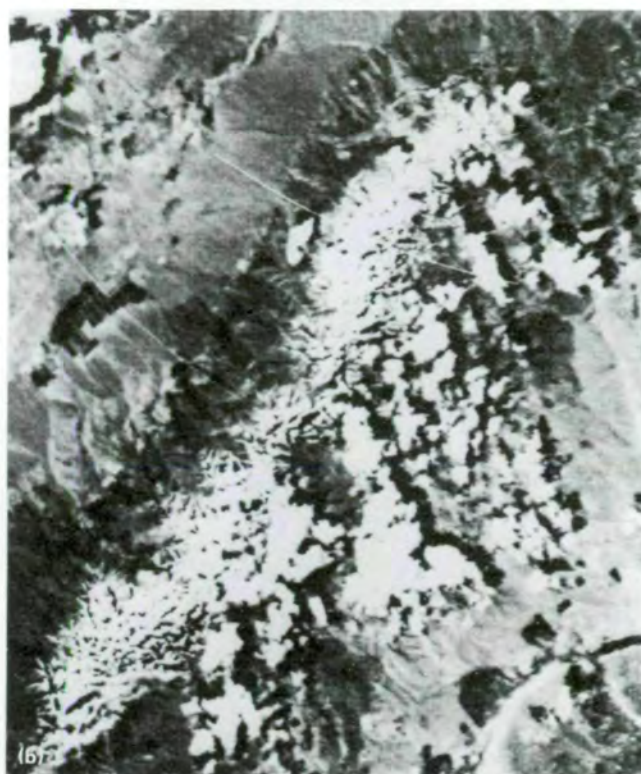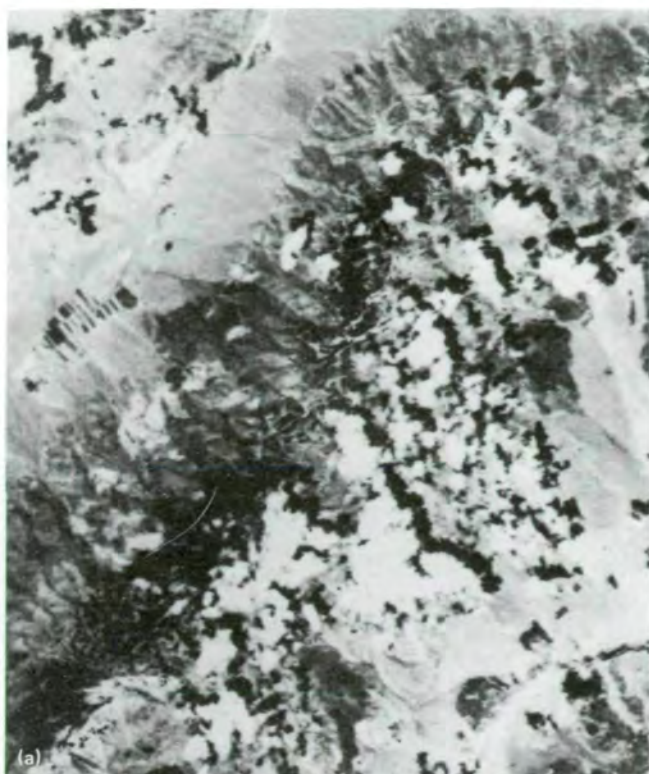
FIGURE 4-23.—S192 data acquired over the White Mountains area in California on June 3, 1973 (ref. 4-41). (a) Visible band 3 (0.52 to 0.56 μm). (b) Near-infrared band 11 (1.55 to 1.75 μm). The change in the background reflectance for snow makes the clouds easier to identify.

resource development. Similar results were reported by Stoeckeler et al. (ref. 4-34).

Ancient water systems.—Skylab photographs enabled Gumerman et al. (ref. 4-44) to study the hydrology of prehistoric farming systems within a large and environmentally diverse area of central Arizona. Hydrologists, geologists, biologists, and archeologists evaluated the adaptation of prehistoric man to the semiarid desert of central Arizona and his creation of land management and water control systems. Ecologically significant subareas, or drainage basins, were selected on the basis of basin area, stream length and order, slopes, bedrock type, and rainfall distribution. Table 4-VII illustrates the usefulness of S190A and S190B photographs for defining environmental parameters. Estimates of available water were established from these parameters and from vegetation communities, and an evaluation of types of prehistoric water management systems was based on these data.

TABLE 4-VI.—*Snowpack Area Within 100-m Elevation Increments for the Five Spectral Classes of Snow Cover*

Elevation, m	Snowpack area, hm², for spectral class —					Total area, hm²
	1	2	3	4	5	
Above 3700	1179	2464	308	108	7	4 066
3600 to 3700	400	1914	694	135	37	3 180
3500 to 3600	129	1868	1858	517	61	4 433
3400 to 3500	45	904	1858	1266	280	4 353
3300 to 3400	13	378	1305	1417	812	3 925
3200 to 3300	7	94	922	1258	1298	3 579
3100 to 3200	6	22	529	793	1540	2 890
3000 to 3100	0	6	213	433	1041	1 693
2900 to 3000	0	1	38	188	535	762
2800 to 2900	0	0	4	54	289	347
2700 to 2800	0	0	1	13	147	161
2600 to 2700	0	0	0	1	95	96
Below 2600	0	0	0	0	79	79
Totals	1779	7651	7730	6183	6221	29 564

TABLE 4-VII.—Evaluation of the Usefulness of S190A and S190B Photographs for Interpreting Environmental Features of Interest to Regional Archeological Studies

Features studied	S190A				S190B	
	Black and white	Color	Color infrared	Enhanced color	Color	Color infrared
Topographical						
Manmade:						
Habitation	Poor	Fair	Poor	Good	Good	Good
Roadways	Poor	Fair to poor	Poor	Good	Very good	Good
Natural:						
Major drainage-ways	Fair	Very good	Good	Very good	Very good	Very good
Minor drainage-ways	Poor	Very good	Good	Good	Very good	Very good
Plains and bajadas	Good	Very good	Good	Good	Very good	Very good
Hills, buttes, and mesas	Good	Very good	Good	Good	Very good	Very good
Mountains	Good	Very good	Good	Good	Very good	Very good
Vegetational						
Regional:						
Vegetation types General density patterns	Poor	Poor	Poor	Poor	Poor	Fair
Riparian	Poor	Poor	Poor	Poor	Fair	Good
Nonriparian	Fair	Fair	Fair	Fair	Fair	Good
Local:						
Differences in vegetation densities on slopes of different exposures	Fair[a]	Fair[a]	Fair[a]	Fair	Fair	Good to fair[b]
Differences in vegetation densities on lower/higher portions of slopes above larger drainages	Fair	Fair	Fair	Fair	Fair	Good to fair[b]
Differences in vegetation densities in drainage channels as a function of adjacent slopes	Poor	Poor	Poor	Poor	Fair to poor[b]	Good to fair[b]
Width of riparian vegetation zones in major drainages	Poor	Fair	Poor	Poor	Fair	Good
Agricultural	Poor	Poor	Fair	Poor	Good	Very good
General rating						
Topography	Fair	Good	Fair	Good	Very good	Very good
Vegetation	Poor	Poor	Poor	Poor	Fair	Good

[a]Difficulties caused by shadows. [b]Some areas better than others.
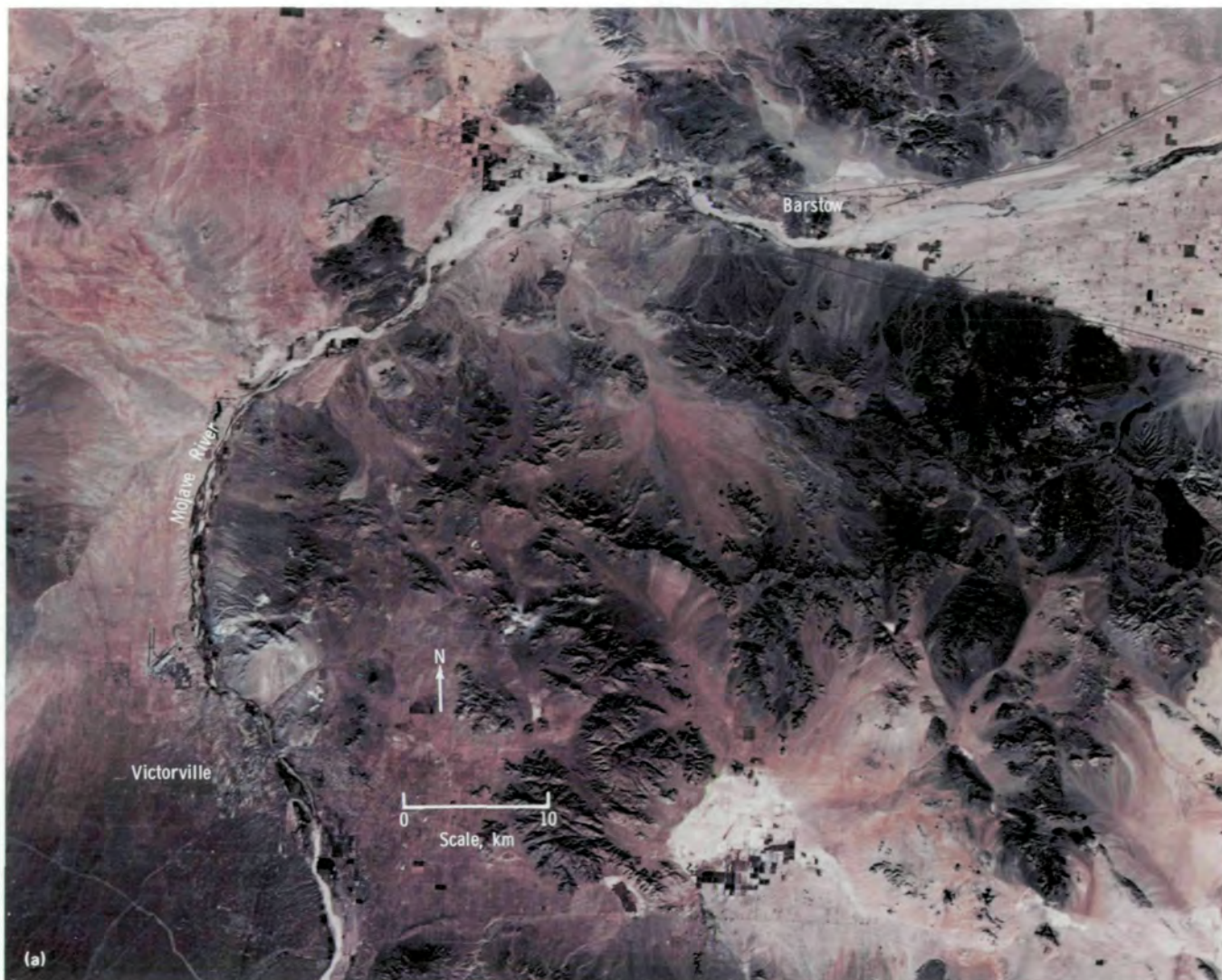
FIGURE 4-24.—South-central Mojave Desert in California. (a) S190B color photograph (SL4-92-349). (b) Geohydrological map based on interpretation of Skylab photographs.

Ground Water

The location of reliable sources and supplies of ground water is of growing social and economic importance in nearly all parts of the world. It has become obvious that ground water exists in limited quantities and that the continued existence of these quantities ultimately depends on the rate of replenishment. For rational resource management, it is important to have the means available for locating ground water reserves.

Although aerial and satellite imagery can provide only indirect evidence of ground water reserves, this evidence can be accurate and definitive under some circumstances.

Skylab photographs and imagery are useful for the assessment of ground water resources, both in terms of spatial distribution and of functioning. According to Colwell et al. (ref. 4-36), arid lands such as the south-central Mojave Desert are most amenable to analysis by photointerpretative techniques, and the information

Explanation

—— — — — Fault (dashed where inferred)

▲▲▲▲▲▲▲▲▲ Geohydrologic unit boundary

●●●●●●●● Drainage province divide

——→ — —→ Direction of ground water movement.
Solid where flow is unimpeded, dashed
where flow is impeded by faults

Alluvium
High porosity and high permeability
surface of infiltration
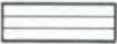
Dune sand
High porosity and high permeability
surface of infiltration

—— Lithologic contact

Lacustrine sediments
High porosity and low permeability
surface of evaporation

Volcanics and hypabyssal intrusives
Low porosity and low permeability
surface of runoff

Igneous and metamorphic
basement complex
Low porosity and low permeability
surface of runoff

N

0   10
Scale, km
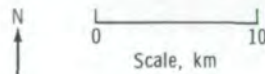
(b)

FIGURE 4-24.—Concluded.

FIGURE 4-25.—Indio Hills and Coachella Valley just north of the Salton Sea in southern California. (a) Enlarged portion of S190B photograph (SL4-92-351). (b) Aircraft view of the Banning Fault in the northern Coachella Valley. The flow of ground water has been blocked by impervious material on the left side of the fault, causing a high ground water table and vegetation growth on the right side of the fault.

generated could be of immediate utility in managing the water resources of these regions. Geohydrological units are delineated by noting such flow barriers as drainage divides, faults, and lithological contacts, which are easily discernible on photographs (figs. 4-24 and 4-25). Lithological units are distinguishable and their permeability may be deduced from lithology. From study of EREP photographs, a generalized model for ground water movement within the south-central Mojave

Desert was postulated by outlining the drainage basins, delineating the individual geohydrological and lithological units, and deducing the hydrological characteristics of the lithological units.

Water-well siting on lineaments.—In central Tennessee, ground water occurs mostly in a network of solution cavities. It seemed reasonable that the lineaments visible in the Skylab photographs might show the existence and location of a major structural system of

FIGURE 4-25.—Concluded.

joints that interconnects this system of cavities and governs the rate at which this ground water can be removed. Accordingly, Moore (ref. 4-45) studied the lineament types revealed by the view from space. He then compiled data on water yields from wells in this area and separated the values of those located on lineaments visible in the Skylab photographs from all the others. He found that the yield of water wells located on these lineaments was approximately six times that of randomly located wells (table 4-VIII). It was concluded that when water-well yields of 1.6×10^{-3} m³/sec (25 gal/min) are required, large savings in time and money can be achieved by locating the wells on lineaments mapped by stereoscopic viewing of Skylab photographs. For wells having yields larger than 6.3×10^{-3} m³/sec (100 gal/min), the potential cost saving between wells randomly located and those on or near stereoscopic and projection linears is approximately $18 000.

Near-surface ground water.—In some areas, the presence of near-surface ground water is clearly, although indirectly, indicated by tonal or textural variations in space photographs. These variations may be caused by differences in surface vegetation, soil composition, or some similar factor (ref. 4-2). Near-surface ground water may represent an important untapped ground water resource in some places or an undesirable buildup of the water table as a consequence of excessive irrigation or poor drainage in others. When combined with a program of ground-based measurements, analysis of the S190B-quality photographs permits the identification and delineation of some types of near-surface ground water with a degree of precision far greater than that possible from conventional ground-survey methods alone (Bannert et al., ref. 4-46; fig. 4-26).
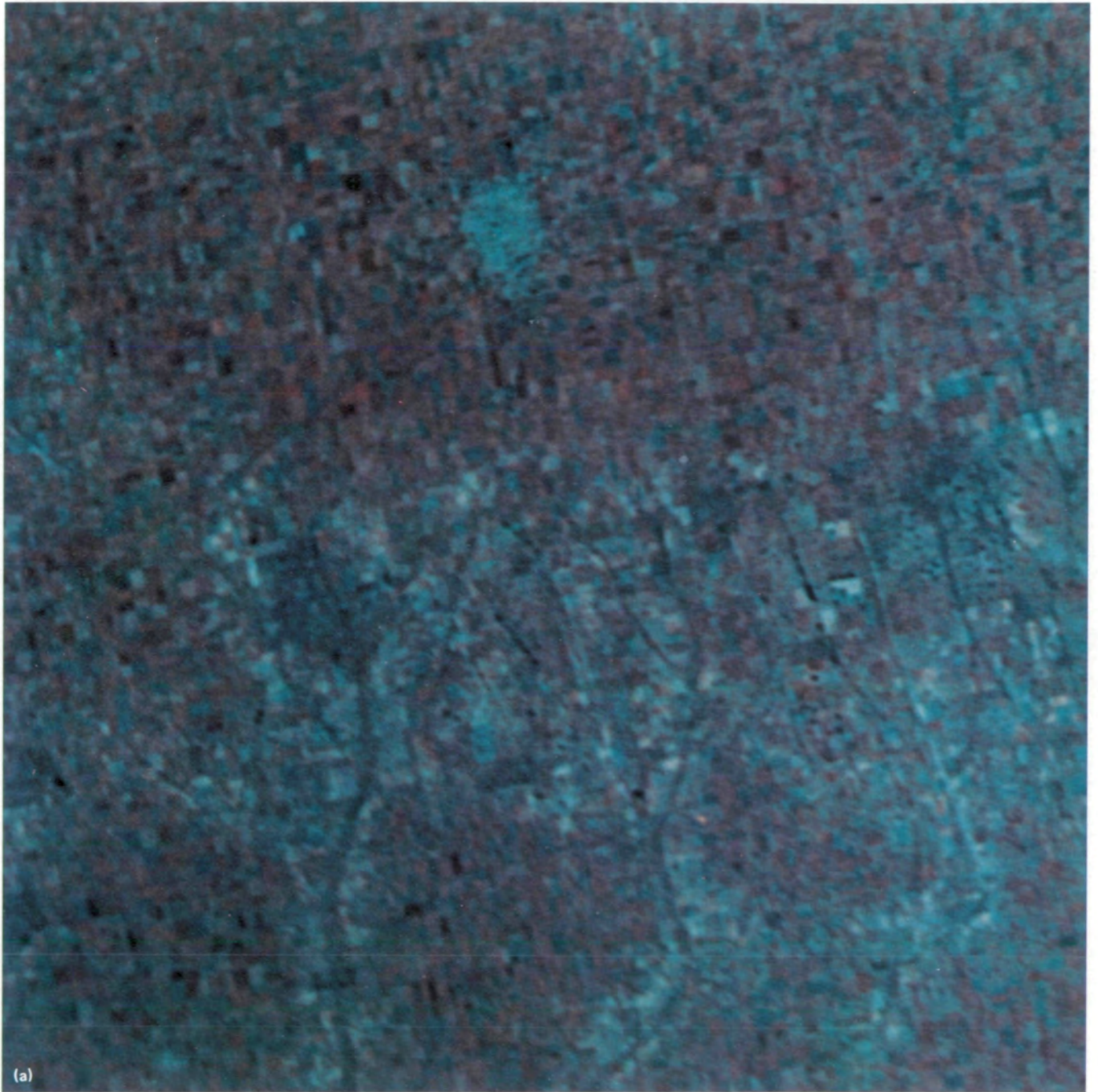
FIGURE 4-26.—Rafaela area, Argentina. (a) Portion of S190A color-infrared photograph (SL3-33-162). (b) Map showing the depths of the ground water in the Rafaela area; the depths were estimated by the interpretation of Skylab photography.
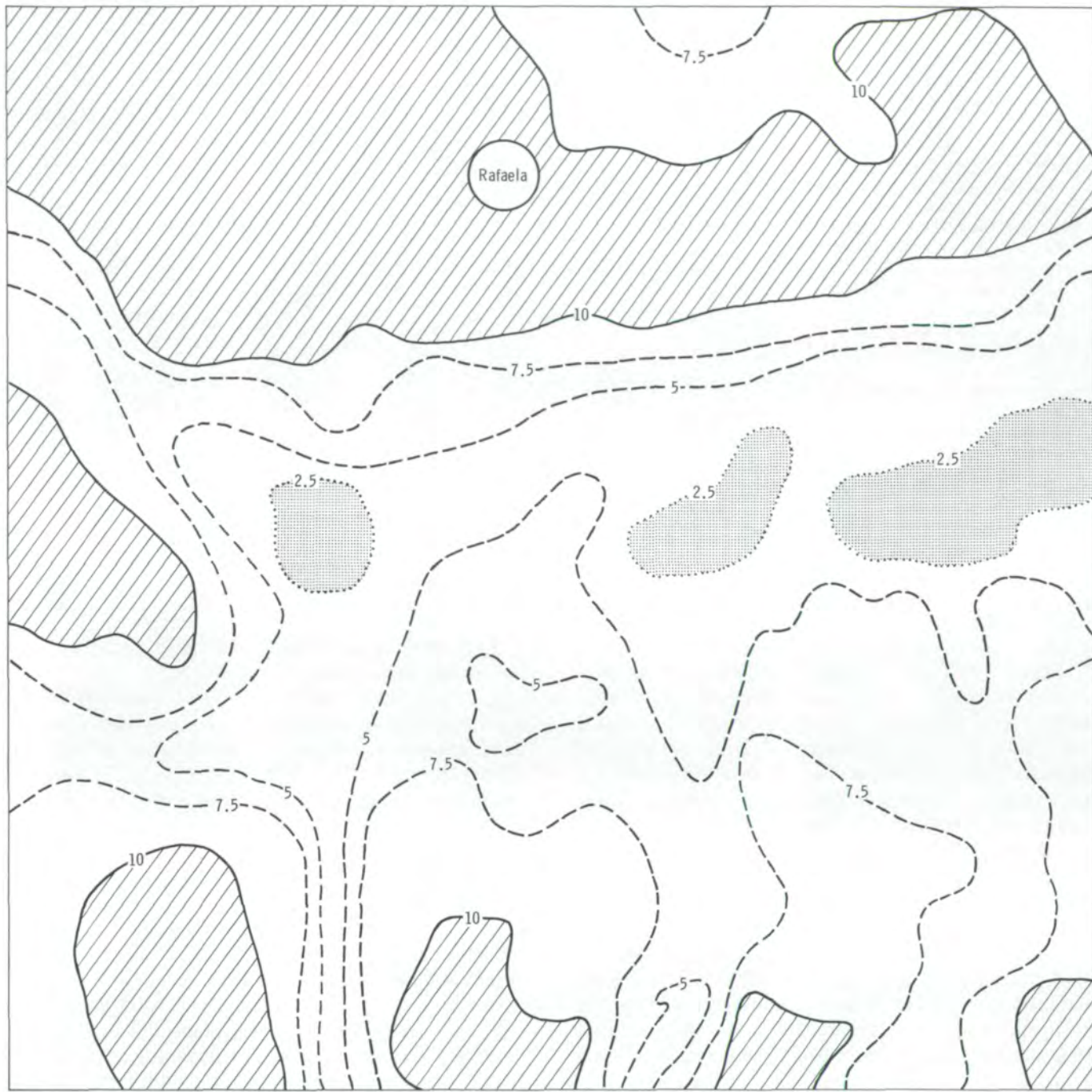
Rafaela

—5— Isolines of depth to ground water in meters	▨ Depth to ground water more than 10 m
▦ Depth to ground water less than 2.5 m	⋯ Bajo

Scale, km
0   10

(b)
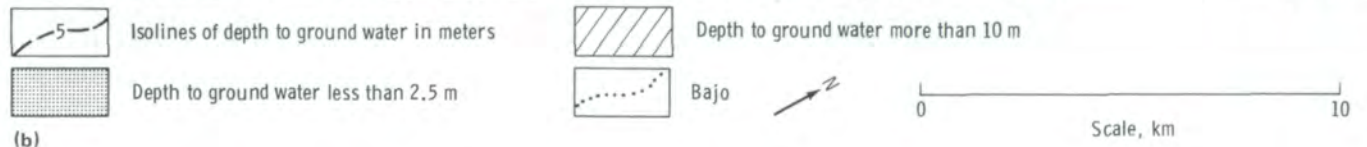
FIGURE 4-26.—Concluded.

*TABLE 4-VIII.—Comparison of Results of Random Drilling With
Locations on or Near Lineaments*

Location of wells	No. of wells necessary to obtain yield, m^3/sec (gal/min), larger than—			
	0.63×10^{-3} (10)	1.6×10^{-3} (25)	3.2×10^{-3} (50)	6.3×10^{-3} (100)
Randomly located	1.8	5.0	11	33
On or near Skylab lineaments:				
Stereoscopic lineaments	1.6	3.3	5.0	14
Projection lineaments	1.9	3.7	7.7	20
Either stereoscopic or projection lineaments	1.8	3.4	6.2	17
Stereoscopic and projection lineaments[a]	1.6	3.3	3.8	5.3
Between Skylab lineaments	1.8	5.6	14	50
On or near Landsat lineaments	2.2	3.7	6.3	43
On or near aerial photograph lineaments	1.6	3.4	6.6	40

[a]Lineaments detected both by stereoviewing and by projection.

SUMMARY

Skylab EREP data provide the geologist with an ideal combination of stereoscopic synoptic view and multispectral coverage of his area of interest. This broad view can reveal regional patterns of geology, landforms, and drainage that are not as obvious on large-scale photographs. The availability of a variety of images for a given area allows an investigator to find the best image or combination of images for study of his particular region. Although S190B color photographs with stereoscopic coverage and high resolution proved to be the most preferred product, all products were found to be useful to some extent, depending on geology, vegetation, topography, and season. Analysis of the EREP data led to a number of geologically significant results.

1. Photogeological reconnaissance and regional maps as good as or better than published small-scale maps can be rapidly prepared.

2. Detailed geological maps were made for arid or semiarid regions for use in conjunction with published data and ground checking.

3. In more heavily vegetated areas, the general structure, particularly lineaments and large folds, was inferred through topographic and drainage analysis.

4. Many previously unknown structures were discovered that were verified by field checking.

5. Active faults and other evidence of recent ground movement were located.

6. Areas were targeted for specialized large-scale ground surveys of various kinds. For example, maps of linear patterns and intensity, where related to rock fracturing, have significance in mineral resource, ground water, and engineering applications.

7. Surface-water and snow-cover inventories were shown to be feasible.

8. Considerable reduction in costs of exploration was documented.

The EREP studies led to the development of new models or hypotheses, or to refinements or rejection of older ideas, which in turn led to a reappraisal of areas formerly considered devoid of economic mineral deposits. The geological investigations and applications described in this section are the beginning of the use of EREP data. Researchers associated with the experiments will extend their applications to other geographical areas, and new users will have the opportunity to use EREP data in their particular areas of interest. As future space platforms are designed and become operational, the lessons learned and the methods tested during the EREP program will contribute to a better understanding of the distribution of the Earth's resources.

REFERENCES

4-1. Quade, Jack G.; Trexler, D. T.; et al.: Geologic Investigation in the Basin and Range of Nevada Using Skylab/EREP Data. NASA CR-144497, 1975.

4-2. Lee, Keenan; Hutchinson, R. M.; et al.: Geologic and Mineral and Water Resources Investigations in Western Colorado, Using Skylab EREP Data. NASA CR-138722, 1974.

4-3. Williams, P. L.: Geology, Structure, and Uranium Deposits of the Moab Quadrangle, Colorado and Utah. U.S. Geol. Surv. Misc. Geol. Inv. Map I-360, 1964.

4-4. Hoppin, R. A.; Caldwell, J.; et al.: Experiment To Evaluate the Feasibility of Utilizing Skylab-EREP Remote Sensing Data for Tectonic Analysis Through a Study of the Big Horn Mountain Region, Wyoming. NASA CR-147543, 1976.

4-5. Houston, R. S.; Marrs, R. W.; and Borgman, L. E.: Multidisciplinary Study of Wyoming Test Sites. NASA CR-147719, 1975.

4-6. Lambert, B. P.; Benson, C. J.; et al.: A Study of the Usefulness of Skylab EREP Data for Earth Resources Studies in Australia. NASA CR-144493, 1975.

4-7. Stoiber, Richard E.; and Rose, William I.: An Investigation of Thermal Anomalies in the Central American Volcanic Chain and Evaluation of the Utility of Thermal Anomaly Monitoring in the Prediction of Volcanic Eruptions. NASA CR-144496, 1975.

4-8. VanderMeerMohr, H. E. C.; and Srivastava, G. S.: Evaluation of EREP Techniques for Geological Mapping: Summary Statements. NASA CR-144494, 1975.

4-9. Morrison, R. B.; Lineback, J. A.; et al.: Applications of Skylab EREP Photographs to Mapping Landforms and Environmental Geomorphology in the Great Plains and Midwest. NASA CR-144491, 1975.

4-10. Olson, Norman K.: Application of Multispectral Photography to Mineral and Land Resources of South Carolina. NASA CR-144109, 1975.

4-11. Cassinis, R.; Lechi, G. M.; and Tonelli, A. M.: Results of Skylab Investigation Over Italy. NASA CR-147396, 1975.

4-12. Merifield, Paul M.; and Lamar, D. L.: Fault Tectonics and Earthquake Hazards in Parts of Southern California. NASA CR-144477, 1976.

4-13. Collins, R. J.; Petzel, G. J.; and Everett, J. R.: Evaluation of the Suitability of Skylab Data for the Purpose of Petroleum Exploration. NASA CR-147468, 1975.

4-14. McMurtry, George J.; and Petersen, Gary W.: Interdisciplinary Applications and Interpretations of EREP Data Within the Susquehanna River Basin. NASA CR-147541, 1976.

4-15. Abdel-Gawad, Monem; and Tubbesing, Linda: Analysis of Tectonic Features in U.S. Southwest From Skylab Photographs. NASA CR-144464, 1975.

4-16. Jensen, Mead LeRoy; and Laylander, Philip: Summary of Space Imagery Studies in Utah and Nevada. NASA Earth Resources Survey Symposium. NASA TM X-58168, vol. IB, 1975, pp. 673-712.

4-17. Bechtold, Ira C.; Reynolds, J. T.; Archer, R. L.; and Wagner, C. G.: An Evaluation of Skylab (EREP) Remote Sensing Techniques Applied to Investigations of Crustal Structure. NASA CR-147458, 1975.

4-18. Goetz, A. F. H.; Abrams, M. J.; et al.: Comparison of Skylab and LANDSAT Images for Geologic Mapping in Northern Arizona. NASA CR-147503, 1976.

4-19. Lee, K.; and Raines, G. L.: An Evaluation of Multiband Photography for Rock Discrimination. Proceedings of the Third Conference on Earth Resources Observation and Analysis Systems (Tullahoma, Tenn.), vol. 3, 1974, pp. 361-396.

4-20. Thomson, F.: Machine Processing of S-192 and Supporting Aircraft Data: Studies of Atmospheric Effects, Agricultural Classifications, and Land Resource Mapping. NASA CR-144503, 1975.

4-21. Chang, David T.; and Isaacs, Ronald G.: Experimental Evaluation of Atmospheric Effects on Radiometric Measurements Using the EREP of Skylab. NASA CR-144500, 1975.

4-22. Jerome, J. E.: Some Features Pertinent in Exploration of Porphyry Copper Deposits. Geology of the Porphyry Copper Deposits, Southwestern North America, S. R. Titley and C. L. Hicks, eds., Univ. Arizona Press, 1966, pp. 75-85.

4-23. Hoffer, Roger M.: Computer-Aided Analysis of Skylab Multispectral Scanner Data in Mountainous Terrain for Land Use, Forestry, Water Resource, and Geologic Applications. NASA CR-147473, 1975.

4-24. Watson, K.; O'Leary, D. W.; and Pohn, H. A.: A Photogeologic Comparison of Skylab and Landsat Images of Southwestern Nevada and Southeastern California. NASA CR-144642, 1975.

4-25. Carlson, J. E.; and Mabey, D. R.: Gravity and Aeromagnetic Maps of the Ely Area, White Pine County, Nevada. U.S. Geol. Surv. Geophys. Inv. Map GP-392, 1963.

4-26. Hose, R. K.; and Blake, C., Jr.: Preliminary Geologic Map of White Pine County, Nevada. U.S. Geol. Surv., 1970.

4-27. Amsbury, David L.; Clanton, Uel S.; and Frierson, Von R.: Small-Scale Imagery: A Useful Tool for Mapping Geological Features in the Texas Gulf Coastal Plain. NASA Earth Resources Survey Symposium, NASA TM X-58168, vol. IB, 1975, pp. 833-849.

4-28. Guillemot, J.: Project Pyralp: Tectonic Relationship Between Pyrenees and Alps (Southern France). NASA CR-140127, 1974.

4-29. Vargas F., Carlos: Interpretacion Geologico-Fisiografica de Una Fotografia Skylab Correspondiente al Area: Santa Cruz-Montero-Buena Vista. Yacimientos Petroleferos Fiscales Bolivianos, Special Report, 1975.

4-30. Austin, C. F.; Austin, W. H., Jr.; and Leonard, G. W.: Geothermal Science and Technology—A National Program. U.S. Naval Weapons Center Tech. Ser. 45-029-72, 1971.

4-31. Duffield, W. A.: Late Cenozoic Ring Faulting and Volcanism in the Coso Range Area of California. Geology, vol. 3, no. 6, 1975, pp. 335-338.

4-32. Anderson, D. H.; and Hall, R. A.; eds.: Geothermal Exploration in the First Quarter-Century. Geothermal Resources Council Special Report No. 3, 1973, pp. 117-144.

4-33. Siegal, Barry S.; Kahle, Anne B.; et al.: The Detection of Geothermal Areas From Skylab Thermal Data. NASA CR-143133, 1975.

4-34. Stoeckeler, E. G.; Woodman, Raymond G.; and Farrell, Robert S.: Multidisciplinary Analysis of Skylab Photography for Highway Engineering Purposes. NASA CR-141942, 1975.

4-35. Trumbull, J. V. A.: The Utility of Skylab Photointerpreted Earth Resources Data in Studies of Marine Geology and Coastal Processes in Puerto Rico and the Virgin Islands. NASA CR-147437, 1975.

4-36. Colwell, Robert N.; Bowden, Leonard W.; et al.: Use of Skylab Imagery to Assess and Monitor Changes in the Southern California Environment. NASA CR-147561, 1974.

4-37. Baker, Victor R.; Holz, Robert K.; et al.: Stream Network Analysis and Geomorphic Flood Plain Mapping From Orbital and Suborbital Remote Sensing Imagery Application to Flood Hazard Studies in Central Texas. NASA CR-144354, 1975.

4-38. Piech, Kenneth R.; Schott, John R.; and Stewart, Kenton M.: S190 Interpretation Techniques Development and Application to New York State Water Resources. NASA CR-144499, 1976.

4-39. Hannah, John W.; Thomas, Garland L.; et al.: Planning Applications in East Central Florida. NASA CR-145415, 1975.

4-40. Yarger, Harold L.; and McCauley, James R.: Skylab Study of Water Quality. NASA CR-144505, 1975.

4-41. Barnes, J. C.; Smallwood, M. D.; and Cogan, J. L.: Study to Develop Improved Spacecraft Snow Survey Methods Using Skylab/EREP Data. NASA CR-144338, 1975.

4-42. Cooper, Saul; Anderson, Duwayne; et al.: Skylab Imagery: Application to Reservoir Management in New England. NASA CR-144514, 1975.

4-43. Anderson, J. R.; Hardy, E. E.; and Roach, J. T.: A Land-Use Classification System for Use With Remote Sensor Data. U.S. Geol. Surv. Circ. 671, 1972.

4-44. Gumerman, George J.; Hanson, John A.; et al.: The Hydrology of Prehistoric Farming Systems in a Central Arizona Ecotone. NASA CR-144492, 1975.

4-45. Moore, G. K.: Hydrologic Significance of Skylab Lineaments in Central Tennessee. NASA CR-144490, 1976.

4-46. Bannert, Dieter; Bender, H.; et al.: Hydrogeological Investigations in the Pampa of Argentina. NASA CR-144488, 1975.

5

Oceans and Atmosphere

WILLARD J. PIERSON,[a†] WILLIAM E. MARLATT,[b]
ZACK H. BYRNS,[c] AND WILLIAM R. JOHNSON[d]

THE OCEANOGRAPHIC PROBLEMS studied in the Earth Resources Experiment Package (EREP) Investigations Program included locating the surface of the ocean relative to the center of the Earth as a function of latitude and longitude; measuring sea-surface temperature more accurately with data from a spacecraft; describing the variation of ocean color and the dynamics of floating ice in space and time; detecting ocean currents and ocean upwelling and the spatial and temporal changes in them; describing erosion, river runoff, sediment transport, and the circulation within bays and estuaries bordering the ocean; assessing ocean dumping; and locating productive fishing areas. The meteorological problems were those of measuring cloud features; identifying the vertical and horizontal distribution of aerosols through the atmosphere both qualitatively and quantitatively; describing the radiation and energy budgets of the atmosphere; identifying characteristic airmass properties; and measuring the winds in the planetary boundary layer over the ocean, as determined by sea-surface roughness, to provide data for improved computer-based numerical weather predictions.

The wind, the oceans, the atmosphere overlying the oceans, and the land are resources for mankind. Because of energy-resource-use rates, NASA and Energy Research and Development Administration

programs are designed to investigate modern methods of obtaining energy from the winds and the waves.

The oceans moderate and influence climate. Evaporation from them provides the water vapor that is transported by the atmosphere to provide rainfall for the land. Changes in oceanic properties can cause floods and drought. The ocean-atmosphere system provides carbon dioxide for plant life, while acting as a buffer to moderate variations in the amount of carbon dioxide. The oceans also serve as a mechanism for the disposal of waste products. Moreover, the oceans are the major means of transporting the goods of the world in ships. It is important, therefore, to understand sea ice, winds, and waves to improve shipping operations.

The study of the oceans and the atmosphere in an interdisciplinary manner involves many aspects of science and technology. Many features of the ocean have been studied using data obtained by spacecraft. The Gemini and Apollo missions yielded many useful photographs of coastal areas from which oceanographic features could be identified. The meteorological satellites currently being used for study purposes have defined such features of the oceans as the outlines of the Gulf Stream from day to day. The operational meteorological satellites used by the National Oceanic and Atmospheric Administration (NOAA) routinely provide such information as sea-surface temperatures and Gulf Stream boundaries.

All EREP instruments were used in the study of oceanographic problems. The Multispectral Photographic Facility (S190) and the Multispectral Scanner (S192) proved to be most useful in investigation of estuaries, bays, and coastlines; the other sensors proved to

---

[a]City University of New York.

[b]Colorado State University.

[c]NASA Lyndon B. Johnson Space Center.

[d]Lockheed Electronics Company, Inc.

[†]Principal Investigator.

be most useful for studying wide scales of variation in the ocean. On the basis of experience in studying the oceans from spacecraft, it was possible to define a new set of problems that could be addressed by the Skylab EREP instrumentation. The Microwave Radiometer/Scatterometer and Altimeter (S193) was primarily designed for use over the ocean to measure the geoid and to determine the wind fields near the surface of the ocean. However, other valuable information was obtained from this particular instrument as an additional benefit through the recognition of uses other than those originally intended.

The ability to use a resource intelligently often depends on a better understanding of the Earth in a geophysical context. The measurement of the position of the ocean surface (relative to the best-fit ellipsoid of revolution, as described later) is required before further steps can be taken to use oceanic resources. Experience gained in this area may eventually lead to better knowledge of ocean currents, to potential locations for undersea mines and oil wells, and to more accurate maps of the ocean floor.

One of the first applications of Earth satellites was the study of meteorological phenomena. Probably the most successful of the American satellites has been the Tiros meteorological series, begun in 1960. Tiros 1 transmitted more than 19 000 photographs of cloud formations and added a new dimension to the understanding of the physics of weather. Since then, an ever-expanding number of orbital and geosynchronous weather satellites, equipped with an impressive array of sensors, have been launched to aid in atmospheric research. The operational use of satellites in day-to-day weather forecasting has become commonplace.

With its nitrogen cycle, carbon dioxide-oxygen cycle, and hydrological cycle, the atmosphere is important to the production of foodstuffs on land. In addition, the atmosphere disposes of industrial wastes in the form of smoke and gases. The atmosphere carries the water evaporated from the sea surface over the land and provides rainfall. The properties of the atmosphere control the rate at which water returns to the atmosphere from the land by a process called evapotranspiration. It is, therefore, not surprising that the EREP Investigations Program for Skylab included the study of both the atmosphere and the oceans.

THE GEOID AS MEASURED BY THE S193 ALTIMETER

For small areas and distances, everyone has an intuitive understanding of the concepts of "level" and "vertical." If the factor of appreciable distance is introduced, however, these concepts need to be modified. For example, the support towers on each side of a long suspension bridge are several centimeters farther apart at the top than at the bottom because of the curvature of the Earth. Nevertheless, each tower is vertical. For distances of several hundreds of kilometers, the concepts of a level surface and a vertical line become more complicated.

The term "sea level" is quite familiar; yet, the sea is not level. Even if it were, the problem of determining the distance from the center of the Earth to any point on the sea surface would still exist. The term for the study of this problem is "geodesy," and the location of the level surface of the sea (even as extended over the continents) is called the geoid.

As a first approximation, the Earth is a sphere with a mean radius of 6371 km. In actuality, there is a difference between the equatorial and polar radii of the Earth of 21.4 km. If an ellipse with these radii is constructed and rotated about the polar axis, the result is an ellipsoid of revolution, or an oblate spheroid that more closely approximates the level surface of the sea.

Sir Isaac Newton was the first to derive the equations that show that the orbit of a spacecraft is an ellipse the orientation and eccentricity of which are determined by the method of placing the spacecraft in orbit. To derive this result, Newton had to assume that the Earth consisted of concentric ellipsoids of revolution, each homogeneous in mass within that layer. The problem is, of course, that for an orbit near the Earth, the Earth is very large compared to the orbiting spacecraft. His famous equation

$$\vec{F} = \frac{G m_1 m_2}{r^2} \tag{5-1}$$

states that the force $\vec{F}$ attracting two masses is given by a universal constant G times the product of these two

masses m_1 and m_2 divided by the square of the distance r between them. The equation for the gravitational force between the Earth and a spacecraft had to be generalized from this equation by integrating over the volume of the Earth with a variable density assigned to the volume elements. It could be expected that the forces acting on a spacecraft such as Skylab would differ from place to place along the orbit depending on the nature of the Earth below. Such is indeed the case, and the actual orbit of a spacecraft, especially if it be rather low, departs substantially from the ellipse derived by Newton. The oblateness causes the orbit to change plane relative to the geometry of the stars, and the inhomogeneities in the distribution of mass in the upper layers of the solid Earth cause the path of the spacecraft to vary about the theoretical ellipse by substantial, measurable amounts.

The problem becomes more complicated over the ocean surface because the surface of the ocean is closer to these inhomogeneous concentrations of mass caused by such factors as the properties of the large plates that form the upper crust of the Earth. The oceans try to reach an equilibrium surface determined by an appropriate integration over the masses in the volume of the solid Earth. If there were no winds generating ocean currents, if there were no ocean tides, if there were no cooling at the poles and no heating at the Equator, and if the oceans did not vary in their saline content, then the surface of the ocean would be level and it would correspond to the concept of the geoid.

The ocean is very nearly level because all the effects cited cause it to depart from the geoid by at most 2 or 3 m (with a few notable exceptions, such as the tides in the Bay of Fundy), whereas the geoid moves toward and away from the center of the Earth by amounts that depart from the ellipsoid of revolution by as much as 100 m.

Sputnik, the first satellite, was launched by the U.S.S.R. in 1957 and tracked by British scientists who used the measurements of its orbit for comparison with previously made measurements based on land distances. The ellipticity of the Earth was confirmed and measured independently in this way. Many subsequent orbital spacecraft have been tracked very carefully, and the perturbations in their orbits have been used to calculate some of the characteristics of the geoid.

Before Skylab, the problems associated with using the orbits of other spacecraft to determine the geoid were becoming increasingly difficult to solve because greater accuracy was required. This difficulty arises because the effects of the smaller scale variations of the geoid fade rapidly with height and hence have little effect on the orbital spacecraft. A lower limit exists at which spacecraft can be orbited before the drag of the upper atmosphere causes them to slow down and fall back to Earth; hence, important details of the geoid cannot be sensed. Programs were developed to generate a geoid by combining spacecraft measurements and the limited number of measurements of gravity variability over the surface of the Earth. The results led to numerous geoids, one being the Marsh-Vincent geoid (or the Goddard Earth Model 6 (GEM-6)), shown in figure 5-1 (ref. 5-1).

The GEM-6 geoid contours the departures of the surface of the ocean, as continued by theory into the continents, in units of meters as if they were measured in terms of the distance from the ellipsoid of revolution. Several features are noteworthy. For example, to this level of definition, the surface of the ocean is 100 m closer to the center of the Earth at a point in the Indian Ocean than is the ellipsoid of revolution. Other areas are as much as 40 or 50 m farther from the center of the Earth than is the ellipsoid of revolution. This figure does not represent the correct geoid because the complete geoid has yet to be measured; nevertheless, many of the major features are correct.

Before the Skylab missions, analysis of orbital data made it possible to distinguish approximately 20 geoid oscillations around the Earth; the shortest oscillation wavelength that could be resolved was approximately 2000 km at the Equator. (The use of precisely obtained gravity measurements allowed shorter wavelengths to be determined, but gravity data are expensive and difficult to obtain.) Altimeter data from Skylab resolved oscillations that are 20 km long and thus produced an improvement in spatial resolution by a factor of 100 in the horizontal dimension.

An investigation of the problem of combining Skylab tracking data and calculations of the orbit with the altimeter measurements of the distance between Skylab and the ocean surface was conducted by Mourad et al. (ref. 5-2). The accurate calculation of the Skylab orbit
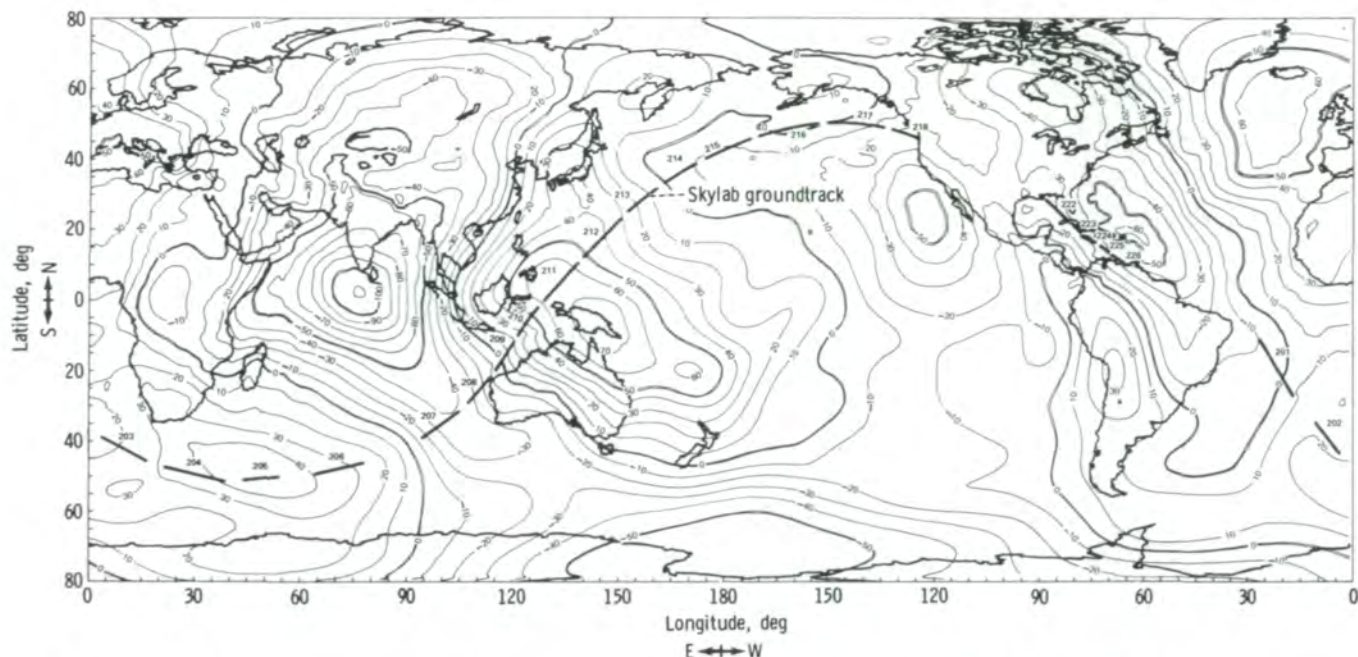
FIGURE 5-1.—The GEM-6 detailed gravimetric geoid with around-the-world groundtrack of a Skylab 4 pass beginning off the coast of Brazil and ending in the Caribbean Sea (from ref. 5-1). Contour intervals are 10 m; groundtrack segments are numbered from 201 to 226.

over a short arc depended on precise knowledge of the spacecraft location and velocity at the start of the arc. It was shown that, for reference ellipsoids that differ in mean radius by 1 part in 60 000 and in flattening by 5 parts in 30 000, the calculated altitudes for Skylab would differ by 10 m after traveling only 10° of longitude. The actual altitude of Skylab varied by as much as 1 km over a 1000-km arc. It is necessary to determine these altitudes to an accuracy of a few meters before the full potential of spacecraft altimetry can be realized. Large bias terms for different Z-axis-to-local-vertical passes indicated large differences from one orbital segment to another.

According to Mourad,

The bias terms recovered for different segments [were] significantly different and had little or no correlation with each other. The general agreement between the altimetry and the a priori geoid profiles demonstrates the viability of the altimetry technique to determine the marine geoid. The short periodic deviations between them, considering their magnitudes, [reflected] the high frequency components of the geoid. It is also evident that

the altimetry sensor is very sensitive to the local geoidal features such as those corresponding to trenches, ridges, and sea mounts. Excellent agreement between the results obtained for the same place at different times (near the Puerto Rico Trench) indicates the self consistency and precision of the altimeter except in the bias term.

The high-frequency components of the geoid are nevertheless easily detected. Examples from the S193 altimeter are given by McGoogan et al. (ref. 5-3). The first pass to be discussed began as the Skylab spacecraft crossed the east coast of the United States and proceeded on a southbound orbit across the island of Puerto Rico. The height of the mean sea level relative to the reference ellipsoid as obtained from the difference of the altimeter range measurement and the computed satellite orbit is shown by the irregular line in figure 5-2(a). The altimeter trace fluctuates as much as 1 m vertically over the distance that was measured. These irregularities are caused by the difficulty of measuring time accurately for the noisy return of the radar pulse in which a change of 1 nanosecond represents a 15-cm change in range.
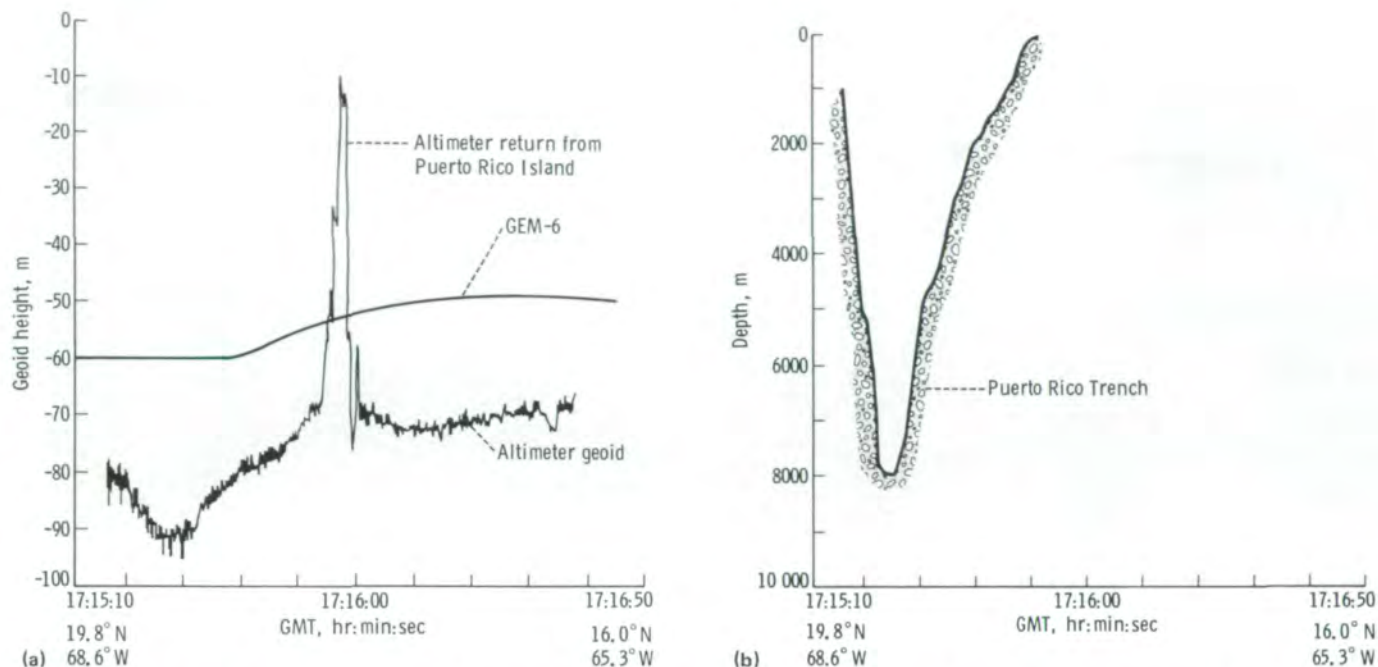
FIGURE 5-2.—Comparison of S193 altimeter data, reference ellipsoid (GEM-6), and submarine topography for southbound Skylab 2 pass 4 over Puerto Rico on June 4, 1973. (a) Measured and theoretical geoids. (b) Corresponding submarine topography for the Puerto Rico Trench.

A smooth curve drawn through the altimeter geoid trace would very nearly represent the level surface of the ocean. Over the relatively short distance of approximately 220 km, the surface of the ocean is 12 m closer to the center of the Earth above the 8-km-deep Puerto Rico Trench (fig. 5-2(b)) because of the variation in the forces that produce the "level" sea surface. On the eastern side of the island is a slight dip but nothing as pronounced as the variation over the trench. A section of GEM-6 data along the same orbit is reproduced in figure 5-2(a). This trace differs from the altimeter measurement by 20 m east of Puerto Rico and by 30 m near the lowest part of the altimeter trace. The 20-m difference could have been caused by an error in locating Skylab in altitude. However, displacing the GEM-6 curve so that it coincides with the right-hand side of the altimeter geoid would still leave substantial differences for the geoid over the Puerto Rico Trench. The EREP passes over the Puerto Rico Trench were repeated many times for slightly different sections of the trench and similar results were obtained each time.

In figure 5-3(a), the altimeter geoid trace is shown from the pass over the Jaseur Seamount in the South Atlantic Ocean, east of Vitória on the coast of South America. The water around the seamount is 4 km deep (fig. 5-3(b)). The seamount rises to within approximately 200 m of the sea surface. As shown in figure 5-3(a), the sea surface rises approximately 10 m with respect to the center of the Earth over this seamount. The reference geoid from figure 5-1 is essentially at the same distance from the center of the Earth along this entire track and, as the altimeter measurements indicate, there is a difference of 12 m from the left side to the right side of figure 5-3(a). Altimeter data from a pass over a seamount near the Cape Verde Islands (fig. 5-4) show the same phenomenon. The sea surface moves away from the center of the Earth by as much as 10 m. A smooth curve through the altimeter geoid would represent very closely the level surface of the sea except for minor effects of, at most, 1 m in these areas.

One of the striking features of the sea bottom is the continental shelf that is adjacent to some, but not necessarily all, continental coasts. Off the eastern coast of the United States in the general area of Florida, the edge of the shelf is called the Blake Escarpment. As shown in figure 5-5(b), the coastal water is initially shallow, then deepens to 1000 m, and finally, over a very short distance, deepens to approximately 4800 m.
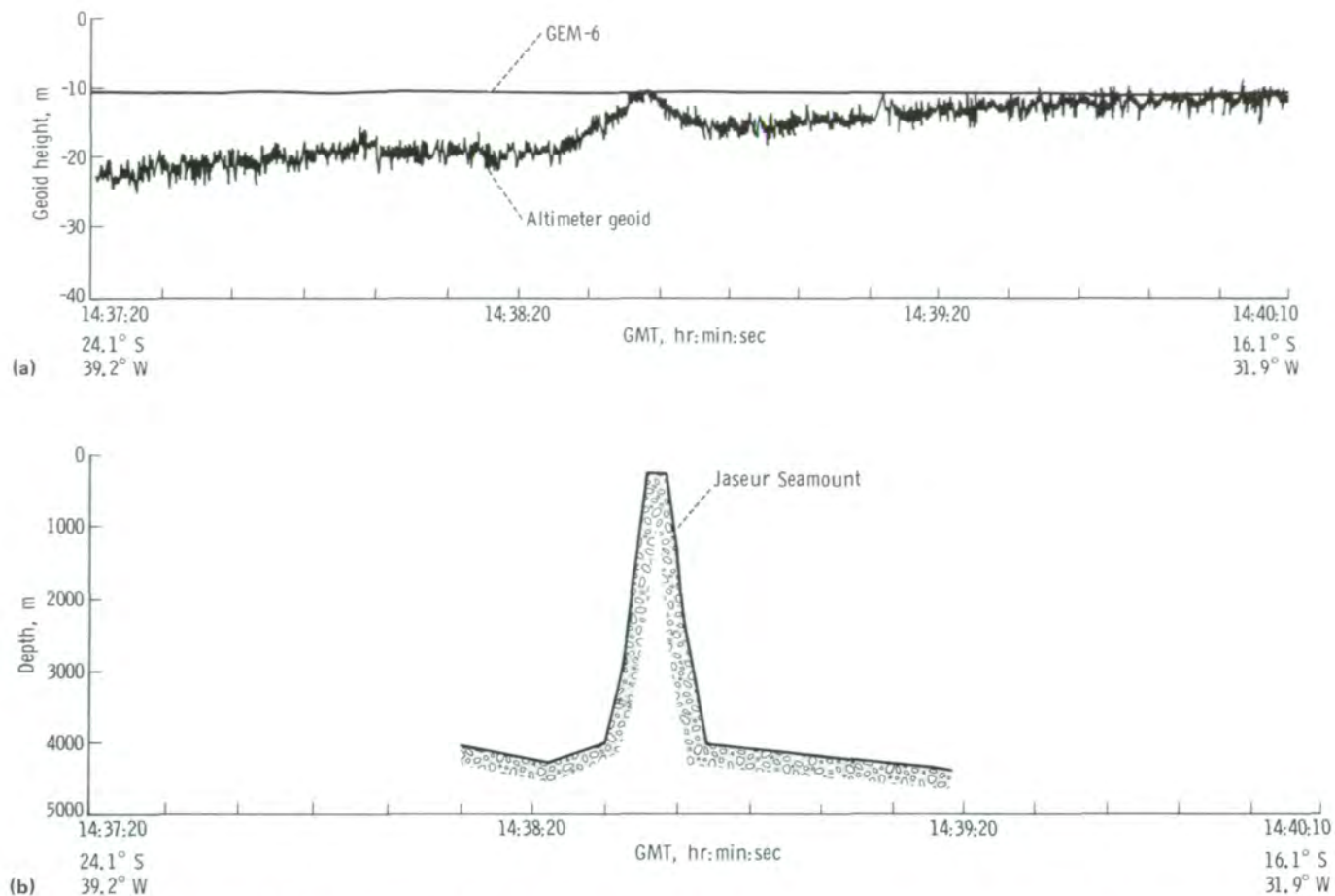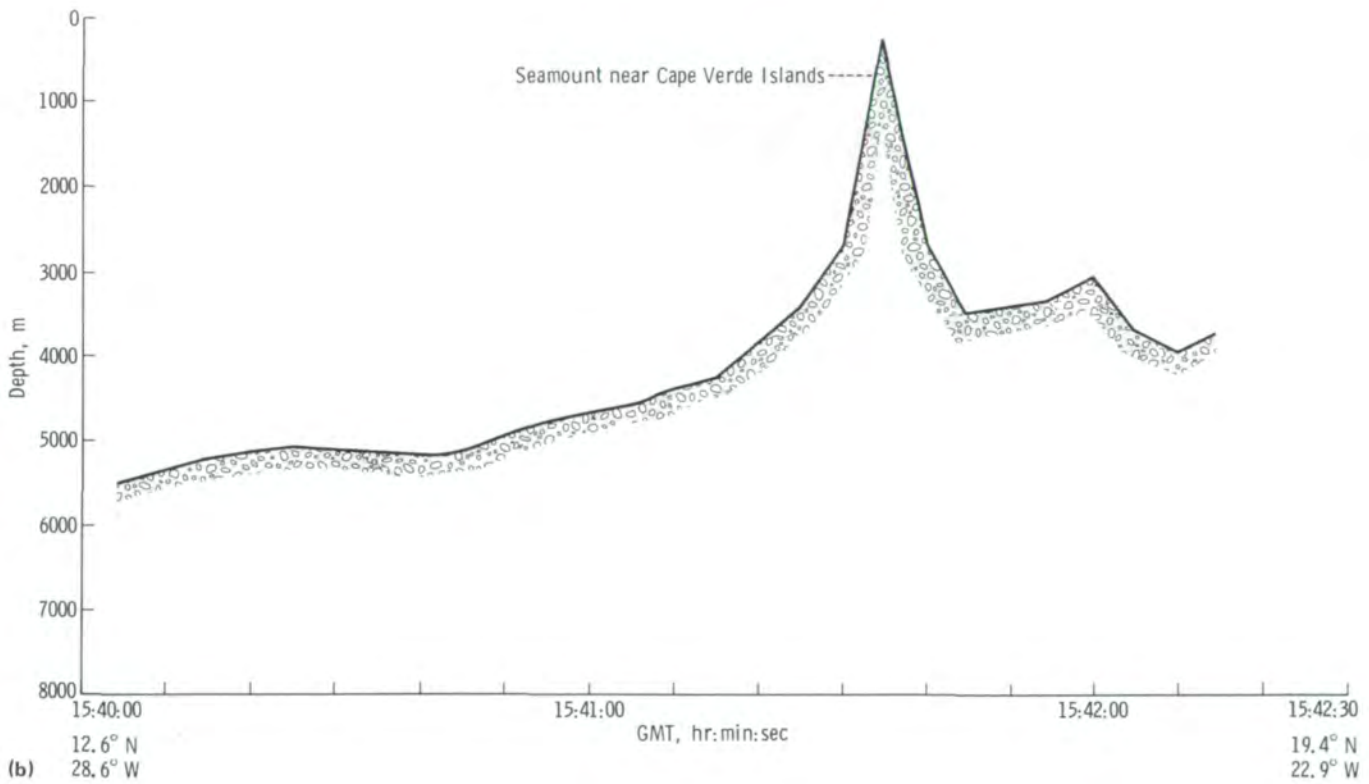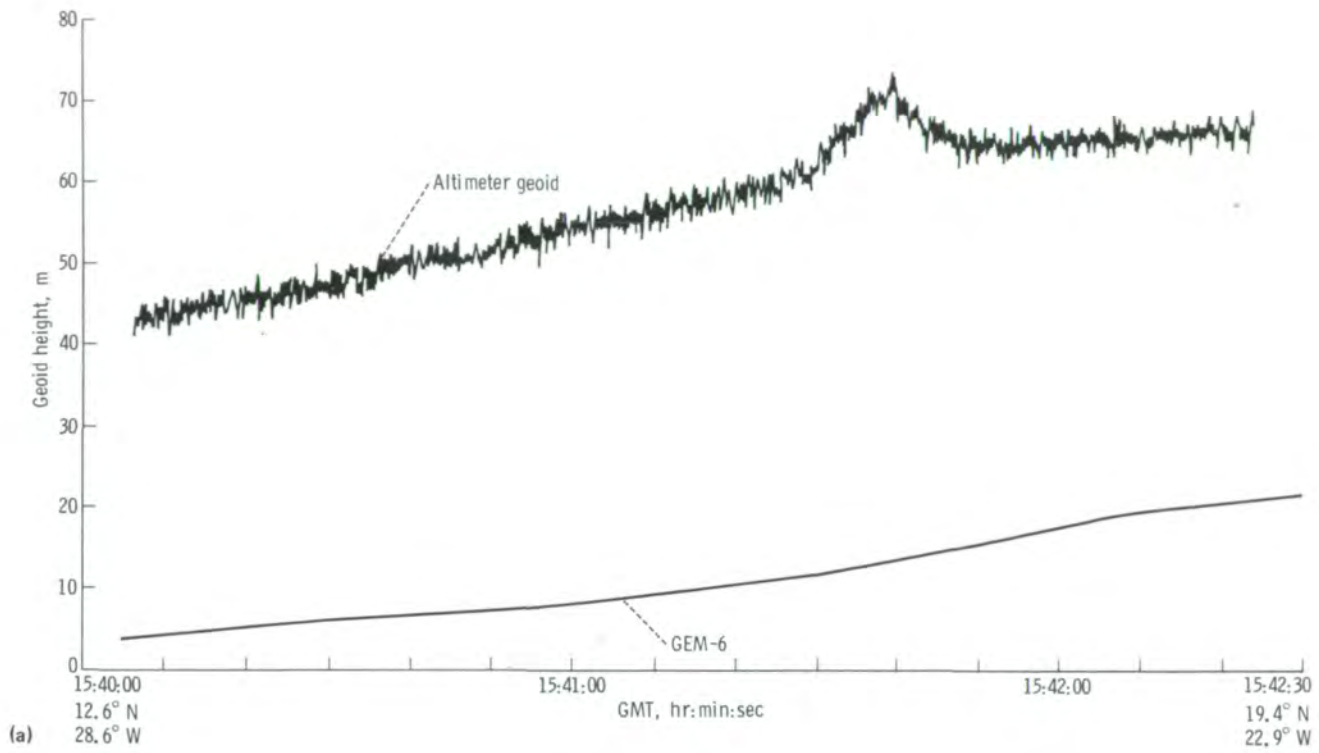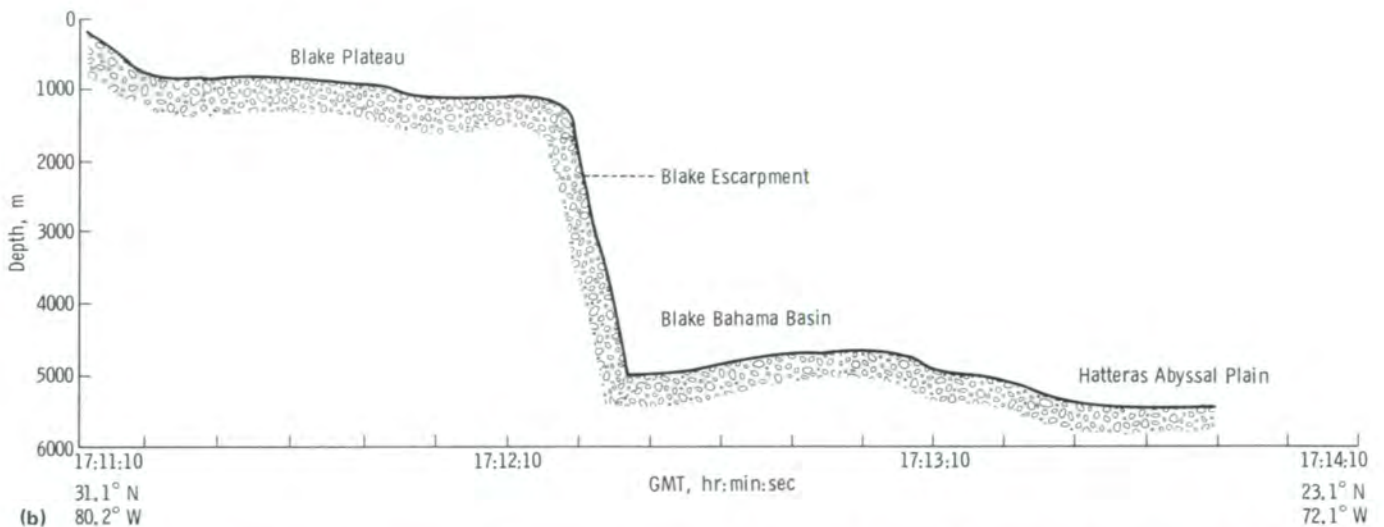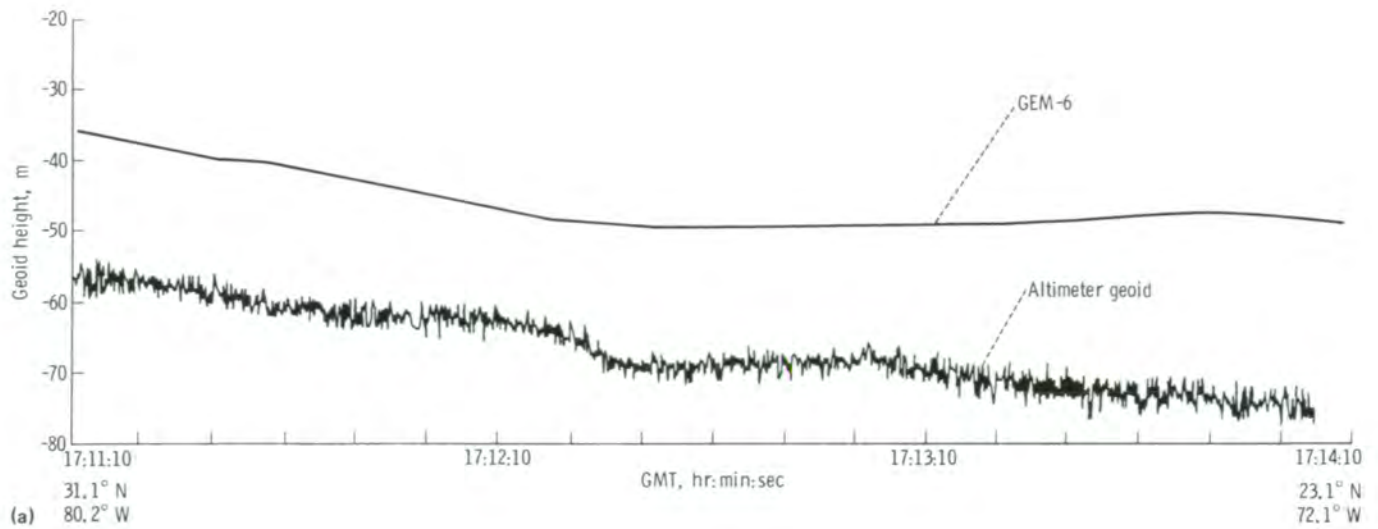
FIGURE 5-3.—Comparison of S193 altimeter data, reference ellipsoid (GEM-6), and submarine topography for northbound Skylab 3 pass 22 over Jaseur Seamount on September 2, 1973. (a) Measured and theoretical geoids. (b) Corresponding submarine topography.

It is important to note that the altimeter trace (fig. 5-5(a)) varies relatively slowly over the western portion out to the edge of the depth increase. Over the Blake Escarpment, the geoid trace moves toward the center of the Earth by 10 m over a very short distance and then rises slightly over the rise in the sea floor to the east. The GEM-6 geoid (fig. 5-1) does not show this very steep change over the Blake Escarpment.

Most of the time, the EREP was operated in the Earth-viewing mode for only 5 or 10 minutes, after which the Skylab spacecraft was returned to the solar-inertial mode. However, on January 31, 1974, the EREP was operated in the Z-axis-to-local-vertical mode for one complete Earth orbit; 26 segments of the geoid were determined for this orbit. (The locations of 23 of the 26 altimeter measurements are plotted on the

GEM-6 model in figure 5-1.) The theoretically derived geoid from spacecraft and gravity data locates major features of the geoid and, along this subspacecraft track, the total range in the distance by which the geoid differs from the ellipsoid of revolution is approximately from −40 to 70 m. In general, the S193 altimeter measured a position for the geoid that reasonably approximated the theoretical curve, as shown in figure 5-6. The greatest discrepancies are for segments 202, 203, 222, and 223.

FIGURE 5-4.—Comparison of S193 altimeter data, reference ellipsoid (GEM-6), and submarine topography for northbound Skylab 3 pass 24 over the Cape Verde Islands on September 3, 1973. (a) Measured and theoretical geoids. (b) Corresponding submarine topography. ⟶

(a)

15:40:00 12.6° N 28.6° W

GMT, hr:min:sec

15:42:30 19.4° N 22.9° W

Seamount near Cape Verde Islands

(b)

15:40:00 12.6° N 28.6° W

GMT, hr:min:sec

15:42:30 19.4° N 22.9° W

FIGURE 5-5.—Comparison of S193 altimeter data, reference ellipsoid (GEM-6), and submarine topography for southbound Skylab 2 pass 4 from the Blake Escarpment to the Hatteras Abyssal Plain on June 4, 1973. (a) Measured and theoretical geoids. (b) Corresponding submarine topography.

Each of these bursts of rapid fluctuations in the altimeter measurement, indicated as a pass on this diagram, could be expanded into a set of curves similar to those previously shown. Several segments during this around-the-world pass also showed some very interesting results.

Segments 209 and 212 and the corresponding submarine topography are illustrated in figures 5-7 and 5-8, respectively. Segment 209 shows no striking correlation

with the submarine topography such as might be expected from the sharp increase in the depth of the ocean represented on the left side of figure 5-7(b). Of interest is that the theoretical geoid (GEM-6) agrees with the altimeter geoid represented on the right side of figure 5-7(a) and departs significantly from it (by approximately 10 m) on the left side.

The deepest point in the ocean is in the Marianas Trench. The S193 altimeter was operated over this
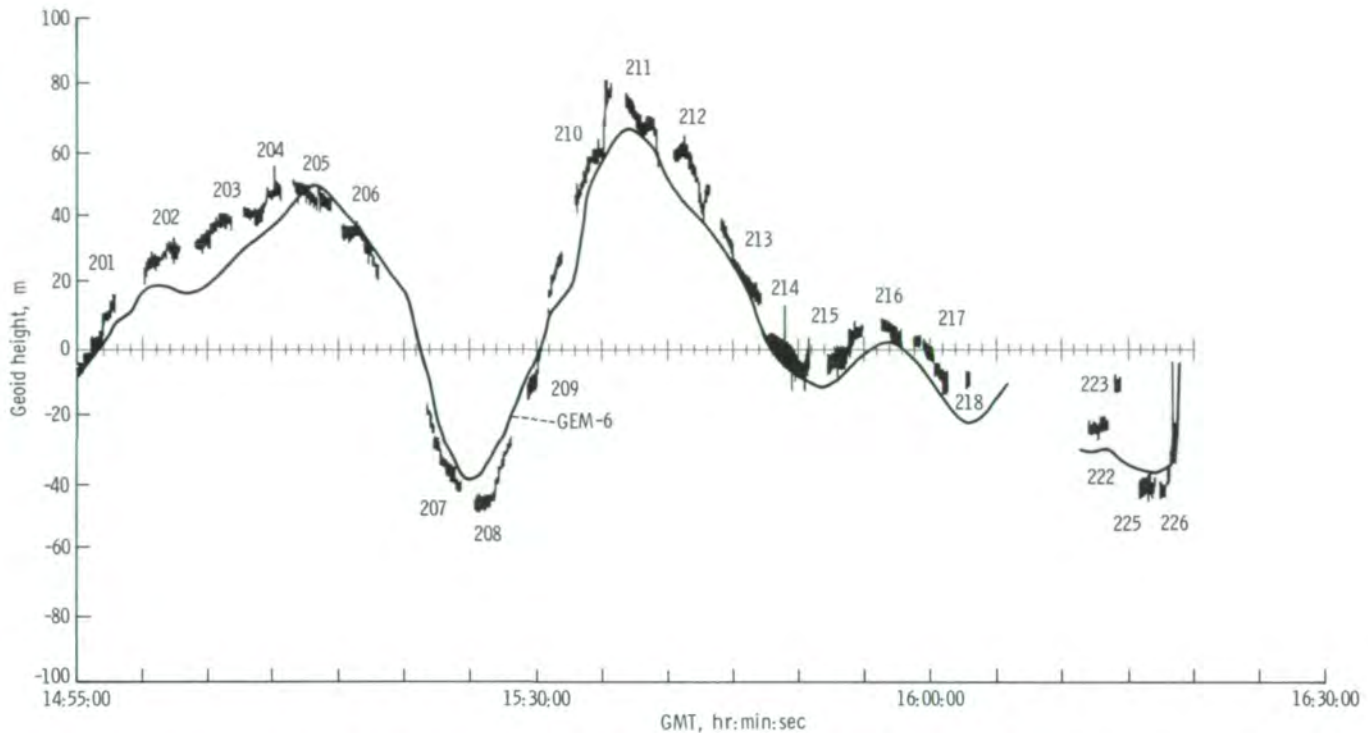
FIGURE 5-6.—Comparison of S193 altimeter data segments and reference ellipsoid (GEM-6) for Skylab 4 around-the-world pass 97 on January 31, 1974.

trench but in a region only approximately 5500 m deep (fig. 5-8(b)). Nevertheless, the Marianas Trench produced a very sharp *V*-shaped feature in the location of the geoid (fig. 5-8(a)). Such effects on the geoid also occurred over the Mid-American Trench (figs. 5-9(a) and 5-9(b)).

The variation of the geoidal surface toward and away from the center of the Earth, as a response to variations in submarine topography, is clearly indicated in figures 5-2 to 5-5. The sea surface need not follow every rise and fall on the sea bottom as was shown in these illustrations. Some portions of the Earth's crust are in isostatic equilibrium; that is, they have risen or sunk as a function of mass to achieve an equilibrium position. Other portions of the crust near and at seamounts and oceanic trenches have not attained this equilibrium. If the seamounts and the trenches just illustrated were in isostatic equilibrium, the geoid would not be expected to respond to their presence. Over some parts of the ocean, this isostatic equilibrium very nearly exists and no remarkable difference in the altimeter geoid is observed over such regions (fig. 5-7).

In the preceding figures, the altimeter traces represent the level surface of the sea, except for relatively minor effects important to oceanography. These traces show that, generally, the level surface of the sea moves away from the center of the Earth over seamounts and toward the center of the Earth over trenches. The estimates of the geoid that were calculated until about 1968 did not include these important features and did not correlate very well with plate tectonics theory. When the radar altimeter concept was first proposed in 1968, Greenwood et al. (refs. 5-4 and 5-5) predicted that the altimeter would resolve the details of the geoid so well that the geoid would begin to show features that would be correlatable with plate tectonics. The illustrations that have been presented show that none of the finer scale fluctuations, such as the rapid variation over the Blake Escarpment, the rises over seamounts, and the dips over the submarine trenches, were in any previous geoidal model. They all correspond to various aspects of plate tectonics theory, and, thus, the theories of geodesy and tectonics are becoming more integrated.
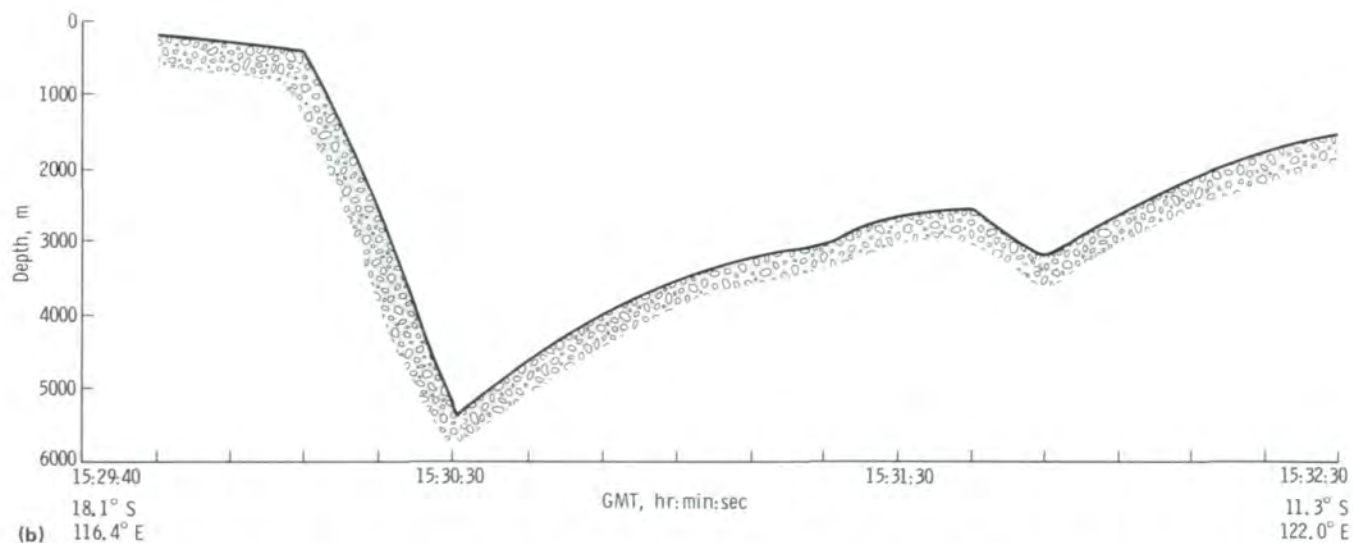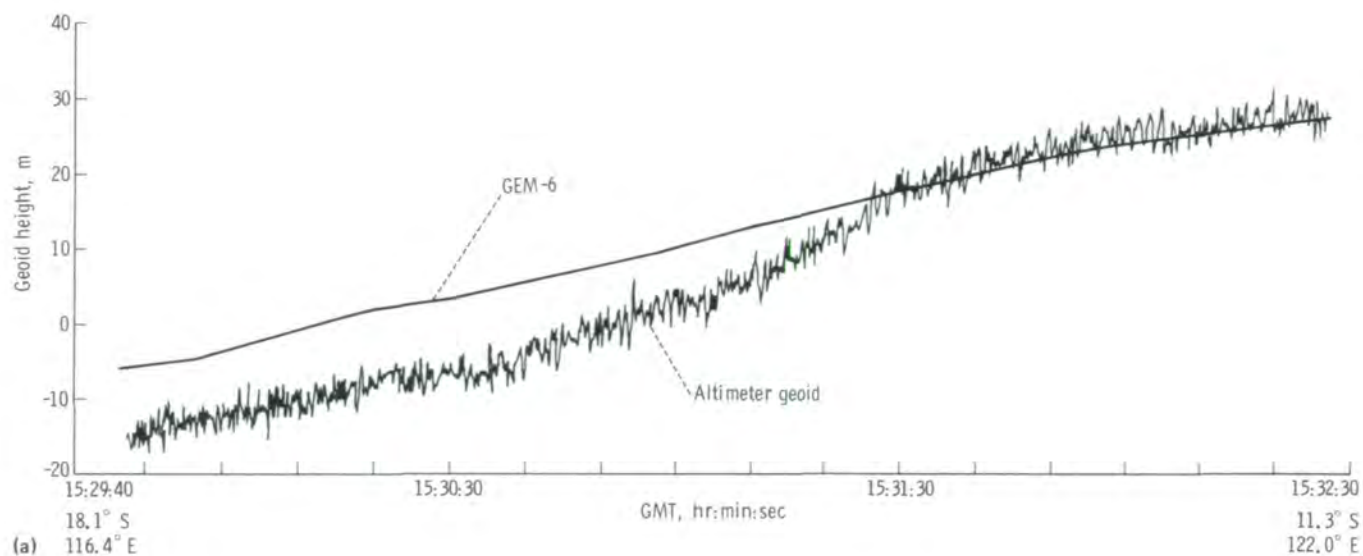
FIGURE 5-7.—Comparison of S193 altimeter data, reference ellipsoid (GEM-6), and submarine topography for segment 209 of Skylab 4 around-the-world pass 97 over the Indian Ocean. (a) Measured and theoretical geoids. (b) Corresponding submarine topography.
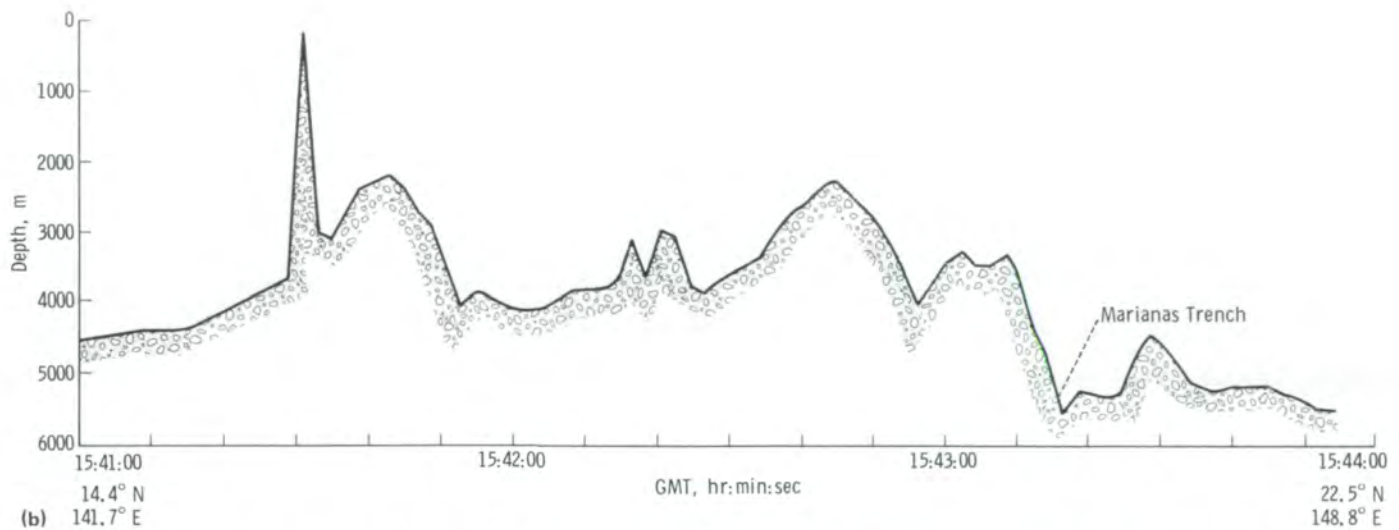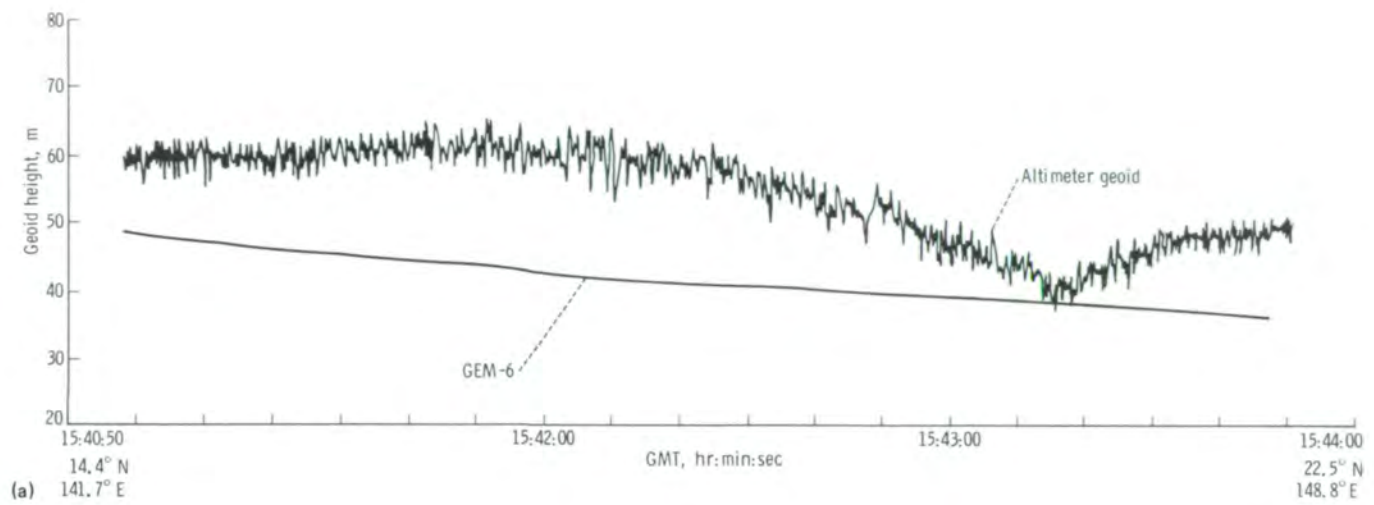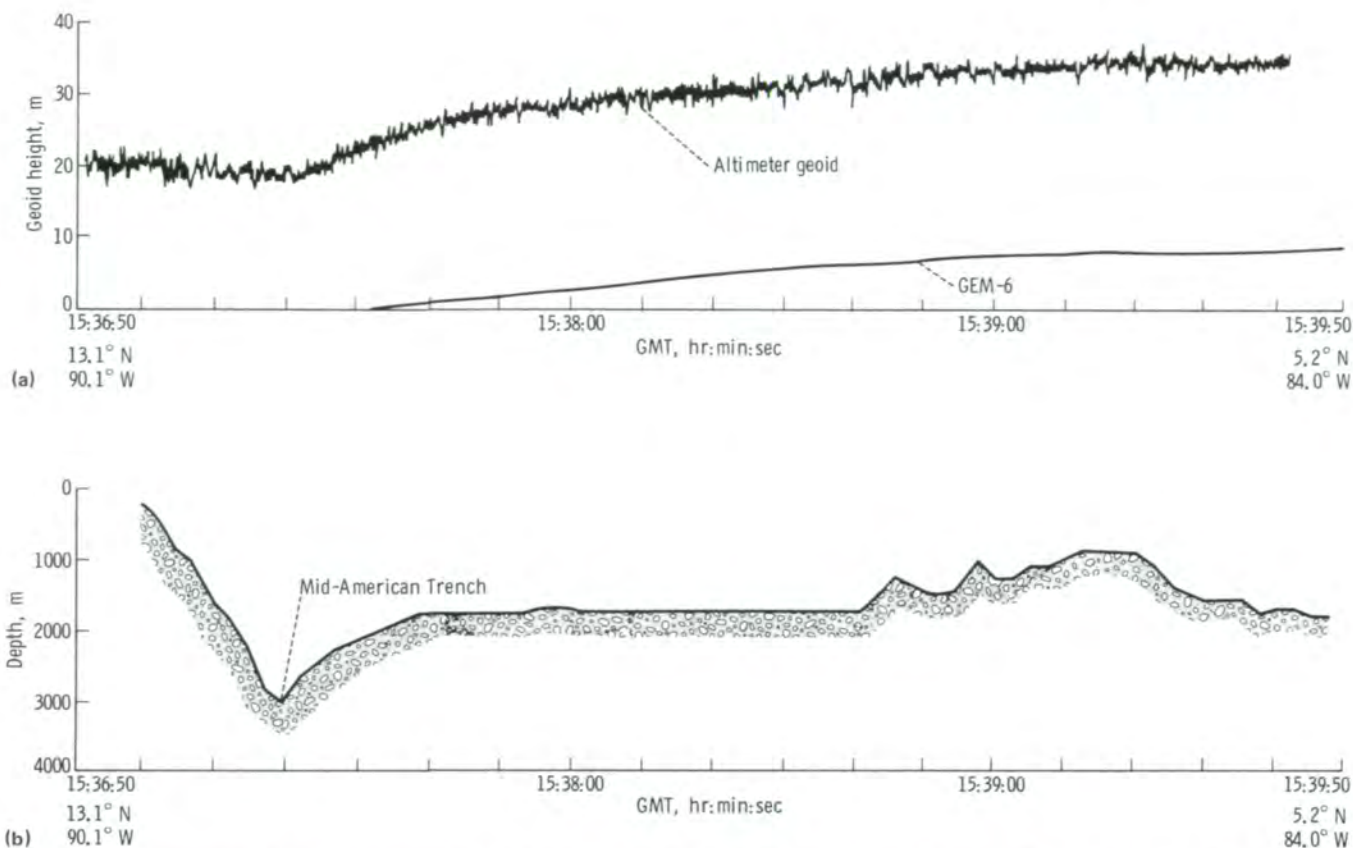
FIGURE 5-8.—Comparison of S193 altimeter data, reference ellipsoid (GEM-6), and submarine topography for segment 212 of Skylab 4 around-the-world pass 97 over the Marianas Trench. (a) Measured and theoretical geoids. (b) Corresponding submarine topography.

FIGURE 5-9.—Comparison of S193 altimeter data, reference ellipsoid (GEM-6), and submarine topography for Skylab 3 pass 18 over the Mid-American Trench on August 11, 1973. (a) Measured and theoretical geoids. (b) Corresponding submarine topography.

OCEANIC PROPERTIES

Water-Surface Temperatures

Sensing systems on operational meteorological satellites routinely acquire image data in the infrared region of the electromagnetic spectrum. From these data, temperatures of cloud tops can be determined and, if an unobstructed view exists between the satellite and the sea surface, the temperature of the sea surface can be estimated. This measurement is made using one wavelength band in the infrared. However, it is necessary to apply corrections, which are predominantly based on climatological concepts, for the intervening atmosphere.

Infrared measurement of sea-surface temperature is difficult because the surface water is undergoing evaporation and there is a very sharp gradient in temperature at the surface of the sea, such that over a verti-

cal distance of approximately 50 mm, the temperature decreases by as much as 1 or 2 K, being colder at the surface. This sharp gradient allows for the flow of heat from the deeper layers of the ocean through the air/sea interface into the atmosphere. What is actually measured is some temperature related to this skin temperature, so a small correction for this effect must be made.

The basic problem, however, is that, as the radiation from the sea surface travels toward the sensor on the satellite, it is both attenuated by the atmosphere and contaminated by atmospheric emission, with the result that signal strength at the satellite is usually lower than it would have been had it traveled through a vacuum. The overall effect is that the infrared temperatures sensed by the recording instrument can be as much as 8 K cooler than the temperature of the sea surface. The single wavelength band measurements can be corrected for this effect; but, because the correction depends on

the actual properties of the intervening atmosphere, occasional errors in measuring the properties can produce unacceptable sea-surface temperatures.

The infrared temperatures of a water surface that would be sensed by integrating over one wavelength band of the Infrared Spectrometer (S191), as compared to integrating over another wavelength band, differ substantially because the extinction coefficients for the intervening atmosphere are functions of wavelength. The basic concept of the experiment conducted by Anding and Walker (ref. 5-6) was to sense two different temperatures in terms of the measurements at two different wavelengths and to calculate their relative extinction coefficients. Then, on the basis of valid linearizing assumptions, the two values of the temperature as plotted against the two relative extinction coefficients were connected by a straight line to extrapolate to the condition in which the relative extinction coefficient would be zero.

This concept was tested in two regions for which surface truth was available, one off Key West, Florida, with surface-truth data obtained on January 8, 1974, and the other in Monroe Reservoir with surface truth obtained on June 10, 1973. In the Key West test, the actual sea-surface temperature was 296 K; the raw infrared measurements at the spacecraft indicated, for the most nearly transparent region of the atmosphere in the infrared, a temperature near 290 K; for the next most transparent region, approximately 289.5 K; and for the more opaque regions, approximately 286.5 K. The relative extinction coefficients were approximately 0.2, 0.33, and 1.4, respectively. When a straight line is fitted to these data, the intercept for a zero relative extinction coefficient is 293.6 K. The error in the method based on the Skylab measurements was thus 2.4 K; if the raw infrared temperatures for the best window had been used, a 6-K difference would have been measured in the infrared. As a check, a model of the theory produced a value of 294.2 K, which indicated some additional sources of error in the S191 data.

A similar experiment was conducted at Monroe Reservoir near Salem, Illinois, where the in situ temperature was measured as 298.0 K. The model yielded 298.6 K, and the value computed from the Skylab measurements was 297.7 K. In this instance, the measurement and the theory differed by only 0.3 K (fig. 5-10).

In addition to Skylab data, Nimbus data (specifically infrared interferometer spectrometer (IRIS)) were used
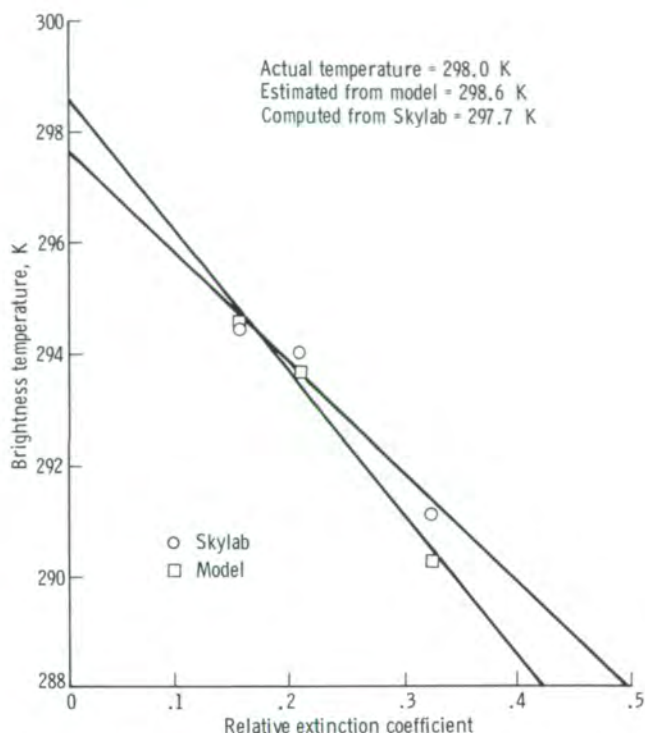

FIGURE 5-10.—Brightness temperature plotted against extinction coefficient for Monroe Reservoir near Salem, Illinois, using S191 data of June 10, 1973 (from ref. 5-6).

to test this hypothesis. It was found that similar results could be obtained with the IRIS data.

The results of this particular experiment show the value of bands in the infrared region for measuring sea-surface temperatures. The next generation of Tiros satellites will contain two bands in the infrared region for more accurate sea-surface temperature measurements.

Temperature, Salinity, and Sea-Surface Roughness

The presence of clouds is a problem in remote sensing of changes in ocean temperature and salinity because clouds preclude the measurement of temperature in the infrared. The main reason for studying the relatively low microwave frequencies, such as those used with the Skylab L-Band Radiometer (S194), is that clouds and rain should have a minor effect on the measurement; hence, in theory, sea-surface temperature should be measurable through clouds if an appropriately chosen frequency is used.

The strength of the passive microwave signal received by the S194 was a function of numerous physical variables as studied by Hollinger and Lerner (ref. 5-7). These variables include the amount of sunglint reflected by the sea surface back to the antenna and the variations in temperature, salinity, and sea-surface roughness. The S194 data were studied in such a way as to isolate these variables to ascertain whether or not, upon removing the effects of all but one cause, the variability due to that cause could be detected.

When operated over the ocean, the S194 obtained data for conditions in which the oceanic salinity varied from approximately 32 to 36.5 parts per thousand. The sea-surface temperature as provided by the Fleet Numerical Weather Central varied from approximately 274 to 301 K, and the windspeed (the cause of sea-surface roughness) varied from 0.5 to 24 m/sec.

Hollinger and Lerner developed techniques to calculate the microwave temperature when the salinity, windspeed, and temperature are known. Then, the effects of two of these three variables were removed so that the remaining one could be studied. Reflected "sunlight" at this wavelength was eliminated simply by not using those data in which it was present. The dependence on salinity was quite weak, and the scatter in the microwave temperatures, after removal of windspeed and temperature effects, was 2 to 3 K about the theoretical curve. As the salinity varied from 32 to 37 parts per thousand, the theoretical temperature curve decreased from 98 to 95 K for a variation of 3 K. The temperature scatter was larger than the range of the salinities.

Near the mouths of rivers and estuaries, where the salinity can typically increase from values near zero in freshwater to 32 to 34 parts per thousand over 15 or 30 km as the ocean is approached, changes in salinity could be detected by an instrument having high spatial resolution. Because oceanographers require salinity measurements to two significant figures past the integer values (in parts per thousand), passive microwave systems are not appropriate remote sensors for salinity measurements in the open ocean.

The sensitivity of the S194 to variations in sea-surface temperature was also studied. The theoretical curve for the antenna temperature that would be measured by the S194 varies from approximately 96 K near a 273-K ocean temperature, through a modest maximum 0.5 K higher at a 288-K ocean temperature, and then dips to 94 K at an ocean temperature of 300 K. Because of the excessively large point scatter throughout this range, it was concluded that the S194, or any other instrument operating at a frequency of 1.4 GHz, was not suitable for measuring either salinities or temperatures of the sea surface on the open ocean.

The last ocean variable studied (ref. 5-7) in S194 measurements was the dependence of the passive microwave temperature on windspeed. The passive microwave temperature increased from approximately 96 K to approximately 103 K as the windspeeds varied from 2.6 to 25 m/sec for the passes that were studied. A regression line yielded an equation indicating that the passive microwave temperature increased at a rate of 0.31 K per 1-m/sec increase in windspeed. The regression equation that was obtained for antenna temperature is given by $T_a = 0.31 W + 95.2$, where W is the windspeed in meters per second. The mean-square difference between the windspeed predicted from the passive microwave temperature and the "observed" windspeed, after removing all these other effects by means of theoretical considerations, was approximately 4 m/sec. The temperature varied approximately 10 or 15 percent about an average value of 98 K.

All the results obtained in this investigation were anticipated, except for the relatively high scatter of the data. The theories concerning instrument measurement capabilities were verified remarkably well. The experiment was successful in verifying the theory of the microwave emission of the sea surface at a frequency of 1.4 GHz. With the theory confirmed at this particular frequency, measurements at a different frequency, at which a greater sensitivity to variations in sea-surface temperature exists, may ultimately permit the determination of sea-surface temperature through clouds. In fact, two five-frequency scanning passive microwave systems are being built for use on the Seasat-A and Nimbus satellites; theoretically, these instruments will be capable of determining sea-surface temperature, surface windspeed, and other sea-surface parameters through clouds.

Water Depth

The conventional methods of ascertaining water depth off a given coastline are sounding (dropping a line from a ship and determining when it hits the bottom) and echo ranging (sending a sound pulse to the bottom and measuring round-trip traveltime). Both methods require considerable time and extremely accurate navigation so that the position of the ship as a

function of latitude and longitude is known for each measurement. The most important areas for the determination of depth are those in which the water depth is less than approximately 30 m. Large amounts of money are spent annually by the maritime nations to update their water-depth charts, especially in areas of important harbors and active navigation. Over the course of 10, 20, or 30 years, the depths of the water in a given region can change. Sandbars can shift their location, new shoals can form, and others can be eroded away. The problem of correctly describing the depth of the water is thus an ongoing problem that requires continuous correction of navigational charts.

In ocean areas characterized by clear water, sunlight in the blue-green portion of the spectrum can penetrate to considerable depth. Although somewhat attenuated, the light can be reflected from the bottom and travel through the water to the spacecraft, if no clouds are present and if the bottom is not excessively deep. This technique is unusable where the water is turbid or discolored, but, over large areas of the ocean, bottom-reflected light can be viewed by the spacecraft and imaged by either a camera or a scanner system such as the S192. Trumbull (ref. 5-8) reported that a stereoscopic view of the bottom could be seen using S190 photographs. He stated that it is possible to separate bathymetric detail and turbid water effects by means of multispectral information in the photographs and in the multispectral scanner data. Images from the wavelength range 0.6 to 0.7 μm show only turbidity features, but images from the wavelength range 0.5 to 0.6 μm show both bathymetric and turbidity features.

According to Polcyn and Lyzenga (ref. 5-9),

The radiance observed over shallow water is the result of sunlight reflecting from the bottom and the water surface, as well as of the scattering of sunlight by the water and the atmosphere. That part of the signal resulting from bottom reflection contains information about the depth of the water through which the light has passed. In order to extract this information, one must first separate the bottom-reflection signal from the rest of the observed signal, and then determine how this signal is related to the water depth.

The two unwanted effects in the spacecraft images are the scattering of light by the intervening atmosphere and the specular reflection of diffuse skylight by the water surface. These effects produce a background signal that must be subtracted to obtain useful data. To determine the amount of unwanted signal to be subtracted from the signals where the bottom has been imaged, data must be collected over deep water where there is no bottom-reflected signal. When the unwanted signal is subtracted, a measured brightness remains that can be related to depth and other physical parameters. These parameters are the atmospheric transmittance, the solar irradiance on the water surface, the bottom reflectance, the index of refraction of water, the light attenuation coefficient of the water, the angle of observation (after refraction under water), and the solar zenith angle (after refraction under water). Some of these parameters can be calculated from theory; others have to be determined for the area in which the depth is to be computed. In particular, the attenuation coefficient and the bottom reflectance need to be determined for each area. Variations in bottom cover can cause differences in reflection.

Three methods for extracting depth information using the theory just described were developed. One was a single-band method. Another used two bands and exploited differences in bottom reflectance and underwater light attenuation differences. The third combined two bands of information in an optimum-decision technique.

The theories were applied to S192 data obtained over eastern Lake Michigan and the western coastal waters of Puerto Rico. The results of the analysis of the latter area are shown in figure 5-11. The vertical axis in the figure is logarithmic and shows the scale for the brightness of the point in the image minus the deepwater brightness level ($V - V_S$). Calibration points (squares for band 3 and circles for band 2) are points for which the depth is known. The agreement is quite good to a depth of approximately 16 m.

These theories were used to produce a bathymetric chart (fig. 5-12(a)) for the waters off the western coast of Puerto Rico with the use of S192 data from bands 2 and 3. For the same region, the conventional depth chart with soundings in fathoms is shown in figure 5-12(b). Over the Escollo Negro region, two line segments were selected for verification. Line 1450 of the digitized version (fig. 5-12(a)) was located and compared with the conventional bathymetric chart, as shown in figure 5-13. In such a verification effort, the observed depths are just as questionable as the Skylab
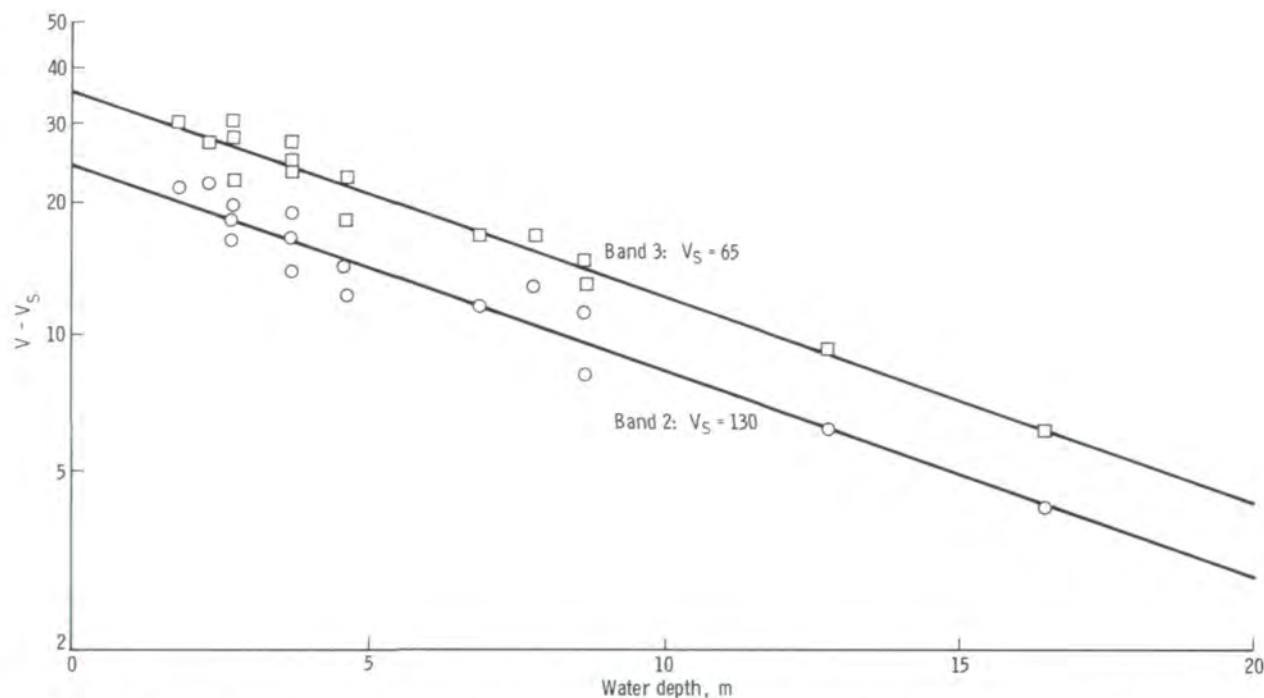
FIGURE 5-11.—Plot of S192 band 2 (circles) and band 3 (squares) signals as a function of depth for Skylab 2 pass 6 over Escollo Negro, Puerto Rico, on June 9, 1973.

depths because of the limited accuracy and the spottiness of data obtained by conventional methods. The agreement is quite good.

Applications to updating world navigational charts and mapping changes in near-shore bottom topography are forecast, based on the results that were obtained from analysis of the Skylab data.

Floating Ice

According to Campbell et al. (ref. 5-10), pack ice begins to form in the Gulf of Saint Lawrence in December and reaches its maximum extent in March, after which it begins to melt and retreat. At that time of the year, the ice interferes with shipping; therefore, it is important to understand the growth and movement of this ice as an aid to safe navigation. The gulf extends from latitude 45° to 50° N and from approximately longitude 58° to 68° W.

The Skylab orbit enabled the Skylab 4 astronauts to obtain photographic and scanner data for the program

conducted by Campbell et al. Because of the 50° inclination of the orbit, successive ascending nodes grouped near latitudes 50° N and 50° S. Consequently, Skylab passed over the gulf on January 6, 11, 14, 18, 19, 20, and 21, 1974, during daylight hours, and handheld-camera photographs were obtained on all 7 days except for January 14, when S190A and S190B photographs and S192 imagery were obtained.

The skies were unusually clear, and the photographs enabled identification of many ice, cloud, and snow features in the gulf region. In winter, many of the extratropical cyclones that form over the United States deepen as they move northward and obtain full development as they travel toward the gulf; thus, this area is one of the cloudiest and windiest regions of North America. In the polar regions of the world, the continuous and effective mapping of floating ice by either photographic or infrared imaging systems on either aircraft or spacecraft is prevented by clouds.

In supporting the Skylab data acquisition, two aircraft, an oceanographic ship, a helicopter, three air-cushion vehicles, and trucks were used to acquire
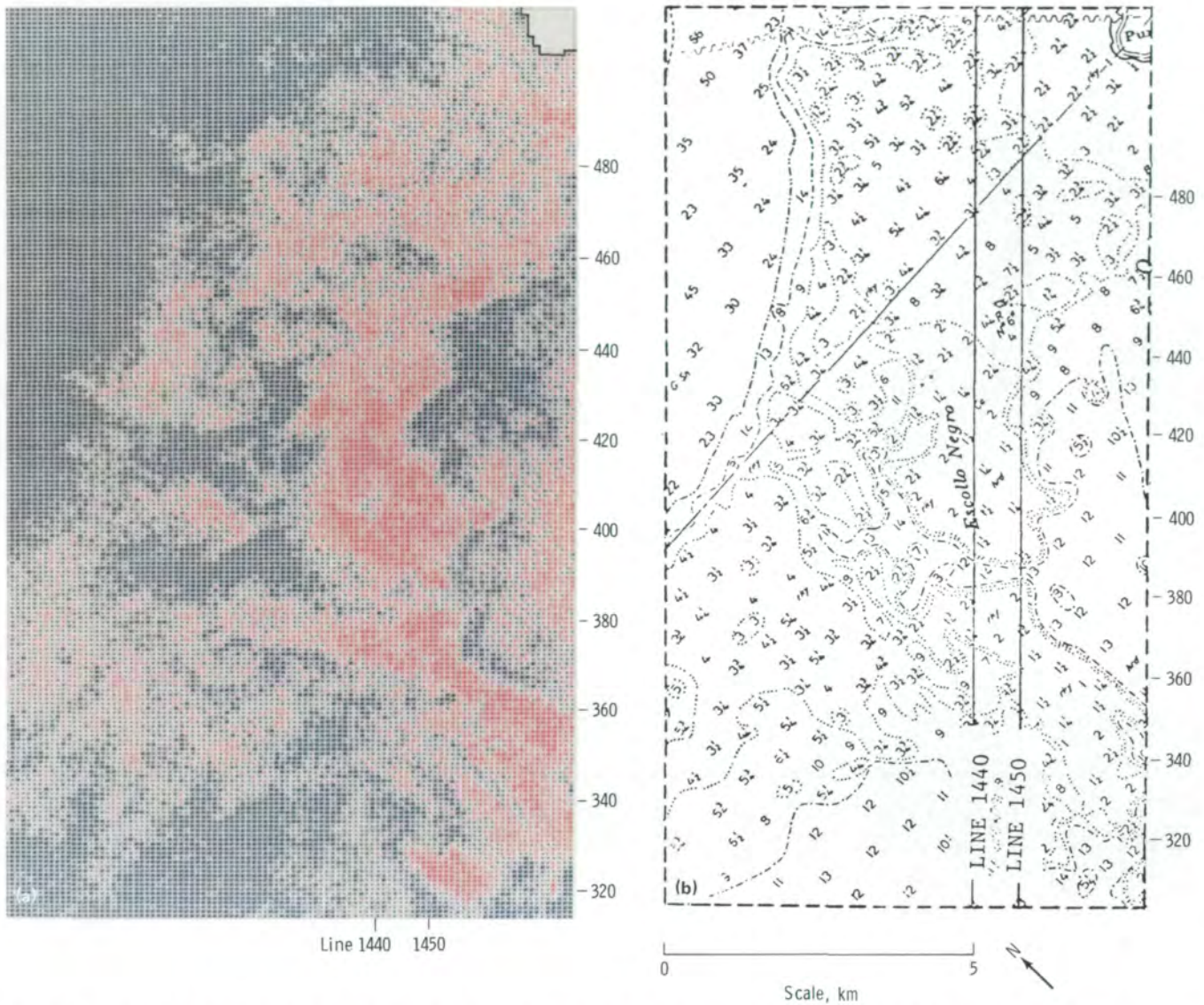
FIGURE 5-12.—Area off western coast of Puerto Rico. Punta Guanajibo is at the upper right-hand corner. The numbers to the right of figures 5-12(a) and 5-12(b) are digital point numbers plotted in figure 5-13. Although figures 5-12(a) and 5-12(b) do not coincide geometrically, the geographic area covered by both figures is approximately the same. (a) Color-coded bathymetric chart obtained from analysis of S192 band 2 and 3 data. The shallowest depths are red; the deepest, blue. (b) U.S. Coast and Geodetic Survey chart of corresponding area (from U.S. Department of Commerce chart 25671) with depths in fathoms. The line and point numbers were extrapolated from figure 5-12(a).

remotely sensed data during the Skylab overpasses. A side-looking imaging radar at a 3-cm wavelength was used on one aircraft, and a passive microwave imaging system was used on another. Other aircraft instruments included an infrared scanner, a multifrequency microwave radiometer, and two RC-8 cameras. The ships and the hovercraft were used to obtain photographs and to measure ice growth, ice thickness, and other conditions. The trucks obtained data on ice near the shores.

Examples of the spacecraft imagery obtained over the gulf from January 14 to 21, 1974, are shown in
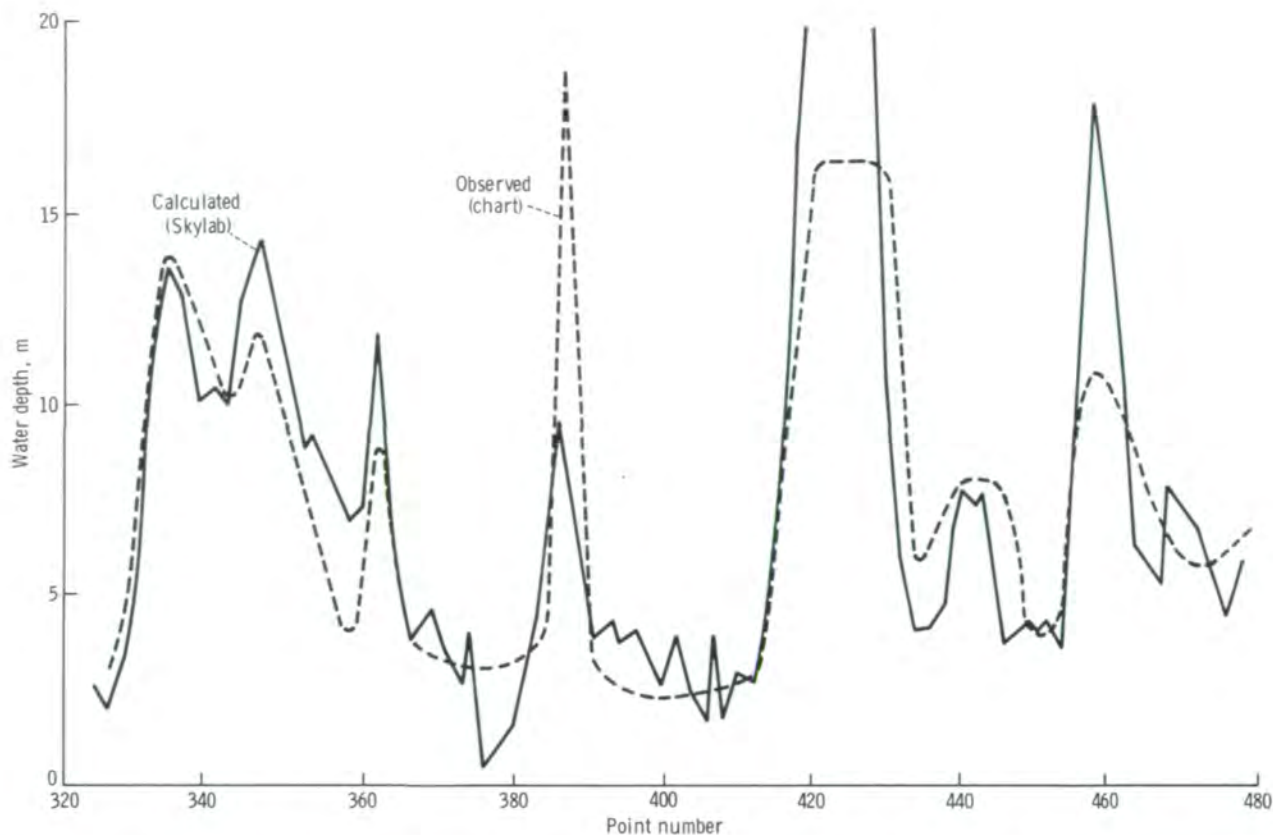
FIGURE 5-13.—Comparison of calculated and charted depths along line segment 1450 (figs. 5-12(a) and 5-12(b)) in the Escollo Negro, Puerto Rico.

figures 5-14 to 5-17. Figure 5-14 shows details of the ice such as color, leads, and coverage around Prince Edward Island on January 14. The ice cover was not as extensive as it was on January 18. The photographs on January 20 document a remarkable growth of the ice over a 2-day period; the rapid eastward extension of the area covered by ice is also evident. The extent of open water areas around Anticosti Island had changed appreciably.

Figure 5-18 is an ice reconnaissance map of the gulf for January 18. This map (one of four in ref. 5-10) is an operational real-time product that uses NOAA-2, Landsat, and aircraft reconnaissance data. Although the Skylab photographs were not used in preparation of the map, there is general agreement between the photo-

graphs and the map. Differences can be seen, however (e.g., the area of open water south of Anticosti Island). The streaming and the eddying of the ice to the southeast of Anticosti Island are important and their changes were traced from analysis of the other photographs.

The aircraft program yielded data from active and passive microwave systems that were analyzed to infer the age of the ice. An example of a side-looking imaging radar product is shown in figure 5-19. The amount of information in side-looking airborne radar imagery is impressive: pressure ridges, shear ridges, floes of all sizes, and plumes are clearly discernible. The radar data currently are useful for interpretation of the surface features of ice but cannot provide information on the age and thickness of the ice.
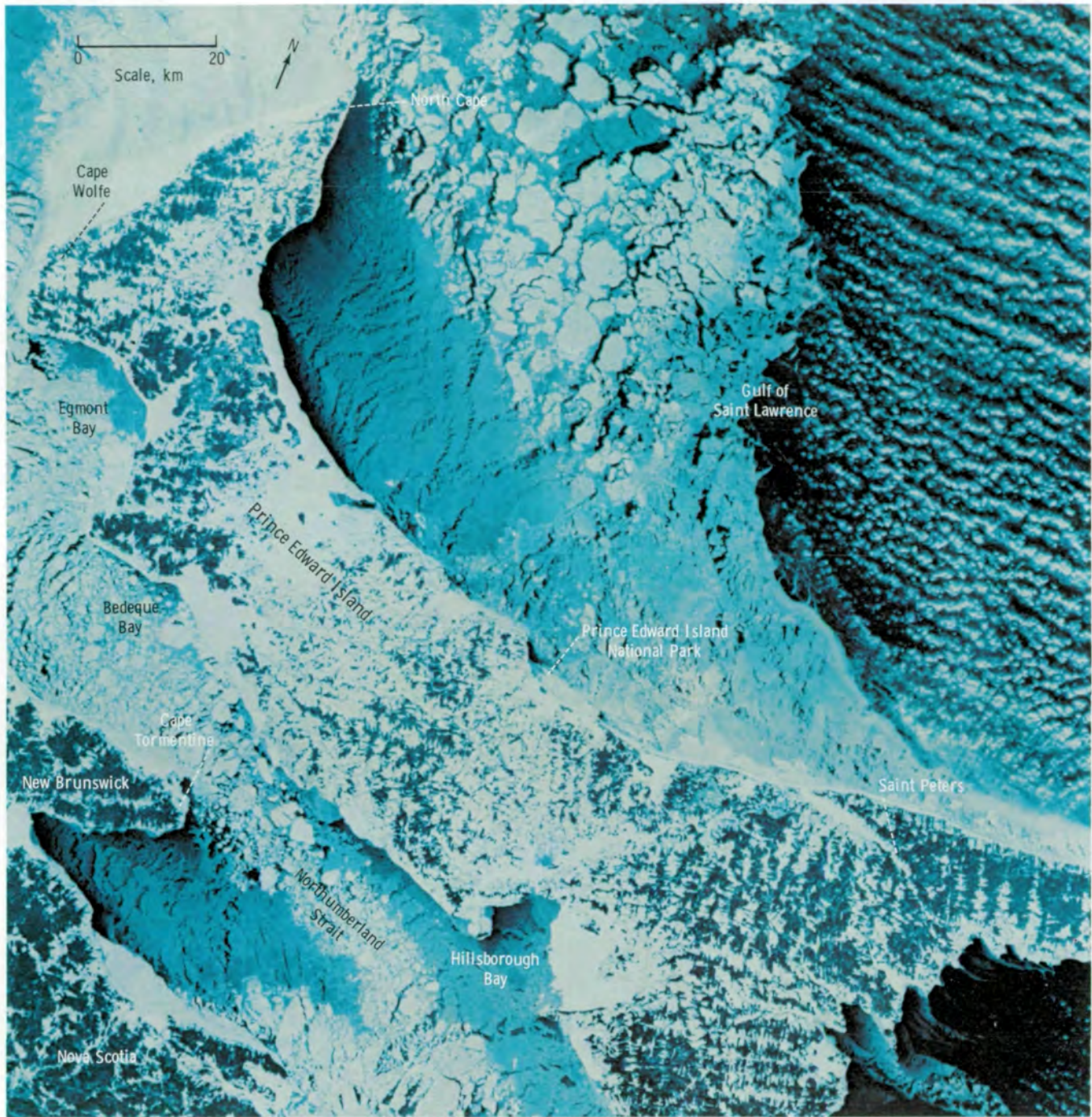
(a)

FIGURE 5-14.—Skylab 4 color photographs of Prince Edward Island and the Gulf of Saint Lawrence taken on January 14, 1974. (a) S190A (SL4-69-058). (b) S190B (SL4-93-041).
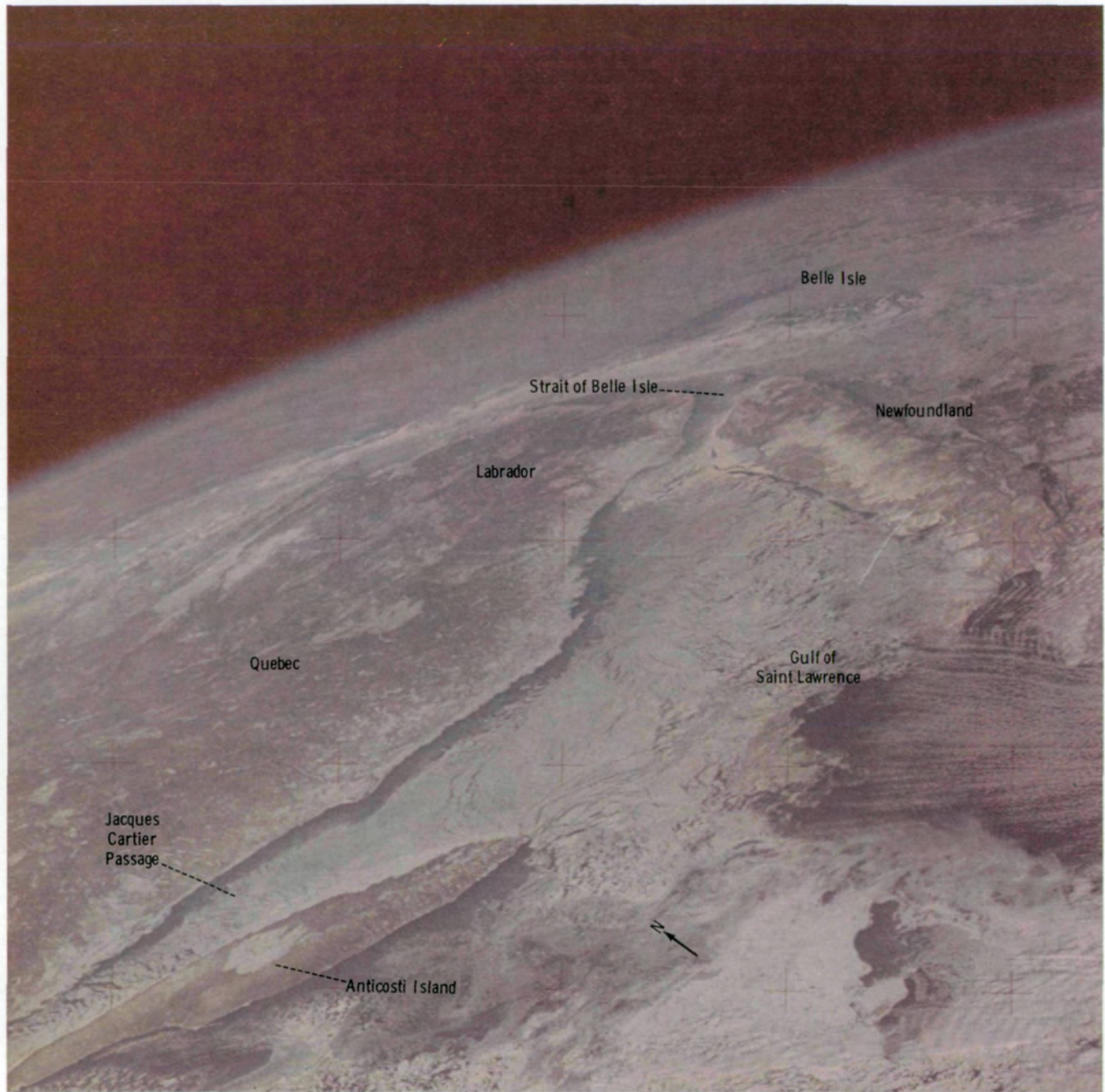
FIGURE 5-14.—Concluded.

FIGURE 5-15.—Skylab 4 color photograph (handheld camera) of the Gulf of Saint Lawrence through the Strait of Belle Isle, viewed obliquely to the northeast, taken January 20, 1974 (SL4-141-4331).
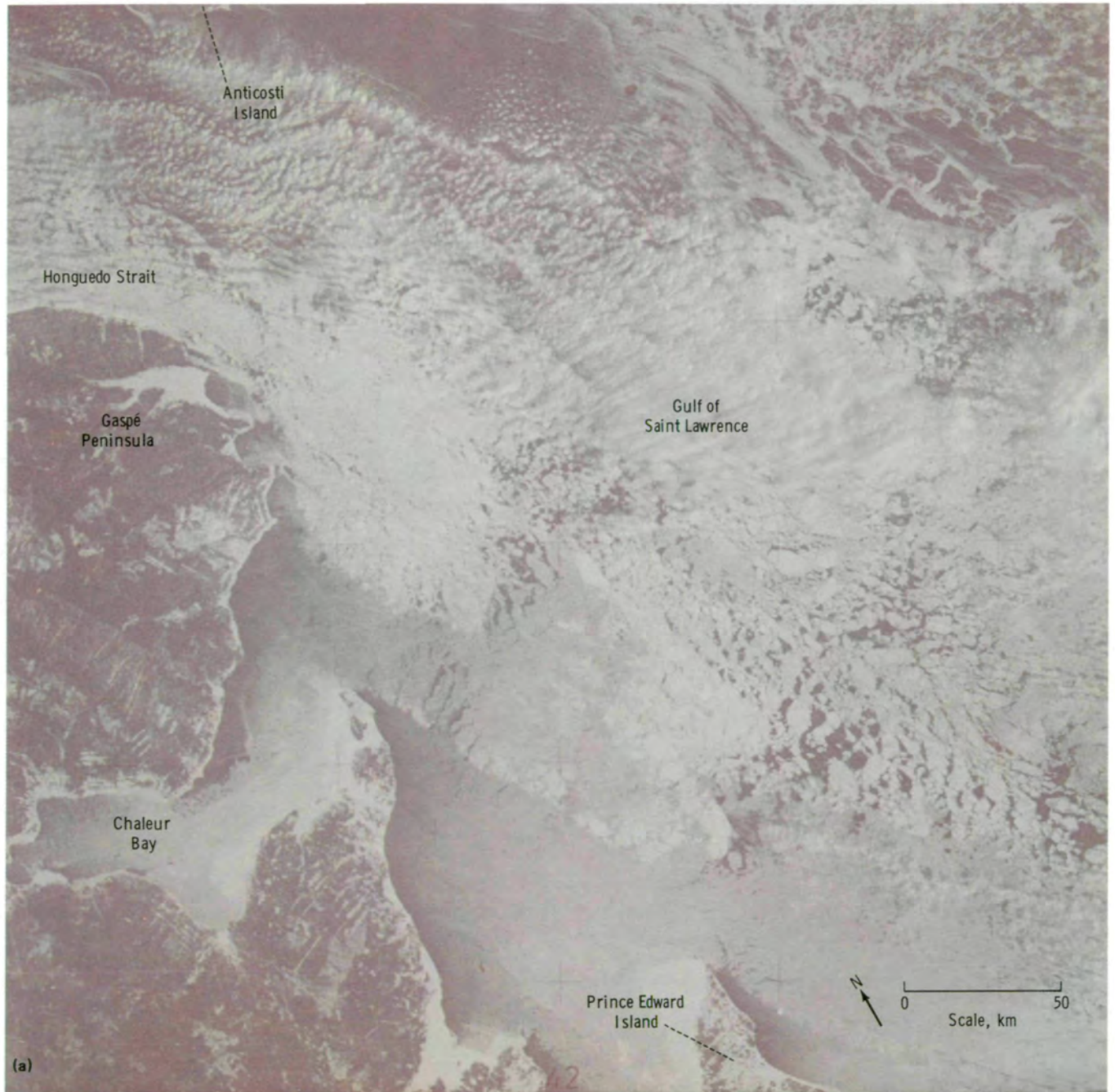
FIGURE 5-16.—Skylab 4 color photographs (handheld camera) of western Gulf of Saint Lawrence and the Gaspé Peninsula. Because of photograph obliquity, scales are approximate. (a) January 18, 1974 (SL4-140-4215). (b) January 20, 1974 (SL4-141-4321).
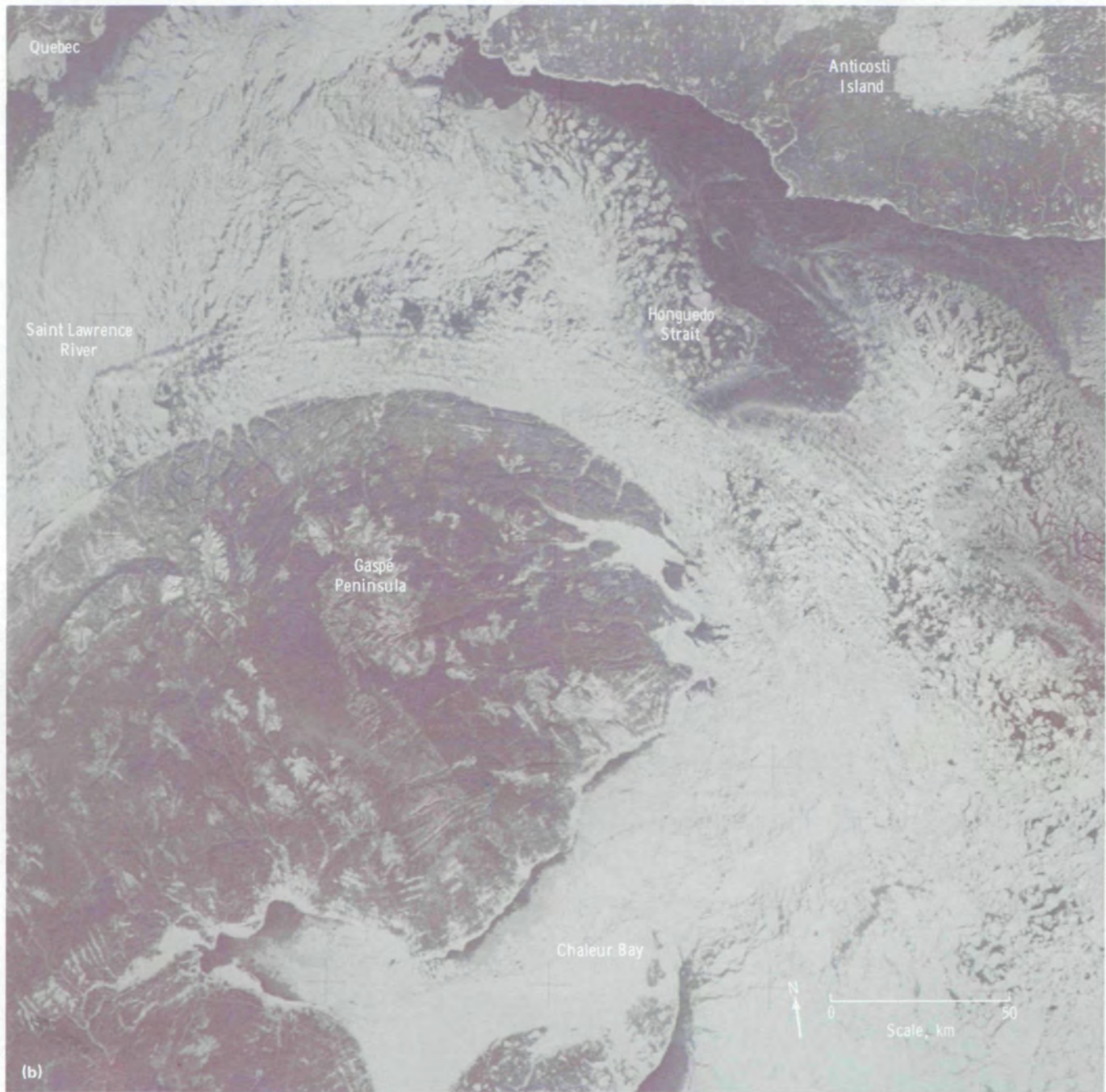
Quebec

Anticosti
Island

Saint Lawrence
River

Honguedo
Strait

Gaspé
Peninsula

Chaleur Bay

N

0   50
Scale, km

(b)

FIGURE 5-16.—Concluded.

FIGURE 5-17.—Skylab 4 color photographs (handheld camera) of northwestern Gulf of Saint Lawrence and Anticosti Island. (a) January 18, 1974 (SL4-140-4216). Scale is approximate. (b) January 20, 1974 (SL4-141-4327). (c) January 21, 1974 (SL4-141-4366).
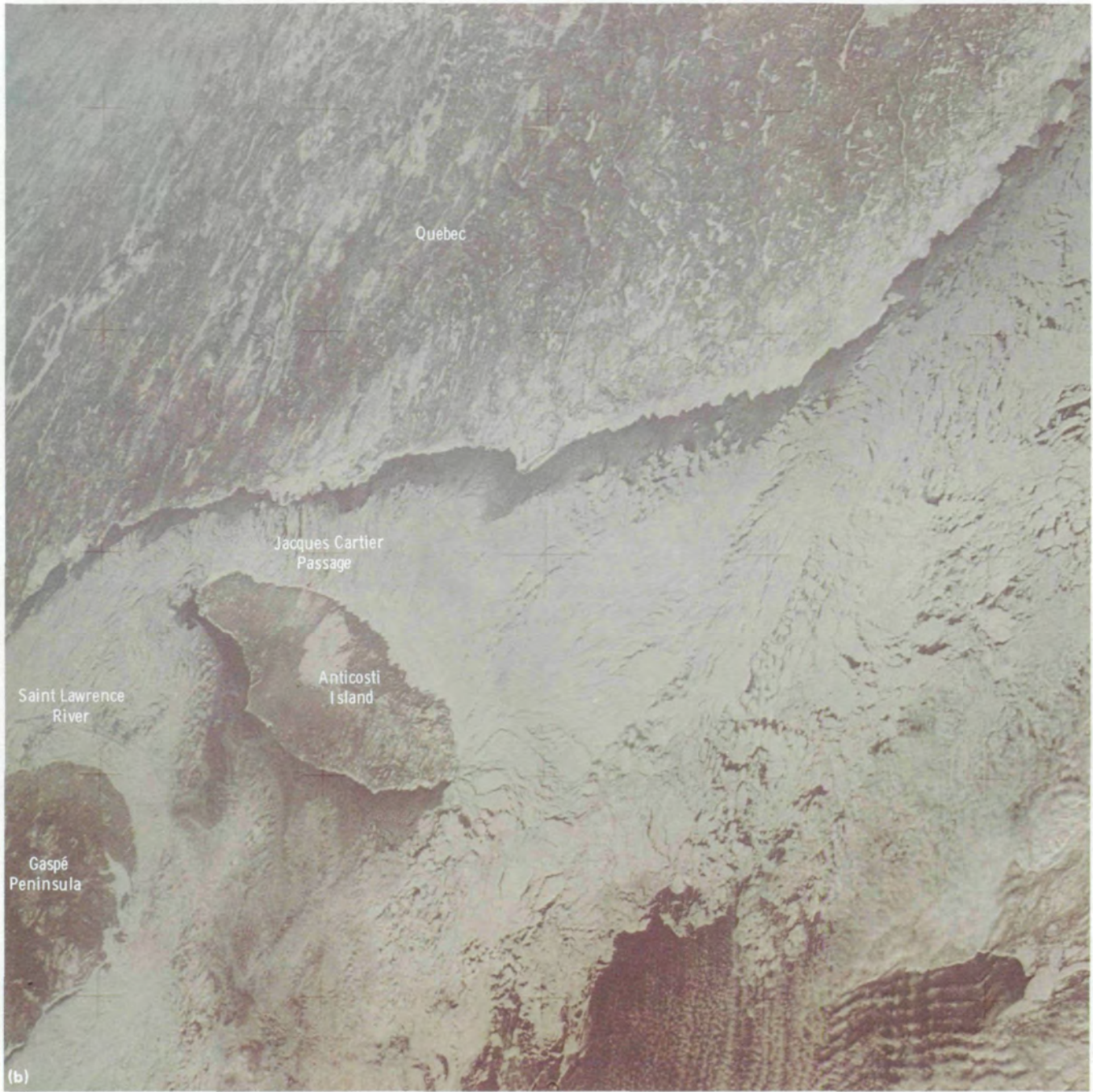
Quebec

Jacques Cartier
Passage

Saint Lawrence
River

Anticosti
Island

Gaspé
Peninsula

(b)

FIGURE 5-17.—Continued.

Labrador

Quebec

Jacques Cartier
Passage
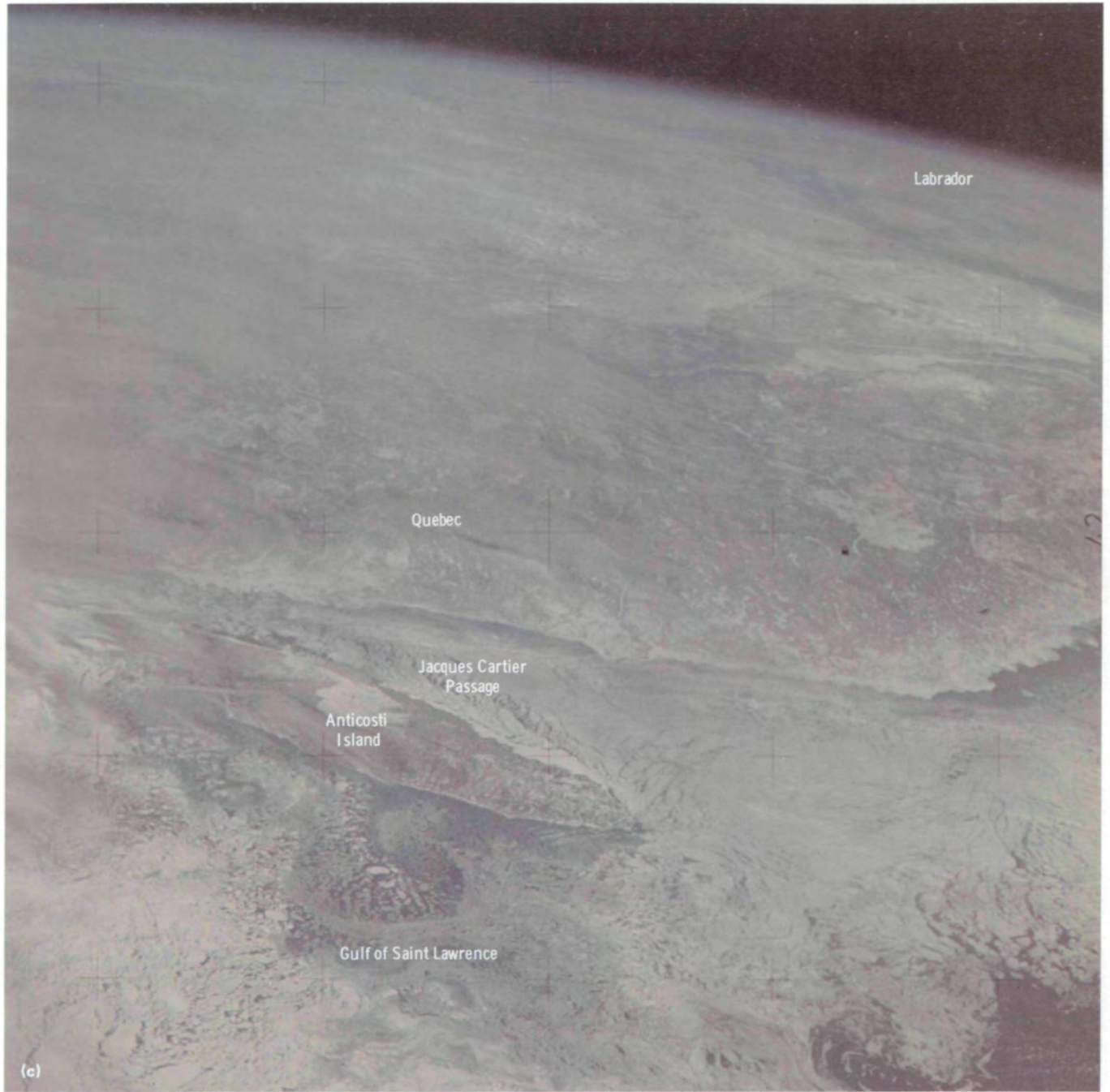
Anticosti
Island

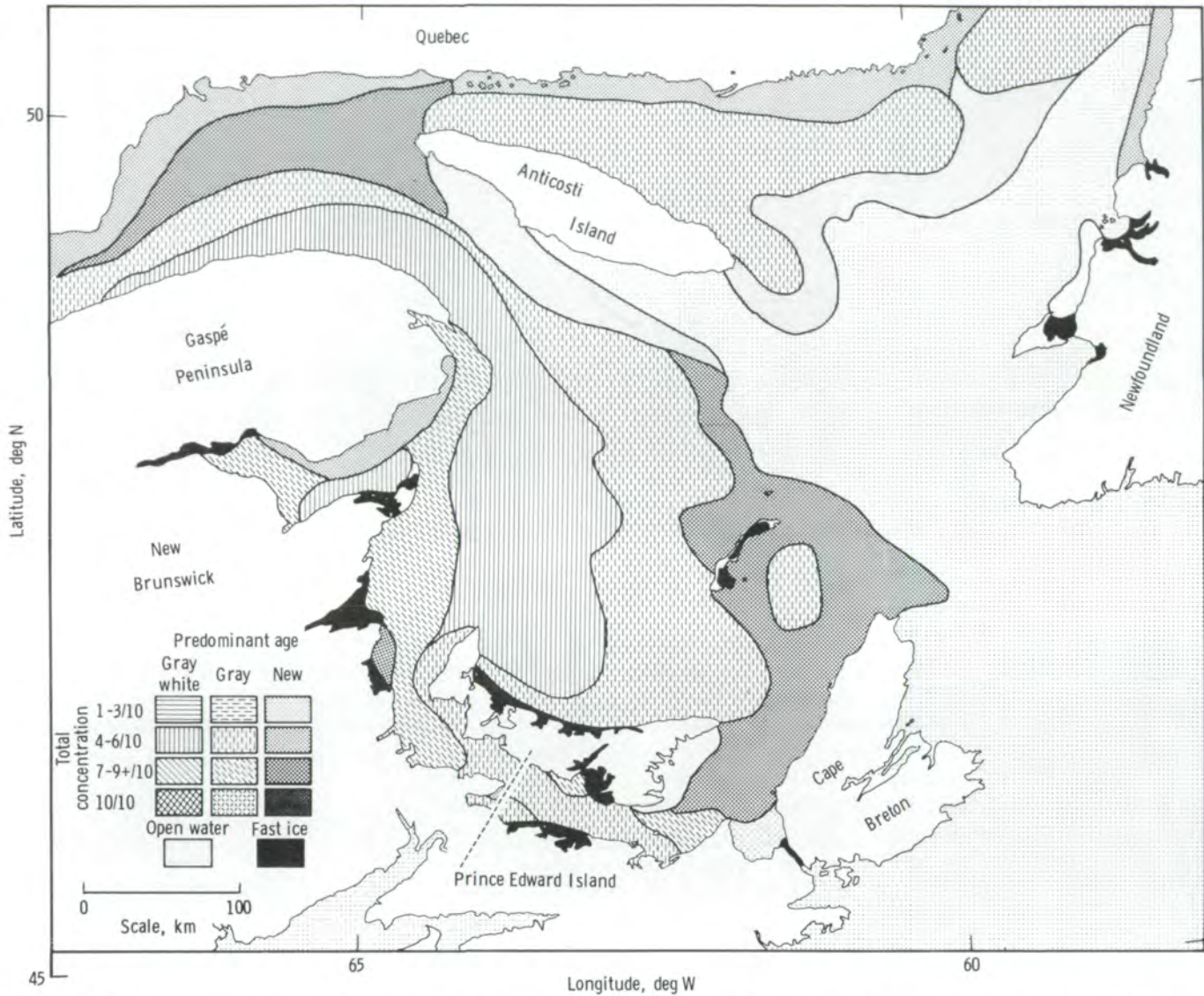Gulf of Saint Lawrence

(c)

FIGURE 5-17.—Concluded.

FIGURE 5-18.—Ice reconnaissance map of the Gulf of Saint Lawrence for January 18, 1974, prepared from aircraft and satellite data. Total concentration is expressed in tenths (i.e., 1-3/10 = 0.1 to 0.3; 7-9+/10 = 0.7 to >0.9); ten-tenths (10/10) is equivalent to 100 percent.

Data from the airborne passive microwave imaging scanner are shown in both horizontal and vertical polarization in figure 5-20(a). Supporting aircraft photographs of different types of ice are shown in figures 5-20(b) to 5-20(d). The microwave temperature (fig. 5-20(a)) is color coded from red as the "warmest" down through the color spectrum as an aid in visual interpretation. The brightness temperature (a term equivalent to the passive microwave temperature) is different for the two polarizations and for different
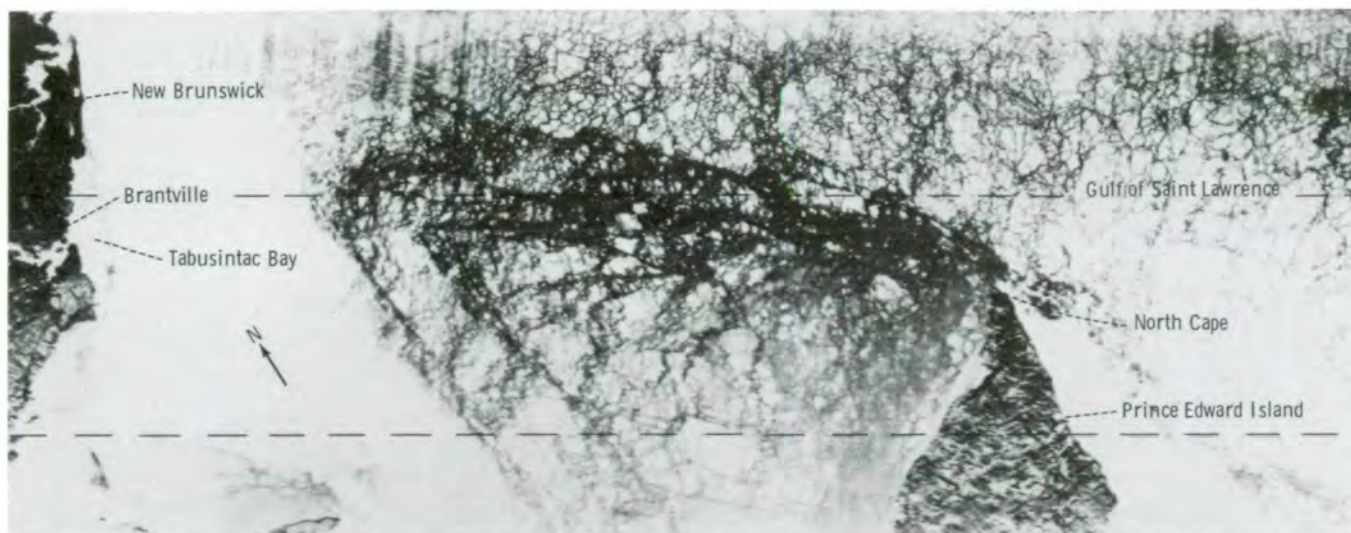
FIGURE 5-19.—Side-looking airborne radar X-band image of a portion of Prince Edward Island and New Brunswick shoreline (taken January 18, 1974, using a 25-km-wide swath). The distance between the horizontal lines is approximately 20 km.

kinds of ice. Analysis of the data showed that (1) the vertically polarized brightness temperature is greater than the horizontally polarized brightness temperature for all ice types, and (2) as the ice ages and thickens, the brightness temperature T increases in both the horizontal H and vertical V polarizations and the difference between the two decreases. These conclusions are summarized quantitatively in table 5-I. The values for vertical polarization increase by 75 K; the values for horizontal polarization increase by 160 K; and the difference $T_V - T_H$ decreases from 130 to 35 K. Passive microwave data are a good means of determining ice age and thickness.

A major conclusion of Campbell's study was that "the best all-weather floating ice remote sensing data can be obtained via the combined operation of passive and active microwave systems." This goal is being fulfilled, at least in part, by existing and planned active and passive microwave instruments on satellites.

Passive microwave imaging systems on Nimbus satellites routinely image ice in the Arctic and Antarctic at a fairly coarse resolution. A radar is being built for Seasat-A that will image ice with a resolution of 20 m

and that will be capable of imaging a 100-km-wide swath through clouds day or night, whenever the satellite transits an interesting region. Extensive plans are being made for use of these data operationally by Canadian and U.S. scientists.

TABLE 5-I.—*Average Brightness Temperature for Uniform Ice Types According to Age*

Ice type	Temperature, K		
	V	H	ΔT
Plumes-water	180	50	130
Frazil-slush	220	120	100
Dark nilas	225	125	100
Thin gray	245	180	65
Gray	255	195	60
Gray-white	240	195	45
Shorefast	245	210	35

50   100   150   200   250   300

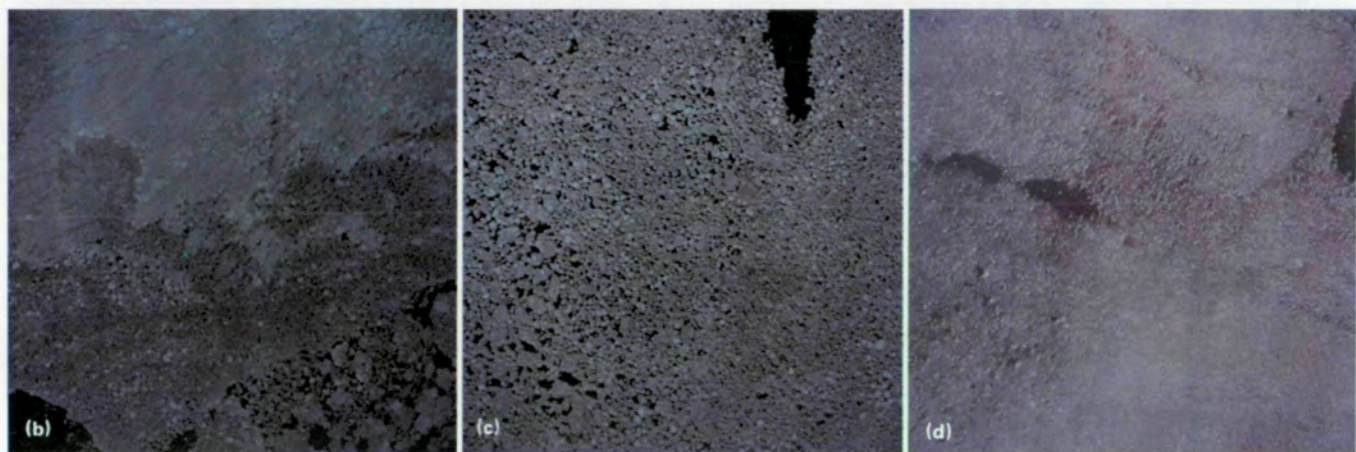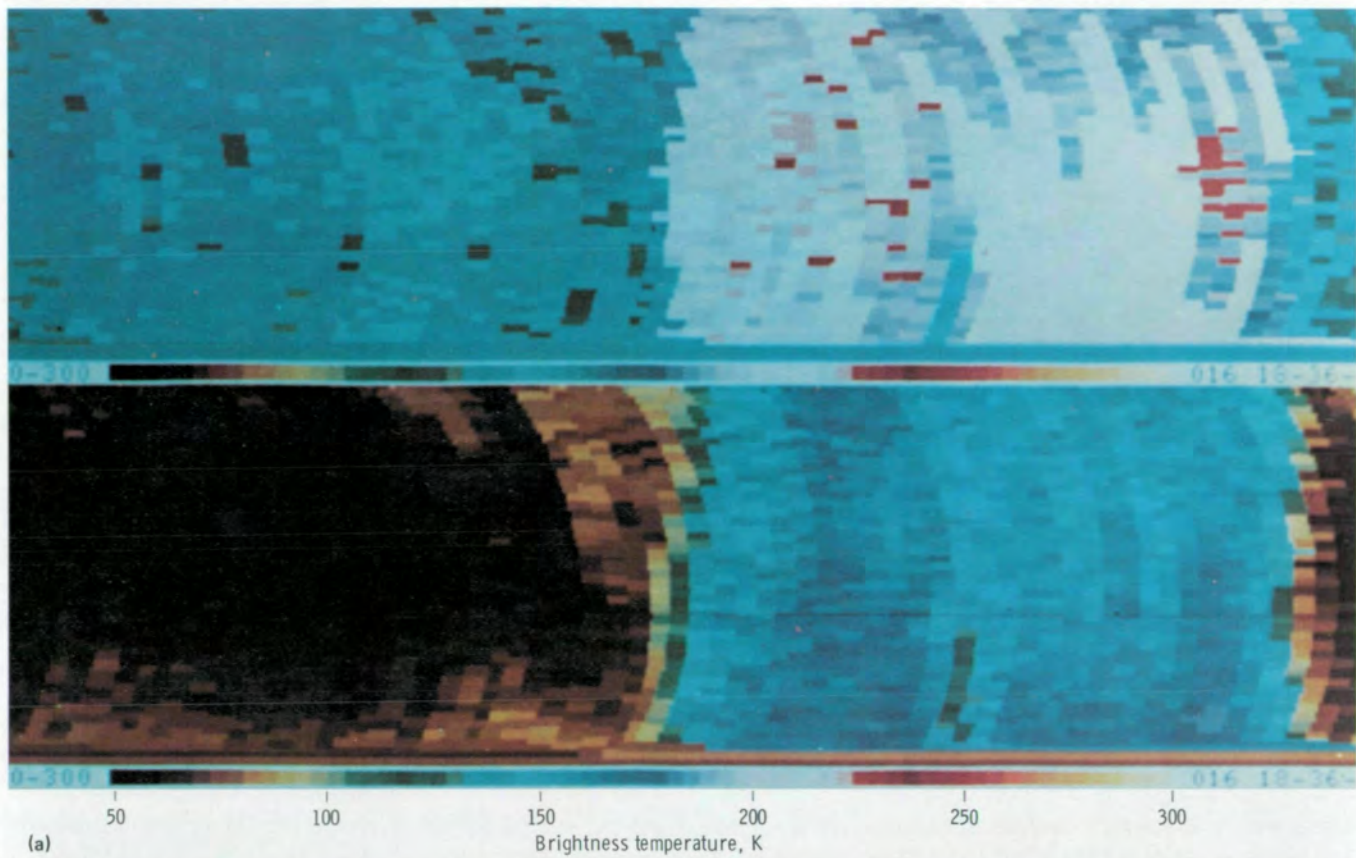(a)   Brightness temperature, K

FIGURE 5-20.—Aircraft imagery and photographs of the Gulf of Saint Lawrence for run 1 of flight 19 on January 16, 1974. (a) Passive microwave imaging system data for sea ice. The upper trace is from the vertical polarization; the lower trace, from the horizontal. (b) Photograph of consolidated pancake and gray-white ice. (c) Photograph of pancake ice. (d) Photograph of slush and frazil.

Fisheries, Chlorophyll, Water Color, and Productivity

The world fishing effort exploits an ocean resource. The total weight of all the fish caught by the major fishing nations increased to a peak in 1972 and then decreased in both the following years. This trend suggests that certain areas are being overfished and that the management of this resource has not been directed toward the concept of maximum sustainable yield.

The presence of fish in a certain area of the ocean depends on the availability of food in the forms of zooplankton and phytoplankton. Phytoplankton, being small plants, require the equivalent of fertilizer and sunlight. The fertilizer, called nutrients, consists of the dissolved nitrates, phosphates, and carbon compounds in the water. Because sunlight only penetrates the first 100 m of the ocean, the food chain in the oceans and estuaries starts in the surface layers.

In many areas of the ocean, the nutrients are not abundant enough to support the food chain and produce large numbers of fish. Midocean areas at latitudes 30° N and 30° S, where the surface waters sink, are particularly devoid of nutrients.

The ocean areas in which nutrients are plentiful are coastal areas with river runoff, Arctic and Antarctic areas where the water overturns each winter to bring submarine nutrients to the surface, and upwelling areas off the western coasts of continents at certain latitudes. In these upwelling areas, the general circulation winds blow toward the Equator, and the drag of the wind on the sea surface forces the coastal water out to sea and thus causes nutrient-rich colder water from several hundred meters below the surface to rise.

Numerous investigations have indicated that water with certain colors, probably caused by phytoplankton, and certain temperatures, often rather narrowly defined, are preferred by various species of fish. If these regions of the ocean could be located, fishing vessels conceivably could be directed to them. The result would be a reduction in the cost of fish and an increase in the availability of these fish to the consumer.

Numerous properties of the ocean surface can be remotely sensed as an aid in locating potential fishing areas. These properties, called signatures, need not necessarily be the same for every area. Those that can indicate the presence of abundant phytoplankton are the temperature variations and the diverse colors of the water. The distinctive colors of the water may be caused by the presence of chlorophyll or by suspended sediments that may indicate nutrient-rich runoff.

Several investigations within the overall concept of fisheries were concerned with detection of the nutrient-rich portions of the surface waters in oceans, bays, and estuaries by means of some direct signature that could be sensed by the Skylab instruments. Eight reports are of interest: Pirie and Steller (ref. 5-11), Nichols (ref. 5-12), Gordon and Nichols (ref. 5-13), Marshall and Bowker (ref. 5-14), Korb and Potter (ref. 5-15), Szekielda (ref. 5-16), Watanabe et al. (ref. 5-17), and Savastano (ref. 5-18).

Areas of upwelling occur along the continental coast and are the location of important fisheries. Coastal upwelling occurs when winds blowing parallel to the shoreline or slightly offshore cause the warm surface waters to move seaward. To replace that loss, waters from depth rise to the surface. The subsurface waters are cooler and contain more nutrients. Pirie and Steller (ref. 5-11) and Szekielda (ref. 5-16) used EREP data to study this phenomenon off the California and West Africa coastal areas, respectively.

An illustration of the sensing of upwelling using EREP data is shown in figure 5-21. The light areas in the water are caused by suspended sediments borne by the rivers that discharge into the ocean along this portion of the California coast. The suspended sediments flow southward along the coast and spread outward into the ocean at discrete regions. (The arrows indicate current direction.) This mixing of the coastal water containing the suspended sediment with the offshore water is not very efficient, with the result that sharp boundaries between the offshore water and the coastal turbid water can be seen. The five fingerlike projections in the upper left portion of the figure illustrate this phenomenon. Three regions (U) that are noticeably darker than the surroundings represent areas without the turbidity associated with the river water. Based on the location of these regions, oceanographers would conclude that they are composed of water that has upwelled from the deeper layers to the west.

Similar effects can be detected in the imagery obtained by operational spacecraft, as shown in figure 5-22. This image, obtained September 11, 1974, from NOAA-3 data (ref. 5-19), illustrates the same phenomenon on a wider scale off the California and Oregon coasts. In this thermal-infrared image, light shades indicate cold water; dark shades, warmer water.
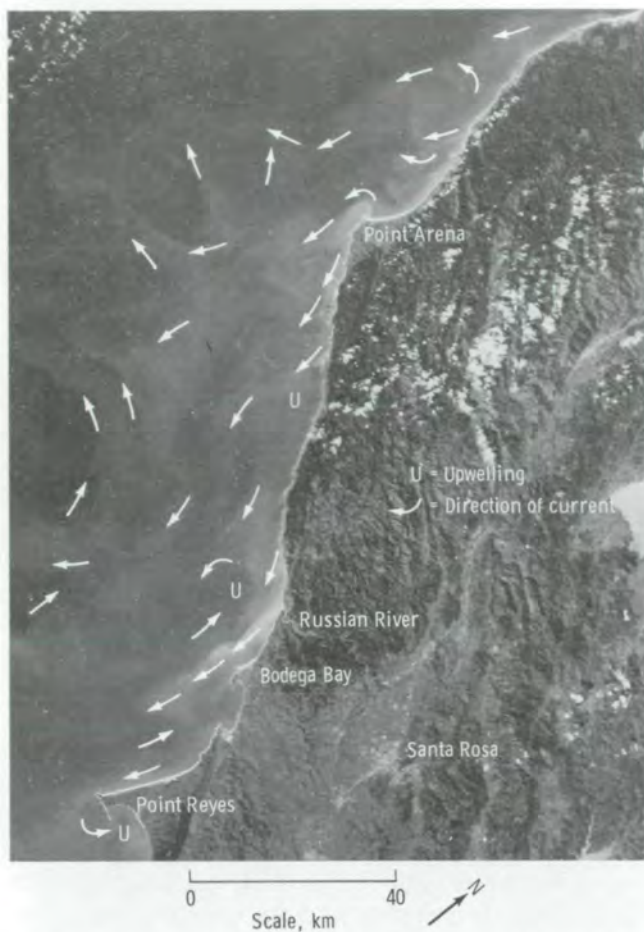
FIGURE 5-21.—Skylab 4 S190A photograph of the northern California near-shore area taken on January 26, 1974 (from ref. 5-11) (SL4-78-069).
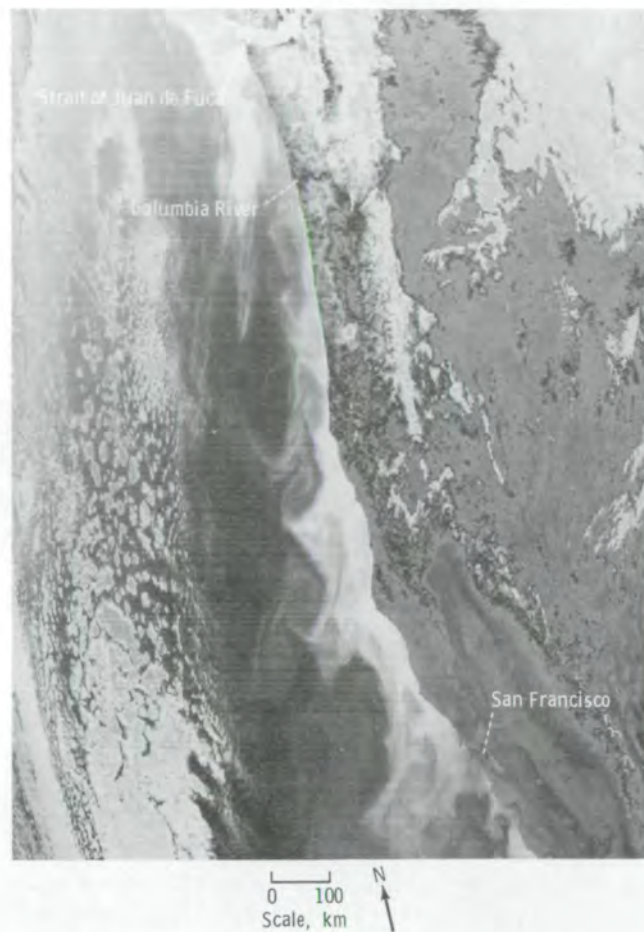

FIGURE 5-22.—Thermal-infrared image of sea-surface temperatures off the California and Oregon coast (NOAA-3 image acquired September 11, 1974).

The light gray along the coast is water with a temperature of approximately 287 K, and the dark gray offshore represents temperatures approximately 6 K warmer. The location and the strength of the upwelling areas along the coast are readily visible in this image; the general patterns are similar to those seen in figure 5-21. The upwelled water mixes with the river water. The result may be high nutrient concentration in the upwelled water, moderate concentration in the mixed river and upwelled water, and low nutrient concentration in the offshore water.

Examination of both these images shows that sharp boundary lines representing zones of discontinuity be-

tween two kinds of surface water are seen as far as 50 km from shore. Most conventional shipboard oceanographic measurement techniques cannot delineate these very complicated patterns. Thus, remote sensing provides oceanographers with the ability to resolve new scales and to investigate new problems in the circulation of the coastal waters. A review of the oceanographic literature more than 10 years old would reveal that most physical oceanographers were unaware of this scale of complexity in sea-surface properties.

That upwelling—or the absence of it—along the western coast of North America is important information desired by the fishery industry is shown in the re-

cent work of Bakun (ref. 5-20) and Bakun and Nelson (ref. 5-21). The first reference provides a tabulation of the daily and weekly upwelling intensities along the western coast of North America from 1967 to 1973. The second discusses the method by which these quantities are computed and describes the climatology of upwelling processes off the coast of Baja California.

These two studies, although not a part of the EREP Program, show how upwelling patterns determined from imagery could eventually be correlated with winds measured by a radar scatterometer. In both cases, the details of the wind fields near the coast are determined from the conventional meteorological information and are then used to compute the stress of the wind on the sea surface, the currents produced by this stress, and the area of upwelling. The volume of water that may be involved in the upwelling seen in figure 5-21 was calculated to be as much as 343 m³/sec per 100 m of coastline. The amount of upwelling peaks in June and July and is still nearly always present both at latitude 39° N, longitude 125° W, and at latitude 36° N, longitude 122° W, in September. For both areas, weekly averages usually exceed 50 m³/sec per 100 m of coastline with peak amounts as high as 250 m³/sec per 100 m of coastline.

An oceanic region similar in circulation and climate to the region off the western coast of North America is off the coast of Spanish Sahara and Mauritania in an area from latitude 18° N to 22° N, longitude 16° W to 18° W. The well-known upwelling phenomenon in this area is caused by meteorological conditions similar to those off California (ref. 5-16). An S190A color photograph off Cape Blanc, where the land is desert, is shown in figure 5-23. The different colors of the water are clearly evident.

Numerous images from both Landsat-1 and Skylab have been obtained for this region and were used to map the ocean color boundaries (fig. 5-24). The plots revealed that the boundaries fluctuated from 10 to 20 to perhaps 40 km from one image to the next and that they were quasi-persistent features of the sea surface in that area. (A feature is defined as quasi-persistent if it lasts several weeks before marked change is observed.)

Analysis of the EREP data shows that upwelling features are relatively small scale compared to major ocean features studied by means of shipboard oceanographic measurements. The same features were observed in the imagery off southern California, and it is evident that remote-sensing techniques make it possible to delineate these areas more accurately. Because the features are quasi-persistent, ample time exists for a fishing fleet to reach the more productive areas.

Many fish caught in the continental shelf waters off the U.S. east coast are adults that matured from fry in the nearby estuarine areas. The fish are hatched in the estuaries and spend their early years in the marshes and shallow areas until they are large enough to venture to sea. Understanding the processes and the phenomenon of these estuaries is thus important in fishery research. A productive food chain in and near the mouths of these estuaries requires dissolved nutrients and sunlight, the same essential conditions that are present off California and north Africa. The dissolved nutrients are derived through runoff from the adjacent landmass and by means of the treated and untreated sewage effluents that are discharged by the coastal cities and towns. A substantial amount of the fertilizer that is used by farmers on their fields is dissolved by rainwater and carried by small streams and brooks into these estuaries as a continuing process.

In contrast to upwelled water, the nutrient-rich estuarine water can have many different origins. Perhaps a primary indicator of its origin is the water color, which depends on the amount of sediments that have been washed down with the water from the land. Three investigators (refs. 5-12 to 5-14) attempted to classify as to chlorophyll and productivity indices the surface features of the waters off the U.S. east coast near Assateague Island, in the lower Chesapeake Bay, and in the Rappahannock River. The results were only partly successful in these particular cases and showed no discernible water-color parameter in the imagery that could be strongly correlated with chlorophyll in the water and only a fair correlation of chlorophyll with turbidity.

The overall result of the study was that it was possible to classify the estuarine waters into numerous major categories according to color and that these categories
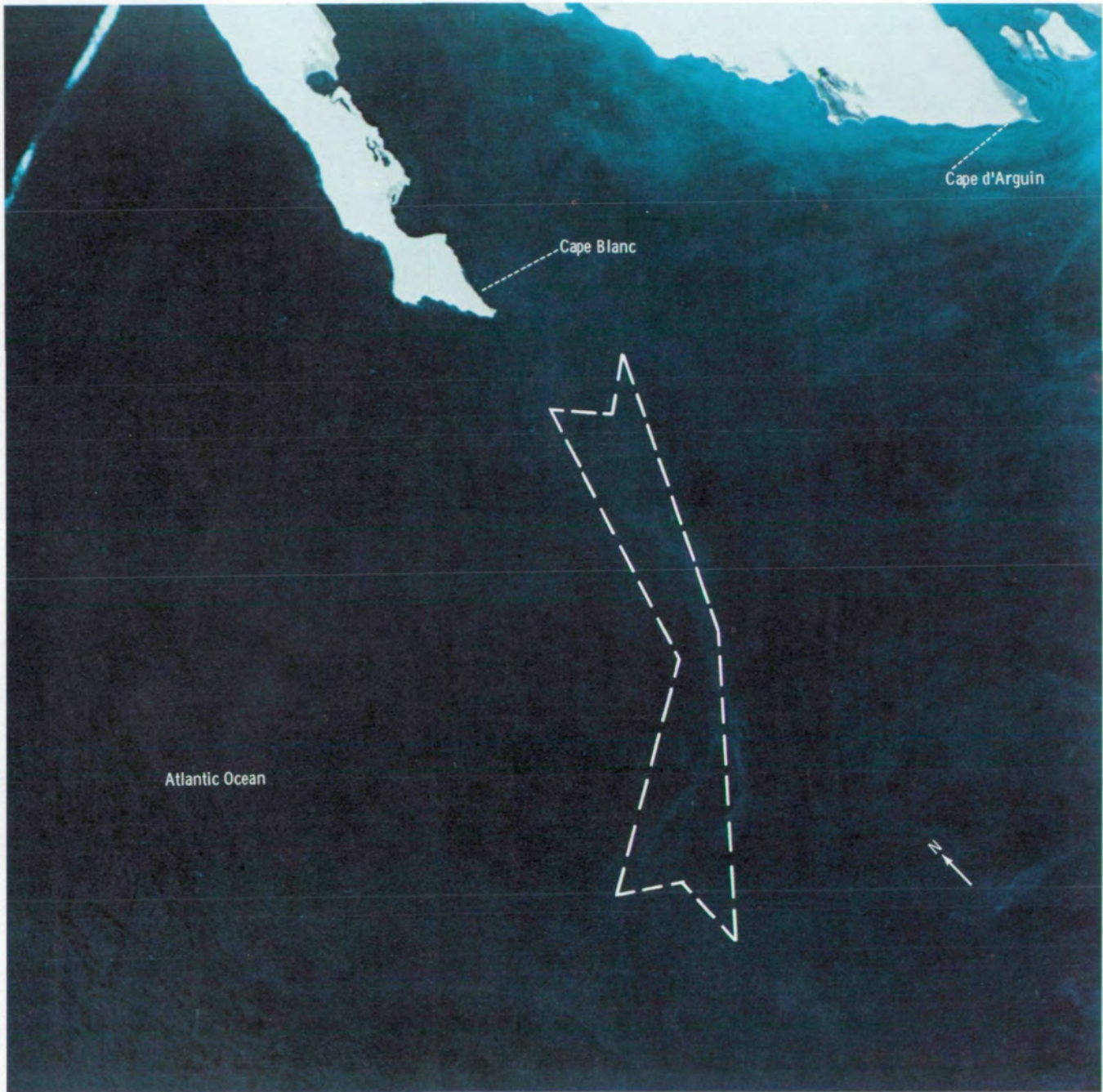
FIGURE 5-23.—S190A color photograph of Cape Blanc area and offshore waters acquired September 4, 1973 (SL3-84-360). An area of upwelling is outlined.
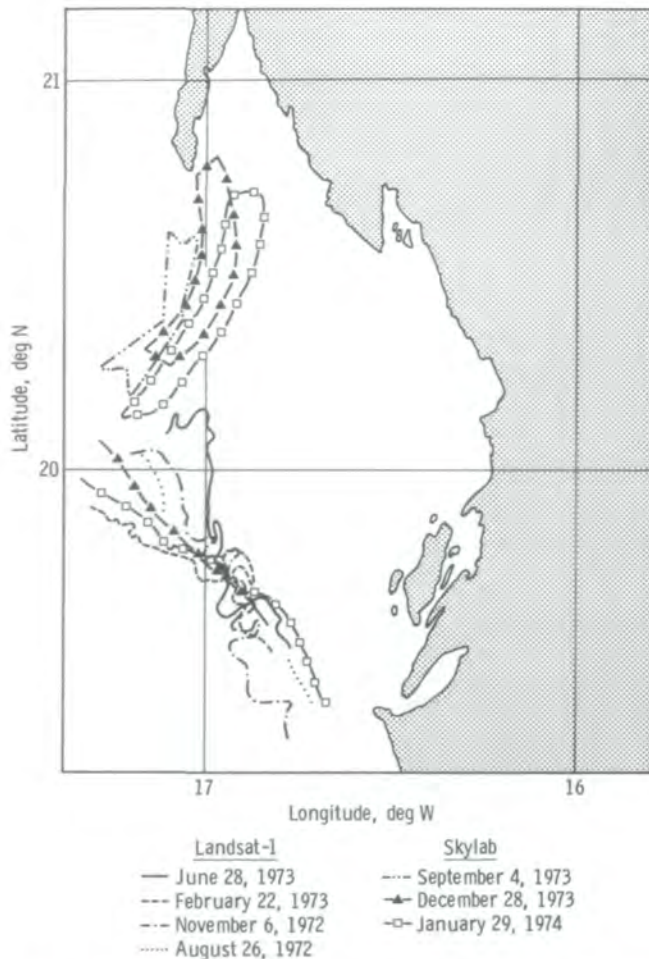
FIGURE 5-24.—Offshore ocean color boundaries derived from Landsat-1 and Skylab data near the western coast of north Africa from August 26, 1972, to January 29, 1974.

The study by Korb and Potter (ref. 5-15) highlights some of the problems of studying ocean features with remote sensing. The surface-truth part of the program was successful; but, of the two EREP data sets obtained for the study areas, one was badly contaminated by Sun glitter and the other had 95 percent cloud cover. They found that the values of chlorophyll in the Matagorda Bay, Texas, area ranged from 1.0 to 14.5 mg/m³ and that the values of turbidity ranged from 0.9 to 25.0 Jackson turbidity units. The correlation coefficient calculated for the chlorophyll and turbidity data was 0.68. This value indicates that the levels of chlorophyll and turbidity were correlated at a confidence level of greater than 99 percent for the bay and near-coast data. Because turbidity can easily be sensed remotely, this result, if it is generally characteristic of coastal regions, would have important implications for studies concerned with the remote sensing of chlorophyll in these regions.

Watanabe et al. (ref. 5-17) used image masking and stereography to study the S190A photographs of Japanese waters in an area south of Hokkaido near latitude 40° N, longitude 145° E. In image masking, the difference between visible (0.5 to 0.6 μm) and near-infrared (0.7 to 0.8 μm) wavelengths is used to identify oceanic patterns or green sea areas and to distinguish them from atmospheric formations. When overlapping photographs were viewed stereoscopically, the clouds could be differentiated from the sea surface and the ocean patterns identified. These latter areas were correlated with abundant phytoplankton that demarked the boundary between the Kuroshio and Oyashio Currents.

In the cited studies, parallel theoretical and observational efforts were made to acquire a better understanding of the various regions and to obtain adequate surface truth. The theoretical effort is assimilated into the body of knowledge for both the direct observations and their future applications to other remote-sensing programs. Just as instruments and systems evolve with time and become progressively better, so do the theories and the techniques used in interpreting the data. It is fully expected that the results of these theoretical investigations will aid in the design of new remote-sensing systems.

The problem of catching fish economically and efficiently was studied using EREP data (except for S193) for the northeastern Gulf of Mexico in cooperation with sport and professional fishermen (ref. 5-18). These fishermen recorded the type, the location, and the time of all catches, and these data were then correlated with

and their positions in the river could be explained on the basis of the tidal circulation in the estuaries. The investigators indicated that repetitive coverage every 2 or 3 hours is needed to study tidal effects. Such coverage is impossible from a low-orbit spacecraft such as Skylab. It may be possible to study phenomena such as these from geostationary satellites on an hour-to-hour basis. However, because of the great distance between the sensor and the target surface, the low resolution of the imagery is a major problem. An alternative is aircraft reconnaissance, and many of the shortcomings of aircraft reconnaissance were discussed in the reports.

information obtained by Skylab and by high-altitude aircraft that overflew the area simultaneously. The primary purpose of the experiment was to ascertain whether remotely sensed data could be correlated with surface measurements and with the types and numbers of fish that were caught.

Conventional meteorological and oceanographic data obtained during this investigation were ocean depth, wave conditions, distance from the shore, chlorophyll content of the water, sea-surface temperature, salinity, water transparency, water color, atmospheric surface pressure, and air temperature. The water temperatures were sensed remotely by two different aircraft over a portion of the total area that was investigated. Chlorophyll-a was sensed remotely and measured at the surface. The remotely sensed chlorophyll data were obtained by a special spectral radiometer flown on a light aircraft at an altitude of 3000 m. The instrument measured the radiance in the spectral region from 390 to 1100 nm and was calibrated at 57 wavelengths in that range. An important feature in the measured chlorophyll content of the waters near the surface of the Gulf of Mexico is that it varies by fairly large amounts over relatively small areas. The content can be as much as four times greater in one place than it is in another just a few kilometers away, and small pockets or regions of zero chlorophyll-a have been observed. The correlation of the values of chlorophyll-a, as measured from an aircraft and as measured from water samples obtained in situ for one flight line, is shown in figure 5-25.

The fish involved were the blue marlin, the white marlin, the sailfish (under the classification of billfish), and the dolphin and wahoo (under the classification of other game fish). During a 2-day period, 67 fish were "raised but not hooked," which probably means that they were sighted and followed the bait for a while but did not take the bait. Of the 171 fish that were hooked (approximately the same number on each day), 58 got away; therefore, 113 fish were caught.

Models based on aircraft data and conventional surface-truth data were developed for predicting the abundance of white marlin in the area. The best model using these techniques had a correlation coefficient of 0.489 and was significant at the 60-percent level. The effect of
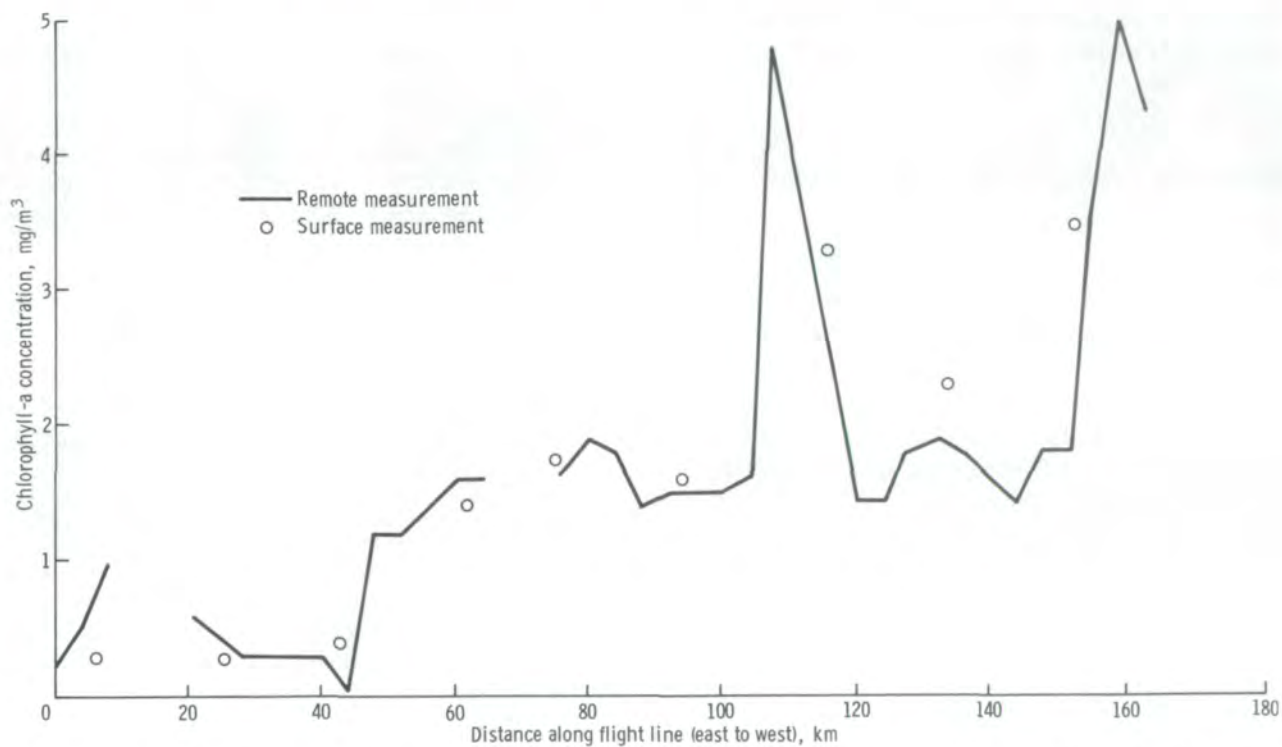

FIGURE 5-25.—Comparison of remote and in situ measurements for chlorophyll-a along a flight line (from ref. 5-18).

remotely sensed EREP data on the prediction models was next determined. Although cloudiness in the area precluded the use of certain sensor data, the S192 data were processed and the radiance values from bands 1 to 7 and from band 13 were used for the cloudless areas in the original test regions. The information content of bands 4 and 5 was eliminated.

The final prediction model for white marlin for one particular day based on a Skylab pass over the area yielded a correlation coefficient of 0.892 (compared to 0.489 without space data) and was significant at the 90-percent level (as compared to the 60-percent level). These results, though based only on data for 1 day and on a subset of the total area that was included in the prediction model, were further evaluated using a model developed from the same surface-truth parameters that were used in the previous model, except that only those test areas for which S192 data were available were used. It was concluded, therefore, that the increase in precision of the model could be attributed to the data from the S192 sensor. Other aspects of the problem, such as trying to remove the effects of sunglint by differencing the measurements made in the different bands, were investigated; the effort was unsuccessful.

The application of these techniques to larger areas of the ocean on a routine basis to improve the efficiency of the various U.S. fishing fleets will not be achieved in the near future. However, this experiment demonstrated the feasibility of a technique that may eventually become extremely useful to the fishing industry.

Coastal Water Interpretation

As demonstrated by their reports, the Principal Investigators who used the EREP data are pioneers in studying potential techniques for improved understanding of the coastal waters around continents and islands. A typical marine scientist conducts research from small, well-equipped coastal vessels from which he acquires point measurements such as catching fish, netting various kinds of plankton, determining chemical and nutrient contents of the water, and measuring currents. The problem with this approach is that it is not possible to cover a large area in great detail, and difficulty is encountered in relating one set of measurements taken at one time and one place to another set of measurements obtained at a different time and a different place.

A significant aspect of the Skylab missions is that the coastal imagery obtained can be used in many different ways to aid in the interpretation of the conventional data obtained by marine scientists. The methods developed in the EREP Program potentially may aid marine scientists in their studies.

Eight Principal Investigators applied photointerpretative techniques such as stereoscopic viewing, densitometric analysis, and color enhancement to EREP imagery to study many coastal and oceanic features. The areas studied were Chesapeake Bay by Nichols (ref. 5-12) and Gordon and Nichols (ref. 5-13); Delaware Bay by Klemas et al. (ref. 5-22); the Seto Naikai, or Inland Sea, and other waters around Japan by Maruyasu et al. (ref. 5-23); New York State water resources (Lake Ontario and Conesus Lake) by Piech et al. (ref. 5-24) (sec. 6 of this report); San Francisco Bay and California coastal waters by Pirie and Steller (ref. 5-11); Puerto Rico waters by Trumbull (ref. 5-8); Block Island Sound by Yost (ref. 5-25); and the Gulf Stream by Maul et al. (ref. 5-26).

The southern Chesapeake Bay, including the Rappahannock Estuary (refs. 5-12 and 5-13), is an area rich in oysters and fish and with relatively mild conditions of tide and river inflow. The tides in such an estuary cause marked changes in the amount of suspended materials that are indicated in circulation patterns. For example, when the water from the lower part of Chesapeake Bay enters the Rappahannock, it can concentrate on one side of the estuary and leave the other side untouched. The tidal currents produce small-scale mixing patterns controlled by changes in the shape and the width of the estuary. In this investigation, S190A and S190B data were analyzed with densitometers and four different estuarine water types were mapped that were related to the water transparency, turbidity, and suspended-sediment load. It was possible to locate small-scale mixing patterns caused by local tidal currents.

In the Delaware Bay study (ref. 5-22), surface truth obtained from boats included measurements of Secchi depth, suspended-sediment concentration, transmissivity, temperature, salinity, and water color. In this investigation, emphasis was placed on coastal land use and vegetation mapping as prepared from EREP photographs and S192 scanner imagery. These products were used to map, at a scale of 1:125 000, 10 land use and vegetation categories that included delineation of the wetlands. A particularly valuable

FIGURE 5-26.—Aerial photograph of red-tide pattern observed in the Sea of Bingo, Japan.

FIGURE 5-27.—Enlargement of S190B photograph showing red-tide patterns (arrows) in the Sea of Bingo, Japan (SL4-89-398).

aspect of the imagery was discrimination of small dispersed areas of marshland that are particularly important in the estuarine food chain. With regard to the marine studies, it was possible to monitor suspended-sediment concentrations, to map surface-current circulations, to locate boundaries of internal systems, to track surface slicks, to follow ocean-waste dispersion, and to monitor ship traffic.

In studies of data obtained during a pass over Japan, Maruyasu (ref. 5-23) used the different colors in the water on a single S190B photograph to trace the tidal currents in the Inland Sea in the vicinity of Kojina Bay. A coinvestigator (Ochiai) analyzed S190B photographs of the Sea of Bingo from the same Skylab pass and higher resolution imagery from an aerial multispectral scanner to map the boundaries of industrial effluents around the coastal industrial zone and to detect oil pollution. An area of red tide was detected in the aerial photograph and in an enlarged portion of an S190B photograph. As described by Ochiai, "The monitoring of the red tide is considered [to be] the most important task for fishery [scientists]." The yellow-colored vortex in figure 5-26 is one red-tide pattern that was sighted in the Sea of Bingo during the observation flight on Janu-

ary 11, 1973; it was also identified in an enlarged S190B photograph (fig. 5-27).

California is an excellent coastal area for demonstrating the potential of use of low-Earth-orbit sensor systems for studying coastal and estuarine processes because of the varied types of features that are encountered. The northern coast is rocky with silt-laden streams and rivers. The southern coast has long, sandy beaches with eroding coastal bluff formations. The streams and rivers of southern California are usually dry during the summer months. In San Pablo Bay, which is in the northern part of San Francisco Bay, sediment transport was traced to areas of known deposition with Skylab imagery and was correlated closely with plots of sediment distribution obtained during the same period by ship surveys (ref. 5-11).

Color-composite enhancements of S192 imagery (bands 4, 6, and 7) provided detailed current and sediment transport patterns. The brightness in the image is proportional to the amount of suspended sediment. The sediment can be seen to flow southward past Alcatraz Island into South Bay. Some of this sediment also flows under the Golden Gate Bridge and can be seen as a boundary far out to sea. An S190A black-and-white

FIGURE 5-28.—Example of discharge of sediment-laden waters from the Carquinez Strait and the distribution in San Pablo Bay in an S190A photograph (SL4-77-071).

photograph of San Francisco Bay illustrates the variation in the sediment load (fig. 5-28).

The patterns of dredged sediment discharges were plotted over a 3-month period. It was found that lithogenous particles, kept in suspension by the freshwater from the combined Sacramento and San Joaquin Rivers, were transported downstream to the estuarine area at varying rates depending on the river-discharge level. To measure the transport in San Pablo Bay, dredged sediments were marked with iridium before discharge near the Carquinez Strait. For May, June, and July 1974, the movements of these tracer sediments were plotted after collection and processing by 82 stations within the bay. This information matched the movements predicted from interpretation of EREP imagery and photographs.

The photographs of San Francisco Bay were taken during a period of exceptionally high freshwater and suspended-sediment discharge. A three-pronged surface

sediment pattern is visible where the Sacramento-San Joaquin River enters San Pablo Bay through the Carquinez Strait. The three prongs extended to areas where maximum deposition historically occurs—the central channel, the southeast shore near Pinole Point, and the northwest flats near the Petaluma River mouth. The S190B color photographs were excellent for spectral and spatial resolution. Spectral analysis of the photographs indicated that the sediment reflection peak was near 0.55 μm. Northwesterly wind was moving surface waters into the southeast bay near Pinole Point.

The S190 photograph and others were processed using narrow-band filters and a densitometer, so as to produce contours of suspended-sediment load as shown in figures 5-29(a) and 5-29(b). A suspensate concentration of approximately 2 mg/liter is quite sufficient to tag a surface-current system and, by using progressively longer wavelength filters, the surface structure of currents with more than 250 mg/liter can be imaged.

Measurements of the suspended-sediment load passing through the Carquinez Strait on January 26, 1974, were made. In the center of the channel, the concentration was approximately 250 mg/liter. A total of approximately 6.3 million metric tons of material passed into the San Francisco Bay during the 1973-74 season. Analysis of the S190A photographs indicates a reflectance shift toward the green from the blue as sediment load increases. This shift explains the excellent detail in the 0.5- to 0.6-μm and in the 0.6- to 0.7-μm bands.

Dredging may be required in the Berkeley Flats area of San Francisco Bay. Use of satellite and aircraft information in this respect will be beneficial, because the sites of shoaling and deposition are detectable. Cost savings using EREP-type data would vary with the placement and the extent of required dredging, but it is possible that savings of several million dollars could result. The techniques outlined in reference 5-11 should be applicable for coastal and estuarine processes studied in other areas of the world.

Excellent EREP photographs were obtained for the study of the coastal processes and waters surrounding Puerto Rico (ref. 5-8). The study of these photographs yielded information concerning many important aspects of the region. The important feature shown in figure 5-30 is the large anomalous blue area, which is also evident in four of the six frames of a simultaneously obtained set of S190A photographs. This intensely dark blue, almost black, area occupies much of the Bahía de Mayagüez (approximately 70
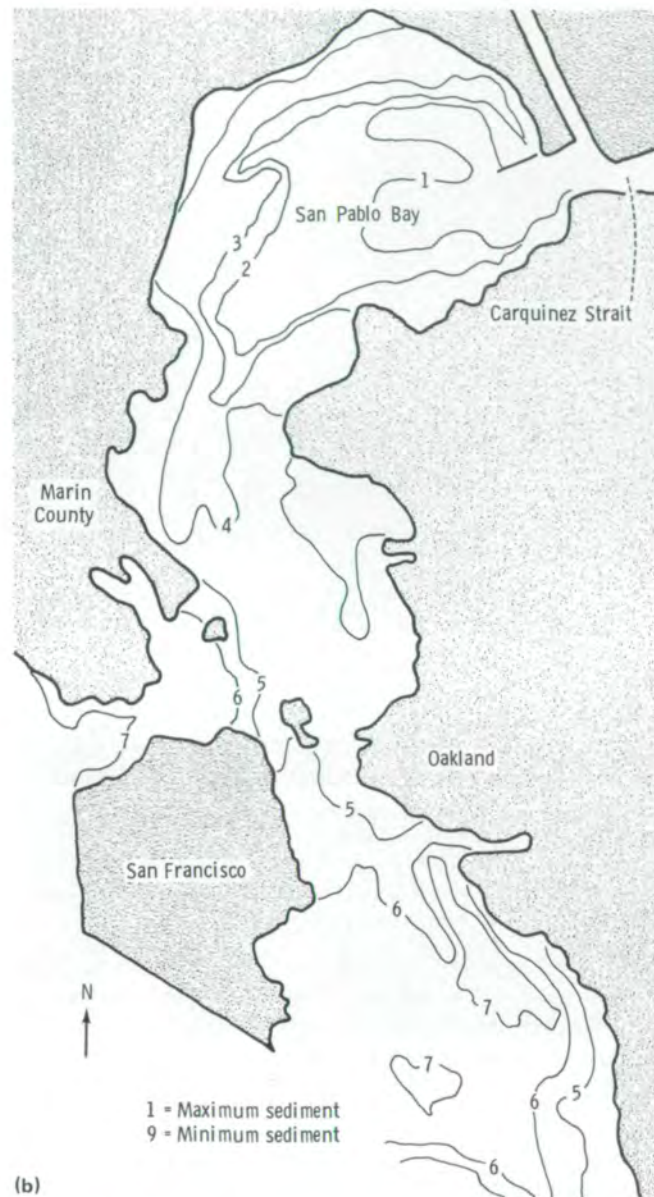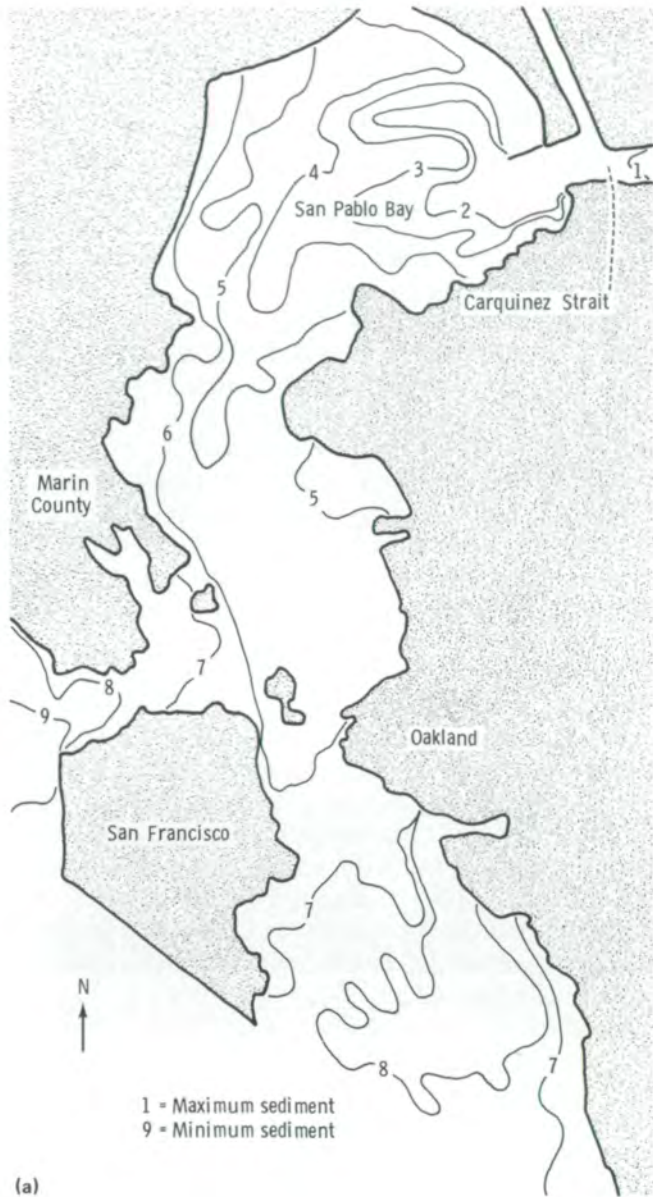
FIGURE 5-29.—Contour plots of suspended-sediment loads in San Pablo and San Francisco Bays. (a) 590 (±10) nm filter. (b) 490 (±10) nm filter.

km²) and is most strongly developed offshore from the city of Mayagüez, in and downwind of an area of known discharge of oily wastewater from tuna packing plants and other industries. The boundary of this deep-blue area on the south coincides with the location of a reef edge; depths in the lighter colored area to the south are generally in the range of 5 to 8 m, whereas depths in the deepest blue area are approximately 183 m. The inten-

sity of blue in the dark-blue area is clearly not a simple function of depth, because nearby deeper areas are not nearly as blue. It seemed evident to Trumbull that this deep-blue area was caused by some effluent on the water surface that changed the spectral reflectance. The presence of the anomaly was unknown before the EREP study.

FIGURE 5-30.—Skylab 2 S190B color photograph of coastal waters off western Puerto Rico (SL2-81-240).

Among the conclusions of the study were the following. The synoptic nature of the EREP information permitted the detection and study of phenomena impossible by any other existing technique. The S190B photographs contained incomparable bathymetric detail in which depths to a maximum of 26 m can be seen in areas of clear water. The turbidity of coastal waters near Puerto Rico is commonly high, reducing water penetration severely or eliminating it entirely. However, depth contours could be produced for certain areas.

Trumbull concluded that Skylab-quality data have particularly high potential for studies of bathymetry, patterns of coastal currents, coastal erosion, sediment transportation and accumulation, effects of coastal works of man, and oil-slick detection in the less well developed coastal areas of the world. Coral reefs and areas of coastal erosion were detected from orbital photographs. Potentially economic quantities of offshore deposits of sand, gravel, and mixed sand and

gravel were readily detectable on orbital photographs of S190 quality, where bottom reflectance can be seen. Field examinations are required for accurate differentiation assessment of the resources.

Currents can be studied in turbid coastal water. (A disadvantage is that, because of current variability in time and space, frequent coverage is necessary.) Effluent discharges and oil slicks of relatively small dimensions are readily detectable. Large, diffuse discharges, potentially dangerous ecologically, can be detected and studied by means of orbital photographs. A limiting requirement for oil-slick detection seems to be that the slick must not be in the Sun-azimuth direction from the center of the photograph.

Photographs of S190B quality can portray the patterns and boundaries of bottom-dwelling plant and animal communities in clear water. It is, however, necessary to make a field check because these patterns are somewhat difficult and sometimes impossible to distinguish from bathymetric patterns. Although stereoscopic effects can be seen in the Skylab photographs, they are not strong enough to show the apparent relief of bathymetric features. Techniques such as those previously discussed are therefore preferred, as compared to attempting to contour depths from stereophotographs. An important point, however, is that the depth of the water can actually be seen from spacecraft altitudes in stereopsis. Both aircraft and spacecraft photographs can be used to identify problem areas and to guide fieldwork from research vessels in a more intelligent way.

In an investigation of Block Island Sound and adjacent New York coastal waters (ref. 5-25), photographic techniques were used that greatly enhanced subtle low-brightness water detail. Photographic contrast-stretching techniques applied to S190A photographs enabled differentiation between two water masses having an extinction coefficient difference of only 0.07. By digitizing S190A multispectral data in registration, a non-homogeneous vertical stratification of Block Island Sound waters with differences in suspended solids of 1 mg/liter was detected. Significant differences between conventional tidal-current charts and the actual patterns of waterflow in Long Island Sound were established. One such difference is the existence of two large counterclockwise gyres heretofore undetected. The average extinction coefficient for white light was measured by ship at Block Island Sound to be 0.335, with a value of 0.400 for the blue band and of 0.554 for

the red band. These optical water characteristics of non-homogeneous surface and subsurface water can be charted. Estimates of suspended particles larger than 5 μm can be made.

Both this section and that on fisheries indicate that marine scientists could profitably use imagery systems such as those on the Landsat satellites but with the spectral bands specially selected to provide high spectral resolution and information in the violet, blue-green, and yellow portions of the visible spectrum, plus one red band. For these bands, the effect of the atmosphere is important because the light from the image is scattered more and, hence, is attenuated. However, the many theoretical analyses in these reports and in the study of aerosols show promising techniques to compensate for the intervening atmosphere. The signal-to-noise ratio of the particular bands in the spacecraft sensor may still be a limiting factor. The problem remains of relating a series of images, often obtained many weeks apart, to point measurements made by conventional techniques to relate the time variations at selected points to the image over an extensive area. The images can serve to assess the problem and identify points at which measurements would be needed.

ATMOSPHERIC PROPERTIES

Some of the energy that drives the global atmospheric circulation is provided by evaporation of water from the ocean surface. The Sun is the primary source of evaporative energy. The water vapor is transferred by vertical air currents through the boundary layer, condenses, and produces clouds and latent heat. Thus, the latent heat of condensation is a driving force of atmospheric circulation, particularly at the lower latitudes.

Further advances in man's understanding and ability to predict require a greater knowledge about the radiation transfer through the atmosphere, the sea-surface temperature patterns, the vertical and horizontal wind fields at different altitudes, and the physical thermodynamic characterization of clouds.

Radiation Transfer

In addition to the need for improving knowledge of the physics of solar and terrestrial radiation transfer

through the atmosphere, it is of major importance that better techniques be developed to correct for the effects of atmospheric attenuation. The Skylab meteorological program placed major emphasis on the study of radiation transfer.

The atmosphere is composed of dry gases (nitrogen, oxygen (O_2), argon, carbon dioxide (CO_2), and trace gases), water vapor (H_2O), and aerosols. Because incoming solar radiation and outgoing terrestrial radiation interact with these atmospheric constituents, the transmission of the beam is selectively modified as a function of wavelength because of the spectral nature of the interacting mechanisms. Radiation at some wavelengths is absorbed by gas molecules (removal of photons from the beam), whereas radiation at other wavelengths is refracted or scattered by molecules and aerosols. Total atmospheric extinction, therefore, is the result of the combined attenuation due to scattering plus absorption.

Atmospheric transmittance may be defined as $T = e^{-\tau}$, where τ is the atmospheric optical depth. An optical depth of 1.0 implies an extinction that would occur in an equivalent vertical path through the mass of the clear atmosphere. Figure 5-31 shows the relationship between atmospheric transmission and wavelength for the spectral interval covered by the S192, excluding the thermal infrared. In the visible region of the spectrum is a slight amount of absorption caused by ozone (O_3) at the shortest wavelengths. However, the most important attenuation mechanisms are those due to scattering by the gaseous (including water vapor) molecules and aerosols.

Chang and Isaacs (ref. 5-27) measured the attenuated direct solar beam on the Great Salt Lake Desert, Utah, during the Skylab pass on June 5, 1973. Figure 5-32 illustrates the spectral modification of incoming solar radiation. The reduced solar intensity that reaches the ground is available for evaporation and warming of the surface, and some may be back-reflected to space by the surface. This back-reflection produces photographs and signals for the S192, and the atmospheric effect has occurred on both the incoming solar beam and the exiting reflected beam.

The absorption and scattering functions for the dry gases in the atmosphere are generally well known (Rayleigh scattering). Extinction by water vapor, liquid water, and ice crystals (cirrus) is not as well understood, even though this factor appears to be of major importance in the heating and cooling of the atmosphere as
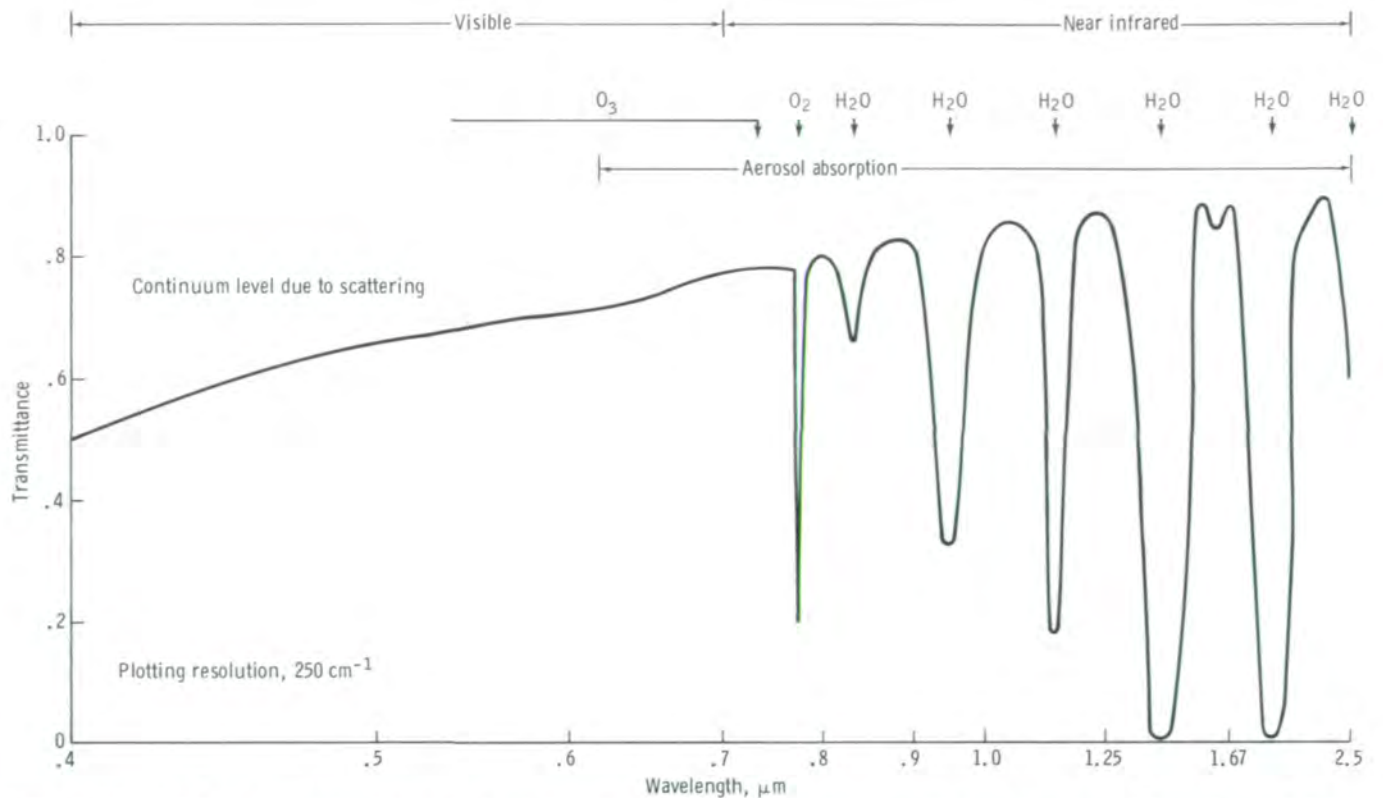
FIGURE 5-31.—Relationship between atmospheric transmission and wavelength for the spectral interval from 0.4 to 2.5 μm (from ref. 5-27).

well as in limiting the accuracy of remotely sensing certain Earth surface features. The extinction of energy is expressed in terms of optical depth.

Aerosol layers may be composed of dry haze, water-coated solid particles, or ice crystals. Sources of aerosols in the atmosphere are numerous and include volcanic eruptions, windborne soil particles, industrial and aircraft pollution, insects, protozoa and other microorganisms, and dust of extraterrestrial origin. The particles usually vary considerably in size, shape, chemical composition, and optical characteristics. In addition, aerosol layers are almost never homogeneous in either the vertical or the horizontal planes. In the atmosphere, an aerosol layer changes the radiative balance and produces both heating and cooling effects. The aerosol backscatter of incoming solar radiation increases the total Earth-atmosphere albedo, whereas the absorption of solar and terrestrial radiation increases the atmospheric temperature (and thus reduces the net radiative cooling). The aerosol number density, particle-size distribution, and location within the atmosphere may be of significant influence on the
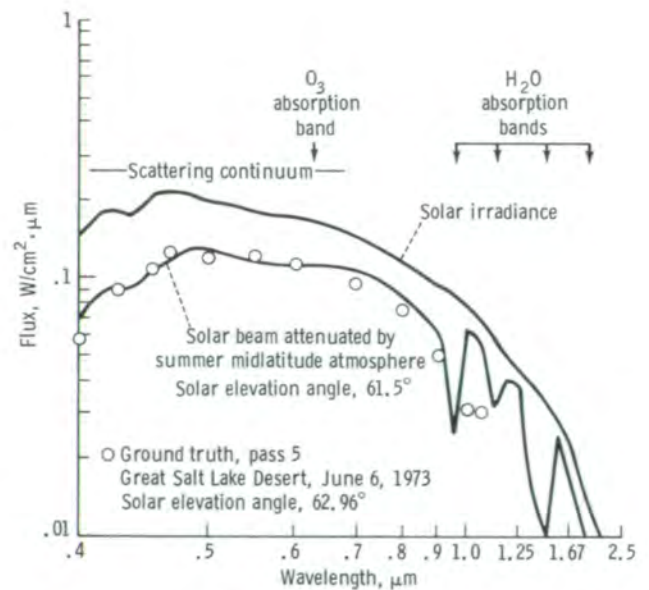

FIGURE 5-32.—Atmospheric effects on incoming solar radiation (from ref. 5-27).

FIGURE 5-33.—Sequence of moonset photographs (35 mm) obtained by Skylab.

strength of the atmospheric circulation. Eight Skylab investigations were devoted either primarily or in part to improving understanding of visible and infrared radiation transfer through aerosol layers (refs. 5-6 and 5-27 to 5-33).

Photographic examples of the results of atmospheric attenuation, refraction, and molecular scatter are seen in figures 5-33 and 5-34. In figure 5-33, the full Moon is seen setting beyond the Earth limb. The distortion of the Moon in the bottom frame results from refraction of the backscattered-reflected solar energy from the Moon through the Earth's atmosphere.

Excellent examples of the manner in which the white light of the Sun is refracted into its component colors are shown in figure 5-34, two series of photographs of the Earth limb as the Sun rises above (fig. 5-34(a)) and sets below (fig. 5-34(b)) the horizon. The red color predominates in the more dense portion of the atmosphere because all other colors of shorter wavelengths have been attenuated; that is, scattered or absorbed. As the molecular density decreases with height above the Earth's surface, the remaining color components appear, until all colors are seen as white light. The blue above the white light is due to scattering by the last remnants of the atmospheric molecules.

Within the dispersion of colors, the horizontal layers seen in frames 4 to 7 (fig. 5-34(a)) are indicative of large changes in the index of refraction. The values of these indices of refraction and their heights are significant and need to be evaluated in the radiation-transfer equations. Future limb-analysis investigations are expected to result in more detailed optical parameters through analysis of forward-scatter radiation, using techniques similar to those used by Tingey and Potter (ref. 5-32) with backscattered radiation.

Stratospheric Aerosols

The residence time of aerosols in the stratosphere has been conservatively estimated to be at least 18 months. Because of the concern about possible chemical and thermodynamic changes resulting from the release of aerosols into the stratosphere by man, many efforts have been made over the past decade to determine aerosol distribution. These efforts have included literally hundreds of aircraft, rocket, and balloon flights as well as ground-based searchlight and laser measurements.

Models based on these measurements yield typical aerosol optical depths of 0.5 for aerosols at altitudes above 20 km with probable variations as great as 5 to 10 times this amount. A stratospheric aerosol optical depth
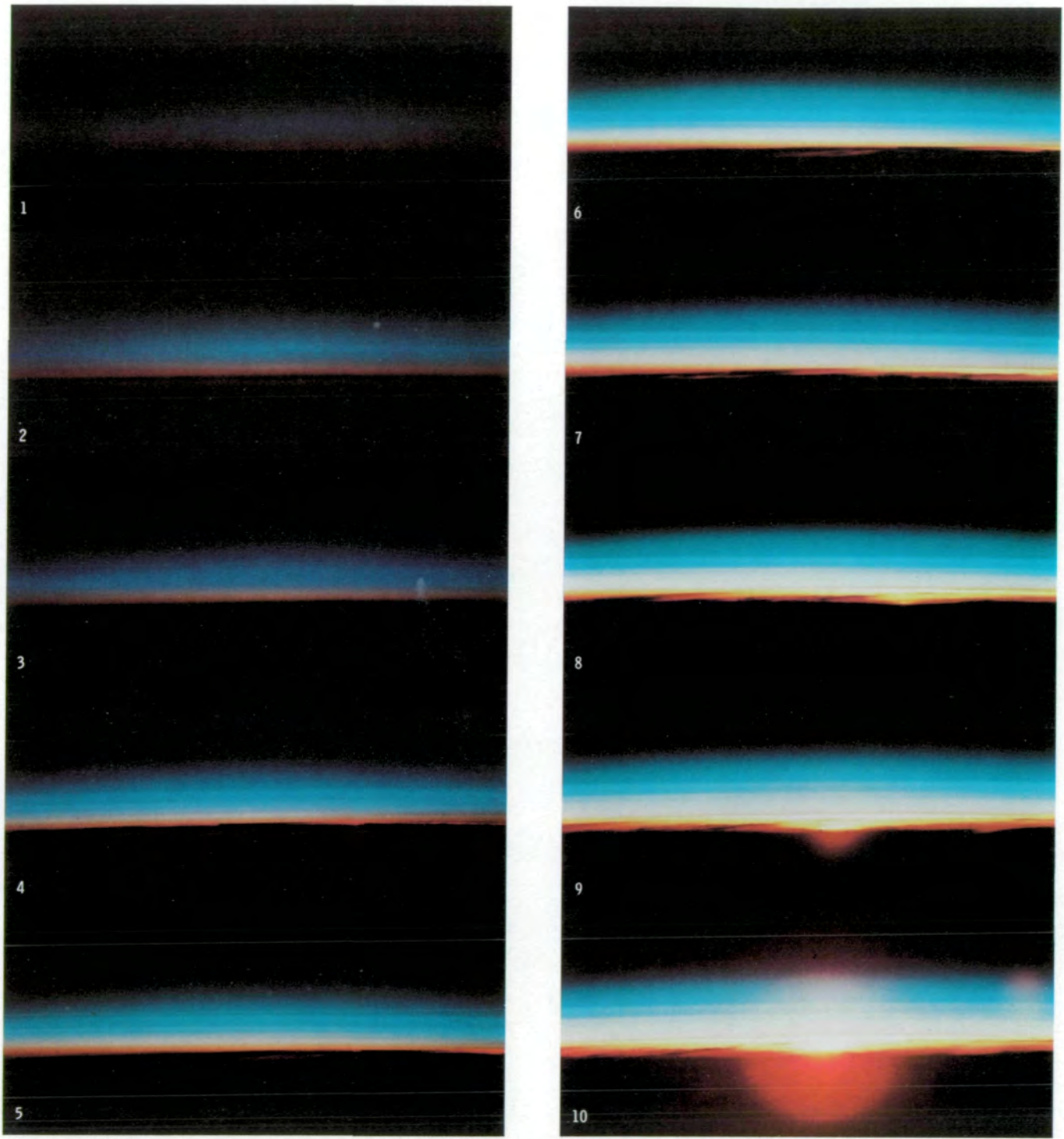
FIGURE 5-34.—Sequences of sunrise and sunset photographs (35 mm) obtained by Skylab 4. (a) Sunrise (SL4-200-7639 to SL4-200-7648). (b) Sunset (SL4-195-7315 to SL4-195-7319).

0   50
Scale, km
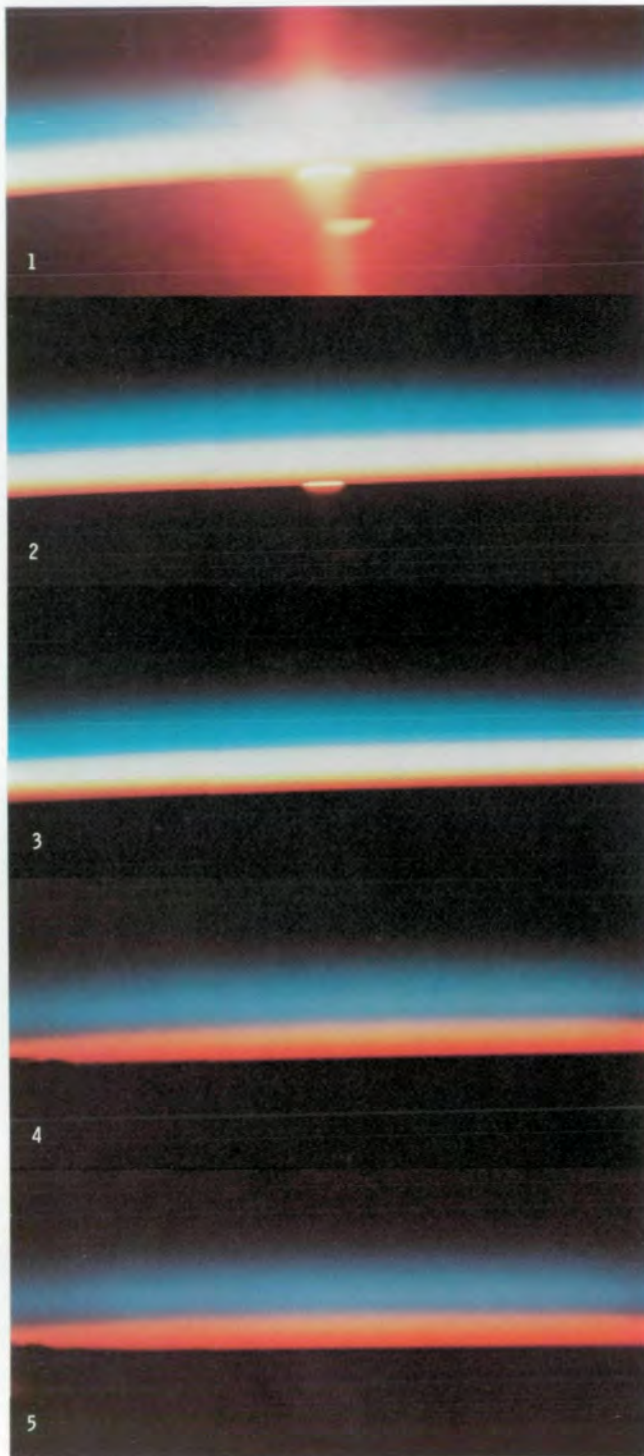
(b)

FIGURE 5-34.—Concluded.

of 2.0 has been shown to cause an error of several percent in classification of ground targets (ref. 5-32). Thus, both scientific and practical reasons exist for the study of the stratospheric aerosol layers.

The Skylab spacecraft usually orbited in a solar-inertial mode. During these periods, it was possible to obtain quantitative measurements of the solar backscatter of the Earth limb (fig. 5-35) to use in studying the distribution of aerosols in the higher atmosphere. Tingey and Potter (ref. 5-32) developed techniques to use limb-brightness measurements (by S190A, S191, and S192) to determine attenuation coefficients of haze layers in the stratosphere. By ratioing the coefficients of attenuation due to aerosols and to dry gases (Rayleigh), they were able to show the location and relative magnitude of haze layers. The results for one S192 pass are shown in figure 5-36; attenuation coefficient peaks associated with haze layers measured by S190A are shown in figure 5-37.

From this work, it was ascertained that several aerosol layers could be identified and that the attenuation coefficients could be evaluated quantitatively. It should be noted, however, that the results of this study were limited by the pointing accuracy of the spacecraft sensor and the absolute calibration of the radiometers. This study unquestionably verified that the limb-brightness technique is useful for evaluating the particulate content of the stratosphere. Aerosol layers were noted at 20-, 40-, 50-, 60-, and 67-km altitudes. Layers at approximately 40, 50, and 55 km appear to be more responsive to longer wavelengths (0.71 μm), whereas layers at 59 and 67 km are more easily detected in the bandpass centered at a wavelength of 0.53 μm. This approach can be used with data from future orbiting platforms to monitor the changes and variations in the stratosphere between 10 and 70 km.

Tropospheric Solar Radiation Attenuation

From the earliest days of aerial photography, it has been known that visible radiation attenuation in the Earth's atmosphere is primarily caused by aerosol scattering. Pioneer work by Lord Rayleigh (ref. 5-34), Mie (ref. 5-35), and, later, Van de Hulst (ref. 5-36) developed general concepts for describing the scattering of light from spheres. (Although it is recognized that most dry aerosols and ice crystals are not spherical, the equations for treating scattering from nonspherical particles are not yet available.) The development of the
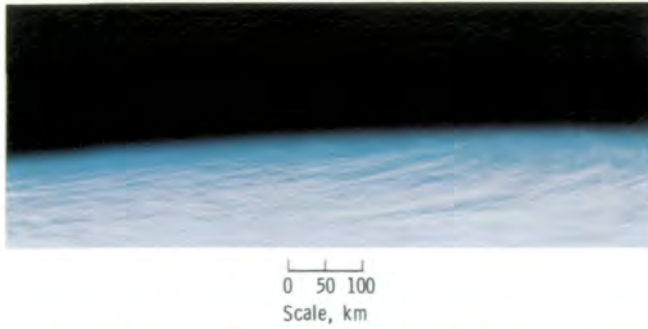
FIGURE 5-35.—S190A color-infrared photograph of solar backscatter from the Earth limb (SL4-52-388). Scale is applicable to limb portion only.
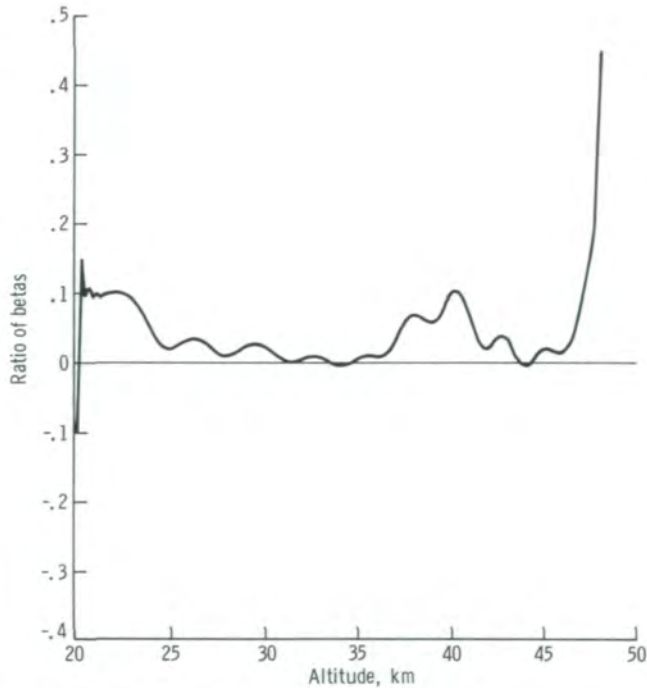

FIGURE 5-36.—Profile of aerosol attenuation in the stratosphere as measured by the Skylab Multispectral Scanner (from ref. 5-32). The ratio of attenuation coefficients (betas) due to aerosols and to dry gases is shown as a function of altitude. Ratio peaks indicate particulate layers.
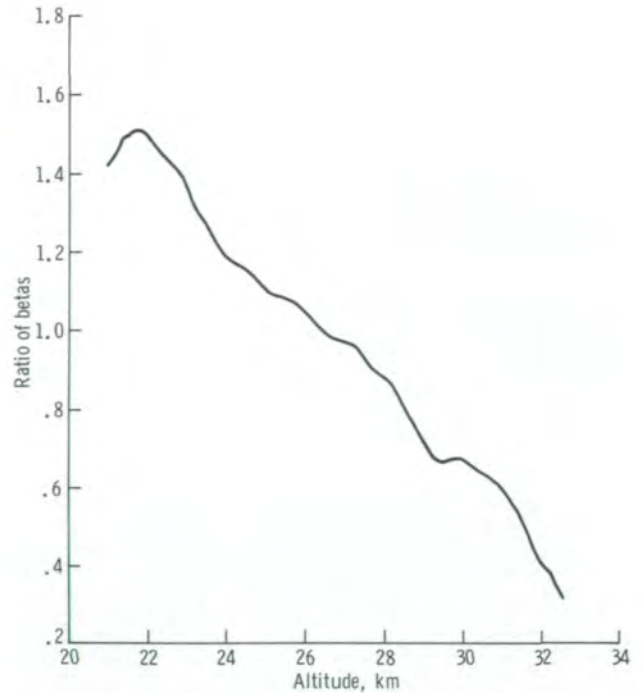
FIGURE 5-37.—Profile of aerosol attenuation in the stratosphere as measured by the Skylab Multispectral Photographic Camera (from ref. 5-32).

mathematical basis for modeling the transfer of radiation through scattering atmospheres is reviewed in the various EREP reports.

A primary function of solar radiation-transfer models is to correct for atmospheric albedo to obtain surface albedo. For the most part, the existing models are only theoretical constructions and thus have very limited applicability to remote sensing. To develop operational models, one must include a synthesis of radiation-transfer theory, surface-reflectivity characteristics, and an appropriate atmospheric description. The fact that few operational visible-spectrum transfer models have been developed is understandable for the following reasons. First, specialized types of accurate data input that are of uncertain availability are required. Second, the high costs associated with model computation time and ground-truth field measurements are often disproportionate to the resources available. Third,

many transfer models for atmospheric correction are not sufficiently accurate to warrant the atmospheric attenuation calculation. In the last case particularly, the discrepancy between theory and measurement results from a lack of understanding of the physical complexities of multiple scattering, the effects of variations in chemical and physical properties of the haze layers, and the lack of knowledge of the distribution of the haze layers in space and time.

Skylab provided a unique opportunity to make accurate comparisons of the results produced by the scattering models to high-quality measurements. The Skylab Concentrated Atmospheric Radiation Project (SCARP) (Kuhn et al., ref. 5-30) included a major field program designed especially to obtain field and aircraft data that could be used to test and compare visible-radiation transfer models through wet, dry, clean, and dirty atmospheres. A distinguishing feature of the study was the use of an aircraft to obtain atmospheric aerosol data. In addition, spectral measurements were made of the surface albedo, and direct measurements of aerosol optical depth were also obtained. The unique set of data collected for this study was considered representative of a large range of varying Earth atmospheres and surface targets with Skylab, aircraft, and ground-based observations collected for a maritime, humid atmosphere near Houston, Texas; a continental, hot, dry atmosphere near Phoenix, Arizona; and a combination dry-atmosphere and low-Sun-angle condition at White Sands, New Mexico.

From this study, it was concluded that single-scattering models are most sensitive to aerosol-refractive-index input and that aerosol optical depth is a critical input for the more refined multiple-scattering models. Of particular interest and practical importance was the evidence that more refined visible-radiation-transfer models are not improved by use of aerosol measurements from aircraft. Only measurements of aerosol optical depth made at the surface are needed to optimize model accuracy. Furthermore, by means of the SCARP measurements, techniques were developed to invert mathematically the surface optical-depth measurements to obtain the aerosol-size-distribution function. These two findings are considered of major importance for future remote-sensing activities.

Numerous Skylab investigations in fields varying from mineral exploration to oceanography included atmospheric corrections to provide more accurate information on true surface albedo (e.g., refs. 5-26 and 5-31). These investigations, although interesting from the standpoint of radiation transfer through the atmosphere for different airmasses and slant ranges, were primarily directed toward improving the measurement accuracy of remotely sensed surface phenomena.

Tropospheric Infrared Radiation Attenuation

In the previous subsection, radiation originating from the Sun, which has a temperature near 6000 K, was discussed. Radiation originating from sources having temperatures of usually less than 320 K is discussed herein.

On a worldwide basis, an average of 27 percent of the direct solar radiation and 20 percent of the energy reflected downward by or conducted from the atmosphere (or a total of 47 percent of the solar energy that reaches the top of the atmosphere) is absorbed by the Earth. The energy that is not used for evaporation and photosynthesis heats the surface and subsequently is reradiated at infrared wavelengths from the surface. In some wavelengths, it is absorbed by certain constituents of the atmosphere, primarily carbon dioxide, ozone, and water vapor, and thus heats the atmosphere. The combined effects of geographical variations in surface temperature and atmospheric absorption drive the "atmospheric engine." Measurements of the radiation budget components from satellites provide data on the energy budget of the Earth. These data comprise a primary information source for numerical weather forecast models. Hence, improvement in understanding the physics of infrared terrestrial radiation transfer through the atmosphere would directly contribute to improved numerical models for global weather forecasting.

A small part of the outgoing infrared radiation originates at the surface and in the clouds and escapes through the atmosphere through radiation "windows," which are the spectral regions between the absorption bands of the gases. Information on various aspects of
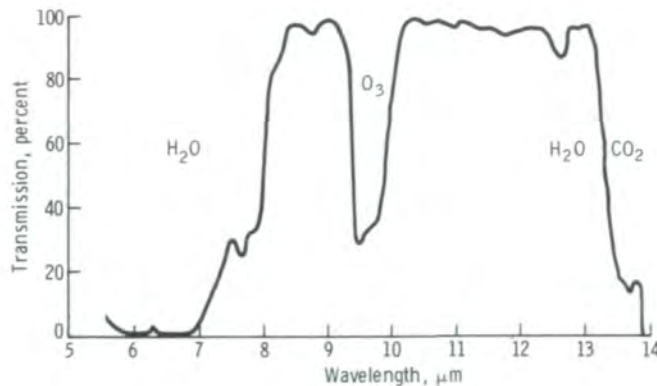
FIGURE 5-38.—Generalized atmospheric transmission in the infrared portion of the electromagnetic spectrum.

the atmosphere and its behavior can be obtained by measuring the upflux of terrestrial radiation at these selected wavelengths. Of particular importance in the measurement of cloud-top and Earth surface temperatures is the atmospheric window in the 8- to 12-μm region of the infrared spectrum. Because atmospheric gases cause little attenuation in this spectral band (fig. 5-38) and because the terrestrial radiation peaks in this region, most of the remote-sensing measurements of surface temperatures for studies in geology, agriculture, oceanography, etc. have been made in this spectral interval. Unfortunately, even in the early days of satellite meteorology, it was noted that at no place in the infrared spectrum was the atmosphere completely transparent. Even in the 10- to 11-μm region, a small amount of outgoing terrestrial radiation is absorbed by the water vapor in the atmosphere. In addition, a significant but usually unknown amount of attenuation occurs as the radiation passes through haze layers and invisible cirrus cloud layers (ref. 5-37). As a consequence, many corrections must be made before radiation measurements from Earth-orbital satellites can be translated into meteorologically meaningful parameters.

During the past decade, numerous theoretical and empirical models have been developed to permit rigorous analytical derivation of Earth surface and meteorological data from infrared-sensor measurements. Most models of infrared radiation transfer developed for remote-sensing applications differ significantly from one another in the manner in which the atmospheric transmissivity for the various gases and particulates is included in the radiation-transfer equations.

Determining the accuracy and utility of these models and investigating their application to the estimation of cloud-top, land, and sea-surface temperatures were major efforts of the EREP Investigations Program (refs. 5-8, 5-29, 5-30, 5-33, and 5-38).

One of the primary objectives of SCARP was to obtain field measurements of the critical parameters used in evaluating these models. Surface, aircraft, and balloonborne sensors obtained pertinent data under the Skylab spacecraft at targets in southeastern Texas and in the Gulf of Mexico (maritime, moist airmasses) and at White Sands, New Mexico, and Phoenix, Arizona (continental, dry airmasses). These data, together with the Skylab S191 measurements, afforded better insight into the mechanisms of infrared radiation transfer through the atmosphere, as well as a statistical comparison of the accuracy of the transfer models in current use (figs. 5-39 and 5-40). The SCARP investigation showed that, when sufficient information is available, the present numerical modeling is adequate for predicting the transfer of infrared radiation through the atmosphere with an accuracy of approximately 1 K.

For most studies, however, ancillary data from surface, aircraft, or balloon measurements are not available. To eliminate this requirement, Anding and Walker (ref. 5-6) developed a technique based on the use of the differential optical properties of the atmosphere in the infrared-window region to infer the atmospheric attenuation. They then used the attenuation values to correct for the effect of the absorption of atmospheric gases on radiometric data. As shown in figure 5-41, they demonstrated that this method of calculating the spectral radiance arriving at the top of a maritime atmosphere compared quite favorably with the S191 measurements. The agreement is excellent in the bandpasses from approximately 11 to 13 μm. For this evaluation, a 100-percent-maritime (wet) aerosol with 23-km sea-level visibility was assumed. To test the application of this method of analysis, the in-band brightness temperatures were computed and plotted against relative extinction coefficients (fig. 5-10).

In addition to the size, shape, and nature of the aerosol particle, the effect of the degree of wetness must be considered. In the Anding-Walker study and in the SCARP maritime study, the aerosol particles were assumed to be water coated. The White Sands and Phoenix aerosols were assumed to be composed of dry quartz. Examples of transmissivity of aerosol layers based on these assumptions are shown in figure 5-42.
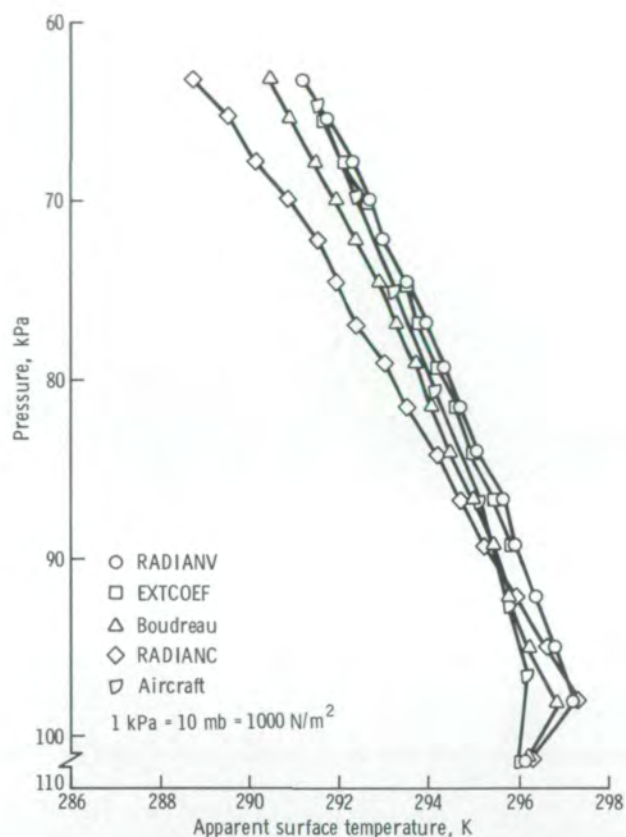
FIGURE 5-39.—Modeled and measured (aircraft) early-morning temperature profiles for Rosenberg, Texas, on August 9, 1973 (from ref. 5-30).

FIGURE 5-40.—Modeled and measured (S191 and aircraft) temperature profiles computed to the top of the atmosphere for Rainbow Valley, Arizona (from ref. 5-30).

The optical depth of the aerosol layers was measured by aircraft instruments for SCARP. When actual measurements were not available, assumptions of optical depth were based on horizontal visibility by Anding and Walker (ref. 5-6), Maul et al. (ref. 5-26), Turner (ref. 5-33), and others. The aerosol problem is further complicated because these layers are tenuous; that is, they change almost continuously in composition, size distribution, and location within the atmosphere. Although the Skylab EREP investigations provided helpful new data, the problem of aerosol attenuation of both visible and infrared radiation has not been solved.

Atmospheric Water, Clouds, and Precipitation

Water, because of its peculiar radiation-absorption characteristics, its changes of state within the normal ranges of atmospheric temperatures, its capability to absorb much of the heat radiated from the Earth's surface, and its large gradients of concentration, both horizontally and vertically in the atmosphere, is an important factor in the energy budget of the atmosphere and a dominant factor in the production of weather events. Earth-orbital satellites have provided major new contributions to knowledge of atmospheric water and have made possible the global assessment of the quantities, the forms, and the distribution patterns of atmospheric moisture as functions of time and space.

Clouds are of major meteorological significance for several reasons.

1. Clouds shield the surface from a portion of the solar radiation. Because of their high albedo, clouds reflect much of the solar energy back to space with the result that areas below clouds are cooler during daytime.

FIGURE 5-41.—Comparison of measured (S191) and calculated spectral radiance for Key West, Florida, on January 8, 1974 (from ref. 5-6). (Sea-surface temperature, 296 K; emissivity, 0.99.)

2. Cloud layers absorb much of the outgoing terrestrial radiation. This absorbed heat is partially reradiated to the surface and the lower layers of the atmosphere. As a result, areas under cloud cover remain warmer at night than they would under clear skies.
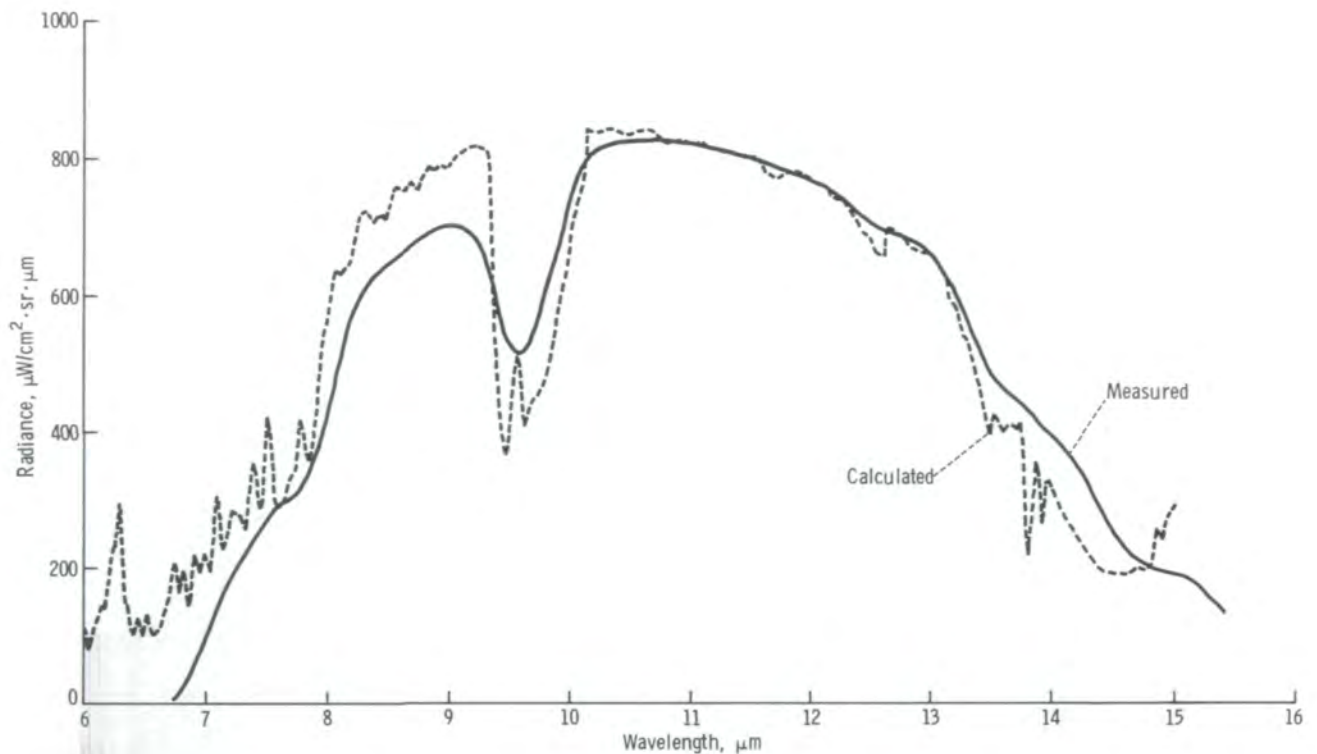
3. Clouds serve as reservoirs of latent heat because the air in them is saturated; they also serve as mechanisms for the transport of energy between latitudes.

4. Cloud cover controls, at least in part, the atmospheric stability. This stability in turn is closely related to the geographical distribution of precipitation and to the type of precipitation received.

Much information about the state of the atmosphere can be derived simply by noting the changing state of the clouds. Nephanalysis, the science of weather analysis from cloud-pattern studies, provides clear indications of atmospheric pressure, temperature, and air circulation, as well as the distribution of moisture itself. Many meteorological characteristics of an airmass may be inferred from satellite-based observations of the clouds associated with it. Sheetlike clouds are usually indicative of slow, widespread lifting of moist air. This type of cloud is often associated with orographic lifting on the windward side of mountain ranges, in the frontal zones between contrasting airmasses, and in areas where the water vapor in warm air passes over cool surfaces, condenses, and produces low stratus or fog. Tower clouds, on the other hand, are formed in areas of marked atmospheric instability with strong vertical air currents.

It is often possible, then, to assess the extent of cloud cover, the type of cloudiness, and the degree of vertical motion from nephanalysis of satellite measurements of clouds. The thickness of unstable layers can be estimated from cloud-top temperatures. The height of cloud bases can be calculated from the geometry of the cloud and from cloud shadow locations on the satellite photograph. Temperature inversions may be inferred by noting where the flattening of cloud tops occurs; such flattening is indicative of the subsidence of warmer, drier air aloft. Phase-change level may be determined by noting the change in cloud outlines

where the sharply defined water clouds give way to the diffuse ice crystal layers.

In addition, it is often possible to identify areas of strong convection from shadows of tall cumulonimbus towers (particularly under low-Sun-angle conditions). Jet-stream cirrus often casts shadows on lower cloud decks, and thin, high cirrus may be identified by its influence on the image of lower clouds. Satellite photographs of cloud patterns show that the cloud elements may be either randomly distributed or organized into some regular formation. Such formations are normally associated with one or more atmospheric and/or topographic factors.

Because other satellite programs are dedicated to obtaining detailed information on the state of the atmosphere, the number of meteorological experiments on Skylab was limited. The capability of man to take high oblique photographs and stereophotographs is unique, and the information gained by the Skylab crewmen's photographic documentation demonstrates forcefully the value of manned space programs. The Skylab 4 crew acquired stereophotographs of numerous classical and unique cloud patterns, including thunderstorms, tropical and extratropical cyclones, mountain wave clouds, convection in cold air passing over warm water, jet-stream cirrus, island vortex and convection effects, sea breezes, cloud streets, and sub-synoptic-scale atmospheric circulations.

The cloud-street orientation seen in figure 5-14(a) is an example of the manner in which cloud rows are used as an indicator of low-level windflow in areas for which radiosonde and surface meteorological observations are not available. Pitts et al. (ref. 5-28) conducted a field program to obtain hourly radiosonde soundings concurrent with photographic data for a cloud-street pattern over Fort Sill, Oklahoma, in June 1973. They learned that the cloud-street orientation conformed to the wind vector at the base of a temperature inversion (cloud-top height) in this case.

The remote measurement of air movement at different altitudes has been attempted by means of various techniques ranging from measurements of cloud-street orientation to the satellite monitoring of the movements of constant-pressure balloons.

In another experiment, Villevieille and Weiller (ref. 5-39) related vertical-wind profiles with cloud-street parameters using satellite photographs. This study presents the theoretical development and algorithms of techniques for calculating important atmospheric
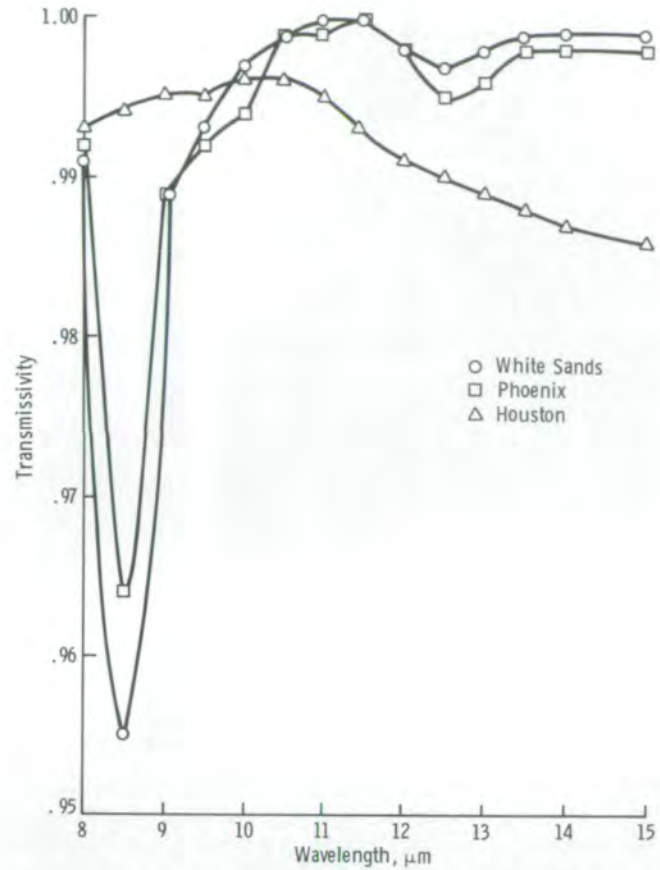
FIGURE 5-42.—Transmissivities due to aerosols computed from EXTCOEF using the aerosol-size-distribution data collected at three test sites (from ref. 5-30).

stability and wind-shear parameters. Further discussion of the methodology of vertical-wind-profile calculations is included in section 6.

In earlier studies, Kuettner (ref. 5-40) and LeMone (ref. 5-41) reported that the range of the ratio of the spacing between the horizontal streets to the height of the temperature inversion was 2 to 4. The EREP data indicated that this spacing ratio was 1.7 for the Fort Sill, Oklahoma, study, which was slightly less than the ratio range found in the earlier studies.

Investigations to describe cloud physical structures using cloud radiance measurements met with varied results. Curran et al. (ref. 5-29) attempted to compare the cloud-top altitudes measured by using 11-μm thermal-infrared (S192 channel 13) radiation with those

FIGURE 5-44.—Ratio of cloud reflectance at 1.61 μm to that at 0.754 μm as a function of cloud optical thickness at the latter wavelength. Bands are formed by two extremes in particle-size distribution, with a small-particle distribution (mean particle radius $\bar{r}$ = 4.5 μm) forming the upper bound and a large-particle distribution ($\bar{r}$ = 16.2 μm) forming the lower (from ref. 5-29).

FIGURE 5-43.—Computer-generated image of the thermodynamic phase of water in an S192 cloud scene (left) as compared to the false-color thermal-infrared image (middle), the color temperature scale for which is shown at right (from ref. 5-29).

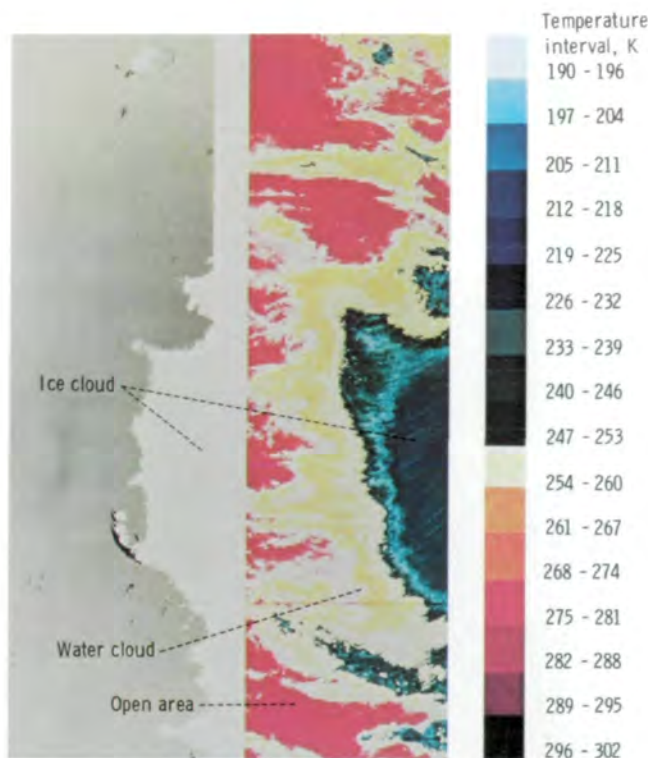using stereoscopic techniques on S190 photographs. A qualitative comparison of cloud-top temperatures with the water phase of the cloud top is shown in figure 5-43 and indicates that future studies of this type can provide useful meteorological information.

Skylab EREP investigations confirmed that infrared sensors on satellites tend to either underestimate or overestimate cloud-top altitudes based on their black-body temperatures. High clouds (15 000 m) were underestimated by approximately 1000 m and low clouds (3500 to 7000 m) were overestimated. These errors were to be expected unless the measurements were corrected for gaseous and aerosol attenuation, because even small errors in temperature result in quite large errors in altitude estimates.

Curran et al. (ref. 5-29) found that the ratio of cloud reflectance at wavelength 1.61 μm to that at wavelength 0.754 μm as a function of the cloud optical thickness at 0.754 μm can be used to distinguish between clouds composed of ice crystals and those composed of liquid droplets (fig. 5-44). When applied to the multispectral scanner, appropriate channel data enabled determination of the thermodynamic phase of the cloud tops. Alishouse et al. (ref. 5-38) and Pitts et al. (ref. 5-28) also ratioed reflectances in the narrow bands in the visible and near infrared to distinguish between ice crystal and water droplet clouds.

Skylab EREP experiments provided some evidence that discrimination is possible among cloud ice crystals, cloud water droplets, and surface snow. However, the need exists to extend discrimination to include super-cooled water droplets, mixes of ice crystals and water droplets, ice crystal stabilization (i.e., agitated in cumulus top as opposed to tropopause stratification), and mixes of surface snow crystal structures.

Because of its spectral reflective and thermal characteristics, snow cover greatly affects both the energy budget at the surface and the regional water balance. New advances in snow-cover mapping using Skylab sensors are discussed in sections 4 and 6.

Soil Moisture

Although the determination of soil moisture content is normally considered in the realm of agriculture, the meteorologist is interested in spatial and temporal variations of soil moisture, particularly in the first few

centimeters below the surface, because the moisture content of the surface soil strongly influences soil thermal properties and evapotranspiration rates. Because water has a greater specific heat than does mineral soil, for a given heat input, moist surface soils will be cooler than dry soils during the day.

Marwitz (ref. 5-42), Davies-Jones (ref. 5-43), and Sasaki (ref. 5-44) have shown that the inflow air source for severe thunderstorms is from the near-surface layer of the atmosphere. Heat and moisture from the soil transferred through this inflow air provide additional energy to the storm system. Beebe (ref. 5-45) reported that the tornado frequency maximums in the Texas Panhandle were centered in a region of extensive irrigation. He concluded that the increased water vapor supplied to these tornado cloud systems was a result of evapotranspiration from the irrigated fields.

In theory at least, the use of microwave frequencies is a direct approach to the measurement of soil moisture. Water has a very high dielectric constant; soils have very low constants. Moist soils therefore have a dielectric constant that is proportional to the relative amounts of water, soil, and air present.

The influences of soil type, surface roughness, and vegetative cover on microwave emission are all wavelength dependent with the strongest effects at the shorter wavelengths (ref. 5-28). A significant advantage of the longer wavelengths is that measurements are not restricted to cloudless skies. At L-band (approximately 21 cm) wavelengths, the atmospheric transmission is close to unity with little influence from clouds or gaseous absorbers.

Several studies were conducted to evaluate the microwave L-Band Radiometer (S194) for soil moisture determination. These results are described in section 6. Pitts et al. (ref. 5-28) compared L-band measurements with an index of antecedent precipitation for two Skylab passes across Oklahoma, New Mexico, and Texas. The antecedent precipitation index (API) is a simple method of characterizing the precipitation history in which

$$\mathrm{API} = \sum_{i=1}^{n} K^i P_i \qquad (5\text{-}2)$$

where P_i is the daily precipitation for each day from n days previous to the current day i and K characterizes
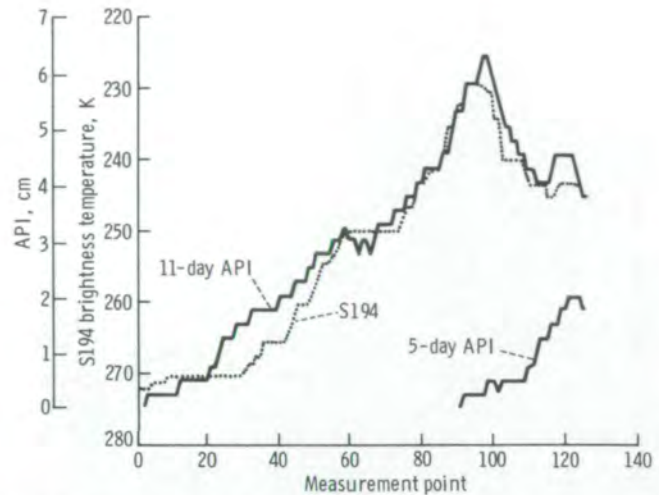
FIGURE 5-45.—Comparison of S194 L-band brightness temperature and average 11-day antecedent precipitation index (API) and 5-day API for June 11, 1973, over southwestern Oklahoma and northeastern Texas (from ref. 5-28). The lack of correlation between the 5-day API and L-band brightness temperatures indicates the necessity of averaging precipitation for longer periods.

the loss of moisture from the soil due to evapotranspiration and deep percolation and is a function of soil type, slope, season, and vegetation.

The antecedent precipitation index is compared with S194 brightness temperature for a Skylab pass across southwestern Oklahoma and northeastern Texas in figure 5-45. From the studies, it is concluded that the L-band of the microwave is well suited for remote sensing of synoptic soil moisture over large areas under a wide variety of weather, vegetation, and terrain conditions.

Measurement of Sea-Surface Winds

The major purpose of the radiometer-scatterometer (ref. 5-46) experiment was to obtain simultaneous measurements of radar backscatter and passive microwave temperatures to demonstrate that the passive microwave temperatures could be used to correct for atmospheric attenuation and that the backscatter measurements, after correction, could be used to determine windspeed and wind direction.

The winds over the ocean surface are very difficult to measure. The windspeeds increase with height, and the rate of increase depends on the difference in temperature between the water and the air. Moreover, the

FIGURE 5-46.—Spectra of waves that exist simultaneously on a water surface with specified windspeeds (from ref. 5-47).

winds are turbulent and fluctuate about an average value in both speed and direction. For improved numerical weather prediction methods, the properly averaged winds need to be measured on an oceanwide scale and on a uniform grid of points. Data obtained from the S193 provided a scientific breakthrough in the field of the meteorology of ocean wind fields.
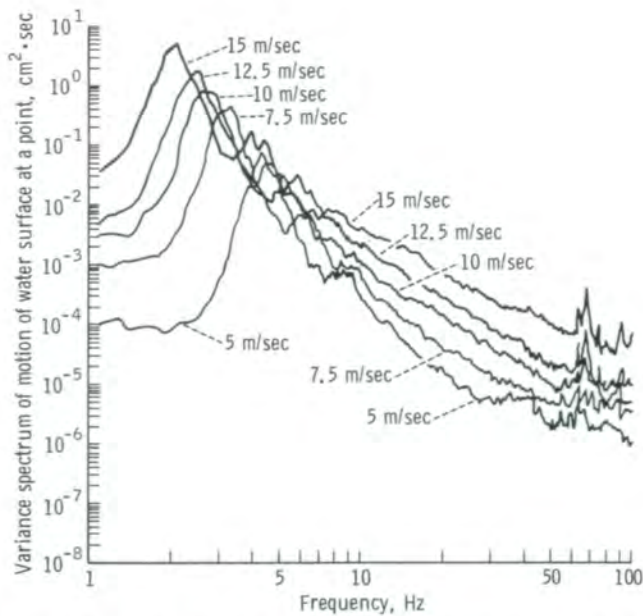
The winds generate waves of all lengths simultaneously on the ocean surface. These wavelengths vary from 0.6 cm to more than 600 m, with the highest waves traveling in the wind direction. Some waves travel in directions that are $\pm 90°$ relative to the wind direction. As the windspeed increases, waves of all lengths grow in height.

That the height of high-frequency capillary waves increases with an increase in windspeed has been shown by measurements made by Mitsuyasu and Honda (ref. 5-47) in a wind-water tunnel. This experiment provides high-frequency-spectrum data to support the theory that capillary wave structure is a dominant factor in radar backscatter, and the data show a power-law windspeed dependence. Figure 5-46 shows that the spectrum of the waves grows with windspeed in the 5- to 30-Hz frequency range when observed as a function of time at a point. The winds in the tunnel for the five curves shown had nominal velocity values of 5, 7.5, 10,

12.5, and 15 m/sec; the curve for the 15-m/sec windspeed corresponded to 33-m/sec winds at an elevation of 10 m above the sea surface.

The growth in height of intermediate-length waves and the increasing roughness of the sea with increasing windspeed are strikingly illustrated by a series of photographs taken from the weather ship *Papa* while stationed in the North Pacific (ref. 5-48). The sea surface becomes increasingly rough as the speed of the wind, as measured just above the surface, increases. The S193 measured this increase in roughness and, at incident angles of 50°, 43°, and 32°, the radar backscatter that was measured for a given relative wind direction increased with windspeed. The measured radar backscatter was correlated both theoretically with sea-surface roughness and winds (ref. 5-49) and directly with the winds by means of multiple-regression techniques (ref. 5-49). Sea roughness is dependent on both wind direction and windspeed. The Skylab results demonstrate that, if the wind direction is known from an independent source, the windspeed can be determined from the backscatter measurement. The Advanced Applications Flight Experiments (AAFE) Langley Radscat Program showed that, as the windspeed increases by a factor of 5, the backscatter increases by more than a factor of 10 (fig. 5-47).

Fung and Chan (in ref. 5-49) succeeded in using the spectral form for the capillary waves shown in figure 5-46 and the available information on the slopes of the longer waves (perhaps 10 m long and longer) to derive a composite theory for backscatter. The large-scale wavy surface was tilted back and forth (in theory), and the backscatter from the small waves, which were approximately 2 cm long, was calculated for the different slopes and summed over the slopes. A typical result is shown in figure 5-48, where the parameter a_o describes the angular spread of the capillary wave spectrum.

Three methods were used to determine the wind-field parameters which were correlated with the S193 data. For Hurricane Ava and tropical storm Christine, one of the methods, used to compute the wind-field characteristics for a 160 000-km² area, was developed for a program independent of Skylab. The model required input information regarding the speed of movement of the storm over the ocean surface, the central pressure, and the radius of maximum winds. Each cell scanned during the Skylab pass over the cyclone was assigned an appropriate wind direction and speed based on this theory.
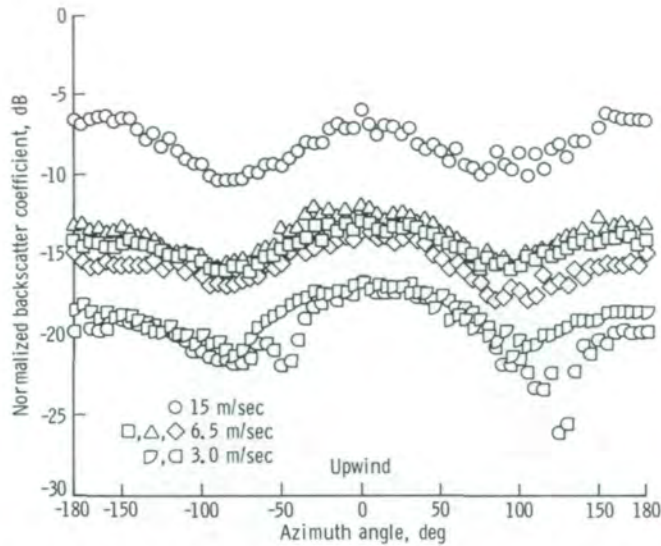
FIGURE 5-47.—Influence of windspeed and wind direction on backscatter intensity from aircraft radar data.

A synoptic analysis for tropical storm Christine based on conventional shipboard data is shown in figure 5-49, in which the rectangular area indicates the S193-scanned width. Conventional data provide very little information on the characteristics of the wind field in a tropical storm because mariners avoid these areas.

Although the winds in Ava and Christine were determined from a theoretical boundary-layer model for an intense moving vortex, the theory was cross checked against data on winds and other parameters obtained by aircraft flights into both storms. For Hurricane Ava, an NOAA C-130 aircraft penetrated to the eye and measured winds near the sea surface at an elevation of approximately 150 m and at other elevations within the storm at the eyewall. These data, together with central pressure determined from dropsondes into the eye, and glitter patterns in the periphery of the storm were used to check the reasonableness of the final model wind field. An example of one check is shown in figure 5-50, in which the winds measured by the aircraft are correlated with the theoretical winds for the appropriate sector of the tropical hurricane (ref. 5-50).

Figure 5-51 (tropical storm Christine) provides a graphic representation of the meteorologically determined vector wind and the measured backscatter value before correction for attenuation and without any concern with the variability of the backscatter value with

wind direction. The arrows that appear to lie in the horizontal plane (with some perspective) are the values of the windspeeds and wind directions, as shown by the appropriate scales, at each of the cells. The spacecraft passed over the bottommost row of cells, which correspond to the nadir measurements. For incidence angles of 31°, 42°, and 50°, the values of the vertically polarized and vertically received backscatter are graphed as vertical bars at each cell. The exact range of variation as a function of windspeed depends on the incidence angle, so these variations in backscatter should be studied along each line at a given incidence angle. For the 31° plot, the backscatter for the low winds in the lower left is approximately −18 dB, increases to greater than −5 dB for one of the cells near the eye, and then decreases with decreasing windspeed to the upper right point. Similar remarks are appropriate for each of the lines scanned for the other two incidence angles. This figure is considered highly significant in that it constitutes the most convincing demonstration of the evident correlation between the winds near the surface of the ocean and the measured value of the radar backscatter.

A second method used to determine the winds in the S193-scanned area was to plot data from all available shipping and coastal reports and perform a streamline isotach analysis of the wind field (ref. 5-49). Streamlines are curved lines everywhere parallel to the reported wind direction, and isotachs are contours of
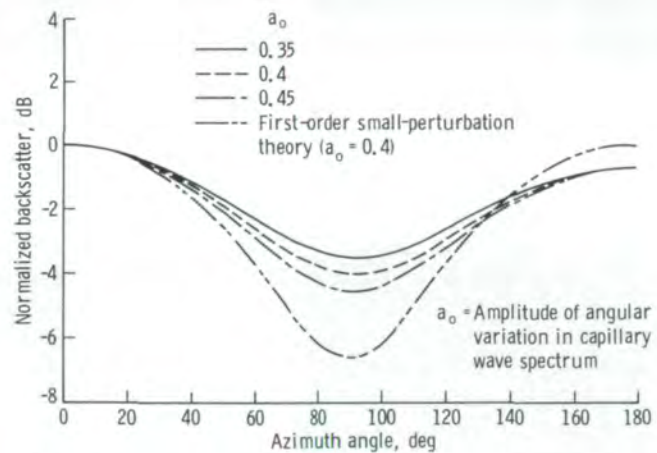
FIGURE 5-48.—Azimuthal dependence of backscatter at 12.9-m/sec windspeed, 13.9-GHz frequency, and 60° angle of radar beam from the vertical at the surface for various choices of a_0 for vertical-transmit/vertical-receive polarization (from ref. 5-49).
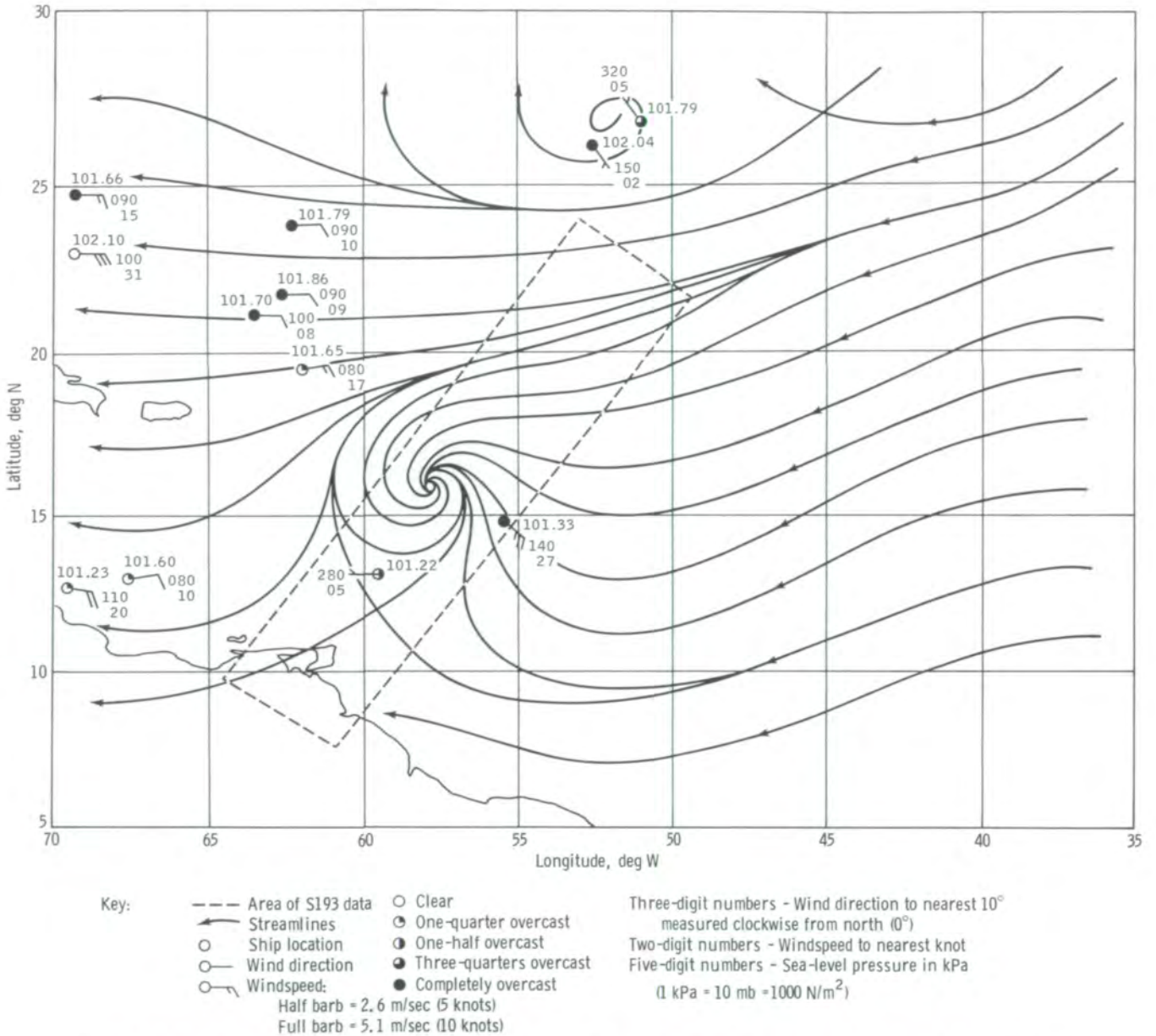
FIGURE 5-49.—Location of S193 pass over tropical storm Christine at 18:00 GMT on September 2, 1973 (after ref. 5-49).

equal windspeed. For the subtropical areas of the world, this analysis was performed for numerous Skylab 2 and 3 passes. The windspeed and the wind direction at each of the cells scanned were then read from the streamline isotach analysis.

The third method of data analysis was a computer technique (ref. 5-49) developed for determining wind in middle-latitude extratropical cyclones and in other changing pressure systems. These systems produce the most important day-to-day wind fields over the ocean. In this analytic technique, the quality of the various reports in the area is weighed by source, depending on whether the reports are made by weather ships, ships with anemometers of known height, ships with anemometers of unknown height, or transient ships that estimate the winds from wave appearance. In some
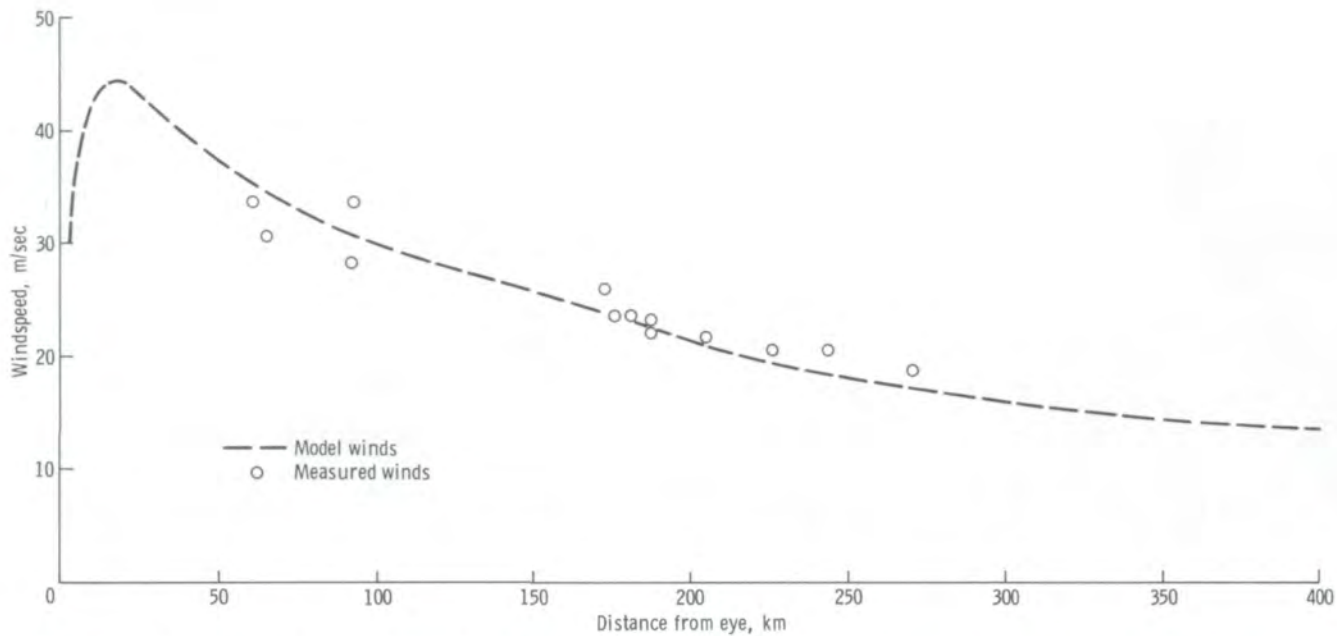
FIGURE 5-50.—Comparison of averaged flight-level (150 m) windspeeds and model winds in the eastern (rear) quadrant of Hurricane Ava (from ref. 5-49).

areas, no reports were available and the winds had to be calculated from the pressure gradients. For many of the cells scanned by the S193 during Skylab 2 and 3, the winds were determined in this way; this technique was used for all the cells scanned during Skylab 4. The procedure corrects for the wind variation with height above the sea surface and refers all winds to an elevation of 19.5 m. It also corrects for atmospheric instability, which produces an additional variation. In effect, the wind with which the backscatter measurement was compared was the wind that would have produced the same wind stress on the sea surface for a neutrally stratified atmosphere.

The scale of the wind fields in extratropical cyclones is illustrated by an analysis performed by Ross (ref. 5-50) as shown in figure 5-52. This cyclone was one of the most intense of the past 20 years. The isobaric pattern and the windspeeds reported by ships near the time of a Skylab pass are shown. The scales involved can be inferred by comparison with the size of the Gulf of Saint Lawrence, which can be seen in the upper left.

The final result of these analyses was provided in an appendix to reference 5-49, in which the measured backscatter values, the passive microwave temperatures, the windspeed and wind direction, the latitude and longitude of the cell, and the time of the observation are tabulated. Table 5-II is taken from reference 5-49. The S193 azimuth is the direction toward which the radar beam is pointing. The aspect angle is the direction of the wind vector relative to the pointing direction of the radar beam. For zero degrees, the beam is pointing upwind; plus is clockwise and minus is counterclockwise.

Correction of the backscatter measurements for the effects of attenuation using the passive microwave measurements was accomplished by using the brightness temperature at an incidence angle of 50°. Differences between the temperatures that were measured and the temperatures that would have been measured (as determined by the sea-surface temperature in the absence of attenuating effects) were calculated. These differences can be shown to be caused by the intervening cloud droplets and rain between the spacecraft and the sea surface. This excess microwave temperature was correlated with attenuation based on independent measurements of the atmospheric temperatures and corresponding attenuations made with a number of ground-based upward-looking passive microwave receivers. This correlation determined the two-way attenuation in decibels for the scatterometer.
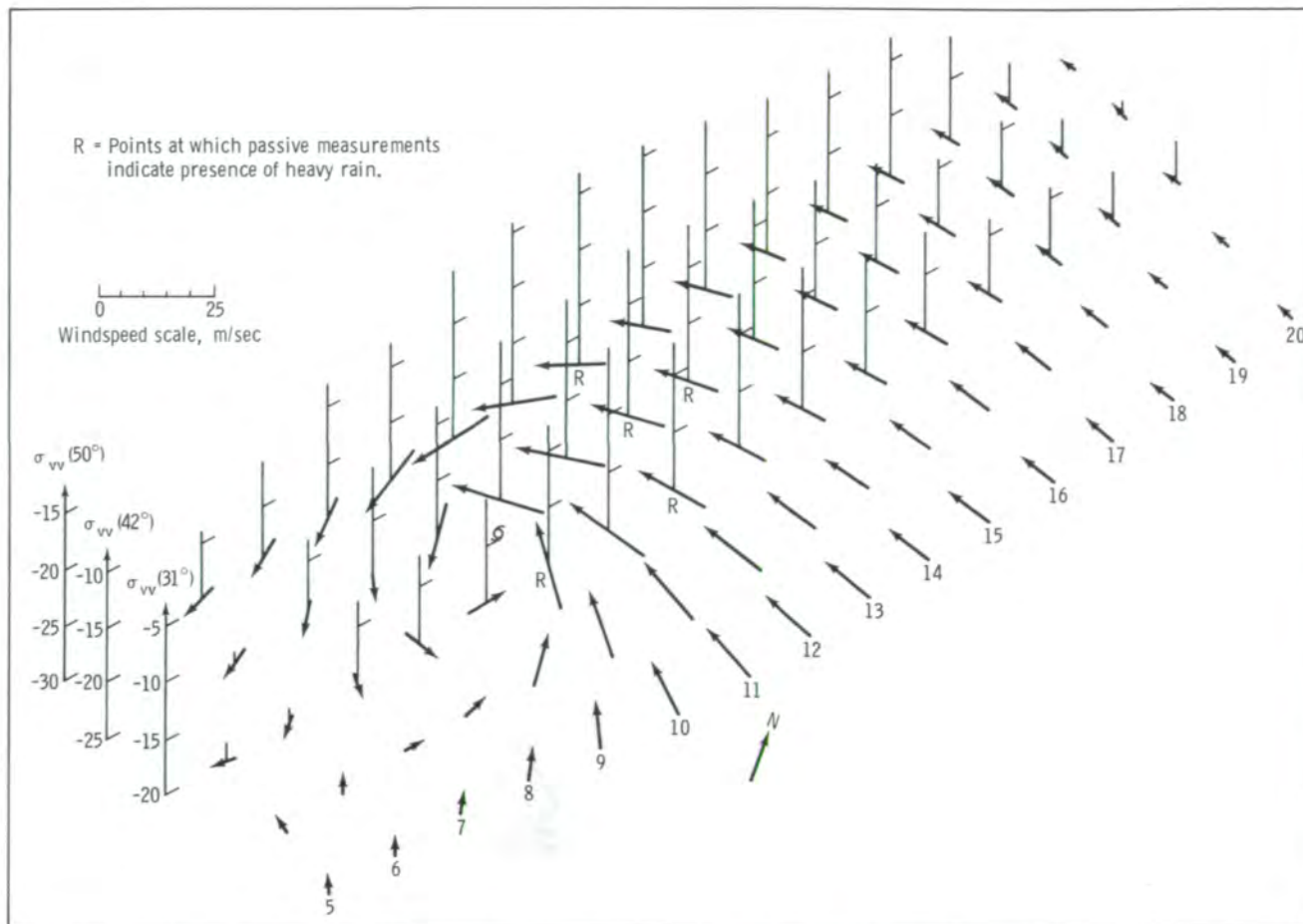
FIGURE 5-51.—Comparison of uncorrected radar backscatter measurements in tropical storm Christine and the vector winds at the cells scanned (from ref. 5-49). The symbol σ_{vv} represents vertically polarized and vertically received backscatter with values expressed in decibels.

For Skylab 2 and 3, a histogram of the attenuation as calculated at each 50° incidence angle is shown in figure 5-53. Because the backscatter values range over 20 dB or more as the windspeeds vary from 3 to 25 m/sec, a 0.2- or 0.3-dB correction is quite small and barely affects the calculation of the windspeed. Attenuation could not be computed for the Skylab 4 data because the antenna was damaged during the repair of the scanning subsystem. However, based on Skylab 2 and 3 results, the inability to correct the attenuation could not have appreciably affected the calculation of the winds.

For certain cells scanned by the S193, the excess

microwave temperatures were extremely high compared to the usual values of the excess microwave temperature just described. These "hot" spots are indicative of large cloud droplets and falling rain. In this situation, the measured backscatter cannot be used to calculate windspeeds because most of it is coming from the clouds and rain. Figure 5-54 shows the marked increases in passive microwave temperature on one of the lines of cells of constant incidence angle over tropical storm Christine. Even for heavy cloud cover in a tropical storm, the attenuation values are not prohibitively large except for the scans in which very sharp peaks
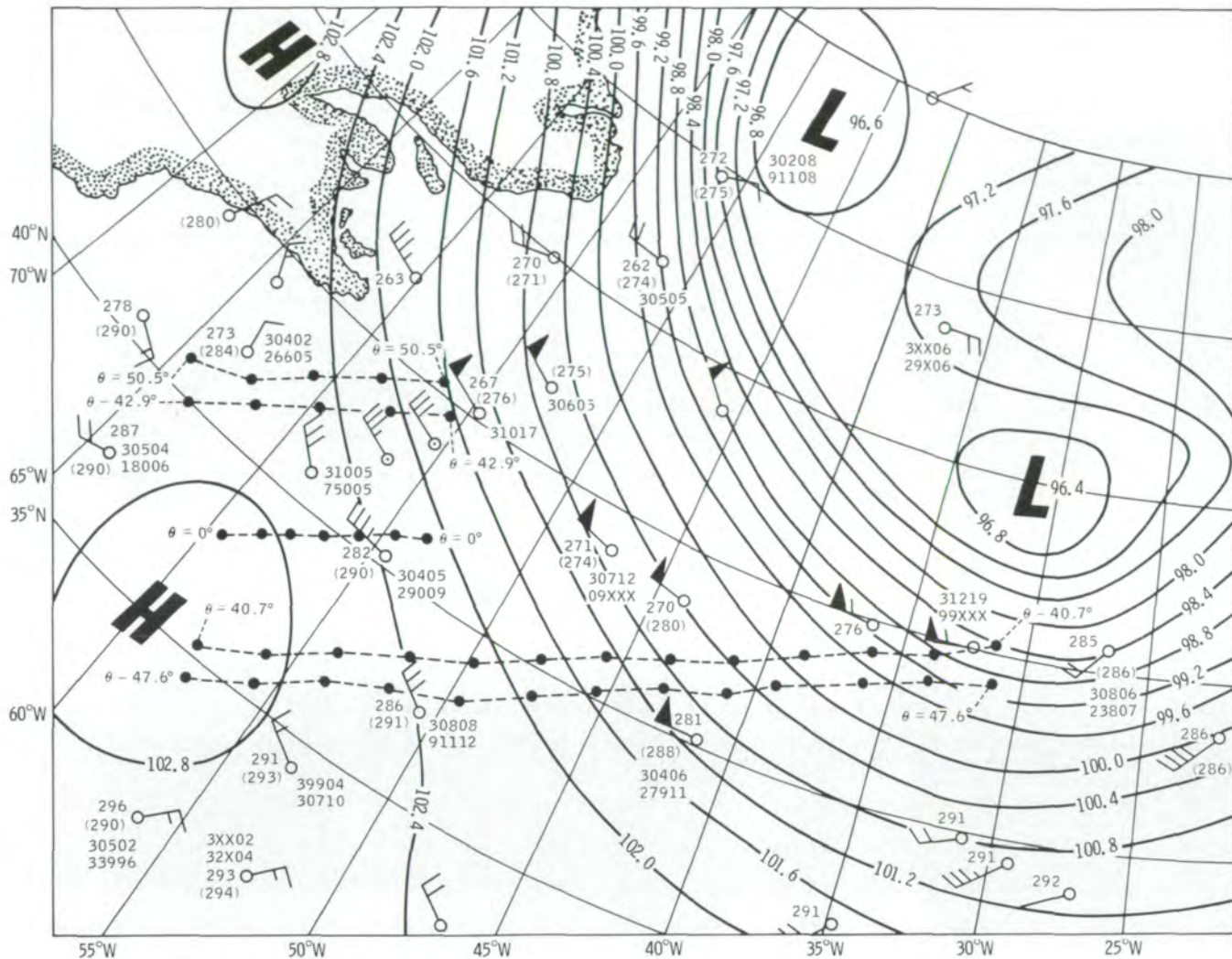
Key:
- Points scanned by S193
- θ Incidence angle of Skylab measurements
- ○ Ship location
- ⊙ Aircraft location
- Wind direction
- Windspeed:
  - Half barb = 2.6 m/sec (5 knots)
  - Full barb = 5.1 m/sec (10 knots)
  - Flag = 25.7 m/sec (50 knots)
- Isobars express sea-level pressure in kPa

  $(1 \text{ kPa} = 10 \text{ mb} = 1000 \text{ N/m}^2)$

Three-digit numbers:
- Air temperature in kelvin (unparenthesized)
- Sea temperature in kelvin (parenthesized)

Five-digit numbers:
- Upper or only set – Sea conditions
- Lower set – Swell conditions

30502
- └── Sea height in half meters
- └── Wave period in seconds
- └── Meteorological code

33996
- └── Swell height in half meters
- └── Swell period in seconds (0 to 4 = 10 to 14 sec or more)
  (5 to 9 = 5 to 9 sec)
- └── Swell direction from which waves come in tens of degrees

99 = Confused conditions
X = Missing data

FIGURE 5-52.—Surface weather chart of extratropical cyclone observed on January 9, 1974 (from ref. 5-50).

TABLE 5-II.—*Merged Meteorological, Oceanographic, Radar Backscatter, and Passive Microwave Data for a Portion of the Pass Over Tropical Storm Christine*

Scan no.	Incidence angle, deg	Scattering coefficients, dB				Antenna temperature, K		Aspect angle, deg	Windspeed, m/sec	Sea temperature, K	GMT, hr:min:sec	Cell coordinates, deg		S193 azimuth angle, deg
		VV[a]	HH[a]	VH[a]	HV[a]	V[b]	H[b]					Lat. N	Long. W	
10.1	49.7	−15.22	−19.26	−25.80	−25.48	175.11	118.20	86.4	20.1	301.16	17:56:32.5	16.55	59.28	312.6
10.2	42.1	−11.27	−13.36	−21.19	−21.05	166.30	127.40	134.1	23.2	301.16	17:56:36.0	16.14	58.44	312.9
10.3	31.0	−7.95	−8.64	−21.08	−21.38	199.10	198.13	−189.2	20.6	301.16	17:56:39.2	15.61	57.52	313.2
10.4	16.6	1.81	2.60	−14.02	−14.30	159.94	168.10	−172.1	16.5	301.16	17:56:42.0	15.03	56.58	314.1
10.5	.9	—	12.25	−4.65	−4.73	134.40	131.29	130.0	13.9	301.16	17:56:44.2	14.45	55.70	6.0
11.1	49.7	−14.33	−18.65	−25.84	−26.11	176.41	118.98	107.3	19.0	301.16	17:56:47.7	17.30	58.68	312.7
11.2	42.1	−11.03	−13.35	−21.83	−21.66	164.66	124.29	128.0	22.1	301.16	17:56:51.2	16.88	57.83	313.0
11.3	31.1	−4.25	−5.73	−16.31	−16.06	165.76	146.69	152.7	20.6	301.16	17:56:54.5	16.35	56.91	313.3
11.4	16.6	2.51	.50	−13.48	−13.25	189.58	165.69	163.6	17.0	301.16	17:56:57.2	15.77	55.98	314.4
11.5	.9	12.04	12.01	−5.04	−5.40	134.88	135.35	119.6	14.4	301.16	17:56:59.4	15.19	55.09	1.4
12.1	49.7	−13.31	−16.05	−24.82	−25.03	184.92	127.92	120.1	17.0	301.16	17:57:03.0	18.05	58.07	312.9
12.2	42.1	−10.43	−12.85	−21.77	−22.06	176.41	128.35	131.9	17.5	301.16	17:57:06.5	17.63	57.22	313.1
12.3	31.1	−7.06	−6.85	−18.14	−18.92	224.57	212.49	145.7	17.5	301.16	17:57:09.8	17.10	56.30	313.3
12.4	16.6	1.85	1.50	−13.47	−14.13	160.74	164.19	154.3	15.4	301.16	17:57:12.5	16.52	55.36	314.7
12.5	.9	12.05	11.85	−4.58	−5.03	133.11	133.60	112.2	13.9	301.16	17:57:14.7	15.93	54.48	.8
13.1	49.7	−13.89	−19.41	−26.33	−26.86	172.82	111.84	126.9	14.4	301.16	17:57:18.2	18.80	57.46	313.1
13.2	42.1	−11.37	−11.87	−22.78	−23.11	207.50	145.53	135.8	14.9	301.16	17:57:21.7	18.37	56.61	313.2
13.3	31.1	−6.46	−8.63	−20.40	−20.84	157.47	132.22	144.5	14.4	301.16	17:57:25.0	17.84	55.68	313.5
13.4	16.7	1.82	.88	−14.03	−14.27	161.75	144.31	150.1	13.9	301.16	17:57:27.7	17.26	54.74	314.9
13.5	.9	—	13.09	−4.23	−4.70	132.71	132.66	102.4	12.9	301.16	17:57:29.9	16.67	53.85	6.6
14.1	49.7	−15.47	−22.13	−28.89	−28.41	171.16	109.68	132.8	12.4	301.16	17:57:33.5	19.54	56.84	313.2
14.2	42.2	−12.21	−14.57	−24.51	−25.33	167.44	119.43	138.5	12.9	301.16	17:57:37.0	19.12	55.99	313.5
14.3	31.1	−7.64	−9.61	−21.97	−22.41	146.38	122.77	145.2	12.4	301.16	17:57:40.2	18.59	55.06	313.8
14.4	16.7	2.05	1.59	−13.91	−14.13	138.55	130.60	148.9	12.4	301.16	17:57:43.0	17.99	54.12	315.1
14.5	1.0	12.90	13.18	−3.77	−4.55	129.21	129.71	102.1	11.3	301.16	17:57:45.2	17.40	53.23	4.9
15.1	49.8	−16.74	−22.43	−29.33	−29.16	170.87	107.82	136.5	10.8	301.16	17:57:48.7	20.30	56.22	313.5
15.2	42.1	−14.31	−18.44	−27.41	−27.89	160.24	115.85	142.4	10.8	301.16	17:57:52.2	19.85	55.36	313.6
15.3	31.2	−10.12	−11.86	−24.55	−24.88	144.94	122.38	146.9	10.8	301.16	17:57:55.5	19.33	54.43	314.1
15.4	16.7	−.27	.09	−14.19	−14.77	174.26	163.53	150.2	10.8	301.16	17:57:58.2	18.72	53.49	314.8
15.5	1.0	13.12	12.97	−4.27	−4.11	127.87	129.39	107.2	10.3	301.16	17:58:00.4	18.14	52.59	359.8
16.1	49.8	−17.33	−23.88	−31.53	−30.92	169.62	105.54	140.3	9.3	301.16	17:58:04.0	21.04	55.60	313.7
16.2	42.2	−16.08	−20.56	−29.87	−29.92	158.24	111.85	144.2	9.3	301.16	17:58:07.5	20.60	54.74	313.8
16.3	31.2	−11.17	−13.15	−26.10	−25.95	145.10	120.45	148.9	9.3	301.16	17:58:10.7	20.05	53.80	314.1
16.4	16.8	1.50	1.09	−14.36	−14.79	132.67	125.86	150.5	9.3	301.16	17:58:13.5	19.45	52.85	315.5
16.5	1.0	—	12.80	−4.04	−4.36	127.85	128.31	130.1	9.3	301.16	17:58:15.7	18.87	51.96	7.9

[a]VV, vertical transmit, vertical receive; HH, horizontal transmit, horizontal receive; VH, vertical transmit, horizontal receive; HV, horizontal transmit, vertical receive.

[b]V, vertical transmit; H, horizontal transmit.

have occurred. The five small R's in figure 5-51 show instances in which the winds could not be calculated from the backscatter in tropical storm Christine because of this effect.

Many different methods were used to study the relationship between the measured backscatter values and the windspeed, all based on the assumption that the meteorologically determined wind direction was correct. All the techniques were variations of multiple-regression schemes. A functional form for the dependence of windspeed on backscatter was used. The various unknown constants in that functional form were determined by minimizing the sums of the squares of the differences between the windspeeds that would be predicted from the radar measurements by means of this analytical form and the meteorological winds. The
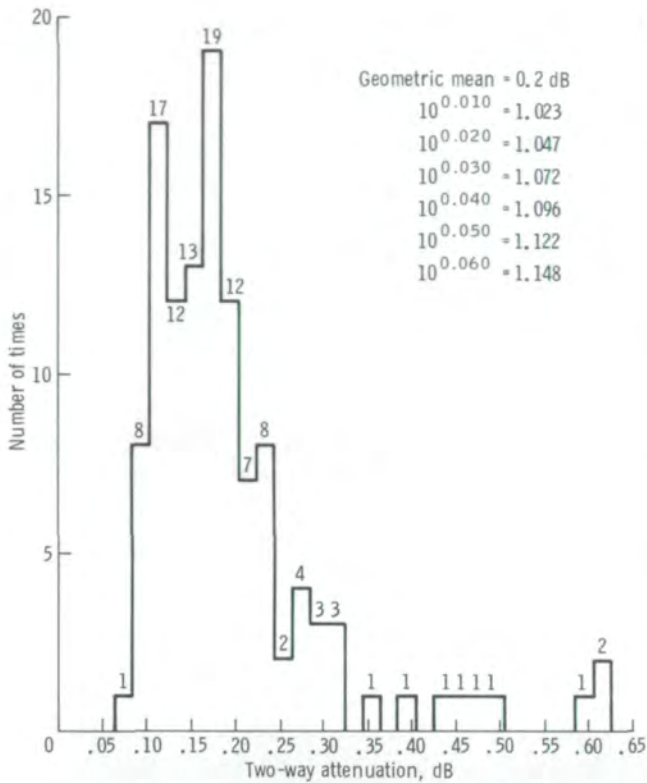
Geometric mean = 0.2 dB

$10^{0.010} = 1.023$
$10^{0.020} = 1.047$
$10^{0.030} = 1.072$
$10^{0.040} = 1.096$
$10^{0.050} = 1.122$
$10^{0.060} = 1.148$

FIGURE 5-53.—Histogram of 118 two-way attenuation values at 50° incidence angles for Skylab 2 and 3 (ref. 5-49).

FIGURE 5-54.—Graph of the values of vertically (circles) and horizontally (squares) polarized passive microwave temperatures at 31° incidence angle for tropical storm Christine (from ref. 5-49).

personnel, are the most accurate. Transient ships provide reports of variable quality depending on whether or not they have anemometers and whether or not the height of the anemometer has been reported. If the ship has no anemometer, the windspeed and wind direction are estimated. Moreover, the reports are from ships that are scattered unevenly over the oceans, being concentrated along the shipping lanes and widely spaced otherwise.

The analysis of the ship reports involves the boundary-layer theory of Cardone (ref. 5-51), in which relationships among the pressure gradients, the air/sea-temperature differences, and the winds are used to form a

results of the analysis of the paired sets of meteorological winds and radar winds were then graphed.

The graph for tropical storm Christine and Hurricane Ava, for all three nadir angles and for cross-polarized radar backscatter, is shown in figure 5-55. The distance of the plotted points from the true value can be caused either by errors in the radar part of the theory or by errors in the determination of the meteorological wind. It was therefore very important to obtain an independent estimate of the errors in the wind, and this estimate was accomplished only for the objective synoptic-scale analyses. It was found that the meteorologically determined surface-truth wind has substantial error.

The winds over the ocean are determined from analysis of ship reports of windspeed, wind direction, surface atmospheric pressure, air temperature, and sea temperature. Some reports are made from weather ships that remain in one place to make scheduled observations like those of a weather station on land. In general, these reports, made by trained meteorological
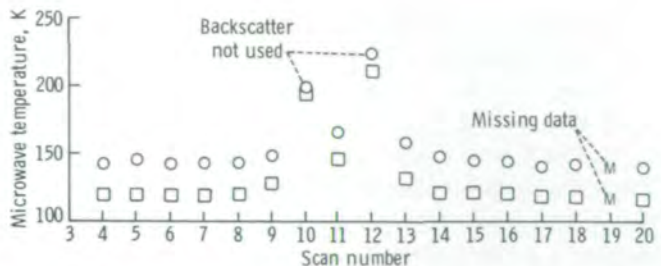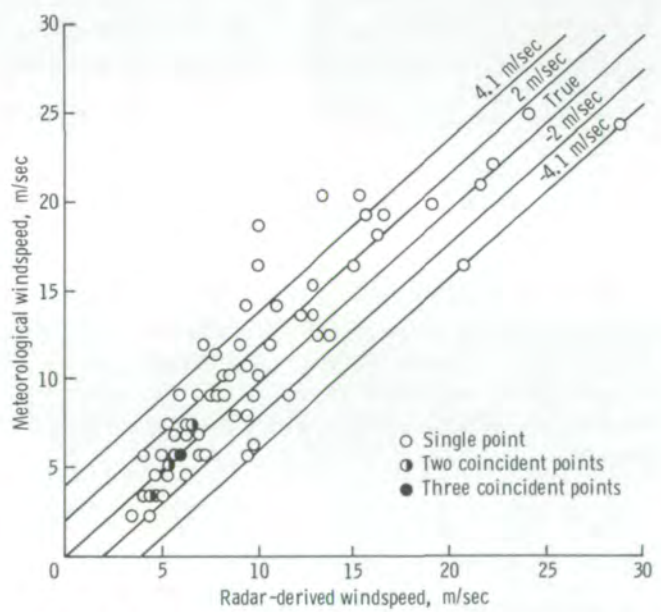

FIGURE 5-55.—Graph of accuracy of wind determination from backscatter values (from ref. 5-49).

continuous field of the vector winds at a fixed height above the sea surface. The accuracy of such an analysis in determining the actual winds depends on the quality and spacing of the available ship reports.

To determine the accuracy of the existing conventional methods for determining the winds near the surface of the ocean, the data were analyzed separately for the entire period by means of a "withheld weather ship" technique. First, the wind fields were analyzed as just discussed with the weather ship data incorporated. Then the weather ship data were removed and the analysis was repeated. The differences between the two resultant winds at points near the weather ship were quite large and depended on the quality of the data that replaced the weather ship data for the area in question. Errors in the specification of the winds were larger than those for a weather ship report when the winds were reported by an ordinary transient ship and still larger if the wind had to be determined from the isobaric pattern and the available boundary-layer theory.

It was possible to partition the total mean-square difference between the radar winds and the meteorological winds into a contribution from the errors in the meteorologically specified winds and a contribution from the radar specified winds. The regression equations yielded a windspeed predicted from the radar backscatter measurement, given the wind direction, so that for the three highest nadir angles, pairs of values of the radar windspeed U_r and the meteorological windspeed U_m were the result. The total variance of these quantities for N samples given by

$$\text{Total variance} = \frac{1}{N} \sum_1^N \left(U_{ri} - U_{mi} \right)^2 \qquad (5\text{-}3)$$

where all samples from 1 to more than 800 were addressed, is a measure of the variation between two different ways of determining the wind. Both U_r and U_m contain errors and differ from the true but unknown value of the windspeed U_T, with the error difference given by

$$U_m - U_r = \left(U_m - U_T \right) - \left(U_r - U_T \right) \qquad (5\text{-}4)$$

Because the total variance is known, it is possible to compute the error variance of the meteorological winds

and the error variance of the radar winds that constitute the total variance.

The term for the meteorological variances was determined by the withheld weather ship technique. The term for the radar variance was determined by comparing different polarizations. The results are provided in table 5-III, as stratified according to the quality of the meteorological surface-truth and windspeed ranges. More than 800 separate cells were scanned by the S193 for these studies during 14 Z-axis-to-local-vertical passes. This amount of data far exceeds that of all previous aircraft programs. The total variance for a large sample should equal the sum of the two parts. It does not because of sampling variability; however, the sums nearly balance. For some categories, the two terms on the right add up to less than the term on the left. The difference is shown under the unexplained variance. The italicized values represent those categories where the two terms on the right exceed the term on the left. Although the errors in the meteorological wind were determined from a different data base, the results nearly balance category by category. Most of the difference between the radar wind and the meteorological wind is due to "errors" in the meteorological wind.

Cardone et al. (ref. 5-49) concluded that the windspeeds computed from the backscatter measurements at each cell, after correction for attenuation and under the assumption that the wind direction was correct, were at least as accurate as those that would have been recorded by a weather ship located at (or near) each cell. It was also stated that this conclusion was a conservative interpretation of the results of the study. The standard deviation of the errors of the radar-measured wind may well be less than half that of the errors in the winds presently reported by weather ships.

The radar backscatter theories developed in this program and the AAFE data were used as a guide in formulating the regression equations that were used. These regression equations with unknown constants, determined from Skylab backscatter measurements and the winds, need not necessarily have agreed with either the theory or the AAFE data. However, they did. The results of one regression method in which radar backscatter is plotted against azimuth angle for three different windspeeds are shown in figure 5-56. The agreement with figure 5-47 as to shape and relative separation is very good. The disagreement as to absolute level can be attributed to S193 recalibration problems during Skylab 4.

TABLE 5-III.—Component Variance Analysis for the Three Highest Nadir Angles

[From ref. 5-49]

(a) Skylab 2 and 3 data

Windspeed range, knots	Type (a)	Variance, (knots)² — Total VVb	HHb	HV/VHb	Meteorological	Radar VV	HH	HV/VH	Unexplained variance, (knots)² (c) VV	HH	HV/VH	Unexplained standard deviation, knots (d) VV	HH	HV/VH	No. of cells scanned VV	HH	HV/VH
e0 to 10	A	11.2	—	—	5.7	1.9	0.9	1.2	3.6	—	—	1.9	—	—	16	—	—
e11 to 20	A	84	9.9	10.4	12.5	1.9	.9	1.2	69.6	3.5	3.3	8.3	1.9	1.8	3	17	16
e21 to 30	A	—	104.0	78.7	19.1	1.9	.9	1.2	—	84.0	58.4	—	9.2	7.6	—	3	3
0 to 10	B	35.5	52.1	51.0	12.9	1.9	.9	1.2	20.7	38.3	36.9	4.5	6.2	6.1	4	8	8
11 to 20	B	27.4	28.5	25.3	25.8	1.9	.9	1.2	.3	1.8	1.7	.5	1.3	1.3	49	48	48
21 to 30	B	99	57.3	47.5	39.5	1.9	.9	1.2	57.6	16.9	6.8	7.6	4.1	2.6	5	2	2
0 to 10	C	6.5	8.8	5.6	12.9	1.9	.9	1.2	8.3	5.0	8.5	2.9	2.2	2.9	9	11	9
11 to 20	C	12.5	13.2	10.2	25.8	1.9	.9	1.2	15.2	13.5	16.8	3.9	3.7	4.1	51	34	37
21 to 30	C	15.5	21.3	13.5	39.5	1.9	.9	1.2	25.9	19.1	27.2	5.1	4.4	5.2	2	2	1
0 to 10	D	—	8.5	6.2	12.9	1.9	.9	1.2	—	5.3	7.9	—	2.3	2.8	—	6	2
11 to 20	D	14.7	17.6	18.1	25.8	1.9	.9	1.2	13.0	9.1	8.9	3.6	3.0	3.0	28	25	26
21 to 30	D	—	66.1	—	39.5	1.9	.9	1.2	—	25.7	—	—	5.1	—	—	1	—
0 to 10	BCD	15.4	22.6	27.5	12.9	1.9	.9	1.2	.6	8.8	13.4	.8	3.0	3.7	13	25	19
11 to 20	BCD	18.7	21.1	18.6	25.8	1.9	.9	1.2	9.0	5.6	8.4	3.0	2.4	2.9	128	107	111
21 to 30	BCD	75.1	44.6	36.1	39.5	1.9	.9	1.2	33.7	4.2	4.6	5.8	2.0	2.1	7	5	3
0 to 10	SYN	11	8.88	10.7	27.9	1.9	.9	1.2	18.8	19.9	18.4	4.3	4.5	4.3	24	39	34
11 to 20	SYN	15.7	13.5	14.0	35.1	1.9	.9	1.2	21.3	22.5	22.3	4.6	4.7	4.7	135	130	127
21 to 30	SYN	55.8	56.2	35.4	55.8	1.9	.9	1.2	1.9	.5	21.6	1.4	.7	4.6	6	6	3
Totals[f]															332	332	316

[a] A-type data are for weather ships and aircraft underflights. The B-, C-, and D-type data are for ship reports of decreasing quality; SYN represents those cells for which the windspeed had to be determined from the isobaric pattern and the boundary-layer theory. The meteorological variance is lowest for type A; the same for B, C, and D; and highest for SYN.

[b] VV, vertical transmit, vertical receive; HH, horizontal transmit, horizontal receive; HV, horizontal transmit, vertical receive; VH, vertical transmit, horizontal receive.

[c] Italicized numbers represent the amounts by which the sum of the meteorological-error variance and the radar-error variance exceeds the total variance.

[d] Italicized numbers are the square roots of the corresponding values in the three corresponding preceding columns.

[e] 0 to 10 knots = 0 to 5.1 m/sec; 11 to 20 knots = 5.6 to 10.3 m/sec; 21 to 30 knots = 10.8 to 15.4 m/sec.

[f] Excluding type BCD.

CONCLUSIONS

Oceans

All Skylab EREP instruments were found to be valuable in studying the oceans. Sea-surface temperatures were measured from orbit by the Infrared Spectrometer. Atmospheric effects on the measurements were corrected to an accuracy of ±1 K by analysis of data in two selected wavelengths sensed by the instrument. The Multispectral Scanner acquired data that were used to portray thermal patterns of ocean currents and upwellings and to determine depth of clear water to 18 m. The Microwave Radiometer/-Scatterometer obtained surface roughness data that verified theories and techniques that will be used in the future to observe sea ice, sea state, and winds over the oceans on a global scale not possible by any other method. Investigators used Microwave Altimeter data

TABLE 5-III.—Concluded

(b) Skylab 4 data

Windspeed range, knots	Type (a)	Variance, (knots)²							Unexplained variance, (knots)² (c)			Unexplained standard deviation, knots (d)			No. of cells scanned		
		Total			Meteorological	Radar											
		VV[b]	HH[b]	HV/VH[b]		VV	HH	HV/VH	VV	HH	HV/VH	VV	HH	HV/VH	VV	HH	HV/VH
[e]11 to 20	A	32.4	0.1	23.2	12.5	6.1	10.5	1.2	*13.8*	*22.9*	*9.5*	3.7	4.8	3.1	3	1	2
[e]21 to 30	A	14.4	16.6	21.8	19.1	6.1	10.5	1.2	*10.8*	*13.0*	*1.5*	*3.3*	*3.6*	*1.2*	5	7	6
[e]0 to 10	B	2.31	6.2	—	12.9	6.1	10.5	1.2	*16.7*	*17.2*	—	*4.1*	*4.1*	—	1	1	—
11 to 20	B	21.7	23.4	25.5	25.8	6.1	10.5	1.2	*10.2*	*12.9*	*1.5*	*3.2*	*3.6*	*1.2*	36	29	28
21 to 30	B	37.6	50.7	67.9	39.5	6.1	10.5	1.2	*8.0*	*.7*	*27.2*	*2.8*	*.8*	*5.2*	29	45	29
>30	B	65.0	81.0	69.4	71.5	6.1	10.5	1.2	*12.6*	*1.0*	*3.3*	*3.5*	*1.0*	*1.8*	4	1	3
11 to 20	C	18.9	10.9	21.2	25.8	6.1	10.5	1.2	*13.0*	*25.4*	*5.8*	*3.6*	*5.0*	*2.4*	12	10	13
21 to 30	C	20.1	76.4	34.6	39.5	6.1	10.5	1.2	*25.5*	*26.4*	*6.1*	*5.0*	*5.1*	*2.5*	11	22	11
>30	C	88.7	67.9	94.3	71.5	6.1	10.5	1.2	11.1	*14.1*	21.6	3.3	*3.8*	4.6	5	5	5
0 to 10	D	3	109.4	—	12.9	6.1	10.5	1.2	*16.0*	*86.0*	—	4.0	9.3	—	1	1	—
11 to 20	D	27.6	37.3	40.2	25.8	6.1	10.5	1.2	*4.3*	*1.0*	*13.2*	*2.1*	*1.0*	*3.6*	50	48	59
21 to 30	D	52.4	109.4	84.8	39.5	6.1	10.5	1.2	6.8	59.4	44.1	2.6	7.7	6.6	49	71	43
>30	D	64.3	41.7	68.0	71.5	6.1	10.5	1.2	*13.3*	40.3	4.7	*3.6*	6.3	2.2	37	15	35
0 to 10	BCD	2.65	57.8	—	12.9	6.1	10.5	1.2	*16.4*	*34.4*	—	4.0	5.9	—	2	2	—
11 to 20	BCD	24.4	29.7	32.9	25.8	6.1	10.5	1.2	*7.5*	*6.6*	*5.9*	*2.7*	*2.6*	*2.4*	98	87	110
21 to 30	BCD	43.6	87.6	72.2	39.5	6.1	10.5	1.2	*2.0*	37.6	31.5	*1.4*	6.1	5.6	89	138	83
>30	BCD	67	49.8	71.1	71.5	6.1	10.5	1.2	*10.6*	*32.2*	*1.6*	*3.3*	*5.7*	*1.3*	46	21	43
0 to 10	SYN	43.2	48.7	6.2	27.9	6.1	10.5	1.2	9.2	10.3	22.9	3.0	3.2	4.8	3	9	4
11 to 20	SYN	32.1	28.5	33.8	35.1	6.1	10.5	1.2	*9.1*	*17.1*	*2.5*	*3.0*	*4.1*	*1.6*	135	118	133
21 to 30	SYN	64.6	80.1	71.4	55.8	6.1	10.5	1.2	2.7	13.8	14.4	1.6	3.7	3.8	79	97	80
>30	SYN	116.6	113.4	82.2	101	6.1	10.5	1.2	9.5	1.9	*20*	3.1	1.4	*4.5*	19	14	19
Totals[f]															479	494	470

[a]A-type data are for weather ships and aircraft underflights. The B-, C-, and D-type data are for ship reports of decreasing quality; SYN represents those cells for which the windspeed had to be determined from the isobaric pattern and the boundary-layer theory. The meteorological variance is lowest for type A; the same for B, C, and D; and highest for SYN.

[b]VV, vertical transmit, vertical receive; HH, horizontal transmit, horizontal receive; HV, horizontal transmit, vertical receive; VH, vertical transmit, horizontal receive.

[c]Italicized numbers represent the amounts by which the sum of the meteorological-error variance and the radar-error variance exceeds the total variance.

[d]Italicized numbers are the square roots of the corresponding values in the three corresponding preceding columns.

[e]0 to 10 knots = 0 to 5.1 m/sec; 11 to 20 knots = 5.6 to 10.3 m/sec; 21 to 30 knots = 10.8 to 15.4 m/sec.

[f]Excluding type BCD.

to demonstrate that the contour of the ocean surface can be measured to an accuracy of ±1 m or better. Information was obtained in passive microwave data that could be used to determine surface roughness and precipitation in the atmosphere.

The L-Band Radiometer results indicate that sea-surface roughness measurements as related to windspeed may be obtained at L-band frequencies when other frequencies are not usable because of precipitation interference. The L-band data were not suitable for measuring sea-surface salinities or temperatures on the open ocean.

The photographs from the Multispectral Photographic and Earth Terrain Cameras were used to dis-
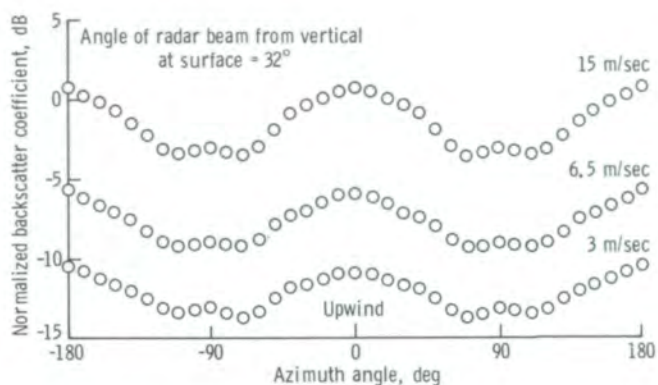
FIGURE 5-56.—Regression curves verifying aircraft data presented in figure 5-47 (from ref. 5-49).

cern and record visible phenomena such as water color, turbidity, depth, current and wave patterns, shoal extent and location, chlorophyll content, and ice types and patterns.

The availability of data acquired simultaneously from two or more instruments provided bases for conclusions that would not be supportable if only one instrument had been used. Study of living marine resources is an example. Certain temperatures are favorable to growth of plant and animal life but locating areas of appropriate temperatures yields inconclusive results in any search for living organisms. If, in addition to data on suitable temperature, water-color information is available from a scanner or a camera, the search area can be reduced. If supplementary information on currents, measured by scanners, cameras, or altimeters, is provided, the results can be further improved.

Subtle gradations of contour, texture, color, and temperature, which are impossible to obtain when measured at or near the surface, can be observed from space and interrelationships can be evaluated. Several investigators used Skylab EREP data containing such information to study ocean currents, which involve most, if not all, of these factors. The superiority of the data acquired from orbit was demonstrated for many applications.

Atmosphere

The Skylab EREP investigations resulted in significant advances in the understanding of the physics of the atmosphere and the interaction between the atmosphere and the land and ocean surfaces. Without doubt, the most significant development in satellite meteorology resulting from Skylab was the use of the microwave spectrum to measure the surface wind over the ocean. The possibilities for obtaining markedly improved wind information across areas of the open ocean will be of major usefulness not only to weather forecasting but also to shipping.

Analytic techniques were developed for and new information was gained on the location and concentration of particle layers in the stratosphere. Skylab provided, for the first time, measurements for studying the spectral transfer of visible and thermal radiation through aerosol layers in the troposphere and permitted realistic evaluation of methods for correcting the effects of atmospheric attenuation for remote sensing of the Earth's surface.

The Skylab EREP photographs provided information for studying the phenomenon of cloud streets— the orientation and spacing of cloud bands as a function of the horizontal wind field. New knowledge was gained and mathematical algorithms were developed to describe the relationship of physical cloud parameters to the vertical wind field.

The Skylab experiments developed techniques for discriminating between cloud ice crystals, cloud water droplets, and surface snow. These experiments will lead to the experimental designs for programs during the Space Shuttle flights to solve the problem of discriminating supercooled water droplets, mixtures of ice crystals and water droplets, and the like.

Several EREP investigations were conducted to ascertain the usefulness of microwave radiometers for soil moisture determination. Although the state of the art in longer wavelength microwave radiometry permitted only synoptic-scale measurements with an instantaneous field of view of 100 km and more in diameter, it was learned that the L-band is well suited for monitoring surface soil moisture under a wide variety of weather, vegetation, and terrain conditions.

Oceans and Atmosphere

The EREP experiments demonstrated that the oceans and the atmosphere over the oceans must be studied jointly and simultaneously. The measurement of the winds over the ocean depends on the properties

of the waves generated by the winds and on ocean temperature measurements. Measurements by means of either infrared or passive microwave instruments have to be corrected for the effects of the atmosphere.

On the basis of Skylab-derived knowledge, improved versions of the S191, S192, S193, and S194 instruments will continue to be built for use on unmanned spacecraft. Multispectral scanners are already onboard the Landsat; an improved altimeter is onboard GEOS-3, and an even more accurate model will be used on Seasat-A. Passive microwave sensors will be included on Nimbus and Seasat-A; dual infrared bands, on Tiros. Radar backscatter will be measured on Seasat-A. The combined study of the oceans and atmosphere will be possible with these new instruments to an extent never before possible.

The Skylab experiment also demonstrated the value of having the spacecraft manned by trained crewmen. The crew's ability to acquire and track a target with the S191 instrument proved useful in acquiring spectral information at a variety of viewing angles. Handheld-camera photography supplemented the EREP data for the floating ice experiment. The experience gained in the combined uses of trained crewmen with complex, new, unproven instruments can be the basis for operational plans for using the Space Shuttle in further scientific study of the Earth.

REFERENCES

5-1. Vonbun, F. O.; McGoogan, J.; Marsh, J.; and Lerch, F. J.: Sea Surface Determination From Space: The GSFC Geoid. NASA TM X-70959, 1975.

5-2. Mourad, A. G.; Gopalapillai, S.; Kuhner, M.; and Fubara, D. M.: The Application of Skylab Altimetry to Marine Geoid Determination. NASA CR-144372, 1975.

5-3. McGoogan, J. T.; Leitao, C. D.; and Wells, W. T.: Summary of Skylab S-193 Altimeter Altitude Results. NASA TM X-69355, 1975.

5-4. Greenwood, J. Arthur; Nathan, Alan; et al.: Radar Altimetry From a Spacecraft and Its Potential Applications to Geodesy. Remote Sensing Environ., vol. 1, no. 1, Mar. 1969, pp. 59-70.

5-5. Greenwood, J. Arthur; Nathan, Alan; et al.: Oceanographic Applications of Radar Altimetry From a Spacecraft. Remote Sensing Environ., vol. 1, no. 1, Mar. 1969, pp. 71-80.

5-6. Anding, David C.; and Walker, John P.: Use of Skylab EREP Data in a Sea-Surface Temperature Experiment. NASA CR-144479, 1975.

5-7. Hollinger, James P.; and Lerner, Robert M.: Analysis of Microwave Radiometric Measurements From Skylab. NASA CR-147442, 1975.

5-8. Trumbull, James V. A.: The Utility of Skylab Photointerpreted Earth Resources Data in Studies of Marine Geology and Coastal Processes in Puerto Rico and the Virgin Islands. NASA CR-147437, 1975.

5-9. Polcyn, Fabian C.; and Lyzenga, David R.: Skylab Remote Bathymetry Experiment. NASA CR-144482, 1976.

5-10. Campbell, W. J.; Ramseier, R. O.; Weaver, R. J.; and Weeks, W. F.: Skylab Floating Ice Experiment. NASA CR-147446, 1975.

5-11. Pirie, Douglas M.; and Steller, David D.: California Coastal Processes Study. NASA CR-144489, 1975.

5-12. Nichols, Maynard M.: Southern Chesapeake Bay Water Color and Circulation Analysis. Water Color and Circulation Southern Chesapeake Bay, Part I. NASA CR-141404, 1975.

5-13. Gordon, Hayden H.; and Nichols, Maynard M.: Skylab MSS vs Photography for Estuarine Water Color Classification. Water Color and Circulation Southern Chesapeake Bay, Part II. NASA CR-141404, 1975.

5-14. Marshall, Harold G.; and Bowker, David E.: The Use of Skylab in the Study of Productivity Along the Eastern Shelf Waters of the United States. NASA CR-144908, 1976.

5-15. Korb, C. Laurence; and Potter, John F.: Ocean Properties. NASA TM X-72961, 1976.

5-16. Szekielda, Karl-Heinz: Dynamics of Plankton Populations in Upwelling Areas. NASA CR-144480, 1975.

5-17. Watanabe, Kantaro; Kuroda, Ryuya; Hata, Katsumi; and Akagawa, Masaomi: Study of Sea Ice in the Sea of Okhotsk and Its Influence on the Oyashio Current. NASA CR-144472, 1975.

5-18. Savastano, K. J.: Application of Remote Sensing for Fishery Resources Assessment and Monitoring. NASA CR-147507, 1975.

5-19. Breaker, Lawrence C.: A Qualitative Look at Sea Surface Temperature off the West Coast of the United States as Seen by UHRR Imagery From the NOAA-3 Satellite. NOAA, Redwood City, Calif., 1974.

5-20. Bakun, A.: Daily and Weekly Upwelling Indices, West Coast of North America, 1967-73. NOAA Tech. Rep. NMFS SSRF-693. NOAA National Marine Fisheries Service, 1975.

5-21. Bakun, A.; and Nelson, C. S.: Climatology of Upwelling Related Processes off Baja California. Paper presented at the Symposium on Fisheries Science at the Autonomous Univ. of Baja Calif., Ensenada, Baja Calif., Feb. 16-22, 1975.

5-22. Klemas, Vytautas; Bartlett, David S.; et al.: Skylab/EREP Application to Ecological, Geological, and Oceanographic Investigations of Delaware Bay. NASA CR-144910, 1976.

5-23. Maruyasu, Takakazu; Ochiai, Hiroaki; and Nakano, Takamasa: Investigation of Environmental Change Patterns in Japan. NASA CR-144569, 1975.

5-24. Piech, Kenneth R.; Schott, John R.; and Stewart, Kenton M.: S190 Interpretation Techniques Development and Applications to New York State Water Resources. NASA CR-144499, 1975.

5-25. Yost, Edward F.: In Situ Spectroradiometric Calibration of EREP Imagery and Estuarine and Coastal Oceanography of Block Island Sound and Adjacent New York Coastal Waters. NASA CR-147469, 1975.

5-26. Maul, George A.; Gordon, Howard R.; et al.: An Experiment to Evaluate Skylab Earth Resources Sensors for Detection of the Gulf Stream. NASA CR-147454, 1976.

5-27. Chang, David T.; and Isaacs, Ronald G.: Experimental Evaluation of Atmospheric Effects on Radiometric Measurements Using the EREP of Skylab. NASA CR-144500, 1975.

5-28. Pitts, David E.; Sasaki, Yoshikazu; and Lee, Jean T., compilers: Severe Storm Environments: A Skylab EREP Final Report. NASA TM X-58184, 1976.

5-29. Curran, Robert J.; Salomonson, Vincent V.; and Shenk, William: The Application of Satellite Data in the Determination of Ocean Temperatures and Cloud Characteristics and Statistics. NASA CR-147539, 1976.

5-30. Kuhn, P. M.; Marlatt, W. E.; and Whitehead, V. S.: The Skylab Concentrated Atmospheric Radiation Project. NASA CR-144481, 1975.

5-31. Thomson, F. J.: Machine Processing of S-192 and Supporting Aircraft Data: Studies of Atmospheric Effects, Agricultural Classifications, and Land Resource Mapping. NASA CR-144503, 1975.

5-32. Tingey, David L.; and Potter, John: Quantitative Determination of Stratospheric Aerosol Characteristics. NASA CR-147444, 1975.

5-33. Turner, Robert E.: Investigation of Earth's Albedo Using Skylab Data. NASA CR-147445, 1976.

5-34. Rayleigh, J. W. Strutt: On the Light From the Sky; Its Polarization and Colour. Phil. Mag., vol. 41, 1871, pp. 107-120 and 274-279.

5-35. Mie, G.: Contributions to the Optics of Dense Media of Special Colloidal Metal Solutions. Ann. Physik, vol. 25, 1908, pp. 377-445.

5-36. Van de Hulst, H. C.: Scattering in a Planetary Atmosphere. Astrophys. J., vol. 107, no. 2, 1948, pp. 220-246.

5-37. Marlatt, W. E.: The Effect of Weather Modifications on Physical Processes. The Microclimate in Ground Level Climatology, R. H. Shaw, ed., AAAS (Washington, D.C.), 1967, pp. 295-308.

5-38. Alishouse, John; Jacobowitz, Herbert; and Wark, David: A Cloud Physics Investigation Utilizing Skylab Data. NASA CR-147474, 1975.

5-39. Villevieille, A.; and Weiller, A. B.: The Possibility of Evaluating Vertical Wind Profiles From Satellite Data. NASA CR-147475, 1975.

5-40. Kuettner, J. P.: Cloud Bands in the Earth's Atmosphere: Observations and Theory. Tellus, vol. 23, no. 4-5, 1971, pp. 404-426.

5-41. LeMone, Margret Anne: The Structure and Dynamics of Horizontal Roll Vortices in the Planetary Boundary Layer. J. Atmos. Sci., vol. 30, no. 6, Sept. 1973, pp. 1077-1091.

5-42. Marwitz, J. D.: The Structure and Motion of Severe Hailstorms. Part I: Supercell Storms. J. Appl. Meteorol., vol. 11, 1972, pp. 166-179.

5-43. Davies-Jones, R. P.: Discussion of Measurements Inside High-Speed Thunderstorm Updrafts. J. Appl. Meteorol., vol. 13, 1974, pp. 710-717.

5-44. Sasaki, Y. K.: Mechanism of Squall-Line Formation as Suggested From Variational Analysis of Hourly Surface Observations. Preprints of the Eighth Conference on Severe Local Storms, American Meteorol. Soc. (Boston, Mass.), Oct. 15-17, 1973.

5-45. Beebe, R. C.: Large Scale Irrigation and Severe Storm Enhancement. Symposium on Atmospheric Diffusion and Air Pollution, American Meteorol. Soc. (Boston, Mass.), 1974, pp. 392-395.

5-46. Moore, Richard K.; and Ulaby, Fawwaz T.: The Radar Radiometer. Proc. IEEE, vol. 57, no. 4, Apr. 1969, pp. 587-590.

5-47. Mitsuyasu, A.; and Honda, T.: The High Frequency Spectrum of Wind Generated Waves. J. Oceanograph. Soc. Japan, vol. 30, no. 4, 1974, pp. 29-42.

5-48. Pierson, Willard J.: The Theory and Applications of Ocean Wave Measuring Systems At and Below the Sea Surface, on the Land, From Aircraft, and From Spacecraft. NASA CR-2646, 1976.

5-49.   Cardone, Vincent J.; Young, James D.; et al.: The Measurement of the Winds Near the Ocean Surface With a Radiometer-Scatterometer on Skylab. A Joint Meteorological Oceanographic and Sensor Evaluation Program for Experiment S193 on Skylab. NASA CR-147487, 1976.

5-50.   Ross, Duncan: A Comparison of Synoptic and Skylab S193/194 Determinations of Ocean Surface Windspeeds. NASA CR-147540, 1975.

5-51.   Cardone, V. J.: Specification of the Wind Field Distribution in the Marine Boundary Layer for Wave Forecasting. Rep. TR 69-1, Geophys. Science Lab., New York Univ., Dec. 1969.

6

Data Analysis Techniques

FABIAN C. POLCYN,[a†] KENNETH R. PIECH,[b†] ALLAN SHAPIRO,[c†]
LARRY B. YORK,[d] AND ANDREW E. POTTER[d]

THE SKYLAB EARTH RESOURCES Experiment Pack-age (EREP) sensors provided a multisensor data base for assessing the use of standard information extraction techniques as well as for developing new techniques. The EREP investigators analyzed data from the photographic, electro-optical mechanical, and microwave sensors in ways that were appropriate to a particular application. In several instances, the investigators developed improvements in remote-sensing analysis techniques or provided results that guided the selection of location of operating bands for future sensors.

Because the space-flight performance of the EREP sensors dictates to a large degree the data-processing and analytical techniques used by individual investigators, the in-flight performance of the EREP sensors and the data analysis techniques used for each sensor are summarized in this section. Other techniques are discussed in sections 2 to 5 and in appendix D.

Of all the sensors onboard, cameras filtered for selected wavelength bands produced photographs having the best spatial resolution. The analytical techniques for the EREP photographic experiments reported in this section are discussed in four general categories: visual analysis of the imagery from different spectral bands and from different sensors; microdensitometry and color encoding; multiband image enhancement and analysis, including image digitization and computer techniques; and data processing that provided input parameters for Earth resources management models.

The EREP optical-mechanical scanner provided multichannel computer-compatible tapes that permitted machine enhancement of surface features based on spectral signature analyses. The techniques used to ensure acceptable recognition accuracies included multiband comparisons, ratio processing, spectral classifications based on statistical tests, mixture processing, and signature-extension schemes. An infrared spectrometer provided high-spectral-resolution data in the visible and infrared bands from preselected test sites so that atmospheric corrections and surface signatures could be developed.

Active and passive microwave sensors, operating at the longest wavelengths used by EREP sensors, provided computer-compatible-tape (CCT) data from which information about the atmosphere, the surface roughness, the soil moisture, and the shape of the Earth could be determined. To achieve the full performance potential of the altimeter, special techniques were developed to determine the antenna pointing angle directly from the radar return and to calibrate range and power output for pulsewidth- and beamwidth-limited conditions. The interpretation of data from the radiometer/scatterometer (RADSCAT) required different statistical methods of analysis for verification and correction. Rigorous methods for computing ocean emission at microwave frequencies for different physical conditions were developed and used to separate various physical parameters from the radiometer data characteristics.

---

[a]Environmental Research Institute of Michigan.

[b]Calspan Corporation.

[c]U.S. Naval Research Laboratory.

[d]NASA Lyndon B. Johnson Space Center.

[†]Principal Investigator.

The data analysis techniques provided for the conversion of sensor data into meaningful application information such as numbers, thematic maps, and boundaries from which decisions could be made, action taken, and new programs initiated. In general, this transformation could not be accomplished without supporting information, surface truth, or a framework of model analysis. The development of suitable models and frameworks for inputting this new form of data supplied by spaceborne sensors is one of the main challenges to the maximum utilization of remote-sensing techniques.

SENSOR FLIGHT PERFORMANCE

The EREP investigators defined their experiments on the assumption that predicted sensor performance levels would be achieved during flight. Therefore, an important task during the EREP data passes was to test the sensors to determine their actual operational performance.

Sensor performance was evaluated in three different areas: (1) functional performance (e.g., camera shutter operation and antenna movement), (2) geometric performance (e.g., spatial distortions in the imagery, pointing accuracy of the antenna), and (3) radiometric performance (e.g., radiometric accuracy and precision). Generally, only the flight data collected for the EREP Principal Investigators were used for the sensor performance evaluation; however, for the lunar or deep-space calibration studies, a restricted amount of data was collected specifically for sensor performance evaluation. Detailed discussion of the performance and engineering evaluation of each sensor is published in an NASA internal document[1] and summarized by Potter et al. (ref. 6-1). A brief summary of the results of the sensor evaluation is presented for each sensor (app. A).

Multispectral Photographic Camera

The Multispectral Photographic Camera (S190A) consisted of six boresighted camera stations, four with spectral filters and black-and-white film, one with high-
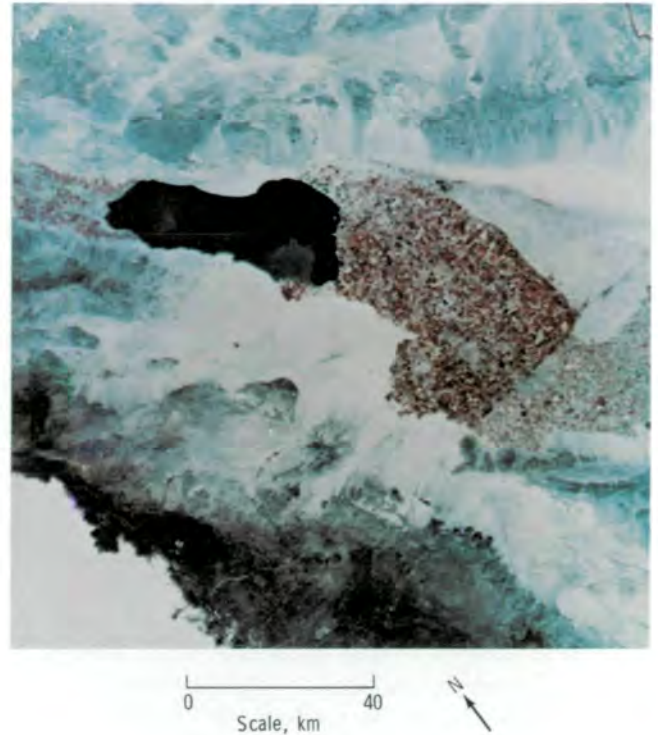

FIGURE 6-1.—Color-infrared imagery of the Imperial Valley and the Salton Sea, California (S-73-1227).

resolution color film, and one with color-infrared film. An example of imagery from the color-infrared camera station showing the Imperial Valley and the Salton Sea, California, is illustrated in figure 6-1. This figure is an enlargement; one entire S190A frame covers a 163-km-square area. Vegetation is delineated by red tones. The same scene, photographed with the high-resolution color camera station, is shown in figure 6-2. To demonstrate the resolution capability of the S190A system, this scene was enlarged. The limit of resolution can be seen in figure 6-3. The measured resolution capability of the camera for this film was approximately 27 m per line pair for high-contrast sites and approximated the value expected from preflight tests. The registration capability of the black-and-white imagery is illustrated in figure 6-4, a composite generated by superimposing enlarged images from three black-and-white camera stations for the Imperial Valley scene (figs. 6-1 and 6-2). The images can be registered to within better than 20 m on the ground, approximately the value expected from preflight tests. The S190A camera was a radiometric
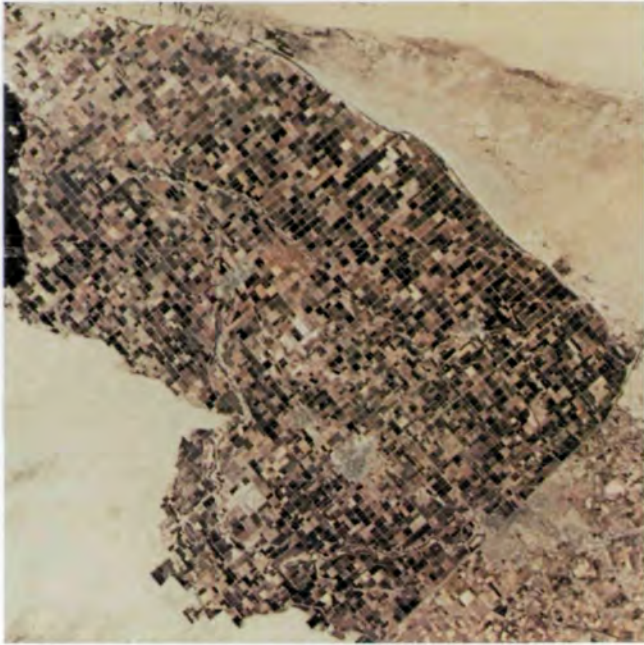
FIGURE 6-2.—The Imperial Valley, California, photographed with high-resolution color film (8× magnification).

camera in that film density could be related quantitatively to the intensity of radiation incident on the lens. In-flight measurements using the ground sites and the Moon established radiometric calibrations accurate to within ±30 percent.

Earth Terrain Camera

The Earth Terrain Camera (S190B), a single camera station, was designed to demonstrate the application of high-spatial-resolution imagery in Earth resource surveys and normally was operated with either high-resolution color or black-and-white film. An S190B image made with high-resolution color film covering a 109-km-square area over Phoenix, Arizona, is shown in figure 6-5. The Sun City Development area, which is used to demonstrate the resolution capability of the camera, is visible in the upper left center of the photograph. Figures 6-6 to 6-8 show successively greater enlargements of this same area. The resolution limit of

the camera system was approached at the magnification shown in figure 6-8. The measured resolution limits were approximately 9 m per line pair from black-and-white film. Performance of the camera was within expected limits for all parameters.

Infrared Spectrometer

The Infrared Spectrometer (S191) measured the radiation from a 0.46-km-diameter area on the Earth in the ranges 0.4 to 2.5 μm and 6.6 to 16 μm. The telescope which collected and transmitted light to the spectrometer could be pointed by a crewman at preselected sites below the spacecraft. Photographs of the scene through the telescope recorded pointing angle and time so that the position of a measured site on the ground could be computed.

The S191 was tested by measurements of calibrated ground sites and areas of the Moon. Typical ground site spectra taken with the spectrometer system are shown in figure 6-9.

Careful analysis of the spectral data indicated that the instrument performance was within preflight specifications in the reflective range, except at the blue end of the spectrum (0.4 μm), where excessive off-band radiation appeared. When viewing similar scenes, relative values in the thermal emissive part of the spectrum were within expected tolerances, but the absolute radiance values were incorrect by variable amounts equivalent to a minimum of 1 K to several kelvins. Postflight analysis of data from the backup spectrometer flown on a helicopter indicated that the probable cause of this error was an incorrect transmission coefficient for the dichroic beamsplitter, which divided the reflective and emissive parts of the spectrum.

Multispectral Scanner

The Multispectral Scanner (S192) provided imagery in 13 spectral bands ranging from the blue (0.4 μm) to the thermal-infrared (12.5 μm) portions of the electromagnetic spectrum. The image data were recorded on magnetic tape for later analysis by high-speed computers. An example of data from the S192 is shown in figure 6-10. Three of the 13 bands (2 infrared and 1 green) were superimposed to make this image. Agricultural features, such as circular irrigated fields,
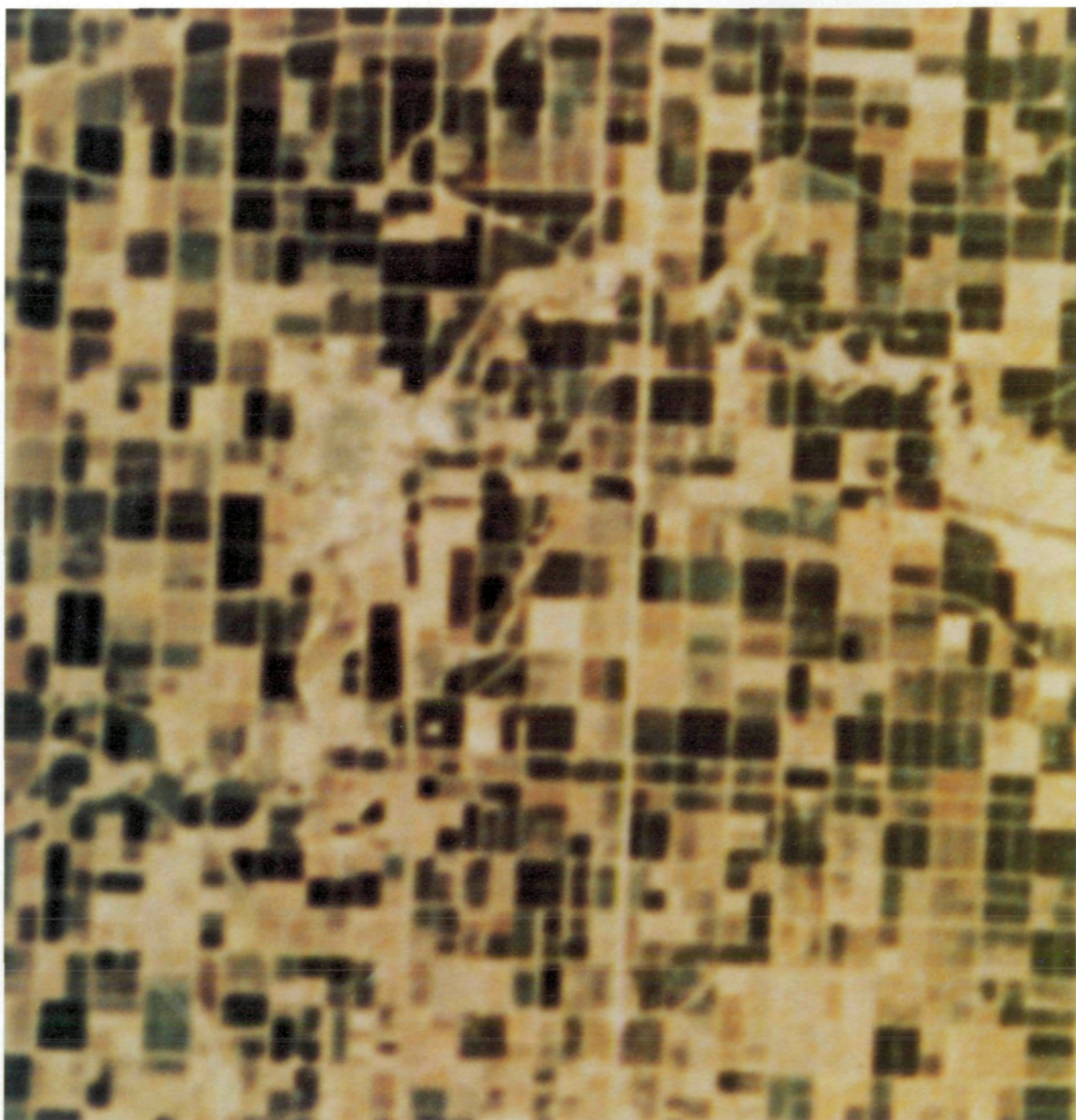
```
0                    2
        Scale, km
```

FIGURE 6-3.—Enlarged area of Imperial Valley, California, photographed with high-resolution color film.

0   Scale, km   10

FIGURE 6-4.—Composite photograph of black-and-white imagery of Imperial Valley, California, generated by superimposing enlarged images from three black-and-white camera stations, showing registration capability.
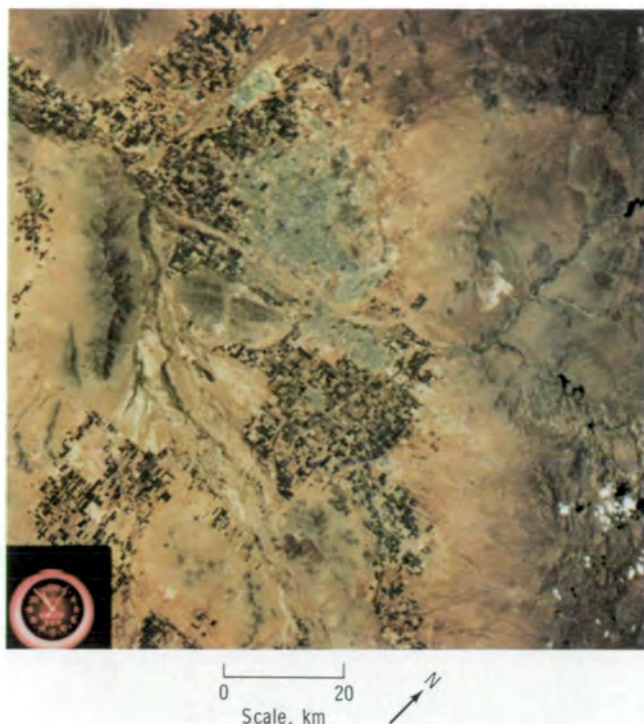
FIGURE 6-5.—An S190B image made with high-resolution color film over Phoenix, Arizona (1.56× enlargement) (SL3-86-011).
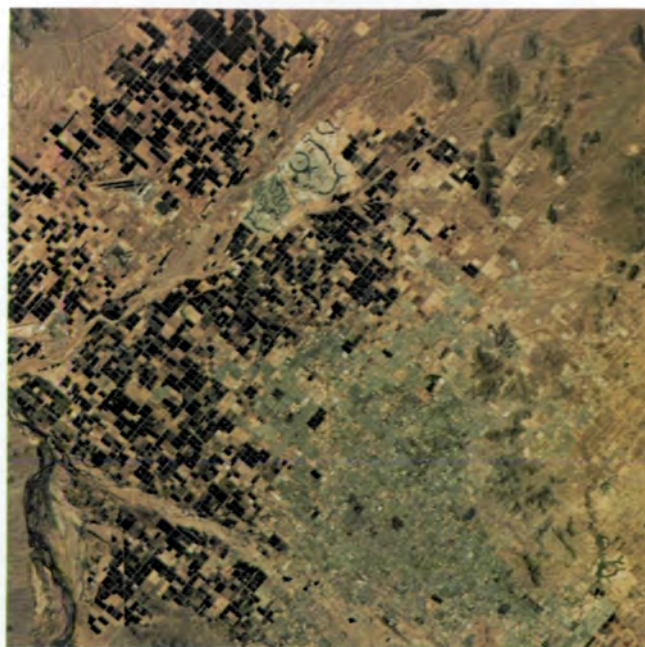

FIGURE 6-6.—Enlargement (3.8× magnification) of S190 image over Phoenix, Arizona.

FIGURE 6-7.—Enlargement (9.45× magnification) of S190 image over Sun City Development area of Phoenix, Arizona.

can be seen clearly in the imagery. Close examination of figure 6-10 reveals that the unfiltered imagery contains a noticeable degree of noise. To determine the effects of this noise on the computer analysis of this imagery, the small outlined area was subjected to computer analysis. The results of this analysis are shown in figure 6-11. The analyzed area is outlined on an S190 photograph on the right, and the results of the computer classification are shown on the left. Agricultural and other features were classified with an acceptable accuracy (greater than 90 percent). The noise in the imagery did not have a major effect on computer classification; apparently, some of the noise was correlated between the different spectral channels. However, the noise was larger than had been expected on the basis of preflight measurements. Consequently, a noise analysis was performed, and two major types of noise were found: high frequency ($\geq$20 kHz) and low frequency ($\leq$20 Hz). In several channels, high-frequency noise at discrete frequencies

FIGURE 6-8.—Enlargement (39.4× magnification) of S190 image over Sun City Development area of Phoenix, Arizona.
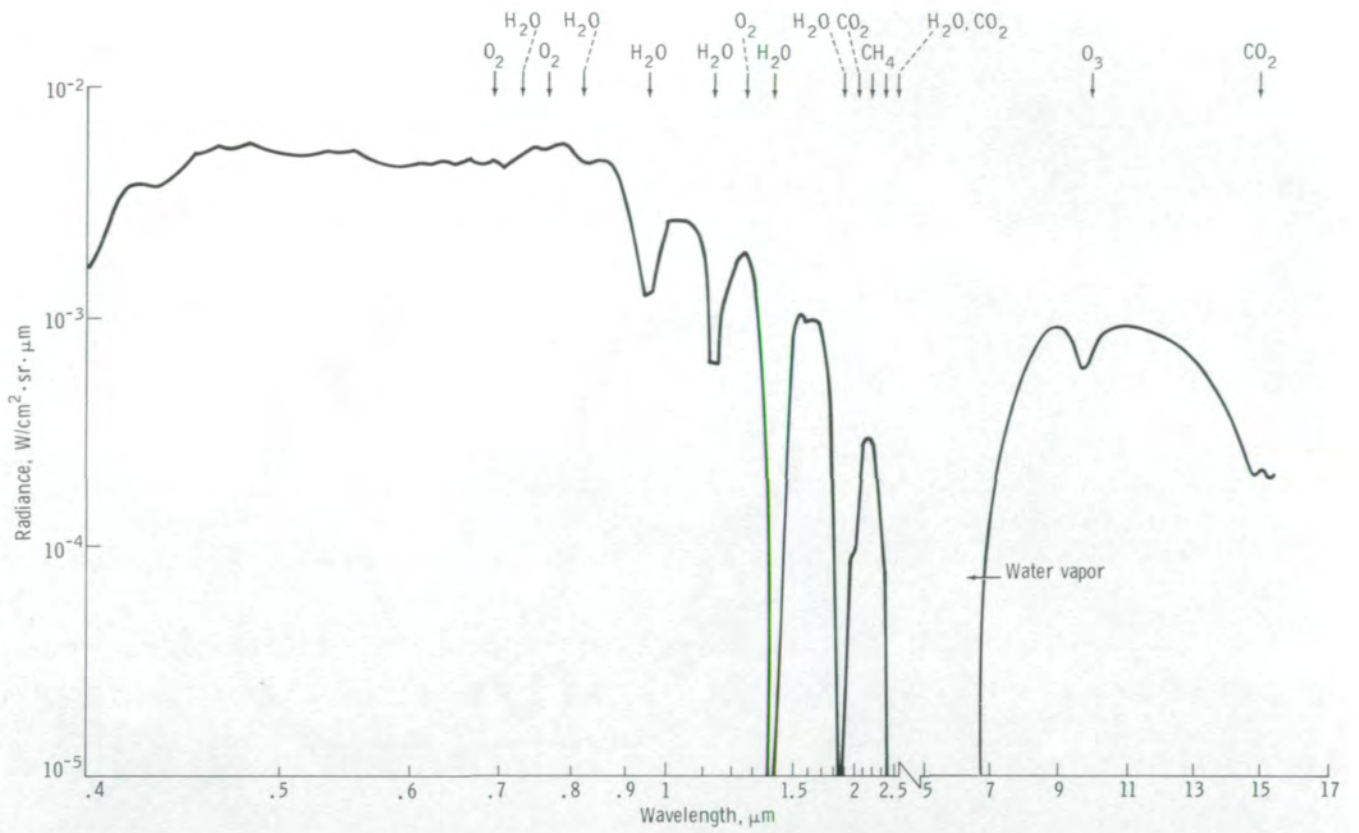
FIGURE 6-9.—Typical S191 spectral data showing peaks for oxygen (O_2), water vapor (H_2O), carbon dioxide (CO_2), ozone (O_3), and methane (CH_4).
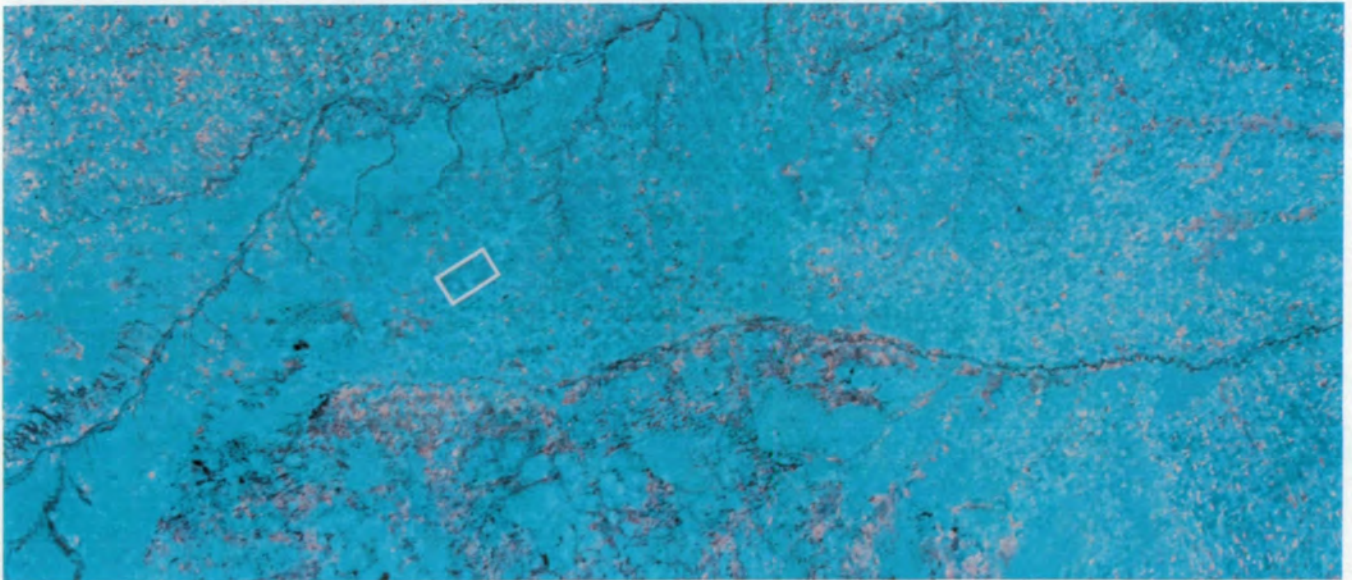

FIGURE 6-10.—S192 Multispectral Scanner imagery of Holt County, Nebraska (S-73-1510).
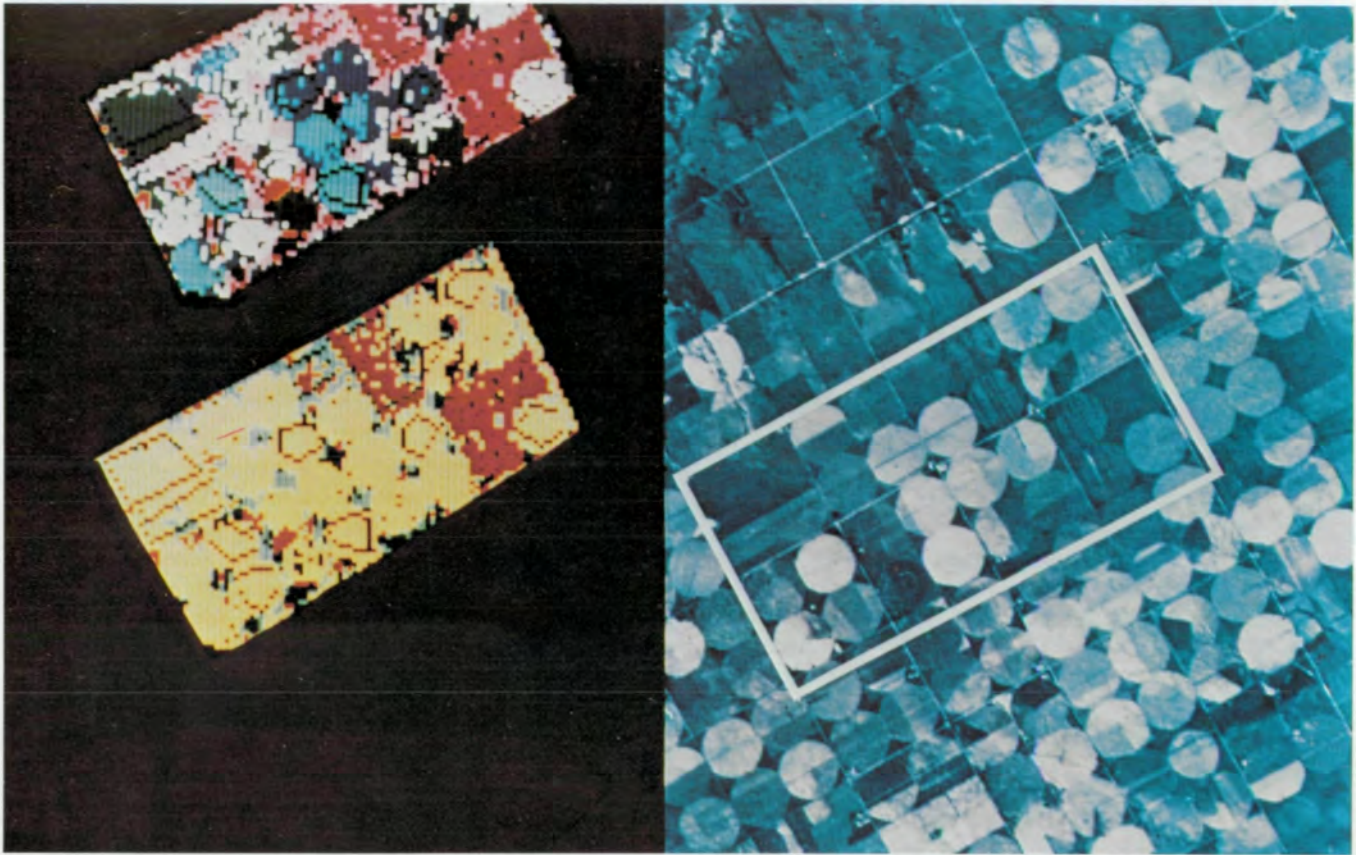
FIGURE 6-11.—Computer analysis of study area (rectangle in fig. 6-10) in Holt County, Nebraska (S-73-2839).

was observed. This noise produced herringbone patterns in the imagery. Because the noise occurred at sharp, well-defined frequencies, it was possible to remove the noise by computer analysis (mathematical filters).

The low-frequency noise was most noticeable in the thermal-infrared channel and produced heavy banding (random noise) in the image. This imagery was not useful for photointerpretation because the banding obscured surface features. Consequently, mathematical filters and every-scan calibration data were used to minimize or remove the noise.

An example of thermal imagery is illustrated in figure 6-12. Low-frequency noise was present before data processing; after processing, the low-frequency noise had been filtered out. Improvement in the quality of imagery for photointerpretation is evident.

The thermal imagery acquired on the first two missions was acceptable for some applications but not for others. As a result, the detectors flown on the Skylab 2 and 3 missions were replaced with an improved thermal detector by the Skylab 4 crewmen. Thermal imagery from the Yuma, Arizona, region (fig. 6-13) was obtained with the improved thermal detector. A substantial improvement is evident in the image quality produced by the detector. The radiometric performance of this thermal detector was such that temperature differences of approximately 0.8 K were equivalent to detector noise.

During initial in-flight checkout and operation, difficulties with the manual alinement and focusing of radiation on the detectors were encountered. In addition, some of the bands had an excessively small dynamic range. Therefore, contingency attenuators
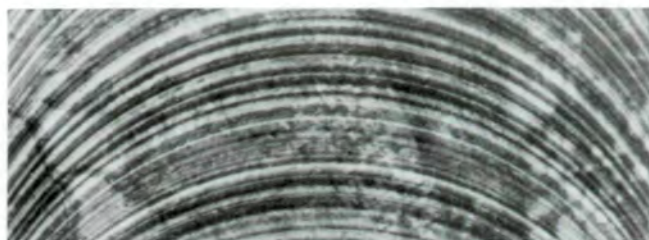
Before processing
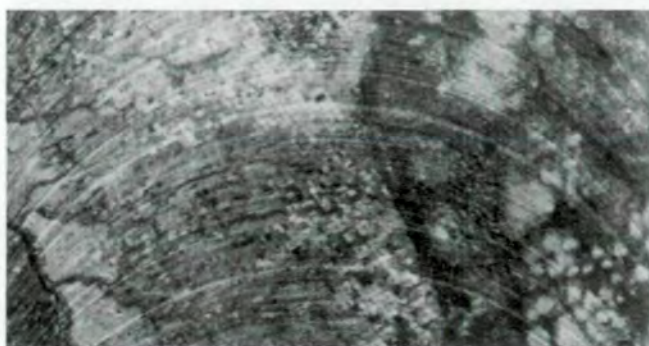
After processing

FIGURE 6-12.—Effects of data processing of S192 Multispectral Scanner thermal imagery (S-74-3154).

were installed by the crewmen. A small percentage of data was lost because of these problems. All other performance factors of the system (band-to-band registration, geometric resolution, radiometric calibration, etc.) were within the limits expected from the preflight calibrations.

Microwave Radiometer/Scatterometer and Altimeter

The Microwave Radiometer/Scatterometer and Altimeter (S193) operated at the K_E-band (2.2 cm) wavelength in three different modes: as a passive radiometer, measuring the microwave energy emitted by the Earth; as an active scatterometer, which sent microwave pulses to the Earth and measured the intensity of the return echo; and as a radar altimeter. All these functions shared the same antenna, which was gimbaled to permit scanning of the Earth in various patterns. The antenna functioned acceptably during the Skylab 2 mission and most of the Skylab 3 mission;

however, near the end of the Skylab 3 mission, the antenna began scanning erratically. Early in the Skylab 4 mission, the crewmen were able to restore the antenna scan in one direction by mechanically pinning it in one axis and by making modifications to the electronic circuits. However, Skylab 4 data proved to be anomalous and very limited amounts of the data were recoverable for the investigators.

Analysis of radiometer performance indicated that emitted radiant power was measured with an accuracy of at least 4 percent (corresponding to a brightness-temperature accuracy of ± 7 K) and with a precision of at least 2 percent (or ± 1.5 K) for typical ground scenes. The scatterometer performance showed that the reflected signal was measured within an accuracy of 4 percent for typical ground scenes, with a precision of at least 2 percent. With this accuracy and precision, the scatterometer was capable of measuring reflected signals that varied in amplitude by a factor of greater than 10 000:1.

Altimeter performance was measured from analysis of the data obtained over regions with known surface contours. The accuracy of the altitude measurement was ± 7 m with a precision of ± 1 m.

With the exception of the antenna, all performance aspects of the S193 during the Skylab 2 and 3 missions equaled or exceeded predicted values.
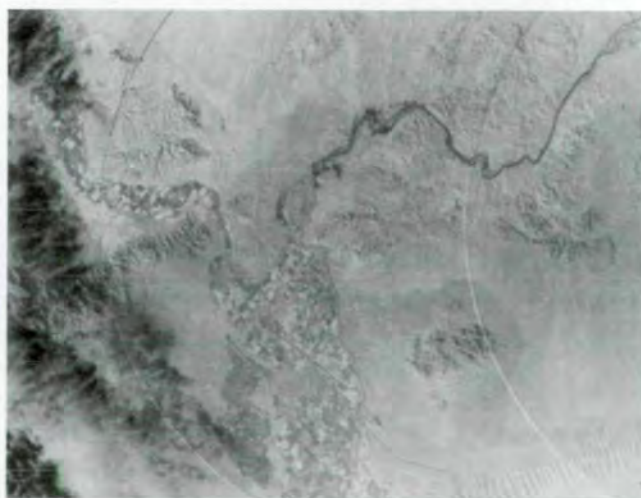

FIGURE 6-13.—Imagery from the Yuma, Arizona, region obtained with the improved S192 thermal detector (S-74-23477).

L-Band Radiometer

The longest wavelength (21 cm) sensor onboard the Skylab vehicle was the L-Band Radiometer (S194), which measured radiant energy from an approximately 124-km-diameter area of the Earth. Effective measurements were limited to a 111-km-wide swath centered about the nadir point. The performance factors of most interest for this passive microwave sensor were its antenna pattern, pointing accuracy, and radiometric accuracy.

Comparison of predicted and observed signals from well-defined surface features were used to define the S194 antenna pattern and pointing accuracy. Both these factors were within a few percent of predicted values. Radiometric performance was determined from measurements of the Sahara Desert, where large sandy areas that have uniform emissivity and temperature exist. A precision of approximately ± 0.2 K and an accuracy of approximately ± 1.7 K at 285 K were found.

THE S190A AND S190B PHOTOGRAPHIC IMAGING SENSORS

The Skylab Program provided a unique opportunity to use photographic imagery in Earth resources investigations. Investigators were able to analyze high-resolution photographs processed under carefully controlled conditions, with known camera performance characteristics, and with a wide range of film and spectral filter combinations. The investigators used both sophisticated data analysis and standard photointerpretation techniques. The advanced techniques included comparison of image information among spectral bands, precise image densitometry, and multiband analysis and enhancement techniques. The application of these sophisticated analysis techniques led to significant results that are discussed in the preceding discipline summary sections.

Almost all the analysis techniques and results are based on two key properties of the Skylab photographs. A brief description of these properties will assist in the understanding and appreciation of most of the techniques developed during the photographic experiments.

First, the Skylab photographs provided investigators with information in many wavelength, or spectral, regions. The spectral data were obtained from filtered black-and-white films or from information in the layers of multiband films, such as color and color-infrared film. In the case of filtered imagery, the spectral bands were defined by the combination of the wavelength transmitted by the filter (filter spectral bandpass) and the wavelength sensitivity of the film (film spectral sensitivity). For the multiband films, the spectral bands were determined primarily by the spectral sensitivity of the individual film layers. The investigators extracted the spectral information from the multiband imagery by separating the information in the individual film bands through a filtering process. Thus, by using either the filtered or the multiband imagery, the Skylab investigators had a wide variety of high-resolution photographic images for Earth resources investigations.

Second, the Skylab photographic experiment package was designed to enable use of the cameras to measure the amount of energy reflected from the Earth. In other words, the Skylab cameras could be used as imaging photometers (devices that measure incident energy). Thus, investigators were able to determine the energy coming from any part of the photographic scene by careful measurements of the density of that part of the image on the exposed film.

Each roll of film had a sensitometric control strip (fig. 6-14) that could be used by the investigator to relate photographic density to the energy that exposed the film. Each control strip consisted of a set of film areas exposed with known amounts of energy. A comparison of the density from a Skylab scene with the same density on the control strip provided a measurement of the energy incident at the film plane in the spacecraft. Also, because the effects of the camera lenses and shutters on exposure energy had been carefully measured, camera effects could be removed from the image data. The photographic image data could be processed to obtain an accurate measure of the energy reaching the spacecraft from any portion of the photographic scene. Thus, the investigators not only had high-resolution photographs that enhanced terrain and resource features, they were also able to extract a measurement of reflected energy in each spectral band being studied and to compare the energy differences among the spectral bands. The ability to measure energy values in the different spectral bands was of fun-
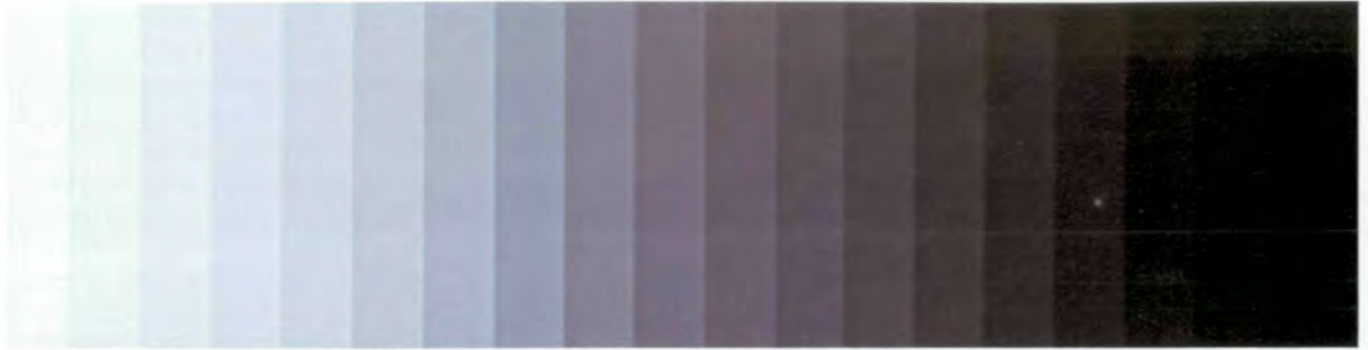
FIGURE 6-14.—Example of a sensitometric control strip for color film. Each step, or square, has been exposed by a different amount of light energy. By measuring the density of each step, investigators obtained the relationship between image density and exposure of the film.

damental importance to several new techniques developed during the photographic experiment.

The data analysis techniques developed from the S190 photographic experiment can be grouped into four categories: (1) techniques arising from the application of conventional photointerpretation methods to the unique data format provided by the Skylab photographs, (2) techniques evolving from various forms of image densitometry, (3) techniques developed from multiband spectral enhancements or analyses, and (4) techniques in which Skylab photographs provided a unique model input for Earth resources analysis.

Photointerpretation Techniques

Conventional photointerpretation techniques principally involve visual evaluation of shapes and patterns on the photographic image (appendix D). The shapes and patterns are defined by the tonal and textural variations within the scene. Interpreters evaluate the patterns discriminated on the basis of their understanding of, and experience with, the physical processes under study. Many successful applications of such conventional photointerpretation analysis can be found in the individual discipline sections of this report. The new approach for Skylab visual analysis techniques is basically an extension of the conventional photointerpretation methods to include, or take advantage of, the unique characteristics of Skylab photographs; namely, the perspective achieved from space (large areal view with high resolution), a wide selection of spectrally filtered images, and the photographic format from which visual comparisons can be made.

Each frame of Skylab imagery covers a large area; the S190A photographs cover approximately 160 km on each side, and the S190B photographs cover approximately 110 km on each side. A high-altitude aircraft flying at 15.24 km with a standard 150-mm focal length, 230-mm format mapping camera would require 50 photographs to cover fully an area 160 km on each side, assuming perfect flight lines and no overlap between photographs. When a standard amount of photographic overlap is allowed, the number of photographs required to cover the 160-km square increases to more than 200. A prodigious effort would be required to correlate these photographs so that an interpreter could recognize large-scale effects occurring over 16 to 160 km.

The Skylab photographic experiment removed this logistical obstacle by providing high-quality, high-resolution photographs covering large areas. Photointerpreters could thus evaluate phenomena at physical scales previously unattainable. For example, figure 6-15 is an S190B color photograph of the Pacific Ocean near Point Arena in northern California. The whitish tones in the water are caused by sediment of varying concentrations. A study of this photograph by Pirie and Steller (ref. 6-2) provided information on the occurrence of upwellings and location of coastal current that would have been impossible from aircraft photographs.

Mapping from aircraft photographs would have required a degree of flight-line accuracy that would have been extremely difficult to achieve over the ocean. The ocean has no landmarks with which to sight a flight line or to orient photographs. Also, aircraft coverage would have required hours of flying, during which the currents could change or lighting conditions could vary. The variation in lighting conditions would cause analysis difficulties because current structures were extracted on

FIGURE 6-15.—The eddy pattern at Point Arena (northern California) is visible as longshore currents move suspended sediments in a southerly direction. The presence of offshore swirl and boundary patterns indicates a slow-moving California Current. Upwellings (U) and current directions (arrows) are indicated. Five fingers, or scalloped patterns, are present offshore on this color photograph (SL4-92-333).

the basis of tonal variation over the ocean. Finally, each aircraft photograph would have brightness changes from side to side across the format caused by differences in angles of illumination and reflection. These brightness changes would also have contributed to analysis difficulties. The problems of flight-line accuracy, time variation, and tonal or brightness fluctuations were minimized by Skylab photographs.

Barnes et al. (ref. 6-3) evaluated the usefulness of EREP data for mapping snow cover. Accurate snow-cover mapping is crucial for runoff prediction and water management. These investigators determined that S190 color and color-infrared photographs could be used to map snowpack extent more accurately than could images provided by any other spacecraft or aircraft system. A key element in the S190 mapping capability was the perspective attributable to large-area coverage. Figure 6-16 depicts snowline regions in central Arizona determined from an S190B photograph and from a concurrent aerial snow survey. The aerial survey snowline is considerably less detailed than the Skylab-delineated snowline, and the position determined from the aerial survey does not fit the topography as closely as the Skylab snowline. The accuracy of runoff prediction is closely related to the accuracy of snowline mapping.

Image analysis techniques using photointerpretation of image patterns were significantly extended in the Skylab photographic experiment by including comparisons of photographic image patterns with patterns found on nonphotographic imagery, such as those from the S192 Multispectral Scanner. Skylab investigators were thus able to extract additional information on such problems as the detection of oceanic upwelling regions for fishery resources, the determination of vertical sediment distribution in coastal waters, the detection of melting snow regions for runoff prediction, and the differentiation of water droplet clouds from snow.

Szekielda (ref. 6-4), for example, used S190 color photographs to study ocean color changes as possible clues to the location of an upwelling. As discussed in section 5, upwelled waters afford an excellent medium for the growth of fish. Monitoring the location of upwelling regions from space is thus extremely important.

Photointerpretation of red and green spectral bands proved useful in determining the vertical distribution of suspended sediments (ref. 6-2). Because penetration of water by red wavelengths is small, an image in the red spectral band depicts only near-surface information. Water penetration in the green spectral region is greater than in the red, and an image in the green spectral region provides detailed information on subsurface sediments. The discrimination of such surface and subsurface effects is depicted in figure 6-17.

Barnes et al. (ref. 6-3) developed a technique for the automatic discrimination between snow and water droplet clouds by comparing S192 imagery in the visible spectral region to that in the middle-infrared (1.6 to 2.4 μm) region. In the latter spectral range, the reflectance of snow is almost zero, whereas water droplet clouds have a high reflectance. A comparison of the visible spectral region, in which both types of objects have high reflectance, with the 1.6- to 2.4-μm region thus permits discrimination. The discrimination technique is of particular significance for automatic snow mapping because cloud discrimination has been recognized as a serious hindrance to eventual machine processing of satellite data for snow-cover mapping.

Similarly, Piech et al. (ref. 6-5) demonstrated that a comparison of red (0.6 to 0.7 μm) and near-infrared (0.8 to 1.0 μm) spectral bands was useful in differentiating atmospheric turbidity that occurs over a large lake from the turbidity that occurs within the lake. The technique is particularly useful in accounting for the effects of very light, wispy clouds or haze. In the near-infrared spectral region, a lake without high sediment load will appear black, whereas a cloud or haze effect will maintain a signal or pattern similar to its pattern in the red spectral band. A comparison of the two spectral bands thus permits discrimination between atmospheric effects and lake effects; this discrimination is important in measuring parameters such as turbidity and chlorophyll concentration.

A comparison of visible and near-infrared bands has also proved useful for detecting snow cover in a melting condition (fig. 6-18). Such snowmelt information is particularly needed in regions where significant portions of the snowpack can melt within a few days, or even hours. A melting snowpack decreases in apparent extent when viewed in the visible and near-infrared bands because of a decrease in the reflectance of melting snow. A comparison of visible and near-infrared bands yields a measure of the melting condition of the snowpack.
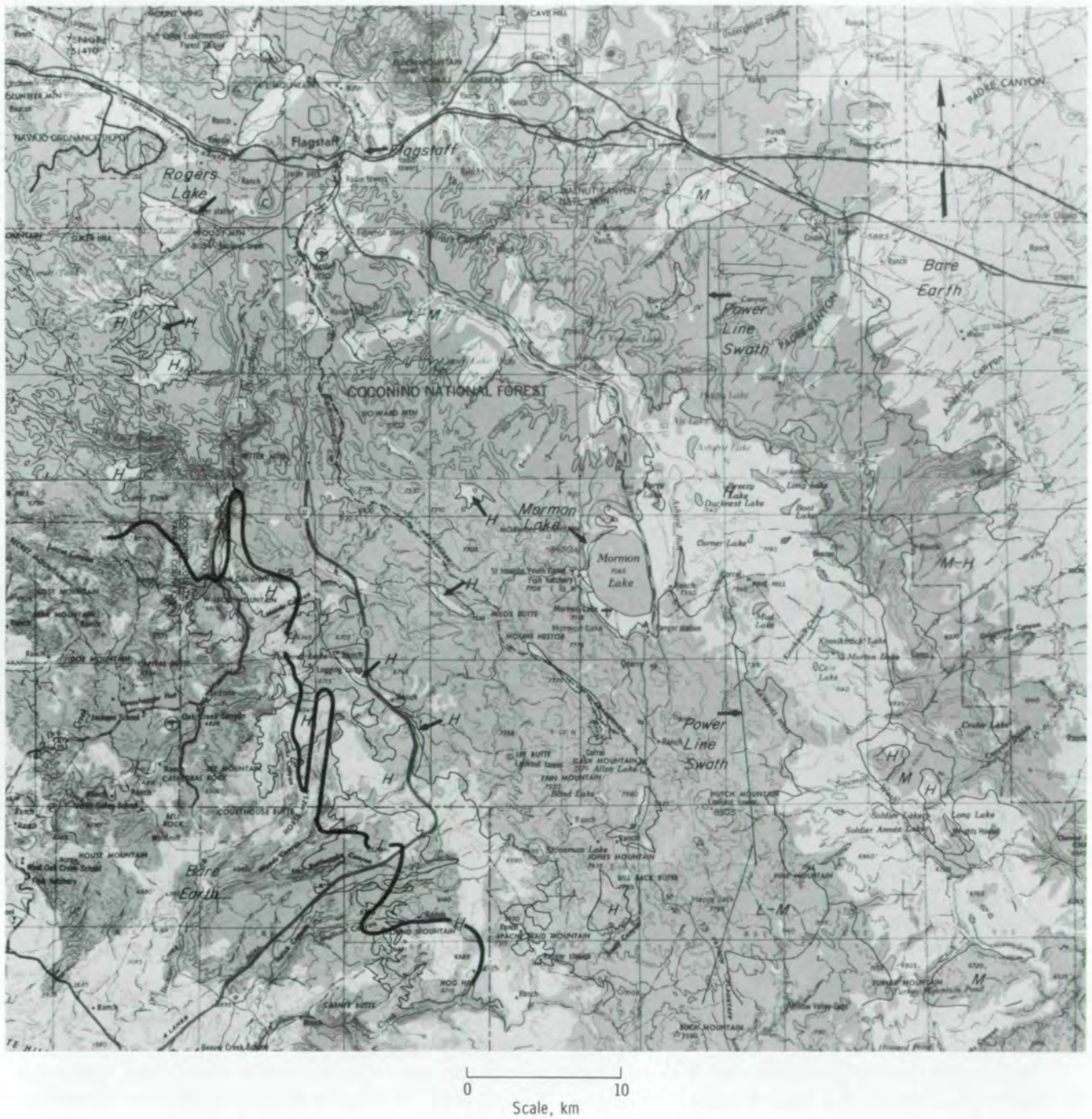
FIGURE 6-16.—Portion of U.S. Geological Survey topographic map showing central Arizona. Thin black lines indicate boundaries of snow areas with differing reflectances as mapped from an S190B photograph; H, M, and L indicate high, medium, and low reflectance, respectively. Heavy black line indicates snow boundary as depicted on aerial survey snow chart.
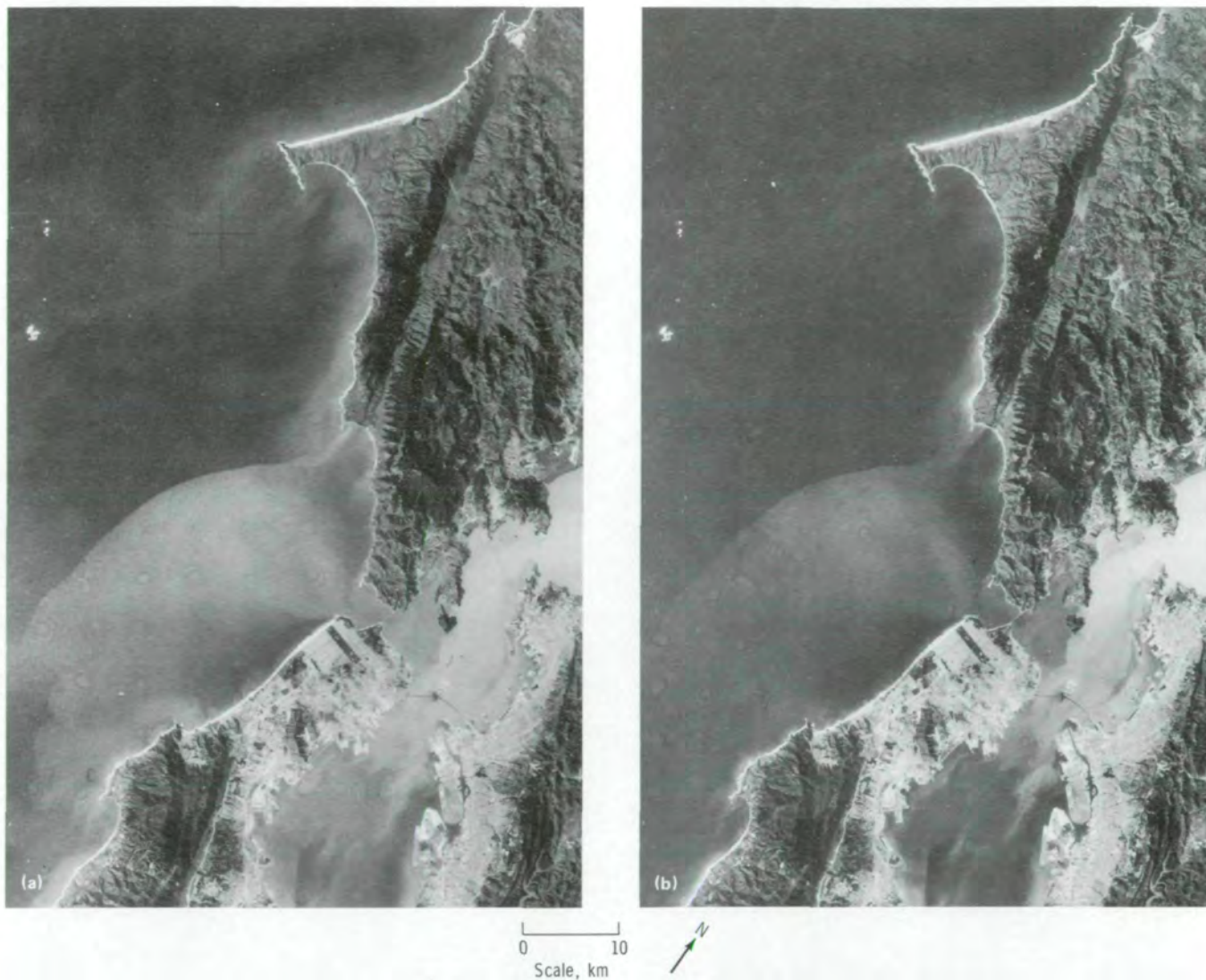
FIGURE 6-17.—Example of the use of different spectral bands in determining the vertical distribution of suspended sediments in coastal waters off Point Reyes, California. (a) Green band (0.5 to 0.6 μm) displays detailed information including the effects of water penetration (SL4-78-071). (b) Red band (0.6 to 0.7 μm) shows surface detail without interference from subsurface sediments (SL4-77-071).

Densitometric Analysis Techniques

A photointerpreter is limited in the ability to discriminate tonal differences within an image. The limitation arises because of visual and psychological constraints in quantifying contrast differences between points of an image that are separated or between points of an image lying in an area of changing image texture. Several Skylab investigators found it desirable to quantify important density or exposure changes occurring within the photographic scene by using various forms of image densitometry.

Some investigators (ref. 6-5) used macrodensitometers to measure density values over a large spot on a photograph, typically approximately 0.5 mm in diameter. A density reading on a 0.5-mm-diameter spot covered a ground area of 1.5 km in diameter on S190A photographs and 0.5 km in diameter on S190B photographs. Other investigators (refs. 6-2 and 6-5) used microdensitometers to measure densities over spot

diameters of approximately 25 μm corresponding to a ground dimension of 75 m in diameter on S190A photographs and 25 m in diameter on S190B photographs. The microdensitometers were used in a manner similar to the use of a macrodensitometer, to measure the density of specific image spots, or to scan the image to provide a trace, or record, of density values from which contours or shapes could be drawn.

Another method used for image densitometry was the application of color-encoding devices, in which a television vidicon scans the photograph and converts the light signal to density values. The density range of the scene is then divided electronically into 10 or 20 ranges of density. Each density range is assigned an individual color, and the photographic scene is redisplayed on a color television screen with the photographic densities encoded as colors. The resulting color patterns can then be interpreted as representing different types of trees or differing sediment concentrations, depending on the problem under investigation.

Densitometry of individual layers of the multiband color or color-infrared films was accomplished by two methods. In one method, a filter transmitting light from one film layer was inserted into the densitometer so that density values were measured for only that film band or layer. In the second method, a black-and-white copy, or separation, of the information on one film layer was made through a filter. Densitometry was then performed on the black-and-white copy of the scene. Regardless of the techniques used, investigators were able to obtain spectral-band information from the multiband films and to apply these data to their resource investigations successfully.

The densitometric analysis techniques were applied not only to Skylab photographs, but to various enhancements of the photographs such as ratio combinations of film layers (ref. 6-5). Application of densitometry to such multiband enhancements is discussed in section 3 and in the following subsection. Densitometry of the original photographs proved most useful in water-quality studies related to coastal dynamics and sediment transport, and in land use studies such as timber differentiation and classification.

Baldridge et al. (ref. 6-6) applied color encoding of color and color-infrared imagery to timber differentiation and analysis. Color encoding was successfully applied to timber mapping, differentiation of hardwood and softwood stands, and evaluation of timber maturity. The infrared-sensitive layer of color-infrared film proved most sensitive and valuable for timber differentiation. Figure 6-19 contains examples of successful delineation of timber maturity from S190B color-or-infrared photographs. This figure shows color encoding of a sample area in Mahoning County, Ohio, containing only three stages of stand maturity. The area was 1 of 16 sample areas in which machine determination of stand maturity from S190B photographs was undertaken. Forest management personnel confirmed the validity of the classification based on the color-encoding techniques in all the sample sites.

Numerous investigators found densitometric analyses of significant value in studies of coastal and estuarine dynamics and of sediment transport (refs. 6-2, 6-4, and 6-7 to 6-9). Welby and Lammi (ref. 6-9) used color-encoding techniques to interpret underwater and shore topography. The Skylab photographs also proved useful in revealing sediment in water bodies. The effect of a period of precipitation on sediment discharged into a major lake was recognized, and the use of orbital photographs for measuring relations between rainfall and sediment load in a drainage basin was shown to be possible.

Szekielda (ref. 6-4) related color changes to particulate concentrations in the study of upwelling areas off the coast of northwest Africa. Gordon and Nichols (ref. 6-8) successfully used color encoding and microdensitometry to analyze southern Chesapeake Bay water color and circulation. Red- and green-band data were found to be the most useful for mapping water types related to transparency, turbidity, and suspended-sediment load. It was further established that suspended sediment could be used as a tracer of water movement to discriminate small-scale mixing patterns and local tidal currents. Large-scale patterns were shown to reflect bottom topography indirectly because the bottom serves as a source of suspended material.

A near-linear relationship between reflected radiance and suspended solids in the concentration range of 20 to 80 p/m was found by Yarger and McCauley (ref. 6-7). Pirie and Steller (ref. 6-2) found that variations in sediment concentration could be observed. Figure 6-20(a) is an S190B photograph of the San Francisco Bay area during a period of high sediment discharge. Microdensitometer traces in the green spectral band are shown in figure 6-20(b), with contour intervals ranging from highest reflectance and highest suspended solids (1) to lowest reflectance and lowest suspended solids (4). Before the Skylab overpass, an iridium tracer was added
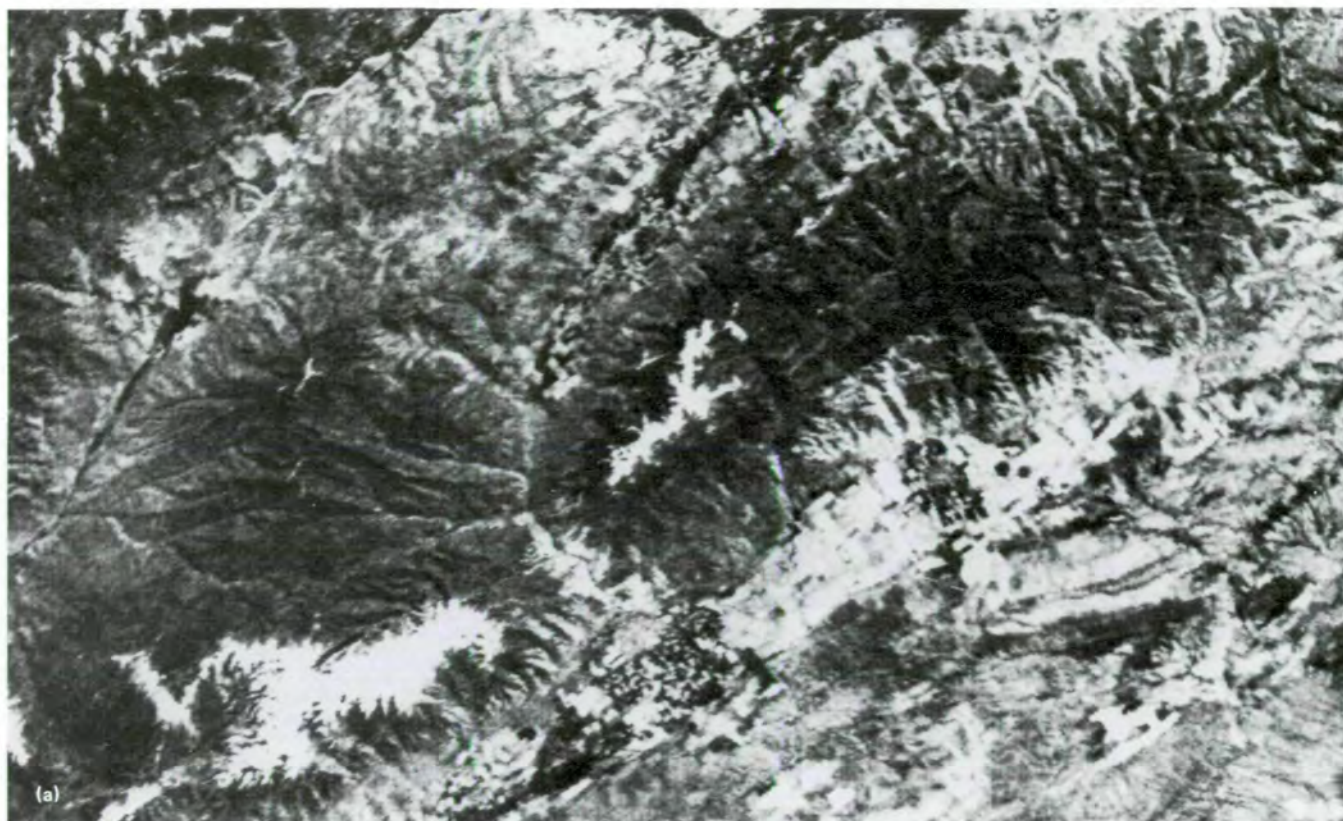
FIGURE 6-18.—An area in Utah including the Mount Nebo Range and San Pitch Mountains. The apparent decrease in the extent of snow cover between these two bands is due to melting snow. (a) Band 3 (0.52 to 0.56 μm). (b) Band 7 (0.78 to 0.88 μm).

to the sediment flow. When fresh and saline waters meet (as in San Pablo Bay), flocculation occurs. Measurement of the amount of tagged sediment in subsequent dredging should therefore correspond with the sediment flow pattern and variations. Figure 6-20(c) indicates the correlation between the brightest regions of flow and the amount of tagged material observed in subsequent dredging of San Pablo Bay. The correlation between the densitometer map and dredging results is very good.

Analyses Using Multiband Spectral Enhancements

Several investigators used data processed from two or more spectral bands. The individual-layer data were combined, either photographically or electronically, with data from other photographic bands to generate displays for interpretation. Hardy et al. (ref. 6-10) investigated land use mapping through combinations of three S190 spectral bands processed on diazo photographic materials to produce maximum color contrast among different land use categories. Colwell et al. (ref. 6-11) digitized densitometric data from four S190 bands and subsequently performed a discriminant analysis on the multiband data to classify crops successfully. Piech et al. (ref. 6-5) used image microdensitometry to determine atmospheric and processing corrections, then photographically and electronically divided two spectral bands (which were corrected for atmospheric and processing effects) to measure eutrophication indices of
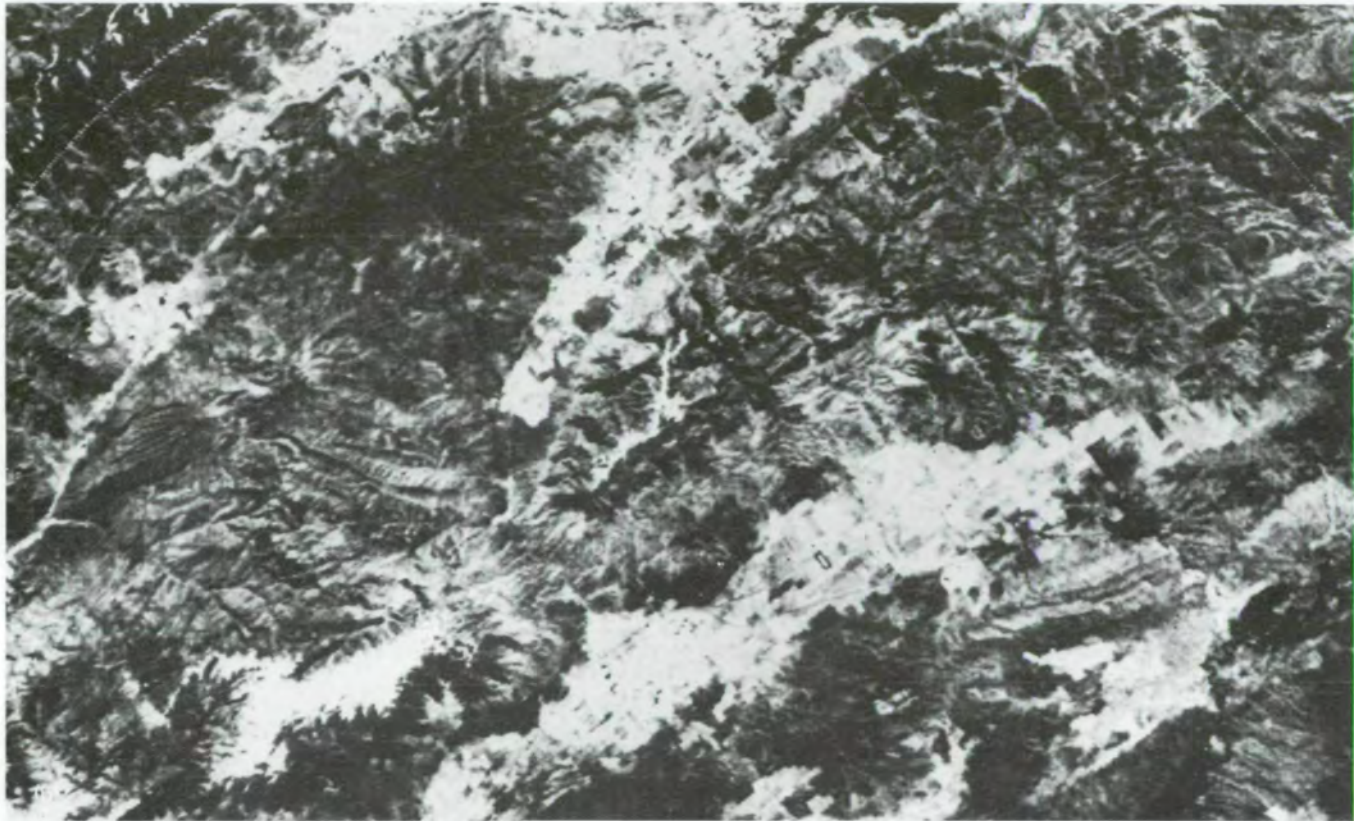
```
0        10        N
   Scale, km
```

FIGURE 6-18.—Concluded.

large lakes. The multiband analyses can therefore be grouped into photographic data reduction, electronic data processing, and a combination of electronic and photographic data analysis.

Photographic data processing.—Hardy et al. (ref. 6-10) used S190 photographs to update an existing New York State land use inventory. A key aspect of this investigation was the development of an inexpensive, systematic procedure for generating enhanced color composites from the filtered S190 photographs. A color prediction model was developed to automate the selection and generation of color composites that maximized color contrast between selected land use categories.

Enlargements were made from the Skylab photographs, and the density range and contrast of the enlargements of each spectral band were standardized, or normalized, so that the density of terrain features would correspond to the exposure range of diazo photographic materials. The diazo photographic materials, which are usually used for line-drawing reproduction, were selected because they are inexpensive to purchase and process.

Density values obtained from each spectral band for known areas representing different land uses are fed into the computerized color prediction model. The model relates the density values in each spectral band for each category of land use to the spectral properties of the various diazo films. The model then produces a combination of spectral-band data and exposure data to maximize the color contrast among the land use catego-

FIGURE 6-19.—Forest-stand maturity analysis of a woodland area in Mahoning County, Ohio. (a) Aircraft photograph of a 52-hm² area containing medium to small saw timber. (From stereographic analysis.) (b) S190B photograph (infrared-sensitive layer only) of area in figure 6-19(a). (c) Image enhancement of S190B photograph showing area in figures 6-19(a) and 6-19(b). Red indicates medium saw timber, green indicates pole and small saw timber, and blue indicates brush and open fields.

ries being examined. Three land use categories can be examined for each composite; a set of color composites used for land use interpretation is shown in figure 6-21. Use of the color-composite data resulted in aggregate errors of approximately 12 percent for Level I land use classification and 25 percent for Level II classification.

Electronic data processing.—Automatic processing of Skylab photographs for crop classification was evaluated by Colwell et al. (ref. 6-11) and Silva (ref. 6-12). In the land use studies, computer processing of photographic density data that had been converted to digital form by scanning with a microdensitometer was used.
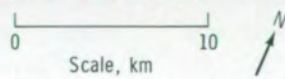
FIGURE 6-20.—Observations of variations in sediment concentration in San Francisco Bay, California. (a) S190B color photograph showing the detailed surface-current structure. The spreading of the waters entering San Pablo Bay and the Pacific Ocean is clearly observable during this high sediment discharge period (SL4-92-336). (b) Green-band density plots from the S190B color photograph with density contours as indicated. Contour intervals represent high (no. 1) to low (no. 4) reflectance (high to low sediment concentration). (c) Dredge disposal plot overlain by suspended-sediment distribution in San Pablo Bay. Correlation between sediment transport pattern and areas of high (10) to low (1) percentage of dredged material can be noted.
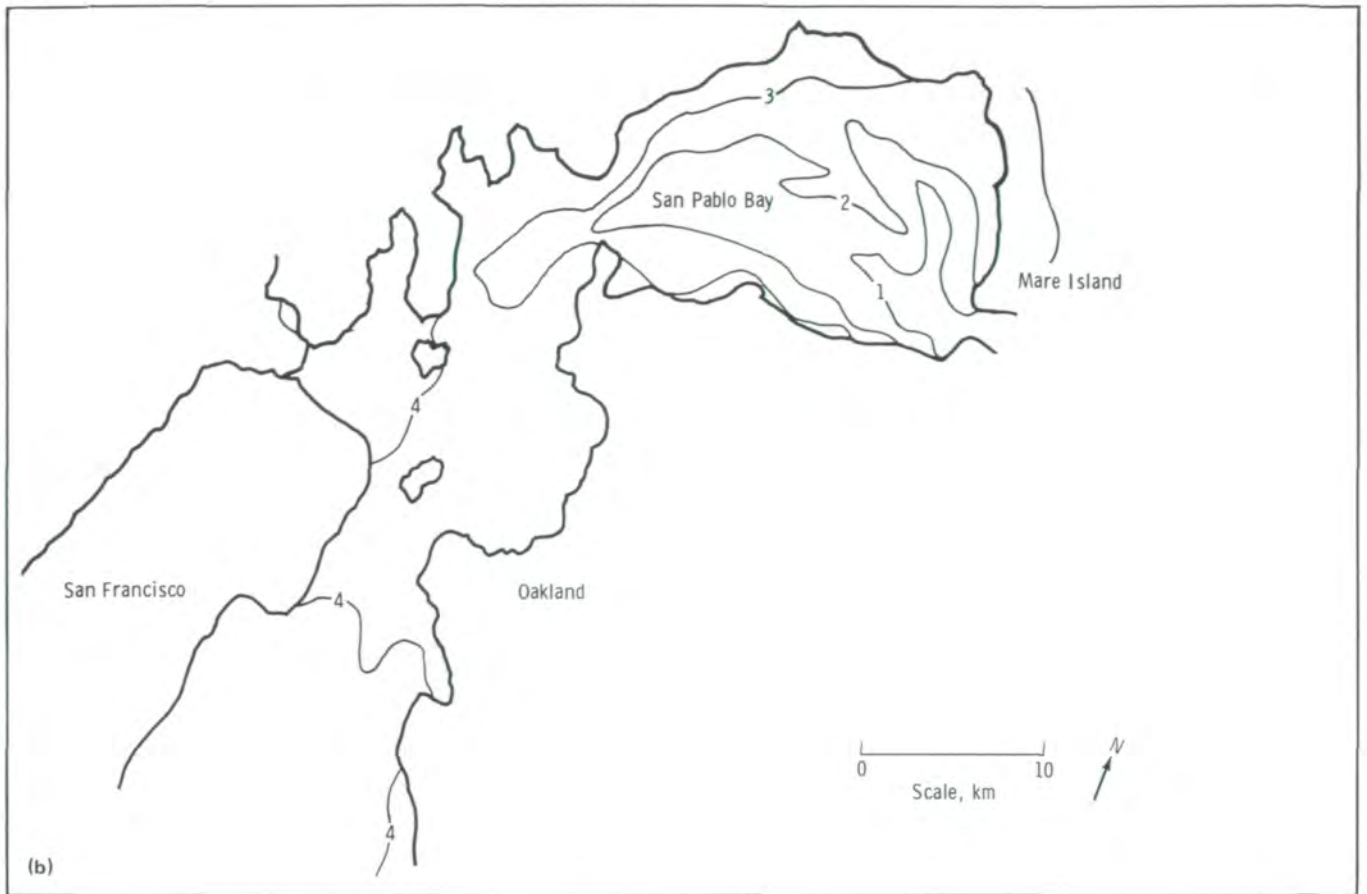
FIGURE 6-20.—Continued.

The four black-and-white bands of the S190A camera (green, red, and two near-infrared spectral bands) were scanned with a microdensitometer using a spot size approximately equivalent to 0.41 hm^2 on the ground (Colwell et al., ref. 6-11). The density measurements were recorded on magnetic tape and processed using pattern recognition algorithms.

The optimum combination of spectral bands was determined, as were interclass divergences, from combinations of crops. A classification map based on the training statistics was then generated. Finally, the data were reprocessed to produce a map wherein a "nearest neighbor algorithm" was used and accuracies of classification were computed.

The classification algorithms were applied with surprising success to data from a set of vegetable crops in the Salinas Valley, California. Analysis of the spectral densities in the four bands permitted classification to an overall accuracy of 49 percent early in the crop cycles and 85 percent later in the crop cycles. The latter accuracy is excellent considering that multidate information was not used in the crop classification.

Silva (ref. 6-12) also digitized S190A photographic data using both color-infrared and black-and-white

Heavy concentration of suspended sediment
Intermediate concentration of suspended sediment
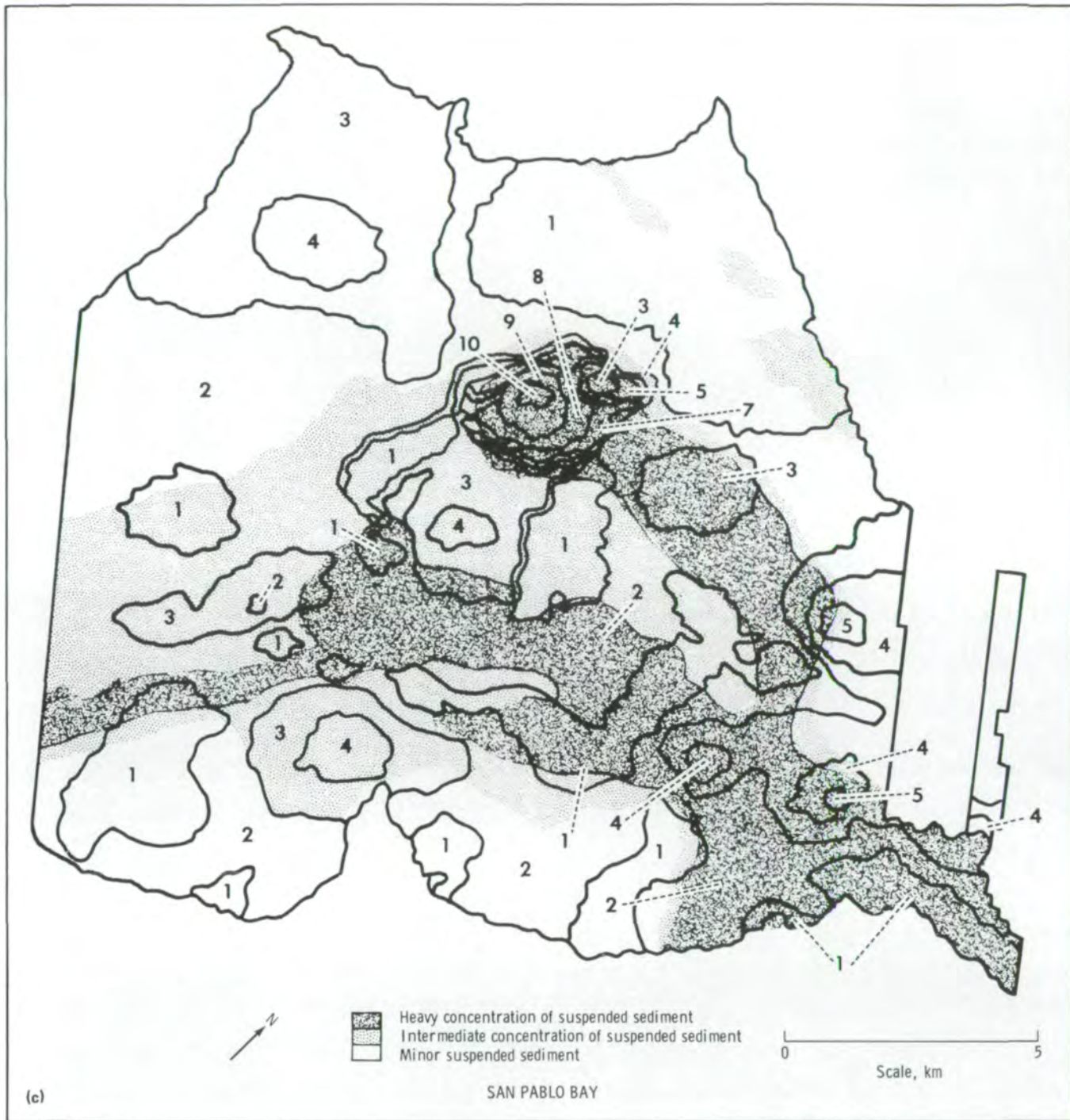Minor suspended sediment

SAN PABLO BAY

FIGURE 6-20.—Concluded.

FIGURE 6-21.—An S190A false-color composite of the Lower Hudson Valley, New York, at a scale of 1:250 000. The color representations are as follows: water, black; vegetation, red; urban areas, blue; agricultural areas, tan-yellow; and major highways, white lines.

multiband frames. The scanning spot was 25 μm in diameter, and lines were scanned at 20-μm intervals. A Kodak 92 filter was used to separate the red layer, a Kodak 93 filter for the green layer, and a Kodak 94 filter for the blue layer. The equivalent ground size for the aperture used was approximately 68 m in diameter. The four black-and-white films of the S190A were also digitized but without filters. A total of 256 different levels of film density was measured, and level 255 was set for the darkest area between frames. The three-channel digitized set defined by the three dye layers of the color-infrared transparency maintained good spatial registration because it was produced from the same transparency. The four-channel digitized set from the four black-and-white films of the S190A camera had to be registered by subjecting an 1100- by 1100-line block of data to a second-order least squares fit using 60 points evenly distributed across the area. The registration was 40 and 70 m for the pair of visible and infrared channels, respectively, but the registration is within two picture elements (pixels) between the visible and infrared bands because of differences in resolution between the two types of emulsion.

Once in proper format, the data were clustered and training fields for each of 12 classes were selected. The digitized color-infrared data were superior to the digitized black-and-white data and had classification accuracies of approximately 80 percent. Some degradation in results was caused by the shoreline of a lake and the narrow course of a river, which did not provide an adequate training set and would be affected by the misregistration between channels.

The successful application of automatic classification from multiband photographic imagery is important because of two characteristics of the photographic data: (1) ease of data storage, which permitted the full multispectral scene from the S190A camera system to be recorded and stored on four 5.72-cm black-and-white film transparencies, and (2) the excellent geometric fidelity of the photographic imagery, which facilitated registration and use of multidate imagery.

Photographic and electronic data processing.—Piech et al. (ref. 6-5) used microdensitometry of image elements to measure atmospheric effects and subsequently to reduce and process the multiband data in the form of target spectral reflectance values. The multiband reflectance analyses were used to obtain the eutrophication indices of large lakes such as Conesus Lake, New York; the relative value, or ratio, of various reflectance bands

is related to eutrophication indices of the lakes (fig. 6-22). The reflectance of a lake is typically approximately 2 to 3 percent, whereas the atmospheric component of the signal at the Skylab spacecraft can have a reflectance of approximately 10 percent. A small change in atmospheric properties from one sampling date to another could thus be misinterpreted as a significant change in lake properties. The accurate measurement of relative reflectance values between spectral bands therefore requires accurate removal of atmospheric signal noise in both spectral bands.

The results of the investigation demonstrated that image microdensitometry could be used to specify accurately the atmospheric component of exposure. Figure 6-23 depicts the relative values of blue- and green-band lake reflectance as measured from the Skylab spacecraft compared to those measured from an aircraft underflight at an altitude of 3048 m. The aircraft measurement techniques had previously been shown to agree consistently with ground measurements of spectral reflectance ratios. The Skylab and aircraft data agree within the system measurement accuracy. The investigators pointed out that increased accuracy in the measurement of reflectance values would be obtained by an increase in image resolution.

Subsequent reduction of the lake spectral data was accomplished by means of a combination of photographic and electronic data processing. A black-and-white photographic copy, or separation, of each spectral band of the S190A color photograph was modified according to the atmospheric effect measured for that spectral band; an appropriate increase in image contrast in each spectral band removed the effects of the atmospheric signal for that spectral band.
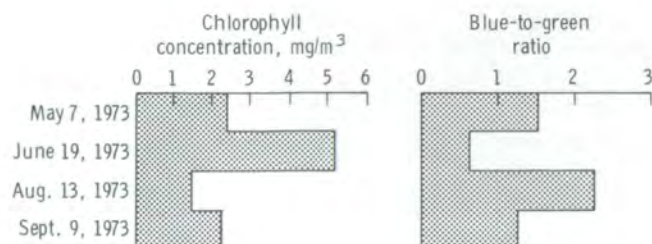

FIGURE 6-22.—An inverse relation is shown between the blue-to-green reflectance ratio and the surface chlorophyll concentration for Conesus Lake, New York, during 1973.
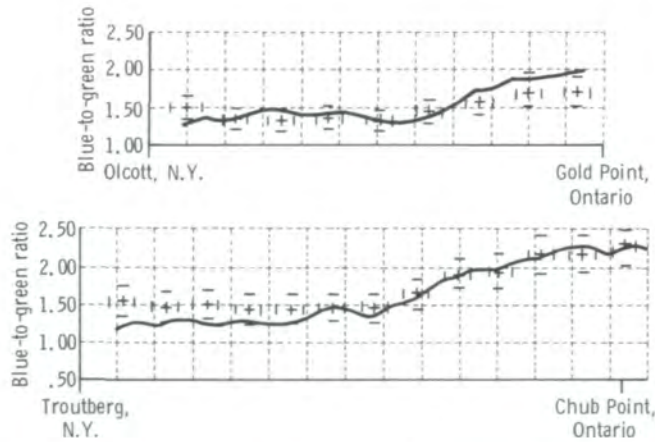
FIGURE 6-23.—Comparison of S190A measurements of blue-to-green reflectance ratio (solid line) with aircraft measurements (crosses and error bars). Each division on the horizontal axes represents 4.8 km (3 s. mi.).

A reversal copy was then made of one of the corrected spectral bands for which relative reflectance values were desired. An overlay of the positive copy of the other spectral band together with the reversal copy comprised a density map proportional to the reflectance ratio values of the lake scene. The data were then extracted, or displayed, using a color-encoding device. The crucial elements to the multiband analysis, however, were the measurement and the removal of atmospheric effects.

Approaches and Model Inputs

The Skylab photographic experiment served as a focal point for several investigations by providing a medium through which large areas could be studied by multidisciplinary teams and through which successful analysis methods could be verified and extended. Although the spectral properties of the Skylab photographs were used in all these studies, the most important characteristics were large-area coverage and high spatial resolution.

Skylab photographs enabled performance of an interdisciplinary study of the hydrology of prehistoric farming systems within a large and environmentally diverse area of central Arizona (Gumerman et al., ref. 6-13; fig. 6-24). Hydrologists, geologists, biologists, and archeolo-

gists evaluated the adaptation of prehistoric humans to the semiarid desert of central Arizona, and their creation of land management and water control systems. Such an analysis required data over thousands of square kilometers and an understanding of the numerous variations in environment over this region. Coverage of such a large region using only ground activities is impossible. Data from Skylab or high-altitude-aircraft systems provide the archeologist with a significant regional perspective for understanding surface geology, hydrology, and vegetation patterns and enable formulation of specific questions and relationships among the environment, prehistoric settlements, and subsistence systems.

The study covered an area extending from the Lower Sonoran Life Zone just north of Phoenix to the Upper Sonoran Life Zone just south of Prescott, including a biological transition zone between the desert floor and the plateau. Ecologically significant subareas, or drainage basins, were selected for study on the basis of basin area, stream length and order, slopes, bedrock type, and rainfall distribution. Estimation of available water was established from these parameters and from vegetation communities. With this information, it was possible to predict with some accuracy the basins most likely to have prehistoric water management systems. Delineation was based primarily on the topography and geometric characteristics of the drainage basins. The drainage information from the Skylab photographs, together with slope and landform data from high-resolution U-2 aircraft imagery, enabled archeologists to discern potential areas of prehistoric utilization.

Within the basins most suited for agricultural purposes, a series of exploitation models for one study area (fig. 6-25) was developed by using the topography, slope, and drainage patterns interpreted from Skylab and U-2 photographs. A decision model developed by Plogg and Garrett (ref. 6-14) was used to evaluate the alternative exploitation schemes for the entire area. The model was informally tested using the remote-sensing interpretations together with statistical data from the traditional sources as inputs. The results provided the archeologists with a fairly comprehensive understanding of the cultural and economic patterns for a large portion of the central Arizona area.

FIGURE 6-24.—Index map of Arizona, showing the location of the Basin and Range, Transition Zone, and Mesa Canyon physiographic complexes. →

Kingman

Flagstaff

Prescott

Test area

34° N

Phoenix

Yuma

Tucson

112° W

Mesa
Canyon
complex

Agua Fria River

Black
Canyon
City

River

34° N

New

Transition Zone complex

N

New River

Lake
Pleasant

112° W

Basin and Range
complex

Interstate Highway
17

0   10

Scale, km
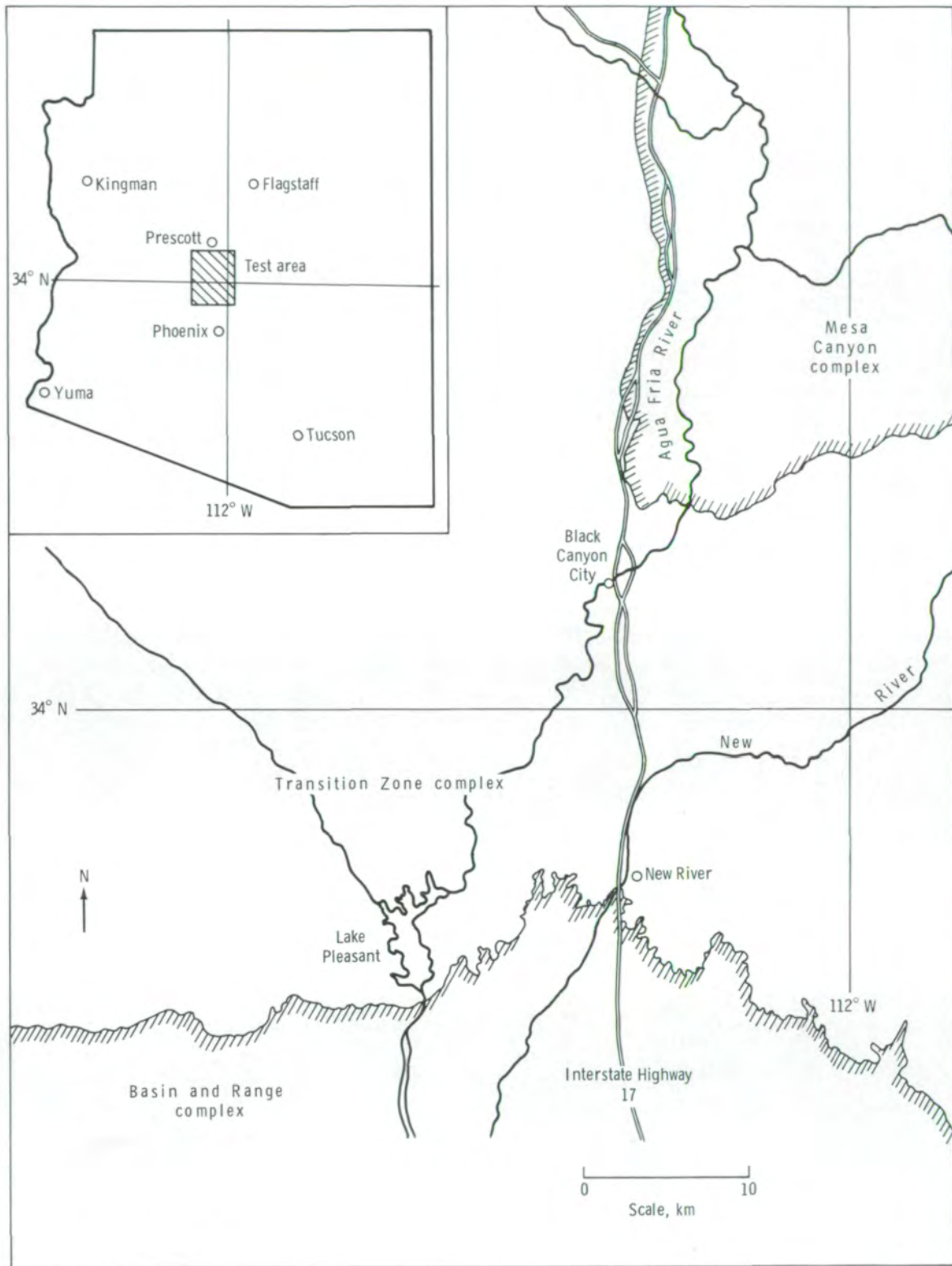
FIGURE 6-25.—Alternative models for exploitation of the central Arizona area by prehistoric civilizations. The organizational schemes define alternatives for social and natural utilization of the area during the period 1000 to 1400 A.D. The models (not to scale) indicate consideration of environmental parameters such as relative areal position, elevation, slope, surface materials, and water availability. (a) Model 1. (b) Model 2. (c) Model 3. (d) Model 4. (e) Model 5. (f) Model 6.

An extension of the precision of multistage sampling of timber volume to a Skylab data base was accomplished by Langley and Van Roessel (ref. 6-15). In multistage sampling, small-scale photographs are used to delineate regions of homogeneous characteristics, large-scale photographs are used to specify field plots of the sample classes for ground measurements, and subsequent ground measurements of yield or volume are used to develop the field plots of the sample classes. The investigators developed a resection technique for the Skylab photographs that permitted accurate location of sample-unit boundaries on the photographs. The subsequent analysis of the inventory precision resulted in the determination of increased economy and efficiency attributable to the space photographs. The precision of the volume estimate could be further improved through the use of multidate photographs; however, Langley emphasized that an increase in resolution to the point at which individual trees can be discriminated would provide the most significant increase in timber-volume accuracy.

THE S192 MULTISPECTRAL SCANNER

Although photographic systems provide better spatial resolution because of simpler construction and the availability of good-quality lenses and modern high-resolution films, optical-mechanical imaging sensors have four advantages relative to the usual photographic system: (1) the sensors operate in spectral regions not available to photographic systems (i.e., generally beyond 1 μm), (2) the position and width of each spectral band can be specified and controlled, (3) the sensors operate simultaneously in several spectral bands wherein each pixel is in both position and time registration across all spectral bands, and (4) the data are better calibrated. As explained previously, the S190A camera system provided registered multiband imagery with color and color-infrared film, and was radiometrically calibrated. However, the spectral bands overlapped to a degree, and their location and width could not be altered. When the multichannel electrical analogs of the scene are recorded on CCT's, a wide range of signal-processing techniques becomes available. Modern, high-speed computers can process the large volume of data generated by satellite sensors.

Thirteen bands of information between 0.4 and 13 μm recorded in the S192 differed from the four-band Landsat systems that operate between 0.5 and 1 μm. A

considerable amount of theoretical work involving statistical decision theory has been applied to the processing of aircraft multispectral scanner data with varying degrees of success. The Skylab S192 sensor was designed to apply these sophisticated schemes to space data, in which both resolution and atmospheric effects were different from those encountered at aircraft altitudes. The question concerning the optimum bands as seen from space for specific disciplines needed to be addressed.

Skylab investigators used S192 data as composite images and computer-compatible tapes to derive parameters of interest for agriculture, water resources, oceanography, land use, and geological and hydrological problems. A few investigators determined the effects of atmospheric attenuation and scattering on the uniqueness of signatures for different classes of objects and on the problems of signature extension.

The unique advantages of the S192 Multispectral Scanner form the basis for discussion of image analysis techniques. In some cases, investigators applied old techniques to new problems, whereas in others, new methods were developed for using the multispectral scanner data. The data analysis techniques are organized into four groups.

1. Single-spectral-band techniques—The investigator used the information in a single spectral band.

2. Two-spectral-band techniques—In some studies, the investigator required the use of only two spectral bands.

3. Multiple-spectral-band techniques—In these investigations, multiple spectral bands, three or more, are used either to generate false-color imagery or to perform multispectral pattern recognition.

4. Imagery use in Earth resource models—For example, a meteorological model may incorporate surface temperature as a key parameter in modeling phenomena such as winds, clouds, or rainfall. The data from the scanner can be used to input surface temperatures into the model and thus infer the meteorological conditions predicted by the model.

Single-Spectral-Band Techniques

The radiometric properties of a single spectral band can be advantageous in some applications research. The general approach for use of single-band radiometric data was to develop empirical correlations between the radiometric intensity and a specific property of the sur-
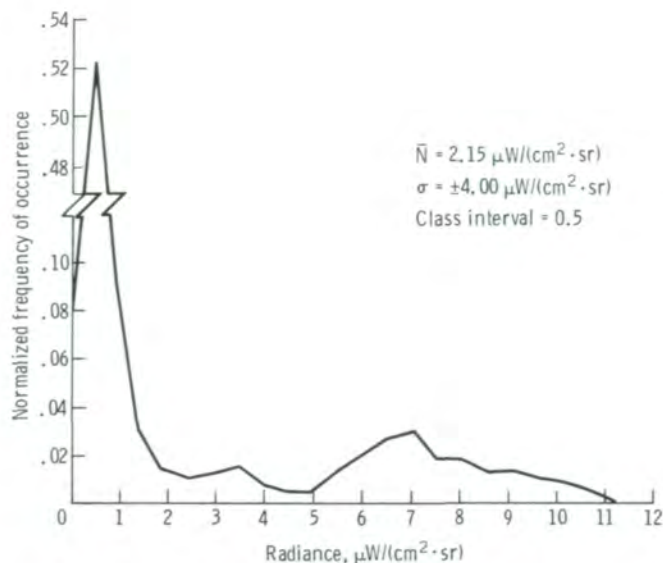
FIGURE 6-26.—A frequency distribution (normalized to unity) of the radiance in band 8. The primary peak at the left represents clear ocean; the broad peak centered at 7 μW/(cm^2·sr) is due to clouds and land.

around the low radiances represents water, whereas the cluster at the high end represents clouds and land. Previous work (ref. 6-16) established the Gaussian distribution of the radiance N reflectance from the ocean; therefore, by a suitable fit of the data for the water reflection, a radiance range of three standard deviations around the mean radiance $\overline{N} = 0.5$ μW/(cm^2·sr) should include all cloud-free pixels.

The range is then spread over the available dynamic range of the display by the conditions (for a negative image)

$$\left. \begin{array}{l} X = 0 \text{ for } N \geqslant \overline{N} + k\sigma \\[2ex] X = \dfrac{M\left[\left(\overline{N} - k\sigma\right) - N\right]}{2k\sigma} \\[2ex] \qquad \text{for } \left(\overline{N} - k\sigma\right) \leqslant N \leqslant \left(\overline{N} + k\sigma\right) \\[2ex] X = M \text{ for } N < \overline{N} < k\sigma \end{array} \right\} \qquad (6\text{-}1)$$

where M is the maximum value allowed by the display, $\overline{N}$ is the mean radiance of the cloud-free data, σ is the standard deviation, and k is an arbitrary constant. By setting $k = 2$, 95 percent of the cloud-free data would be recorded over the full range of the display. Detection of anomalies on the ocean surface would be improved by this method of enhancement.

The problem of area measurement using digital values and finite spatial resolution leads to errors for those pixels containing parts of two classes. Gilmer and Work (ref. 6-17) faced this problem in attempting to measure lakes and pond areas and their changes. Usually, all water areas are underestimated. Using the 1.55- to 1.75-μm band of the S192, pixels within the boundary of each lake in their test site were counted. In terms of percentages, higher errors were more frequent for smaller ponds and for those with irregular shapes. Because of the conical scan, the actual errors varied depending on the size and shape of the conical scan direction.

face. By the careful choice of spectral band, a great variety of surface conditions can be mapped, including soil salinity, land use patterns, and lake outlines. In addition to radiometric intensity data, the single-spectral-band imagery contains information on the spatial distribution of intensities. Fourier transformation can be used to analyze the spatial frequencies in single-band image data and to correlate them with geologic or hydrologic features of the surface. In the following paragraphs, specific examples of these techniques are summarized.

Maul et al. (ref. 6-16) used S192 imagery to study cloud features over the Atlantic Ocean between Florida and Cuba. One analytical technique used was the automatic detection of clouds to specify free areas for further sea-surface temperature or ocean color measurements. Band 8 (0.98 to 1.08 μm) was chosen because of its high atmospheric transmissivity and high water absorption. Figure 6-26 shows the frequency distribution for the water and cloud signals in band 8. The cluster

Techniques Involving Two Spectral Bands

The intensity of radiation received by the multispectral scanner from a given element of the Earth's surface is influenced primarily by the reflectance of the surface and the Sun angle. However, other factors such as the angle or slope of the surface and the amount of atmospheric haze or cirrus clouds over the surface influence the intensity of received radiation. To a first approximation, the effects of illumination, angle, haze, and clouds can be suppressed by dividing the intensity in one band by the intensity of a different spectral band. The band ratio is largely a function of the difference of surface reflectivity at the two wavelengths. Several investigators used this general technique in their investigations.

Vincent et al. (ref. 6-18) used S192 and S191 data to study the feasibility of using ratios of spectral-band signals to map iron compounds in the exposed surfaces of rocks and soil and to differentiate silicate rock types. A general investigation of laboratory spectra had been

TABLE 6-I.—Ranking of Simulated S192 Bands for Producing Automatic Recognition Maps of Rock, Mineral, and Soil Classes [a]

Rank	Band	
	Number	Wavelength, μm
1	12	2.10 to 2.34
2	8	0.93 to 1.05
3	2	0.45 to 0.50
4	11	1.55 to 1.73
5	5	0.60 to 0.65
6	4	0.54 to 0.60
7	7	0.77 to 0.89
8	9	1.03 to 1.19
9	10	1.15 to 1.28
10	6	0.65 to 0.73
11	3	0.50 to 0.55
12	1	0.42 to 0.45

[a]Based on discriminant analysis of 211 laboratory spectra.

conducted (ref. 6-19) by which the best bands for discriminating rock, mineral, and soil classes were determined. Tables 6-I and 6-II show the rankings of the simulated S192 bands for single-band and two-band-ratio processing, respectively. The value of operating satellite sensors in narrow bands such as those employed in EREP is shown by the orderings. Using laboratory and field spectra, optimum spectral ratios were determined for mapping iron compounds. Comparison of the results of S190B photointerpretation and single-level slicing methods was also performed. Not all optimal ratios could be formed with the data set available, but those bands in the red, near infrared, and thermal infrared proved most useful. After suitable conversion and noise-reduction steps, three ratios were formed from the data.

$$\frac{\text{Band 8}}{\text{Band 7}} = \frac{0.93 \text{ to } 1.05 \ \mu m}{0.77 \text{ to } 0.89 \ \mu m}$$

$$\frac{\text{Band 11}}{\text{Band 7}} = \frac{1.55 \text{ to } 1.73 \ \mu m}{0.77 \text{ to } 0.89 \ \mu m}$$

$$\frac{\text{Band 12}}{\text{Band 11}} = \frac{2.10 \text{ to } 2.34 \ \mu m}{1.55 \text{ to } 1.73 \ \mu m}$$

The ratios $R_{8/7}$ and $R_{11/7}$ were chosen to differentiate ferric and ferrous materials. For proper implementation of the technique, the signal from atmospheric path radiance must be subtracted from the scene elements by using the darkest object subtraction method. Specifically, an analysis of the darkest objects in the scene is made, the mean value is calculated, and that value is subtracted from all pixels. After subtraction, the range of the ratio is adjusted for maximum contrast. For the test site shown in figure 6-27(a), the ratio image $R_{8/7}$ was constructed and is shown in figure 6-27(b). This ratio proved best for separating ferric, ferrous, and nonferrous classes of materials. The color codes define the range (low to high) of ratio values. The basaltic and acidic rocks are imaged in the test site as blue (low ratio), which is indicative of ferrous compounds. The

TABLE 6-II.—Twelve Best Band Ratios for Producing Automatic Recognition Maps of Rock, Mineral, and Soil Classes From Simulated S192 Scanner Data [a]

Rank	Ratio
1	$R_{7/5} = \dfrac{L_7\,(0.77 \text{ to } 0.89\,\mu m)}{L_5\,(0.60 \text{ to } 0.65\,\mu m)}$
2	$R_{3/2} = \dfrac{L_3\,(0.50 \text{ to } 0.55\,\mu m)}{L_2\,(0.45 \text{ to } 0.50\,\mu m)}$
3	$R_{8/4} = \dfrac{L_8\,(0.93 \text{ to } 1.05\,\mu m)}{L_4\,(0.54 \text{ to } 0.60\,\mu m)}$
4	$R_{10/9} = \dfrac{L_{10}\,(1.15 \text{ to } 1.28\,\mu m)}{L_9\,(1.03 \text{ to } 1.19\,\mu m)}$
5	$R_{12/11} = \dfrac{L_{12}\,(2.10 \text{ to } 2.34\,\mu m)}{L_{11}\,(1.55 \text{ to } 1.73\,\mu m)}$
6	$R_{7/3} = \dfrac{L_7\,(0.77 \text{ to } 0.89\,\mu m)}{L_3\,(0.50 \text{ to } 0.55\,\mu m)}$
7	$R_{4/2} = \dfrac{L_4\,(0.54 \text{ to } 0.60\,\mu m)}{L_2\,(0.45 \text{ to } 0.50\,\mu m)}$
8	$R_{4/3} = \dfrac{L_4\,(0.54 \text{ to } 0.60\,\mu m)}{L_3\,(0.50 \text{ to } 0.55\,\mu m)}$
9	$R_{7/2} = \dfrac{L_7\,(0.77 \text{ to } 0.89\,\mu m)}{L_2\,(0.45 \text{ to } 0.50\,\mu m)}$
10	$R_{7/4} = \dfrac{L_7\,(0.77 \text{ to } 0.89\,\mu m)}{L_4\,(0.54 \text{ to } 0.60\,\mu m)}$
11	$R_{8/3} = \dfrac{L_8\,(0.93 \text{ to } 1.05\,\mu m)}{L_3\,(0.50 \text{ to } 0.55\,\mu m)}$
12	$R_{8/7} = \dfrac{L_8\,(0.93 \text{ to } 1.05\,\mu m)}{L_7\,(0.77 \text{ to } 0.89\,\mu m)}$

[a]Based on discriminant analysis of 211 laboratory L spectra.

high-ratio values (reds and oranges) relate to the ferric sediments that flank the slopes of the highlands. As the concentration of ferric iron decreases in the surficial deposits of the valley floors, the color shifts to yellow and green, an indication of intermediate values (fig. 6-27(b)).

The ratio process produced images that were much less influenced by variations in illumination and terrain shadows, a problem that reduced the effectiveness of single-band enhancement techniques. In one case, fault location related to the abruptness of a color-boundary change was enhanced.

The bands found useful in this investigation should help to define the optimum placement of bands for future multispectral scanner sensors. Current Landsat bands are excessively broad; Landsat band 7 integrates both bands used in the $R_{8/7}$ ratio.

Yarger and McCauley (ref. 6-7) found band ratios that gave best results for a statistical correlation with inorganic suspended solids in three Kansas reservoirs. The CCT's for the S192 data were used to select the proper pixels within each of the reservoir images for the nine bands analyzed. The pixels were averaged, and the signal level was converted to radiance levels.

The most effective bands were ratioed, and the values were plotted as a function of suspended solids (fig. 6-28). The red/green ratio improved the correlation with suspended load when compared to individual-band performance. The ratio of infrared/green also exhibited a good linear correlation with suspended load. Agreement with Landsat data is also shown.

The effectiveness of the ratio method to discriminate between ice crystals and water droplet clouds was studied by Curran et al. (ref. 6-20) and Pitts et al. (ref. 6-21). These authors found that the infrared band centered at 1.65 μm ratioed with a lower wavelength band has potential for separating ice clouds, liquid water droplet clouds, and snowfields.

Techniques Involving Multiple Spectral Bands

Three or more spectral bands can be combined to produce a false-color image. In this way, the spectral bands invisible to the human eye can be rendered visible and used for interpretation of the scene. The generation of false-color images and their analysis was a major use of the Skylab multispectral scanner data. A second method for analysis of multiple-spectral-band data involved the use of pattern recognition techniques and digital computers. Many methods for computer-aided analysis of multispectral image data have been developed during the past decade, and these methods were applied to the Skylab multispectral scanner imag-

ery with generally successful results. Examples of the application of false-color imagery and computer-aided analysis of multispectral image data are summarized in paragraphs which follow.

In processing S192 data, the approach taken by Colwell et al. (ref. 6-11) was to determine the best combination of four channels that could be used to effectively classify an area. This approach was selected to minimize processing-time costs without sacrificing classification accuracy.

Each of the 22 scientific data output (SDO) channels (app. A, table A-I) of S192 scanner tape was inspected on a television monitor to screen out unusable data on the basis of noise level or saturation. Three channels were used in a color monitor to facilitate the selection of training fields. Coordinates of selected fields were determined from a grid network displayed simultaneously with the tape data. After selection of training sets, conventional statistical analysis of the data was performed.

The data were reclassified using the nearest neighbor algorithm as well as a threshold algorithm by which a point was reclassified only if a stated probability of correct classification was attained. In a preliminary test, SDO channels 2, 3, 8, and 12 were determined as necessary for classification; for another test, channels 2, 3, 8, 9, 10, and 12 were found to produce usable results. Later, for an extended area, nine channels (2, 6, 8, 9, 10, 12, 18, 20, and 21) were used to determine the best combination of four channels. Classification tests made using channels 8, 18, 20, and 21 resulted in high accuracy, especially when the nearest neighbor algorithm was used. This result was expected because the nearest neighbor algorithm reclassifies each point as one of a defined set of crop classes, whereas the second classification technique using the threshold algorithm reclassifies a point as one of the defined set or defines it as unclassified. Further studies with EREP data yielded results based on analysis of all 22 channels for an area in northern Fresno, California, containing a variety of crop types in different states of maturation.

The best combination of four spectral bands for discriminating crop subclasses was determined to be 4, 7, 9, and 11, with band 10 or band 8 serving as a suitable substitute. However, the complexity of the agricultural scene investigated resulted in an overall performance accuracy of 57 percent. After reclassification into 13

classes for 22 subclasses, the performance accuracy increased to greater than 66 percent.

The studies showed that, depending on the agricultural environment, season, and state of maturity, the optimum combination of bands will vary. For a limited inventory of one or two crops, single bands might be adequate. The importance of the near-infrared region was particularly demonstrated.

Silva (ref. 6-12) analyzed S192 data for an Indiana test site by clustering of signal levels which showed that separation of 13 subclasses was possible. A separability measure was used to find the best 4 of the 12 bands evaluated; namely, bands 3, 7, 8, and 11. The four Skylab bands gave better results than four bands used to simulate Landsat bands, but this result could be due to both information and noise differences.

Overall, the performance of the S192 optimum four bands was better than the results obtained with digitized photographs and was essentially equal to results obtained from analysis of Landsat data taken the day before the Skylab pass, despite the fact that the Skylab data were noisier. Figure 2-11 in section 2 (Land Use and Cartography) shows the color-coded results for nine land use classes.

The classification procedure used the pattern recognition algorithms that have been implemented in a software package called LARSYS (ref. 6-22). Training fields for 12 classes, representing approximately 0.3 percent of the study area, were scattered throughout the study area.

The training fields were evaluated using a clustering routine to determine whether further division of the 12 classes was necessary to ensure that each of the resulting spectral classes represented a unimodal distribution. Assuming that the spectral data of the samples for each spectral class had normal (Gaussian) distribution, the N-dimensional mean vector and the N by N covariance matrix of the multispectral data sets were computed for each class, where N represents the number of channels of spectral information in each data set. The mean vectors and covariance matrices were used in the actual classification routine, which incorporates the maximum-likelihood decision rule (ref. 6-23) with the a priori probability of occurrence for each class being equal.

A modified divergence rule was used to select the best 4 of the 12 bands in the Skylab S192 data set evalu-
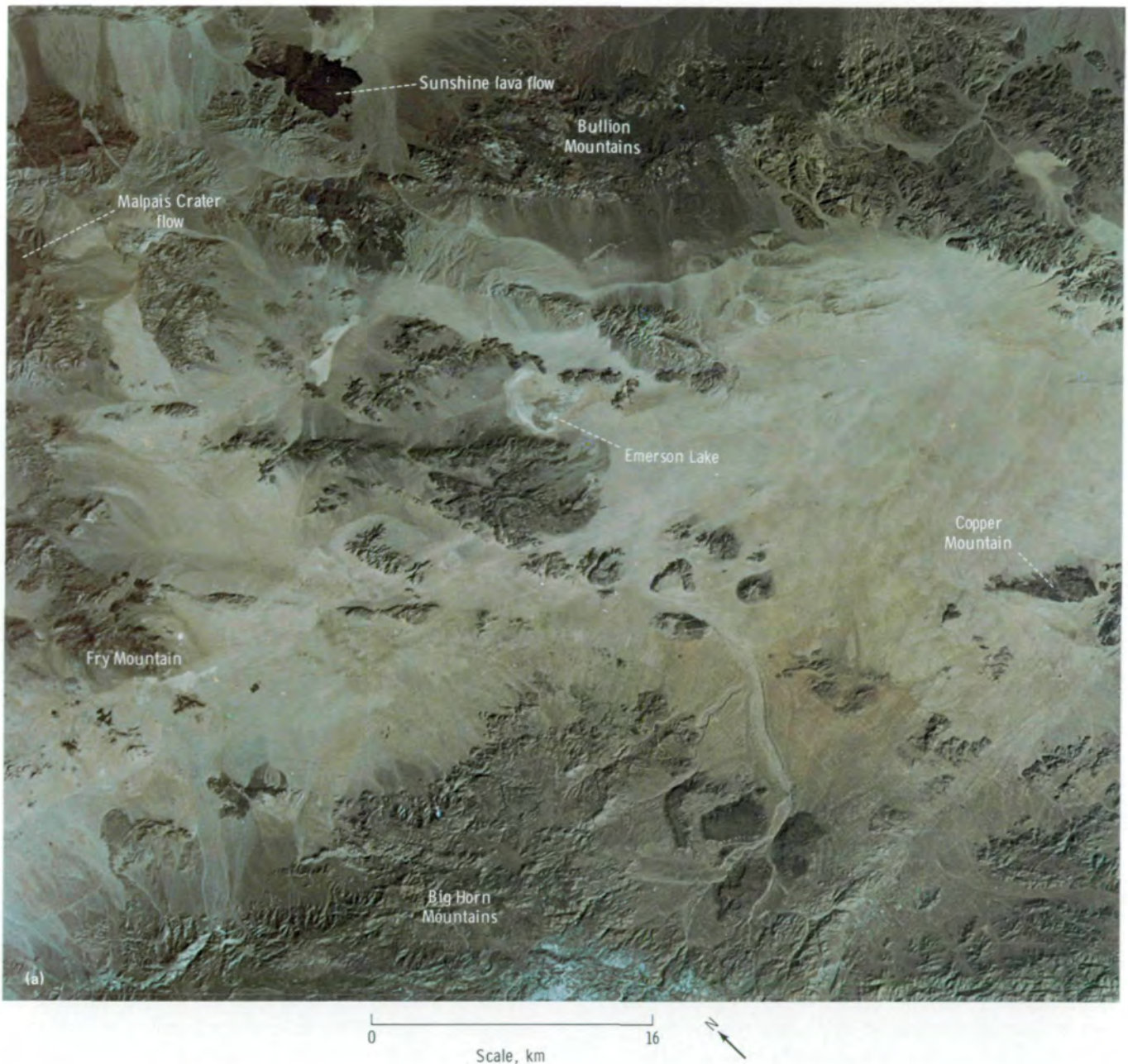
FIGURE 6-27.—The Pisgah Crater test site in California. (a) S190B photograph (SL4-92-351). (b) Color-coded $R_{8/7}$ ratio image (January 26, 1974).

ated. Divergence is used because it is a measure of separability between two density functions that represent two classes of objects. This modified divergence (called transformed divergence) was extended to a multiclass case to choose the best four bands in two separate ways.

First, the average of the transformed divergence for all possible class pairs was maximized; then, the minimum transformed divergence of all possible class pairs was maximized. It cannot be shown, however, that either of these methods is optimal. Four bands were selected for

Low
ratio

N

High
ratio

Ratio
uncalculated
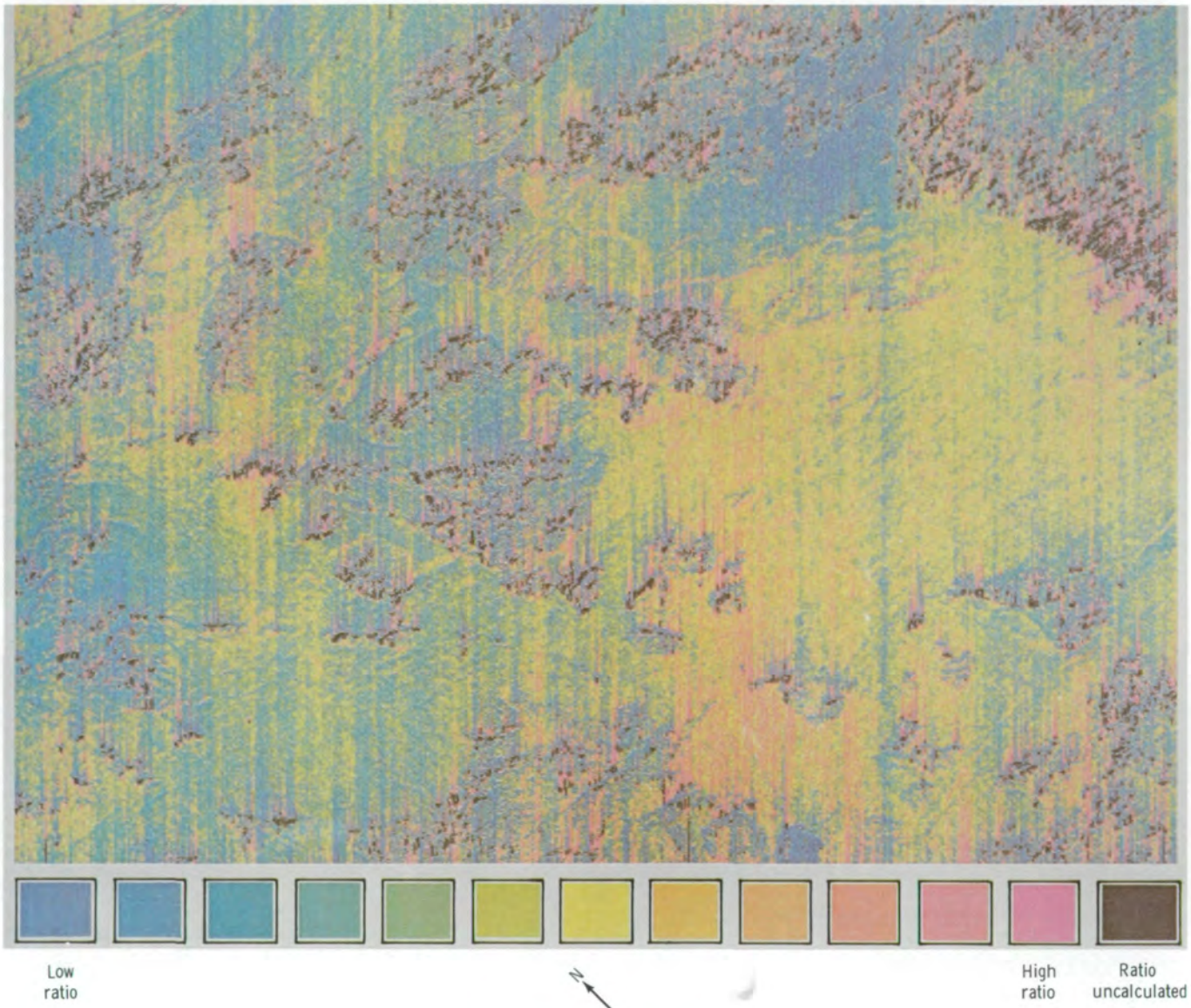
FIGURE 6-27.—Concluded.

the classification to reduce computer costs and to determine whether the bands selected included any spectral bands not available in the other data sets.

The products obtained in the study include the transformed divergence measures for the separability of each pair of classes in each data set, the classification maps, and the classification performance results. The classification performance results were obtained by selecting six test areas scattered throughout the study area representing the classes under consideration.

FIGURE 6-28.—Radiance ratios as a function of suspended solids. The data were taken over three southeastern Kansas reservoirs during the period July to September 1973.

Photographs were projected onto the classification map of these test areas, and a point-by-point check of the classification was done. The points from all six test areas were combined to obtain performance results for each class and for the overall classi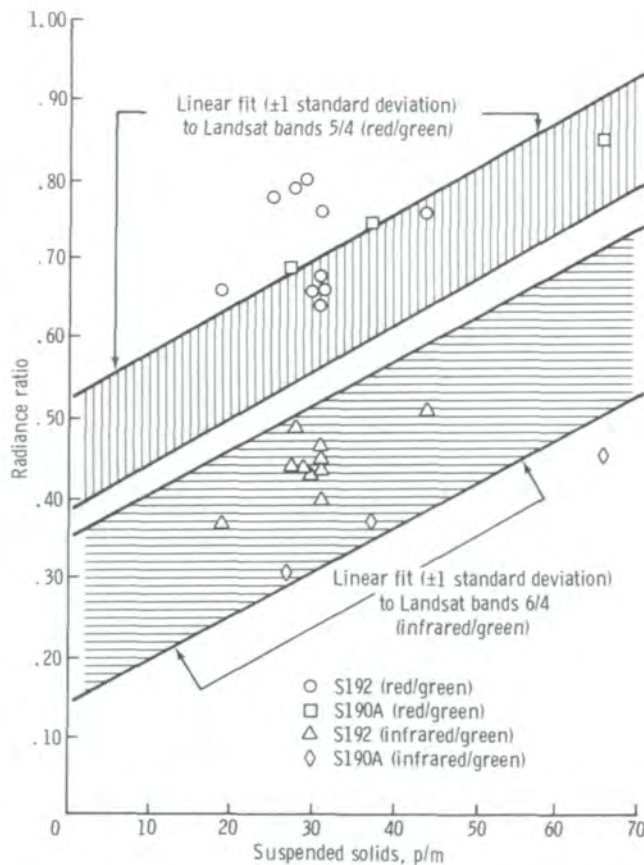fication performance represented by the total number of points classified correctly divided by the total number of test-area points.

In the processing of S192 data by Goetz et al. (ref. 6-24), scan lines were added or deleted where necessary to correct for scale. Unusual lines were modified by inserting an average of neighboring lines and thereby reducing the noise level. The high-data-rate channels (1 to 16) were merged into a single band equivalent to the low-data-rate channels (17 to 22). Geometrical rectification was performed as a preliminary step to compensate for a 5.5° cone angle and for the 110° scan arc motion of the sensors. A correction was also made for spacecraft

motion and Earth rotation during the acquisition time of a given frame. In the process, 1240 original samples along a scan line were reduced to 1056 samples/line.

Once in this form, images can be easily made to fill the dynamic range of the display medium by means of contrast enhancement. Pairs of images having intensities I_1 and I_2 were compared by a ratio algorithm of the form

$$I_o = a \frac{I_1}{I_2} + b \qquad (6\text{-}2)$$

where I_o is the output image intensity and the two constants a and b are chosen to maximize contrast and may change for different scenes. This technique proved useful for temporal and spectral comparisons.

One classification algorithm that was used is called stepwise linear-discriminant analysis (ref. 6-24). It consists of finding a transform that minimizes the ratio of the difference between group-multivariate means to the group-multivariate variances.

A second technique used was a hybrid approach. First, for each spectral band, the means $\overline{X}$ and the standard deviations $\hat{\sigma}$ for each category are computed. The paired categories are compared for each band and determined to be separable if they satisfy the relation

$$\frac{\overline{X}_1 - \overline{X}_2}{C\left(\hat{\sigma}_1 + \hat{\sigma}_2\right)} > 1 \qquad (6\text{-}3)$$

where C is a constant. The hybrid classification combines two existing classification schemes, the parallelepiped algorithm and the Bayesian maximum-likelihood function.

The parallelepiped algorithm approximates a hyperellipsoid that is defined by computing means, variances, and covariances based on the assumption of a Gaussian distribution for the signal variations for each category in the selected wavelength bands. Decision boundaries, related to the number of standard deviations about the mean, can be defined by the computer operator. Each band is considered a vector component;

i.e., the set of spectral bands for a given category is a vector in multidimensional space. Ideally, all pixel vectors for a given category will cluster about a well-defined mean with small variances that fall within a narrow ellipsoid.

Maximum-likelihood processing depends on the knowledge of a priori probabilities. The data set can be integrated to define the probabilities, but the likelihood usually is defined by the multivariate Gaussian probability density function.

Goetz et al. (ref. 6-24) used an interactive unsupervised clustering algorithm. The interactive technique incorporates a self-grouping method based on the best partitioning of N objects into g groups by maximizing the variations between groups and minimizing the variations within groups. Several criteria then can be considered in selecting the best grouping. The methods using the various criteria are time consuming and require large-computer capabilities. Some random sampling of the scene to give the initial clustering is performed to make the technique more practical.

Other investigators, such as Sattinger et al. (ref. 6-25), in studying techniques for land-cover inventories, deleted the two doubly sampled thermal channels. First, noise levels and dynamic ranges were assessed by making a histogram of the data values in each spectral band. Some differences were noted in the histograms for even- and odd-numbered SDO's. By this process, only the better data channels were used.

An optimum band selection program was invoked, and the best six bands were determined. In order of preference, these were 0.78 to 0.88, 1.55 to 1.75, 0.98 to 1.08, 0.68 to 0.76, 0.52 to 0.56, and 0.62 to 0.67 μm. It appeared that the choice was dependent on the signal-to-noise ratio and on spectral contrast.

Seasonal comparisons using March to June data were considered best. By means of supervised classification techniques, the best single-band delineation (1.55 to 1.75 μm) was used as a base onto which 2.6-km^2 grid sections were transferred. The section lines had been traced from a 1:120 000-scale color-infrared transparency spatially registered to the digital map of S192 data by a transfer scope. This grid enabled better location reference for the training sets when analyzing the S192 digital data. Thirty-five separate sets were designated to encompass the wide variability of the categories of interest. Enlargements (8×) of S190B photographs proved valuable in selecting boundaries of training sets and judging the homogeneity of fields.

Means and variances for each training set were computed with all boundary pixels excluded from calculations. A test for signature statistical uniqueness was made by computing the probability of misclassification for all possible pairs of signatures. Each pairwise probability of misclassification provides a measure of the separability between two multidimensional statistical distributions. It represents an average of the probabilities that samples from distribution A will be mistaken as B and that samples from distribution B will be mistaken as A. The results vary between zero (the two distributions well separated) and 0.5 (the two distributions superimposed). The classification rule used is the best linear decision rule used to classify multispectral data (ref. 6-25).

Based on the results of the pairwise calculation, the 35 signatures were aggregated into a smaller number of composite signatures by combining groups of signatures having high probabilities of misclassification. Classes defined by photointerpretation of high-altitude-aircraft photographs and composite signature analyses of S192 data can give different results. For example, for the scene classes identified on high-altitude-aircraft photographs taken in June 1972, there were three nonforested wetland classes, a flooded forest, brush fields, three types of forest crown cover, aspen regeneration sites, and a pine plantation. On the other hand, for the composite signature classes of the S192 data (acquired in August 1973) of the same scene, there were only two nonforested wetland classes and only one general forest class with the other classes remaining the same. Time and seasonal differences between the two sets of data could explain the different groupings. After the categories were selected, the optimum spectral bands were determined (table 6-III). Further studies comparing Landsat discrimination with selected S192 bands showed the significance of band 11 for improving performance as well as the value of using more channels (i.e., more than four).

Field checks were made to verify choices of training sets and their particular character. Finally, after redefining the training sets on the basis of onsite inspection, classification probabilities for each category were calculated. The expected classification performance for the best linear rule classifier was calculated.

Figure 6-29 illustrates the spectral separability of the 12 classes using the best 2 spectral bands. In this figure, the relative location, the shape, and the orientation of the distributions provide a graphic illustration of their

TABLE 6-III.—*Selection of Optimum Bands for Composite Signatures From S192 Data*

Spectral band, μm	Signal-to-noise ranking (a)	Ranking of bands		Landsat band corresponding to S192 band
		Seven major signatures	Four brush and tree signatures	
0.41 to 0.46	12	9	6	—
0.52 to 0.56	4	4	8	4
0.56 to 0.61	8	11	12	—
0.62 to 0.67	9	10	4	5
0.68 to 0.76	6	7	3	6
0.78 to 0.88	3	1	1	—
0.98 to 1.08	7	3	5	7
1.09 to 1.19	5	5	10	—
1.20 to 1.30	10	6	11	—
1.55 to 1.75	1	2	2	—
2.10 to 2.35	2	8	7	—
10.20 to 12.50	11	12	9	—

[a]The highest signal-to-noise ratio is ranked 1.

statistical uniqueness. The computer separated the classes using the six best bands, chose weighted probabilities for the scene (based on color-infrared photographic results), and determined a threshold value that corresponded to the 0.001 level of rejection for six degrees of freedom. Pixels having values exceeding the threshold were unclassified. The accuracies of classification range from 72 to 82 percent, depending on the grouping of the final categories and the averaging of statistics over 2.6 km². Some limitations of accuracies are expected from the nature of the available signal-to-noise ratio, the misregistration of bands, the geometric distortion, and the scan-line-straightening procedures.

A technique for obtaining accurate crop area estimates in agricultural areas characterized by ground resolution sufficiently large to create a high probability that the scanner will integrate a mixture of objects was developed by Nalepka et al. (ref. 6-26). Figure 6-30 displays the nature of the problem over 2.5 km². In this example, the number of pure field pixels is only 30 percent of the total pixels that cover the scene. Thus, the impact of this technique can be significant, because the more mixture pixels in a scene, the greater the chance for error. Conventional classification techniques are not adequate for such a case.

For this technique, a small number of signatures having sufficient separation are desired not only to avoid degenerate signatures (one signature equaling a linear
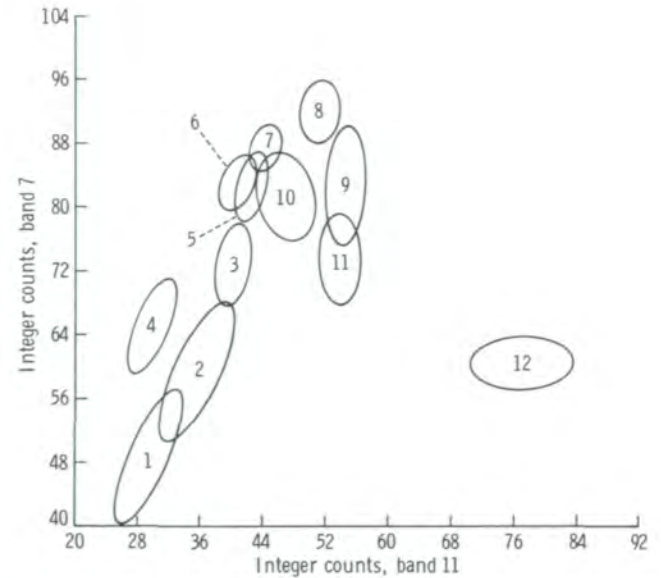
Distribution number	Scene class	Distribution number	Scene class
1	Deep/shallow marsh	7	Sparse forest with under-story
2	Shrub swamp		
3	Flooded forest	8	Aspen regeneration
4	Pine plantation	9	Agriculture
5	Dense forest without understory	10	Brush
		11	Herbaceous
6	Intermediate to dense forest with under-story	12	Bare soil

FIGURE 6-29.—**Two-channel Gaussian representation of the 12 composite signatures used for data classification. Signatures used for data classification axes represent first two optimum wavelength bands.**

combination of two others) but to keep processing time practical. Processing time is proportional to $m(m + 1)/2$, where m is the number of signatures.

In performing classification, signatures based on pixels are derived. For best results, center pixels or field pixels are more desirable for avoiding the ambiguities of border points and mixtures. Nalepka et al. (ref. 6-26) identified field pixels for training purposes by inscribing a small polygon within the boundaries of a training field.

In general, an inset I was defined that is calculated by

$$I_\alpha = \frac{D_\alpha}{P_\alpha} B + R_\alpha + L + S \text{ pixels} \quad (6-4)$$

where α indicates the scan direction x or the alongtrack direction y

D_α is the size of the resolution cell in the direction of α (The S192 data were oversampled by 10 percent; therefore, a digital resolution cell is not equal to a pixel.)

P_α is the size of the pixel in the direction of α

B is the inset necessary to ensure that the pixel does not include the boundary between fields; typically, $B = 0.5$ pixel

R_α is the error due to misregistration effects; e.g., if one channel is misregistered from the others by R pixels, this channel could still be imaging across the field boundary when the other channels are imaged entirely within the field. For conic data corrected for misregistration, $R_x = 0.32$ and $R_y = 0$. For scan-line-straightened data, $R_x = 1 + M\sin\theta$ and $R_y = 1 + M\cos\theta$, wherein M is the maximum misregistration in conically scanned data (found to be 1.13) and θ is the angle between the line tangent to the conically scanned data at the point being considered and a line in the alongtrack or flight direction. To develop one measure for the entire scan line, the maximum values of $\sin\theta$ and $\cos\theta$, which is 1, are used. Thus, $R_x = 2.13$ and $R_y = 2.13$

L is the error due to field location errors

S is the error due to movement of individual pixels as a result of the nearest neighbor scan-line straightening. Therefore, for conically scanned data, $S = 0$; for straightened data, $S = 0.5$ pixel

Thus, the inset to be used for conically scanned data would be

$$\left.\begin{aligned} I_x &= \left(\frac{81}{72}\right)0.5 + 0.32 + L \\ &= 0.90 + L \text{ pixels} \\ I_y &= \left(\frac{81}{72}\right)0.5 + 0 + L \\ &= 0.58 + L \text{ pixels} \end{aligned}\right\} \tag{6-5}$$

The inset to be used for scan-line-straightened data would be

$$I = \left(\frac{81}{72}\right)0.5 + 2.13 + L + 0.5$$

$$= 3.21 + L \text{ pixels} \tag{6-6}$$

where $I = I_x = I_y$.

This technique was applied to an urban scene to determine the amount of vegetative and impervious material. Such information is useful to geographers, urban planners, and urban climatologists. Most pixels could be mixtures. Five classes of interest were defined: green vegetation, concrete, other impervious materials

☐ Field center pixels	
▨ Mixture pixels	

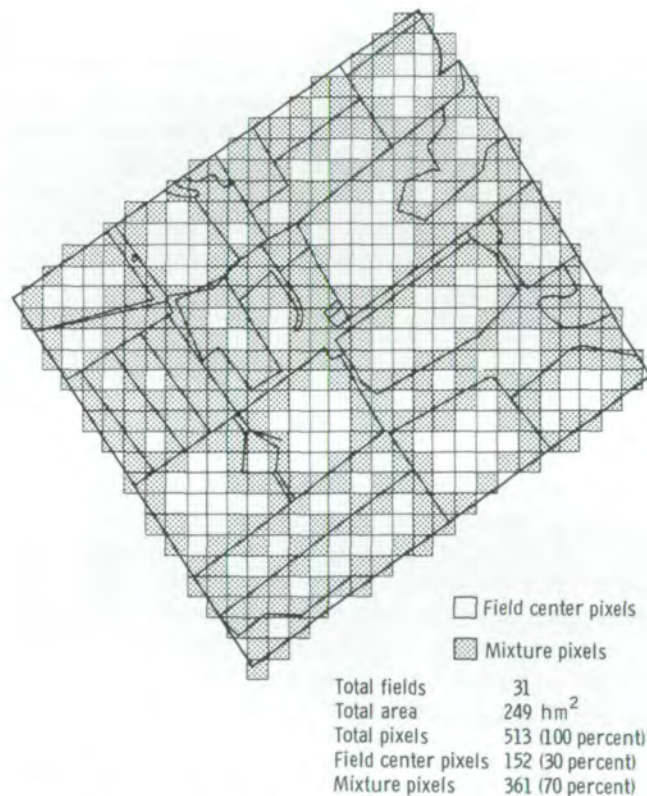|	
Total fields	31
Total area	249 hm^2
Total pixels	513 (100 percent)
Field center pixels	152 (30 percent)
Mixture pixels	361 (70 percent)

FIGURE 6-30.—Display of mixture pixels in section 109, Locke Township, Michigan.

(roofs, asphalt, etc.), bare soil, and water. A statistical test for a measure of separateness (approximately the distance, in standard deviations, between the signature mean and the hyperplane through the other signature means) showed that the five classes were degenerate. Data with limited signal ranges and less than optimum spectral contrasts are not suitable for mixture processors.

Results of this investigation indicate that, because of misregistration in line-straightened data, processing should be performed on a conical format. Finer spatial resolution should be considered for future sensors to reduce the number of field pixels for better training signatures. Also, the design of future sensors should incorporate a means of adjusting scanner gain and offset parameters to match the radiance characteristic of individual scenes better so that the available dynamic range is used. Long atmospheric paths add a sizable constant radiance and attenuate the reflectance radiance to cause reduced contrast.

Signature extension is a process by which the training statistics from one scene may be modified and used to classify features in a second scene that may differ geographically or temporally. Use of this process reduces the need for extensive ground truth and for retraining signatures without incurring an intolerable loss in accuracy. Nalepka tested several signature-extension algorithms on the S192 data (ref. 6-26). The data were grouped into 10 clusters that were identified from training statistics. One of the first methods attempted involved dark-object signature correction. The technique assumes, band by band, that the signal levels generated by dark objects represent mostly path radiance and can be used to generate a correction algorithm. Because of the haze, the correction factor tends to be greater as the wavelength becomes shorter. Significant improvement in classification accuracy occurred; in particular, the recognition was unexpectedly accurate where the haze was densest (i.e., the dark level correction was greatest). However, the algorithm showed some tendency to misclassify bright features as darker features. The need for a multiplicative signature correction in conjunction with an additive correction feature was made evident.

A second method, involving an adjustment for the mean level of the signal over an extended scene, was tried and produced slightly less successful results. In the technique, the correlation between averages over portions of the training scene and of the signature-extension scene is used to estimate a correction for the mean levels of each training signature in each band. The method required similar percentages of ground cover. The results showed nearly the same correction factor for the shorter wavelength bands, although differences were noted at the longer wavelength bands. This result suggests a bias in favor of darker materials, which absorb shorter wavelengths; at longer wavelengths, the scene has more contrast and vegetation is more reflective.

A third method incorporated both a multiplicative and additive signature correction (MASC) factor by using a least squares regression to match training cluster mean signal levels with local cluster mean levels based on the ordering and spacing of those signature means within a chosen data band. Because mathematical modeling of the illumination variations indicated that the variations should be both multiplicative and additive, use of MASC was expected to produce a realistic signature correction factor. A test performed using only the 1.55- to 1.75-μm band for classifying a Michigan agricultural test site showed that more than one band should be used to help match the clusters from differing portions of an extended scene. When there are variations alongtrack, clustering algorithms cannot be expected to produce sets of signatures from two different scenes that are in close correspondence; some method is needed to identify and omit noncorrelating clusters during the cluster-matching procedure that leads to calculations of signature correction factors.

Simonett (ref. 6-27) used the S192 data to extract land use information. Contrast-enhanced, geometrically rectified gray-level maps for the test areas were printed for the spectral bands (4 and 8) providing the greatest visual discrimination of land use (cover) categories. Noise-reduced, line-straightened data were used and reformatted for further analysis. Contrast enhancement was accomplished by a technique called histogram equalization (ref. 6-28), in which a nonlinear (several to

one) mapping of input gray levels to output gray levels is defined and the input data are effectively spread across the entire usable dynamic range of the output display. Because only land use was of interest, only the range pertinent to land features in a given spectral band was transformed. The output print matched the scale of U.S. Geological Survey (USGS) 7.5' quadrangle maps for ease in comparing results with ground truth and in selecting computer training sites.

Finally, ground-truth and scanner digital data were merged by generating a data file consisting of map information on field boundaries, land use boundaries, and 13 spectral data values. Thus, within each individual record of the data file, the analyst had access to the gray levels from all S192 bands, the pixels that were assigned to known fields, and the land use represented by the pixels. The 22 SDO's were reduced to the best 13 spectral bands based on a selection process.

Field signatures were computed to give the means and the covariance matrix, and a signature file was generated. By means of a stepwise discriminant analysis technique (refs. 6-29 and 6-30), the best set of spectral bands for discriminating various land use categories was found. Composite group signatures (a function of how a given scene is to be divided) were used to calculate a set of cross-product terms to form a matrix for both within-group cross products and total cross products. The total cross-product matrix was directly proportional to the variance-covariance matrix for all the data treated as a single data set. The within-group cross-product matrix was directly proportional to a weighted sum of the variance-covariance matrix for each group. A given spectral band provides a good discriminant between groups if the total variance for all the data (diagonal element of the total cross-product matrix) is much greater than the variance obtained by treating the data in groups (diagonal element of the within-group cross-product matrix). Spectral values are assumed to have a multivariate Gaussian distribution throughout. The best spectral band for discriminating among all groups was selected by calculating the likelihood ratio to test the equality over all groups for each spectral band. The process is repeated to find successive combinations of bands that discriminate best among groups, given that

specific bands have already been selected. In applying the stepwise discriminant analysis, only the best field signature representing the group selected for analysis was used. In addition, an estimate of the spectral separability of the input data classes at each step was made using the transformed divergence measure (ref. 6-31). The technique was used to examine 87 test sites with signatures calculated for 609 fields and to separate them into relatively broad land use classes (Level I)—urban, agricultural, forest, water, and wetlands—and more specific land uses (Level II).

For the broad classification, five bands were found to be important. These bands were 11, 9, 13, 5, and 6, in order of decreasing value. Again, spectral coverage in the near infrared, together with the red and thermal-infrared bands, proved to be crucial.

Further examination to determine separability within each broad class was undertaken. However, the similarity of the spectral signatures for Level I classes, the complexity of the spatial distribution, the lack of multidate coverage, the presence of noise, misregistration, and different sampling rates between channels influenced the final outcome. The best results were obtained for large fields, in which some of the effects were not as important. In general, the best five bands for discriminating the general classes were not the same bands for discriminating elements within a class; therefore, a two-stage processing technique was implemented.

In the first stage, an unknown pixel signature was assigned to one of five general levels and that information was stored. In the second stage, the best five spectral bands for discriminating within one of the five general levels were selected. A maximum-likelihood classification algorithm was used during each of the two stages with equal a priori probabilities assumed for each class.

Natural grouping of signal levels, or clustering, was also tested. The distance measure used in the clustering is the reduction of the divergence measure for an assumed diagonal covariance matrix. Use of this procedure reduced computer-processing time but resulted in some loss of discrimination. The investigation revealed the value of multidate imagery because of the character of outlying elements within certain groups.

Thresholding within two standard deviations of the mean was performed only during the second stage. To check classification accuracy, all fields having signatures were stratified as either training or test fields. The results varied from an overall accuracy greater than 70 percent for Level I separation, with forests classified at 84 percent and water at 96 percent. Thresholding reduced the number of misclassified pixels.

Two important conclusions were reached concerning the improvement of classification accuracies. These were the need for multidate coverage to help in the spectral separability of classes and the need for higher spatial resolution in proper registration to reduce the problems of mixed pixels.

Hoffer (ref. 6-32) performed a computer analysis on S192 data taken over mountainous terrain and classified the scenes for a variety of applications. As an initial step before computer classification, the data were geometrically corrected and made compatible with Landsat, aircraft, and digital topographic data. The digital topographic data were used to obtain elevation information, and an interpolation technique was developed to compute slope and aspect (fig. 6-31). All data sets were matched to an X-Y grid base and stored on a single computer tape for ease in multisensor comparisons. Twenty channels were available for further analysis; i.e., 13 bands of the S192, 4 bands of the Landsat multispectral scanner, and 3 channels of ground information (elevation, aspect, and slope). The information was geometrically corrected to a 1:24 000 scale to match the USGS 7.5′ quadrangle topographic maps.

Two different processing techniques were developed and applied. The modified clustering technique provided generally better results than did either the standard supervised procedures or the standard clustering procedures used previously. Machine time was significantly reduced, classification accuracy was increased, and man/machine interactions were improved.

The modified clustering technique is essentially a combination of the supervised and nonsupervised classification procedures. It is designed to overcome disadvantages inherent in both approaches. The modified clustering technique is performed in four steps.
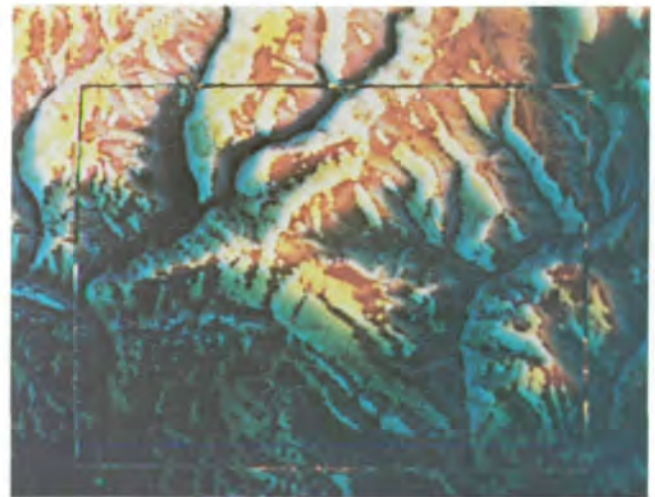

FIGURE 6-31.—False-color composite of topographic data. A red filter was used to denote elevation; a blue filter, slope; and a green filter, aspect.

1. Several training areas of approximately 1600 pixels each are selected over the entire study site to be classified.

2. Each training area is clustered separately. The results are compared to a supporting data map for accuracy, and reclustering is performed if necessary.

3. The results from all training areas are combined using the separability algorithm, and a single set of training statistics for the chosen categories is developed.

4. The training area is classified again as a preliminary check, statistical parameters are modified if necessary, and only then is the entire study site classified.

A newly developed algorithm, extraction and classification of homogeneous objects (ECHO), provided more accurate classification in a more useful format than did conventional per-point classification. This classifier uses an algorithm that first defines the boundary around an area of similar spectral characteristics

Key

White – snow
Light blue – Douglas fir
Dark blue – water
Medium green – ponderosa pine
Dark green – spruce-fir

Dark brown – soil and exposed
    rock outcrop
Orange-brown – aspen
Yellow – gambel oak
Red – hay and pasture

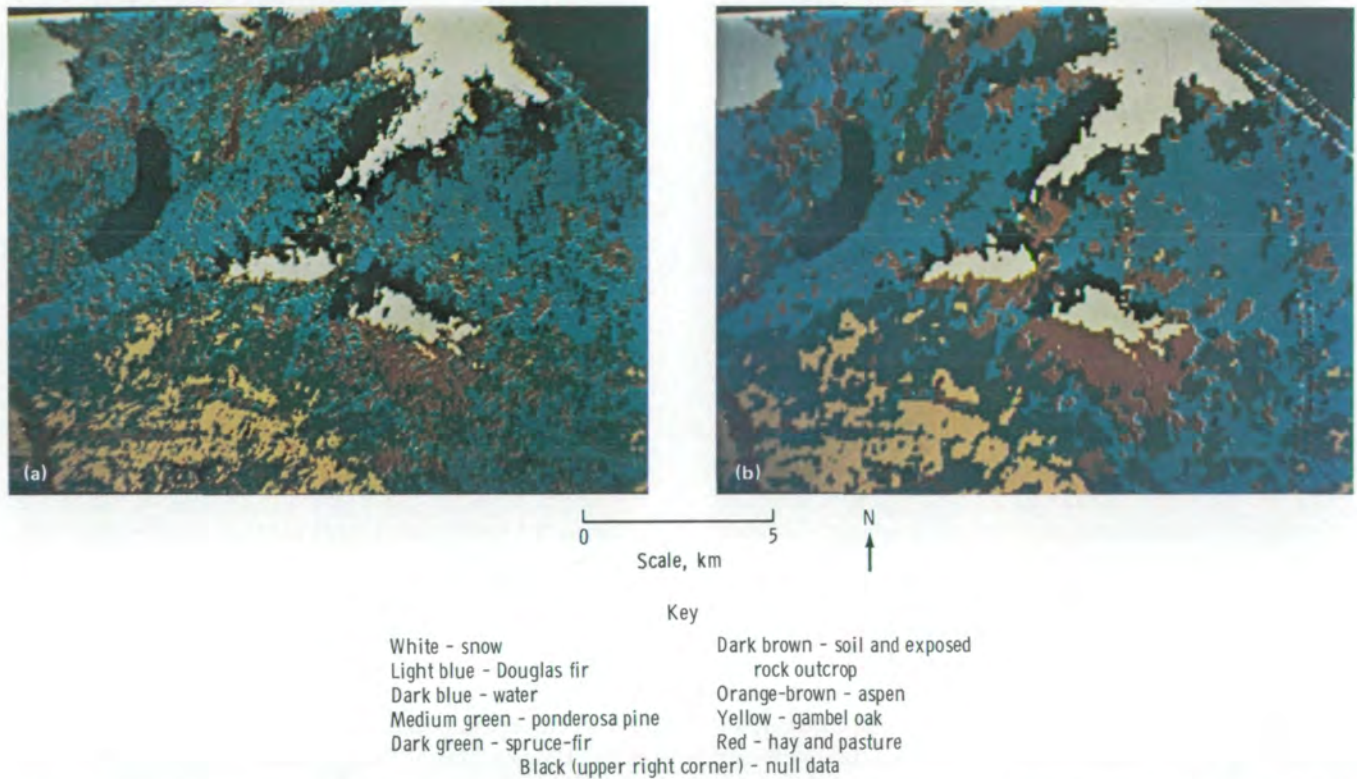Black (upper right corner) – null data

FIGURE 6-32.—Comparison of "per point" and ECHO classification results for forest cover types. (a) Per-point classification. (b) ECHO classification.

and then classifies the area within the boundary as a single spectral class. The classifier specifies the boundaries as part of the procedure and is not dependent on the analyst for specifying boundaries. The output format proved acceptable to those agency personnel interested in a generalized cover-type map. The classification results of the two approaches are shown in figure 6-32. The per-point classifier results do not have the smoothing effect shown by the ECHO classifier results.

Overall evaluation of computer processing revealed that four-band classification was optimal from the standpoint of best accuracy and least expense; a significant increase in classification costs resulted from an in-

crease in the number of bands beyond four. However, for different classes of objects, various combinations of four wavelength bands were needed for accurate discrimination. Thus, future satellite sensors should operate with more than four bands but need to analyze with only a subset of four bands, depending on the scene composition. For example, in analyzing a land use (forest cover) scene, 85 percent overall classification accuracy was achieved using the four bands located at 0.46 to 0.51, 0.78 to 0.88, 1.09 to 1.19, and 1.55 to 1.75 μm.

Acreage estimates of forest cover types were highly correlated with measurements from standard photointerpretation techniques. The value of the technique in

which slope and aspect were monitored together with the spectral signature was proved when spectral differences between forest cover types were found to be influenced significantly by topographic relationships, whereas spectral variations within individual forest types were related to differences in standard density. The consideration of these factors resulted in a substantial improvement (10 percentage points) in classification performance.

An evaluation of the priority for the various bands supported the use of six bands (spaced two in the visible, two in the near infrared, one in the middle infrared, and one in the thermal infrared) for the application area defined as land use and forest cover. When the techniques were applied to the mapping of hydrological features, the different classes of snow were tabulated as a function of elevation and spectral signature. This class difference arose from various mixtures of snow and forest cover within each scanner resolution element and possibly from snow-melting conditions.

The "layered classifier" approach was used and provided better differentiation between snow and clouds and better snow-cover class tabulation by comparison to conventional maximum-likelihood classification techniques. The thermal-infrared band proved valuable in measuring reservoir temperatures accurately after a two-point nonlinear calibration technique was used to process the S192 data. The high elevation of the reservoir and the transmission characteristics of the 10.2- to 12.5-μm band led to close agreement between satellite measurements and reference measurements for the same portion of the reservoir.

A tabulation of the watershed area extent of each spectral class of snow indicates that remote-sensing data can be effectively used to predict water runoff from mountain snowpack areas. On a regional basis, this information would aid reservoir and watershed management planners.

Thomson (ref. 6-33) investigated the effects of variation in the atmospheric state on pattern recognition performance. The question of whether preprocessing must be altered along a flight track is crucial to the success of signature extension. Based on a comparison of results

obtained using a combination of four-band optimum sets, a Landsat analog, and optimum seven-band sets from the S192 sensor, the following conclusions are noted.

At atmospheric conditions equivalent to horizontal visibilities of approximately 10 km, adequate performance (greater than 65 percent correct classification) can be achieved within visibility variations of ± 3 to ± 4 km. If greater variations are found, data-preprocessing corrections must be made to maintain adequate performance. As better sensors are constructed, more care must be taken in selecting a set of bands and in determining their number and location. For example, although seven optimum bands gave better performance under noise-free conditions for a given set of environmental factors than did four optimum bands, the seven-band results were more sensitive to changes in atmospheric visibility.

In analysis of S192 data, Wiegand et al. (ref. 6-34) used the 0.78- to 0.88-μm band to visually differentiate water, vegetation, and bare soil on a cathode-ray tube in a study of eight saline areas in southern Texas. Simple linear correlation analyses were used to relate field electrical conductivity EC_e measurements to the mean multispectral scanner digital values for both bare soils and vegetation test areas. In one test area, bands 6 to 11 of the multispectral scanner correlated well, but the difference between the signal from bare soil and vegetation in the 1.2- to 1.3-μm band (in Landsat, 0.8 to 1.1 μm) correlated best with the amount of electrical conductivity or salinity.

Hannah et al. (ref. 6-35) used S192 CCT's to obtain land use information for Orlando and Lakeland, Florida. Band 13 imagery indicated that commercial-industrial regions, newly formed residential areas, and wooded residential areas could be separated on the basis of temperature. The land use maps prepared for these urban areas were derived from analysis of bands 4, 6, 11 or 12, and 13. The maximum-likelihood procedure was used principally, although less accurate schemes for classification were applied. These schemes were based on measurements of least distances from the point being classified and on determination of the three
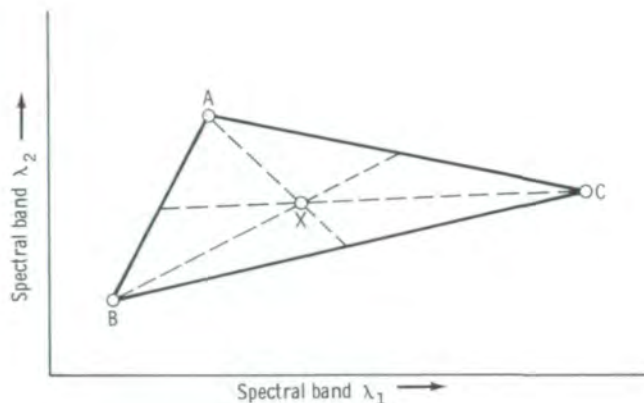
FIGURE 6-33.—Geometric interpretation of means of signature mixtures. In the case illustrated, the unknown X is a mixture of three pure materials, A, B, and C, which form the vertices of the signature simplex.

nearest classes by least distance and use of maximum likelihood to choose among them.

In a different approach, McMurtry and Petersen (ref. 6-36) used wave-number analysis. Each band inspected in the Fourier transform domain was found to provide unique wave-number information about particular scenes. This method is suggested for studying lineaments and geologic structures such as folds and fracture traces.

If the lineaments are related to fracture traces and appear as a line of discontinuous spikes in intensity relative to the surrounding intensity, they will have the distinctive wave number k ($k = 1/\lambda$, where λ is spatial wavelength) response for a lineament from $k = 0$ to the Nyquist wave number. Several filter functions can also be used with this method. For geology, a filter function called the strike-selective filter can be used to check for lineaments first observed by photointerpretation. If the lineaments exist, the digital format can be enhanced as shown in reference 6-36. Other features can also be enhanced by using this method (ref. 6-37).

Functions that take the derivative of the signal such as high- and low-pass frequency filters can also be applied. Filter analysis can aid in deciding which bands to use for the analysis of a particular parameter and can aid in selecting a subset of bands for color displays.

In a technique first outlined by Horwitz et al. (ref. 6-38), a proportion estimation algorithm is used to estimate the percentage of area occupied by different objects within the field of view (FOV). Geometrically, three objects as seen in two spectral bands can be depicted (fig. 6-33). Points A, B, and C represent the pure spectra of each object. If an instantaneous FOV contains a mixture of all three materials, then the signature X must lie within the triangle formed by connecting the vertices at A, B, and C. By extending a line from one vertex through the unknown point within the triangle and intersecting the opposite side, an estimate of the pairwise proportion of the pure materials constituting the unknown element can be made by taking the inverse ratio of the lengths into which the leg is divided.

The concept can be extended into N-dimensional space so that at least $N-1$ spectral bands of information are required to estimate mixtures of N objects satisfactorily. Some degradation in estimates is expected if one material is very similar to the weighted average of the others.

The value of the S192 spectral resolution was demonstrated by Poulton and Welch (ref. 6-39), in the study of rice-yield prediction. The crop calendar for rice begins with a bare unflooded stage, progresses to a fully green vegetative state, and eventually becomes a changing yellow during ripening. Thus, spectral discrimination at the proper season was found to be a dominant factor. For a test area in Louisiana, interpretation of an S192 color composite yielded a higher accuracy than did analysis of the S190A and S190B photographs taken at the same time. Figure 6-34 is a comparison of the three images. The Skylab S192 color composite using bands 1, 7, and 9 had better contrast and thus aided in the differentiation of rice in various stages of maturity from other crops when the field size was greater than 6 to 8 hm².
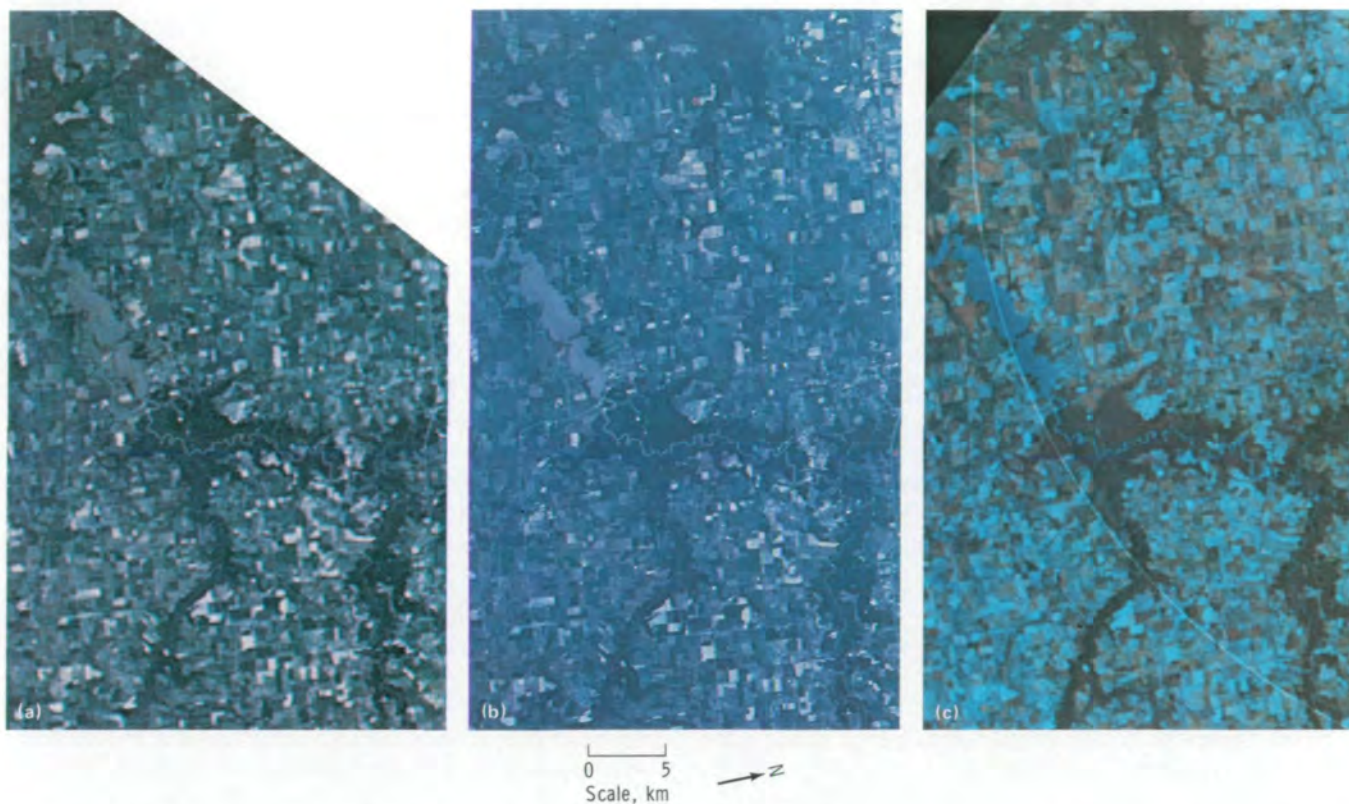
0   5
Scale, km

FIGURE 6-34.—Data taken in August 1973 of the Louisiana coastal plain rice region. Note the improvement in field contrasts in the S192 color composite compared to the conventional photographic products. (Original scale, 1:327 000.) (a) S190A color (SL3-22-120). (b) S190B color (SL3-83-056). (c) S192 color composite.

In geology, Goetz et al. (ref. 6-24) separated different lithologic units most effectively by using bands outside the range available in the current Landsat regions. They found that bands 0.46 to 0.51, 0.98 to 1.08, and 1.20 to 1.30 μm from both field spectral analysis and enhanced color composites gave the best separation (fig. 6-35). For this particular site, thematic maps produced by three classification algorithms were not as accurate as results obtained by photointerpretation of computer-enhanced imagery. Among the three algorithms tried, the linear-discriminant algorithm seemed to be the most efficient. The need for operational satellites capable of imaging in the far-reflective-infrared region was expressed.

Houston et al. (ref. 6-40) investigated the potential of S192 data by using both visual qualitative examination and densitometric quantitative measurements. Except for the detection of red beds in band 2 (0.46 to 0.51 μm) and better contrast of small, closed anticlines in band 4

(0.56 to 0.61 μm), the near-infrared bands provided the best contrast for different rock units (band 8, 0.98 to 1.08 μm; and band 9, 1.09 to 1.19 μm). Relative density values for 15 lithologic units on each S192 band were measured by a video densitometer, and results showed that bands 7, 8, and 12 yielded the highest total contrast values. Computer analysis of the S192 data for geologic applications confirmed the value of the near infrared in enhancing contrast between lithologic units. The digital

FIGURE 6-35.—Enhancements of geologic units by S192 composite compared to S190 photographs. (a) Simplified geologic map of the Coconino Plateau showing distribution of geologic units. (b) S190A false-color-infrared composite photograph. The green band is displayed as blue, the red band as green, and the infrared band as red. The stream in the upper portion of the frame is Cataract Creek. (c) S192 false-color composite made from bands 2, 8, and 10. Area included is slightly less than that shown in figure 6-35(b). →
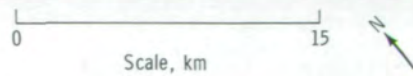
Unconformity

Miocene? - Recent		Alluvium, reworked Tertiary gravels, and Tertiary gravels	Cenozoic		Permian	Kaibab Formation	Alpha member	Unconformity	Dolomite: unit 6		Paleozoic

Legend entries:

Alluvium, reworked Tertiary gravels, and Tertiary gravels — Cenozoic

Basalt flows, landslides, and basalt talus

Unconformity

Moenkopi Formation — Triassic, Mesozoic

Dolomite: unit 6

Sandstones and shales (locally gypsiferous) with underlying dolomite: units 4 & 5 — Alpha member

Siltstones and shales (locally gypsiferous) with underlying dolomite: units β, 1, 2, & 3 — Beta member

Older Paleozoics — Pennsylvanian

Kaibab Formation / Permian / Pennsylvanian — Paleozoic

(a)

N ↑

Scale, km 0 — 15

Scale, km 0 — 64

Mapped area — Utah / Arizona, Grand Canyon, 64, 66, Flagstaff

— — — — Contact, dashed where approximate

⌐—?— Fault, dashed where approximate, dotted where concealed, queried where uncertain; bar and dot on downthrown side

⊢—?— Monocline, dashed where approximate, queried where uncertain; arrow indicates direction of inclination

⊢—— Anticline, showing plunge of axial trace

⊢—— Syncline, showing plunge of axial trace

DATA ANALYSIS TECHNIQUES   303

0   15
Scale, km

N

FIGURE 6-35.—Continued.

0   Scale, km   15

FIGURE 6-35.—Concluded.

tapes for the 13 S192 bands were analyzed by constructing alphanumeric maps and computing pairwise clusters from two-dimensional frequency histograms of test sites. Histograms for each of 78 possible pairs from 13 bands were analyzed, and maps were made of the best contrast pairs. A further analysis of reflectance vectors for the test region resulted in a decision to use weighting factors. One particular method, designated Q-mode factor analysis, was conducted with more than 100 000 points, and results indicate that this method is useful. If matrix D is an m by m ($m = n$) data matrix of reflectance values in the i-th channel for the j-th pixel, the columns of matrix D will be normalized to unit length L by the formula

$$L_j = \left(\sum_{i=1}^{n} D_{ij}^2 \right)^{1/2} \tag{6-7}$$

representing the square root of the sums of each matrix element squared, and by the new matrix

$$Z_{Q_{ij}} = \frac{D_{ij}}{L_j} \tag{6-8}$$

Each column of Z_Q represents the reflectance at a given location after its brightness has been adjusted to the same general intensity.

By taking the cosine of the angle between two normalized reflectance vectors, a test of similarity is easily made. The cosine will have a value of 1 if the vectors are identical and will have a value of 0 if the vectors are different (perpendicularly). A computer algorithm was developed that facilitated factor comparison (ref. 6-40) of large numbers of pixels by Q-mode analysis. Table 6-IV is an example of the factors computed by the Q-mode method for varying wavelength λ. The use of the factors in making a new alphanumeric map shows the manner in which outcrops of enriched rocks could be enhanced or the densest vegetated areas could be delineated.

Haefner (ref. 6-41) found that, for operational mapping of dynamic features such as snow, preference should be given to digital data to take advantage of near-real-time classification. By combining information from band 11 (1.55 to 1.75 μm), band 7 (0.78 to 0.88 μm), and band 2 (0.46 to 0.51 μm), snow could be separated from clouds. The test area was first classified into 29 different categories but later reduced to 5 main classes: snow in Sun, snow in shadow, clouds, snow-free area in Sun, and snow-free area in shadow. Data were prepared from digital tapes following the standard procedures of (1) data reformatting to match available computer systems, (2) delineation, (3) statistical evaluation of sampling areas, (4) classification of classes based on euclidean distance, and (5) data display with geometric corrections for maplike output.

Goldman and Horvath (ref. 6-42) researched the detection of oilspills on the ocean with S192 data, which were expected to be useful for this application because of the spectral resolution choices and the wide area of effective coverage (68.5 km). Difficulties were expected because of the uncertainty in the nature of oil-to-background contrast. Slicks that have a center thick enough to inhibit the diffuse upwelling radiation from the water would appear darker than the surrounding water. Because oil has a higher specular reflectance than that of water, the water may be dark and the specular reflectance of the oil may dominate; in such cases, the oil would appear bright in contrast against the background. Chlorophyll and suspended particles complicate the spectral contrast further. In almost all cases, however, for moderate-thickness films, the reflectivity of at least the thin portions of oil on water should be uniformly higher than that of water alone. Techniques for ratioing total radiance values from one band to another can help separate these effects and perhaps be used to confirm the location of an oilspill.

Statistical analysis of the noise in the S192 data was performed before the detection method was attempted. Mean values and standard deviations were computed for a test area. The results showed that a small reflective anomaly could not be detected with single-band analysis only.

Spatially coherent weighted sums were generated to reduce noise effects using four channels (SDO's 3, 7, 9, and 15). Weighted summations, incorporating ratios of the standard deviation, equalized the noise contribution

TABLE 6-IV.—*Summary of Eigenvalues and Factors Computed by Q-Mode Analysis of Hyattville, Wyoming, Area S192 Data*

i	Factors				Band
	1st[a]	2d[b]	3d[c]	4th[d]	
1	0.10240	0.18692	−0.23624	−0.09554	Green yellow (0.56 to 0.61 μm)
2	.14507	.28924	−.45414	−.19125	Orange red (0.62 to 0.67 μm)
3	.12920	.28356	.23215	−.01564	Near infrared (0.78 to 0.88 μm)
4	.13420	.35157	−.22595	.11777	Middle infrared (1.55 to 1.75 μm)
5	.12151	.28651	−.34220	.11615	Middle infrared (2.10 to 2.35 μm)
6	.51754	−.23440	−.19352	.73040	Thermal infrared (10.20 to 12.50 μm)
7	.16102	.40116	.32231	.11809	Near infrared (1.20 to 1.30 μm)
8	.15241	.31609	.36925	.00438	Near infrared (0.98 to 1.08 μm)
9	.62774	−.37827	.27163	−.26939	Thermal infrared (10.20 to 12.50 μm)
10	.32864	.06362	−.25477	−.36177	Violet blue (0.46 to 0.51 μm)
11	.16681	.35972	.31071	.06647	Near infrared (1.09 to 1.19 μm)
12	.26852	−.05455	−.05456	−.41396	Violet (0.41 to 0.46 μm)

[a] $j = 1$; $\lambda_j = 0.98844$ μm.

[b] $j = 2$; $\lambda_j = 0.00517$ μm.

[c] $j = 3$; $\lambda_j = 0.00203$ μm.

[d] $j = 4$; $\lambda_j = 0.00148$ μm.

of all channels used in the summation. Values of the sums falling within the highest and lowest 10 percent of the range were isolated and designated special points. If an oilspill were present in the scene analyzed, it would, with high probability, have special points adjacent to each other.

Because the results over a 600-pixel area gave only a random distribution, no oilspill could be confirmed. However, the technique proved valuable because confirmation of an oilspill with Landsat bands 4 and 6 was successful when ratios of radiance were taken after subtracting the background radiance from all values in the scene.

Pirie and Steller (ref. 6-2) studied coastal circulation and sediment loading using S192 color composites of images specially prepared by a linear expansion of the image density range so that contrast was enhanced for small density changes. Bands 4, 6, and 7 were used to enhance interpretation in analysis of coastal processes (fig. 6-36). The detail seen in the enhancement is considered unique. Variations in suspended-sediment load are easily seen, and comparisons to known sediment-distribution maps show close correlation. Areas on the enhancement that appear to be receiving the greatest amounts of surface sediment closely correspond to the areas of maximum deposit as seen from ground-sampled surveys.

Water-depth relations were established from analysis of S192 visible band imagery by Trumbull (ref. 6-43) and by Polcyn and Lyzenga (ref. 6-44). Band 3 (0.52 to 0.56 μm) was most useful for water penetration; color coding by Polcyn improved contrast which aided in relating data values and water depth. Further discussions are presented in section 5.

Imagery Use in Earth Resource Models

The 13 S192 bands have provided investigators a wide range of spectral data for study of Earth resources with predictive models. The examples discussed in this section illustrate the use of S192 imagery in models that are used to predict climate changes, wind fields, atmospheric effects, and soil moisture.

```
  |_____|      N
  0                   5      /
        Scale, km          /
```
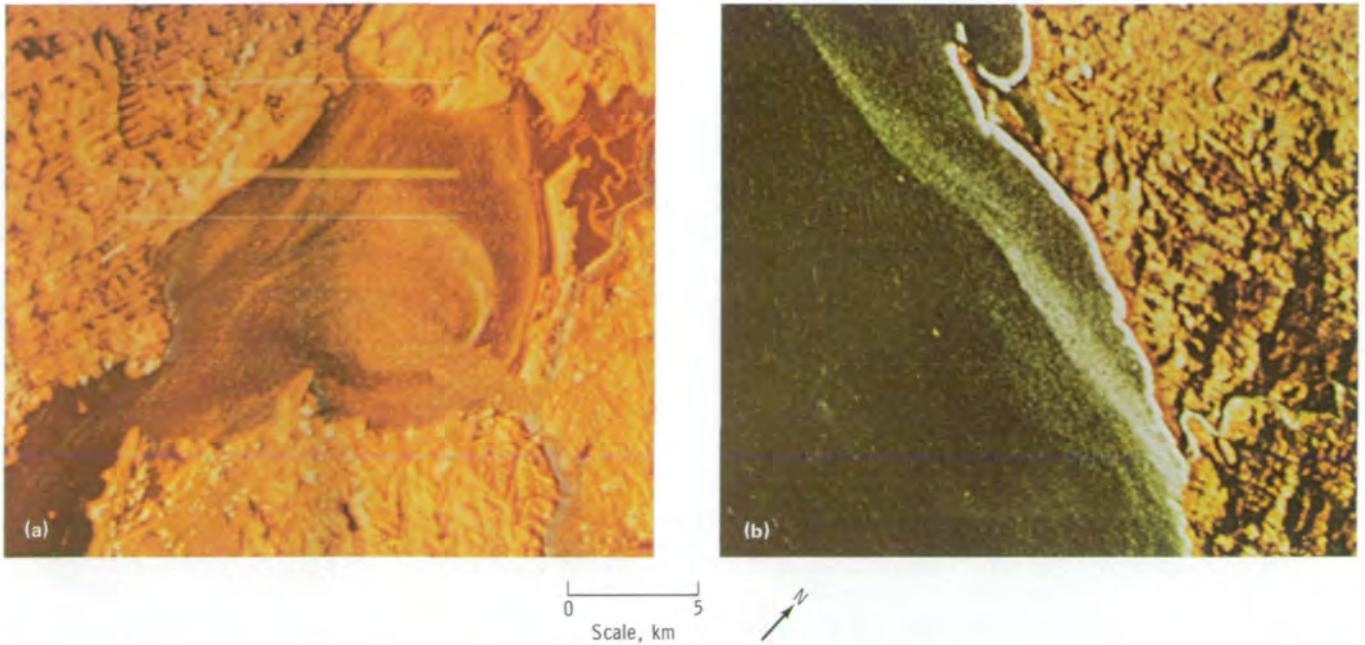
FIGURE 6-36.—Color composites made from S192 computer tape data of northern California. These enhancements were made by merging and color-filtering linearly stretched Skylab computerized images of three scanner bands. Each band was individually filtered to maximize sediment transport and surface-current characteristics. (a) San Pablo Bay. (b) The Russian River-Bodega Bay area.

Alexander et al.[2] used the thermal band of the S192 to construct observed-temperature maps for comparison with predicted-temperature maps produced by use of a surface-climate simulation model. By considering the effect of land-use-related components of urban climates (such as the heat-island effect), better information on climatological consequences of land use changes can be derived from the model and future urban design can be made more effective. This model enables extrapolation of remote-sensing results at a given time to other times of the day or year while allowing for changes in the input parameters. Data obtained by an imaging radiometer enable construction of a matrix of spatial averages over all types of urban surfaces that is far superior to point-sampling tables. Earlier research had demonstrated the value of time-sequential remotely sensed data. The simulation model is based on the familiar energy conservation equation relating

$$R + S + H + L = 0 \qquad (6-9)$$

where net radiation R, soil heat flux S, sensible heat flux H, and latent heat flux L are expressed in terms of meteorological-geographical parameters and surface temperature. A temperature equilibrium model is used to search for the specific surface temperature that balances the equation. Profiles of soil temperature as a function of depth are updated after each iteration. The Skylab EREP experiment led to improvements in a second version of the model that incorporated estimates of geographical terrain parameters in the form of (1) wetness fraction (irrigated lawn cover and tree cover), (2) silhouette ratio (the ratio of the vertical silhouette area in a tract to the horizontal area of that tract), and (3) observation height (mean vertical height that obstructs airflow and also increases the area of absorbed radiation). These factors were even more valuable because they could be deduced from remotely sensed imagery.

[2]Robert H. Alexander, John E. Lewis, Jr., et al., "Applications of Skylab Data to Land Use and Climatological Analysis," unpublished Final Report, NASA-USGS Agreement T-5290-B, 1976.

From space, the temperatures defined for a pixel can be ambiguous when several objects are in the same resolution element. To calibrate the scanner, a method is used to account for the atmospheric path influence on surface-temperature estimates. A gray-window model (ref. 6-45) was used in the form

$$R_z = E[E_{bb}(\overline{T})] + (1 - E)R_o \qquad (6\text{-}10)$$

where R_z is the radiance in watts per centimeter squared micrometer steradian received by the spaceborne scanner, R_o is the surface radiance, E is the emissivity of the airpath, and $[E_{bb}(\overline{T})]$ is the equivalent black-body radiance of the airpath at mean temperature $\overline{T}$.

Both atmospheric path convections and two-target temperature-calibration procedures were used to finally relate scanner digital values to true surface temperatures. The results were encouraging. However, when the model prediction and S192 temperature maps were compared, the model produced values lower than those observed. Further refinements of the model and better classification of land cover are recommended. The use of computer-derived classification from multispectral scanner data was considered a promising alternative.

Villevieille and Weiller's (ref. 6-46) use of models concerned the evaluation of vertical wind profiles. The convective cell in the atmosphere can be considered a stationary phenomenon that is spatially repetitive with an interior sinusoidal vertical wind variation along the vertical axis and two perpendicular horizontal axes.

One example of a wind field W would be

$$W = W_m \cos\left(l_x\right) \cos\left(m_y\right) \sin\left(n_z\right) \qquad (6\text{-}11)$$

where $l = 2\pi/L_x$, $m = 2\pi/L_y$, and $n = 2\pi/L_z$ define the wave numbers of wavelengths L_x, L_y, and L_z, respectively, that can be measured from satellite photographs. In the presence of "cloud streets," L_x is the spacing between the centers of two consecutive clouds in a single street, L_y is twice the spacing between the axes of two streets, and L_z is twice the thickness of the convective layer.

Several different cell types were studied by means of a method in which numerical techniques were used,

friction forces were considered, and wind profiles at the interior of the convective layer were obtained for a given characteristic dimension. The method was applied using S190B data obtained over Bordeaux, France, to determine spacings L_x and L_y. Values of other parameters needed were obtained from radiosonde measurements. Figure 6-37 shows a comparison of the predicted profile and the actual profile as measured by radiosonde.

The cell type determined the minimum interval energy dissipation. The results warrant further comparisons. If successful, interstreet spacing and street directions derived from satellite measurements could be coupled with mean thermal gradients derived from surface temperatures supplied by a very high resolution radiometer or other future satellite systems to make feasible the operational use of the model.

Aldrich et al. (ref. 6-47) used an aircraft to obtain satellite-matched forest terrain-reflectance measurements so that corrections for atmospheric effects could be made. The aircraft platform afforded more versatility than would a tower-mounted instrument, which can only measure signatures over an area equivalent to a few pixels of satellite data. With multidate coverage, the possibility of measuring time changes in vegetative spectral signatures was feasible. Also, information of importance for signature-extension techniques in computer-aided classification schemes could be obtained.

The aircraft instrumentation consisted of an upward-pointing irradiance meter and a downward-pointing radiometer. In this instrument, silicon diode detectors were filtered to match the S190 sensors and the Landsat-1 multispectral scanner bands.

A video camera monitored the flight track so that targets actually measured could be verified in real time. At low altitude, which minimizes effects of the atmospheric path, the aircraft radiance N_a is

$$N_a \approx \frac{\rho H}{\pi} \qquad (6\text{-}12)$$

where ρ is reflectance, H is irradiance, and Lambertian reflection is assumed. Satellite radiance N_s can be equated to the sum of two effects: the path radiance N_p, and a term proportional to surface reflectance by the
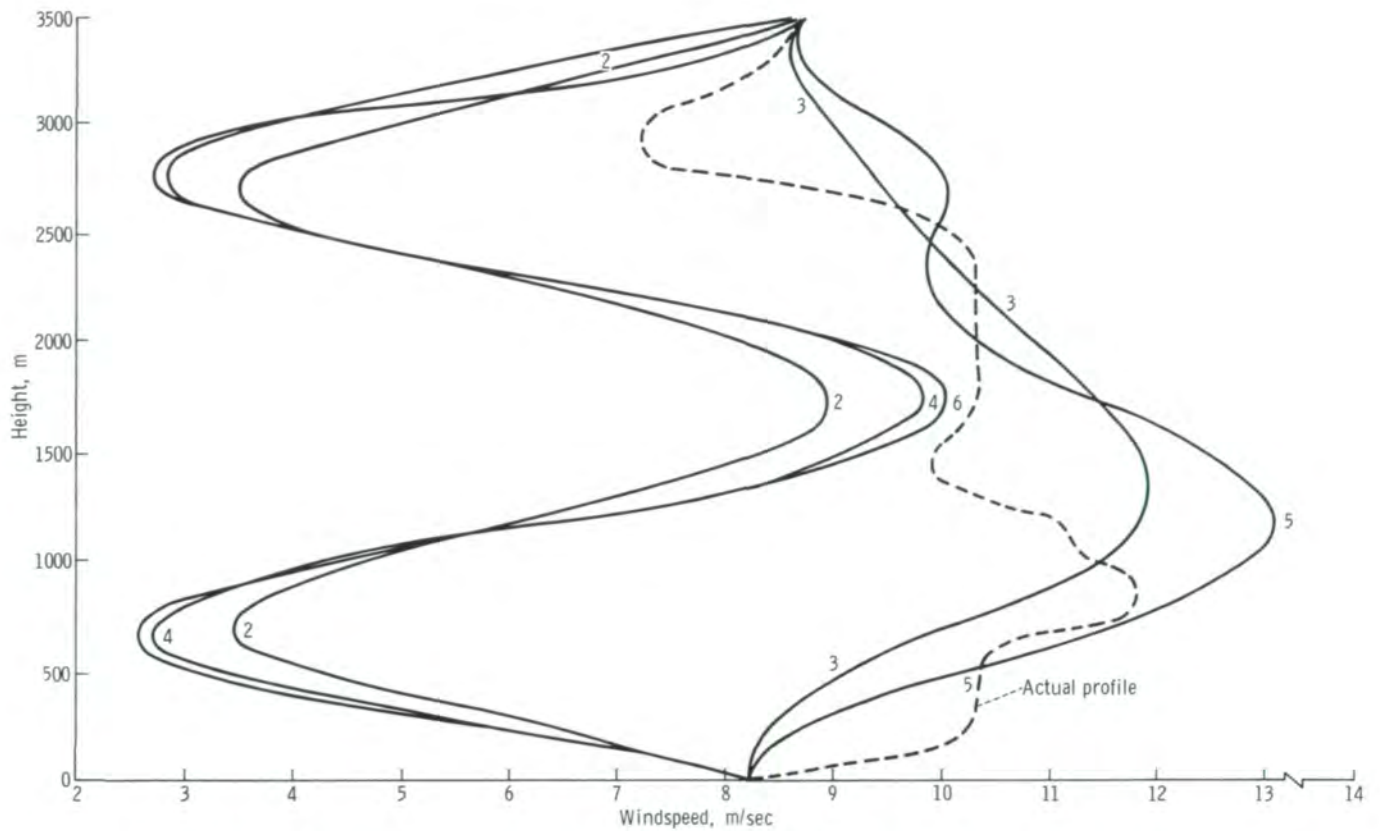
FIGURE 6-37.—Comparison of actual wind profile with calculated profiles corresponding to cell types 2 through 6.

product of total irradiance and atmospheric transmittance τ.

$$N_s = N_p + \rho \frac{H\tau}{\pi} \qquad (6\text{-}13)$$

The FOV of the instrument is 2.6°; therefore, at a 300-m altitude, the ground resolution is 13 m. The output was recorded on an airborne chart recorder and later sampled at 20-m intervals. Calibration was performed in a laboratory using National Bureau of Standards traceable standards. Ratios of radiance to irradiance were calculated from these values for areas that could be related to satellite pixels. Skylab S190A photographs were scanned with a digital microdensitometer. Density was calibrated by a comparison of measured duplicate densities produced by the same exposures applied to the

original film. After suitable conversion from digital satellite counts to diffuse density and relative exposure, an equivalent radiance N was computed from the relation

$$N = \frac{4F^2}{\pi tT} E \qquad (6\text{-}14)$$

where E is absolute exposure; F is the camera lens f-number; t is integrated exposure time; and T is total transmittance of lens, filters, and window.

Thus, by measuring Skylab data for N_s and using the low-altitude reflectance measurements for ρ for at least three different ground reflectors, estimates of N_p and τ can be derived and used for correcting atmospheric effects. At satellite altitudes, total irradiance is assumed to be that of solar input.

In a plot of N_s as a function of ρ, the intercept on the radiance axis gives N_p, whereas the slope is proportional to beam transmittance and irradiance. When the correct values are known, new radiance values can be corrected and adjusted to earlier radiances derived from scene classes of the same reflectance.

In a Skylab EREP investigation (ref. 6-48), a method developed by Colwell (ref. 6-49) was applied to the S192 sensor data to determine surface soil moisture in the presence of partial vegetation cover. The reflectance of bare soil decreases for increasing soil moisture (fig. 6-38). The difference in reflectance between wet and dry soils is greater in the reflective infrared than in the visible part of the spectrum. Also, as the amount of green vegetation cover increases, the near-infrared (0.7 to 1.1 μm) reflectance increases but red reflectance decreases because of chlorophyll absorption. If soil moisture is to be inferred from a field with partial vegetation cover, some means for removing the effects of vegetation cover independent of the effects of variable soil moisture is needed. Fortunately, the near-infrared/red reflectance ratio is more sensitive to the amount of vegetation cover than is either of the single bands. In addition, the ratio is insensitive to soil moisture. Figure 6-39 summarizes the important relationship that suggests the method will work to normalize the effects of both soil type and soil moisture. From these trends, an algorithm was developed in the form

$$\text{Soil moisture} = A' - B'\rho_{ir} \pm C'\rho_{ir}^2 + \frac{D'\rho_{ir}}{\rho_r}$$

$$\pm E'\left(\frac{\rho_{ir}}{\rho_r}\right)^2 \tag{6-15}$$

where A', B', C', D', and E' are constants; ρ_{ir} is infrared reflectance; and ρ_r is red reflectance. The ρ_{ir}^2 term is a correction for the nonlinearity of the effects of both soil moisture and vegetation, and the $(\rho_{ir}/\rho_r)^2$ term is a correction for the nonlinearity of the relationship between percent cover and the infrared/red reflectance ratio.

A specific relation was formed after simulating the reflectance of canopies with 30 combinations of soil moisture and vegetation cover and after finding the
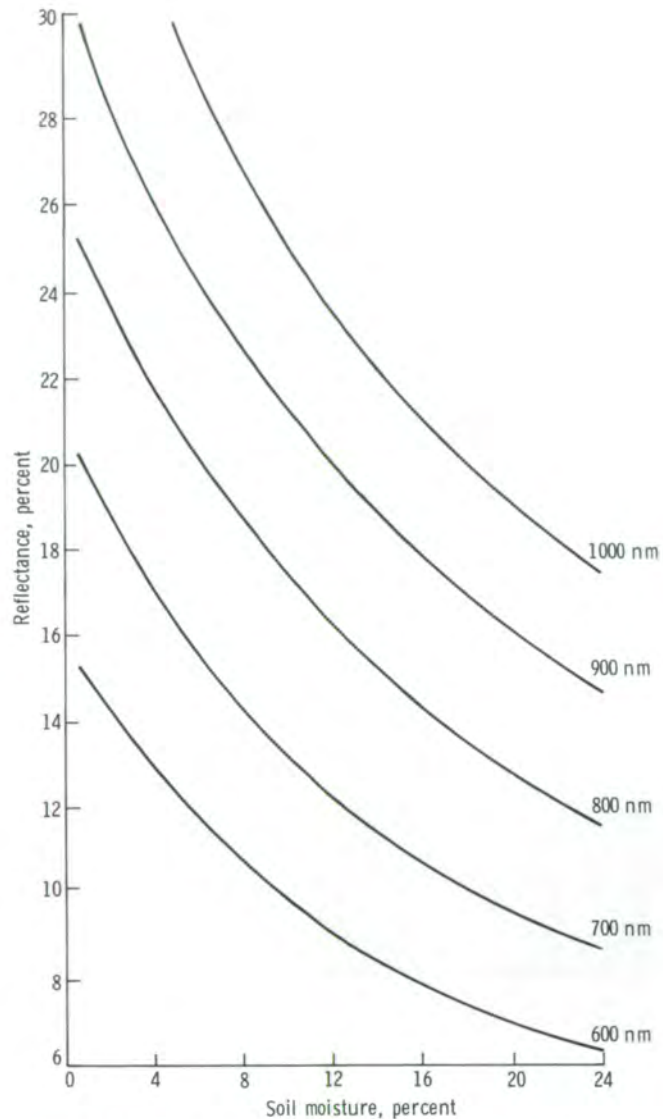

FIGURE 6-38.—Percent reflectance for bare soil as a function of percent soil moisture at various wavelengths.

standard least squares regression relation. The specific equation became

$$\text{Soil moisture} = 19.79 - 0.02\rho_{ir} - 0.066\rho_{ir}^2$$

$$+ 5.06\frac{\rho_{ir}}{\rho_r} - 0.067\left(\frac{\rho_{ir}}{\rho_r}\right)^2 \tag{6-16}$$
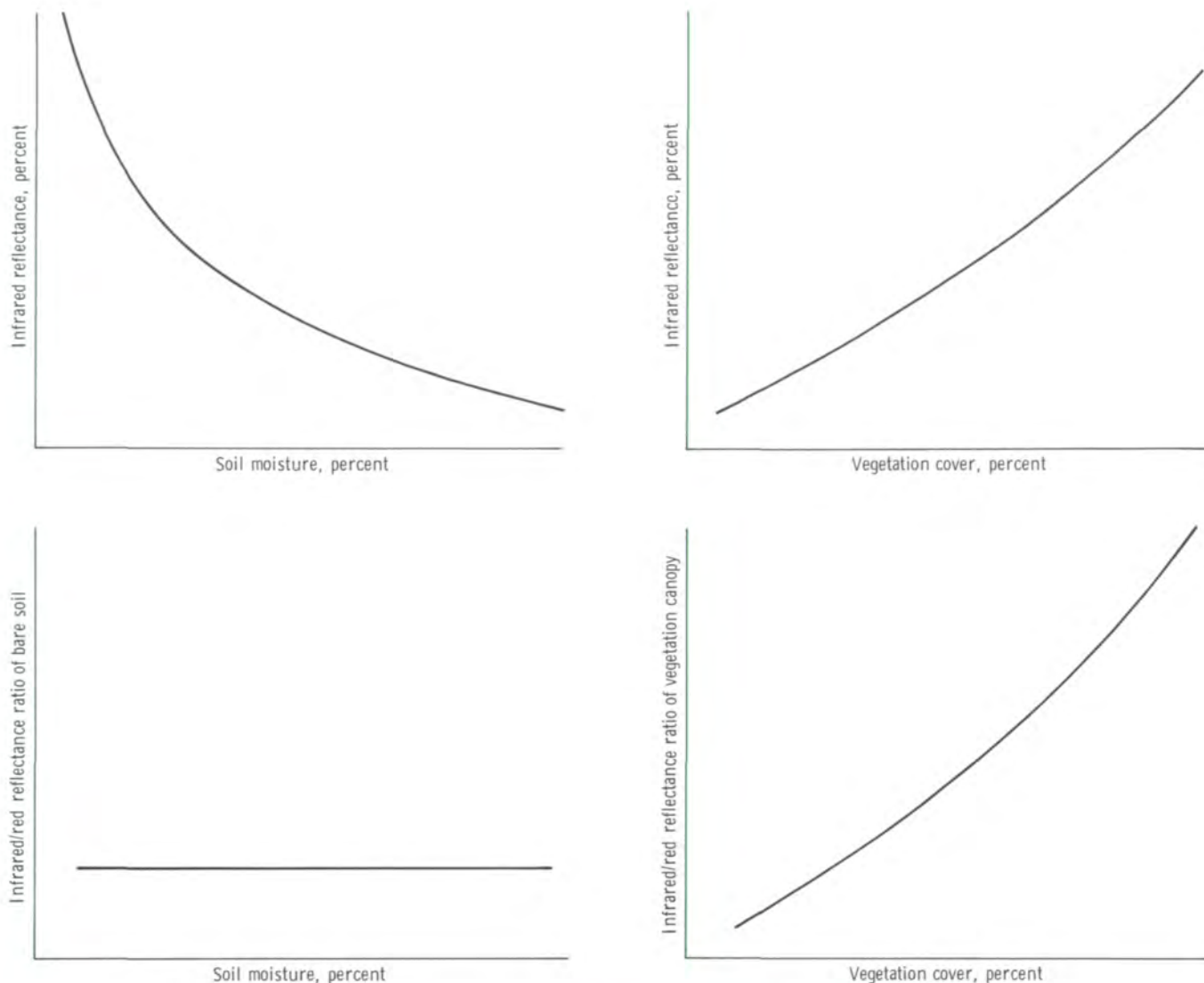
FIGURE 6-39.—The relationships from which the soil moisture algorithm was developed.

The correlation index R^2 of 0.95 for the values used in this algorithm indicates the effectiveness of the algorithm in correcting for the effects of variable vegetation cover and in accurately predicting the surface soil moisture. Such modeling can be useful in determining sensor requirements (spectral bands and signal-to-noise characteristics) for future satellite systems in specific applications. For example, the modeling suggests that a noise equivalent reflectance difference NE $\Delta\rho$ of 0.5 percent or more might be required in the near-infrared spectral band for estimating surface soil moisture in variably vegetated terrain.

The advantage of a remote-sensing technique for the determination of surface soil moisture under variable vegetation-cover terrain is the ability to map large areas and to locate homogeneous areas with different surface soil moisture regimes. When this technique was applied to aircraft multispectral data similar to the S192 imagery, positive results were obtained. In figure 6-40, a portion of the test site that was mapped is shown; the map gives the areal distribution for soil moisture. Techniques using only one band failed to show correlation with soil moisture. Under certain conditions, the use of the ratio infrared/red reflectance, together with the scanner thermal data, will improve the significance of the regression equation for soil moisture.

Because of better registration between bands, S192 conical data were used to construct a land-cover map of an area in southeastern Ontario, Canada. A particular feature of this map was the 10 classification categories shown in figure 6-41. These classes (water; marsh; mixed conifer/hardwood; hardwood; suburban; quarry and bare soil; undifferentiated herbaceous; and low-, medium-, and high-percent green herbaceous cover) are suggested as being pertinent to hydrological problems dealing with runoff, water balance, and water management applications. The map was made in two key steps. First, an unsupervised clustering algorithm was used on six polygon-shaped test sites chosen from aircraft underflight imagery 1 day after the Skylab pass. Second, the reflectance ratio $R_{10/6}$ was used to determine the percent cover of green vegetation. The final classification was performed using 30 signatures to define 8 classes. Water was also recognized as a level slice from the near-infrared band. Probabilities of correct classification were computed using a program to generate 1000 points for each signature with a normal distribution. A best linear classification rule was used to obtain correct probabilities of classification that were greater than 90 percent correct for six of the eight classes and approximately 77 percent correct for two classes, which were suburban and undifferentiated vegetation. This result was expected because of the mixed nature of the class defined.

Comparison with Landsat recognition classes for the same area showed similar results for 75 percent of the scene. The maps were reasonably equivalent in their information content. Most of the differences could be accounted for by differences in training-set signatures used.
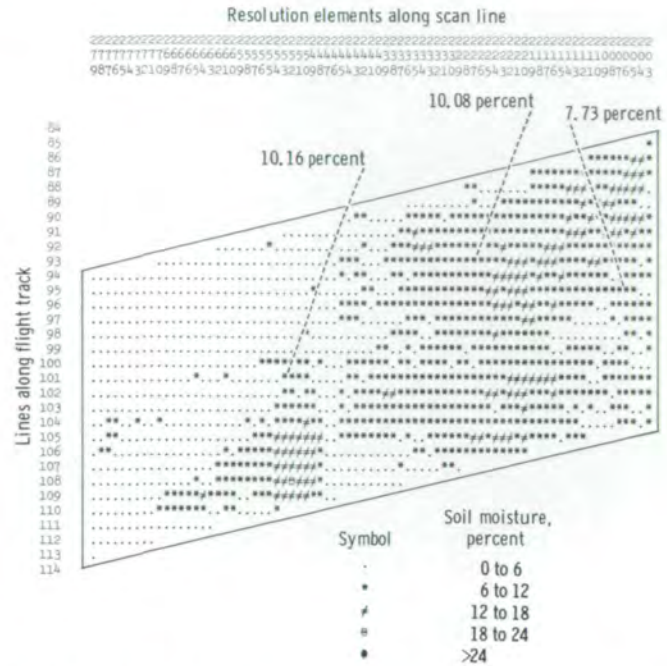

FIGURE 6-40.—A map of scanner-indicated soil moisture (Ontario, Canada). Each data point represents an area approximately 9 m (30 ft) on a side. Three sampled soil moisture values are shown for comparison.

An extensive modeling program to use S192 imagery for delineation of optimum fishing areas in the Gulf of Mexico was performed by Savastano (ref. 6-50). Detailed discussion of the model is presented in section 5.

THE S191 INFRARED SPECTROMETER

Although the S191 Infrared Spectrometer was not an imaging device, it was designed to obtain critical information about the spectral transmission of the atmosphere and about reflection characteristics of ground classes of terrain important to Earth resources applications. This knowledge is useful directly in the study of atmospheric processes and in the design of multispectral scanners such as the S192. The search for the optimum spectral bands for a given application is one of the major problems in remote-sensing research.
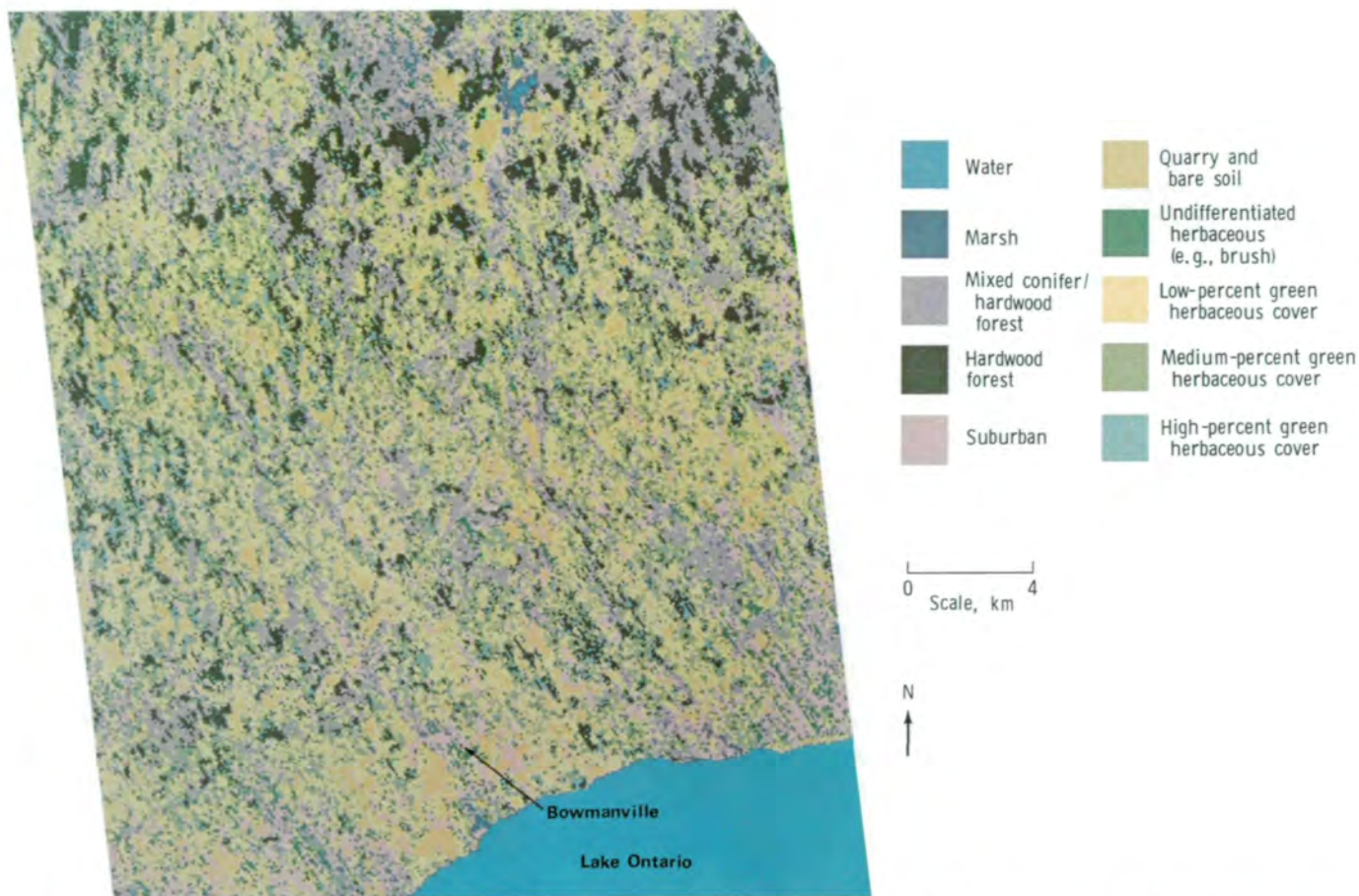
FIGURE 6-41.—Color-coded S192 recognition map of southeastern Ontario, Canada. The map was generated from data obtained September 1973. The skew apparent in the map results from the use of non-scan-line-corrected data.

The S191, providing continuous spectra over a wide range, was manually pointed at selected targets to obtain the spectral characteristics of represented areas on the surface. Data in two ranges were obtained: between 0.4 μm in the violet and 2.5 μm in the near infrared, and between 6.6 and 16.0 μm in the thermal infrared. Scan time was 1 second, and the ground area coverage was approximately 500 m in diameter.

Data were collected in six spectral segments across the two ranges (appendix A); with appropriate reduction and calibration procedures, the data were reduced to a form suitable for analysis. Many Skylab investigators used the sensor for atmospheric radiative transfer experiments, whereas others found it useful in measuring the surface radiance more accurately.

Anding and Walker (ref. 6-51) integrated the radiance values from the two portions of the thermal band on each side of the ozone absorption band and ratioed the values to offset the effect of atmospheric influences on sea-surface temperature measurements. This technique of using two thermal bands such as those available from the S191 Infrared Spectrometer offers an attractive alternative to correcting radiance values for atmospheric temperatures, moisture, and aerosol content. Further discussion of Anding and Walker's investigation is found in section 5.

Silva (ref. 6-12) used the output data in the thermal infrared to compare the data on spectral radiance measured by the S191 with data derived from surface measurements using both a ground spectroradiometer and a pyrheliometer to determine the spectral radiance and the spectral atmospheric transmission. The spectral path radiance, as computed from S191 measurements and as predicted by atmospheric models (ref. 6-52), is

compared in figure 6-42 for the visibility condition present at the test site (Lake Monroe, Indiana). The temperature of the lake was measured, and figure 6-43 shows the comparison of the spectral radiance derived from the S191 and that due to a black body at the temperature measured. Agreement of the results within experimental error verified both the atmospheric model and the feasibility of detailed spaceborne spectroradiance measurement.

To derive quantitative measurements of stratospheric aerosol characteristics, Tingey and Potter (ref. 6-53) used S191 data in the 0.4- to 2.5-μm band to acquire high-spectral-resolution data for increments of 2.4 km of altitude at the Earth limb. As an initial step, some signal averaging was introduced to improve the signal-to-noise ratio at the low radiance value encountered. Compared with the S192, the S191 proved to be more sensitive but less accurate in its absolute radiometric calibration. However, analysis of the S191 data proved that aerosol layers could be detected in several spectral bands at various altitudes measured from the top of the atmosphere. It was found that layers at altitudes of 42, 50, and 55 km are more responsive to longer wavelengths, whereas layers at 59 and 66 km were more responsive to wavelengths near 0.53 μm. Knowledge of the distribution of aerosols is of interest in astronomy, meteorology, air-quality surveys, and remote sensing.

In geology, Vincent et al. (ref. 6-18) applied S191 data to the problem of differentiating basaltic rocks from dacite. Atmospheric models from Anding et al. (ref.
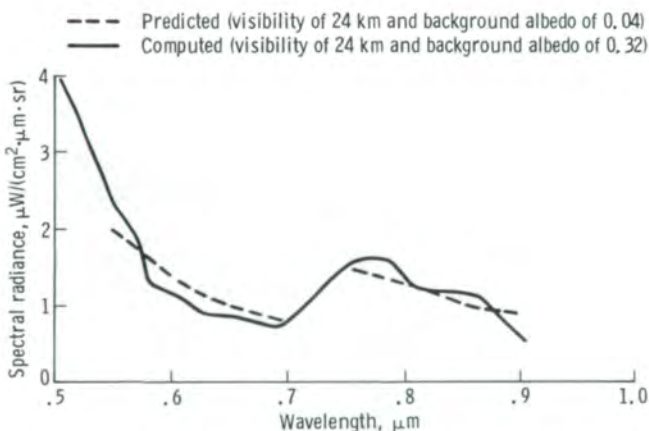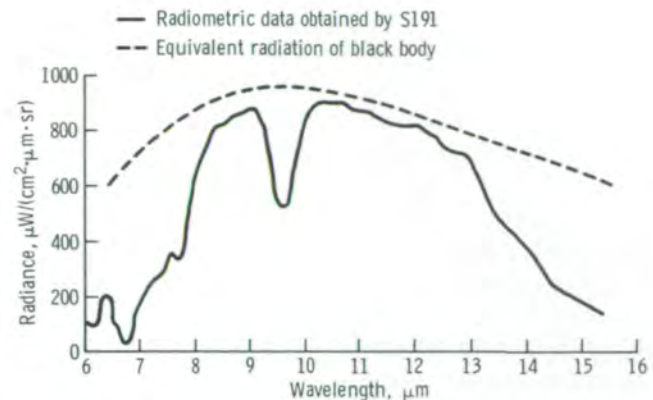

FIGURE 6-43.—Comparison of radiance measured by S191 over Lake Monroe, Indiana (June 10, 1973), with equivalent radiance for a 297.7-K (24.5° C) black body.

6-54) and radiance data at Yucca Flat, Nevada, were used to calculate the average spectral radiance at the surface. To compute spectral emissivities for basalt and dacite, corrections for the different temperatures of the two materials were made. The ratios of the two emissivities were calculated by averaging emissivity in the short-wavelength band and dividing by the average emissivity in the long-wavelength band. This calculation was accomplished for different bandwidths proposed for future space sensors; in each case, however, the emissivity ratios for basalt and dacite were different, an indication that the materials could be separated by means of ratio techniques operating in the thermal-infrared bands.

In oceanography, Maul et al. (ref. 6-16) used the S191 nadir data to develop methods for recovering the ocean color spectrum through the atmosphere. These results validated measurements for wavelengths greater than 0.5 μm. More data on marine aerosol properties are needed before a quantitative determination of the ocean color spectrum from spacecraft altitudes can be made.

MICROWAVE SENSORS

The Skylab EREP instruments greatly expanded the microwave remote-sensing program from space by including both active and passive microwave instruments for measuring the scattering and emitting properties of the Earth's surface. The S193 instrument operated at a frequency of 13.9 GHz both as an altimeter and as a

FIGURE 6-42.—Comparison of computed and predicted path radiance.

combination radiometer/scatterometer. The latter instrument was designed to provide both vertical and horizontal polarization data at five incidence angles (0° to 48°). The S194 radiometer provided an additional frequency at 1.4 GHz for gross resolution studies of emission.

The altimeter sensor utilized the high-range-resolution capability of radar to measure the surface height variations along the satellite groundtrack. The primary objective of the altimeter experiment was to establish its potential as a remote sensor of both the geoid over the ocean and the topography over land.

The backscatter experiment provided information to radar designers concerning the range of backscatter coefficients expected from space for a variety of surfaces, angles of incidence, polarizations, and geometric configurations. Also investigated was the dependence of the backscatter on the geometrical characteristics and the physical state of land areas and on the surface roughness over the oceans.

Similarly, it was of interest to determine the range of brightness temperatures that could be expected for different polarizations and incidence angles as sensed by a radiometer in space. Also to be investigated were relations between the brightness temperature and the physical state of land areas, the oceanographic surface parameters, and the atmospheric variations. Over ocean areas, the simultaneous RADSCAT observations could be used to provide corrections for the atmospheric attenuation of the backscatter measurements.

Several new techniques and special analysis procedures were developed to convert the raw microwave measurements to meaningful data for interpretation and comparison with other independent information. For the altimeter observations, special techniques were developed for (1) the accurate determination of the antenna pointing angle from the radar return, (2) the calibration and correction of the normalized radar cross section for pulsewidth/beamwidth-limited conditions, (3) deterministic and statistical analysis of the radar return for evaluating terrain reflection characteristics, and (4) the modeling of surface characteristics to reduce intrinsic noise of the altimeter height measurements and to separate the height biases.

Two approaches were used for the S193 RADSCAT data investigations. One was a general investigation in which brightness temperature and backscatter were categorized for the different incidence angles and polarizations to provide surface signature data for future microwave sensor design. In the second approach, the microwave signature was correlated with specific parameters such as ocean windspeed, soil moisture, and vegetation cover. Using the second method, investigators confronted a basic problem of determining the validity and accuracy of the ground-truth parameters, and several techniques were used to separate the uncertainty of the ground-truth parameter from the inferred parameter as measured by the microwave sensor from space (sec. 5).

The S194 radiometer data obtained over the oceans were used primarily to verify the theoretical relations of the microwave brightness temperature to ocean surface variables such as windspeed, sea-surface temperature, and salinity. The different techniques and analyses used to establish the relations between the measured microwave signature and the corresponding physical parameters of the Earth surface are discussed in the following subsections.

The S193 Altimeter Experiment

The altimeter precision needed for geodetic measurements over the oceans required a careful analysis of all potential error sources that contribute to the final error in the geodetic height determination. McGoogan et al. (ref. 6-55) derived the geodetic height h_g from

$$h_g = h_s - h_a - \Delta h \qquad (6\text{-}17)$$

where h_s is the satellite height above a reference spheroid as obtained from the satellite tracking data; h_a is the altitude measured by the altimeter; and Δh represents the dynamic ocean effects due to tides, winds, and currents. As indicated by McGoogan, Δh can be considered negligible relative to the expected precision of approximately 1 m root mean square (rms), and no correction was made for it.

The major errors are due to orbital uncertainties and altimeter measurement inaccuracies. Because the altimeter is used primarily to determine the higher frequency geoidal components, methods for short-arc analysis were developed in which systematic error effects due to air drag, thrusting, and geopotential errors could be minimized. Comparison between short-arc analysis with extensive tracking coverage and longer arc
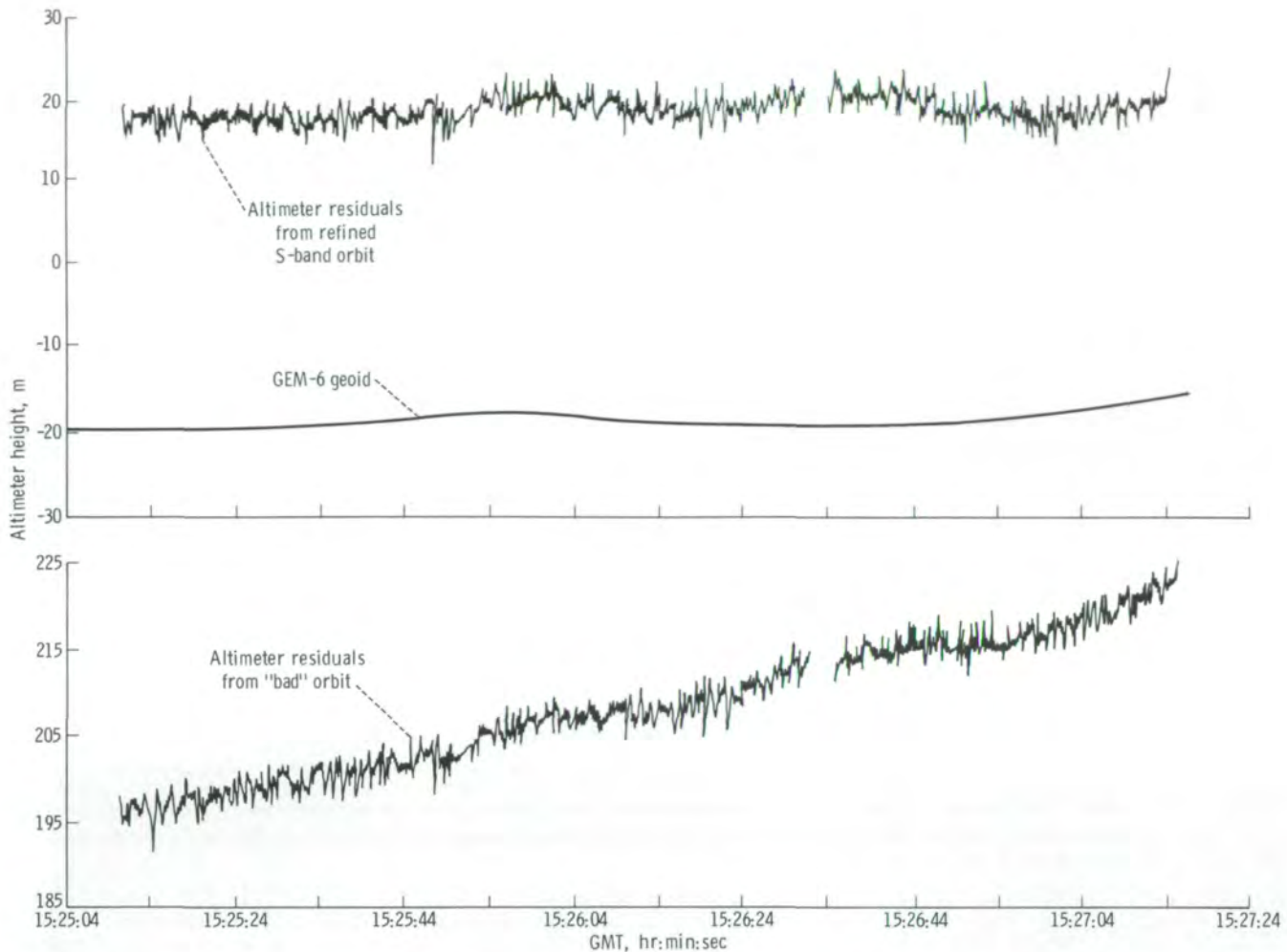
FIGURE 6-44.—Effect of orbital errors illustrated by Skylab altimeter residuals (pass 8, mode 3). A reference geoid, Goddard Earth Model 6, is shown for comparison.

analysis with reduced tracking coverage showed that a significant bias and tilt could be introduced by orbit uncertainties (fig. 6-44). McGoogan developed techniques to estimate the orbital accuracy for each pass; and potential bias values from −20 to 135 m, depending on the quality and quantity of the tracking coverage, were obtained for different passes.

The error sources that contribute to the measured altimeter height h_a were separated into three main categories corresponding to the basic instrument delays, the pointing error, and the atmospheric path delay. The basic instrument errors were reduced by careful preflight and in-flight calibration of the system delays and by use of range-tracker design information.

To determine the pointing angle, two new techniques were developed. In one technique, the radar return was used directly for pointing-angle analysis. Because the altimeter operated in essentially a beamwidth-limited condition, the mean radar return waveform consisted of a stretched pulse having a trailing edge that corresponded to the angular variation of the antenna gain. When the antenna pointed off-nadir, the increase of the antenna gain in the off-nadir direction increased the amplitude of the trailing edge relative to the peak amplitude. A plot of the theoretical relation for various off-nadir pointing angles ξ is shown in figure 6-45(a), and a plot of a measured waveform is shown in figure 6-45(b). The pointing angle could be measured from the
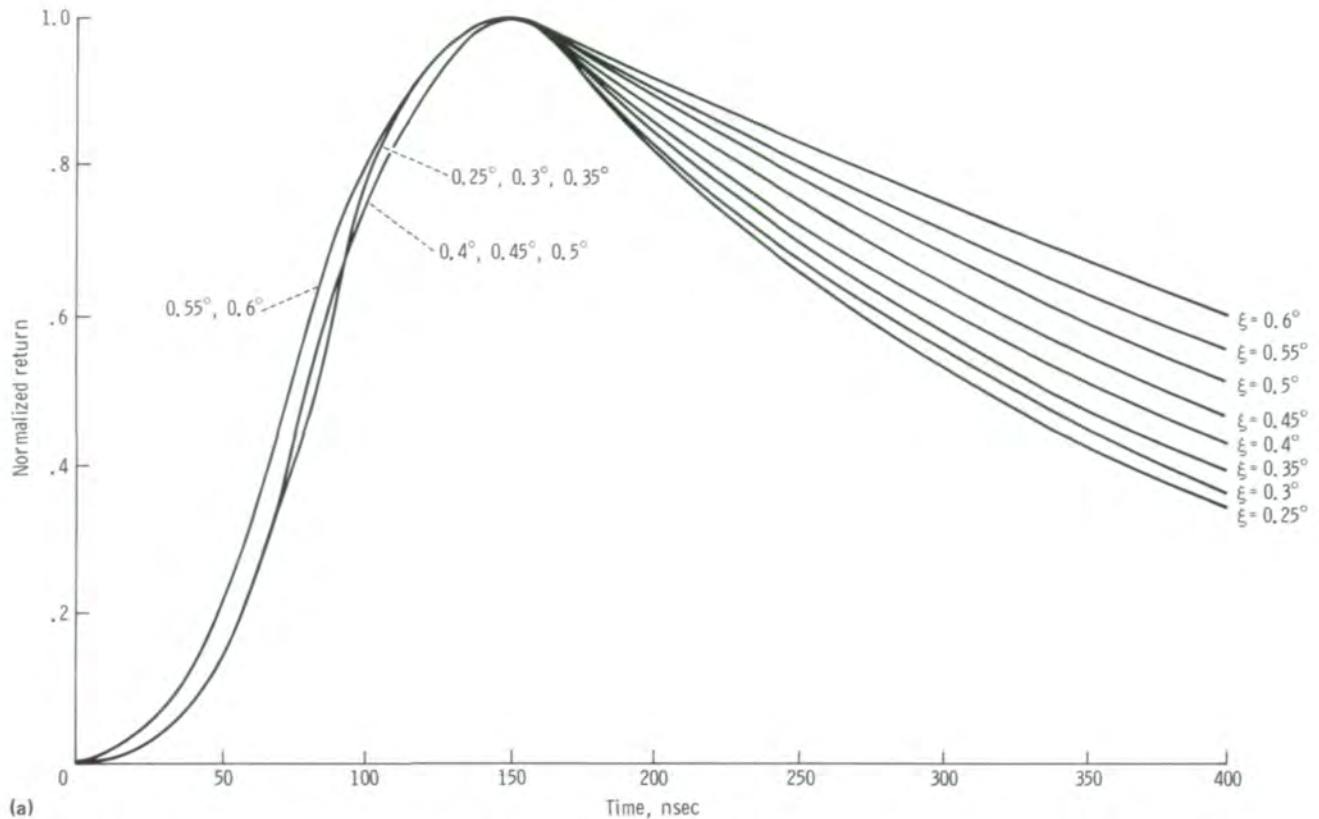
FIGURE 6-45.—Effect of pointing-angle variations on radar returns normalized to unity. (a) "Flat sea" return for no jitter. Height is 435 km (235 n. mi.). (b) Comparison of measured mean return and theoretical return for a 100-nanosecond transmitted pulsewidth (pointing angle 0.5° off-nadir). Error bars are based on one standard deviation σ.

deviation of the trailing edge with an uncertainty of ±0.05°.

The waveform method can be used only when the off-nadir pointing angle is less than one-half a beamwidth (0.6°); beyond this angle, the accuracy of the method is degraded because the leading edge starts to spread out. For larger off-nadir angles, the statistical characteristics of the range-tracker "jitter" (range fluctuations) were analyzed to deduce the pointing angle. Range jitter is produced by the intrinsic noise of the radar return due to the electromagnetic reflection properties of the ocean surface. An example of this technique is shown in figure 6-46. As mentioned previously, the leading edge stretches out as the off-nadir angle increases above 0.6°. The range-tracker-jitter amplitude and frequency response is related to the slope of the risetime, and increasing the risetime will increase the range-tracker jitter and reduce the bandwidth, as indicated in figure 6-46(c).

After the off-nadir pointing angle was determined, preflight calibration data were used to convert pointing-angle offset to effective height corrections. The corrections and calibration of the data reduced the absolute rms height error from 20 to 10 m; however, relative errors for any given pass should be less than 1 m.

The corrected altimeter geoid height data were plotted for all operating passes and compared with a reference geoid (Goddard Earth Model 6 (GEM-6)) and with ocean-bottom topography where available. Several interesting relationships between the measured geoid and the sea trenches and mountains were discovered. (See sec. 5, entitled "Oceans and Atmosphere.")

Mourad et al. (ref. 6-56) used the calibrated altimeter data from four passes to further investigate the effects of the orbit and instrument noise on the results. A "best estimate" of the geoidal profile along the satellite groundtrack was obtained by applying the generalized least squares collocation method (GLSCM) to the

$\xi = 0.55°$
$\xi = 0.5°$
$\xi = 0.45°$

⊥̸̸ᵩ Estimated 1σ confidence bounds
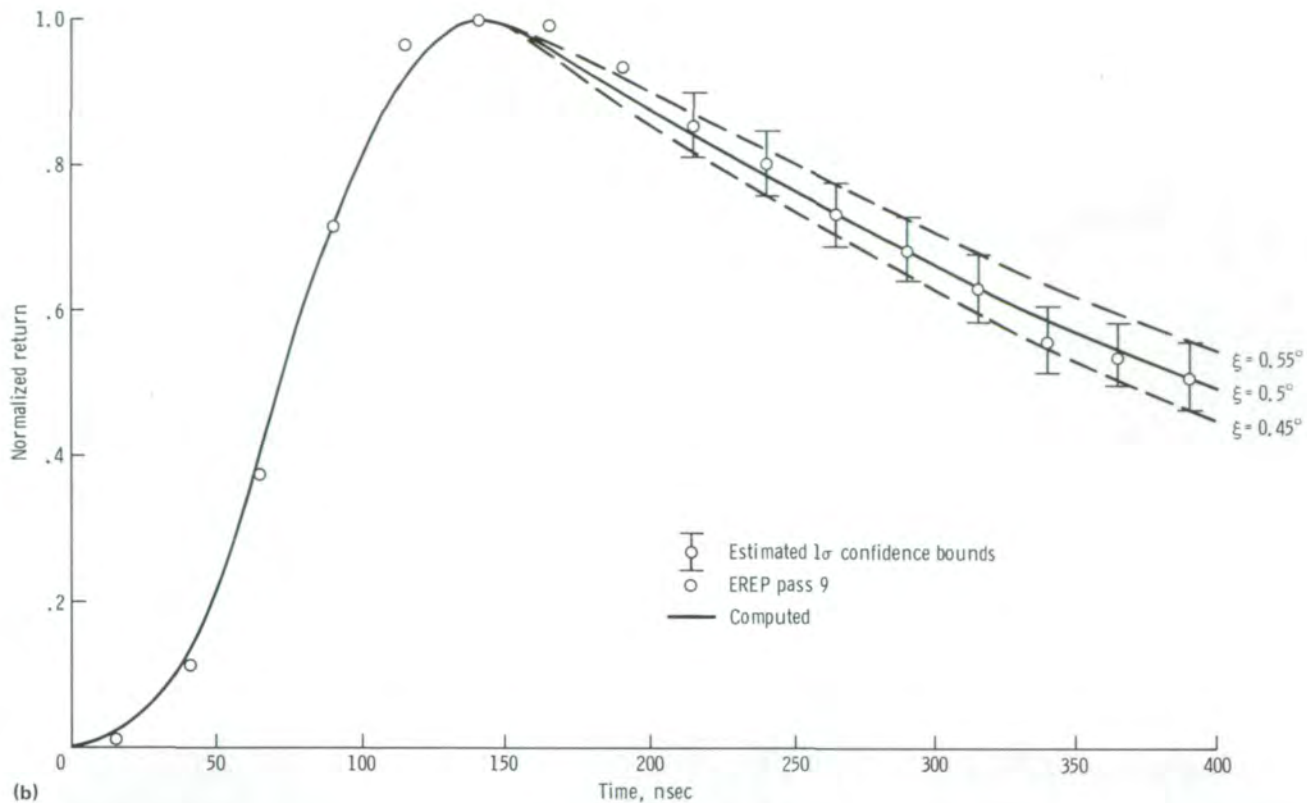○ EREP pass 9
—— Computed

(b)

Time, nsec

FIGURE 6-45.—Concluded.

altimeter height observations. The analysis consisted basically of three steps.

1. The geoidal height was obtained as before (eq. (6-17)) by subtracting the measured altimeter height from the computed satellite height relative to a reference spheroid. This residual was then modeled as the sum of the expected random height signal and the intrinsic random range noise of the altimeter. For short arcs (<450 km), the signal can be expressed as the sum of a calibration constant reflecting the systematic orbit, altimeter and environmental errors, and the random height signal having variations bounded by the expected frequency characteristics of the global geoidal height distributions.

2. Using the signal spectral characteristics, the intrinsic range noise was reduced by applying the GLSCM to the residual values (filtering).

3. The filtered residuals were then compared with the Marsh-Vincent (M-V) geoid (Goddard geoid 73 (GG-73)), and by using weighting functions that corresponded to the reduced noise level of the altimeter measurements and the uncertainty of the M-V geoid, the GLSCM was reapplied to determine a calibration constant and the geoidal height deviations relative to the ground-truth M-V geoid. Several segments of the short-arc tracks were combined in the GLSCM solution by constraining the adjacent geoidal height values of the segments to be equal.

The values of the calibration constant reflecting potential altimeter and orbital biases varied between 20 and 50 m for passes 4 and 7 and compared with estimated orbital biases of 20 to 30 m (ref. 6-55) for the same passes.

Ground truth, consisting of the free-air gravity anomalies, the bottom topography, and the reference M-V geoid along the Skylab groundtrack, was assembled and compared with the derived geoid profile. An example of the results is shown in figure 6-47. The
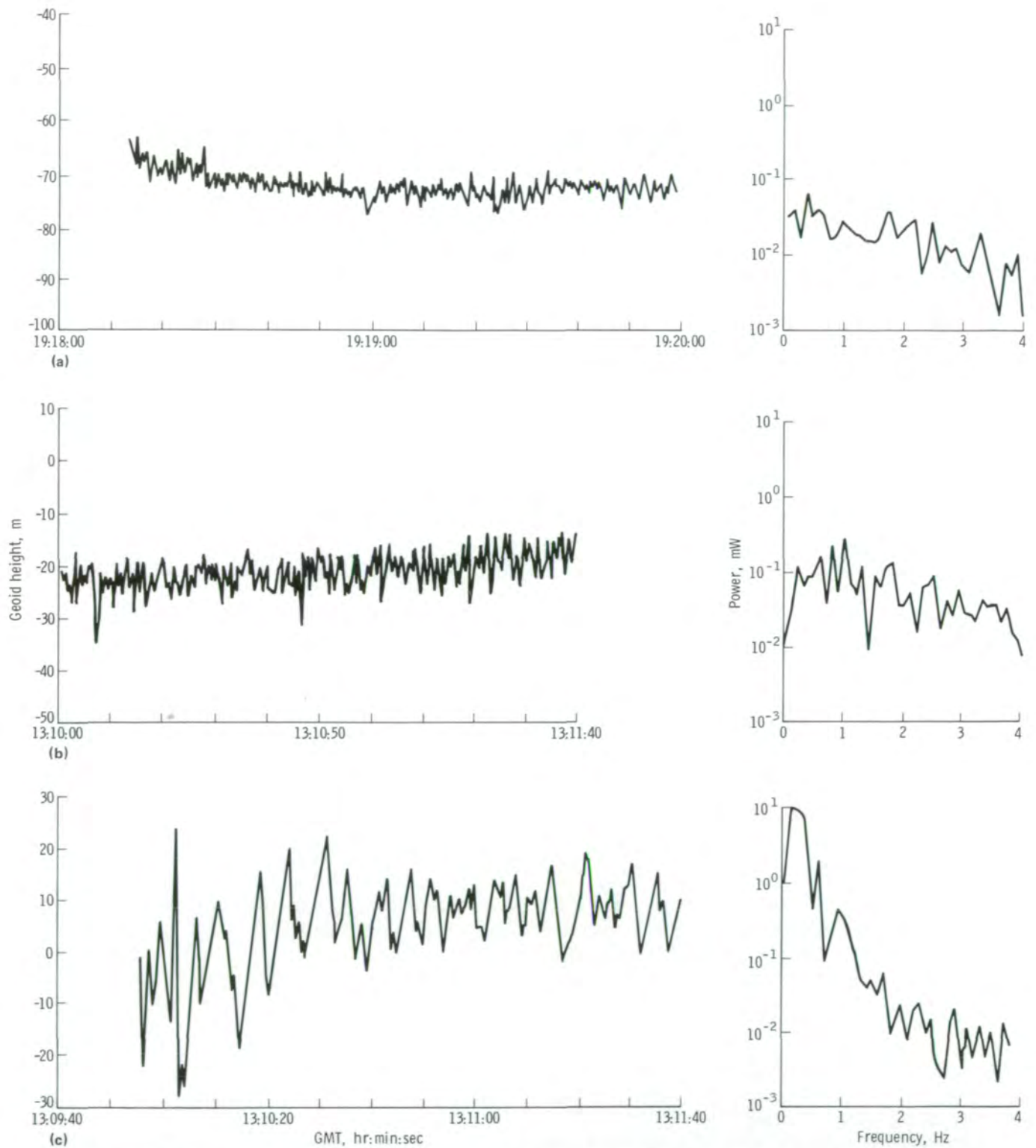
FIGURE 6-46.—Off-nadir pointing-angle effects on range and power spectrum. (a) Skylab 4 pass 38/86; $\xi = 0.6°$. (b) Skylab 2 pass 9; $\xi = 1.1°$. (c) Skylab 3 pass 21/32; $\xi = 1.4°$.
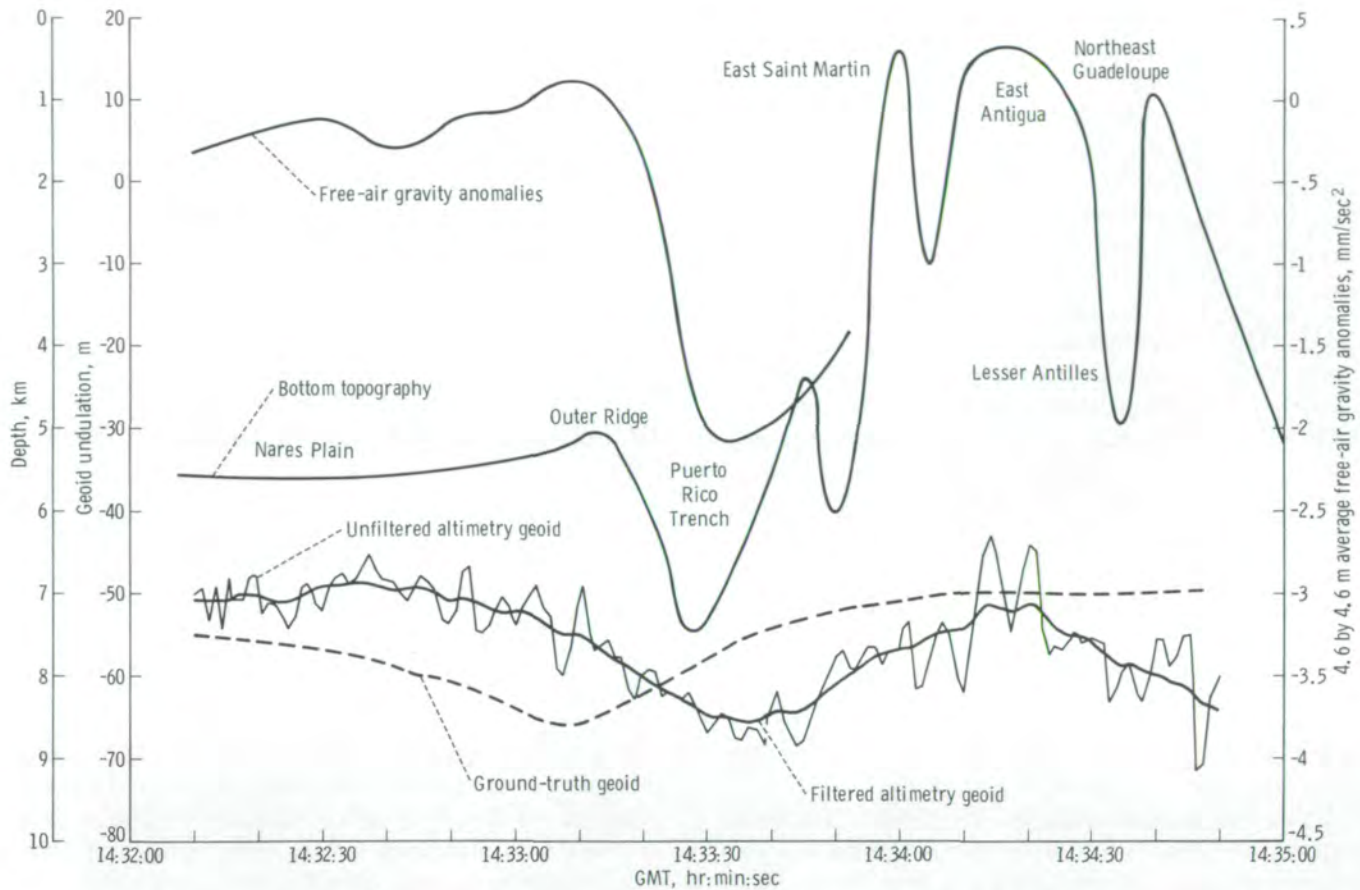
FIGURE 6-47.—Geoid undulations computed from Skylab altimetry data (pass 7, mode 5).

relatively large and slow frequency fluctuations of the unfiltered altimeter geoid were caused by a large off-nadir angle (1.25°; ref. 6-55). The application of the GLSCM effectively suppresses these noise fluctuations, as seen by the resultant filtered altimeter geoid. The depression of the altimeter geoid is displaced horizontally by approximately 200 km relative to the ground-truth geoid (GG-73) but agrees with the locations of the Puerto Rico Trench and the free-air gravity anomaly. Other results of Mourad's analysis that illustrate the altimeter sensitivity to the fine structure of the geoid are discussed in section 5.

The determination of values of the normalized radar cross section $\sigma°$ of the ocean at near-nadir angles and their accuracy was derived by Brown (ref. 6-57) from the altimeter data and calibration curves. The radar cross section $\sigma°(\hat{\psi}_0)$ is expressed by

$$\frac{\sigma°\left(\hat{\psi}_0\right)}{L_P} = \frac{P_{POM_{cal}}}{\hat{P}_{CDS}} \frac{\rho}{\hat{F}\left(h,\xi,\tau_P\right)} K \qquad (6\text{-}18)$$

where $\hat{\psi}$ is the incidence angle that produces the peak amplitude; $\hat{\psi}_0 = \sqrt{c\tau_P/h}$
c is the speed of light
h is the altimeter altitude
L_P is the path loss
$P_{POM_{cal}}$ is the peak of the mean power as obtained from the automatic gain control (AGC) calibration curves at receiver temperature T_r

$\hat{P}_{CDS}$ is the in-flight received-power measurement obtained in the calibration data submode (CDS)

ρ is the correction factor for the change of measured waveform relative to the waveform used in calibration, and the conversion from the mean of peak values of the received power measured by the altimeter to the peak of the mean values needed to compute $\sigma°$

$\hat{F}(h,\xi,\tau_p)$ is basically the convolution of the system point-target response with the flat surface impulse response and is a function of the radar parameters, the antenna pattern, the pointing angle ξ, and the time delay τ_p at which maximum value is obtained

K represents the system losses obtained from preflight calibration

Brown (ref. 6-57) computed values of $\sigma°$ for each of the passes during which the pointing angles were less than 0.8°. The pointing angle was derived from the waveform return as described previously.

Using the pointing angle and the measured antenna pattern, the function $\hat{F}$ could be computed. Because the antenna pattern was asymmetrical, two values for $\hat{F}$ were computed, one with the pointing angle assumed to be in the roll direction (ξ_r) and one assigned to the pitch direction (ξ_p). For Skylab 2 and 3, the values of $\hat{F}$ as a function of ξ are shown in figure 6-48. Typical values of $\sigma°(\hat{\psi})$ for small incidence angles ($\hat{\psi} = 0.5°$) varied between 8 and 16 dB.

Brown (ref. 6-57) also performed an error analysis to establish the uncertainty of the derived values of $\sigma°$ as a function of the pointing angle. Estimates of errors due to uncertainties in calibration, to $\hat{F}$, and to dominant bias were made, and the resultant error was computed. The Skylab 2 and 3 results show that absolute and relative rms errors of 0.7 and 0.3 dB, respectively, are achieved for a known pitch angle of 0° to 0.5°. When the antenna pattern was degraded, as in Skylab 4, rms errors of approximately 4 and 0.5 dB were obtained for absolute and relative values, respectively, with pitch angles of 0° to 0.5°.

Altimeter performance over terrain in the United States was investigated by Shapiro et al. (ref. 6-58) to evaluate the capability of the sensor to profile terrain
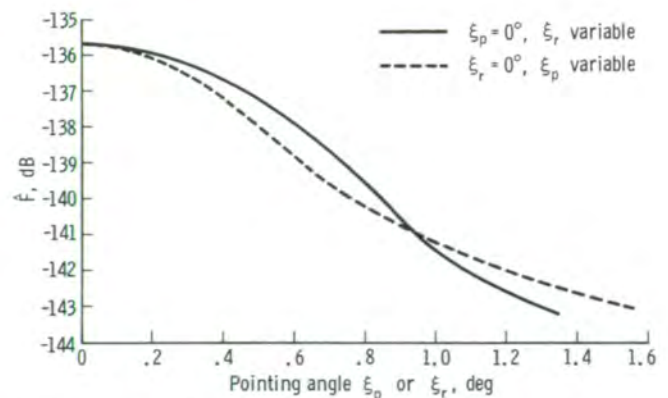

FIGURE 6-48.—$\hat{F}$ as a function of $(0°,\xi_r)$ and $(\xi_p,0°)$ for Skylab 2 and 3.

topography along the satellite groundtrack. The non-homogeneity of terrain topography within a footprint reduced the potential height accuracy but provided relatively reliable tracking over most areas having small height variations. In general, the existence of high-reflectivity patches provided a waveform on which the split-gate range tracker could operate. The mean reflected power relative to the ocean return for different types of terrain is listed in table 6-V. The values decrease with increasing terrain complexity. The large received power at nadir over the salt flats is equivalent to a radar backscattering coefficient of 32 dB and, when compared with the Moore et al. (ref. 6-59) value of 14 dB at 1.5° incidence angle, indicates a highly specular return. Generally, a dominant specular return provided the required waveform for proper range-tracker operation as shown both by the dropoff of the backscatter between 0° (altimeter operation) and 1.5° (scatterometer operation) over the same type of terrain, and by the waveform analysis. In figure 6-49, a typical example of the radar return waveform from farmland in Iowa is compared with the water return waveform from Lake Michigan. The terrain return is similar to a point-target return with a sharp trailing edge, whereas the trailing edge of the Lake Michigan return is stretched by the diffuse return of the water surface. Also shown is the correlation between the temporal (equivalent to a spatial resolution of 70 m) amplitude variations at the risetime portion of the individual radar returns (100/sec). The analysis shows that the amplitude of the water return decorrelated for a displacement of 70 m along the track, whereas the land return is correlated for

TABLE 6-V.—*Dynamic Range of Peak Terrain Radar Return Relative to Ocean Return*

Type of terrain	Radar return, dB
Salt flats	20
Lakes	10
Ocean, deserts	0
Valleys, plains, cities, swamps	−5
Ridges, canyons, dry lakes	−10
Hills, ranges, mountains	−12
Cliffs, forest	−16

several hundred meters. Thus, it can be deduced that specular patches of approximately a few hundred meters exist and that the altimeter measures the height to these bright spots within the altimeter footprint.

Figure 6-50 shows an altimeter output and topographic map profile. An example of the altimeter profile over Arizona is shown in figure 6-50(b) compared with the power return (fig. 6-50(a)) and an equivalent topographic profile (fig. 6-50(c)) obtained from a 1:250 000-scale contour map. The large received-power variations could not be correlated directly with the topographic variations because they also depend significantly on surface roughness, soil type, and soil moisture. Additional variations are caused by instrumental effects of the narrow AGC sampling gate.

The correlation between the altimeter profile and the map profile shown in figure 6-51(a) gives a correlation coefficient of 0.92 when the altimeter profile is shifted by approximately 7 km backwards relative to the map profile. A corresponding mean height difference of approximately −15 m and an rms height variation of ±35 m were computed, and the results are shown in figure 6-51(b). The backward shift has been detected in all passes and is probably due to the inertial response of the range tracker to height variations.

The results show that an altimeter, such as the S193, profiles the subsatellite groundtrack topography but acts as a low-pass filter (as opposed to altimeter geoidal operation over the ocean) because it responds primarily to the lower specular areas within the footprint. Future altimeters should provide for both specular and diffuse returns and should have additional sampling gates available so that the vertical structure within a footprint can be determined.
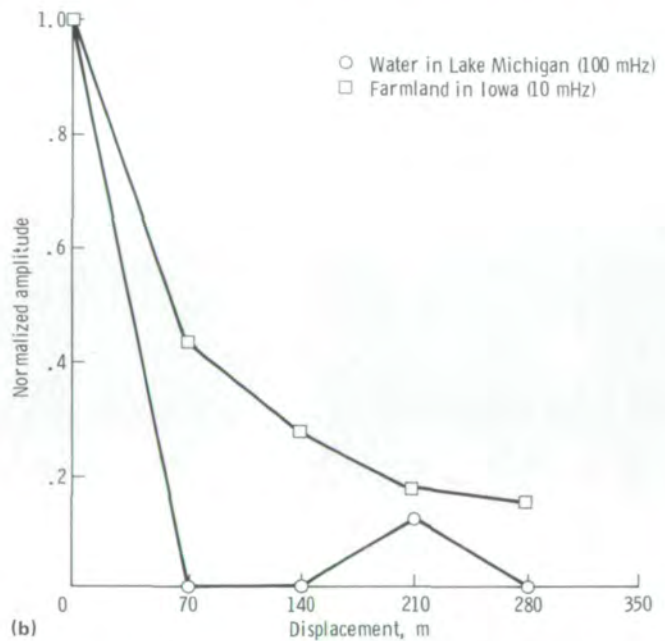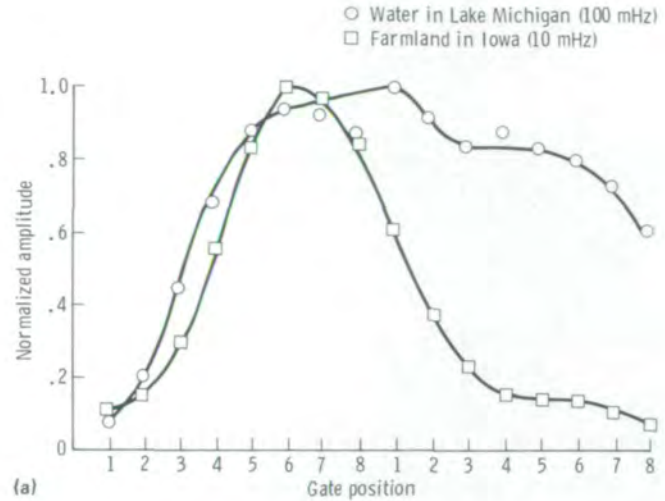

FIGURE 6-49.—Comparison of terrain waveforms obtained on Skylab 3 pass 17. (a) Radar return. (b) Autocorrelation.

The S193 RADSCAT and S194 Radiometer Experiments

An overall evaluation of the RADSCAT measurements was made by Moore et al. (ref. 6-59) to determine the relationships of the measurement parameters to
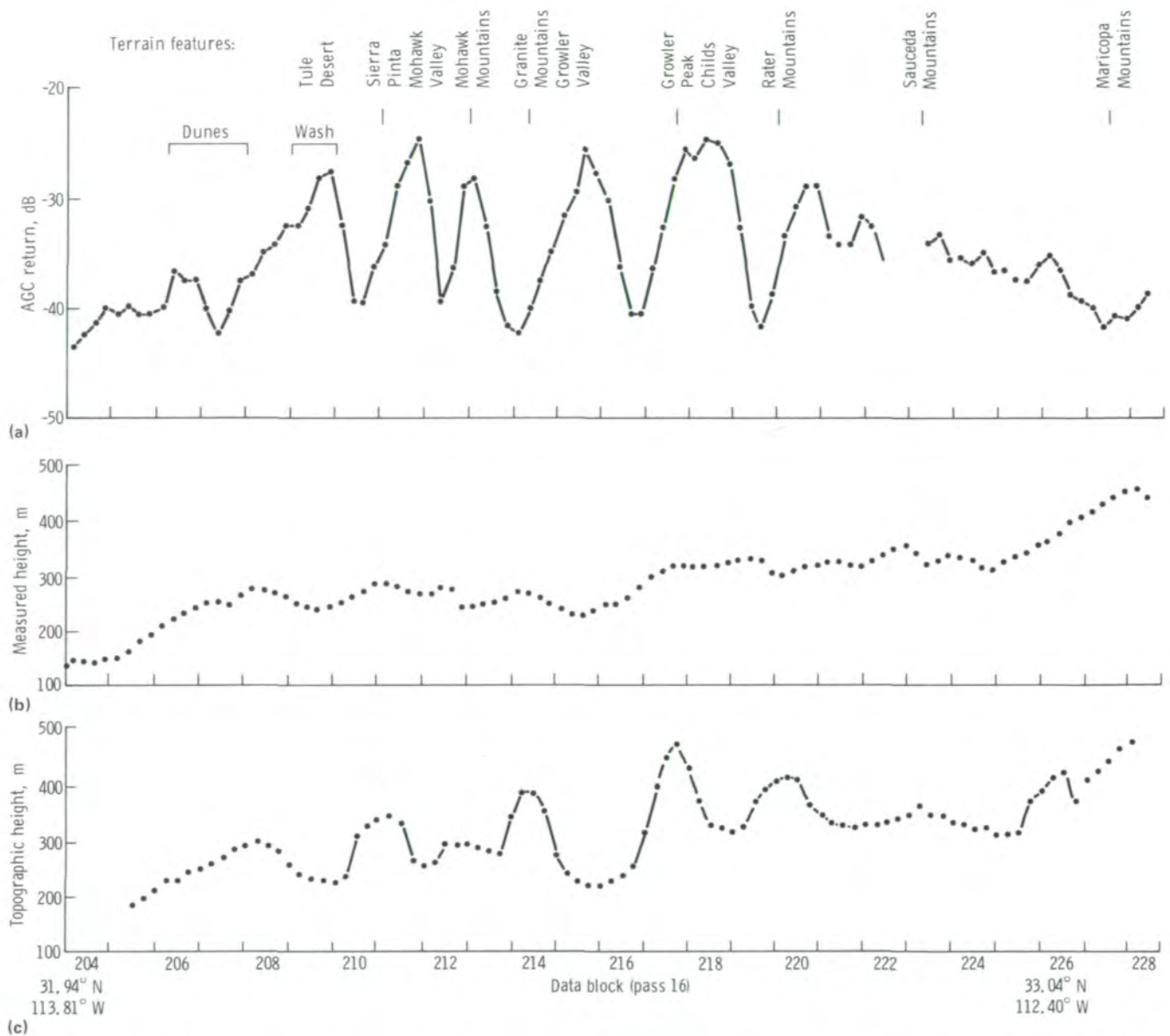
FIGURE 6-50.—Skylab altimeter output and topographic map profile for Arizona test site. (a) Altimeter power return. (b) Altimeter profile. (c) Topographic profile translated for maximum cross correlation with radar height.

polarization, incidence angle, soil moisture, type of terrain, and vegetation cover. Data obtained over the United States, Brazil, and the oceans were categorized, and specific test areas in which large anomalies were observed were used to establish potential correlation with the physical parameters of the observed areas.

The angular dependence (approximately 1.5° to 52°

for the S193 radiometer) of the brightness temperature T_B over the continental United States is summarized in figure 6-52(a) for vertical-transmit/vertical-receive (VV) antenna polarization. Also shown is the number of samples for each data point and the upper and lower decile values. The mean brightness temperature over land is approximately constant at 268 K with a decile
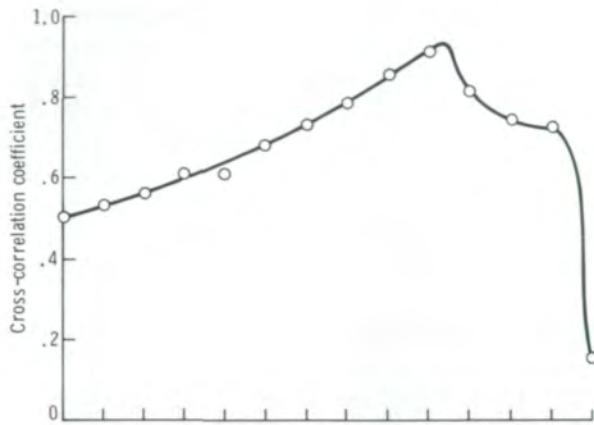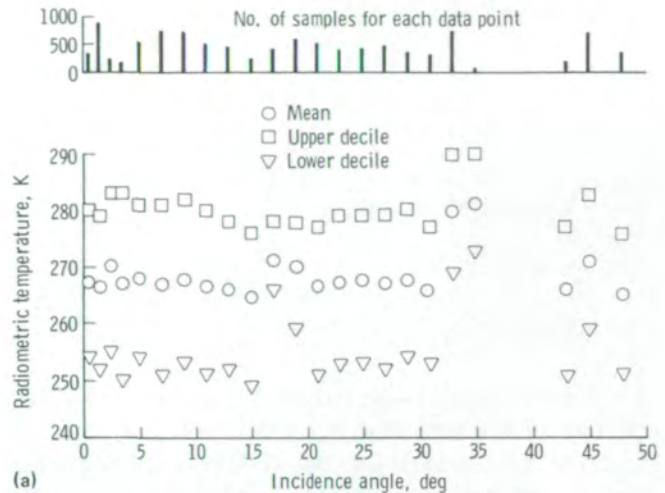
(a)
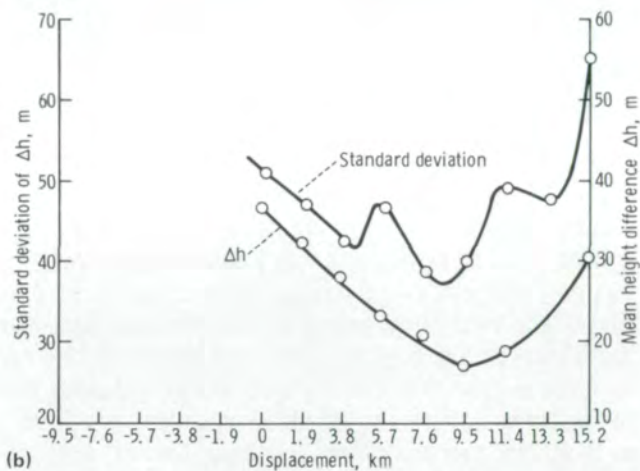
(b)

FIGURE 6-51.—Mean and standard deviation of height difference
and cross correlation of altimetry ground height as a function of map
elevation (Skylab 3 pass 16, data blocks 204 to 228). (a) Correlation
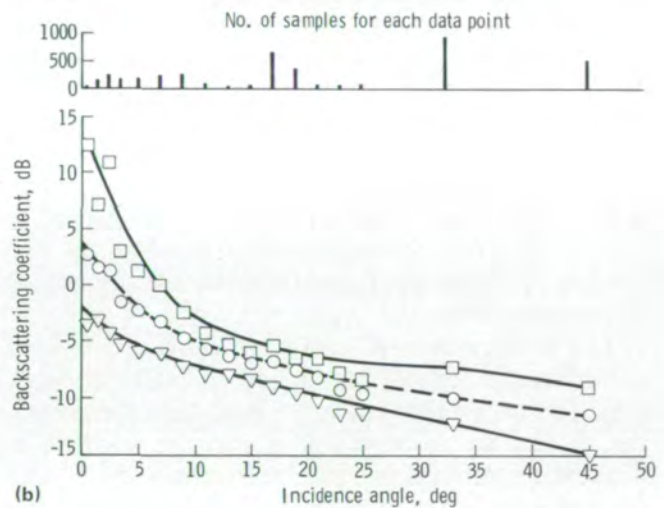between altimeter profile and map profile. (b) Mean height
difference.

(a)

(b)

FIGURE 6-52.—Summary of angular dependence of brightness tem-
perature and backscatter for VV antenna polarization during Skylab
2 and 3. (a) Angular radiometric response from S193 radiometer
operations. (b) Angular scatterometric response from S193 scat-
terometer operations.

value range of approximately ±15 K for all incidence
angles. This relationship agrees with a Lambert's law
model for very rough surfaces.

The mean backscatter response over land shown in
figure 6-52(b) reveals a two-step dropoff with incidence
angle θ; this relationship can be analytically expressed
by a best fit to the data by

$$\left.\begin{array}{l} \sigma°(\theta) = 1.7e^{-(\theta/5.6°)} \quad \text{for } 0° < \theta < 11° \\[2ex] \sigma°(\theta) = 0.4e^{-(\theta/29.6°)} \quad \text{for } 11° < \theta < 45° \end{array}\right\} \quad (6\text{-}19)$$

The decile values around the mean value are relatively
small (≈ 4 dB) for angles larger than $10°$ because of
spatial averaging of the large footprint (>100 km^2).

The angular dependence of the brightness tem-
perature over the oceans for both vertical and horizon-
tal polarizations agrees with a slightly rough surface
model, whereas the mean backscatter ocean response

follows a one-step dropoff given by

$$\sigma^\circ(\theta) = 16e^{-(\theta/6.1^\circ)} \qquad (6\text{-}20\text{a})$$

for VV polarization and

$$\sigma^\circ(\theta) = 22e^{-(\theta/5.3^\circ)} \qquad (6\text{-}20\text{b})$$

for horizontal-transmit/horizontal-receive (HH) polarization, where $0^\circ < \theta < 45^\circ$.

Statistical analysis of the different measurement parameters over land showed a low correlation between the brightness temperature and the backscatter coefficient and a high correlation between horizontal and vertical polarization as well as between the microwave backscatter measurements at different incident angles for $\theta > 15^\circ$. These results imply (1) that active and passive microwave measurements over terrain are sensitive to different surface and/or atmospheric characteristics, whereas the use of multiple polarization, at least for the given spatial resolution, is redundant, and (2) that side-looking radar performance can account for the far-range effects.

The backscatter coefficients are compared to land use categories for different incidence angles in figure 6-53. The σ° values overlap for most land use categories, except for the high values over the salt flats in Utah, water surfaces at an incidence angle of 1.5°, and the low water values at incidence angles of 33° and 46°. An attempt to distinguish different types of terrain by a statistical decision procedure applied to the microwave data was unsuccessful for two reasons. The larger scatterometer footprint generally included different land use categories; and other factors, such as soil moisture, may dominate the microwave terrain response.

To establish a more precise correspondence between the physical state of the terrain and the microwave data, some uniform land areas over which large deviations in the microwave data were observed were studied in detail. A uniform rangeland groundtrack in Texas showed a large change in brightness temperature (288 to 236 K) and backscatter signal (-11 to -7 dB). To determine whether this change could be related to soil moisture, the pattern of precipitation along the groundtrack for 5 days preceding the overpass and on the day of the overpass was studied. Using the 5-day antecedent precipitation index (API) as an estimate of the soil moisture distribution along the satellite groundtrack, a correlation between the microwave data and the soil moisture was computed. The result indicated a relatively high correlation (-0.76 for land emission and 0.62 for backscatter). Results by Eagleman et al. (ref. 6-60) show that the correlation is improved if the API estimate of soil moisture is extended over 10 days.

Another area in which large changes in backscatter and emission were observed was the Great Salt Lake Desert in Utah. Brightness changes of approximately 70 K between the surrounding terrain and the desert were observed by the S193 sensor at a frequency of 13.9 GHz (fig. 6-54), by the S194 sensor at 1.4 GHz (fig. 6-55), and by the Nimbus-5 radiometer at 19.35 GHz. The Nimbus-5 spacecraft had passed over the area many times in 1972 and 1973. Corresponding large anomalies in backscatter are indicated in figure 6-53. To explain this large change in emission and backscatter over an apparently dry and smooth region, a two-layer surface model was assumed in which the low emission and the large backscatter could be associated with a subsurface brine layer having a dielectric constant considerably larger than that of the surrounding area. This model was based on the history of the region, which was originally covered by Lake Bonneville. The measurements indicated that the thickness of the dry surface layer may vary from 1 m to 10 cm over the Great Salt Lake Desert.

The large uniform forest and savanna-type areas in Brazil provided an opportunity to investigate the effect of different biomes on microwave radiation and scatter. The S193 backscatter pattern delineated the boundary between the relatively wet rain forests and the dryer savanna and thornbush region. A pseudoimage signature of the region obtained at VV and HH antenna polarizations is shown in figure 6-56. These detailed investigations have demonstrated that soil moisture is the most significant influence in terrain microwave emission and backscatter and that soil moisture may mask the roughness features of the observed terrain.

The S194 radiometer observations over water surfaces were evaluated by Hollinger and Lerner (ref. 6-61) to determine the response of the radiometer to various oceanographic parameters. A rigorous and systematic method was developed to compute the expected antenna temperature and compare it with the measured values.
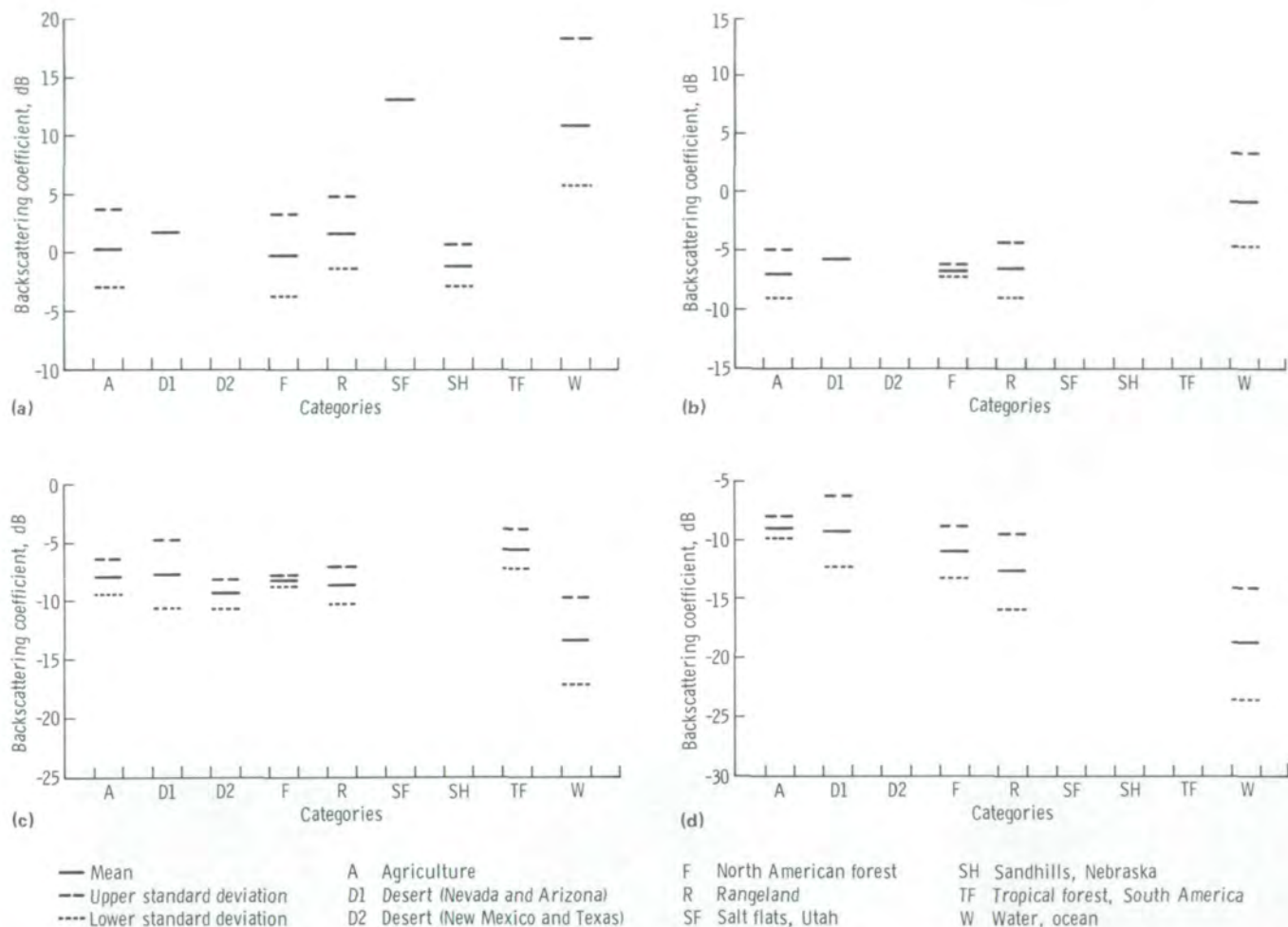
FIGURE 6-53.—Comparison of backscattering coefficient for various terrain categories at four incidence angles from Skylab 2 and 3 data obtained using the S193 scatterometer and VV antenna polarization. (a) $\theta = 1.5°$. (b) $\theta = 17°$. (c) $\theta = 33°$. (d) $\theta = 46°$.

The antenna temperature T_A was obtained from

$$T_A = \frac{A_e}{2K} \int \left(I_t I_a + Q_t Q_a + U_t U_a + V_t V_a \right) d\Omega \quad (6-21)$$

where K is Boltzmann's constant, A_e is the effective antenna area, I_t, Q_t, U_t, and V_t are the Stokes parameters of the total radiation, I_a, Q_a, U_a, and V_a are the Stokes parameters of the antenna pattern in the proper reference frame, and Ω is the solid angle over which the integration is performed.

The use of the Stokes parameters in equation (6-21) permits the cross-polarized components of the emitted, reflected, and atmospheric radiation to be simply summed and then to interact directly with the antenna polarization characteristics. A computer program was developed to compute the Stokes parameters as a function of the oceanographic and instrumental parameters in several steps.

First, the dielectric constant of seawater was computed as a function of radiometer frequency, sea-surface temperature, and salinity. From the computed dielectric values, the horizontal and vertical Fresnel reflection coefficients for water as a function of incidence angle were determined. The Fresnel reflection coefficients
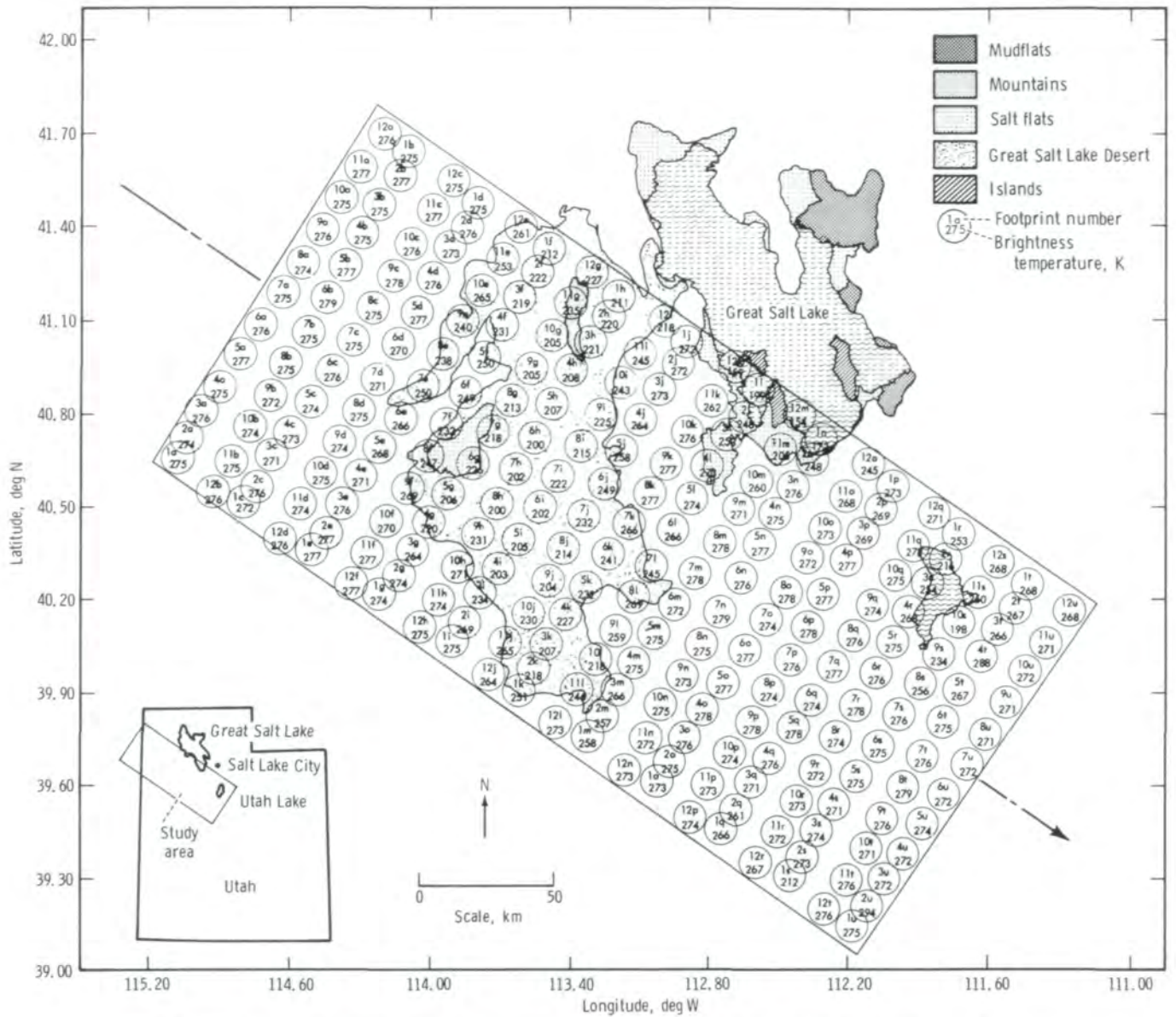
FIGURE 6-54.—S193 radiometer (13.9 GHz) footprints over the Great Salt Lake Desert, Utah (June 5, 1973).

were then modified to account for the surface roughness by using the empirical relation for differential brightness temperature

$$\Delta T_B = 0.134 U f^{1/2} \tag{6-22}$$

where U is the windspeed in knots and f is the frequency in gigahertz.

The Stokes parameters of the emitted and reflected components were then obtained by multiplying the proper combination of horizontal and vertical reflection coefficients by the equivalent black-body radiation. For

FIGURE 6-55.—S194 (1.4 GHz) brightness temperature as a function of distance from the center of the footprint over the Great Salt Lake Desert, Utah.
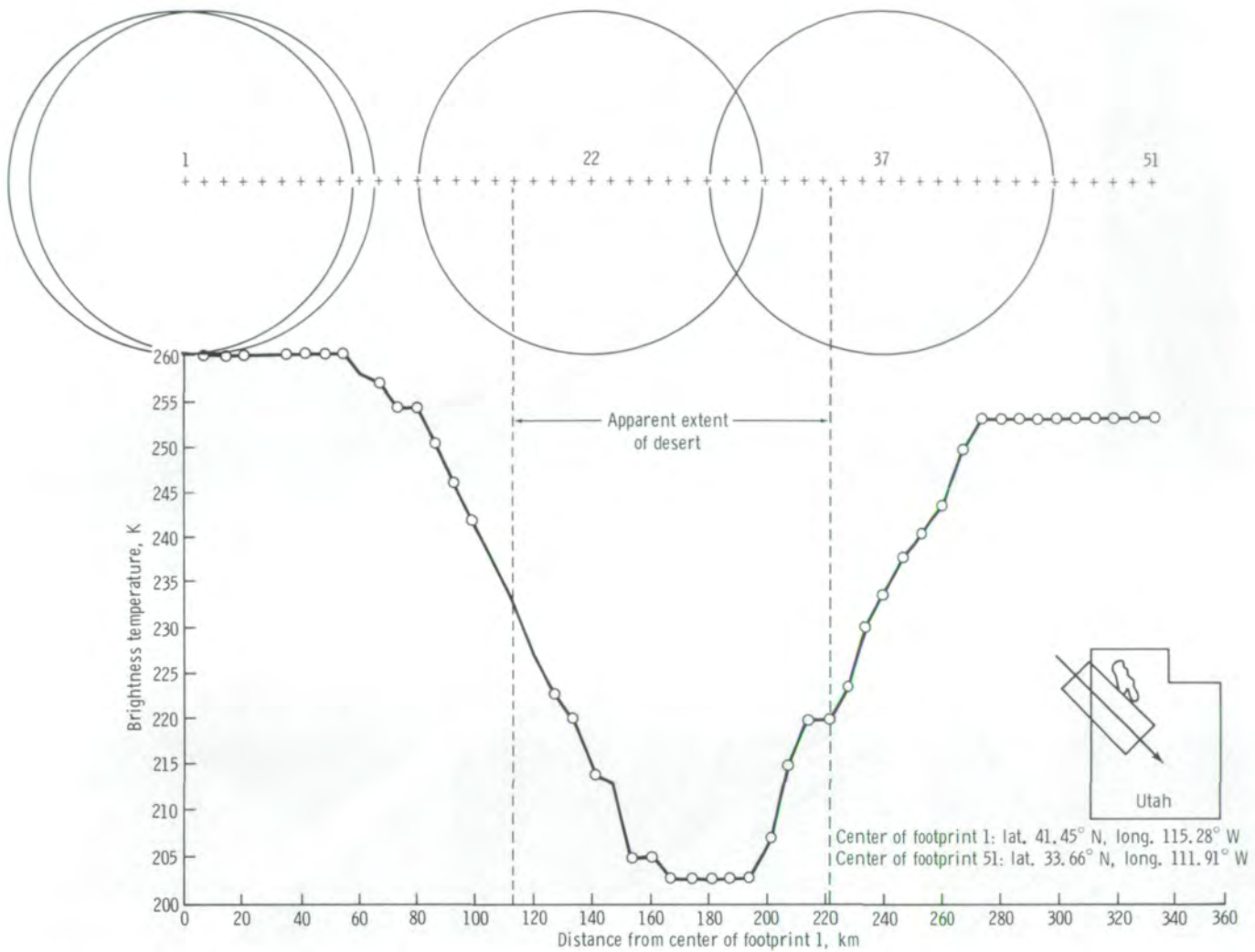
the emitted component, the black-body radiation is obtained from the Rayleigh-Jeans approximation to Planck's black-body radiation law.

The sky radiation needed for the determination of the reflected component of the Stokes parameters was separately computed from simplified atmospheric models. For this purpose, the absorption coefficients for oxygen, water vapor, and liquid water were determined as a function of frequency and then integrated

along the path of propagation to obtain both the downward-looking and the upward-looking radiation. The resultant values were then used to compute the reflected and atmospheric Stokes parameter components as well as the atmospheric attenuation. A final step in the program transformed the satellite coordinate system of the antenna pattern to the coordinate system of the observed surface so that the integration shown in equation (6-21) could be performed.
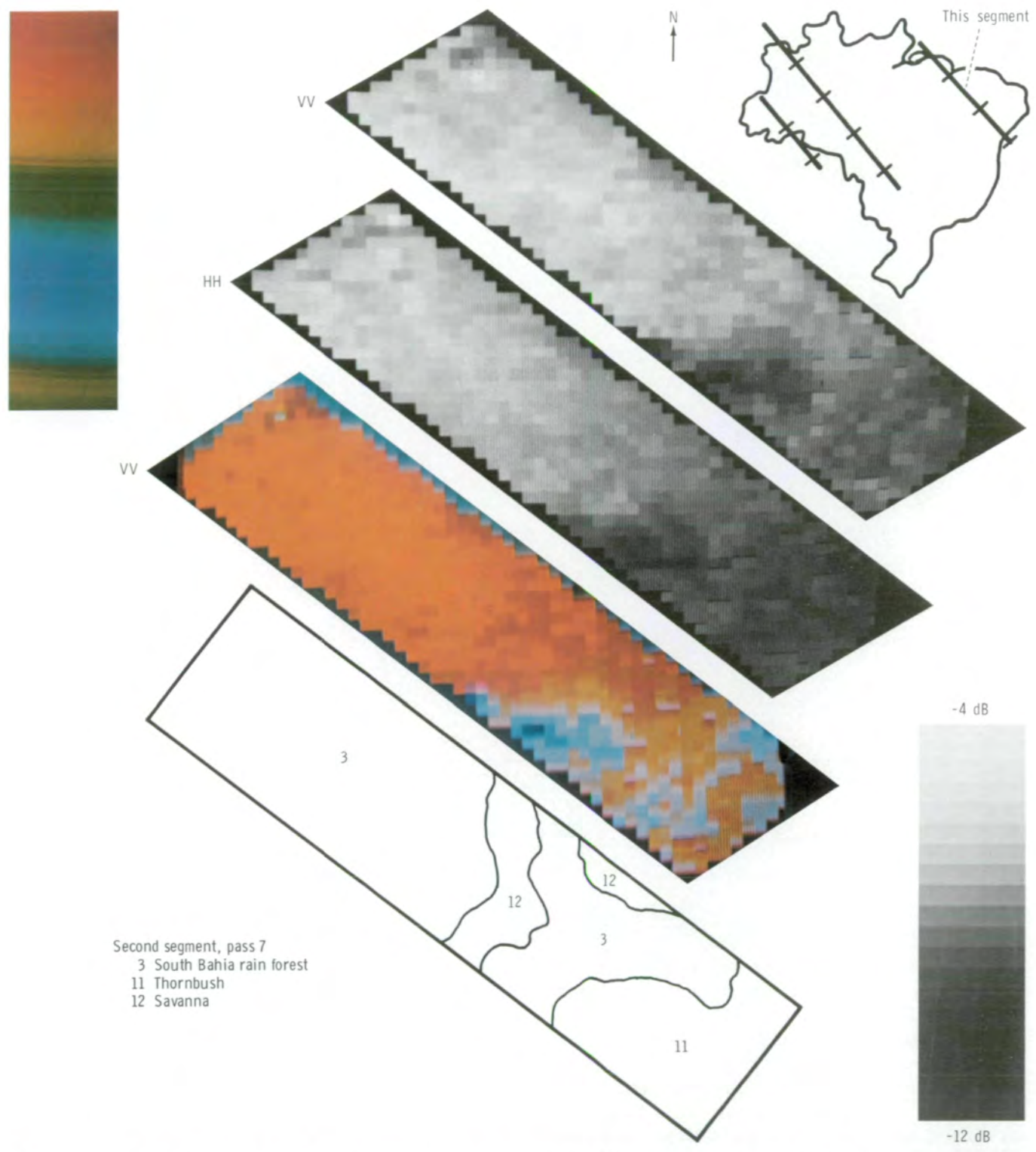
FIGURE 6-56.—Pseudoimages produced from backscatter response with crosstrack-contiguous, pitch 29° mode of S193 operation over Brazil.

Second segment, pass 7
  3 South Bahia rain forest
  11 Thornbush
  12 Savanna

The integration was made by mapping the S194 antenna beam pattern ($\theta_{3\,dB} = 15°$) by a grid of 1728 points out to 41° off-nadir so as to include the major side lobes. The height, the longitude, and the latitude at nadir were used as reference points for each observation; then, the position within the antenna beam was computed for every 10° in azimuth and 0.5° nadir angle to a maximum of 18°, and every 2° nadir angle to a maximum of 41°. For mixed land and water surfaces, each point was then identified as being on either land or water and the inputs to the models were adjusted accordingly. The land radiation was obtained from S194 measurements when land was known to fill the antenna beam completely. A separate program designed to compute the contribution of sunglint as a function of Sun elevation angle and windspeed was used primarily to eliminate extreme data points.

The S194 radiometer measurements were calibrated over three areas characterized by calm seas (windspeed $U < 2.6$ m/sec (5 knots)), minimum atmospheric loss, and availability of very good ground-truth data (passes 9 and 23). Using this calibration, the computed and measured antenna temperatures for all data (31 passes) were compared. The mean value of the difference is -0.0035 K with a standard deviation of 1.3 K. The small resultant error indicated that the theoretical relationships between the brightness temperature and salinity, sea-surface temperature, and windspeed could be directly used to predict the 21-cm radiometer sensitivity to these parameters.

The evaluation of the RADSCAT performance as a wind sensor over the ocean required the development of new techniques and models to provide the best estimate of the windspeed for a given measured value of the normalized radar cross section. Although previous theoretical and experimental investigations had indicated that the measured radar cross section is related to the sea-surface roughness and that the surface roughness in turn can be related to the surface windspeed, considerable scatter in the data precluded the establishment of quantitative relationships. The S193 RADSCAT observations provided, for the first time, a large data base, a wide range of wind conditions, and different instrumental and geometric configurations (polarization and incidence angles) so that the methods of statistical analysis could be effectively used.

The basic approach as used by Cardone et al. (ref. 6-62) was relatively simple. The values of the measured

backscatter coefficients as a function of position and time were accumulated and compared with the corresponding surface-truth windspeed values. Then, using a theoretical relationship between backscatter and windspeed, the best-fit relationship between the two parameters was established. The implementation of this approach, however, was much more complex. In addition to the accumulation and evaluation of the large amount of data, the data had to be stratified according to quality and quantity, and according to the range of windspeed and windspeed direction, so that more meaningful and accurate relationships could be derived.

Because the quality of the conventional sea-surface-truth windspeed values was known to be highly variable, a special effort was made to improve the estimate of the wind vector at a given location and time by utilizing all available data sources as near to the location and time of the Skylab pass as possible. The wind data were classified according to quality (obtained from aircraft, weather ships, transient ships, etc.), and special models were used depending on the kind of weather systems and locations.

The analysis for Hurricane Ava illustrates the techniques used to acquire regional wind-field data. Beginning with the launch of Skylab, a systematic search was made for weather disturbances near the Skylab groundtrack to provide a large range of windspeeds for data interpretation. In early June 1973, it was apparent that a tropical storm would develop into a hurricane off the southwest coast of Mexico and that it would intersect with a Skylab pass on June 6. Preparations for obtaining S193 measurements were made, and the storm was tracked by U.S. Air Force aircraft. The National Oceanographic and Atmospheric Administration (NOAA) aircraft used in support of the Skylab observations was dispatched to Acapulco, Mexico, to fly through the eye of the hurricane on June 6, the day of the expected Skylab pass. The measurements made by the aircraft (fig. 6-57) were then used directly as input boundary conditions to a hurricane model described by Cardone et al. (ref. 6-62) to derive a first estimate of the streamline-isotach distribution of the wind field. The modeled wind field was then refined by including all ship reports and data from other aircraft near the hurricane. The resultant composite analysis of the surface wind field is shown in figure 6-58. The solid lines (streamlines) are parallel to the wind direction, and the dashed lines (isotachs) are contours of constant
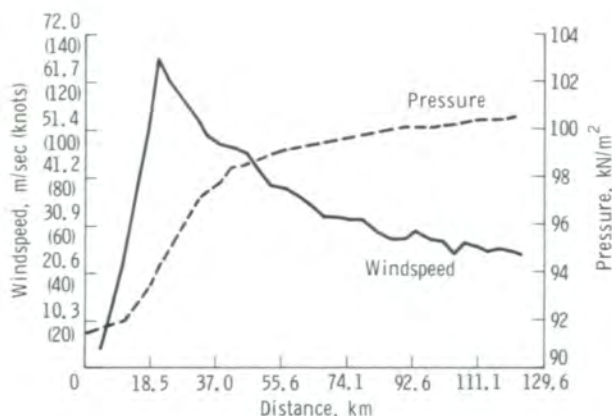
FIGURE 6-57.—Variation of flight-level windspeed and pressure (extrapolated to surface pressure) at an altitude of 3048 m (10 000 ft) during the NOAA C-130 aircraft penetration of Hurricane Ava, June 6, 1973.

windspeed. The circles indicate the position of the cells observed by the RADSCAT instrument. The wind vector at each position can be obtained directly from the chart by proper interpolation.

The backscatter coefficients were derived separately for each cell and time, corrected for atmospheric attenuation as obtained from the simultaneous radiometer measurements, and cataloged for each polarization and incidence angle. All measurements were referred to the five nominal incidence angles by correcting the values of the backscatter coefficients for small deviations from the nominal angles.

To establish the dependency of the backscatter coefficients on windspeed or of the windspeed on the backscatter coefficients, two methods were used. In the first method, all backscatter values were transformed to upwind direction by using the measured effects of wind direction (by the Advanced Applications Flight Experiment RADSCAT Program) as a conversion factor. Then, using the formal power relation obtained from an updated theory of backscatter, which included the effects of wind direction, a regression analysis was performed to minimize the variance between the predicted radar wind velocity U_r and the meteorological wind velocity U_m. The relation used in the analysis was expressed in both logarithmic and power law form as

$$\left. \begin{aligned} \log U_{(m/sec)} &= b_0 + b_1 \sigma^\circ_{(dB)} \\[2ex] U_{(knots)} &= \beta_0 \sigma^{\circ\,\beta_1} \end{aligned} \right\} \quad (6\text{-}23)$$

The computed coefficients b_0, b_1 and β_0, β_1 for predicting the windspeed from the backscatter are shown in table 6-VI for the log model and in table 6-VII for the power law model, respectively. These tables show the sensitivity of calculations of the windspeed to changes in radar cross section as a function of both polarization and incidence angle, and indicate that the largest changes in backscatter for a given change in windspeed occur between incidence angles of 30° and 50°. The inverse of the parameters was also computed and showed that better agreement was obtained for the power law because of more uniform weighting of the lower windspeeds.

In the second method, the predicted radar wind is expressed as a combination of upwind, downwind, and crosswind velocity components and the aspect angle (the angle between the wind direction and the antenna direction). By an iterative method using both polynomial and power law relations, an effective power law is obtained for determining new coefficients, which are now functions of the aspect angle. The nonlinear relations used in the iteration process indicated that the deviations could be improved if the data were stratified for different wind-range intervals. The data were further stratified according to the source of the surface truth, such as weather research ships (type A) or aircraft, and transient ships (types B, C, and D), and were used for final error analysis.

To confirm the consistency of the results, the variance of the surface-truth values and the radar values of windspeed were first separately computed. The surface-truth windspeed variance was obtained using a withheld weather ship analysis, in which the value measured by the weather ship was assumed to be the true windspeed. The variance of the radar windspeed values was obtained by comparing the windspeed values obtained at the four different polarizations for each cell. It was then assumed that, if the results were consistent, the total variance of the difference between the meteorological wind and the radar wind should be the sum of the two variances. The results are shown in table 5-III in section 5. Residual variances are generally obtained only when the sample sizes are small. This finding increases the confidence that the assumed

FIGURE 6-58.—Composite streamline-isotach analysis for Hurricane Ava, June 6, 1973. The streamlines (solid) show the direction of airflow. The isotachs (dashed lines) show windspeed in meters per second (knots). ⟶
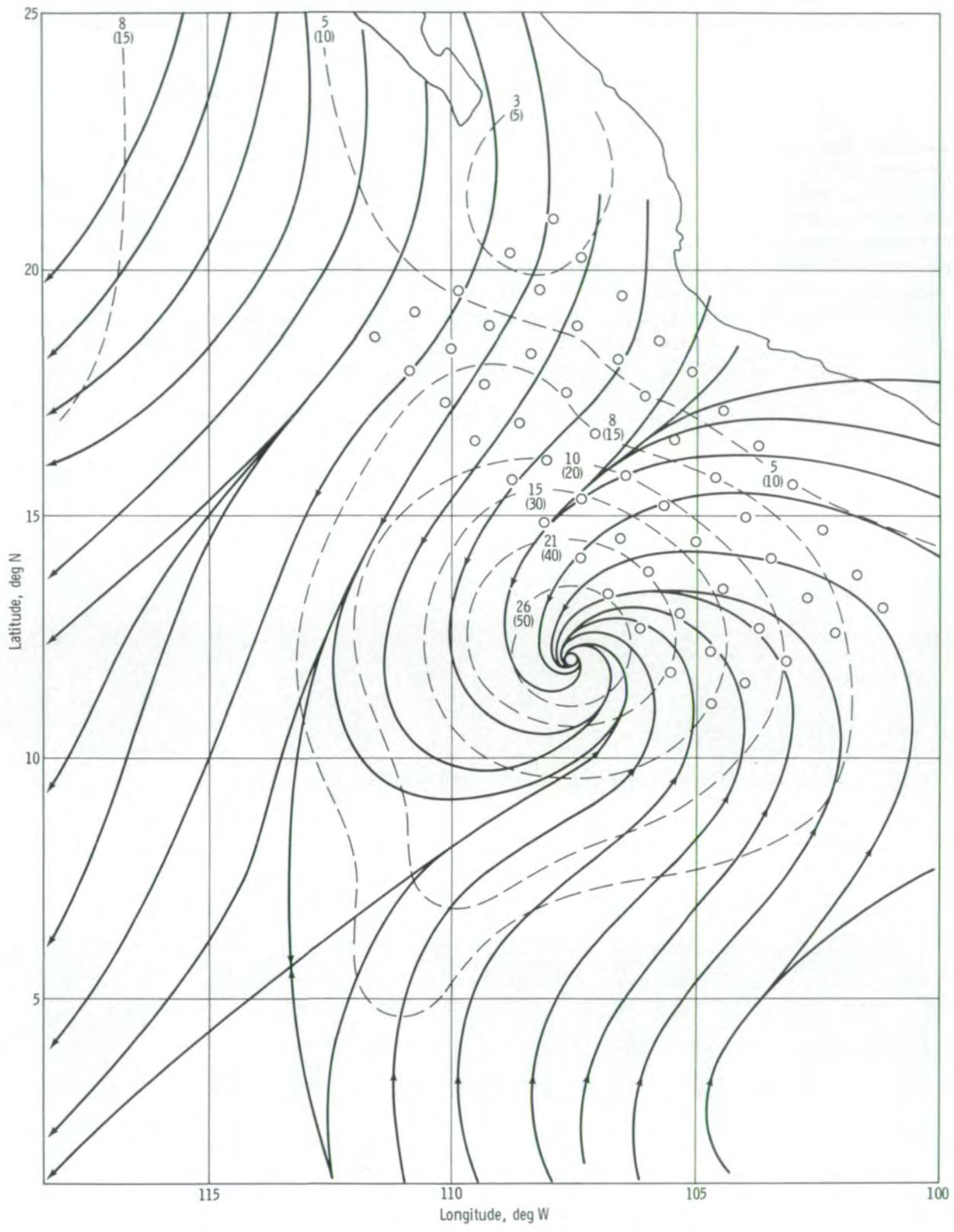
models and techniques used are valid and that the radar values, which have a constant variance of 0.98 m/sec (1.9 knots) squared, are generally more reliable than the values obtained from ship observations.

The brightness temperature and backscatter anomalies measured by the S193 over a groundtrack in Texas on June 5, 1973, were related to the 5-day API by Moore et al. (ref. 6-59) as previously described. The 5-day API is a convenient moisture parameter because it requires only the daily precipitation, which is routinely reported by the weather stations. However, it is known that the actual soil moisture content may be considerably different from the value predicted by the 5-day API

because it neglects the effects of the soil type and the runoff routing on the surface.

To establish a more accurate ground-truth base of soil moisture for both S193 and S194 measurements, Eagleman et al. (ref. 6-60) determined the soil moisture directly along the groundtrack of the satellite. Soil samples, collected at 7-km intervals near the time of the Skylab overflight for each 2.5-cm layer down to a depth of 15 cm, were weighed and dried in the laboratory, and the soil moisture (in percentage by weight) for each location and layer was determined. To compare the Skylab measurements with the ground-truth soil moisture values, the sampled soil moisture values were

TABLE 6-VI.—*Linear Regression Estimates of Backscatter Coefficients* [a]

$$[\log U_{(m/sec)} = b_0 + b_1 \sigma^\circ_{(dB)}]$$

Nadir angle, deg	Polarization (b)	b_1	Estimated standard error of b_1	b_0	Standard error of b_0	No. of observations
50	VV	0.0290	0.0027	1.387	0.159	124
	HH	.0301	.0025	1.541	.154	121
	VH	.0311	.0025	1.786	.150	110
	HV	.0322	.0026	1.811	.149	114
43	VV	.0260	.0023	1.279	.149	134
	HH	.0277	.0023	1.389	.144	133
	VH	.0317	.0023	1.762	.133	126
	HV	.0303	.0023	1.721	.137	127
32	VV	.0342	.0030	1.236	.134	147
	HH	.0345	.0031	1.271	.136	146
	VH	.0238	.0021	1.445	.133	141
	HV	.0276	.0022	1.545	.128	140
17	VV	.0827	.0100	.731	.190	146
	HH	.0706	.0098	.737	.198	145
	VH	.0905	.0116	2.164	.195	136
	HV	.0887	.0112	2.131	.195	141
1	VV	−.1163	.0179	2.368	.218	134
	HH	−.1148	.0177	2.349	.223	140
	VH	−.1425	.0167	.274	.208	136
	HV	−.1383	.0158	.291	.206	136

[a] The scattering coefficients were adjusted to upwind direction and the nadir angles listed before regression.

[b] VV, vertical transmit, vertical receive; HH, horizontal transmit, horizontal receive; VH, vertical transmit, horizontal receive; HV, horizontal transmit, vertical receive.

interpolated both in time and space by using the climatic water-balance technique developed by Thornthwaite and Mather (ref. 6-63). In this method, the potential evapotranspiration rate is estimated from the mean daily temperature and the value is adjusted to the day of the year and to the latitude. The actual evapotranspiration is then computed from the estimated potential evapotranspiration rate, the precipitation, and the available soil moisture, which depends on the soil type at the given location. Contour maps of the resultant soil moisture, such as that shown in figure 6-59(a), were then produced.

Similar distributions of S193 brightness temperature

TABLE 6-VII.—*Power Law Regression Estimates of Backscatter Coefficients*

$$[U_{(knots)} = \beta_0 \sigma^{\circ \beta_1}]^a$$

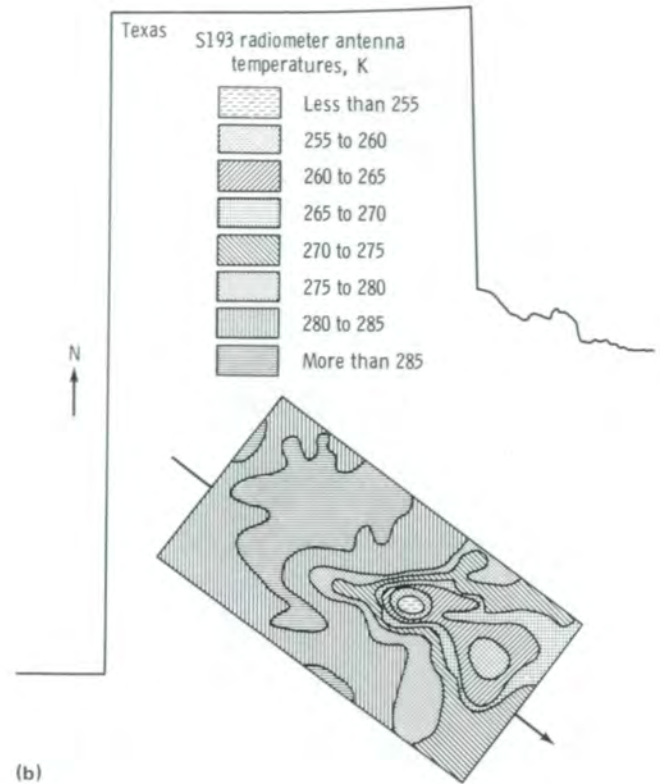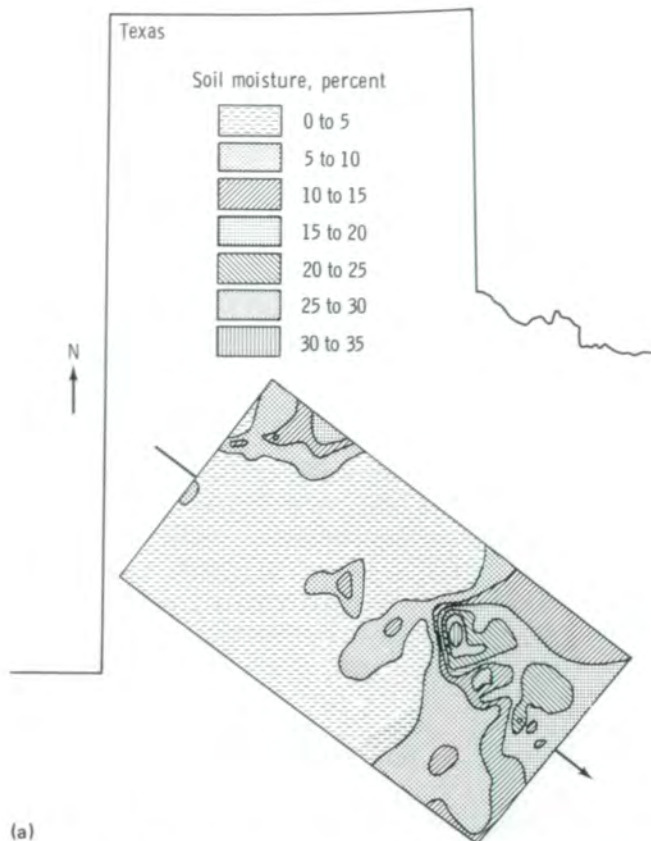| Nadir angle, deg	Polarization (b)	β_0	β_1	Number of cases	rms difference
50	VV	82.87	0.4196	124	5.5
	HH	102.5	.3748	121	5.2
	VH	137.2	.3263	110	4.4
	HV	140.9	.3318	114	4.4
43	VV	61.64	.3881	134	5.2
	HH	84.40	.4000	133	4.9
	VH	136.1	.3414	126	4.1
	HV	134.0	.340	127	4.2
32	VV	36.41	.3594	147	3.8
	HH	42.55	.3847	146	3.9
	VH	75.90	.2881	141	3.7
	HV	75.75	.2878	140	3.7
15	VV	11.82	.6284	146	4.7
	HH	12.16	.484	144	5.2
	VH	279.8	.8778	136	4.9
	HV	206.4	.7924	141	5.0
0	VV	373.2	−1.070	134	4.7
	HH	529.3	−1.182	140	4.7
	VH	4.250	−1.345	136	4.7
	HV	3.571	−1.533	136	4.2

[a]1 knot = 0.5144 m/sec.

[b]VV, vertical transmit, vertical receive; HH, horizontal transmit, horizontal receive; VH, vertical transmit, horizontal receive; HV, horizontal transmit, vertical receive.

and backscatter were derived and are shown for the same test site in figures 6-59(b) and 6-59(c), respectively. The large footprint of the S194 radiometer observations did not permit presentation of such a high-resolution distribution, and a comparison between the S194 data and the ground-truth soil moisture was obtained by weighted averaging of the soil moisture content within the footprint.

The results of the analysis of five passes indicate that the highest correlation was obtained between the 21-cm (S194) brightness temperature and ground-truth soil moisture (fig. 6-60) because the 21-cm radiometer is more sensitive to soil moisture than the 2.2-cm RADSCAT and is less sensitive to surface roughness and atmospheric variations. The equivalent comparison between the 2.2-cm brightness temperature and soil moisture is shown in figure 6-61 for the Texas test site used by Moore (ref. 6-59). The correlation increases, in this case, from −0.76 with a 5-day API to −0.91 with the direct soil moisture content determination. A comparison of soil moisture with the backscatter measurements, however, shows a reduced correlation.

A comparison of the different sensor sensitivities to soil moisture is shown in figure 6-62 for the same size resolution cell. The poor response of the backscatter measurements is believed to be due to the large incidence angle (30°), at which roughness effects dominate the response. Other significant results of Eagleman's analysis indicate that horizontal polarization radiometry at 2.2 cm is less sensitive to soil moisture than is vertical polarization, that the best correlation is obtained with the top 2.5-cm-layer soil moisture, and that the height of the vegetation cover may modify the soil moisture measurements.

The performance of microwave sensors of soil moisture as a function of incidence angle was investigated by Stucky (ref. 6-21). For this purpose, the June 11 pass over Texas, made using sensors that operated in the intrack-contiguous mode, was selected. The soil moisture parameter was expressed as the API for 11 and 6 days with a recession value (i.e., loss of moisture due to evapotranspiration and subsurface runoff) of 0.9. The daily precipitation was limited to 5 cm because it was assumed that any excess value would produce runoff and would not contribute to soil moisture. Interpolation between station API's and the API's at the footprint center was obtained by a distance-dependent circular weighting function that combined at least three station API's.

(a)

Texas

Soil moisture, percent

- 0 to 5
- 5 to 10
- 10 to 15
- 15 to 20
- 20 to 25
- 25 to 30
- 30 to 35

N ↑

(b)

Texas   S193 radiometer antenna temperatures, K

- Less than 255
- 255 to 260
- 260 to 265
- 265 to 270
- 270 to 275
- 275 to 280
- 280 to 285
- More than 285

N ↑

(c)

Texas

S193 scatterometer return, dB

- More than -8.0
- -8.0 to -8.5
- -8.5 to -9.0
- -9.0 to -9.5
- -9.5 to -10.0
- -10.0 to -10.5
- Less than -10.5

N ↑

FIGURE 6-59.—Geographic distribution of various parameters over the Texas test site, June 5, 1973 (Skylab 2 pass 5). (a) Soil moisture content. (b) S193 radiometric temperature. (c) S193 scattering coefficient.
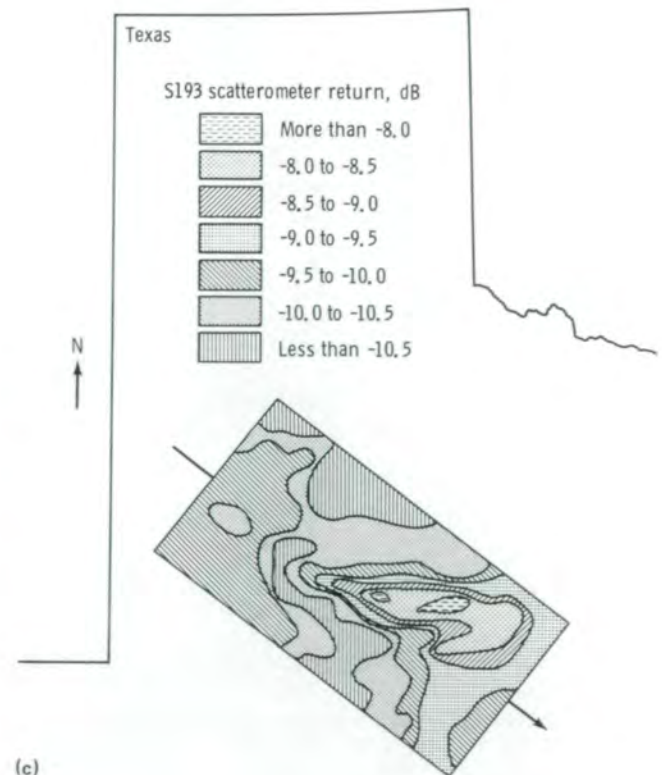
A relatively high correlation of soil moisture with 2.2-cm brightness temperature was obtained only for small incidence angles and for the 10-day API (fig. 6-63). The 6-day API neglected significant contribution to soil moisture of earlier precipitation, and at the larger angles, the effect of surface roughness and the atmospheric variations became more significant. Correlation coefficients between brightness temperature and backscatter decreased linearly with increasing incidence angle, starting with a maximum of -0.95 at $2°$ nadir angle.

McFarland (ref. 6-21) used the concurrent S194 measurements for comparisons with computed API's.
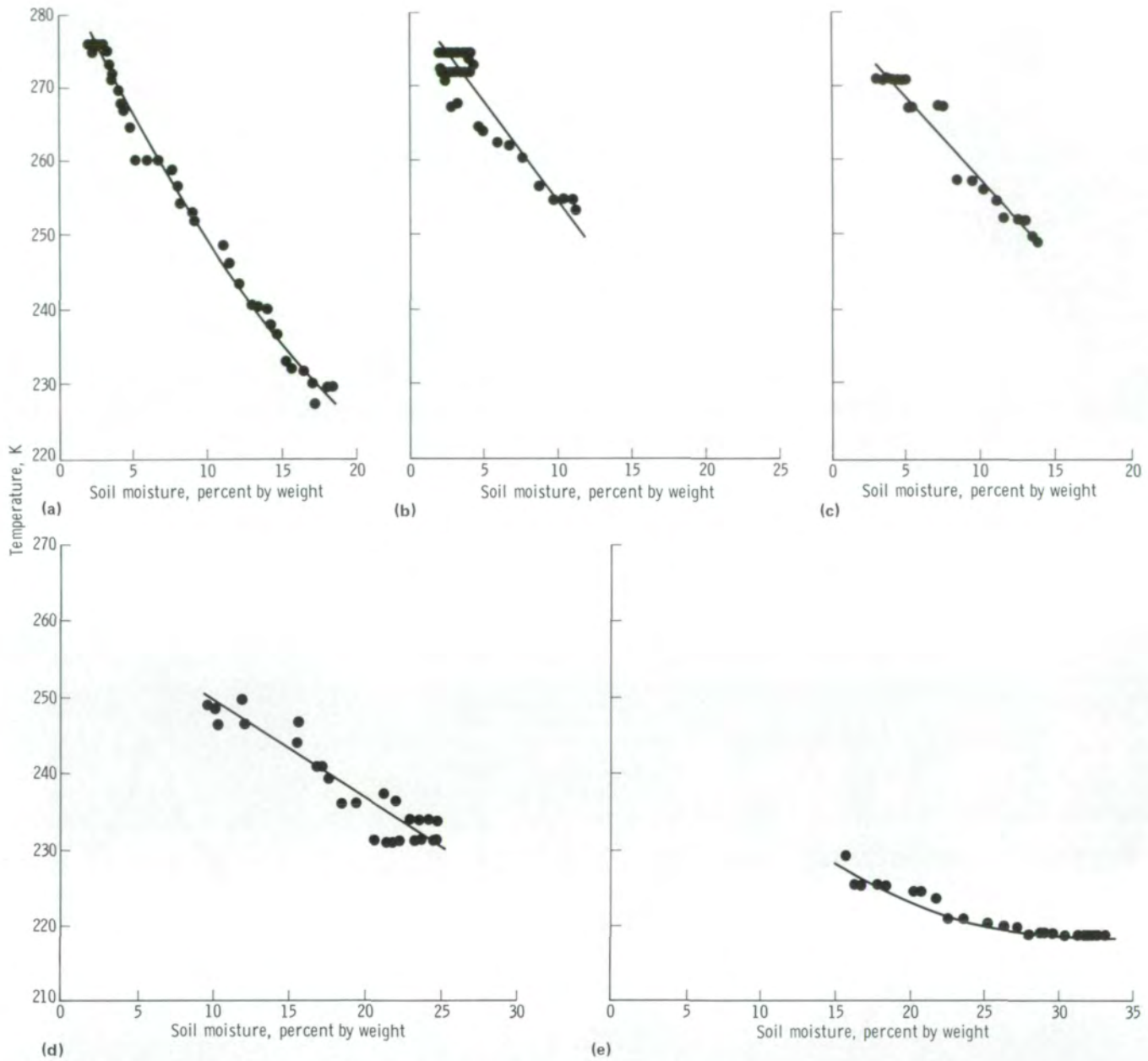
FIGURE 6-60.—The relationship between S194 brightness temperature and soil moisture content for five separate data sets. The correlation coefficient r is shown for each set. (a) Texas, pass 5; $r = -0.99$. (b) Texas, pass 16; $r = -0.96$. (c) Texas, pass 38; $r = -0.98$. (d) Kansas, pass 10; $r = -0.95$. (e) Kansas, pass 38; $r = -0.97$.

Excellent agreement was obtained with the 11-day API as shown in figure 6-64, but another pass showed anomalies that could be correlated with irrigation and cultivation. Thus, although the 11-day API represents a good estimate of soil moisture, there are areas in which a remote sensor such as the S194 would produce a more accurate determination of the true soil moisture content.
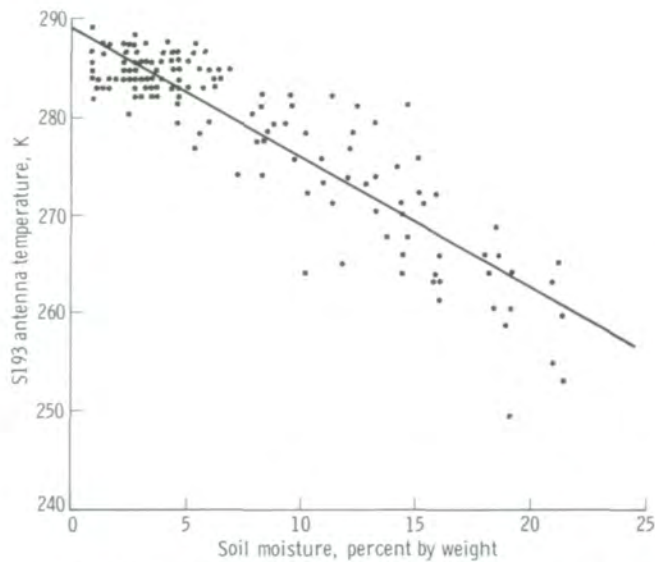
FIGURE 6-61.—S193 antenna temperature as a function of soil moisture content for the Texas site, pass 5, at 29.4° pitch and VV polarization ($r = -0.91$).
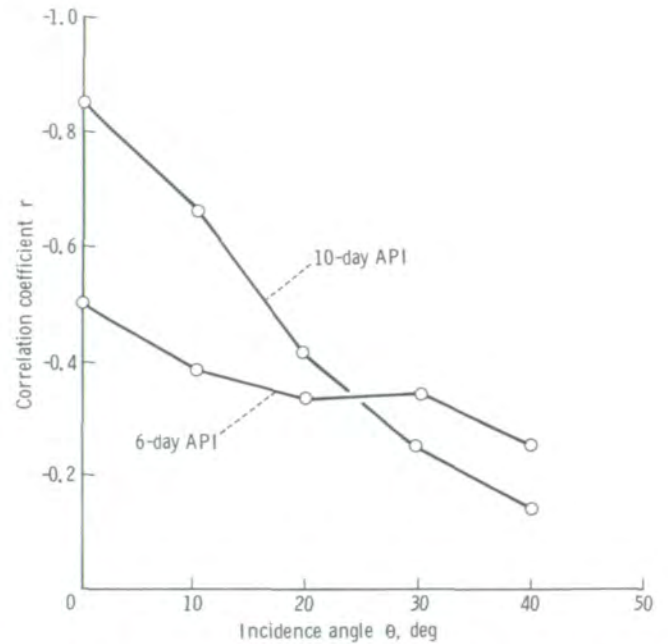
FIGURE 6-63.—Correlation of S193 apparent brightness temperatures with the 6- and 10-day weighted API sets for five incidence angles.
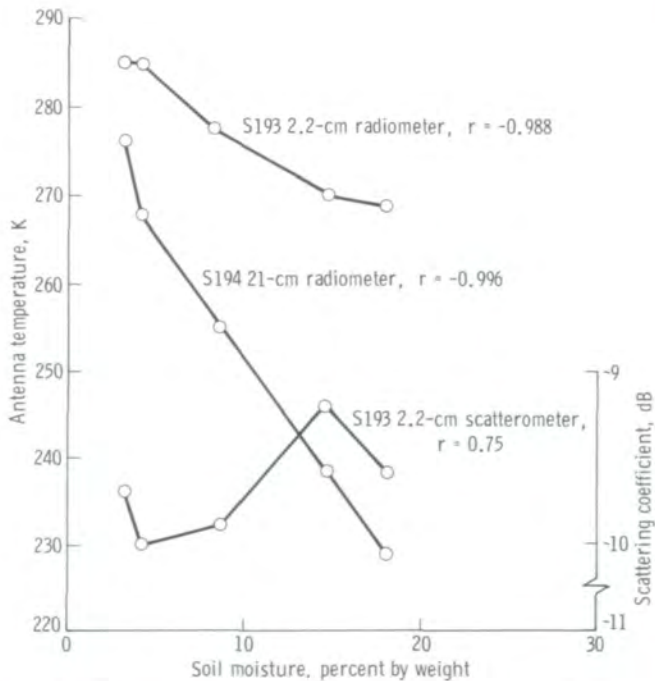

FIGURE 6-62.—A comparison of the response of the two radiometers and the scatterometer to the soil moisture content when averaged for the same size resolution cell.
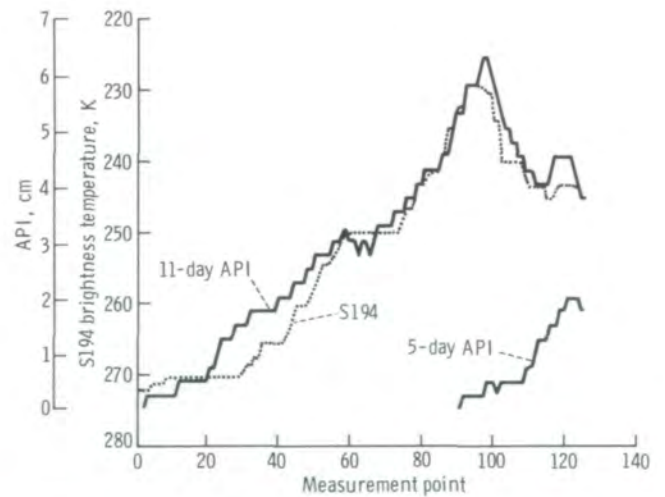

FIGURE 6-64.—S194 L-band brightness temperature and footprint average of 11-day API for June 11, 1973. The 5-day API data are shown for comparison.

SUMMARY

The results of the Skylab EREP photographic experiment demonstrate that sensitometrically controlled, multiband photography constitutes a powerful tool for investigating Earth resources problems. The multiband characteristics of the photographic data were crucial for both visual and machine analysis of the data. The three most desired improvements in the photographic data are larger scales, better resolution, and more frequent coverage. The larger scales would make machine analysis of the data simpler because image densitometry of an object becomes easier as the image size of the object increases. Improved resolution would assist visual and machine interpretation and increase analysis accuracy. The desire for more frequent and repetitive coverage is not endemic to the photographic experiment; investigators using other sensors also expressed this need. However, the demonstrated ability to handle atmospheric and processing differences occurring between coverage dates has improved the potential value of multidate analyses and has undoubtedly led to increased requests for such coverage. Image digitization and computer analysis of photographic data offer perhaps the most significant and adaptable analysis approach for complex, multidate problems, and realization of the potential of this form of image analysis is only beginning.

The electrical recording of multichannel data from the S192 Multispectral Scanner enabled use of a wide range of signal-processing techniques and led to several developments in data manipulation by which the advantages inherent in multispectral remote sensing can be applied. In some cases, single bands outside the photographic region showed sufficient contrast and provided information for a particular use. Examples include the use of the 1.2- to 1.3-μm band for correlation to electrical conductivity or salinity, the thermal band to help differentiate commercial-industrial-residential land uses from natural vegetated areas, and the 1.55- to 1.75-μm band to separate waterfowl habitats from other land features.

The digital format enabled machine enhancement of detail by contrast-stretching a particular range of signals to match the display medium. By color translation and by overlaying images from two or more bands, improvements in discrimination of features in water, geological, and agricultural scenes were demonstrated.

The tape recording of the several channels also permitted the ratioing of a pair of channels that aided in the separation of ferric, ferrous, and nonferrous classes of materials. The ratio of spectral bands in the red/green region resulted in better correlation with suspended solids in reservoirs than either individual band. The ratio of infrared/red spectral bands was found useful in correlating soil moisture differences in the presence of partial vegetation cover.

The full potential of the multispectral data set was realized when computer analysis of the entire spectral range was performed. Subsets of optimum spectral bands were chosen by various statistical decision algorithms, and computer recognition of objects by using both supervised and unsupervised classification techniques was achieved with varying degrees of success. Modified clustering techniques led to reduced machine time, higher classification accuracies, and improved man/machine interactions.

Classification accuracies were improved by using different preprocessing rules. Atmospheric effects in the data were removed to improve accuracies, and atmospheric effects on the choice of channels were explored. Mixture-processing techniques were used to improve results whenever the resolution element contained a mixture of objects such as found near boundaries between classes. Signature-extension schemes were explored and information about elevation, aspect, and slope helped to improve recognition accuracies, particularly for scenes of mountainous regions. The use of statistical factor analysis in N-dimensional space, where N is the number of spectral bands, was explored and found valuable in the enhancement of rock outcrop and dense vegetation.

The S192 data also were used in studies of urban microclimate and in vertical wind profile analyses. The value of multiband scanner data was demonstrated especially for bands beyond those now available in Landsat. These should be incorporated in future space sensors.

The S191 Infrared Spectrometer data were useful in obtaining information about the spectral transmission of the atmosphere and reflection characteristics of terrain classes. Ratios of spectral emissivities in the short- and long-wavelength bands are useful in differentiating basaltic rocks from dacite. The S191 data were used in the study of the ocean color spectrum. Results agreed well with measurements for wavelengths greater than

0.5 μm. More data on aerosol properties are needed to achieve similar results for wavelengths less than 0.5 μm.

The major objectives achieved by the EREP microwave investigators can be summarized in three areas: sensor performance evaluation, building of a data base for microwave sensor system design, and establishment of potential application areas.

The altimeter precision was validated, and methods for determining and correcting for pointing-angle and orbital errors were developed. Ocean radar cross sections for altimeter operation were determined with high precision, the electromagnetic reflection mechanism for both ocean and terrain was established, and measurements of terrain topography were shown to be feasible.

The scatterometer observations provided a large data base of backscatter coefficients as a function of surface reflecting and scattering properties, incidence angle, and polarization, and established the sensitivity of a scatterometer to windspeed for a large range of surface-truth windspeed values. Similarly, a large data base of brightness-temperature variations over the ocean and terrain was cataloged for different surface conditions, incidence angles, and polarizations. Theoretical relationships between variations of the physical ocean parameters of salinity, surface wind, and sea-surface temperature and the ocean brightness temperature were developed and verified with the S194 measurements. Potential application for determining soil moisture by long-wavelength radiometer observations was confirmed.

The results of the microwave investigations have both short- and long-term implications. The experience gained with the Skylab altimeter was immediately applied to the design and operation of the Geodetic Earth Orbiting Satellite C altimeter, which is now in orbit. Further refinements are planned for the Seasat altimeter (to be launched in 1978). The Seasat spacecraft will also include an improved version of a scatterometer that can determine both windspeed and wind direction.

The results of the Skylab altimeter terrain observations provide basic information for improved surface topography determination by altimetry if the altimeter sampling capability of the radar return is expanded. This concept is being considered for the Space Shuttle, which will orbit the Earth, and for unmanned spacecraft that will orbit the Moon and the planets.

The catalog of backscatter coefficients and brightness temperatures will help radar and radiometer designers to provide optimum microwave system performance for a variety of applications.

Finally, the availability of higher spatial resolution performance of passive microwave sensors at the longer wavelengths will enable significant global synoptic measurements of soil moisture content.

REFERENCES

6-1. Potter, A. E.; Grandfield, A. L.; and Williams, C. K.: Flight Performance of the Skylab Earth Resources Experiment Package. The Skylab Results, Advances in the Astronautical Sciences, vol. 31, pt. 2, William C. Schneider and Thomas E. Hanes, eds., American Astronautical Society (Tarzana, Calif.), 1975, pp. 605-633.

6-2. Pirie, Douglas M.; and Steller, David D.: California Coastal Processes Study. NASA CR-144489, 1975.

6-3. Barnes, James C.; Smallwood, Michael D.; and Cogan, James L.: Study to Develop Improved Spacecraft Snow Survey Methods Using Skylab/EREP Data. NASA CR-144388, 1975.

6-4. Szekielda, Karl-Heinz: Dynamics of Plankton Populations in Upwelling Areas. NASA CR-144480, 1975.

6-5. Piech, Kenneth R.; Schott, John R.; and Stewart, Kenton M.: S190 Interpretation Techniques Development and Applications to New York State Water Resources. NASA CR-144499, 1975.

6-6. Baldridge, Paul E.; Goesling, P. H.; et al.: Utilizing Skylab Data in On-Going Resources Management Programs in the State of Ohio. NASA CR-134938, 1975.

6-7. Yarger, Harold L.; and McCauley, James R.: Skylab Study of Water Quality. NASA CR-144505, 1975.

6-8. Gordon, Hayden H.; and Nichols, Maynard M.: Skylab MSS Versus Photography for Estuarine Water Color Classification. Water Color and Circulation Southern Chesapeake Bay, Part II. NASA CR-141404, 1975.

6-9. Welby, Charles W.; and Lammi, J. O.: Utilization of EREP Data in Geological Evaluation, Regional Planning, Forest Management, and Water Management in North Carolina. NASA CR-144104, 1975.

6-10. Hardy, Ernest E.; Skaley, J. E.; et al.: Enhancement and Evaluation of Skylab Photography for Potential Land Use Inventories. Part I and Part II. NASA CR-144473, 1975.

6-11. Colwell, Robert N.; Benson, Andres S.; et al.: Agricultural Interpretation Technique Development. NASA CR-144486, 1975.

6-12. Silva, Leroy F.: A Study of the Utilization of EREP Data From the Wabash River Basin. NASA CR-147412, 1976.

6-13. Gumerman, George J.; Hanson, John A.; et al.: The Hydrology of Prehistoric Farming Systems in a Central Arizona Ecotone. NASA CR-144492, 1975.

6-14. Plogg, F.; and Garrett, C.: Explaining Variability in Prehistoric Southwestern Water Control Systems. Paper presented at the 35th Annual Meeting of the Society for American Archeology (Mexico City, Mexico), 1970.

6-15. Langley, Philip G.; and Van Roessel, Jan: The Usefulness of Skylab/EREP S-190 and S-192 Imagery in Multistage Forest Surveys. NASA CR-147439, 1976.

6-16. Maul, George A.; Gordon, Howard R.; et al.: An Experiment to Evaluate Skylab Earth Resources Sensors for Detection of the Gulf Stream. NASA CR-147454, 1976.

6-17. Gilmer, David S.; and Work, Edgar A., Jr.: Utilization of Skylab (EREP) System for Appraising Changes in Continental Migratory Bird Habitat. NASA CR-147542, 1975.

6-18. Vincent, R.; Wagner, H.; Pillars, W.; and Bennett, C.: Assessments of Mapping Exposed Ferrous and Ferric Iron Compounds Using Skylab EREP Data. NASA CR-144504, 1976.

6-19. Vincent, R. K.; and Pillars, W. W.: Skylab S-192 Ratio Codes of Soil, Mineral, and Rock Spectra for Ratio Image Selection and Interpretation. Proceedings of the Ninth International Symposium on Remote Sensing of Environment, Environmental Research Institute of Mich. (Ann Arbor, Mich.), 1974, pp. 875-896.

6-20. Curran, Robert J.; Salomonson, Vincent V.; and Shenk, William: The Application of Satellite Data in the Determination of Ocean Temperatures and Cloud Characteristics and Statistics. NASA CR-147539, 1976.

6-21. Pitts, David E.; Sasaki, Yoshikazu; and Lee, Jean T., compilers: Severe Storm Environments: A Skylab EREP Final Report. NASA TM X-58184, 1976.

6-22. Phillips, T. L., ed.: LARSYS Version 3.1 User's Manual. Vol. 2. Laboratory for Applications of Remote Sensing, Purdue Univ. (West Lafayette, Ind.), 1973.

6-23. Swain, P. H.: Pattern Recognition: A Basis for Remote Sensing Data Analysis. NASA CR-130757, 1973.

6-24. Goetz, A. F. H.; Abrams, M. J.; et al.: Comparisons of Skylab and Landsat Images for Geologic Mapping in Northern Arizona. NASA CR-147503, 1976.

6-25. Sattinger, I. J.; Sadowski, F. G.; and Roller, N. E. G.: Analysis of Recreational Land Using Skylab Data. NASA CR-144471, 1976.

6-26. Nalepka, R. F.; Morganstern, J.; et al.: S-192 Analysis: Conventional and Special Data Processing Techniques. NASA CR-144506, 1975.

6-27. Simonett, David S.: Application of Skylab EREP Data for Land Use Management. NASA CR-147457, 1976.

6-28. Eberlein, R.; Vanderburg, G. L.; Rosenfeld, A.; and David, L. S.: Edge and Line Detection in ERTS Imagery: A Comparative Study. NASA CR-138963, 1974.

6-29. Anderson, Theodore W.: An Introduction to Multivariate Statistical Analysis. John Wiley & Sons, Inc., 1958.

6-30. Rao, C. R.: Linear Statistical Interference and Its Applications. John Wiley & Sons, Inc., 1965.

6-31. Swain, P. H.; Robertson, T. V.; and Wacker, A. G.: Comparison of the Divergence and B-Distance in Feature Selection. LARS Information Note 020871, Purdue Univ. (West Lafayette, Ind.), 1971.

6-32. Hoffer, Roger M.: Computer-Aided Analysis of Skylab Multispectral Scanner Data in Mountainous Terrain for Land Use, Forestry, Water Resource, and Geologic Applications. NASA CR-147473, 1975.

6-33. Thomson, F. J.: Machine Processing of S-192 and Supporting Aircraft Data: Studies of Atmospheric Effects, Agricultural Classifications, and Land Resource Mapping. NASA CR-144503, 1975.

6-34. Wiegand, Craig L.; Richardson, Arthur J.; et al.: Soil Salinity Detection. NASA CR-144403, 1975.

6-35. Hannah, John W.; Thomas, Garland L.; Esparza, Fernando; and Millard, J. J.: Planning Applications in East Central Florida. NASA CR-145415, 1975.

6-36. McMurtry, George J.; and Petersen, Gary W.: Interdisciplinary Applications and Interpretations of EREP Data Within the Susquehanna River Basin. NASA CR-147541, 1976.

6-37. Selzer, Robert H.: The Use of Computers to Improve Biomedical Image Quality. Proceedings of Fall Joint Computer Conference, vol. 33, pt. 1, Dec. 1968, pp. 817-834.

6-38. Horwitz, Harold M.; Nalepka, Richard F.; Hyde, Peter D.; and Morganstern, James P.: Estimating the Proportions of Objects Within a Single Resolution Element of a Multispectral Scanner. Proceedings of the Seventh International Symposium on Remote Sensing of Environment, Environmental Research Institute of Mich. (Ann Arbor, Mich.), 1971, pp. 1307-1320.

6-39.   Poulton, Charles E.; and Welch, Robin I.: Plan for the Uniform Mapping of Earth Resources and Environmental Complexes From Skylab Imagery. NASA CR-144484, 1975.

6-40.   Houston, R. S.; Marrs, R. W.; and Borgman, L. E.: Multidisciplinary Study of Wyoming Test Sites. NASA CR-147719, 1975.

6-41.   Haefner, Harold: Snow Survey and Vegetation Growth in the Swiss Alps. NASA CR-147395, 1976.

6-42.   Goldman, Gary C.; and Horvath, Robert: Oil Pollution Detection and Monitoring From Space Using Skylab. NASA CR-144502, 1975.

6-43.   Trumbull, James V. A.: The Utility of Skylab Photointerpreted Earth Resources Data in Studies of Marine Geology and Coastal Processes in Puerto Rico and the Virgin Islands. NASA CR-147437, 1975.

6-44.   Polcyn, Fabian C.; and Lyzenga, David R.: Skylab Remote Bathymetry Experiment. NASA CR-144482, 1976.

6-45.   Pease, Robert W.: Mapping Terrestrial Radiation Emission With a Scanning Radiometer. Proceedings of the Seventh International Symposium on Remote Sensing of Environment, Environmental Research Institute of Mich. (Ann Arbor, Mich.), 1971, pp. 501-510.

6-46.   Villevieille, A.; and Weiller, A. B.: The Possibility of Evaluating Vertical Wind Profiles From Satellite Data. NASA CR-147475, 1975.

6-47.   Aldrich, Robert C.; Dana, Robert W.; et al.: Evaluation of Skylab (EREP) Data for Forest and Rangeland Surveys. NASA CR-147440, 1975.

6-48.   Polcyn, Fabian C.; Rebel, Diana L.; and Colwell, John E.: Analysis of Hydrological Features of Portions of the Lake Ontario Basin Using Skylab and Aircraft Data. NASA CR-147456, 1976.

6-49.   Colwell, J. E.: Bidirectional Spectral Reflectance of Grass Canopies for Determination of Above Ground Standing Biomass. Ph. D. Dissertation, Univ. of Mich. (Ann Arbor, Mich.), 1973.

6-50.   Savastano, K. J.: Application of Remote Sensing for Fishery Resources Assessment and Monitoring. NASA CR-147507, 1975.

6-51.   Anding, David C.; and Walker, John P.: Use of Skylab EREP Data in a Sea-Surface Temperature Experiment. NASA CR-144479, 1975.

6-52.   Malila, William A.; and Nalepka, Richard F.: Atmospheric Effects in ERTS-1 Data, and Advanced Information Extraction Techniques. Proceedings of the Symposium on Significant Results Obtained From the Earth Resources Technology Satellite-1, Goddard Space Flight Center (New Carrollton, Md.), Mar. 5-9, 1973, vol. I, sec. B, pp. 1097-1104.

6-53.   Tingey, David L.; and Potter, John: Quantitative Determination of Stratospheric Aerosol Characteristics. NASA CR-147444, 1975.

6-54.   Anding, D. C.; Kauth, R.; and Turner, R. E.: Atmospheric Effects on Infrared Multispectral Sensing of Sea-Surface Temperature From Space. NASA CR-1858, 1971.

6-55.   McGoogan, J. T.; Leitao, C. D.; and Wells, W. T.: Summary of Skylab S-193 Altimeter Altitude Results. NASA TM X-69355, 1975.

6-56.   Mourad, A. G.; Gopalapillai, S.; Kuhner, M.; and Fubara, D. M.: The Application of Skylab Altimetry to Marine Geoid Determination. NASA CR-144372, 1975.

6-57.   Brown, G. S.: Reduced Backscattering Cross Section ($\sigma°$) Data From the Skylab S-193 Radar Altimeter. NASA CR-141401, 1975.

6-58.   Shapiro, Allan; Thormodsgard, June M.; and Okada, J. M.: Skylab Altimeter Observations Over Terrain. NASA CR-144498, 1975.

6-59.   Moore, Richard K.; Ulaby, Fawwaz T.; et al.: Design Data Collection With Skylab Microwave Radiometer-Scatterometer S-193. Vols. I and II. NASA CR-144537 and NASA CR-144538, 1975.

6-60.   Eagleman, J. R.; Lin, W.; et al.: Detection of Soil Moisture and Snow Characteristic From Skylab. NASA CR-144485, 1975.

6-61.   Hollinger, James P.; and Lerner, Robert M.: Analysis of Microwave Radiometric Measurements From Skylab. NASA CR-147442, 1975.

6-62.   Cardone, Vincent J.; Young, James D.; et al.: The Measurement of the Winds Near the Ocean Surface With a Radiometer-Scatterometer on Skylab. NASA CR-147487, 1976.

6-63.   Thornthwaite, C. W.; and Mather, C. W.: Instructions and Tables for Computing Potential Evapotranspiration and Water Balance. Publications in Climatology, vol. 10, no. 3, 1957, pp. 185-311.

APPENDIX A

EREP Sensor Systems[a]

Roy L. Eason[b]

PRELIMINARY SENSOR SELECTION

The rationale for selecting the Earth Resources Experiment Package (EREP) sensors was based on the desire to explore various portions of the electromagnetic spectrum; on the need for correlating data among the various sensors; on the status of sensor development; and on the adaptability of the sensors, as a package, to the mission requirements. The sensor selection, as first considered in 1969, resulted in the proposal of four sensors.

For investigations in the visible portions of the spectrum, the prime candidate was a camera system. A multiband, high-resolution camera system was proposed to provide data correlation with other remote-sensor systems. The potential of the multiband camera system was demonstrated during the Apollo 9 mission. The spectral regions and film/filter-combination proposals were based on experience gained during the NASA Earth Resources Aircraft Program, the Apollo Program, and other multispectral photographic studies.

The second sensor proposed was a wide-range imager that would extend observations from the visible through the near-infrared into the far-infrared portion of the spectrum (0.5 to 2.4 μm and 10.5 to 12.5 μm). The shorter wavelengths were proposed to overlap the multiband camera system. Other bands were proposed to extend into the near infrared with the longer wavelengths extending into the thermal infrared. The longer wavelengths were to permit monitoring of nighttime surface emissions.

An infrared spectrometer was proposed to extend measurements from 3.2 to beyond 14 μm. This wavelength range would provide correlation with the wide-range imager at 10.5 to 12.5 μm.

A microwave system that was a combination radar scatterometer and passive microwave radiometer operating at approximately 10 GHz (3 cm) was proposed. The advantages of this system were that it could operate day or night and that it was not generally affected by clouds and weather. The objectives of this system primarily concerned measurements of the winds over the oceans, the capability for snow mapping, and measurement of rainfall. Portions of this type of system had been used in the NASA aircraft program and in the Nimbus satellite program.

Later in the Skylab Program, three additional sensors were proposed for the EREP system.

1. The L-band 1.4-GHz passive radiometer for measurement of soil moisture and oceanographic data

2. A radar altimeter applicable to both geodesy and oceanography (This system was to be capable of measuring the distance from the spacecraft to the surface of the oceans within an accuracy of 1 to 2 m.)

3. An Earth terrain camera system to provide higher resolution data to serve as a truth source for the other sensors and to assist those investigators interested in mapmaking (This camera system was similar to the high-resolution camera flown on the Apollo 14 mission.)

THE EREP SYSTEM

The following five systems were selected for EREP. (See fig. A-1.)

1. The Multispectral Photographic Facility (S190) consisting of the Multispectral Photographic Cameras (S190A) and the Earth Terrain Camera (S190B)

2. The Infrared Spectrometer (S191)

3. The Multispectral Scanner (S192)

FIGURE A-1.—Skylab spacecraft, showing locations of EREP sensors (SL3-114-1659).

- L-band Radiometer (S194)
- Infrared Spectrometer (S191)
- Multispectral Photographic Camera (S190A)
- Earth Terrain Camera (S190B)
- Microwave Radiometer/Scatterometer and Altimeter (S193)
- Multispectral Scanner (S192)

4. The Microwave Radiometer/Scatterometer and Altimeter (S193)

5. The L-Band Radiometer (S194)

Figure A-2 shows the wavelength coverage of the Earth-viewing EREP Skylab sensors. The EREP ground coverage is shown in figure A-3.

Photographic Systems

Cameras provided the primary source of information for most of the Skylab investigators. The carefully designed cameras and films used for the EREP were not fundamentally different from conventional cameras and films.

Images are formed on films by different wavelengths or colors of light. Each film has a different sensitivity to the various wavelengths of light. Figure A-4 shows the wavelength sensitivity of one of the Skylab films (Eastman Kodak (EK) 3414). This film is similar to the commercially available Plus-X film; however, it is capable of achieving higher resolution and is coated on a thinner base. The thin base permits a large volume of film to be packed into a small space.

The Skylab cameras used the wavelength sensitivity of the films to photograph the Earth in well-defined col-
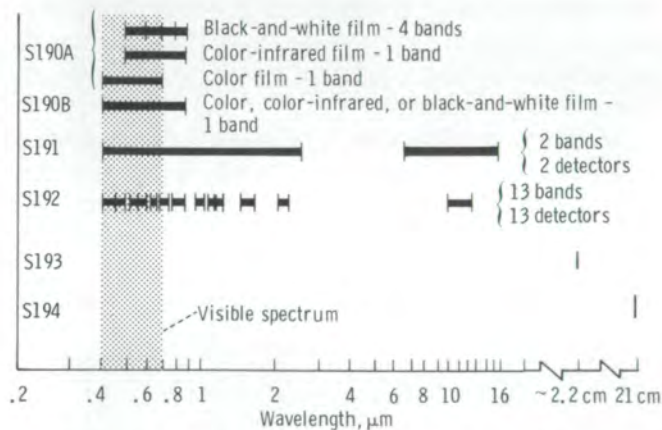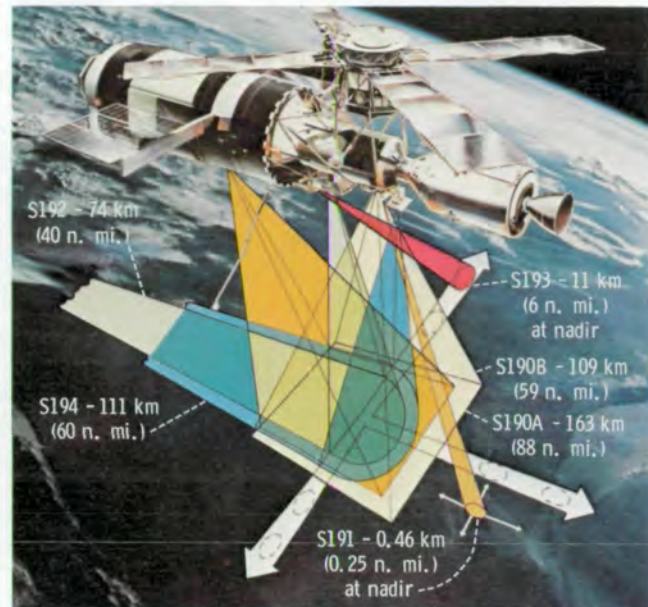

FIGURE A-3.—The ground area coverage provided by EREP sensors (S-73-005-S).

or, or wavelength, regions by placing a filter over the camera lens. The effect of placing a filter that transmits only red light over EK-3414 film is shown in figure A-5. Use of the filter results in the film recording information in the red wavelength region only. Color films do not need such filtration to record an image in spectral bands. An ordinary color film has three light-sensitive layers, each of which is sensitive to a different group of wavelengths. One film layer records only blue light, a second layer only green light, and a third layer only red light (fig. A-6). The information recorded on each of these film layers can be separated by means of several analysis techniques that are described in section 6 of this report.

Whereas standard color film has the normal blue-, green-, and red-sensitive layers (fig. A-7(a)), color-infrared film does not have a blue-sensitive layer but instead has a layer sensitive to infrared wavelengths. Because the human eye is not sensitive to infrared wavelengths, the information on this film layer is made
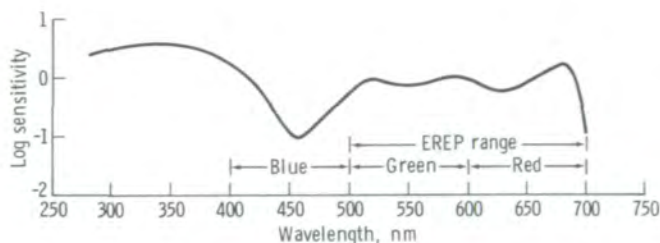

FIGURE A-2.—Wavelength sensitivity of Earth-viewing Skylab sensors.

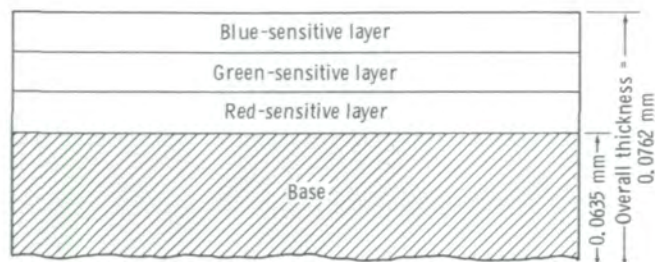FIGURE A-4.— Wavelength sensitivity curve for EK-3414 film.

FIGURE A-6.—Cross section of a typical color emulsion layer.

visible after development by having the infrared layer appear red. The red-sensitive layer is made to appear green, and the green-sensitive layer appears blue. This rather complicated situation in which red is not red and green is not green is depicted schematically in figure A-7(c). The apparent confusion is more than justified, however, by the amount of information obtained by making infrared wavelengths visible in a photograph. Color-infrared film is particularly valuable in vegetation studies. Figure A-7(b) contains a color-film image of the same scene shown in figure A-7(d).

The photographic image is determined not only by the film used but also by the camera. Three camera characteristics are most important: focal length, aperture, and shutter speed. At a fixed distance, the focal length of a camera determines the size of an object relative to the size of a photograph on which it appears. Thus, a telephoto lens with long focal length will make a distant object appear larger on a photograph than it would appear if a short-focal-length lens were used. A long-focal-length lens will also provide better reproduction or resolution than a short-focal-length lens of equal quality. The detail reproduction in a photograph can be limited not only by lens distortions but also by film

grain. A view of exposed film under high magnification will reveal a nonuniform pebbly, or grainy, appearance called graininess. A long-focal-length lens will map a smaller object onto the limiting graininess to achieve better resolution because of the small blur circle. The focal length cannot be increased arbitrarily. It is more difficult and expensive to make a high-quality lens of longer focal length. A long-focal-length lens also covers less area. The field of view (FOV) is decreased with a long-focal-length lens, and a small FOV can be a disadvantage in Earth resources studies.

The aperture and shutter parameters of a camera affect the amount of energy reaching the film during the exposure. The camera aperture (f-stop) represents the ratio of the focal length to the diameter of the lens aperture. The amount of energy reaching the film is proportional to the square of the ratio of aperture diameter to focal length.

Multispectral Photographic Cameras (S190A).—Six high-precision cameras with matched optical systems were mounted and boresighted to form the camera assembly shown in figure A-8. Each camera had an f/2.8 lens with an aperture variable to f/16 in 0.5-stop increments and a focal length of 15.2 cm. At a nominal
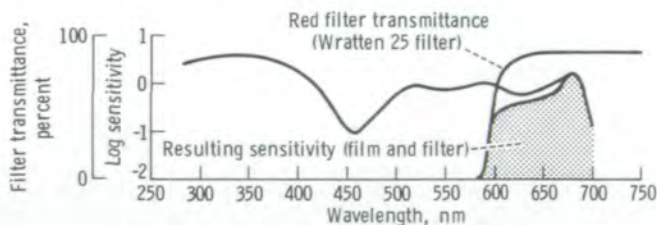
FIGURE A-5.—Wavelength sensitivity curve for EK-3414 film showing filtering to transmit only red light.

FIGURE A-7.—Color as opposed to color-infrared spectral layer. (a) Sensitivity curve for color film. (b) Color photograph of the Yuma, Arizona, area taken on January 26, 1974 (SL4-92-356). (c) Sensitivity curve for color-infrared film. (d) Color-infrared photograph of the Yuma, Arizona, area taken on January 14, 1974 (SL4-93-057). →

(a)

Relative sensitivity

Blue   Green   Red

Wavelength, nm

(b)

(c)

Relative sensitivity

Green   Red   Infrared

Wavelength, nm

(d)

FIGURE A-8.—Multispectral Photographic Cameras (S190A). (a) Magazines (S-72-44415). (b) Lenses and filters (S-72-44416).

spacecraft altitude of 435 km, the 21.2° FOV provided ground coverage of a square area approximately 163 km on each side (1:2 900 000 scale, approximately).

The film width was 70 mm, the shutter speeds were 2.5, 5, and 10 milliseconds, and the six shutter mechanisms were synchronized to within 0.4 millisecond. Programed camera rotation, variable from 10 to 30 mrad/sec, compensated for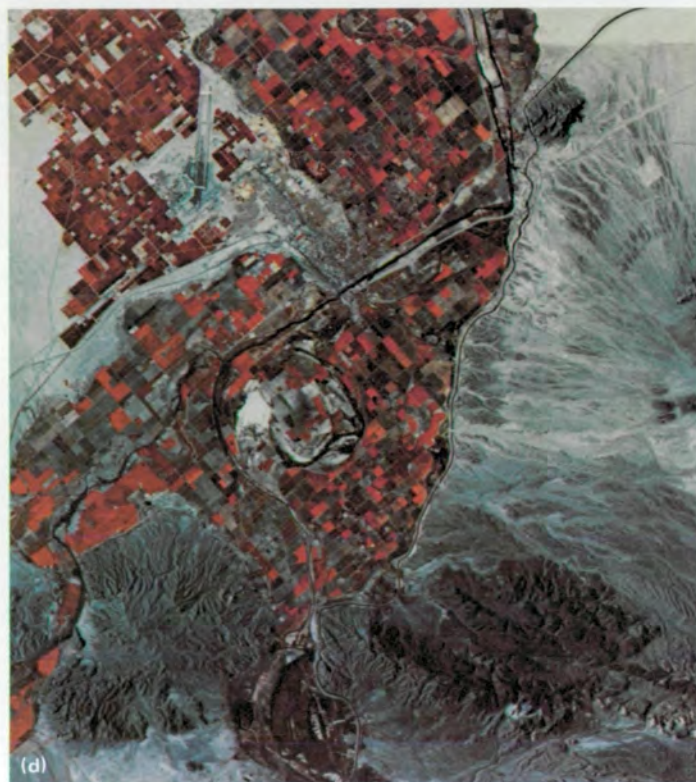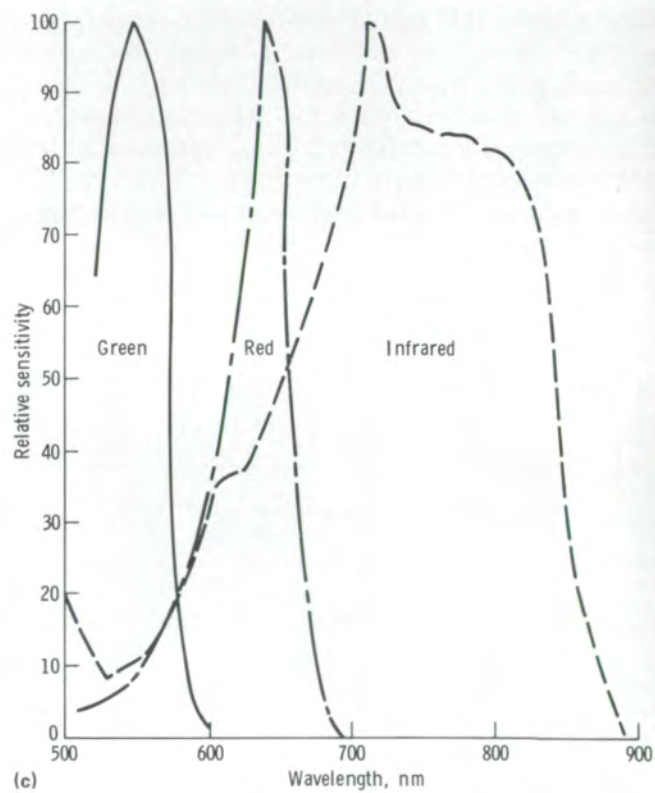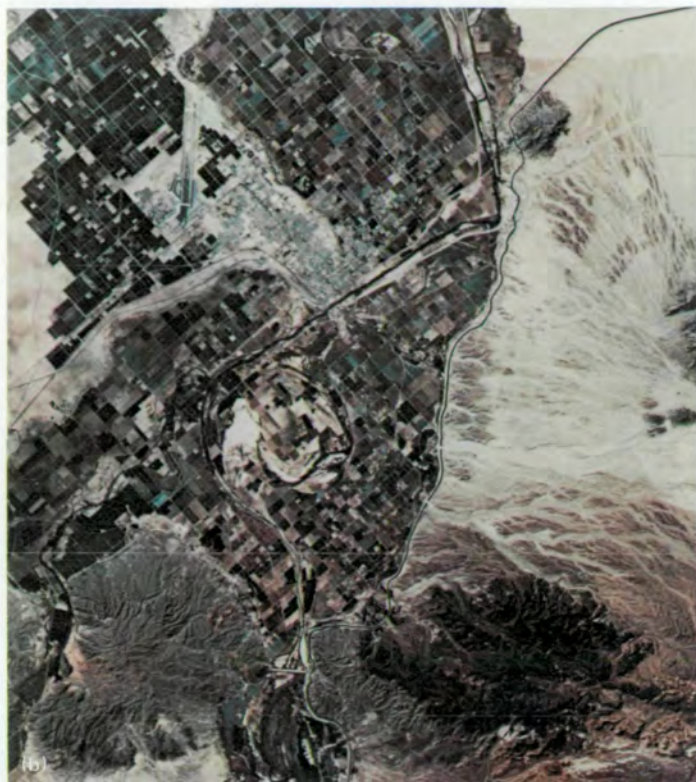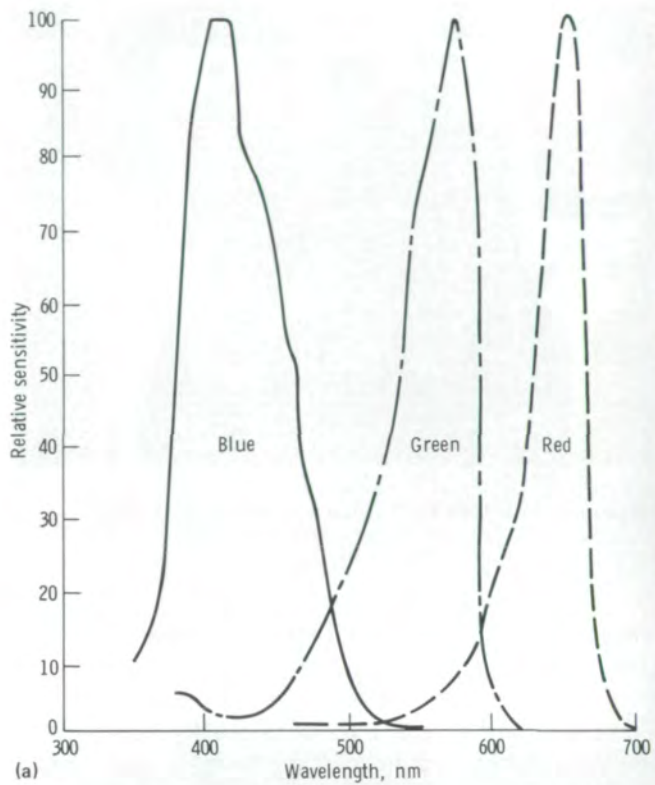 the forward motion of the spacecraft, and photographs could be taken singly or in automatic series in 2- to 20-second intervals. To provide for stereoscopic viewing, 60-percent overlaps were obtained using 10-second intervals.

Figure A-9 shows six sample images acquired by the S190A cameras and includes information on film types and spectral ranges. The S190A data were usually furnished to the Principal Investigators in the form of contact positive and negative transparencies (70 mm) and enlarged transparencies (280 mm).

Earth Terrain Camera (S190B).—The Earth terrain single-lens camera assembly (fig. A-10(a)) had an f/4 lens and a focal length of 45.7 cm with a focal-plane shutter. Programed camera rotation, variable from 0 to 25 mrad/sec, compensated for the forward motion of the spacecraft. The 14.24° FOV provided ground coverage of a square area approximately 109 km on each side (1:950 000 scale, approximately).

The film width was 12.7 cm, and the shutter speeds were 1/100, 1/140, and 1/200 second. Sequence photography intervals were possible from 0 to 25 frames/min.

To provide for stereoscopic viewing, 60-percent overlaps were obtained using a rate of 9.5 frames/min. Figure A-10(b) is an image of an area taken with the Earth Terrain Camera. Data were usually furnished to the Principal Investigators in the form of positive and negative contact transparencies (140 mm) and enlarged transparencies (280 mm). Unless otherwise stated, "color film" should be assumed in S190B discussions throughout this report. The S190B film types used onboard the spacecraft were EK-3414 black-and-white high-definition aerial (0.5 to 0.7 μm), special order SO-242 high-resolution aerial color (0.4 to 0.7 μm), SO-131 high-resolution color-infrared aerial (0.5 to 0.88 μm), and EK-3443 color-infrared (0.5 to 0.88 μm).

Station	Wavelength, μm	Film	
		Color	Type
1	0.7 to 0.8	Black-and-white (B&W) infrared	EK-2424
2	0.8 to 0.9	B&W infrared	EK-2424
3	0.5 to 0.88	Color infrared	EK-2443
4	0.4 to 0.7	Color	Special order (SO) 356
5	0.6 to 0.7	B&W visible	SO-022
6	0.5 to 0.6	B&W visible	SO-022
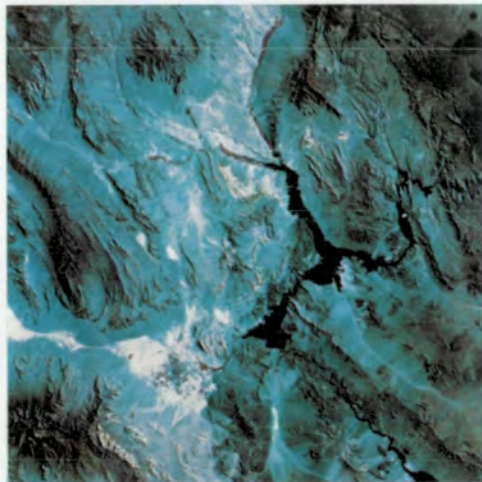
Station 1 Station 2 Station 3 Station 4 Station 5 Station 6

FIGURE A-9.—S190A sample data taken over Las Vegas, Nevada; Lake Mead; the Colorado River; and the Hoover Dam. Data on film parameters for each station are contained in the table on the facing page.

Magazine assembly

Lens cone

Camera control box

Forward motion compensation mechanism

(a)

Ft. Walton Beach

Panama City

(b)

FIGURE A-10.—Earth Terrain Camera (S190B). (a) Camera assembly. (b) Sample data taken over northwestern Florida (SL3-88-141).

Spectroradiometric Sensors

Remote sensing depends on receiving energy from an object or a scene, viewing or recording it, and analyzing the received energy to deduce some of the characteristics of the scene. In recording the energy of an Earth scene with a space sensor, the many variables considered can generally be divided into two classes: those variations that affect or influence some characteristics of the scene, such as temperature and moisture, and those variations that, although they influence the radiation received at the sensor, do not represent scene characteristics. Examples are the intervening atmosphere and contamination around the recording instrument. The most influential agent within the wavelengths previously discussed is the atmosphere. The alterations of radiation passing throu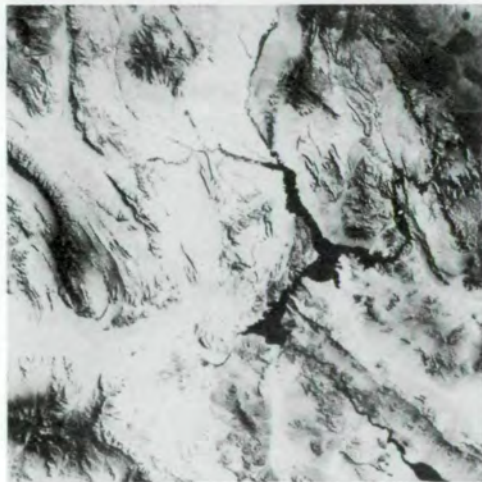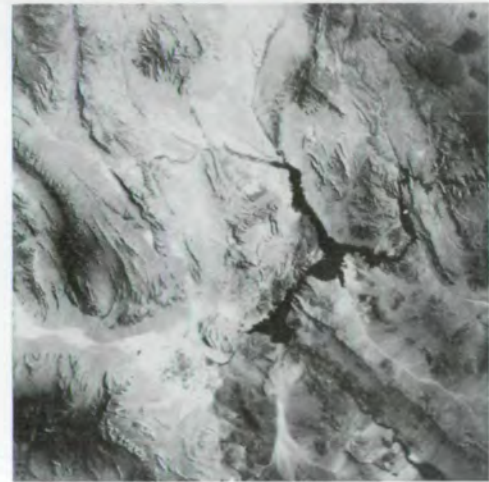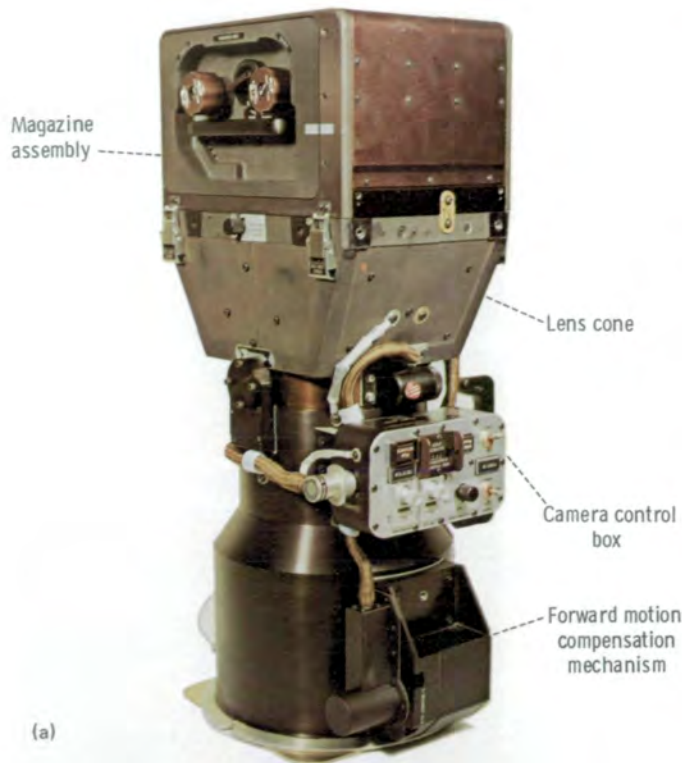gh the atmosphere have serious ramifications for remote sensing. The S191 Infrared Spectrometer was designed to investigate correction factors that might be applied. Although called an infrared spectrometer, the sensor operated in both the reflective (0.4 to 2.5 μm) and emissive (6.6 to 16 μm) wavelength intervals.

The basic principle concerned viewing a single homogeneous scene long enough to record the radiance values over the entire wavelength range and thereby obtaining a plot of energy level as a function of wavelength for the target scene. If the energy levels departing from ground level are known (either from direct measurements or by inference) and if they are compared to the levels received at the sensor, the major differences can be attributed to the intervening medium. Even if there are no differences, however, one cannot assume the medium has no effect. For example, at some wavelengths, the medium may completely absorb the emissions of the ground scene and replace the absorbed radiation with its own emissions. The experimenter relies on the spectral details of the comparison to unravel the confounding effects of the atmosphere.

Infrared Spectrometer (S191).—The S191 Infrared Spectrometer was unlike the other visible and infrared recording sensors (cameras and multispectral scanner) and also unlike many other infrared systems in that no image was acquired or derived.

The S191 sensor (fig. A-11(a)) was composed of a filter-wheel spectrometer that spectrally scanned the radiation entering its aperture and a tracking telescope alined along the spectrometer line of sight that enabled the crewman to acquire and track the test site and take
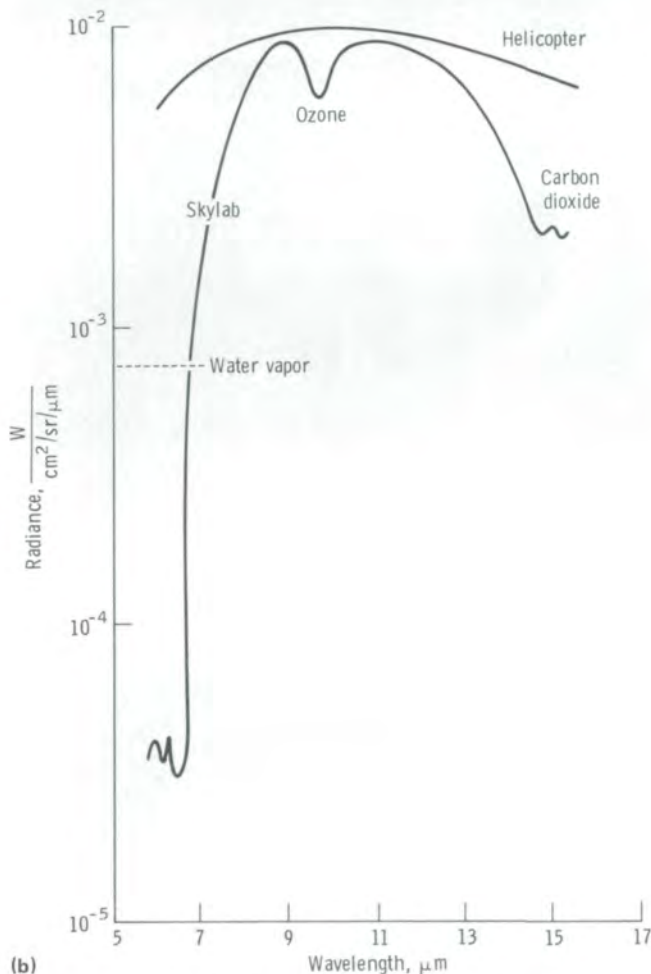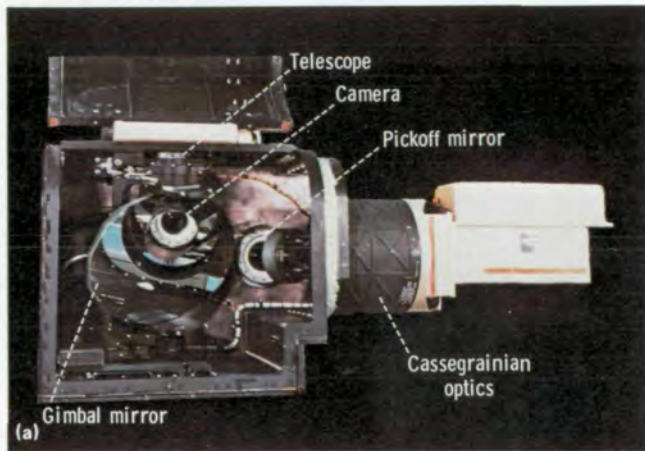
(b)

FIGURE A-11.—Infrared Spectrometer (S191). (a) Instrument. (b) Sample data.

16-mm photographs of the scene. Incoming radiation, recorded at 1 spectral scan/sec from a Cassegrainian collecting telescope, was split into short-wavelength (0.4 to 2.5 μm) and long-wavelength (6.6 to 16.0 μm) bands by a dichroic beamsplitter. The detector alternately sensed radiation from the external target and from the internal reference sources.

Visible and near-infrared energy was detected by a silicon and lead sulfide sandwich detector; thermal energy was detected by a mercury-cadmium-tellurium detector that was cooled to 90 K by a miniaturized closed-cycle engine. In-flight calibration spectra recorded before and after each data-gathering pass enabled conversion of the spectral voltage signals to radiance values. The data from this experiment sensor were furnished to the Principal Investigators in the form of computer tapes and 16-mm film.

Typical spectral data obtained with the spectrometer are shown in figure A-11(b). The lower spectrum was obtained when the Skylab spacecraft was over White Sands, New Mexico, on a foggy morning. Only the thermal region of the spectrum is shown. For comparison, the line at the top of the figure shows the spectrum measured by a similar spectrometer mounted in a helicopter. The difference between the two is due to energy being absorbed in the atmosphere by carbon dioxide, ozone, and water vapor. The differences at the various wavelengths illustrate atmospheric effects on data recorded above the atmosphere.

Multispectral Scanner (S192).—Another method of forming an image is through a point-by-point reconstruction of an area that has been scanned by an optical mechanical scanner. Each point actually represents the integrated energy from a small area called a picture element (pixel) or resolution cell. The size of the picture element on the ground is governed by the optical design parameters of the sensor and the height of the satellite. The energy from each pixel is collected by an optical assembly and focused onto a detector. The detector converts the energy received at each instant into an analog electrical signal that can be amplified and recorded. The electrical signal varies in direct proportion to the changes in the amount of energy received at the detector and thus carries information about changes in the reflection or emission of radiation from the objects scanned.

The mechanical movement (usually rotation) of a mirror in the optical assembly produces the scan lines perpendicular to the satellite track. As the spacecraft

moves, each line is scanned so that successive lines will fall exactly adjacent to each other and a continuous swath of the Earth can be mapped. The scan lines can be curved or straight depending on the method chosen to generate the scan motion. The quality of the data depends on the swath width, defined by the unobstructed angle through which the scanning mirror is designed to rotate, and is limited by changes in the atmospheric path lengths and in the size of the pixel for off-nadir angles and by the available electrical bandwidths for tape recording or telemetry of the image data.

Variations in spacecraft height or velocity or in mirror scan rotation can cause an underlap or overlap of adjacent lines that must be corrected during image reconstruction at a ground facility. If the height increases, as when viewing the Earth obliquely, the width of the area scanned will increase; and, if no change is made in the rotational speed of the mirror or in the forward velocity of the spacecraft, overlapping lines will be sensed. For contiguous imagery, the width of each line on the ground must equal the distance the spacecraft moves while scanning each line.

By using the proper optical design and an array of detectors, a set of coincident spectral bands can be obtained for each line. In storing the signals on a multiband recorder, a multispectral set of data is made available to the analyst for interpretation. One of the advantages of an optical mechanical scanner is that it can collect radiation in spectral regions outside as well as coincident with those viewed by a camera, particularly infrared wavelengths beyond 1 μm. The particular design for an optical mechanical scanner used for the EREP was called the Multispectral Scanner (S192) (fig. A-12).

This optical electromechanical scanner collected incoming radiant energy using a rotating mirror in the image plane to scan the scene conically. A spherical mirror was the major element of a folded reflecting telescope that had a 43.2-cm entrance pupil. The energy scanned in the image plane passed through a reflective Schmidt corrector mirror and through a field stop that was the entrance slit of a prism spectrometer. A dichroic mirror then separated the short wavelengths (0.41 to 2.35 μm) from the long thermal wavelength band (10.2 to 12.5 μm). The spectrally dispersed electromagnetic energy received from the scene simultaneously irradiated 13 detectors. Each detector responded to a specific wavelength band as given in table A-I. The multispectral scanner had 22 scientific data outputs. One scientific data output (SDO) was assigned to each
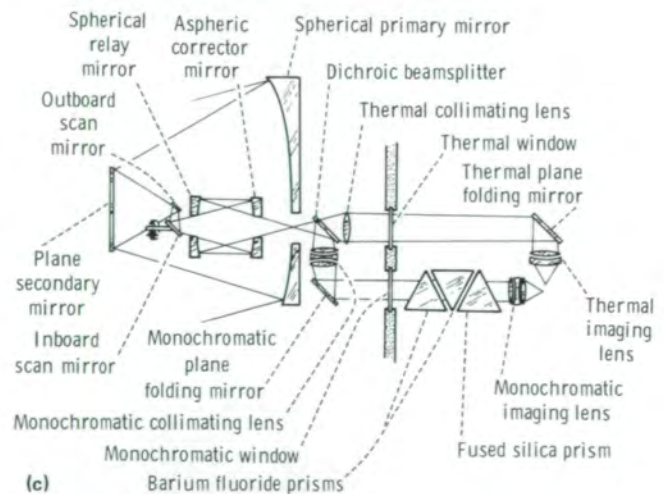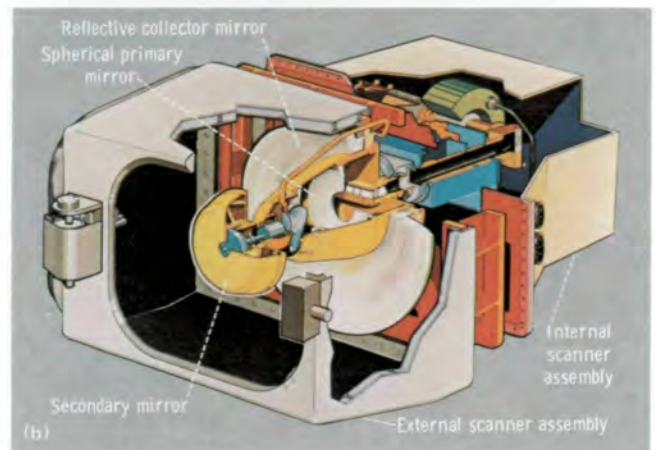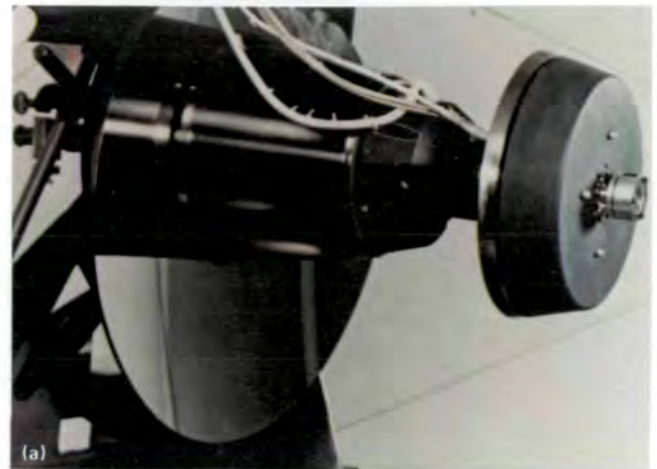

FIGURE A-12.—Multispectral Scanner (S192). (a) Cutaway diagram. (b) Scanner optics. (c) Lens system.

TABLE A-I.— Detectors and Corresponding Wavelength Bands for the Multispectral Scanner (S192)

Detector no.	Band		SDO
	Color	*Wavelength, μm*	*(or channel)*
1	Violet	0.41 to 0.46	22
2	Violet-blue	0.46 to 0.51	18
3	Blue-green	0.52 to 0.56	1, 2
4	Green-yellow	0.56 to 0.61	3, 4
5	Orange-red	0.62 to 0.67	5, 6
6	Deep red and infrared	0.68 to 0.76	7, 8
7	Near infrared	0.78 to 0.88	9, 10
8	Near infrared	0.98 to 1.08	19
9	Near infrared	1.09 to 1.19	20
10	Near infrared	1.20 to 1.30	17
11	Middle infrared	1.55 to 1.75	11, 12
12	Middle infrared	2.10 to 2.35	13, 14
13	Thermal infrared	10.20 to 12.50	15, 16, 21

detector sampled at 1240 times/scan (bands 1, 2, 8, 9, and 10). Two SDO's were assigned to the detectors sampled at 2480 times/scan (bands 3, 4, 5, 6, 7, 11, 12, and 13). Band 13 was assigned an additional redundant SDO.

Each detector produced an electronic signal that corresponded to the average value of the radiance received in its spectral band from the area on the Earth's surface in the instantaneous FOV of the instrument. The detector outputs were amplified, converted to digital values, multiplexed, buffered, and recorded on magnetic tape.

The 0.182-mrad FOV measured by each detector provided an instantaneous ground coverage of a square area 79 m on each side. Although the scan assembly rotated a full 360°, only the forward 110° were used to obtain surface data with the calibration data taken on the remainder of the scan. The corresponding sweep angle viewed from the sensor was 10.4°, which provided a groundswath width of 74 km.

Because the original thermal detector (Y-3) had less than specified sensitivity, a more sensitive detector (X-5) was installed in January 1974 during the Skylab 4 mission. Checkout of this instrument was accomplished January 15 to 17, 1974.

An example of the multispectral scanner imagery is shown in figure A-13. The data from this experiment were furnished to the Principal Investigators in the form of imagery (from one SDO per detector) and computer tapes.

Active and Passive Microwave Sensors

Microwave sensors operate in the millimeter to meter region of the electromagnetic spectrum. Because the longer wavelengths require larger antennas for a given angular resolution, higher resolution microwave space sensors usually operate at the shorter wavelengths, with the exception of special applications.

An active microwave sensor transmits repetitive pulsed bursts of energy that are directed in a given direction by the antenna beam. A discontinuity, such as the atmosphere/lithosphere interface, will reflect or scatter a part of the energy back to the transmitting antenna, where it is accepted by the receiver between the transmitted bursts. After the receiver, which is designed to match the transmitted signal characteristics for optimum detection, converts the radiofrequency energy to video frequencies, signal processing is performed. In remote-sensing applications, in which the effect of either the Earth's surface or the atmosphere on the transmitted radiation is measured, the geometric configuration of the observations will depend on both the target characteristics and the radar system parameters. Generally, when the spatial resolution depends only on the antenna size, the operation is termed beamwidth limiting and is used to measure the amount of backscatter from a given area within the antenna beam (scatterometer). To derive a radar signature for each measurement, the measured backscatter is normalized relative to the beamwidth-limited area. The resultant radar cross section per unit area, or backscatter coefficient, will depend only on the surface characteristics, the incidence angle, and the polarization for which the values were determined.

The backscatter coefficients measured by a scatterometer are estimates of the mean return of a noiselike signal. To reduce fluctuations as well as increase the signal-to-noise ratio, a long pulse is transmitted. For a monostatic radar that uses the same transmitting and receiving antenna, the transmitted pulsewidth cannot exceed the expected round-trip traveltime ($2R/c$, where R is the range and c is the electromagnetic wave propagation speed), so that the received and transmitted energy will not interfere. The pulsewidth used for the Skylab scatterometer was approximately 4 milliseconds for higher incident angles.

The active sensor can also be used as an altimeter to measure precisely the spacecraft height relative to the subsatellite groundtrack. Narrow transmitted pulses are

Band 1   N↑   Band 2

Band 3   Band 4

Band 5   Band 6

(a)   Band 7   Band 8
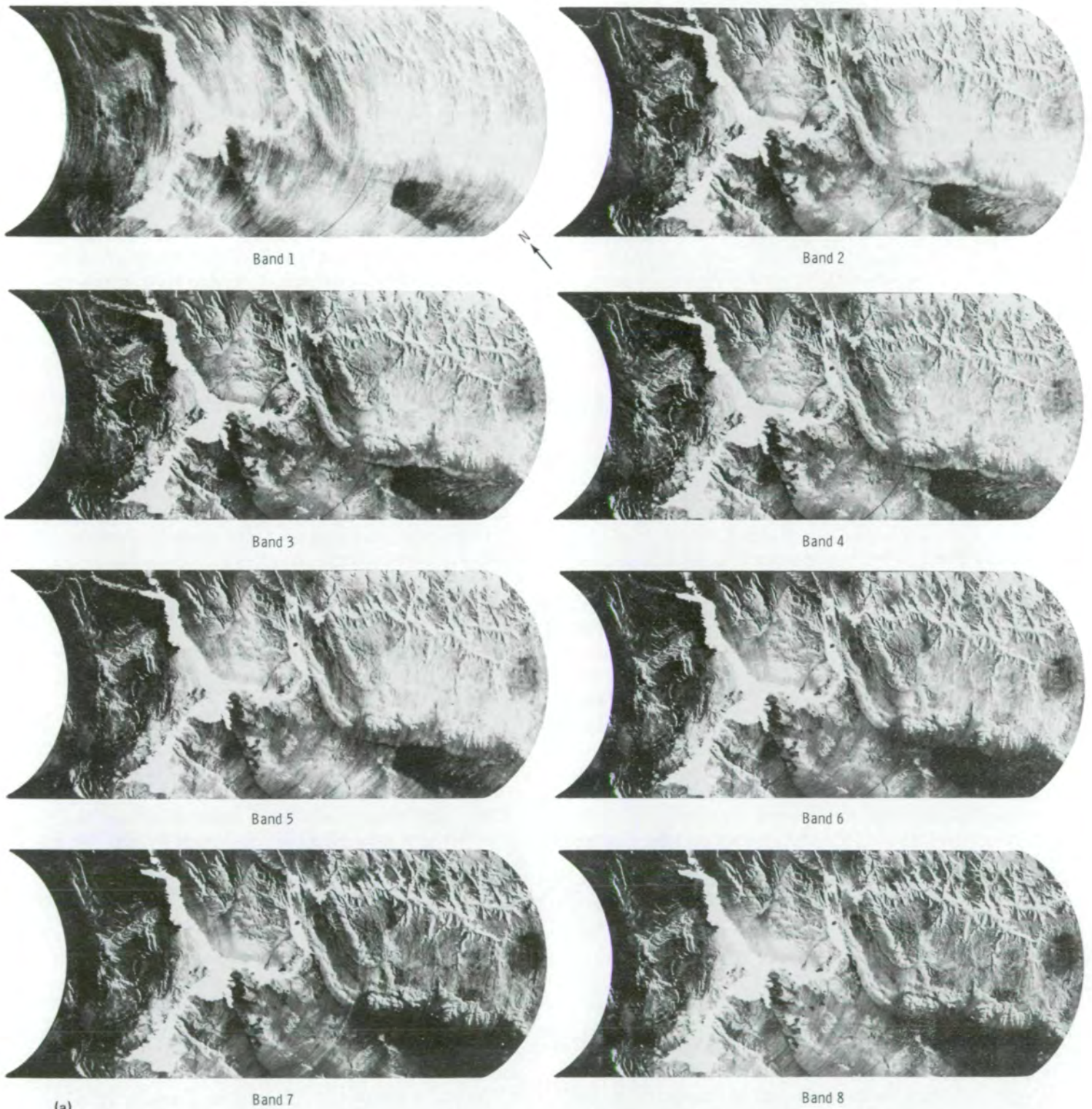
FIGURE A-13.—Imagery from the 13 S192 detectors taken over Las Vegas, Nevada; Lake Mead; the Colorado River; and the Hoover Dam. (a) Bands 1 to 8. (b) Bands 9 to 13.

Band 9

Band 10

Band 11

Band 12

Band 13

(b)
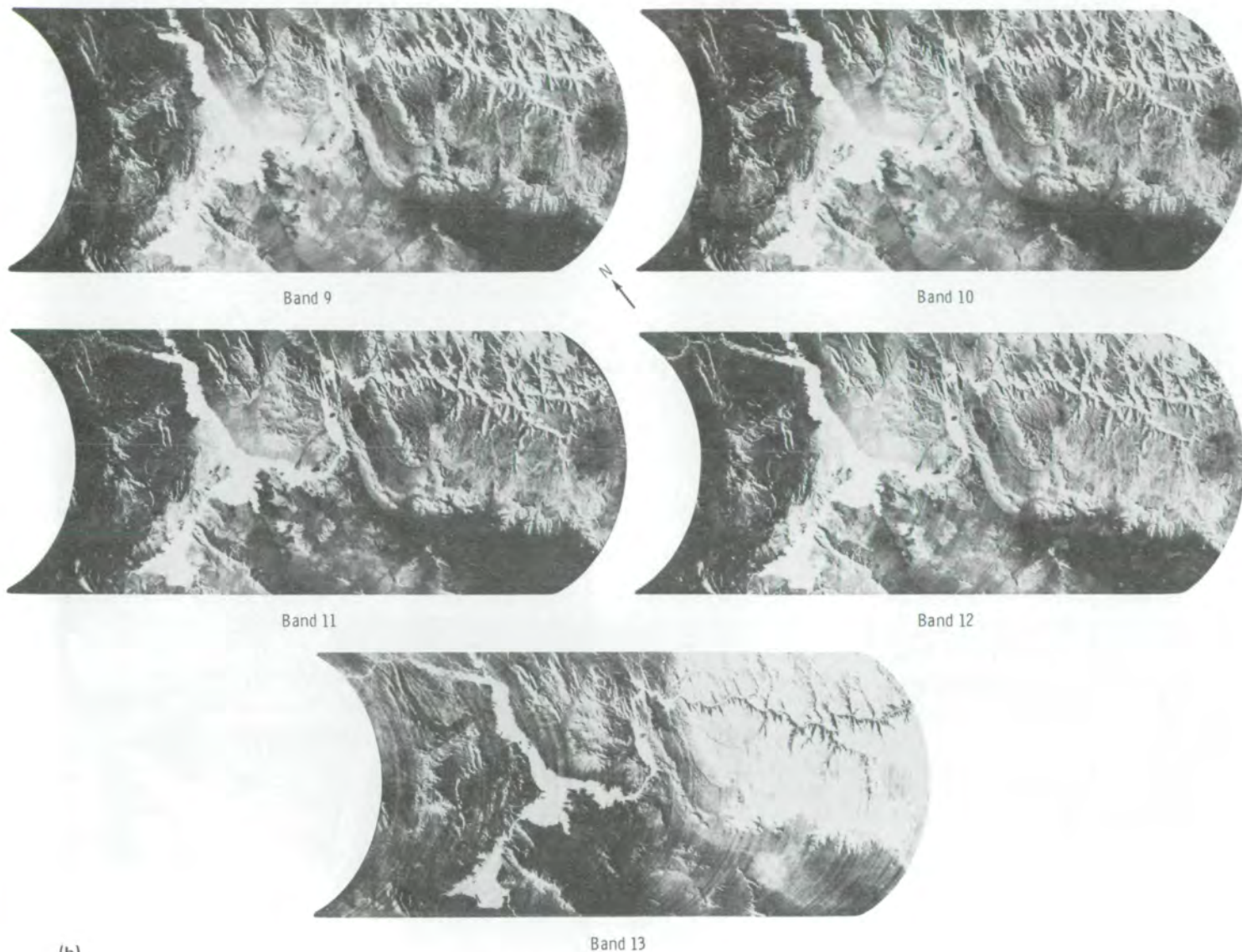
FIGURE A-13.—Concluded.

used for this application, and the arrival time of each pulse relative to the transmitted time is measured. Time precision (1 nanosecond = 15 cm) is easily obtained, and a profile of the subsatellite groundtrack can be obtained by plotting a time history of the altimeter measurements. At nadir, the spatial resolution is pulsewidth limited rather than antenna beamwidth limited (fig. A-14), if sufficiently narrow transmitted pulses are used.

The operation of both the scatterometer and the altimeter is based on the reflective properties of a rough surface. However, when smooth areas are encountered, the scatterometer will become inoperative at larger incidence angles, whereas the altimeter, operating at nadir, will be activated by mirrorlike returns that preserve the transmitted pulse shape. In this case, the effective area of reflection is reduced to the first Fresnel zone, which may be only a fraction of the pulsewidth- or beamwidth-limited area (fig. A-14). The size of the Fresnel zone depends only on the platform height and the radar wavelength and thus is independent of both the pulsewidth and the antenna size.
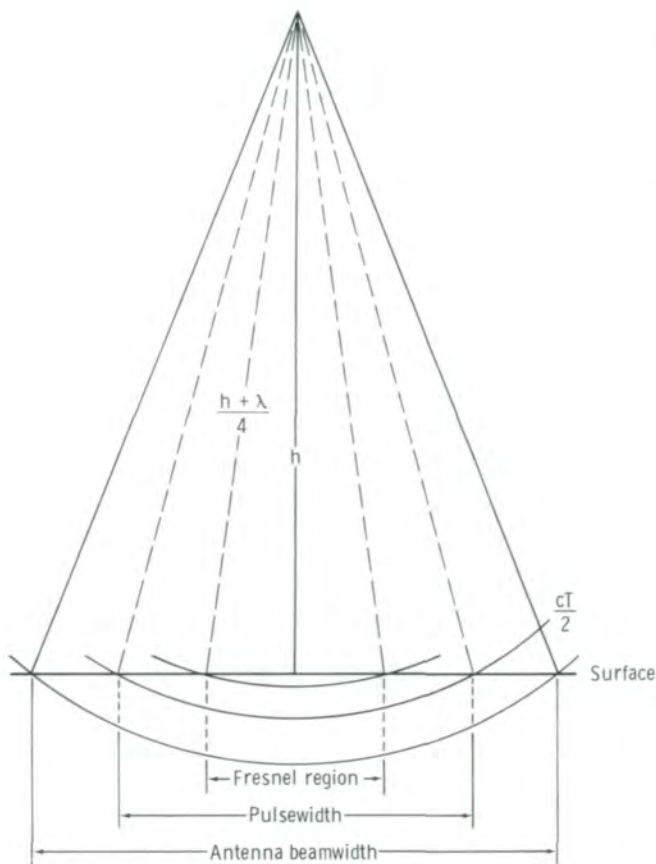
FIGURE A-14.—Antenna beamwidth, pulsewidth, and Fresnel region, where c is electromagnetic wave propagation speed, T is time, h is height, and $\lambda/4$ is quarter wavelength.

Passive microwave receivers have many components similar to radars. An antenna is focused on those targets that are emitting the wavelengths of electromagnetic radiation. Generally, the passive receiver bandwidth is much broader than radar bandwidths because the naturally generated radiation is much weaker. Passive microwave receivers therefore require very sophisticated calibration techniques involving internal radiation sources and a consideration of the internally generated receiver noise.

The measurements made by passive microwave receivers are converted to passive microwave temperatures, which are interpreted in terms of the temperature of the target and its emissivity. These physical properties change for each target.

Microwave Radiometer/Scatterometer and Altimeter (S193).—The active microwave scatterometer, the

passive microwave radiometer, and the altimeter shared one antenna (fig. A-15). The radiometer and scatterometer functions of S193 were combined into a single instrument. Features of microwave radiometry were incorporated in the radar scatterometer design to improve the accuracy of the backscatter measurements.

From radiometer measurements, the brightness temperature of the Earth's surface within the 1.6° half-power point of the antenna pattern was determined as a function of incidence angle from 0° (vertical) to 48° with a bandwidth of 0.200 GHz centered at a frequency of 13.9 GHz for two polarizations. The mean value of the Earth's thermal noise signal was determined by sufficiently long integration of the received signal. The

FIGURE A-15.—Microwave Radiometer/Scatterometer and Altimeter (S193).
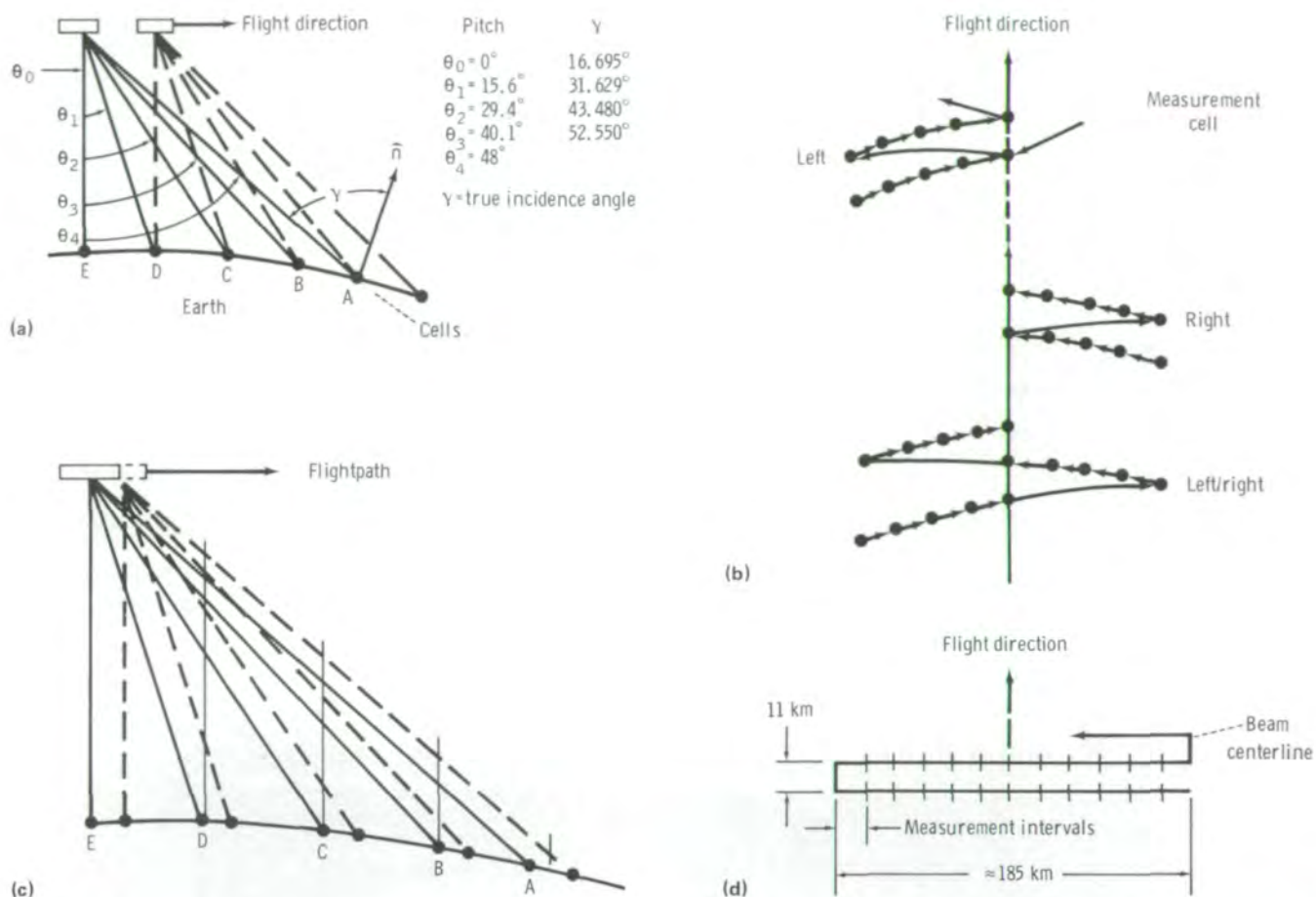
FIGURE A-16.—Radiometer and scatterometer data. (a) Intrack noncontiguous scanning mode with varied pitch angle θ; $\hat{n}$ is the local vertical vector. (b) Crosstrack noncontiguous scan mode. (c) Intrack contiguous scan mode. (d) Crosstrack contiguous scan mode.

measured energy, converted to brightness temperature, was compared to the mean noise energy from two known internal temperature sources for calibration to yield an accurate proportional measurement of the microwave emission of the Earth within the antenna half-power points.

The scatterometer measured the radiation backscatter from the Earth at a center frequency of 13.9 GHz as a function of incidence angles from 0° (vertical) to 48° for different polarization combinations and scanning modes as shown in figure A-16. The calculated scattering coefficient was related to the roughness and the dielectric properties of the surface reflections. Several measurements of the scattered return signal (which resembles thermal noise) and receiver noise were taken and integrated to obtain an accurate measurement of

average return power, from which the backscattering coefficient was calculated. Concurrent operation of the radiometer and the scatterometer enabled collections of values of the backscattering coefficient and apparent black-body temperatures for each surface area. This method resulted in the ability to study emissivity effects from reflectivity effects in the same area.

An example of radiometer/scatterometer data (in two polarizations) collected from Hurricane Ava off the coast of Mexico is shown in figure A-17. The winds at the closest approach of the S193 sensors to the center of the hurricane had speeds of approximately 90 km/hr, with 10-m wave heights. The changes in the backscatter as this spacecraft passed by the storm were caused by changes in surface roughness, as slightly attenuated by the clouds. As the windspeeds increased near the storm
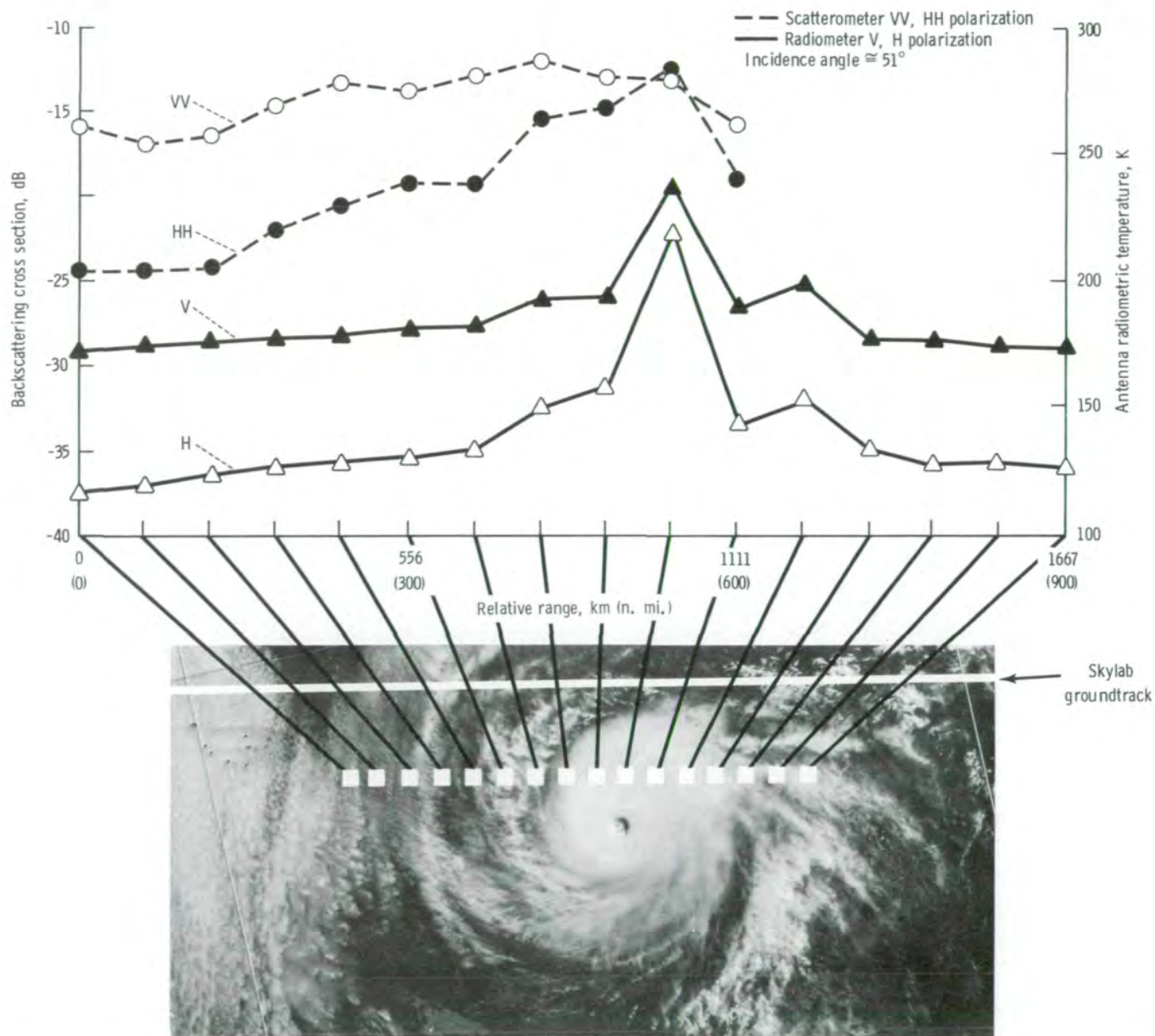
FIGURE A-17.—Radiometer and scatterometer data from Hurricane Ava. (V = vertical transmit; H = horizontal transmit; VV = vertical transmit, vertical receive; HH = horizontal transmit, horizontal receive.)

center, the scattered signal intensity increased because of increased surface roughness. The microwave temperature increased because of both thickening clouds and increased roughness. These data were analyzed to determine the feasibility of using the passive microwave data to correct the radar data for attenuation and then determining the windspeed.

The S193 altimeter was designed to operate in a preprogramed sequence of approximately 3 minutes. Each sequence consisted of a data acquisition and system calibration subsequence. To increase the flexibility of the system and to study the various effects of different system parameters, five different combinations of pulsewidth, receiver bandwidth, and off-nadir

TABLE A-II.— Basic Sequence of
Altimeter Operation

	Transmitter		IF[b] filter bandwidth (receiver), MHz	Antenna pointing angle, deg	No. of data frames (c)
Step	Submode (a)	Pulsewidth, nsec			
Mode 1 (pulse shape)					
0	DAS-1	100	10	Subsatellite	50
1	DAS-2	100	100	Subsatellite	61
2	DAS-3	100	100	0.431 pitch	61
3	CDS-1	100	100	NA[d]	7
4	CDS-2	100	10	NA	5
5	CDS-3	100	10	NA	5
Mode 5 (pulse compression)					
0	DAS-1	100	10	Subsatellite	16
1	DAS-2	130	100	Subsatellite	99
2	DAS-3	20	100	Subsatellite	51
3	CDS-1	20	100	NA	7
4	CDS-2	130	100	NA	7
5	CDS-3	100	10	NA	5

[a]DAS = data acquisition step; CDS = calibration data step.

[b]Intermediate frequency.

[c]One frame corresponds to approximately 1 second of data.

[d]Not applicable.

Figure A-18.—Skylab 2 groundtrack for altimeter data.

angle were available. The basic sequence of operation for modes 1 and 5, which were most frequently used in the altimeter operation, is shown in table A-II.

An example of the altimeter data over an anomaly in the gravitational field of the Earth is shown in figures A-18 and A-19. Because of this anomaly, the mean sea level deviates considerably from the spherical Earth model ellipsoid representing the shape of the Earth. These illustrations show a 20-m depression of mean sea level as obtained directly from the altimeter sensor. The altimeter measurements correlate with independent measurements of sea level in this region.

L-Band Radiometer (S194).—The objective of the L-Band Radiometer was to evaluate the applicability of a passive microwave radiometer to the study of the Earth from orbital altitudes. The radiometer measured the brightness temperature of the terrestrial surface along the spacecraft groundtrack to a high degree of accuracy.

The S194 sensor (fig. A-20) had a fixed antenna with a 3-dB (half power) beamwidth of 15.0°. The energy received by the antenna was integrated at a rate that ensured a minimum of 80-percent ground coverage overlap. The receiver provided a digital representation of the 0- to 350-K input radiometric temperature range. The system had an internal calibration network referenced to a fixed hot- or cold-load input.

The radiometric brightness temperature was measured with a resolution of ±1.0 K at a wavelength of approximately 21 cm. The system operated at a center frequency of 1.4125 GHz with a bandwidth of 27 MHz. Operating at this frequency, the sensor provided measurements that were minimally affected by meteorological conditions.

The 3-dB beamwidth implies that 50 percent of the energy received by the antenna was received in the 15°
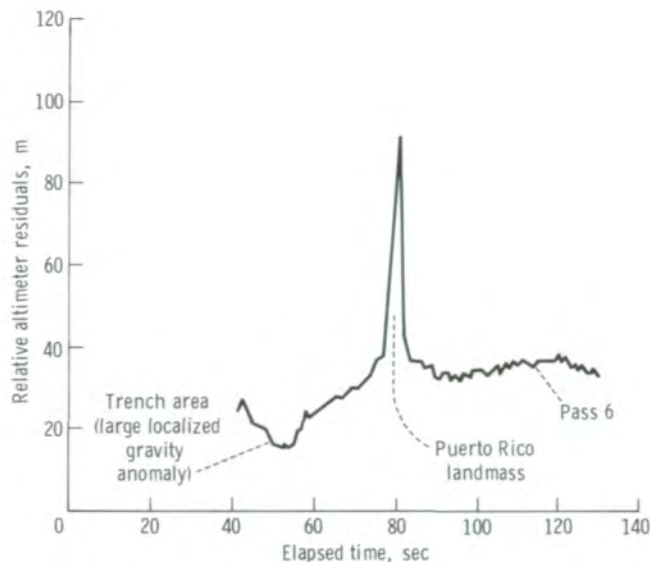
FIGURE A-19.—Altimeter range measurements.

FIGURE A-20.—L-Band Radiometer (S194).

by 13.9° solid pyramid centered about the vertical axis. The antenna received more than 90 percent of the energy available in a first-nulls beamwidth (primary lobe) that encompassed a swath width of approximately 282 km at the 435-km orbital altitude, and the signature was influenced by the entire view area. However, the signature recorded by the facility was influenced to a much larger degree by the brightness of the material contained within the 3-dB beamwidth: a 111-km swath centered about the nadir point. Data output was eighteen 10-bit words/sec. Sensor radiometric calibration was acquired by viewing the Moon and deep space.

Examples of the data produced by the S194 sensor are shown in figures A-21 and A-22. The spacecraft moved from Baja California across the Gulf of California and on into Mexico along the groundtrack shown in the map at the top of figure A-21. The antenna footprint is shown as circles on the flightpath. The solid circle represents the half-power point on the antenna pattern and corresponds to a circular area 124 km in diameter. The first null in the antenna pattern is shown by the dashed circle representing 285 km in diameter. The plot in the lower portion of figure A-21 shows the radiometer response along this groundtrack.
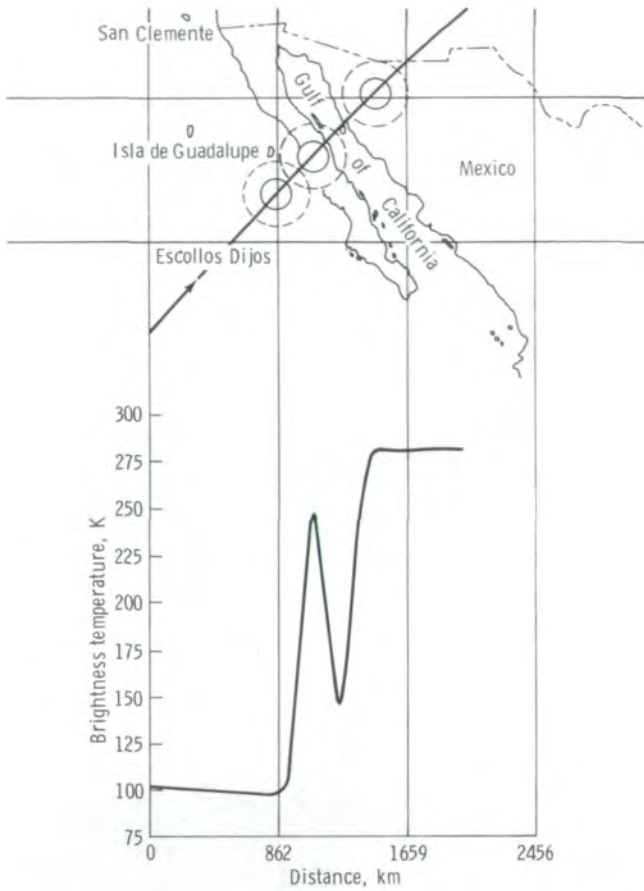
FIGURE A-21.—L-Band Radiometer data from Baja California.
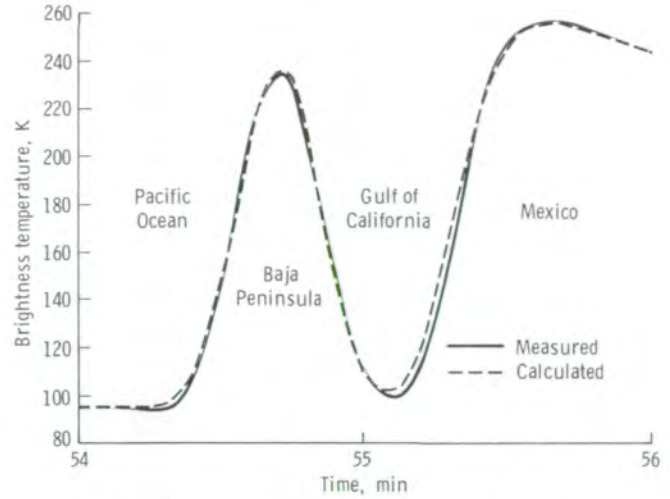
FIGURE A-22.—Brightness temperature plots of data from the L-Band Radiometer.

Radiometer response is shown in terms of microwave brightness temperature. The low temperature of the sea is caused by its low emissivity. Land surfaces have emissivities approaching that of a black body, so that the microwave temperatures for land surfaces are close to actual temperatures.

Correlations were obtained between moisture content of the soil and radiometric data from S193 and S194. The correlations indicate that microwave sensors may be quite useful for such measurements in the future.

Page Intentionally Left Blank

APPENDIX B

Skylab EREP Principal Investigators[a]

United States

ALABAMA

Robert R. Jayroe
NASA George C. Marshall Space Flight Center
Huntsville

ARIZONA

George Gumerman
Prescott College
Prescott

CALIFORNIA

Monem Abdel-Gawad
North American Rockwell Corporation
Thousand Oaks

David C. Anding
Science Applications, Inc.
La Jolla

Ira C. Bechtold
Bechtold Satellite Technology Co.
City of Industry

R. Gordon Bentley
Bureau of Land Management
Riverside

Robert N. Colwell
School of Forestry and Conservation
University of California
Berkeley

A. Earl Davis
Resources Agency of California
Sacramento

Alexander F. H. Goetz
NASA Jet Propulsion Laboratory
Pasadena

Robert C. Heller
USDA/FS
Pacific Southwest Forest and Range Experiment
  Station
Berkeley

Philip G. Langley
Earth Satellite Corporation
Berkeley

Dale F. Leipper
Department of Oceanography
U.S. Naval Post Graduate School
Monterey

Ronald J. P. Lyon
School of Earth Sciences
Stanford University
Stanford

Paul M. Merifield
Earth Science Research Corporation
Santa Monica

Douglas Pirie
U.S. Engineer District
San Francisco

Charles E. Poulton
Earth Satellite Corporation
Berkeley

363

CANAL ZONE

Jack E. Staples
Inter-American Geodetic Survey
Fort Clayton

COLORADO

Peter M. Kuhn
NOAA/ERL/APCL
Boulder

Keenan Lee
Colorado School of Mines
Golden

Roger B. Morrison
U.S.G.S.
Denver

Harry Smedes
U.S.G.S.
Denver

Kenneth Watson
U.S.G.S.
Denver

DELAWARE

Vytautas Klemas
College of Marine Studies
University of Delaware
Newark

Karl-Heinz Szekielda
College of Marine Studies
University of Delaware
Newark

DISTRICT OF COLUMBIA

Robert H. Alexander
U.S.G.S.
Washington

John C. Alishouse
NOAA/NESS
Washington

Richard R. Anderson
Department of Biology
The American University
Washington

James P. Hollinger
Microwave Remote Sensing Section
U.S. Naval Research Laboratory
Washington

Allan Shapiro
U.S. Naval Research Laboratory
Washington

David S. Simonett
Earth Satellite Corporation
Washington

FLORIDA

John W. Hannah
Brevard County Planning Department
Titusville

Aaron L. Higer
U.S.G.S.
Miami

George A. Maul
NOAA/AOML
Miami

Duncan Ross
NOAA/AOML
Miami

ILLINOIS

Ravinder K. Jain
U.S. A.C.E.
Champaign

INDIANA

Roger M. Hoffer
LARS
Purdue University
West Lafayette

LeRoy F. Silva
LARS
Purdue University
West Lafayette

Charles Wier
Department of Natural Resources
Indiana Geological Survey
Bloomington

IOWA

Richard Hoppin
Department of Geology
The University of Iowa
Iowa City

KANSAS

J. R. Eagleman
University of Kansas/CRINC
Lawrence

R. K. Moore
University of Kansas/CRINC
Lawrence

Harold L. Yarger
Kansas Geological Survey
University of Kansas
Lawrence

LOUISIANA

Robert H. Cartmill
NASA Earth Resources Laboratory
Slidell Computer Complex
Slidell

MAINE

Ernest G. Stoeckeler
Maine State Highway Commission
Bangor

MARYLAND

Ronald Brooks
Wolf Research & Development Corporation
Riverdale

Morton Keller
NOAA/NOS
Rockville

C. Lawrence Korb
NASA Goddard Space Flight Center
Greenbelt

William E. Shenk
Meteorology Branch
NASA Goddard Space Flight Center
Greenbelt

R. Lawrence Swanson
NOAA/NOS
Rockville

K. M. Weaver
Maryland Geological Survey
The Johns Hopkins University
Baltimore

MASSACHUSETTS

James C. Barnes
Environmental Research & Technology, Inc.
Lexington

David T. Chang
Environmental Research & Technology, Inc.
Lexington

Saul Cooper
Reservoir Control Center
U.S. A.C.E.
New England Division
Waltham

H. T. U. Smith
Department of Geology
University of Massachusetts
Amherst

MICHIGAN

J. Braithwaite
Environmental Research Institute of Michigan
Ann Arbor

Robert Horvath
Environmental Research Institute of Michigan
Ann Arbor

Lester V. Manderscheid
Department of Agricultural Economics
Michigan State University
East Lansing

Richard F. Nalepka
Environmental Research Institute of Michigan
Ann Arbor

Fabian C. Polcyn
Environmental Research Institute of Michigan
Ann Arbor

Irvin J. Sattinger
Environmental Research Institute of Michigan
Ann Arbor

Frederick J. Thomson
Environmental Research Institute of Michigan
Ann Arbor

Robert E. Turner
Environmental Research Institute of Michigan
Ann Arbor

Robert K. Vincent
Environmental Research Institute of Michigan
Ann Arbor

MISSISSIPPI

Charles W. Bouchillon
Institute of Environmental Studies
Mississippi State University
State College

William H. Stevenson
National Marine Fisheries Service
NASA National Space Technology Laboratories
Bay St. Louis

NEVADA

Jack Quade
Mackay School of Mines
University of Nevada
Reno

NEW HAMPSHIRE

Richard E. Stoiber
Department of Earth Sciences
Dartmouth College
Hanover

NEW YORK

Ernest E. Hardy
New York State College of Agriculture
Cornell University
Ithaca

William Harting
Tri State Transportation Commission
New York

Kenneth R. Piech
Calspan, Inc.
Buffalo

Willard J. Pierson, Jr.
CUNY Institute for Marine and Atmospheric
  Sciences
The City College
New York

Edward Yost
Science Engineering Research Group
C. W. Post Center
Long Island University
Greenvale

NORTH CAROLINA

Lee S. Miller
Engineering & Environmental Sciences Division
Research Triangle Institute
Research Triangle Park

Charles W. Welby
North Carolina State University
Raleigh

NORTH DAKOTA

Harvey K. Nelson
Bureau of Sport Fisheries and Wildlife
Northern Prairie Wildlife Research Center
Jamestown

OHIO

A. G. Mourad
Battelle Memorial Institute
Columbus Laboratories
Columbus

David C. Sweet
Ohio State Department of Development
Columbus

OKLAHOMA

Robert J. Collins, Jr.
Eason Oil Company
Oklahoma City

PENNSYLVANIA

George J. McMurtry
Office for Remote Sensing of Earth Resources
The Pennsylvania State University
University Park

SOUTH CAROLINA

N. K. Olson
Division of Geology
South Carolina State Development Board
Columbia

SOUTH DAKOTA

Victor I. Myers
Remote Sensing Institute
South Dakota State University
Brookings

TENNESSEE

Gerald K. Moore
U.S.G.S.
Nashville

TEXAS

Victor R. Baker
Department of Geological Sciences
The University of Texas at Austin
Austin

Thomas L. Barnett
NASA Lyndon B. Johnson Space Center
Houston

R. Bryan Erb
NASA Lyndon B. Johnson Space Center
Houston

William G. Hart
USDA/ARS
Citrus Insects Research
Weslaco

Harbhajan S. Hayre
Department of Electrical Engineering
Wave Propagation Laboratories
University of Houston
Houston

David E. Pitts
NASA Lyndon B. Johnson Space Center
Houston

James V. A. Trumbull
U.S.G.S.
University of Corpus Christi
Corpus Christi

Craig L. Wiegand
USDA
Rio Grande Soil & Water Research Center
Weslaco

UTAH

M. L. Jensen
Department of Geological & Geophysical Sciences
University of Utah
Salt Lake City

VIRGINIA

Alden P. Colvocoresses
U.S.G.S.
McLean

William J. Hargis, Jr.
Virginia Institute of Marine Science
Gloucester Point

William J. Kosco
U.S.G.S.
McLean

Harold G. Marshall
Department of Biology
Old Dominion University
Norfolk

John D. McLaurin
James W. Schoonmaker, Jr.
U.S.G.S.
McLean

Joseph T. Pilonero
U.S.G.S.
McLean

Doyle G. Smith
U.S.G.S.
McLean

WASHINGTON

William J. Campbell
U.S.G.S.
University of Puget Sound
Tacoma

Troy A. Crites
Kent Junior High School
Kent

David L. Tingey
Boeing Space Center
The Boeing Company
Kent

WISCONSIN

Joseph B. Zmolek
Lourdes High School
Oshkosh

WYOMING

Robert S. Houston
Department of Geology
University of Wyoming
Laramie

International

ARGENTINA

O. Dominquez
Instituto Nacional de Technobgia Agropecuarra
Buenos Aires

Eduardo J. Methol
Direccion Nacional de Geologia y Mineria
Buenos Aires

Rodolfo Liendo Soula
Direccion General de Fabricaciones Militares
Buenos Aires

AUSTRALIA

N. H. Fisher
Bureau of Mineral Resources, Geology and Geophysics
Canberra City

BOLIVIA

Carlos Brockmann
Director, Servicio Geologico de Bolivia
La Paz

BRAZIL

Luis Henrique de Azevedo
Berilo Langer
Ministry of Mines and Energy
DNPM - Project RADAM
Rio de Janeiro

Fernando de Mendonca
Instituto de Pesquisas Espaciais (INPE)
São Jose dos Campos
São Paulo

CANADA

R. A. Stewart
Topographical Survey Directorate
Surveys & Mapping Branch
Department of Energy, Mines and Resources
Ottawa, Ontario

K. P. B. Thomson
Canada Centre for Inland Waters
Burlington, Ontario

CHILE

Hector Inostroza
Reinaldo Aldunate
Instituto Hidrografico de la Armada
Valparaíso

ENGLAND

P. G. Mott
Hunting Surveys Ltd.
Boreham Wood, Hertfordshire

R. M. Shackleton
Research Institute of African Geology
University of Leeds
Leeds

J. L. Van Genderen
Department of Geography
The University of Sheffield
Sheffield

FEDERAL REPUBLIC OF GERMANY

Deiter Bannert
Geological Survey of the Federal Republic of Germany
Hannover

J. Bodechtel
Institut für Allgemeine und Mineralogie
  der Universität München
München

Klaus Giessner
Geographisches Institut
University of Technology
Hannover

Peter Kronberg
Geologisches Institut
Technische Universität Clausthal
Zellerfield

Franz K. List
Free University of Berlin
Lehrstuhl für Angewandte Geologie
Berlin

Gunther Stuckmann
Geographisches Institut
University of Technology
Hannover

FRANCE

Jacques Guillemot
Institute Français du Petrole
Rueil-Malmaison

M. Villevieille
Bureau d'Etudes Meteorologie Spatiales
Paris

INDIA

P. R. Pisharoty
Indian Space Research Organization
Physical Research Laboratory
Ahmadabad

IRAN

K. Ebtehadj
The Plan Budget Organization
Tehrān

ISRAEL

Joseph J. Otterman
Tel Aviv University
Department of Environmental Sciences
Ramat Aviv

ITALY

Roberto Cassinis
Geolab
Milan

O. E. Fischnich
Food and Agricultural Organization
Rome

Attilio Moretti
Servizio Geologico d'Italia
Rome

JAPAN

Takakazu Maruyasu
Institute of Industrial Science
University of Tokyo
Tokyo

Kiyoshi Tsuchiya
Forecast Division
Japan Meteorological Agency
Tokyo

Kantaro Watanabe
Kyoto Gakuen University
c/o Kobe Marine Observatory
Kobe

MALAYSIA

J. B. Ahmad
Geological Survey of Malaysia
Ipoh

MALI

Mamadu Konate
Department of Mines and Geology
Ministry of Industrial Development and Public Works
Koulouba, Bamako

MÉXICO

Francisco Arzate
Ministry of Public Works
Mexico City

Luis Del Castillo
Univ. Nal. Aut. de México
Instituto de Geofisica de Exploracion
Ciudad Universitaria

Carlos Acosta Del Campo
Consejo de Recursos Naturales
No Renovables
México 7, D.F.

Nicolas Sanchez Duron
Direccion General de Agricultura
Baldera

Jose Amando Diez Perez
Secretaria de Recursos Hidraulicos
Pisco

Arturo Gonzalez Salazar
Comision Federal de Electricidad
Pisco

Carlos Castillo Tejero
Instituto Mexicano del Petroleo
México 14, D.F.

Jorge F. Vaca
Comision de Estudios del Teritorio Nacional
Secretaria de la Presidencia
San Antonio

NETHERLANDS

H. E. C. van der Meer Mohr
International Institute for Aerial Survey and Earth
    Sciences (ITC)
Enschede

SWITZERLAND

Harold Haefner
University of Zürich
Zürich

THAILAND

Pradisth Cheosakul
National Research Council
Bangkok

VENEZUELA

Jose Antonio Galavis
Chief, Marine Geology Division
Ministry of Mines and Hydrocarbons
Centro Simón Bolívar
Caracas

APPENDIX C

Photograph Index

Skylab Earth Resources Experiment Package (EREP) photographs cited in the discipline summary sections are listed by geographic areas. Reproduction of the photographs can be obtained from the Earth Resources Observation Systems (EROS) Data Center, Sioux Falls, South Dakota 57198.

Geographic location	Photograph no.	EROS Data Center identification no.	Figure no.
Africa			
Mauritania	SL3-84-360	G30A843600000	5-23
Asia			
Japan	SL4-89-398	G40B893980000	5-27
	Aircraft	—	5-26
Atlantic Ocean			
Puerto Rico	SL2-81-240	G20B812400000	5-30
	S192	—	5-12(a)
Europe			
France	SL3-34-321	G30A343210000	4-14
Sicily	SL3-87-355	G30B873550000	4-18
Moon and Earth limb			
Moon and Earth limb	SL3-119-2253	G370119225300	5-33, upper frame
	SL3-119-2254	G370119225400	5-33, center frame
	SL3-119-2255	G370119225500	5-33, lower frame
Earth limb	SL4-200-7639	G470200763900	5-34(a), frame 1
	SL4-200-7640	G470200764000	5-34(a), frame 2
	SL4-200-7641	G470200764100	5-34(a), frame 3
	SL4-200-7642	G470200764200	5-34(a), frame 4
	SL4-200-7643	G470200764300	5-34(a), frame 5
	SL4-200-7644	G470200764400	5-34(a), frame 6
	SL4-200-7645	G470200764500	5-34(a), frame 7
	SL4-200-7646	G470200764600	5-34(a), frame 8
	SL4-200-7647	G470200764700	5-34(a), frame 9

Geographic location	Photograph no.	EROS Data Center identification no.	Figure no.
Moon and Earth limb			
Earth limb	SL4-200-7648	G470200764800	5-34(a), frame 10
	SL4-195-7315	G470195731500	5-34(b), frame 1
	SL4-195-7316	G470195731600	5-34(b), frame 2
	SL4-195-7317	G470195731700	5-34(b), frame 3
	SL4-195-7318	G470195731800	5-34(b), frame 4
	SL4-195-7319	G470195731900	5-34(b), frame 5
	SL4-52-388	G40A523880000	5-35
North America			
Great Lakes Region	SL3-40-016	G30A400160000	4-21(a), 4-21(b)
Canada	SL4-93-041	G40B930410000	5-14(b)
	SL4-69-058	G40A690580000	5-14(a)
	SL4-140-4215	G470140421500	5-16(a)
	SL4-140-4216	G470140421600	5-17(a)
	SL4-141-4321	G470141432100	5-16(b)
	SL4-141-4327	G470141432700	5-17(b)
	SL4-141-4331	G470141433100	5-15
	SL4-141-4366	G470141436600	5-17(c)
	SLAR[a]	—	5-19
	[b]RC8-70-061	625900700, roll 61	5-20(b)
	[b]RC8-70-044	625900700, roll 44	5-20(c)
	[b]RC8-70-050	625900700, roll 50	5-20(d)
	S192	—	6-41
South America			
Argentina	SL3-34-165	G30A341650000	3-6(a)
	SL3-33-162	G30A331620000	4-26(a)
Brazil	SL3-33-093	G30A330930000	3-5(a)
	SL3-83-361	G30B833610000	3-2(a)
United States			
Alabama	SL4-93-152	G40B931520000	2-17
	S192	—	5-43
Arizona	SL4-90-305	G40B903050000	2-29(a)
	SL3-86-011	G30B860110000	2-7(a), 6-5
	SL4-92-356	G40B923560000	A-7(b)
	SL4-93-057	G40B930570000	A-7(d)
	S190A	—	6-35(b)
	S192	—	6-35(c)
	SL4-90-306	G40B903060000	4-8
	S192	—	4-10(a), 4-10(b)
	SL4-94-237	G40B942370000	4-19(b)
	S-74-23477 (S192)	—	6-13

[a]Side-looking airborne radar.

[b]Aircraft camera.

Geographic location	Photograph no.	EROS Data Center identification no.	Figure no.
United States			
California	SL2-04-121	G20A041210000	3-3(a)
	SL2-03-121	G20A031210000	3-3(b)
	S192	—	3-4
	SL3-87-111	G30B871110000	4-6
	SL4-92-333	G40B923330000	6-15
	SL4-78-071	G40A780710000	6-17(a)
	SL4-77-071	G40A770710000	6-17(b)
	S-73-1227	—	6-1
	SL4-92-336	G40B923360000	6-20(a)
	S192	—	6-36
	SL4-92-351	G40B923510000	6-27(a)
	S192	—	6-27(b)
	SL4-94-013	G40B940130000	4-11(a), 4-11(b)
	cS-75-31982	—	4-11(c)
	SL4-76-078	G40A760780000	4-15(a), 4-15(b)
	SL4-92-335	G40B923350000	4-17(a), 4-17(b)
	S192	—	4-17(c)
	S192	—	4-23(a), 4-23(b)
	SL4-92-349	G40B923490000	4-24(a)
	SL4-92-351	G40B923510000	4-25(a)
	Aircraft	—	4-25(b)
	SL4-77-071	G40A770710000	5-28
	SL4-78-069	G40A780690000	5-21
	NOAA-3 image	—	5-22
Colorado	SL2-09-017	G20A090170000	2-1(a)
	SL3-21-331	G30A213310000	2-1(b)
	SL3-21-004	G30A210040000	3-7(a)
	Aircraft	—	3-9(a)
	Aircraft	—	3-9(b)
	Aircraft	—	3-9(c)
	Aircraft	—	3-9(d)
	SL2-81-020	G20B810200000	3-8(c)
	SL2-15-010	G20A150100000	3-8(a)
	SL2-15-009	G20A150090000	3-8(b)
	S192	—	3-8(d)
	SL2-10-016	G20A100160000	4-22(a), 4-22(b)
	S192	—	4-22(c)
	S192	—	3-13
	S192	—	2-12(a)
	S192	—	6-31
	S192	—	6-32(a), 6-32(b)
Connecticut	SL3-88-276	G30B882760000	2-8(a)
Florida	SL3-88-141	G30B881410000	A-10(b)
Georgia	SL4-90-046	G40B900460000	3-11
Indiana	S192	—	2-11

cGround camera.

Geographic location	Photograph no.	EROS Data Center identification no.	Figure no.
United States			
Kentucky	SL4-90-032	G40B900320000	2-18(a), 2-18(b)
Louisiana	SL3-83-056	G30B830560000	6-34(b)
	SL3-22-120	G30A221200000	6-34(a)
	S192	—	6-34(c)
Maryland	SL2-15-174	G20A151740000	2-20(a)
	SL3-39-123	G30A391230000	2-20(b)
	SL3-83-166	G30B831660000	2-13(a)
	SL3-83-166	G30B831660000	2-3(a)
	SL3-15-172	G30A151720000	2-3(b)
Mississippi	SL4-92-295	G40B922950000	2-6
Nebraska	S-73-1510 (S192)	—	6-10
	S-73-2839	—	6-11
Nevada	SL3-25-059	G30A250590000	A-9, station 1
	SL3-26-059	G30A260590000	A-9, station 2
	SL3-27-059	G30A270590000	A-9, station 3
	SL3-28-059	G30A280590000	A-9, station 4
	SL3-29-059	G30A290590000	A-9, station 5
	SL3-30-059	G30A300590000	A-9, station 6
	S192	—	A-13
	S192	—	4-9(a), 4-9(b)
	SL3-28-057	G30A280570000	4-12(a)
	S192	—	4-16
New Jersey	SL3-86-303	G30B863030000	2-21(a)
New York	S190A	—	2-5(a), 2-5(b)
	SL3-88-274	G30B882740000	2-2(a)
	SL3-87-300	G30B873000000	2-2(b)
	S190A	—	6-21
North Dakota	S192	—	2-22
Ohio	Aircraft	—	6-19(a)
	S190B	—	6-19(b)

Geographic location	Photograph no.	EROS Data Center identification no.	Figure no.
United States			
Oklahoma	SL4-90-144	G40B901440000	4-13(a)
South Dakota	SL2-08-113	G20A081130000	4-5(a)
	SL2-09-121	G20A091210000	4-5(b)
	SL2-81-316	G20B813160000	4-20(b)
Texas	SL4-94-111	G40B941110000	2-25(a)
	SL4-93-326	G40B933260000	3-1(a)
	SL4-91-005	G40B910050000	3-1(b)
	Aircraft	—	3-1(c)
Utah	SL3-83-300	G30B833000000	2-19
	S192	—	6-18
	SL2-81-016	G20B810160000	4-1(a)
	SL2-10-010	G20A100100000	4-2(a)
Wyoming	SL3-88-018	G30B880180000	4-3(a)
	SL2-82-146	G20B821460000	4-4(a)
Skylab and engineering photographs			
S191 engineering instrument	—	—	A-11(a)
S192 engineering instrument	—	—	A-12(b)
EREP sensors	SL3-114-1659	G370114165900	A-1
S190 engineering instrument	S-72-44415	—	A-8(a)
	S-72-44416	—	A-8(b)
S193 engineering instrument	—	—	A-15
S194 engineering instrument	—	—	A-20
EREP sensor coverage	S-73-005-S	—	1-3, A-3

Page Intentionally Left Blank

APPENDIX D

Principles of Photographic and Digital Data Analysis

In this appendix, the methods and terms most commonly used in the analysis of photographs and images[1] and in the preprocessing and analyzing of multispectral scanner digital data are discussed. The analysis of microwave data requires highly specialized techniques; therefore, detailed discussion of procedures and methods for analyzing such data is contained in section 6.

Fundamentals of Photographic Interpretation

ROBERT N. COLWELL[a]

Photographic interpretation involves the systematic examination of negative or positive prints and transparencies for the purpose of identifying objects and judging their condition or significance. This process requires planning a sequence of activities which includes defining the data geometry, enhancing the data, identifying the data characteristics, and interpreting the results.

PHOTOGRAPHIC GEOMETRY

The first step in photointerpretation is to establish the method of acquiring the data and its significance in reference to a set of known features or relationships. By this means, the interpreter can define the general proportional perspective of features on the photograph and can form a standard for measurement of specific objects.

The geometric relationships among film negative, camera lens, and target for vertical photographs are illustrated in figure D-1. Three principal points that define the positions *a*, *b*, and *c* on the film correspond to
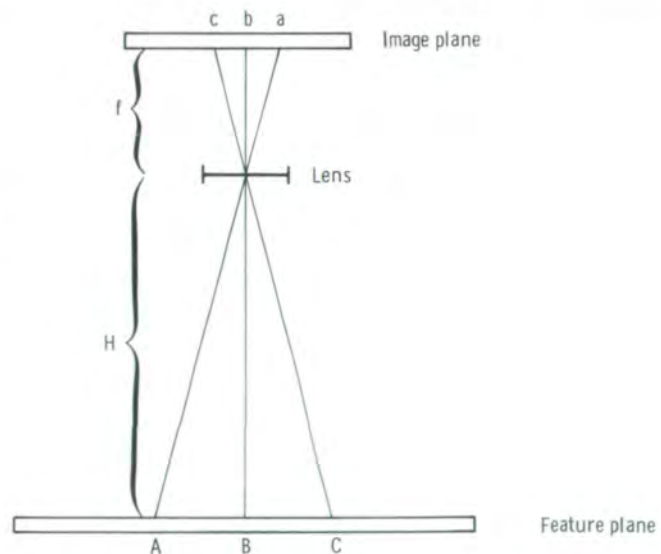
FIGURE D-1.—Diagram illustrating the imaging of ground objects in vertical aerial photographs.

---

[1] Positive prints and transparencies are often referred to as "images." In this report, "image" or "imagery" is defined as a print or a transparency generated from electronic data (i.e., multispectral scanner).

[a] University of California at Berkeley.

points A, B, and C on the imaged surface. The perpendicular distance f from the camera lens to the film is the focal length of the camera.

The scale S is the relationship between a distance on the photograph and the corresponding distance on the ground. For example, in figure D-1,

$$S = \frac{ab}{AB} \qquad (D1)$$

The larger the denominator of the fraction, the smaller is the scale of the photograph. The scale of the photograph can also be determined from the relationship between the camera focal length f and the camera altitude H at the instant of photography. Then,

$$S = \frac{f}{H} \qquad (D2)$$

For example, the scale of the original film image of the Skylab Earth Terrain Camera (S190B) with a 45.7-cm focal length, taken at a spacecraft altitude of 435 km, is

$$\frac{0.457}{435\ 000} \text{ or } \frac{1}{951\ 860}$$

This fraction indicates that one measurement unit on the photograph corresponds to 951 860 of the same units on the ground. Thus, the scale of the photograph is approximately 1:950 000.

PHOTOINTERPRETATIVE EQUIPMENT

Photointerpreters use equipment for three general purposes: viewing, measuring, and transferring or recording detail. Measuring instruments may be used on single photographs or stereoscopic pairs. Viewing equipment is used to increase the interpreter's ability to scan or study photographs. Some of these instruments provide a stereoscopic (three dimensional) view of overlapping photographs under various magnifications, whereas others provide only a two-dimensional but magnified view of objects on photographs. Light tables aid the photointerpreter in screening and selecting photographs, judging the importance or quality of the photographs, and examining transparencies or nega-

tives. The stereoscope, a binocular viewing instrument that through a combination of lenses, mirrors, and prisms provides a three-dimensional view of photographs, is one of the most important instruments used in photointerpretation. The stereoscopic principle is used in measuring and plotting instruments that are designed primarily for viewing photographs and/or images generated from multispectral scanners (e.g., S192) or enhancement of photographs. Measurement is also done with a hand lens on which a scale has been etched. Various ruler-type and caliper-type scales are also used. To transfer information from the photograph to a base map or descriptive chart, optical and mechanical devices are used. In many Earth Resources Experiment Package (EREP) experiments, zoom transfer scopes were used to optically converge the scale of the photograph with that of the base map. Optical devices were used to enlarge or reduce the photographs and aid in the transfer of data. Proportional dividers and pantographs can also be used to transfer small amounts of detailed information.

PHOTOGRAPH ENHANCEMENT

Enhancement devices are equally as useful on photographic and electronically derived images for increasing the amount of information that can be interpreted by the analyst. Forms of enhancement include density slicing, color coding, and combining multiple images into a single composite. Some analysts advocate the use of multiple lantern-slide projectors or other optical devices for this purpose, whereas others prefer electronic devices such as closed-circuit television equipment. A combination of optical and electronic devices is especially useful when several multidate or multiband images of the same area, each containing different information, are available.

In addition to the advantages common to both optical and electronic enhancement techniques, some important relative advantages and limitations are associated with each technique. Generally, optical enhancement methods and techniques provide better spatial resolution (i.e., higher definition) and enable the use of simpler and less costly equipment. However, electronic methods and techniques offer advantages based on their capability to quickly select and mathematically expand data, to assign color hues, to combine multidate and multiband data for analysis, and to geometrically correct an image or a photograph.

PHOTOGRAPH CHARACTERISTICS

The synoptic view of Earth provided by space photographs requires the analyst to revise his concepts of the significance of shape, size, shadow, tone, color, texture, and pattern characteristics of objects in the image. As an example, much of the EREP data consists of vertical photographs covering in excess of 26 000 km^2 of the Earth surface. From this new perspective, some features assume greater importance in space photographs than in the ground view and details that may predominate in the ground view may be nearly indistinguishable from space.

The shape of an object as seen in the plan view portrayed by a vertical photograph provides an important and sometimes conclusive indication of its structure, composition, and function. For example, in the vertical view of a forest, its economic and recreational value may be apparent. The vertical view of a landform may show effects of tectonic and erosional processes. To the motorist, a cloverleaf intersection is an incomprehensible maze; to the analyst, however, the form and function of the intersection are clearly evident. Shape is valuable to the interpreter because it establishes the class of objects to which an unknown object must belong; shape frequently enables a conclusive identification, and it aids in the understanding of significance and function of the object.

The size of an object is one of the most useful clues to its identity. By measuring an unknown object on a photograph, the interpreter can eliminate from consideration groups of features or phenomena. Size can also be used to formulate sets of possible inferences that may help to identify significance. For example, measurement of the length of a runway can indicate whether or not an airfield can accommodate large jet aircraft.

Shadow in vertical photographs sometimes aids the interpreter by providing dimensional representations of landforms or other objects of interest. Although shadows can affect the photointerpreter's depth perception, they are often an invaluable aid in estimating heights or depths of objects. In nearly flat terrain, subtle variations on the surface which would otherwise be difficult to detect are emphasized by shadows. However, because objects in the shaded area reflect so little light to the spacecraft camera, they are rarely visible in space photographs.

Tone and color perception are important elements in the analysis of photographs. On black-and-white photographs, distinctions between objects are observed only in tones of gray. On color photographs, hue brightness and saturation as well as tone can be used to distinguish objects. The color of surface objects, particularly when viewed from space, rarely corresponds to the ground-level perceptions. A body of water may appear in tones ranging from white to green to black, depending on the Sun angle, the viewing angle, and the condition of the surface reflecting light to the camera lens. A black asphalt road may appear very light in tone because of its smooth surface. When the photointerpreter understands the factors that govern the photographic tone or color of objects of interest, these characteristics become major clues to their identity or composition.

Texture in photographs is the result of tonal repetitions in groups of objects too small to be discerned as individual objects. Thus, the size of an object required to produce texture varies with the scale of the photograph. In large-scale (1:5000) photographs, trees can be seen as individual objects and their leaves or needles, although not seen separately, contribute to the texture of the tree crowns. Similarly, in small-scale (1:250 000) photographs, the individual tree crowns, although not seen separately, may contribute to the texture of the whole stand of trees. Thus, the texture of a group of objects (e.g., a timber stand of a certain species composition) may be distinctive enough to serve as a reliable clue to the identity of the objects.

Scientists have stressed the pattern, or the spatial arrangement and association, of objects as an important clue to their origin, to their function, or to both. Geographers and anthropologists study settlement patterns and their distribution to understand the effects of diffusion and migration in cultural history. Outcrop patterns provide geologists clues to geological structure, and drainage patterns have orderly association with structure, lithology, and soil texture. The varying relationships between vegetative elements and their environment produce some characteristic patterns of plant association.

Many regional patterns and associations that formerly could be studied only through laborious ground observation are clearly and quickly visible in space photographs. Moreover, these photographs may capture many significant patterns, such as fracture traces and tonal "anomalies" that the ground observer might overlook or misinterpret because of his limited field of view. The trained observer appreciates the significance of space photographs chiefly through his understanding of patterns and associations on the Earth surface.

INTERPRETATIVE ACTIVITIES

The interpreter observes characteristics of the photograph or image and determines the identity and significance of the objects they represent. The analysis process occurs in a time sequence beginning with a search process that results in the detection of important features, some of which may require measurement. Measurement is followed by consideration of the features in terms of collateral information, usually nonpictorial, from the interpreter's special field of knowledge. On the basis of these actions, hypotheses concerning the identity and significance of the features are formed. Finally, the interpreter must evaluate the identity and significance. In some instances, it may be possible to perform field checks to validate his deductions as to the identity of an object. Thus, the five important sequential activities of photointerpretation include search techniques, the use of indicators, measurement, deductive reasoning, and field checking.

Interpretation begins with close examination of all details that are considered relevant. However, most experienced interpreters prefer to begin by scanning the photograph or image as a whole. It is usually necessary to study the photograph or image with reference to an index map or a photomosaic which serves as an index map. A large-scale map, preferably topographic, is useful as a base map.

Many characteristics may provide indications as to the identity of an unknown object. No single indicator is likely to be infallible; but if all or most of the indicators lead to the same conclusion, the conclusion is probably correct. Photointerpretation, therefore, is highly dependent on the science of probabilities. The principle involved, known as "convergence of evidence," requires that the interpreter first recognize basic features or types of features and then consider their arrangement (pattern) in the areal context. Several alternative interpretations may be possible. With the aid of photointerpretative keys, critical examination of the evidence usually reveals that all interpretations except one are unlikely or impossible.

Photointerpreters can measure the exact dimensions of features using scales and other instruments. Generally, however, photointerpretative measurement involves making visual estimates of the size and shape of an object. A reasonably correct estimate of dimensions is essential to correct identification. Plotting and drawing to known scales may also be regarded as further activities of measurement.

By means of deductive reasoning based on the previously described activities, the interpreter can identify objects and features on the photograph or image. On the basis of these deductions, the interpreter documents his response by labeling (naming or describing) the identified features. The labeled products are often called thematic or classification maps.

Much scientific knowledge has been tested by the patient correlation of photographed or imaged features with ground features by means of careful field checking. Many established correlations are taught as basic principles in the various photointerpretation disciplines. Nevertheless, in almost every interpretative task, unknowns or uncertain conclusions will arise that must be checked in the field. The interpreter should conduct field checking whenever feasible to validate his work. Some types of work require field correlation before and after the interpretation. The amount of fieldwork necessary varies with the requirements for accuracy, the complexity of the area, the quality of the photographs or images, and the ability of the interpreter.

Digital Analysis Techniques

Roger M. Hoffer[b] *and A. Victor Mazade*[c]

Current procedures for processing and analyzing digital data from the EREP Multispectral Scanner (S192) or similar systems involve four primary activities: preprocessing, display and enhancement, analysis and classification, and evaluation. Although many variations and combinations of these activities provide a flexible analytical system, this section is intended to give a very brief overview of techniques used by many investigators.

[b]Purdue University.

[c]Lockheed Electronics Company, Inc.

PREPROCESSING

Preprocessing involves various manipulations that make the data more usable. It is important to note that no actual data analysis or interpretation occurs in this phase of the activity. A major preprocessing activity performed on the digital data is editing, in which the portion of the data of particular interest to investigators is located and extracted from the total data set. Optical-mechanical systems record scanner data in either a straight or a conical scan-line configuration. Landsat is typical of the former, whereas EREP (S192) is characteristic of the latter. Because most users of digital data do not have the capability to display conical scan-line formats, a special preprocessing of the S192 data was required to display the data in approximately the correct geometric output format. Because geometric distortion across the scene makes the location of specific geographic features difficult, the conical scan-line data were resampled and data tapes reconstructed so that the data could be displayed using straight scan-line display equipment. This process enabled the users to display the data with their own equipment and still obtain output products having reasonably accurate geometric fidelity. The third major task of preprocessing and reformatting involves digital filtering of the data to improve the data quality (signal-to-noise ratio). Preliminary work with the S192 data indicated that some wavelength bands were extremely noisy. These noise patterns were complex and included both systematic and random noise. To decrease the effect of the systematic noise, a series of digital noise filters was developed, and much of the S192 data was preprocessed with the digital noise filters.

For selected Earth resources studies, some investigators have subjected their data sets to a geometric correction and rotation sequence designed to correct for the orbital path of the satellite and to enable display of the data at a geometrically correct scale. Other investigators have performed additional data preprocessing to adjust the data values to a particular discipline requirement, including merging the data for bands with two scientific data outputs, or have transformed the data by mathematical methods into an entirely new set of values. A few investigators have registered their scanner data to other data sets, such as Landsat-1 data or U.S. Geological Survey topographic maps.

DISPLAY AND ENHANCEMENT

The display of computer-enhanced data can assume several forms. One of the more common procedures is to illuminate imagery of three individual wavelength bands of the original satellite data through appropriate color filters to obtain false-color composites. Using digital data, channels can be assigned to the three color guns of a cathode-ray device and thus create a false-color-composite image. This approach has been successfully used for the Landsat data. Numerous combinations of false-color-composite images can be obtained.

A variety of mathematical functions can be applied to the digital data to enhance display. The data value range may be expanded or compressed to increase or decrease contrast, or data value ranges may be segmented with colors assigned to identify different ranges. Data values may be combined by addition and subtraction or may be ratioed to emphasize degrees of similarity or difference between channels. By taking mathematical transforms of groups of channels, entirely new data sets may be formed to isolate a particular feature in the data.

ANALYSIS AND CLASSIFICATION

During the past decade, considerable progress has been made in the development of computer-aided analysis techniques involving the application of pattern recognition theory to multispectral scanner data. The basic procedure used for analysis of multispectral scanner data normally includes the following steps.

1. Definition of the parameters of the classification problem

2. Selection of a classification technique

3. Identification of areas within the scene for which reference data (i.e., ground truth) are known

4. Calculation of various statistical parameters for the area of interest

5. Classification of the data into spectral classes

6. Display and/or tabulation of the classification results

The first step in classification consists of the formulation of a set of objectives against which the final results will be measured, the establishment of a procedural analysis plan, and the selection of a data set.

The objectives may include such items as the desired accuracy standards or informational content of the final product. The procedural plan outlines the major steps and contingencies to be followed and defines the classification algorithm to be used. A data set that is appropriate for the objectives is selected. The set may include a small area about which detailed information is desired, may be a test area from which inferences to a much larger area are possible, or may actually include a relatively large geographic area (i.e., several thousand square hectometers).

Sample areas for which detailed reference data (i.e., ground truth) are available are identified in the data set to develop a truly representative set of training statistics. Reference data may also include results of field surveys or radiometric measurements made at the time of data collection, as well as information from photographs and maps. The sample areas are located within the data set and labeled for future use. Some of the sample areas are designated "training areas," and the reflectance values of these areas are used to define the classification statistics. Other sample areas, designated test areas, are reserved for evaluating the accuracy of the final product.

The two basic classification techniques are supervised and unsupervised. In the supervised technique, the computer, in essence, compares the statistical parameters of each point (picture element or pixel) with the statistical parameters of known surface features selected by the analyst. Based on probability decisions defined by the classification algorithm used, the computer assigns each data point to the most similar defined feature type. This supervised classification technique is used when the features of known interest are easily located in the data set and are homogeneous in character. For example, when an analyst knows that a particular agricultural crop was imaged in a specific portion of the data, this area can be identified and used as a "training field" from which spectral reflectance values can be determined. Such training fields are defined for several crop species and cover types. The data values for each remaining data point in the scene then are compared to the reflectance values of the training data and classified, on the basis of the probability

parameters, into one of the crop species or cover-type categories defined by the training data. After classification, the analyst may also assign a "threshold" parameter that defines the maximum amount of difference acceptable between the data point reflectance values and the reflectance values of the known feature type. If the probability decision falls below a defined threshold level, the data are displayed as a blank.

In the unsupervised technique, often called "clustering," the data points are classified on the basis of similarity to other data points in the scene. The computer examines the spectral signature of each data point in the scene and then statistically divides the entire scene into the number of spectral classes or groups specified by the analyst. This technique is used when features of known interest cannot be specifically located in the scene or are not homogeneous. For example, an analyst interested in a wild-land area containing a very complex mixture of cover types may program the computer to classify the scene into 12 or 16 groups having similar spectral characteristics. After the classification has been performed, the analyst attaches a significance to the classes on the basis of some other reference information, such as an aerial photograph.

Some analysts use a combination of the two techniques to take advantage of the special features of each. Regardless of the technique, it is important to recognize that, in most cases, the results obtained are as much a function of the manner in which the analyst has interfaced with the data as they are of the particular algorithm being used. Analyst skills in quantifying the overall objectives and in understanding the computer-processing system are of critical importance in the effective use of computer-aided analysis techniques.

Classification of the data is accomplished by the computer, using one of several possible algorithms available. The maximum likelihood based on Gaussian distribution has been commonly used in the past and was the algorithm used in several of the Skylab investigations. Other decision strategies can be used that employ functions based on linear discrimination or geometric proximity (nearest neighbor). The computer time required for the actual classification task may range from a few seconds to several minutes, depending

on the number of wavelength bands in the data set, the number of spectral classes defined, the type of computer, and the efficiency of the software. It is also important to recognize that the classification can be extended to relatively large geographic areas. It is these types of classification tasks, involving thousands or millions of square hectometers, that most effectively use the power of the computer (e.g., rapid classification and tabulation of large quantities of data).

Display of the classification results is normally accomplished by using either an image-type or a tabular format. Image-type formats, often obtained from a standard computer line printer, print out a symbol that is distinctive for each classification category. The symbols are arranged in the sequential fashion of the data and present a geographic distribution of the results. Direct image formats provide similar information but use cathode-ray tubes or film recorders to display the results, often with colors to indicate the various cover types and to identify their location. This technique is useful for comparing the results with maps or aerial photographs.

Tabular formats may be summary statistics that indicate the number of data points classified into each category. These formats are used when estimates of the total area of a class type are desired, such as the number of square hectometers of hardwood forest in the scene. Because each data point or resolution element of satellite data represents an area on the ground (approximately 0.56 hm²/resolution element for the reformatted S192 data), a conversion factor is applied to determine the number of square hectometers in each cover type of interest. The percentage of the entire classified area, as well as the area covered by each of the species or cover types of interest, can be rapidly calculated.

ANALYSIS EVALUATION

Analytical results are evaluated using both qualitative and quantitative techniques. The analyst may obtain a quick subjective impression by comparing the display of the classification results with an aerial photograph or a thematic map. When satisfied that the product is generally acceptable, he then undertakes a more objective evaluation. Quantitative evaluation is extremely important for assessing the accuracy of the classification obtained at different times of the year or for comparing results obtained from the use of different combinations of wavelength bands in the analysis.

In the most common approach, test areas reserved during the preliminary analytical stages are evaluated by comparing the known reference information with the classification results. Any data point classified into the same category as defined by the reference information is called "correct"; others are errors. Standard statistical techniques are then used to determine the quantitative accuracy and significance based on the number of correct and erroneous data points in the test area. Depending on the number and adequacy of the test areas, the tested accuracy can be projected to the entire scene.

Another test can be performed by comparing the total area classified in a category with the total area derived from some other source, such as census-type data or areas obtained by interpretation of aerial photographs. Classification errors for individual data points may be averaged over the entire scene. For example, if the number of "forest" data points misclassified as "other" is equal to the number of "other" data points misclassified as "forest," the total area of the forest may be correct even though numerous individual data points may be misclassified.

Many researchers believe that the major potential advantage of digital processing is the quantitative nature of the available information. Preprocessing activities facilitate accurate formatting of the geometric and radiometric quality of the data to fit the user's specific requirements. Display and enhancement techniques can be used to emphasize features of particular interest. Analysis and classification can be accomplished in a consistently accurate and systematic manner. Statistical evaluation steps indicate the degree of classification accuracy within a scene and among different scenes. With these tools, the computer-assisted analyst can make scientifically valid, objective decisions concerning the Earth's resources.

Page Intentionally Left Blank

APPENDIX E

Standard Weather Symbols
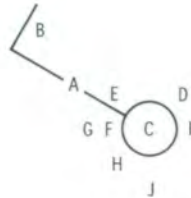
A, B
Wind Direction and Windspeed

Symbol	Speed, knots	Speed, m/sec
◎	Calm	Calm
—	1 - 2	0.5 - 1
＼	3 - 7	1.5 - 3.6
＼	8 - 12	4.1 - 6.2
＼	13 - 17	6.7 - 8.7
＼	18 - 22	9.3 - 11.3
＼	23 - 27	11.8 - 13.9
＼	28 - 32	14.4 - 16.5
＼	33 - 37	17 - 19
＼	38 - 42	19.5 - 21.6
＼	43 - 47	22.1 - 24.2
＼	48 - 52	24.7 - 26.7
＼	53 - 57	27.3 - 29.3
＼	58 - 62	29.8 - 31.9
＼	63 - 67	32.4 - 34.5
＼	68 - 72	35 - 37
＼	73 - 77	37.6 - 39.6
＼	103 - 107	53 - 55

⟶ (wind direction)

A Direction from which wind is blowing (See symbols at left.)
B Windspeed (See symbols at left.)
C Extent of cloud cover (See symbols below.)
D Barometric pressure reduced to sea level, kilopascals (millibars)
E Air temperature at time of reporting, kelvin
F Weather condition at time of reporting (See symbols below.)
G Visibility, meters
H Dewpoint temperature, kelvin
I Pressure change during the 3-hr period preceding observation, kilopascals (millibars)
J Height of base of lowest cloud, meters

Missing or unavailable data are indicated by "M" in the proper location.

C
Cloud Cover

Symbol	Percent covered
○	Clear
◔	Up to 10
◔	20 to 30
◑	40
◑	50
◕	60
◕	70 to 80
◖	90 or overcast with openings
●	Completely overcast
⊗	Sky obscured

F
Present Weather Conditions

Symbol	Explanation
∿	Visibility reduced by smoke
∞	Haze
،	Intermittent drizzle (not freezing), slight
••	Continuous rain (not freezing), slight
⦂•	Continuous rain (not freezing), moderate
✳	Intermittent snow, slight
▽	Slight rain showers
▽	Slight snow showers

Temperature

Kelvin	Fahrenheit
311	100°
305	90°
300	80°
295	70°
290	60°
285	50°
280	40°
275	30°
270	20°
265	10°
260	0°
255	-10°
250	-20°
245	-30°
240	-40°
233	

Pressure

Kilopascals	Millibars	Inches of mercury (32° F)
105.5	1055	
105	1050	31
104.5	1045	
104	1040	
103.5	1035	30.5
103	1030	
102.5	1025	
102	1020	
101.5	1015	30
101	1010	
100.5	1005	
100	1000	29.5
99.5	995	
99	990	
98.5	985	29
98	980	
97.5	975	
97	970	
96.5	965	28.5
96	960	
95.5	955	